POST-ELASTIC BEHAVIOUR OF REINFORCED CONCRETE FRAME-WALL COMPONENTS AND ASSEMBLAGES SUBJECTED TO SIMULATED SEISMIC LOADING

A thesis
submitted in partial fulfilment of the requirements
for the degree of
Doctor of Philosophy in Civil Engineering
at the University of Canterbury

by

David D. Spurr

University of Canterbury
Christchurch, New Zealand
1984

ABSTRACT

This thesis investigates aspects of the behaviour of reinforced concrete frame-wall components and assemblages under high intensity simulated seismic loading.

An experimental study was made of the post-elastic behaviour of four beam-column specimens and two 7 storey × 1 bay reinforced concrete frame-wall specimens. The observed responses of the specimens were used for both direct assessment of the response characteristics and for evaluating a computer program developed for analysing the response of ductile reinforced concrete structures under post-elastic cyclic loading. Two of the beam-wall specimens and the two frame-wall specimens were loaded through very large displacement cycles in the final stages of the tests to observe their failure modes.

Subsequent to the experimental work a static frame analysis computer program was developed to model the behaviour of reinforced concrete frame-wall components and assemblages under large displacement post-elastic load reversals. The program utilizes an inelastic "layered" section analysis procedure to evaluate member responses. This is capable of modelling accurately softening of the section responses due to Bauschinger effect in the steel. Models were also developed for evaluating inelastic anchorage deformations at the ends of members and inelastic sliding shear deformations in plastic hinge zones.

In developing the computer program emphasis was placed on minimizing computation time in order to ensure that it was suitable for analysing reasonable sized frames. Emphasis was also placed on developing a stable and efficient solution procedure.

ACKNOWLEDGEMENTS

The research described in this thesis was carried out in the Department of Civil Engineering of the University of Canterbury, between 1971 and 1979. Professor H.J. Hopkins was Head of Department until 1977, and Professor R. Park from 1978 onwards.

I wish to express my deepest gratitude to Professor T. Paulay under whose supervision this investigation was conducted; also to Mrs. Paulay for her forebearance for so many years.

I wish also to gratefully thank the following organisations and people:

The University Grants Committee for their financial support during the first three years.

The Civil Engineering Department of the University of Canterbury for their financial and logistical support for the work.

Certified Concrete Limited for donating concrete for the frame-wall specimens.

Dr. A.J. Carr for his assistance with parts of the theoretical work.

Messrs. J. Byers, R. Payne, G. Balantine, J. Sheard, J. Van Dyk and other technicians who assisted with construction and testing of the test specimens; Mr. H. Patterson for his photographic work.

The staff of the University of Canterbury Computer Centre.

The New Zealand Ministry of Works and Development, and particularly Mr. R.B. Shephard, Assistant Chief Structural Engineer, for their support and encouragement to complete this thesis.

Dr. D.L. Hutchison for reading, and his useful comments on the draft, and his family for making time available to him.

Messrs. R. Holbrook, M. Singh, Mrs. J. Anderson and the others who did much of the draughting.

Mrs. H. Pepere, Mrs. C. Brown, Ms. C. Hinton and Mrs. S. Carlyle, for typing the manuscript.

My parents for their support and encouragement throughout the study and particularly my mother who traced most of the diagrams for the theoretical chapters.

Finally, I would like to express my deepest gratitude to my wife, Sara, for her support, encouragement and forebearance while this thesis was being written, and especially to thank her for carrying most of the burden of bringing up our baby son for the past year.

TABLE OF CONTENTS

LIST OF SYMBOLS

Chapter 2

Scalar Notation:

a = shear span

A_k = area of kth layer of section (Figure 2.8)

AL = length of rigid end block, Node 1 end (Fig. 2.2)

AX = rigid end block offset, Node 1 end (Fig. 2.2)

BL = length of rigid end block, Node 2 end (Fig. 2.2)

BX = rigid end block offset, Node 2 end (Fig. 2.2)

C_e = $C_e(L,AL,BL,AX,BX,N_1,N_2)$ = term used to describe the element configuration

d = distance from compression face to centroid of tension reinforcement

d'' = distance along the tension reinforcement to last inclined crack originating from the end of a member, refer Fig. 2.6

e_v = allowance for the effect of inclined cracks on the stresses induced in the flexural reinforcement

EA = section axial rigidity

EI = flexural rigidity taken about the section reference axis, R_A

EI_c = flexural rigidity taken about the section centroid

FA = first moment of axial rigidity taken about R_A

GA = section shear rigidity

jd = distance between the centroid of compression and the centroid of the tension bars

ℓ_a = anchorage length (Fig. 2.5)

L = clear span of the deformable portion of a member

M = moment applied at the end of a member (Fig. 2.6)

N_1 = cosine θ (Fig. 2.7)

N_2 = sine θ (Fig. 2.7)

p = fraction of the reference force vector applied to a structure (Eq. 2.28)

$\overline{p}$ = prescribed maximum increase in p during a load increment

p_{LR} = prescribed maximum increase in p during a load reversal

q_v = section shear force

R_A = member (or section) reference axis

R_x = T_f/T_s

t_c = distance to R_A from the instantaneous elastic centroid of a section

t_k = distance to kth layer from R_A

T_f = force induced in tension bars due to flexure only

T_s = total force induced in tension bars

V = total shear force

V_s = component of shear force carried by the transverse reinforcement (Fig. 2.6)

x = distance along a member (Fig. 2.6)

α = minimum inclination of cracks to R_A (Fig. 2.6)

α = specific degree of freedom in a multi-degree of freedom system

$\overline{\alpha}$ = nodal degree of freedom specified for displacement control (Section 2.5.5.1)

δ = deflection at prescribed degree of freedom

$\overline{\delta}$ = prescribed maximum increase in δ during a load increment

δ_{LR} = prescribed maximum increase in δ during a load reversal

Δ = incremental quantity

$*\Delta$ = normalized energy residual, solution convergence tolerance (Section 2.5.7)

Δ_{ph} = integral of axial strains of a model plastic hinge (Section 2.2.3.3)

ϵ_k = strain imposed at kth layer of a section

η = location of a segment integration point (Fig. 2.3)

η = V_s/V (Section 2.2.4)

θ = inclination of member axis to global X axis

θ_{ph} = integral of curvature over a model plastic hinge (Section 2.2.3.3)

$*\pi$ = energy residual (Fig. 2.21)

π_T = total energy (Fig. 2.21)

σ_k = stress at kth layer of a section

ϕ_{ea} = fraction of anchorage length designated "elastic zone"

ϕ_{pa} = (inelastic anchorage deformation)/(integral of strains over the model plastic hinge zone)

Vector and Matrix Notation:

$\mathbf{A}$ = member flexibility matrix

$\mathbf{C}$ = compatibility transformation matrix

$\mathbf{C}_N$ = nonlinear component of $\mathbf{C}$

$\mathbf{E}$ = equilibrium transformation matrix

$\mathbf{f}$ = section flexibility matrix

$\mathbf{F}$ = initial stress component of an element stiffness matrix

$\mathbf{K}$ = structure stiffness matrix

$\mathbf{K}_e$ = element stiffness matrix

$\mathbf{q} = \mathbf{q}(q_1, q_2, q_3)$ = forces acting at section R_A (axial force, moment, shear force)

$\mathbf{r} = \mathbf{r}(r_1, r_2, r_3)$ = member forces (Fig. 2.3)

$\mathbf{R}$ = nodal forces acting on the structure

$\mathbf{R}_e$ = element nodal forces (Fig. 2.7)

$\mathbf{R}_o$ = fixed initial nodal forces acting on structure (Section 2.5.1)

$\mathbf{R}_{ref}$ = reference nodal force vector applied to structure in increments (Section 2.5.1)

$\mathbf{S}$ = member stiffness matrix

$\mathbf{T}$ = differential compatibility transformation matrix (Section 2.4.3)

$\mathbf{T}_L$ = first order (linear) compatibility transformation matrix (Section 2.2.5)

$\mathbf{v} = \mathbf{v}:(v_1, v_2, v_3)$ = member displacements (Fig. 2.3)

$\mathbf{v}_a = \mathbf{v}_a:(v_1, v_k)_a$, k = 2 or 3 = member displacements due to deformations within the anchorage regions at the ends of the deformable members (Section 2.2.3.3)

$\mathbf{V}$ = structure nodal displacements

$\mathbf{V}_e$ = element nodal displacements

$\mathbf{V}_{ref}$ = structure nodal displacements due to $\mathbf{R}_{ref}$

$\boldsymbol{\epsilon} = \boldsymbol{\epsilon}:(\varepsilon_1, \varepsilon_2, \varepsilon_3)$ = section strains measured at R_A (axial, flexural, shear)

Left superscripts:

i = increment numbers (0, 1, ...)

*g = components due to geometric nonlinearities (Table 2.2)

*m = components due to material nonlinearities (Table 2.2)

* = component due to out-of-balance actions arising from both geometric and material nonlinearities

Right superscripts:

(j) = iteration number

T = matrix transformation

Subscripts:

r = force resisted

s = secant value

t = tangential value

Chapter 3

A,B,C,D = model constants for strain hardening branch of the monotonic steel stress-strain curve (Eq. 3.1 to 3.3)

C = normalized strain term in the Ramberg-Osgood function (Eq. 3.4)

CL = strain limit (Section 3.6)

CU = strain limit (Section 3.6)

KN = curve number (Fig. 3.12)

E_o = elastic modulus of steel before a bar has been yielded (initial elastic modulus)

E_{xo} = current elastic modulus of steel at a plastic strain of ε_{xp}

E_y = assumed minimum fictitious yield modulus = $\phi_y . E_o$ (Section 3.8.1)

r = Ramberg-Osgood curve coefficient (Section 3.4)

R-O = Ramberg-Osgood (abbrev.)

X = normalized stress term in Ramberg-Osgood function (Eq. 3.4)

ε_s = steel strain

ε_{sy} = steel yield strain (Fig. 3.1)

ε_{sh} = steel strain at onset of strain hardening

ε_{su} = steel strain at ultimate

ε_{xo} = strain origin for R-O curve

ε_{cm} = plastic component of maximum compression strain

ε_{tm} = plastic component of maximum tension strain

ε_{xp} = plastic strain corresponding to current steel strain, ε_s

ν = Poisson's Ratio

σ_s = steel stress

σ_{sy} = steel yield stress

σ_{su} = ultimate stress

σ_{ch} = characteristic stress = $\phi_{ch} \cdot \sigma_{tc}$

σ_{xo} = stress origin for R-O curve

σ_{tc} = stress difference between the tension and compression envelope curves

ϕ_{ch} = characteristic stress ratio, experimental constant

ϕ_y = fictitious yield modulus ratio, see E_y

Chapter 4

A_s'' = area of confining steel bar

b'' = width of confined concrete

d'' = depth of confined concrete

E_c = initial tangential elastic modulus of the concrete

f_c' = compressive strength of the concrete

f_t' = tensile strength of the concrete

R_c = reduced loading modulus for concrete previously strained beyond ε_o

s = tie spacing

w = concrete density

z = slope of descending branch of concrete stress-strain relationship (Fig. 4.1)

ε_c = concrete strain

ε_m = maximum compressive strain imposed

ε_o = strain at maximum compressive stress (f_c')

ε_{cr} = strain at which unconfined concrete crushes

ε_{oo} = residual plastic compression strain in concrete (Fig. 4.1)

ε_{20} = strain boundary between the falling branch and constant stress regions of the envelope curve ($\sigma_c = 0.2\ f_c'$, Fig. 4.1)

ε_{50u} = strain defining z for unconfined concrete (Fig. 4.1)

ε_{50h} = strain defining z for confined concrete (Fig. 4.1)

ρ = parameter defining the shape of the initial loading curve $= \varepsilon_o f_c'/E_c$. Can vary from 1.5 for a cubic curve to 2.0 for a quadratic curve

ρ'' = confining steel ratio

σ_c = concrete stress

Chapter 5

A_{int} = interlock rigidity (along individual crack)
A_{vi} = shear area of the concrete section
b_n = net width of concrete at the level of the dowel reinforcement
c = crack width
EA_{conc} = concrete component of section axial rigidity
f'_c = concrete compressive strength
f'_t = concrete tensile strength
G_{int} = interlock component of shear modulus
J = variable defining state of cracking and shear strain (Eq. 5.9)
K_{int} = experimental constant relating G_{int} and ε_{ave} (units of stress)
q_{conc} = component of shear force resisted by the compression block
q_{int} = component of shear force resisted by interlock action
q_v = section shear force
Δ = incremental quantity
δ_v = shear displacement
ε_{ave} = average effective axial strain (Eq. 5.6)
ε_c = section strain at concrete layer
ε_e = effective axial strain (Section 5.4.3)
ε_v = shear strain
ε_{xv} = coupling strain (Eq. 5.9)
ε_{oo} = residual plastic compression strain in concrete
μ = coefficient of shear friction
ϕ_g = experimental constant relating concrete component of shear rigidity to EA_{conc}
ϕ_{xv} = experimental constant defining the effective slope of cracks
ϕ_{unl} = experimental constant relating the section loading and unloading shear rigidities

Chapter 6

e_v = allowance for effect of inclined cracks on the stresses induced in the flexural reinforcement (Section 2.2.4)
E_o = steel elastic modulus before plastic straining
f'_c = concrete compressive strength
K_{int} = experimental constant for interlock component of shear model (Chapter 5)

$*\Delta$ = normalized energy residual, tolerance for convergence (Section 2.5.7)

ε_{cr} = strain at which unconfined concrete crushes

ε_s = steel strain

ϕ_{pa} = ratio of inelastic anchorage rotation to rotation of model plastic hinge (Section 2.2.3.3)

ϕ_y = fictitious yield modulus ratio (see Section 3.8.1)

ϕ_g = experimental constant for concrete shear modulus (Chapter 5)

ϕ_{unl} = experimental constant for shear unloading (Chapter 5)

ϕ_{xv} = experimental constant defining effective slope of cracks (shear model, Chapter 5)

Chapter 7

a = shear span

A_v = area of transverse reinforcement

d = distance from compression face to centroid of tension reinforcement

d_w = value of d for wall

e_v = allowance for effect of inclined cracks on the stresses induced in the flexural reinforcement (Section 2.2.4)

E_c = initial tangential modulus of concrete

E_o = elastic modulus of steel before plastic straining

f'_c = concrete compressive strength (152 dia. × 305 cylinders)

f_r = concrete modulus of rupture

f'_t = concrete tensile strength

f_{su} = ultimate strength of steel

f_y = yield strength of steel

jd = distance between centroid of compression and centroid of tension

K_{int} = experimental constant for interlock component of shear (Chapter 5)

LR = load reversal

ℓ = distance between reference axes of the wall and column

ℓ_a = modelled anchorage length (Section 2.2.3)

M_B = total moment acting at base of frame-wall specimen

M_C = column base moment

M_W = wall base moment

P = net axial load

P_g = axial load due to gravity loads

P_x = axial load due to lateral loads

s = stirrup spacing

V_B = total shear force acting at base of frame-wall specimen

δ_{7y} = assumed yield deflection at level 7

ε_c = concrete strain

ε_{cr} = strain at which unconfined concrete crushes

ε_{sh} = strain at onset of steel strain hardening

ρ = concrete density

ρ_s = tension steel content (ratio)

ρ'_s = compression steel content (ratio)

ϕ = strength reduction factor

ϕ_{pa} = ratio of inelastic anchorage rotation to rotation of model plastic hinge (Section 2.2.3.3)

ϕ_g = experimental constant for concrete shear modulus (Chapter 5)

ϕ_{xv} = experimental constant defining the effective slope of cracks (shear model, Chapter 5)

Chapter 8

a = shear span

d = effective depth (distance from the compression face to centroid of the tension steel)

DF = Ductility Factor (Fig. 8.2)

e_v = coefficient determining the effect of inclined cracks on the flexural bar stresses

f'_c = concrete compressive strength

ℓ_a = model anchorage length of flexural reinforcement

LR = load reversal number

P = load acting at end of cantilever

P_{dep} = dependable strength (19)

P'_i = ideal strength, based on measured steel and concrete properties

P_y = yield strength

Δ = deflection at end of cantilever

Δ_y = yield deflection

θ = beam rotation (Δ/a for cantilever)

μs = microstrain

ϕ = strength reduction factor (19)

ϕ_{pa} = anchorage model coefficient defining extent of inelastic deformation in the anchorage region (Section 2.2.3.3)

Chapter 9

b_w = width or thickness of wall

d_b = bar diameter

d_w = distance from compression face of wall to tension centroid

DF_b = beam displacement ductility factor

e_v = coefficient determining the effect of inclined cracks on the flexural bar stresses

E_c = initial tangential elastic modulus of concrete

f'_c = concrete compressive strength (152 dia. × 305 mm cylinders)

f'_t = concrete tensile strength

I_g = gross moment of inertia of concrete section

ℓ_w = horizontal length of wall

LR = load reversal

M_b = total moment acting at base of specimen

M_{by} = value of M_b at onset of yield in the walls

M_w = moment acting at base of wall

v_u = maximum nominal shear stress

V_w = shear acting at base of wall

δ_7 = deflection at level 7

δ_v = beam shear displacement

δ_{v1} = shear displacement between level 0 and 1

δ_{w1} = wall deflection at level 1

δ_{w7} = wall deflection at level 7

Δ = incremental quantity

ϵ_{sy} = steel yield strain

ϕ_o = flexural overstrength factor

1. INTRODUCTION

1.1 BACKGROUND

Most reinforced concrete buildings designed to current seismic design standards can be expected to be subjected to several cycles of large plastic deformations during a severe earthquake. This design philosophy recognises that reinforced concrete can be detailed for adequate ductility to sustain such deformations without failure, and that generally it is neither economical nor practical to design a structure to remain elastic under seismic loading of an intensity which occurs only very infrequently.

Extensive experimental and theoretical research over the last 30 years has considerably improved understanding of the types of detailing necessary to achieve adequate ductility. However, there are still many areas where uncertainty exists and even the best design codes contain clauses which are little more than intuitive guesses.

At the same time, developments in analytical procedures have not kept pace with the rapid increases in computer capabilities. Although models capable of accurately simulating various component responses have been developed for some time, no general structural analysis program has become available which can simulate the response of whole frames or buildings to a similar level of accuracy. Analyses for design and even research are still carried out using comparatively crude analytical models.

Although some of the more sophisticated computer models presently available have been shown to be capable of simulating overall displacements of frame structures with reasonable accuracy, they can not accurately predict the internal force distributions, especially where different types of elements are involved, e.g., a mixture of wall and frame elements. In addition, none of the general frame analysis programs available accurately model inelastic sliding shear deformations. These deformations can significantly affect the response of structures which have members with small shear span to

depth ratios.

Ideally, development of a computer model simulating the elasto-plastic response of a generalised structure should interact with a programme of parallel experimental work. Through interplay of the two phases of work, a better understanding of the actual mechanisms controlling the structure's elasto-plastic response should be possible.

1.2 REVIEW OF PREVIOUS WORK

This review is limited to experimental and analytical investigations related to the post-elastic behaviour of reinforced concrete frame and frame-wall structures subjected to high intensity seismic loading.

1.2.1 Experimental Studies

Large numbers of post-elastic cyclic load tests have been carried out on components of reinforced concrete frame buildings such as isolated beams and beam-column sub-assemblages. Examples of these include tests carried out at the University of Canterbury (1, 2, 3, 4, 5, 6, 7), at the University of California, Berkeley (8, 9, 10, 11, 12, 13), and at other institutions (14, 15, 16, 17, 18). Many important results from these tests are now embodied in design codes (19, 20, 21) which have greatly improved the quality of detailing in ductile regions of reinforced concrete beams and columns; for example by limiting tension steel content relative to the compression steel content, providing adequate lateral ties to confine core concrete and compression bars, providing sufficient shear steel to resist the full design shear force in beam plastic hinge zones, and by ensuring the adequacy of anchorage and beam-column joint details. Other tests have also shown the advantages of using various inclined bar arrangements for improving shear performance (22, 23, 24), and of moving beam plastic hinges away from column faces to protect the beam-column joints (24, 25, 26, 27).

A number of seismic load tests have also been carried out on structural walls (28, 29, 30, 31), but the variety in geometry and load conditions that can occur means that many aspects, such as wall

buckling, have not been adequately investigated.

Another area which has not been fully investigated is the effect of floor slabs cast integrally with the beams. In addition, there have been few experimental studies testing medium scale frame or frame-wall assemblages. Several monotonic load tests have been carried out, e.g. (32). However, very few studies have involved pseudo-static cyclic load tests on full assemblages.

More recently, there has been a trend to performing dynamic load tests. Several medium to large scale, typically 1 bay x 1 bay reinforced concrete frame structures, have been tested on large shaking tables in the United States of America (33, 34, 35, 36) and Japan (37, 38). The results from these tests have generally been used for evaluating various analytical component models used in dynamic analysis computer programs.

1.2.2 Analytical Studies

Most inelastic seismic analyses of frame or frame-wall buildings are performed with computer programs which use frame (line) elements for modelling beams, columns and often walls, and in some cases, two-dimensional finite elements for modelling walls, e.g. DRAIN-2D (39). The first programs used to predict post-elastic responses using line elements, were generally simple elasto-plastic formulations in which plastic hinging was simulated by inserting real hinges at locations where yielding occurred. The structures were then re-analysed and any forces due to post-yield loading added to the forces existing at the time yield occurred, e.g. (32). Formulations were later developed in which the basic frame element was modified by the addition of spring sub-elements at each end, to model plastic hinge and joint deformations (40). Although more sophisticated line elements have been developed, the basic two-spring model has remained in dominant use.

With time, spring models used have been improved from the original simple bi-linear models to the well-known Clough degrading stiffness model (41) and subsequently to the more sophisticated variations (42,43).

Analytic spring models which allow for local buckling of reinforcing bars, pinching of hysteresis loop due to inelastic shear deformations, and partial failure or loss of strength of a member, have also been developed (44, 45, 46).

The last two decades have also witnessed the almost separate development of models for reinforced concrete section analysis based on postulated material constitutive relationships for concrete and steel (12, 47, 48, 49). Most of these models assume a linear distribution of strain over the section depth which is subdivided into a number of concrete and steel elements, i.e., "layered" models. The overall response is then computed from the imposed strain history and the constitutive laws for each material. For many practical cases, this type of analysis has been shown to be capable of very accurately predicting the moment-curvature responses of reinforced concrete sections, even when they are subjected to a number of quite large post-elastic load reversals.

However, despite the number and inherent accuracy of the models produced, only a very small number of them have been developed past the section analysis stage. Kent (48) incorporated his model into a beam analysis program. Later, Menegotto and Pinto (50) incorporated a section model into a general frame analysis program, although the largest analysis reported was of a four-member (twelve-element) frame. The only other post-elastic section models known by the author to have been incorporated into line element frame programs are a simple monotonic load model by Blaauwendraad (51) and a cyclic analysis model developed by Taylor (52). The latter model was based on simple bi-linear steel and concrete responses and was used in a wall element that Taylor incorporated in a dynamic analysis program developed by Sharpe (53).

The fact that the layered section models have not found wider use is basically attributable to two reasons. The first is simply that the cost of most of the models in terms of computer time and/or storage is so large as to make them impracticable for any reasonably-sized frame analysis. The second reason is that, until recently, the

models were capable of computing only flexural responses. Even if feasible, the cost of computer time required for accurately computing the flexural response would rarely be justified if errors in calculating other components such as anchorage and particularly shear deformations were likely to invalidate the accuracy of the results.

1.3 AIMS AND SCOPE OF PRESENT WORK

The aims of this study were to investigate the behaviour of reinforced concrete frame-wall assemblages subjected to high intensity earthquake loading and to develop a general frame analysis computer program capable of modelling more accurately the post-elastic seismic response.

The first part of the study was experimental and involved testing four small beam-wall specimens (TB1-TB4) and two quarter-scale 7 storey x 1 bay frame-wall specimens (FSW-1 and FSW-2) under pseudo-static simulated seismic loading. The four small specimens were models of the beam-wall junctions in the frame-wall specimens and were to the same scale as the larger specimens. These small specimens were tested to provide detailed information about the response of the scale beams, which could not have been obtained from the indeterminate frame-wall specimens. Areas of particular interest in these tests were the flexural, shear, and anchorage responses and the susceptibility of the plastic hinge zones to buckling at high ductilities. In the frame-wall tests, the main areas of interest were the effects of interaction between the individual elements and the behaviour of both the wall plastic hinge zone and the columns under varying axial loads.

The second part of the study consisted of developing a computer program to simulate the response of reinforced concrete frame and frame-wall structures.

Data from both series of tests were used to evaluate this frame analysis program, which in turn was used to help interpret the experimental responses.

The frame analysis program is based on a standard frame (line) element idealisation which was extended to incorporate a reinforced concrete section model for determining the inelastic response of the members. The section model used is similar to those developed by Kent (48), Thompson (44) and others for moment-curvature section analyses,* but with the additional capability of modelling sliding shear and anchorage deformations. Emphasis was placed on development of models for steel, anchorage and sliding shear response, and on developing suitable solution procedures. In addition, the large amount of detailed calculation that would be required for computer analysis of a reasonably-sized structure, made both model and coding efficiency matters of prime concern.

The theoretical part of this study represents only one step in the process of developing a comprehensive computer model for analysing reinforced concrete buildings subjected to high intensity seismic loading. As currently coded, the program is capable of analysing only plane frame(-wall) structures. It is largely orientated towards predicting responses and has only a very limited capability for assessing ultimate failure criteria. The inelastic shear model is not designed for analysing elements with shear span to depth ratio of less than about 2. Another important limitation is that no allowance has been made for the effect of torsion or warping distortions in integral slab-beam members.

One important consideration in developing the models used in the program was that they be efficient enough to be used in dynamic analyses of reasonable sized structures. However, a dynamic analysis capability has not been incorporated at this stage as the scope of the project was limited to developing the models and evaluating them against measured responses obtained from pseudo-static load tests on reinforced concrete specimens.

---

* In these models, responses are evaluated at steel and concrete sub-element level using accurate constitutive response algorithms.

1.4 FORMAT

As noted in the preceding section, the experimental work for this study was carried out before developing the frame-analysis computer program. This order has, however, been reversed in the presentation which follows. The first five chapters (2-6) describe and evaluate the theoretical model, and the last three chapters (7-9) describe the experimental tests and present and evaluate the results.

The reason for this reversal is primarily to allow the computer model to be used for evaluating the experimental responses, without unnecessary duplication of description.

2. FRAME ANALYSIS COMPUTER PROGRAM

SUMMARY

This chapter outlines the general formulation used in the computer program written for analysing reinforced concrete structures subjected to high intensity cyclic load reversals. The program is restricted to static analyses of two-dimensional structural assemblages, but the basic principles are applicable to three-dimensional and dynamic analysis problems. Although primarily developed for inelastic analyses of frame or frame-wall structures, the program is also suitable for analysing any other type of structure that can be idealised as a planar frame or truss element assemblage, including those where geometric nonlinearities are significant.

2.1 INTRODUCTION

The use of analytical models based on realistic material constitutive idealizations for evaluating the post-elastic behaviour of reinforced concrete beam and column sections is now well established. A number of the section analysis models developed have shown reasonably good correlation with observed moment-curvature responses, e.g. (12, 17, 47, 48). However, only a few attempts (50) have been made to incorporate this type of section analysis into a general frame analysis procedure. Part of the reason for this has been the large computation time and strain history storage requirements for some of the more refined section models. Also the member flexural response only contributes one component of the overall response of the structure and without allowance for other significant components there would be little justification in carrying out a refined flexural analysis.

The computer program described in this section was developed with the intention of extending the degree of refinement available for moment curvature analyses, to general analyses of frame assemblages. Emphasis was placed on development of models for the steel, anchorage and sliding shear responses, and on adapting the Newton-Raphson solution procedure to make it suitable for analysing the complex structural behaviour encountered in this type of application.

2.2 STRUCTURAL IDEALIZATION

Line element idealizations of both frame and frame-wall structures have long been used in elastic linear and geometrically nonlinear formulations, and have also often been retained as a primary idealization of frame members for materially nonlinear analyses (50, 51). This approach is also adopted in the present study.

In this section, only aspects related to the longitudinal idealization of the individual elements are considered. Details of the transverse section idealizations are considered in Section 2.3.

2.2.1 General Plane Frame Element

The basic frame element idealization used is shown in Figures 2.1 and 2.2. As indicated, general two-dimensional rigid end blocks are provided for, permitting the local member axes to be defined independently of the end node locations. Seven configuration terms, jointly characterised as the element configuration

$$C_e = (L, AL, BL, AX, BX, N_1 = \cos\theta, N_2 = \sin\theta),$$

are used to describe this element (See Figure 2.2).

Physically, each element consists of the following basic components:

(a) Two 2-dimensional rigid end blocks, one at either end.

(b) The clear span deformable region of the member.

(c) Two deformable anchorage regions, one at either end of the clear span.

The latter two components jointly constitute the deformable part of the element, which is generally referred to simply as the 'member'.

2.2.2 Member Segmentation

Under post-elastic loading conditions, there can be substantial variations in rigidity along the length of a member. In order to permit realistic representation, individual members are therefore subdivided into a suitable number of prismatic segments. Each segment has an associated transverse section specified at some point along its length (Figure 2.3). The response of the segment at this integration point is determined using

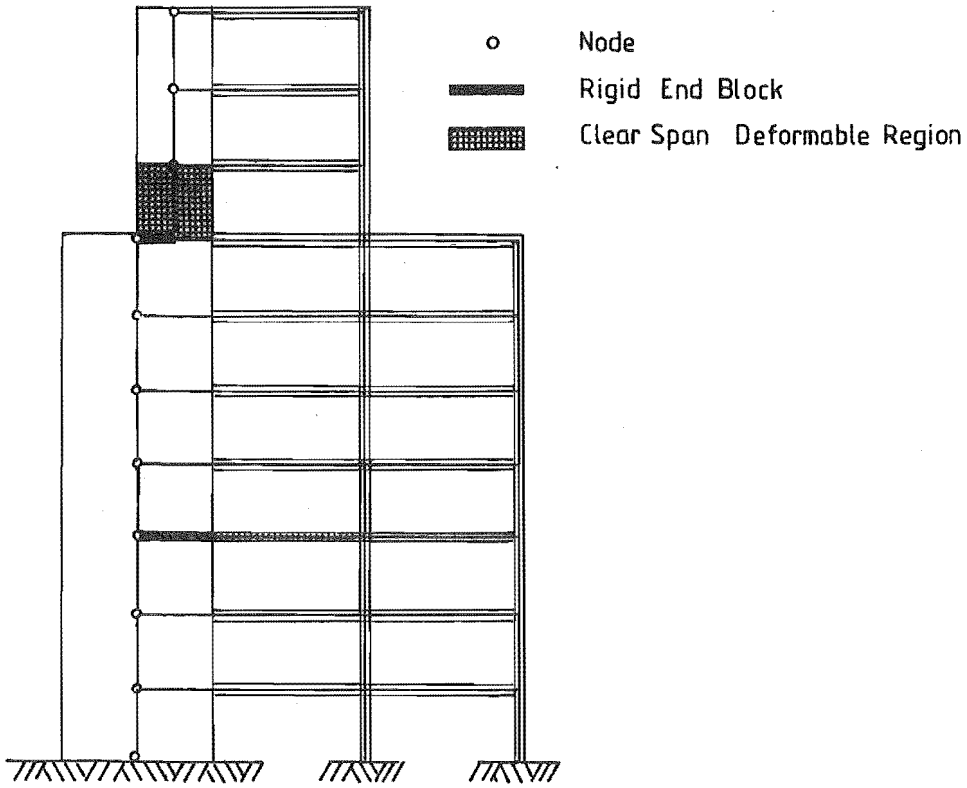

FIGURE 2.1 : LINE ELEMENT IDEALIZATION TO STRUCTURAL FRAME-WALL ASSEMBLAGE

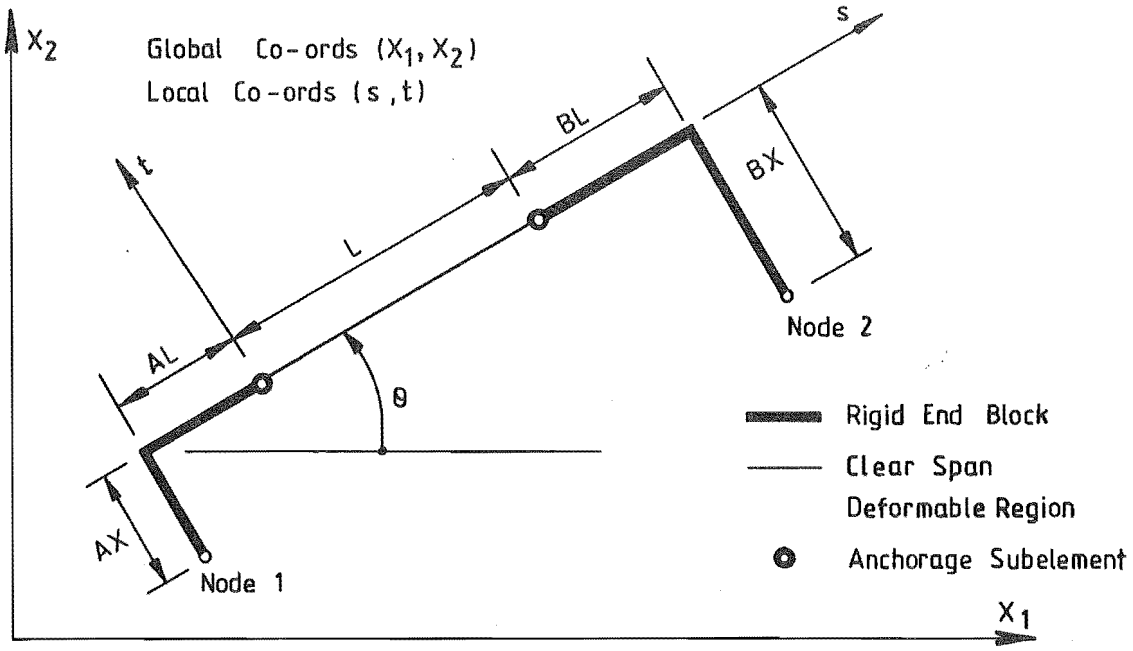

FIGURE 2.2 : GENERAL PLANE FRAME ELEMENT

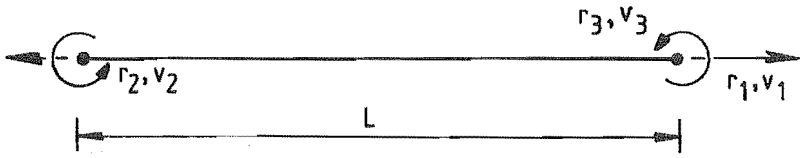

(a) Member Force and Displacement Degrees of Freedom

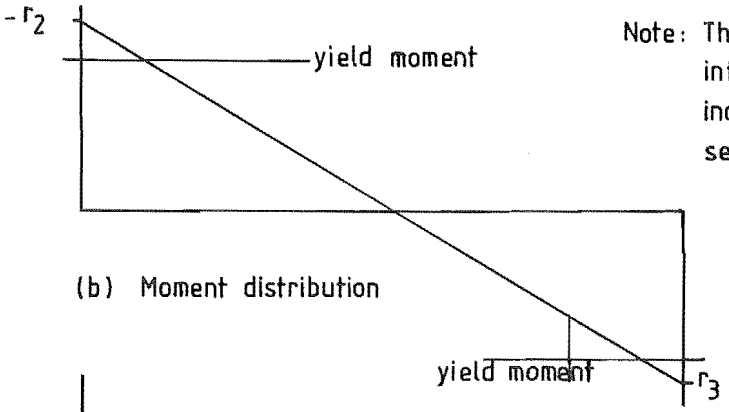

(b) Moment distribution

Note: The transverse section integration points are specified independently of the member segmentation.

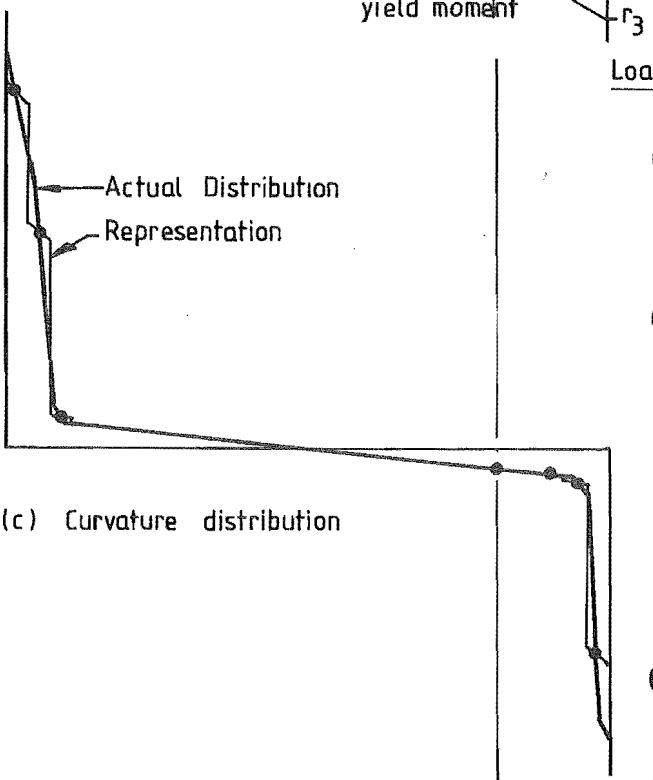

(c) Curvature distribution

Loading at transverse section

$$q_n = \begin{bmatrix} 1 & \cdot & \cdot \\ \cdot & \eta_n - 1 & \eta_n \\ \cdot & 1/L & 1/L \end{bmatrix} \cdot r$$

$$q_n = \left\{ \begin{matrix} q_1 \\ q_2 \\ q_3 \end{matrix} \right\}_n = \text{Imposed section forces at n}$$

$$r = \left\{ \begin{matrix} r_1 \\ r_2 \\ r_3 \end{matrix} \right\} = \text{Member forces}$$

Section strain

$$\epsilon_n = f_n \cdot q_n$$

$$\epsilon_n = \left\{ \begin{matrix} \epsilon_1 \\ \epsilon_2 \\ \epsilon_3 \end{matrix} \right\}_n = \text{Section strain at n}$$

f_n = Section flexibility matrix (Section 2.3.2)

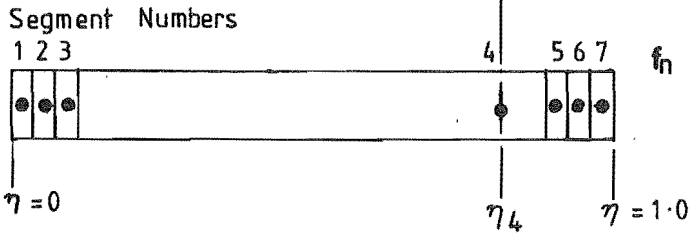

(d) Member Segmentation

FIGURE 2.3 : SEGMENTATION FOR A DOUBLE YIELDING BEAM MEMBER

one or other of the section analysis models described in Section 2.3, depending on the type of section specified (refer Table 2.2, steps 31 to 37).

This type of member idealization is simple and flexible with the segments and integration points able to be located and concentrated to suit each particular situation considered. Furthermore, a coarse member idealization can be satisfactorily used in most situations, e.g. a double yielding beam can be acceptably represented by as few as 3 segments (Figure 2.4). Because of the flexibility of the procedure, most straight frame members can be represented analytically as a single element. This means that the required number of external degrees of freedom, and hence the cost of solving the external force-displacement relationships, is kept to a minimum.

Two other types of member idealization involving analytic integration, the first assuming a linear variation of strain and the second, a linear variation of rigidity between the transverse section integration points, were investigated. However, it was considered that these would not significantly improve the member representation, and that the additional complexity would not be warranted. Furthermore, for equivalent levels of representation, the prismatic segment idealization used generally requires one less section integration point than other methods. Numerical quadrature methods, which are commonly used in general finite element applications, were not considered to be appropriate for the present type of application. These methods are relatively inflexible insofar as the location of integration points is concerned and a larger number of integration points would almost certainly be necessary to provide an equivalent level of representation. This is particularly true in cases where large plastic deformations may be confined to a small portion of the member length, or where a coarse idealization is necessary. Menegotto and Pinto (50) used a numerical procedure to integrate the post-elastic responses of reinforced concrete members. However, a significantly higher density of section integration points appears to have been required than was found to be necessary for the prismatic segment representation. In the example given in reference (50), 132 section integration points were used to model a 4 member frame.

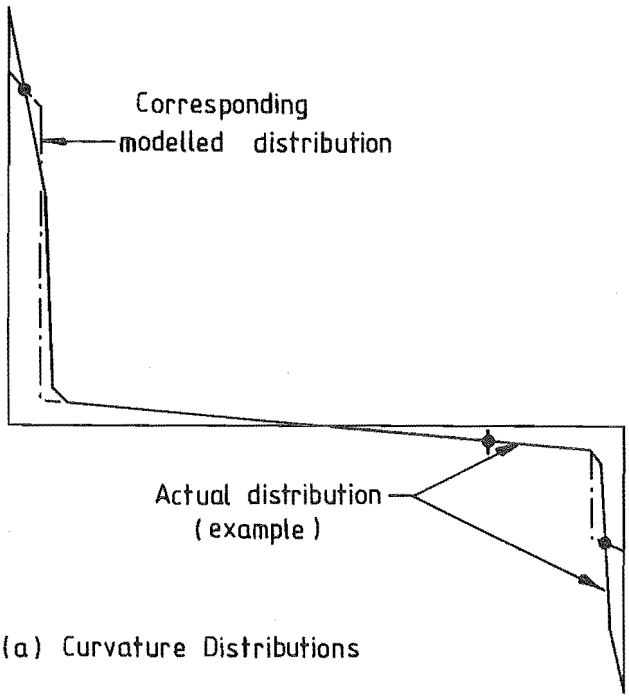

(a) Curvature Distributions

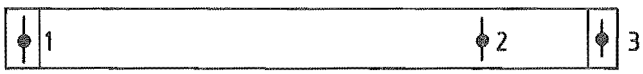

(b) Prismatic Segment Idealization

NOTE:

The modelled curvature is approximately equal to the actual curvature at each integration point (-⊕-). Because the section rigidities are assumed to be constant over the length of each segment (prismatic segment idealization), the slope of the modelled curvature distribution within a segment is proportional to the moment gradient.

FIGURE 2.4 : COARSE IDEALIZATION OF A DOUBLE YIELDING BEAM MEMBER

By using a prismatic segmentation, the same frame could be modelled with as few as 12 integration points.

2.2.3 Anchorage Subelement

Beam-column and beam-wall joints and anchorage deformations can have a substantial influence on the overall response and flexibility of a reinforced concrete structure. Consequently, regardless of the degree of sophistication of an analytic model, the response of a structure cannot, in general, be accurately predicted from consideration only of the deformations within the clear spans of the members.

Although many experimental measurements of joint-anchorage zone deformations in beam-column subassemblages have been made (17, 54), there is still not sufficient information to be able to accurately predict these deformations under generalized loading or structural conditions. Development of a suitably general anchorage model would require a major experimental investigation. The model used in this study is therefore only approximate and is valid only for the range of anchorage behaviour considered.

2.2.3.1 Components of Joint-Anchorage Deformation

In general, the total deformation within a joint-anchorage region comprises three main components:

(a) Joint shear deformation.

(b) Overall slip of the anchored reinforcement relative to the concrete, i.e. the amount of slip at points where the bars are unstressed.

(c) Cumulative elongation (or shortening) of the member flexural reinforcement in the anchorage zone, including that due to yield penetration.

Test measurements of the contributions of the joint shear deformation and the overall slip of the anchorage reinforcement have shown that these components vary considerably depending on the specific details of the specimen. In a number of early beam-column subassemblage tests, a

major portion of the subassemblage flexibility was due to these deformation components.

The variability of this behaviour, together with the deterioration of the resistance mechanisms, make it difficult to model these components with any reliability. Moreover, these types of deformations are generally undesirable and, in most instances, can be largely suppressed by suitable detailing.

Because of the above factors, the analytic model described in this section makes allowance only for deformations resulting from elongation or shortening of the member reinforcement in the anchorage zone. The proportion of total member deformation contributed by this mechanism varies less, and even in a well-detailed joint, is generally significant over the full load range, regardless of the state of structural deterioration. It is emphasised, therefore, that the analytic model developed is applicable only to situations where the joint shear deformation and overall bar slip do not become significant. The experimental responses used for checking and calibrating the model were specifically selected to ensure that these conditions were satisfied.

2.2.3.2 Modelling of Anchorage Deformations in Non-Yielding Applications

One approximate and commonly used method of allowing for anchorage deformability in elastic and elasto-plastic frame analyses is to use artificially long member clear span lengths (55). This method was used in the present study for modelling anchorage deformations of columns and other members in which the forces were expected to remain below yield level, and which were represented by non-yielding member idealizations. However, this method is not, in general, suitable for modelling anchorage deformations of members subjected to significant inelastic flexural deformations.

2.2.3.3 Analytic Model for Inelastic Anchorage Deformation

This anchorage model is based on the observed behaviour of the anchorage regions of the small scale beam-wall and frame-wall specimens tested as a part of this study. These tests are described in detail in Chapters

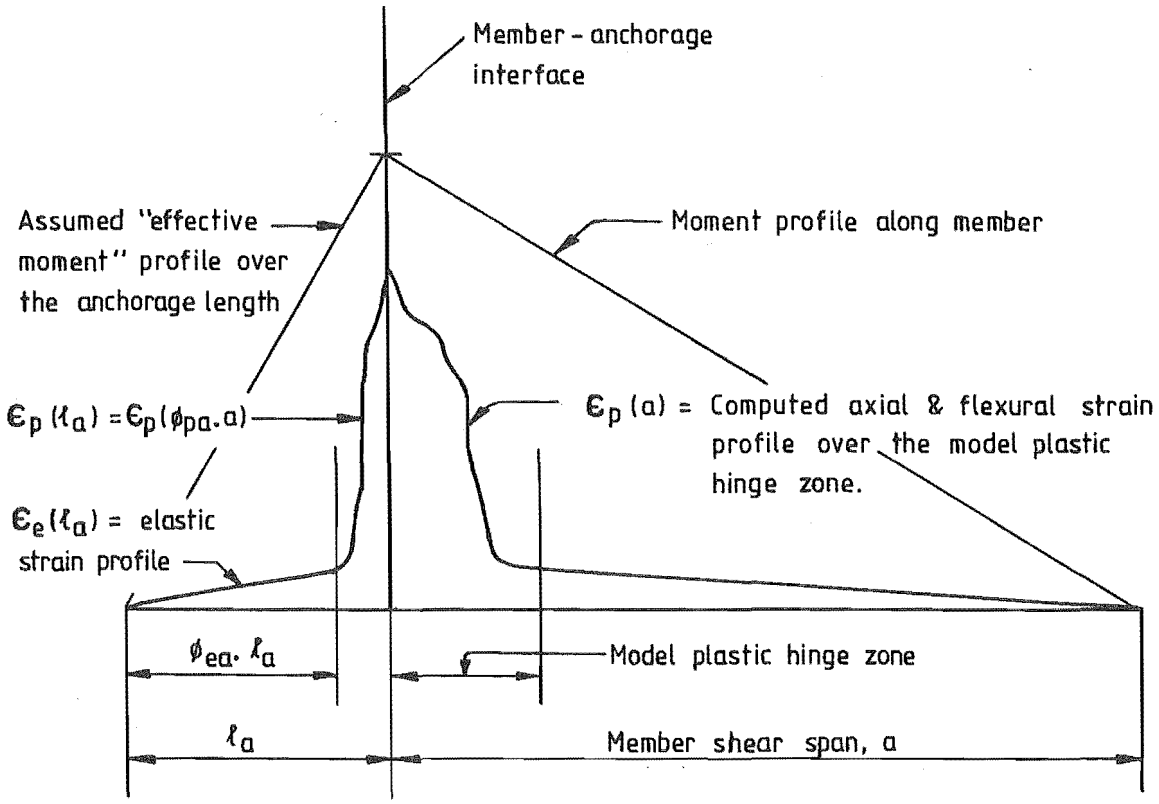

(a) Strain distribution

Note: k = 2 at ? = 0
= 3 at ? = 1·0
(Refer to Fig. 2·3)

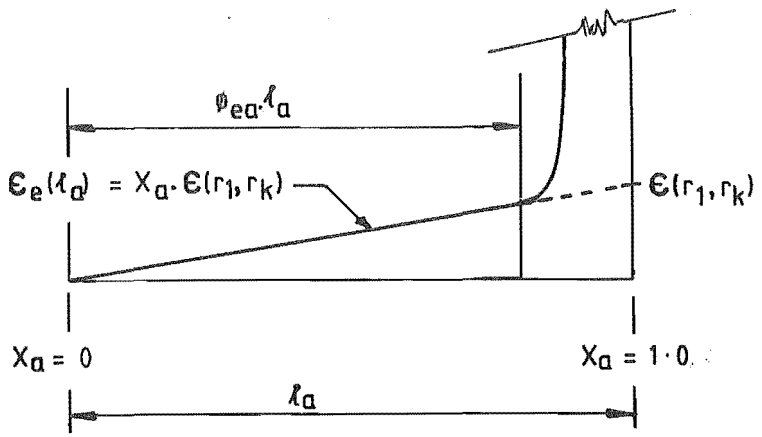

(b) Elastic strain profile detail

$\epsilon(r_1, r_k) = (\epsilon_{1,e}, \epsilon_{2,e})$ are the elastic axial and flexural strains at the member anchorage interface and (r_1, r_k) are the forces acting on the member section at the interface.

FIGURE 2.5 : INELASTIC ANCHORAGE MODEL

7, 8 and 9. One of the main features of the behaviour of the anchorage regions of these specimens was that the relative contribution of the anchorage deformations to the flexural component of the beam and wall end deflections was approximately independent of both the load intensity and the number of preceding load cycles, i.e. there was no deterioration of the anchorage responses relative to the flexural response of the member clear span regions. A similar behaviour was also evident in the wall specimens tested by Wang, Bertero and Popov (31). It must be emphasised, however, that all beam and wall reinforcing bars in these specimens were well anchored, and that this type of behaviour would not be expected in situations where there was significant overall slip of the anchored bars.

In order to simulate this behaviour, the modelled anchorage deformations are assumed to occur over a fixed anchorage length. As shown in Figure 2.5, this length is subdivided into "elastic" and "inelastic" (yield penetration) zones. It is also assumed that there are only axial and flexural deformations within the anchorage region. The elastic components of the anchorage deformation are computed based on the linear strain distribution shown in Figure 2.5b.

The elastic strains ($\varepsilon_{1.e}$, $\varepsilon_{2.e}$) are computed based on the response of the member section at the interface, assuming that the reinforcement and concrete are infinitely elastic*. The inelastic components of anchorage deformation are not computed independently but are, instead, taken as being equal to a specified fraction, ϕ_{pa}, of the integral of the strains over a specified region of the member, normally taken as the maximum extent of the plastic hinge zone, and referred to as the 'model plastic hinge zone'.

The total deformation at the anchorage-member interface is given by

---

* concrete fracture excepted.

$$\mathbf{v}_a = \begin{Bmatrix} v_{1.a} \\ v_{k.a} \end{Bmatrix} = \tfrac{1}{2}\,\phi_{ea}^2 \cdot \ell_a \cdot \begin{Bmatrix} \varepsilon_{1.e} \\ \varepsilon_{2.e} \end{Bmatrix} + \phi_{pa} \cdot \begin{Bmatrix} \Delta_{ph} \\ \theta_{ph} \end{Bmatrix}, \quad k = 2 \text{ or } 3 \qquad \ldots (2.1)$$

where $v_{1.a}$ = axial elongation of the anchorage zone,

$v_{k.a}$ = rotation of the anchorage-member interface,

Δ_{ph} = integral of axial strains over the model plastic hinge,

θ_{ph} = integral of curvature over the model plastic hinge,

ϕ_{ea} = fraction of anchorage length designated "elastic zone",

ϕ_{pa} = (inelastic anchorage deformation)/(integral of strains over the model plastic hinge zone),

ℓ_a = anchorage length.

Typically, values of $\phi_{ea} = 0.6 - 0.8$ and $\phi_{pa} = 0.1 - 0.35$ were used in the analyses performed in this study. However, as with the anchorage length, the actual values used in any particular analysis could only be approximately assessed on the basis of the little experimental data that was available, and allowing for such factors as the reinforcement arrangement in the anchorage zone. Also, although both axial expansion and rotation of the anchorage zone are modelled, the values for the model constants were determined largely from a consideration of the rotational deformations.

The validity of the approach used for computing the inelastic components of anchorage deformation depends, in part, on the forces throughout the model plastic hinge zone being representative of the "effective moments" within the anchorage zone (Figure 2.5). The forces imposed on individual members of a frame or frame-wall structure subjected to seismic loading normally satisfy this condition, although some difficulties may arise in situations where a significant portion of the total member forces results from gravity forces distributed along the member axis. Evaluating the inelastic components of anchorage deformation directly from the forces at the member-anchorage interface would not significantly improve the accuracy of the analysis as sufficiently accurate general bond stress-slip relationships were not available.

2.2.4 Shear Induced Stresses in Flexural Reinforcement

The frame element used in the computer program is not capable of directly modelling shear induced stresses in the flexural reinforcement, such as those caused by inclined cracking. These stresses can be significant in short members and, in many of the analyses performed in this study, an approximate allowance was made in an attempt to simulate the phenomenon.

The approach used made allowance only for the effect of inclined cracking. This was done by reducing the modelled area of the main bars by an amount such that the stress induced by moment alone was equal to the stress induced in the full area of the bars by flexure and shear. The allowance for tension induced as a result of inclined cracking was determined from the assumed crack pattern shown in Figure 2.6. In accordance with the notation in this diagram, the total forces induced in the tension reinforcement in regions 0 to d" and d" to a are respectively

$$(T_s)_{0\text{-}d''} = (M - 0.5V_s\, x^2/d'')/jd$$

$$= V(a - 0.5\eta x^2/d'')/jd \qquad \ldots (2.2a)$$

$$(T_s)_{d''\text{-}a} = V(a - x + e_v)/jd \qquad \ldots (2.2b)$$

where T_s is the bar tension force at a distance x from the fixed end, V is the total applied shear force, V_s is shear force carried by the stirrups, $\eta = V_s/V$ and $e_v = (\cot \alpha - 0.5\eta \cot \alpha)jd$ for shear reinforcement perpendicular to the member axis (95). For the analyses made in this study, α was assumed to be 45^o (giving d" = jd) and η taken as 1.0 over the full length of the shear span. Using these values therefore gave bar reduction factors ($R_x = T_f/T_s$) for regions 0 to d" and d" to a respectively as

$$(R_x)_{0\text{-}d''} = (a - x)/(a - x^2/2d'') \qquad \ldots (2.3a)$$

$$(R_x)_{d''\text{-}a} = (a - x)/(a - x + e_v) \qquad \ldots (2.3b)$$

with $e_v = 0.5jd$.

Because of the approximations involved (e.g. $\eta = 1.0$), analyses were generally performed both with ($e_v = 0.5jd$) and without ($e_v = 0$) allowance for the effect of inclined cracks, in an attempt to assess the validity of the approach used.

The inability to model tensile stresses at the point of contraflexure (Figure 2.6c) means that, even with allowance for inclined cracking, this type of element is likely to be satisfactory only for members with shear span to depth ratios greater than 2 to 3.

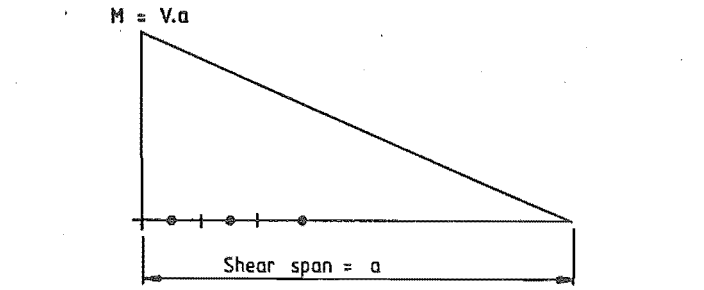

(a) Moment diagram, with member segmentation indicated

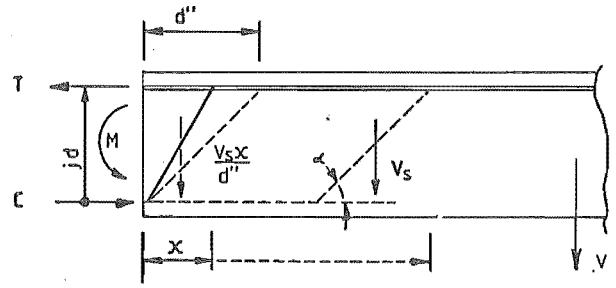

(b) Assumed crack pattern

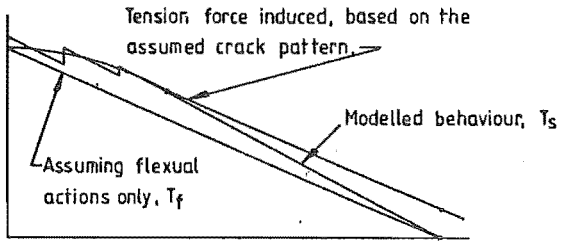

(c) Tension force induced in the main bars

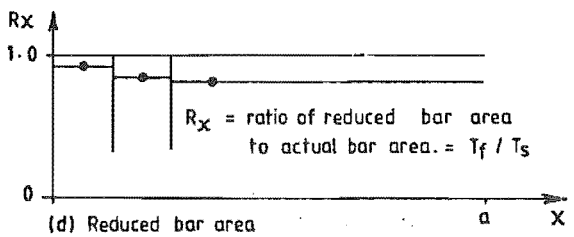

(d) Reduced bar area

FIGURE 2.6 : EFFECT OF INCLINED CRACKS

2.2.5 Element Nodal Force-Displacement Relationships for Small Displacements

As is common in frame analysis formulations, the element stiffness matrix is computed in two stages: first, establishing the member force-displacement relationships in terms of a local Eulerian reference system, and secondly, transforming these to form the element nodal force-displacement relationships.

The member and element nodal degrees of freedom employed are shown in Figure 2.7, and are defined such that for the element AB, subjected to the nodal displacements $\mathbf{V}_e$: $(V_1, V_2, V_3, V_4, V_5, V_6)$, the consequent member displacements, member forces, and nodal forces, are given by $\mathbf{v}$: (v_1, v_2, v_3), $\mathbf{r}$: (r_1, r_2, r_3), and $\mathbf{R}_e$: $(R_1, R_2, R_3, R_4, R_5, R_6)$ respectively. Consistent with these definitions and with the usual stiffness matrix notation, the member force displacement relationships are given by

$$\mathbf{r} = \mathbf{S}.\mathbf{v} \qquad \ldots (2.4)$$

where $\mathbf{S} = \mathbf{A}^{-1}$ is the 3×3 member stiffness matrix, and $\mathbf{A}$ is the 3×3 member flexibility matrix computed from the flexibilities of the individual segments and the anchorage regions at each end of the member (Table 2.2, step 38).

The transformations required for the second stage are given by the first order compatibility and equilibrium relationships (Figure 2.7) can be expressed in matrix notation as

$$\mathbf{v} = \mathbf{T}_L.\mathbf{V}_e \qquad \ldots (2.5)$$

$$\mathbf{R}_e = \mathbf{T}_L^T.\mathbf{r} \qquad \ldots (2.6)$$

where

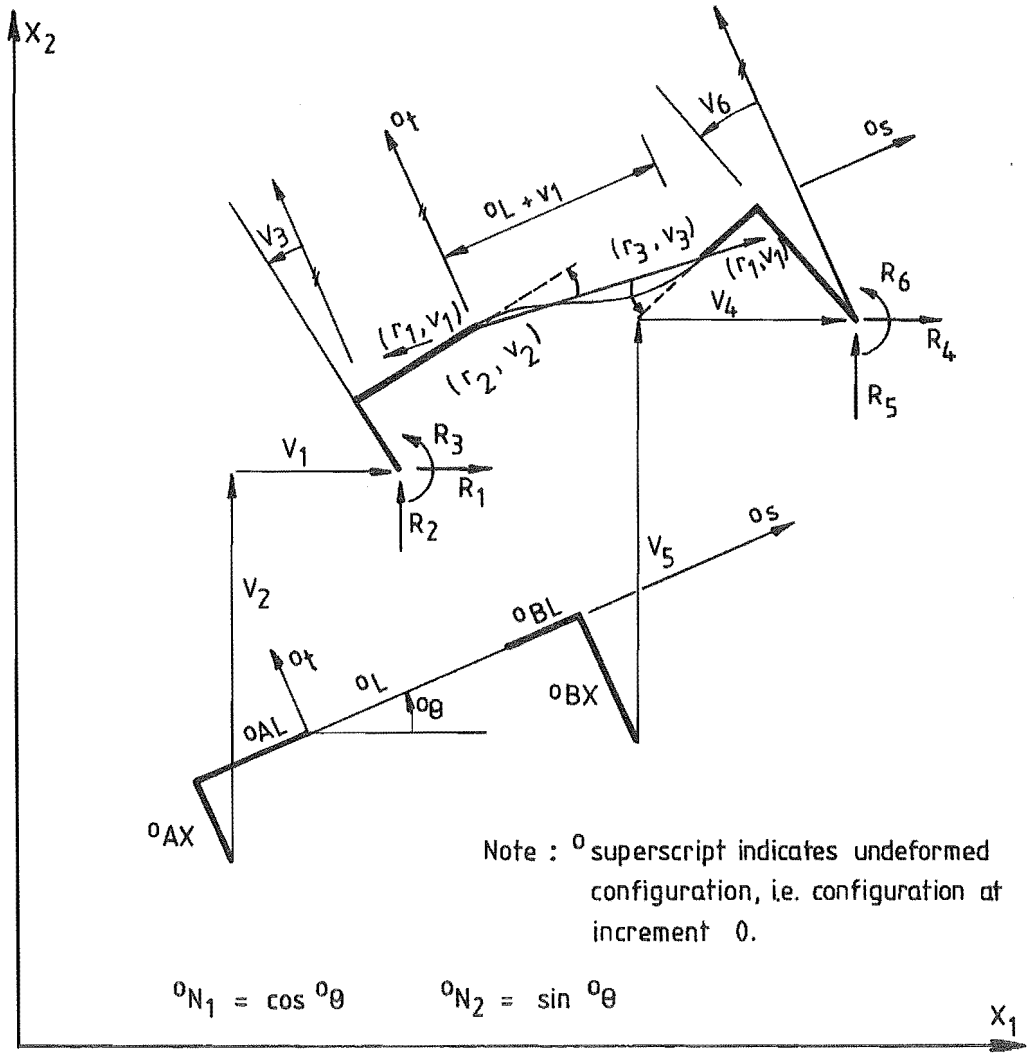

First Order Compatibility Relationships

$$v_1 = (V_4-V_1).{}^oN_1 + (V_5-V_2).{}^oN_2 + {}^oAX.V_3 - {}^oBX.V_6$$

$$v_2 = \{(V_4-V_1).{}^oN_2 - (V_5-V_2).{}^oN_1 + {}^oAL.V_3 + {}^oBL.V_6\}/{}^oL + V_3$$

$$v_3 = \{(V_4-V_1).{}^oN_2 - (V_5-V_2).{}^oN_1 + {}^oAL.V_3 + {}^oBL.V_6\}/{}^oL + V_6$$

First Order Equilibrium Relationships

$$R_1 = -r_1.{}^oN_1 - (r_2 + r_3)/{}^oL.{}^oN_2$$

$$R_2 = -r_1.{}^oN_2 + (r_2 + r_3)/{}^oL.{}^oN_1$$

$$R_3 = r_1.{}^oAX + (r_2 + r_3)/{}^oL.{}^oAL + r_2$$

$$R_4 = r_1.{}^oN_1 + (r_2 + r_3)/{}^oL.{}^oN_2$$

$$R_5 = r_1.{}^oN_2 - (r_2 + r_3)/{}^oL.{}^oN_1$$

$$R_6 = -r_1.{}^oBX + (r_2 + r_3)/{}^oL.{}^oBL + r_3$$

FIGURE 2.7 : FORCE AND DISPLACEMENT DEGREES OF FREEDOM FOR A GENERAL TWO-DIMENSIONAL PLANE FRAME ELEMENT

$$\mathbf{T}_L = \mathbf{T}_L({}^oC_e) = \begin{bmatrix} -{}^oN_1 & -{}^oN_2 & {}^oAX & {}^oN_1 & {}^oN_2 & -{}^oBX \\ -{}^o\left(\frac{N_2}{L}\right) & {}^o\left(\frac{N_1}{L}\right) & {}^o\left(\frac{AL}{L}\right)+1 & {}^o\left(\frac{N_2}{L}\right) & -{}^o\left(\frac{N_1}{L}\right) & {}^o\left(\frac{BL}{L}\right) \\ -{}^o\left(\frac{N_2}{L}\right) & {}^o\left(\frac{N_1}{L}\right) & {}^o\left(\frac{AL}{L}\right) & {}^o\left(\frac{N_2}{L}\right) & -{}^o\left(\frac{N_1}{L}\right) & {}^o\left(\frac{BL}{L}\right)+1 \end{bmatrix} \quad \ldots (2.7)$$

is the linear compatibility transformation matrix, and $\mathbf{T}_L^T$, the transpose of $\mathbf{T}_L$, is the linear equilibrium transformation matrix. Combining Eqs. 2.4 to 2.6, thus gives the required nodal force-displacement relationships

$$\mathbf{R}_e = \mathbf{K}_e({}^oC_e).\mathbf{V}_e \quad \ldots (2.8)$$

where $\mathbf{K}_e({}^oC_e) = \mathbf{T}_L^T.\mathbf{S}.\mathbf{T}_L$ is the element stiffness matrix, based on the undeformed element configuration ${}^oC_e$ and defined in terms of the structure global co-ordinates.

The modifications required to be made to incorporate geometric non-linearities, are described in Section 2.4.

2.3 SECTION MODELS

Three reinforced concrete section models are included in the frame analysis computer program: a general inelastic model, suitable for analysing the response of a section under high intensity reversed cyclic loading, and two "non-yielding" models.

Although the overall inelastic response of a structure is largely determined by the behaviour of the member plastic hinge zones, it is still often necessary to provide section integration points in regions where the reinforcing steel always remains elastic. Examples of such applications include many column and wall members and the central region of double yielding beam members (Figure 2.3). Clearly, for efficient representation of such members, it is desirable to use alternative and substantially less expensive non-yielding section idealizations at these integration points.

2.3.1 Section Model Limitations

The analytic section models incorporated in the frame analysis computer program are based on the following simplifying assumptions:

(a) The normal and shear strain distributions over the section depth are assumed to be linear and uniform respectively.

(b) Ductile flexural behaviour is assumed, i.e. the shear reinforcement provided is assumed to be sufficient to prevent a diagonal tension failure at any stage during loading.

(c) While both normal and shear stress actions are considered, the behaviour of these actions is assumed to be such that there is no direct coupling between them, i.e. no terms coupling normal and shear stress actions appear in the section flexibility matrix.

(d) The effects of shrinkage, residual concrete tension, local buckling of the reinforcing bars, flexural bond slip at the interface of the concrete and steel, and time effects such as creep, rate of loading (Section 7.3.3) and strain ageing (Appendix C), have been ignored.

Assumptions of this type are customary for inelastic section analyses, and have generally been shown to provide a realistic basis for modelling the moment-curvature responses of rectangular flexural members (12, 44). The inclusion of inelastic shear deformations in the present analysis is simply a refinement of the traditional flexural section idealization. Consequently, although the generality of the shear model is restricted, the established applicability of the assumptions is not affected.

It is important, however, to recognise that the range of established applicability is limited, and that there are a number of commonly encountered applications where this type of section idealization may be unsatisfactory. Two important applications in this class are very short members where diagonal tension effects dominate (see Section 2.2.4), and non-rectangular sections where shear lag or section warping is significant, e.g. monolithic slab-beam construction.

2.3.2 Response Parameters

As indicated in Table 2.2, the section response parameters required by the global Newton-Raphson (N-R) solution procedure in the general frame sections of the program are:

(a) The section tangential flexibility matrix, $\mathbf{f}_t$, which in accordance with the limited section definition adopted (Section 2.3.1), is given by

$$\mathbf{f}_t = \begin{bmatrix} f_{11} & f_{12} & 0 \\ f_{21} & f_{22} & 0 \\ 0 & 0 & f_{33} \end{bmatrix}_t \qquad \ldots (2.9)$$

where $f_{11} = 1/EA + t_c^2/EI_c$, $f_{12} = f_{21} = t_c/EI_c$, $f_{22} = 1/EI_c$, and $f_{33} = 1/GA$ are the components of the section flexibility matrix; $t_c = -FA/EA$ is the distance from the instantaneous elastic centroid of the section to the member reference axis, R_A; $EI_c = EI - t_c^2.EA$ is the tangential flexural rigidity of the section taken about the instantaneous elastic centroid; and EA, FA, EI and GA are the section tangential* values of axial rigidity, first moment of axial rigidity, flexural rigidity and shear rigidity, determined relative to R_A in accordance with the appropriate section model.

(b) The total section forces resisted, $\mathbf{q}_r : (q_1, q_2, q_3)_r$, where q_1, q_2 and q_3 are the axial, flexural (i.e. moment) and shear force components determined relative to the member reference axis, R_A. These forces are determined directly from the appropriate section analysis model described in the following subsections.

---

* Under certain conditions secant moduli are substituted for the tangential values. (Refer Sections 2.3.4, 3.8 and 4.4).

2.3.3 Fully Inelastic Section Model

This model is designed to allow as general representation of reinforced concrete sections as is practicable within the limitations discussed in the preceding section. The geometric representation is relatively standard, although it is more flexible than has been used in many inelastic section models.

Each section is subdivided into a number of single degree of freedom steel or concrete subelements or layers (Figure 2.8). In addition, there is a single shear degree of freedom for each section. Only aspects related to the geometry and properties of the subelements and to the response of the complete sections are discussed here. The relevant material constitutive relationships used to model the elastic and post-elastic responses of the subelements are discussed separately in Chapters 3 to 5.

2.3.3.1 Steel Subelements

Each steel subelement is defined in terms of the area (A), the location (t), and the steel type of the bar group represented by the subelement. Any number or distribution of subelements (or "layers") can be used, e.g., each individual bar, or layer of bars, in a section could be modelled as a separate subelement, although this would not normally be warranted for sections with large numbers of bars.

In this study, up to 9 subelements were used to model reinforcement in a wall section. This was done only for comparing analytic and experimental responses. For most practical purposes, the bars could have been grouped into a smaller number of subelements without affecting the accuracy of the results. Most beam and column sections can be accurately modelled with 2 to 4 steel subelements.

The steel type specifications define the shape of the monotonic stress-strain relationship for each subelement, i.e. elastic modulus, yield strength, shape of strain hardening curve, and ultimate strain. (These properties are discussed further in Chapter 3). Different steel types can be specified for each subelement, although normally only one or two

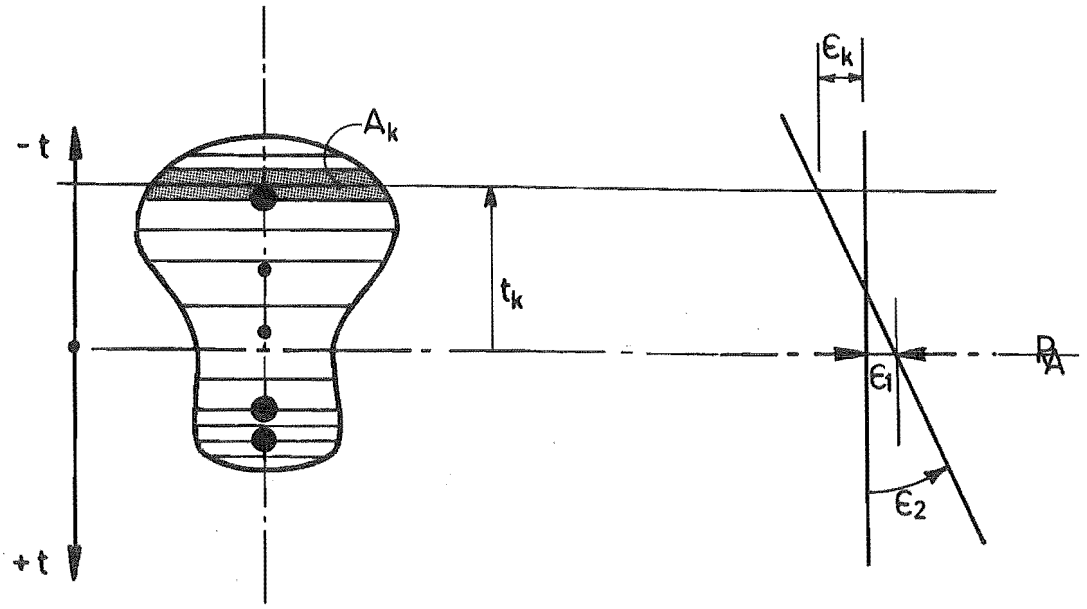

(a) General section segmentation

(b) Strain profile
$\epsilon : (\epsilon_1\ \epsilon_2\ \epsilon_3)$
(Shear strain ϵ_3 not shown)

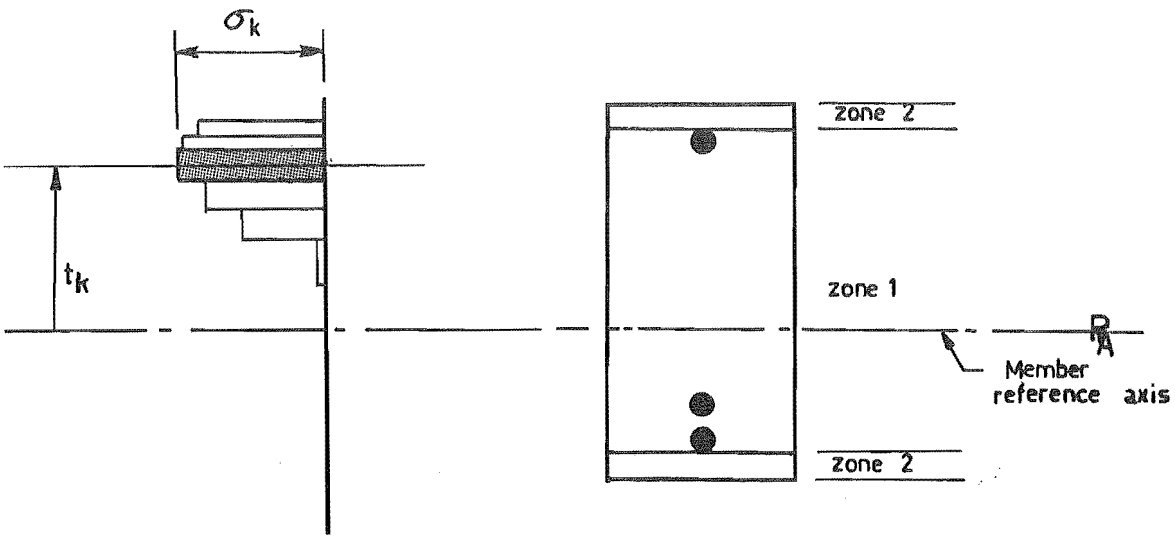

(c) Concrete stress profile

(d) Typical concrete zoning for rectangular section

— Steel subelement

— Concrete subelement (layer)

FIGURE 2.8 : GENERAL INELASTIC SECTION MODEL

steel types would be used per section, e.g. to model different grade bars.

The data input format also requires the orientation of each steel subelement to be specified. This provision was made to allow inclined bars to be analysed and was included when the program was developed for the incremental-pure iteration technique (Section 2.5.2). However, this capability is not functional for the Newton-Raphson solution procedure (Section 2.5.3) as inclined bars would introduce coupling between the section shear and normal stress actions (cf. Section 2.3.1).

2.3.3.2 Concrete Layers

In addition to the standard discretization of the concrete section, the model allows for two separate concrete zones such that

(a) Two different slopes for the descending branch of the concrete stress-strain relationship are permitted.

(b) Concrete spalling is permitted only in the No. 2 zones (Figure 2.8).

(c) Different shear moduli may be specified for the two zones.

The provision of separate zones is designed to allow differentiation between either confined and cover concrete, or web and flange regions of a section.

In this study, between 10 and 14 concrete layers were normally used to represent beam and column sections, and between 14 and 18 to represent wall sections. (See also Section 6.2).

2.3.3.3 Shear Deformation

Two options for modelling shear are provided in the general inelastic section model. The first is a full inelastic shear analysis as described in Chapter 5. This is designed to model sliding shear deformations of the type occurring in the plastic hinge zones of conventionally reinforced members. In the second option, the shear response is assumed to be elastic, with a single value of shear modulus

for the full shear area. This option was used for modelling the behaviour of plastic hinge zones in situations where the shear forces were largely resisted by inclined reinforcement.

2.3.3.4 Section Response*

The response for each section is determined in terms of the section tangential rigidities $(EA, FA, EI, GA)_t$ and the forces resisted by the section $\mathbf{q}_r:(q_1, q_2, q_3)_r$. In accordance with the section definitions for this model and with the notation in Figure 2.8, these are:

$$\begin{aligned} EA_t &= \sum_k A_k(\partial\sigma_k/\partial\epsilon_k) \\ FA_t &= \sum_k t_k.A_k(\partial\sigma_k/\partial\epsilon_k) \\ EI_t &= \sum_k t_k^2.A_k(\partial\sigma_k/\partial\epsilon_k) \\ GA_t &= \partial q_v/\partial\epsilon_3 \end{aligned} \qquad \ldots (2.9)$$

and

$$\mathbf{q}_r = \left\{ \begin{array}{l} q_1 = \sum_k \sigma_k A_k \\ q_2 = \sum_k \sigma_k A_k t_k \\ q_3 = q_v \end{array} \right\} \qquad \ldots (2.10)$$

where $\partial\sigma_k/\partial\epsilon_k$ are the values of tangential elastic modulus of each layer computed from the relevant steel or concrete response models, $\partial q_v/\partial\epsilon_3$ is tangential shear rigidity, σ_k is the concrete or steel normal stress computed for each layer, and q_v is the shear force resisted by the section.

2.3.4 Elastic Cracked Concrete Section Model

In this model, all the material responses, with the exception of concrete fracture, are assumed to remain elastic. Consequently, no complex load history terms are involved and it is possible to directly evaluate the

---

* In order to simplify the notation used in this section, the superscripts for increment, i, and iteration, j, numbers are not shown.

response over the section as a whole.

The material section idealizations used in this model are discussed below:

2.3.4.1 Steel Section

Since the steel remains completely elastic, only 3 parameters, the axial rigidity EA_s, the first moment of axial rigidity FA_s, and the steel flexural rigidity EI_s (all evaluated at the member reference axis R_A), are needed to describe the steel response (Figure 2.9a). Individual bars are not considered during the analysis stage and consequently the number of bars in each section does not effect the analysis cost.

2.3.4.2 Concrete Section

The concrete section for this model is, at present, restricted to either a rectangular or T shape (see Figure 2.9b). Two further simplifications are:

(a) Initial fracture results in loss of the tension capacity of the concrete over the entire section.

(b) Secant rigidities are used as approximations to the corresponding tangential values, i.e. the tangential components of rigidity associated with changes in neutral axis depth are disregarded. (Note that for the N-R* procedure, the section rigidities directly affect only the solution convergence, not the accuracy of the solution).

2.3.4 3 Section Response

Consistent with the section definitions (a) and (b) above and with the notation of Figure 2.9, the section rigidities for this idealization are given by (all values referenced to R_A):

---

* Newton-Raphson iteration procedure (Section 2.5.3).

$$EA = EA_s + EA_{fc} + EA_{wc}$$

$$FA = FA_s - EA_{fc}.t_f - EA_{wc}.t_w$$

$$EI = EI_s + EA_{fc}.t_f^2 + EA_{wc}.t_w^2 + \frac{1}{12}(EA_{fc}.d_f^2 + EA_{wc}.d_w^2) \quad \ldots (2.11)$$

and $GA = GA_{wc}$

The corresponding forces resisted by the section are then computed as

$$\mathbf{q}_r = \begin{Bmatrix} q_1 = EA.\varepsilon_1 - FA.\varepsilon_2 \\ q_2 = EI.\varepsilon_2 - FA.\varepsilon_1 \\ q_3 = GA.\varepsilon_3 \end{Bmatrix} \quad \ldots (2.12)$$

where $\boldsymbol{\epsilon}$: $(\varepsilon_1, \varepsilon_2, \varepsilon_3)$ are the imposed section strains.

2.3.4.4 Application

Since both the computation time and core storage requirements for this section model are very small, these factors do not impose significant constraints on application, e.g. only four strain history terms are required to be stored as compared with more than one hundred to model a section with two reinforcing bars using the general inelastic section model. However, because of the restrictions imposed by the idealizations used for the concrete response and section geometry, a second and more general non-yielding section model has also been provided.

2.3.5 General Non-yielding Section Model (Type C Section Model)

This section model employs a combination of the steel and shear rigidity idealizations used in the elastic cracked concrete model, the concrete section geometry idealization used in the general inelastic model and the simplified inelastic constitutive relationship for concrete described in Section 4.3. The forces resisted by the section, $\mathbf{q}_r$, and the section rigidities EA, FA, EI and GA are thus evaluated in accordance with the respective component idealizations as previously described.

The greater generality of the concrete idealization makes this section model more expensive to use than the elastic cracked concrete model. Nevertheless, there is still a significant saving in comparison with the general inelastic section model, and the model is therefore useful for applications such as at critical sections of members with high axial loading and/or high yield reinforcement or at sections not conforming with the restrictive geometry requirements of the elastic cracked concrete model.

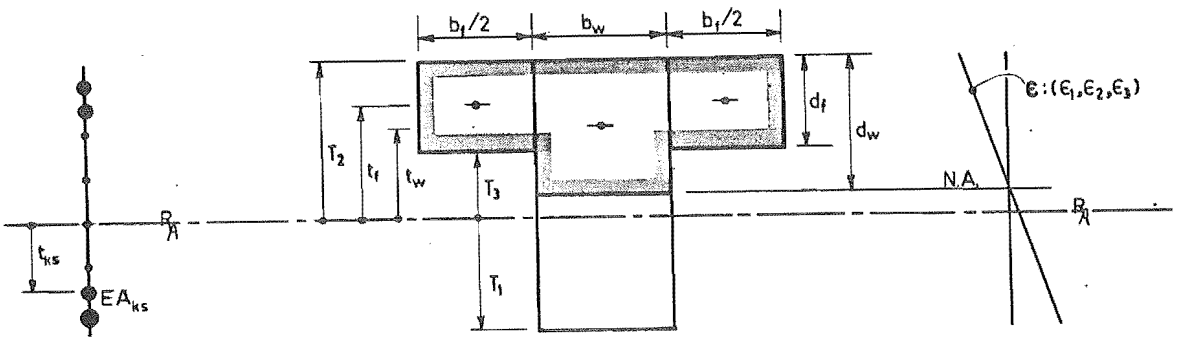

$$EA_s = \sum_{ks} EA_{ks}$$

$$FA_s = \sum_{ks} EA_{ks}.t_{ks}$$

$$EI_s = \sum_{ks} EA_{ks}.t_{ks}^2$$

$EA_{fc} = (E_c.b_f).d_f$

$EA_{wc} = (E_c.b_w).d_w$

$GA_{wc} = G.b_w.(T_1 - T_2)$: Constant.

(d_f, d_w, t_f, t_w) are re-evaluated for each new iteration.

FIGURE 2.9 : ELASTIC CRACKED CONCRETE SECTION MODEL

2.4 GEOMETRIC NONLINEARITY

In many frame analysis computer programs, nonlinearities arising from change of geometry are either neglected altogether or allowance is made only for the so-called "P-Δ" effect, usually determined on the basis of the net gravity load at each floor level. However, the inclusion of all change of geometry effects has only a minimal effect on the total computational effort, particularly for analyses which include material nonlinearities, since iteration is already required.

In the present case, all of geometry effects associated with rigid body displacements of the basic member have been incorporated in the frame analysis procedure, but the member force-displacement relationships have not been modified. Consequently, only the equilibrium and compatibility transformation matrices are affected. In applications where local buckling effects are important, these can be readily accounted for by using several elements to represent each member likely to be affected (56).

2.4.1 Types of Geometrically Nonlinear Formulation

There are two basic types of geometrically nonlinear formulation. In the first, generally referred to as the Lagrangian formulation, the analysis variables are always referenced to the undeformed configuration, while in the second, generally referred to as the moving co-ordinate or updating formulation, the reference configuration displaces with the structure. Both types of formulation are included in the present computer program, although, because of the manner in which it is applied, the latter is referred to herein as a "recursive formulation". Both approaches are based on second order approximations to the incremental displacements at the element nodes.

2.4.2 Nonlinear Compatibility and Equilibrium Transformation Matrices, Lagrangian Formulation

Unlike the linear transformation matrices considered in Section 2.2.5, the nonlinear compatibility and equilibrium transformation matrices are not the transpose of one another. Because of this, the notation

$$ {}^{i}\mathbf{R}_e = \mathbf{E}({}^{i}C_e).{}^{i}\mathbf{r} \qquad \ldots (2.13) $$

$$ {}^{i}\mathbf{v} = \mathbf{C}({}^{o}C_e, {}^{i}\mathbf{V}_e).{}^{i}\mathbf{V}_e \qquad \ldots (2.14) $$

is introduced where i is the current increment, $\mathbf{E}({}^{i}C_e)$ is the 6×3 Lagrangian equilibrium transformation matrix evaluated for the current element configuration ${}^{i}C_e$, equating the element nodal forces ${}^{i}\mathbf{R}_e$ to the member forces ${}^{i}\mathbf{r}$, and $\mathbf{C}({}^{o}C_e, {}^{i}\mathbf{V}_e)$ is the 3×6 Lagrangian compatibility transformation matrix expressed in terms of the undeformed configuration, ${}^{o}C_e$, and the element nodal displacements, ${}^{i}\mathbf{V}_e$, relating the local member displacements, ${}^{i}\mathbf{v}$, to the element displacements, ${}^{i}\mathbf{V}_e$. As indicated, Eq. 2.14 is a second order approximation to the true compatibility relationships.

The matrix $\mathbf{C}({}^{o}C_e, {}^{i}\mathbf{V}_e)$ can be decomposed into linear and nonlinear components such that

$$ {}^{i}\mathbf{v} = [\mathbf{T}_L({}^{o}C_e) + \mathbf{C}_N({}^{o}C_e, {}^{i}\mathbf{V}_e)], {}^{i}\mathbf{V}_e \qquad \ldots (2.15) $$

where $\mathbf{T}_L({}^{o}C_e)$ is the linear compatibility transformation matrix used in Section 2.2.5, and $\mathbf{C}_N({}^{o}C_e, {}^{i}\mathbf{V}_e)$, which contains only first order terms in ${}^{i}\mathbf{V}_e$: ${}^{i}(V_1, V_2, V_3, V_4, V_5, V_6)$, is the nonlinear component of $\mathbf{C}({}^{o}C_e, {}^{i}\mathbf{V}_e)$.

2.4.3 Nonlinear Differential Force-Displacement Relationships, Lagrangian Formulation

The differential compatibility transformation matrix, $\mathbf{T}({}^{o}C_e, {}^{i}\mathbf{V}_e)$, relating the differential member displacements d to the differential element nodal displacements, $d\mathbf{V}_e$, is obtained by partially differentiating Eq. 2.15 with respect to each of the six components of ${}^{i}\mathbf{V}_e$ in turn, giving

$$ \mathbf{T}({}^{o}C_e, {}^{i}\mathbf{V}_e) = [\mathbf{T}_L({}^{o}C_e) + 2\mathbf{C}_N({}^{o}C_e, {}^{i}\mathbf{V}_e)] \qquad \ldots (2.16) $$

The equilibrium transformation matrix $\mathbf{E}({}^{i}C_e)$ is related to this compatibility transformation matrix by the virtual work equation (56)

$$ {}^{i}\mathbf{R}_e^T.\mathbf{U} = {}^{i}\mathbf{r}^T.\mathbf{u} = {}^{i}\mathbf{r}^T.\mathbf{T}({}^{o}C_e, {}^{i}\mathbf{V}_e).\mathbf{U} \qquad \ldots (2.17) $$

which equates the work done by the forces ${}^{i}\mathbf{R}_e$ and ${}^{i}\mathbf{r}$, which are in equilibrium, undergoing arbitrary compatible virtual displacements of $\mathbf{U}$ and $\mathbf{u} = \mathbf{T}({}^{o}C_e, {}^{i}\mathbf{V}_e).\mathbf{U}$. Since this equation holds for any set of virtual displacements that is applied to the element, then

$$ {}^{i}\mathbf{R}_e = \mathbf{T}^T({}^{o}C_e, {}^{i}\mathbf{V}_e).{}^{i}\mathbf{r} \qquad \ldots (2.18) $$

Comparing Eqs. 2.13 and 2.18 gives

$$ \mathbf{T}({}^{o}C_e, {}^{i}\mathbf{V}_e) = \mathbf{E}^T({}^{i}C_e) = \mathbf{T}({}^{i}C_e) \qquad \ldots (2.19) $$

where $\mathbf{T}({}^{i}C_e)$, like $\mathbf{E}({}^{i}C_e)$, has the same form as $\mathbf{T}_L({}^{o}C_e)$ in Eq. 2.7, but is computed based on the current configuration ${}^{i}C_e$.

Substituting $\mathbf{T}^T({}^{i}C_e)$ for $\mathbf{T}^T({}^{o}C_e, {}^{i}\mathbf{V}_e)$ in Eq. 2.18, and expressing the resulting relationship in differential form gives

$$ d\mathbf{R}_e = \mathbf{T}^T.d\mathbf{r} + d\mathbf{T}^T.{}^{i}\mathbf{r} \qquad \ldots (2.20) $$

where $d\mathbf{T}^T.{}^{i}\mathbf{r} = \mathbf{T}^T({}^{i}C_e, d\mathbf{V}_e).{}^{i}\mathbf{r}$, and can be rearranged into the form

$$ d\mathbf{T}^T.{}^{i}\mathbf{r} = \mathbf{F}({}^{i}C_e, {}^{i}\mathbf{r}).d\mathbf{V}_e \qquad \ldots (2.21) $$

where $\mathbf{F}({}^{i}C_e, {}^{i}\mathbf{r})$ is the initial stress component of the 6×6 element tangential stiffness matrix.

Hence, differentiating Eq. 2.4 and combining with Eqs. 2.16, 2.20 and 2.21 gives the required differential force-displacement relationship

$$ d\mathbf{R}_e = \mathbf{K}_{et}.d\mathbf{V}_e \qquad \ldots (2.22a) $$

$$ \text{where } \mathbf{K}_{et} = \mathbf{T}^T({}^{i}C_e).\mathbf{S}_t.\mathbf{T}({}^{i}C_e) + \mathbf{F}({}^{i}C_e, {}^{i}\mathbf{r}) \qquad \ldots (2.22b) $$

is the 6×6 element tangential stiffness matrix and $\mathbf{S}_t$ is the 3×3 member

TABLE 2.1 : ELEMENTS OF $\mathbf{T}({}^{i}C_e)$ AND $\mathbf{F}({}^{i}C_e, {}^{i}\mathbf{r})$

(a) Transformation Matrix, $\mathbf{T}({}^{i}C_e)$

The elements of this matrix are obtained directly from consideration of equilibrium of the updated configuration. Consequently, the individual elements are the same as for $\mathbf{T}_L({}^{o}C_e)$, but with ${}^{o}C_e$ replaced by ${}^{i}C_e$, i.e.

$$\mathbf{T}({}^{i}C_e) = \begin{bmatrix} -{}^{i}N_1 & -{}^{i}N_2 & {}^{i}AX & {}^{i}N_1 & {}^{i}N_2 & -{}^{i}BX \\ -{}^{i}\left(\frac{N_2}{L}\right) & {}^{i}\left(\frac{N_1}{L}\right) & {}^{i}\left(\frac{AL}{L}\right)+1 & {}^{i}\left(\frac{N_2}{L}\right) & -{}^{i}\left(\frac{N_1}{L}\right) & {}^{i}\left(\frac{BL}{L}\right) \\ -{}^{i}\left(\frac{N_2}{L}\right) & {}^{i}\left(\frac{N_1}{L}\right) & {}^{i}\left(\frac{AL}{L}\right) & {}^{i}\left(\frac{N_2}{L}\right) & -{}^{i}\left(\frac{N_1}{L}\right) & {}^{i}\left(\frac{BL}{L}\right)+1 \end{bmatrix}$$

(b) Initial Stress Stiffness Matrix, $\mathbf{F}({}^{i}C_e, {}^{i}\mathbf{r})$

The elements of the matrix $d\mathbf{T} = \mathbf{T}({}^{i}C_e, d\mathbf{V}_e)$ are given by $\lim_{\Delta\mathbf{V}_e \to 0} [\mathbf{T}({}^{i}C_e, \Delta\mathbf{V}_e) - \mathbf{T}({}^{i}C_e)]$.
Transposing this matrix, post multiplying by ${}^{i}\mathbf{r}$, and rearranging, gives

$$\mathbf{F}({}^{i}C_e, {}^{i}\mathbf{r}) = \mathbf{F}({}^{i}C_e, {}^{i}r_1) + \mathbf{F}({}^{i}C_e, {}^{i}r_2 + {}^{i}r_3)$$

where

$$\mathbf{F}({}^{i}C_e, {}^{i}r_1) = {}^{i}\left(\frac{r_1}{L}\right) \cdot {}^{i}\begin{bmatrix} N_2^2 & -N_1.N_2 & -AL.N_2 & -N_2^2 & N_1.N_2 & -BL.N_2 \\ & N_1^2 & AL.N_1 & N_1.N_2 & -N_1^2 & BL.N_1 \\ & & AL(AL+L) & AL.N_2 & -AL.N_1 & AL.BL \\ & & & N_2^2 & -N_1.N_2 & BL.N_2 \\ \text{symm.} & & & & N_1^2 & -BL.N_1 \\ & & & & & BL(BL+L) \end{bmatrix}$$

$$\mathbf{F}({}^{i}C_e, {}^{i}r_2 + {}^{i}r_3) = {}^{i}\left(\frac{r_2+r_3}{L^2}\right) \cdot {}^{i}\begin{bmatrix} -2N_1.N_2 & (N_1^2-N_2^2) & (AL.N_1+AX.N_2) & 2N_1.N_2 & -(N_1^2-N_2^2) & (BL.N_1-BX.N_2) \\ & 2N_1.N_2 & -(AX.N_1-AL.N_2) & -(N_1^2-N_2^2) & -2N_1.N_2 & (BX.N_1+BL.N_2) \\ & & -AX(L+2AL) & -(AL.N_1+AX.N_2) & (AX.N_1-AL.N_2) & (AL.BX-BL.AX) \\ & & & -2N_1.N_2 & (N_1^2-N_2^2) & -(BL.N_1-BX.N_2) \\ \text{symm.} & & & & 2N_1.N_2 & -(BX.N_1+BL.N_2) \\ & & & & & BX(L+2BL) \end{bmatrix}$$

tangential stiffness matrix determined in accordance with Section 2.2.2 such that $d\mathbf{r} = \mathbf{S}_t.d\mathbf{v}$. The individual elements of the matrices $\mathbf{T}({}^{i}C_e)$ and $\mathbf{F}({}^{i}C_e, {}^{i}\mathbf{r})$ are given in Table 2.1. The use of the current configuration to compute these matrices does not invalidate the Lagrangian description*, but is simply the most convenient approach. The transformation matrix can, alternatively, be computed in terms of ${}^{o}C_e$ and ${}^{i}\mathbf{v}_e$ from consideration of either equilibrium or compatibility. However, the derivation based on compatibility must be approached with caution, as the compatibility relationships, which contain second order displacement terms, are not unique, i.e. they may be expressed in several ways, only one of which will lead to the result given in Eq. 2.16. This is similar to the problem of nonuniqueness encountered in energy based formulations (57).

The order of approximation to the current configuration required for computing $\mathbf{K}_{et}$ is ${}^{i}C_e = C_e({}^{o}C_e, {}^{i}\mathbf{v}_e)$, i.e. only a first order approximation to the current configuration is required. Thus, from Figure 2.10 the required current values for the seven configuration parameters are:

$$ {}^{i}L = {}^{o}L + {}^{i}_{o}e.{}^{o}L \qquad \ldots (2.23a) $$

$$ {}^{i}AL = {}^{o}AL - {}^{i}_{o}\phi_3.{}^{o}AX \qquad \ldots (2.23b) $$

$$ {}^{i}BL = {}^{o}BL + {}^{i}_{o}\phi_6.{}^{o}BX \qquad \ldots (2.23c) $$

$$ {}^{i}AX = {}^{o}BX + {}^{i}_{o}\phi_3.{}^{o}AL \qquad \ldots (2.23d) $$

$$ {}^{i}BX = {}^{o}BX - {}^{i}_{o}\phi_6.{}^{o}BL \qquad \ldots (2.23e) $$

$$ {}^{i}N_1 = {}^{o}N_1 - {}^{i}_{o}\phi_m.{}^{o}N_2 \qquad \ldots (2.23f) $$

$$ {}^{i}N_2 = {}^{o}N_2 + {}^{i}_{o}\phi_m.{}^{o}N_1 \qquad \ldots (2.23g), $$

where

$$ {}^{i}_{o}e = -\{{}^{o}N_1({}^{i}v_1 - {}^{i}v_4) + {}^{o}N_2({}^{i}v_2 - {}^{i}v_5) - {}^{o}AX.{}^{i}v_3 + {}^{o}BX.{}^{i}v_6\}/{}^{o}L $$

---

* Because ${}^{i}C_e$ is defined in terms of ${}^{o}C_e$ and ${}^{i}\mathbf{v}_e$.

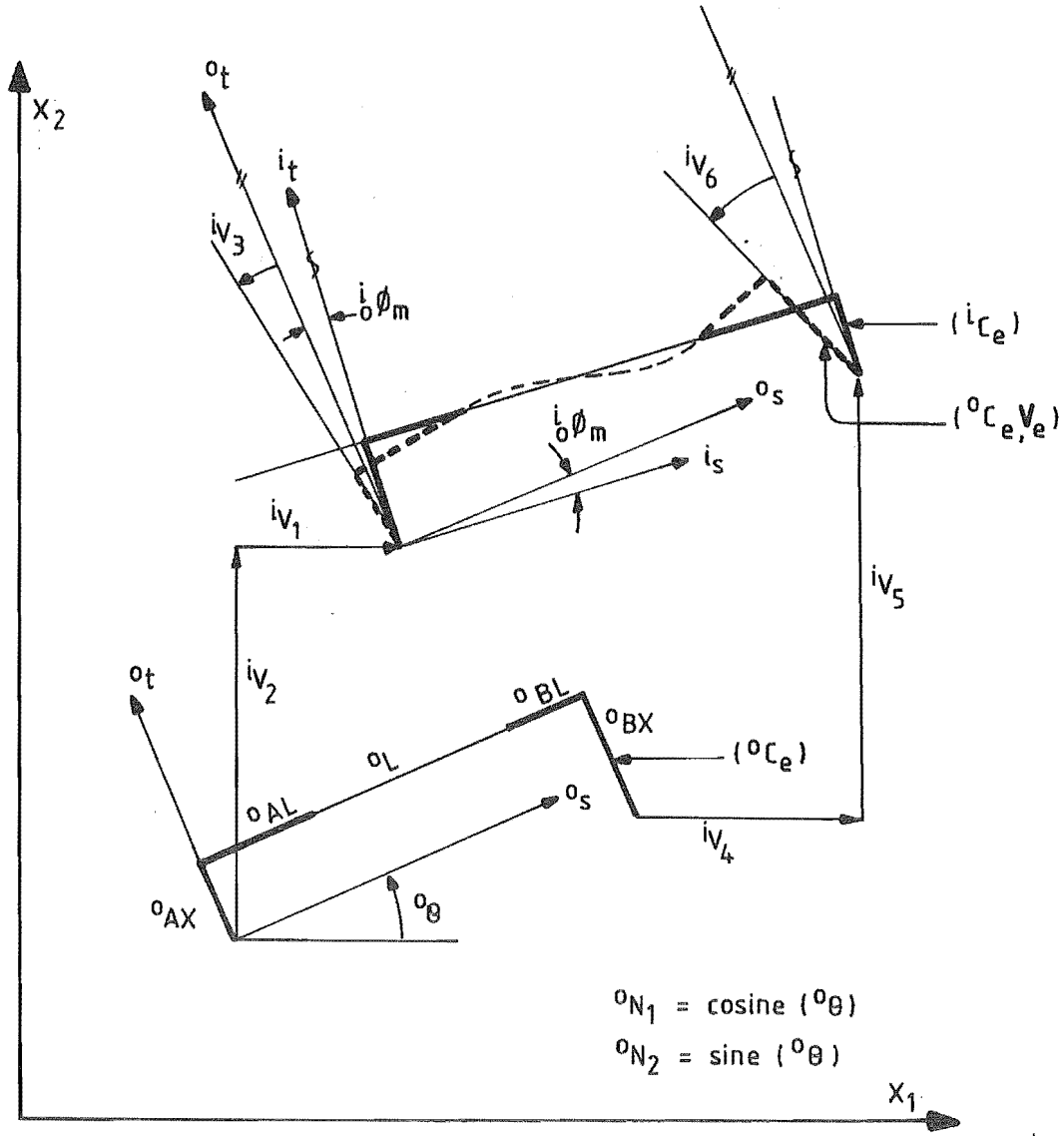

FIGURE 2.10 : CONFIGURATION UPDATING PROCESS

$$ {}^{i}_{o}\phi_m = -\{{}^{o}N_1({}^{i}v_2 - {}^{i}v_5) - {}^{o}N_2({}^{i}v_1 - {}^{i}v_4) + {}^{o}AL.{}^{i}v_3 + {}^{o}BL.{}^{i}v_6\}/{}^{o}L $$

$$ {}^{i}_{o}\phi_3 = v_3 - {}^{i}_{o}\phi_m $$

$$ {}^{i}_{o}\phi_6 = v_6 - {}^{i}_{o}\phi_m $$

These values are recomputed at every increment, i, based on the undeformed configuration.

The evaluation of the out-of-balance nodal forces requires use of the compatibility transformation matrix $\mathbf{C}$. This is not based solely on the current configuration, but can be readily computed from Eqs. 2.15 and 2.16, which give

$$ \mathbf{C}({}^{i}C_e) = 0.5[\mathbf{T}({}^{i}C_e) + \mathbf{T}_L({}^{o}C_e)] \qquad \ldots (2.24) $$

Since $\mathbf{T}({}^{i}C_e)$ is already required for computing $\mathbf{K}_{et}$, this approach is more efficient than computing $\mathbf{C}({}^{o}C_e, {}^{i}\mathbf{V}_e)$ directly.

2.4.4 Recursive Formulation

Although the range of applicability of the second order Lagrangian formulation is adequate for the large majority of practical analysis problems, the relationships employed for computing ${}^{i}C_e$, i.e. Eqs. 2.23, are in a form readily adaptable to recursive evaluation. This can be achieved virtually without additional cost, simply by retaining the updated configuration parameters and using them, rather than the original values, ${}^{o}C_e$, to compute the new configuration in the next increment. In this procedure, the incremental displacements, $\Delta\mathbf{V}_e$, replace the total displacements, ${}^{i}\mathbf{V}_e$ used in Eqs. 2.23, and the updating is characterized by the recursion relation

$$ {}^{i}C_e = C_e({}^{i-1}C_e, \Delta\mathbf{V}_e) \qquad \ldots (2.25) $$

To gain advantage from this improvement, the compatibility matrix required for evaluating the out-of-balance forces must also be applied incrementally.

Thus the required compatibility transformation matrix is given by

$$\mathbf{C}({}^{i}C_e) = 0.5[\mathbf{T}({}^{i}C_e) + \mathbf{T}({}^{i-1}C_e)] \qquad \ldots(2.26)$$

The matrices $\mathbf{T}({}^{i}C_e)$ and $\mathbf{F}({}^{i}C_e, {}^{i}r)$ given in Table 2.1, are functions only of the current configuration and member forces, and thus, are unaffected by the change in updating procedure.

The only errors of approximation made in this procedure involve second or higher order terms in the incremental displacements, $\Delta\mathbf{V}_e$, in Eqs. 2.25 and 2.26. Consequently, within the limits to which geometric and constitutive representation have been satisfied, the obtained results will converge to the correct solution with increment refinement, regardless of the total strains or displacements involved. However, although the solution over any individual load increment is of second order accuracy, the improvement with increment refinement is, because of cumulating errors, only first order. The solution convergence with refinement of increment size was found to deteriorate significantly with increasing total displacements and because of this, additional higher order terms in the incremental displacements were introduced into the recursive relations for updating the configuration parameters. The relationships now used are:

$$i_L = {}^{i-1}L.c_m/\phi_L \qquad \ldots (2.27a)$$

$$i_{AL} = {}^{i-1}AL.c_3 - {}^{i-1}AX.s_3 \qquad \ldots (2.27b)$$

$$i_{BL} = {}^{i-1}BL.c_6 + {}^{i-1}BX.s_6 \qquad \ldots (2.27c)$$

$$i_{AX} = {}^{i-1}AX.c_3 + {}^{i-1}AL.s_3 \qquad \ldots (2.27d)$$

$$i_{BX} = {}^{i-1}BX.c_6 - {}^{i-1}BL.s_6 \qquad \ldots (2.27e)$$

$$i_{N_1} = {}^{i-1}N_1.c_m - {}^{i-1}N_2.s_m \qquad \ldots (2.27f)$$

$$i_{N_2} = {}^{i-1}N_2.c_m + {}^{i-1}N_1.s_m \qquad \ldots (2.27g)$$

where

$$c_m = 1 - 0.5\,\phi_m^2$$

$$s_m = \phi_m - \phi_m^3/6$$

$$c_3 = 1 - 0.5(v_3 - \phi_m)^2$$

$$s_3 = (v_3 - \phi_m) - (v_3 - \phi_m)^3/6$$

$$c_6 = 1 - 0.5(v_6 - \phi_m)^2$$

$$s_6 = (v_6 - \phi_m) - (v_6 - \phi_m)^3/6$$

$$\phi_L = 1 - \{{}^{i-1}N_1(v_1-v_4) + {}^{i-1}N_2(v_2-v_5) - {}^{i-1}AL.v_3^2/2 - {}^{i-1}BL.v_6^2/2 - {}^{i-1}AX(v_3-v_3^3/6) + {}^{i-1}BX(v_6-v_6^3/6)\}/{}^{i-1}L$$

$$\phi_m = \phi_t - \phi_t^3/3$$

and

$$\phi_t = -\{{}^{i-1}N_1(v_2-v_5) - {}^{i-1}N_2(v_1-v_4) - {}^{i-1}AX.v_3^2/2 + {}^{i-1}BX.v_6^2/2 + {}^{i-1}AL(v_3-v_3^3/6) + {}^{i-1}BL(v_6-v_6^3/6)\}/({}^{i-1}L.\phi_L)$$

Because of the approximation made in Eq. 2.26, the formulation remains a second order procedure. However, since only fourth or higher order terms in $\Delta\mathbf{V}_e$ are neglected in the updating process, there are no significant cumulating errors, regardless of the total displacements imposed. The extra computation required because of these modifications has only a minimal effect on the total computational time per increment, i.e. approximately 1% or less for a combined materially and geometrically nonlinear analysis.

Note also that, because the same code is used for both formulations, these relationships, with ${}^{o}C_e$ substituted for ${}^{i-1}C_e$ and ${}^{i}\mathbf{V}_e$, for $\Delta\mathbf{V}_e$, are also used in the Lagrangian formulation.

2.5 NUMERIC SOLUTION PROCEDURES

The inelastic response of a reinforced concrete structure subjected to high intensity cyclic loading is one of the most complex problems likely to be encountered in any structural analysis. Analyses employing realistic constitutive material responses, place a very high demand on the numeric solution procedure, both in terms of solution stability and reliability, and in terms of solution efficiency.

The reinforced concrete analyses formulations developed by Franklin*(58), Blaauwendraad*(51), and Menegotto and Pinto (50) all used solution procedures based on some form of pure iteration. An incremental form of this iteration technique was originally used in the present computer program. However, this solution procedure was never fully implemented for post-yield analyses, and was later replaced by a solution procedure based on the generalized Newton-Raphson (N-R) iteration technique. The version of the N-R solution procedure incorporated into the program includes a number of modifications which were found to be necessary in order to ensure reliable and efficient solution convergence. These modifications mainly involve the solution formulation at the constitutive response level, and are discussed in Chapters 3 and 4. However, one important modification made to the global procedure, was the introduction of a displacement control capability.

Although not all problems with the constitutive responses have been fully resolved, the N-R based procedure nevertheless proved to be a highly effective and efficient solution procedure for analysing both geometrically and materially nonlinear structures.

This section discusses various aspects related to the general load application and solution procedures provided in the frame analysis computer program and gives a detailed description of the displacement control procedure that was developed.

2.5.1 Load Incrementation

The loading capability provided in the computer program allows for a single application of a fixed initial load $\mathbf{R}_o$ (e.g. to model gravity

---

* These formulations were for monotonic load analyses only.

loads), followed by repeated increments of a separate load vector $\Delta\mathbf{R} = \Delta p.\mathbf{R}_{ref}$. The total load applied to the structure at the end of any increment, i, is therefore:

$$ {}^{i}\mathbf{R} = {}^{i}p.\mathbf{R}_{ref} + \mathbf{R}_{o} \qquad \ldots (2.28) $$

where $\mathbf{R}_{ref}$ is the reference force vector for incremental loading,
${}^{i}p = {}^{i-1}p + \Delta p$ is the total fraction of $\mathbf{R}_{ref}$ applied to the structure,
$\Delta p = \overline{p}$ for standard force iteration (e.g. N-R), or
$= f(\overline{\delta})$ for displacement controlled iteration (Section 2.5.5),
$\overline{p}$ is the prescribed maximum force increment, and
$\overline{\delta}$ is the prescribed maximum displacement increment.

The increments $\overline{p}$ and $\overline{\delta}$ can be varied from increment to increment, although this is rarely necessary. Almost all analyses in this study were performed with constant increments of $\overline{p}$ and $\overline{\delta}$. With constant increments, the loading can be applied either monotonically or cyclically in materially nonlinear analyses, or can be made to trace the entire equilibrium path of a geometrically nonlinear response in which both bifurcation and "looping" occur. For cyclic load analyses, the limits of each load reversal can be specified in terms of force, displacements, or number of increments. The type of limit (i.e. force, displacement, etc.) can be varied from load reversal to load reversal, or, if desired, both force and displacement limits can be specified for the same load reversal, i.e. the load reversal could be limited by either force or displacement, depending on which limit is reached first.

2.5.2 Incremental-Pure Iteration

The incremental-pure iteration technique is characterised by the recurrence relation

$$ {}^{i}\mathbf{V}^{(j)} = [\mathbf{K}_{s}({}^{i}\mathbf{V}^{(j-1)})]^{-1}.\Delta\mathbf{R} + {}^{i-1}\mathbf{V} \qquad \ldots (2.29) $$

where $\mathbf{V}$ is the vector of the nodal displacements, $\Delta\mathbf{R}$ is the vector of the incremental nodal forces, $\mathbf{K}_{s}$ is the incremental secant stiffness matrix of the structure, and i and j denote the i^{th} increment and the

j^{th} iteration respectively. The iteration procedure operates by repeated solving of the governing force-displacement equations ($\Delta \mathbf{R} = \mathbf{K}_s . \Delta \mathbf{V}$), i.e. repeated evaluation of ${}^{i}\mathbf{V}^{(j)}$ in Eq. 2.29. This is carried out using an equation solver based on standard Gauss elimination (Section 2.5.6). The stiffness matrix used for each solution is computed based on the latest estimate of the displacement of the structure, i.e. ${}^{i}\mathbf{K}_s^{(j)} = \mathbf{K}_s({}^{i}\mathbf{V}^{(j-1)})$. Each improvement in the accuracy of the displacements ($\mathbf{V}$) leads to a better estimate of $\mathbf{K}_s$, and this in turn provides a still better estimate of $\mathbf{V}$. This process continues until $\mathbf{K}_s$ and $\mathbf{V}$ converge to their correct values.

Examples of this type of solution convergence are shown in Figure 2.11a for a 1 degree of freedom structure and in Figure 2.11b, for the local response at an internal element, α, in a multi-degree of freedom structure. The changes in local force (r_α) between iterations shown for the latter example are due to interaction between the local element and the surrounding structure. The total force applied to the structure (${}^{i}\mathbf{R}$) remains constant during the iteration process. In the example shown, the reduction in force on the element will have resulted in a net increase in the force carried by other parts of the structure. Similar force redistributions also occur with the N-R and other iterative solution techniques.

Several researchers have used pure or incremental-pure iteration techniques to analyse nonlinear responses of reinforced concrete structures (50, 58). However, this type of iteration technique has several characteristics which made it unsuitable for analysing the more complex responses considered in this study. Three of the more important of these are discussed below:

(a) The convergence rate can be very slow if the response is highly nonlinear, e.g. such as at the onset of steel yielding (Figure 2.11c). In analyses of individual reinforced concrete sections, this problem can be minimised by inserting intermediate load steps. However, this is impracticable in analyses of large structures, where yielding may be initiated at a number of sections during a single load increment. Also, if the change

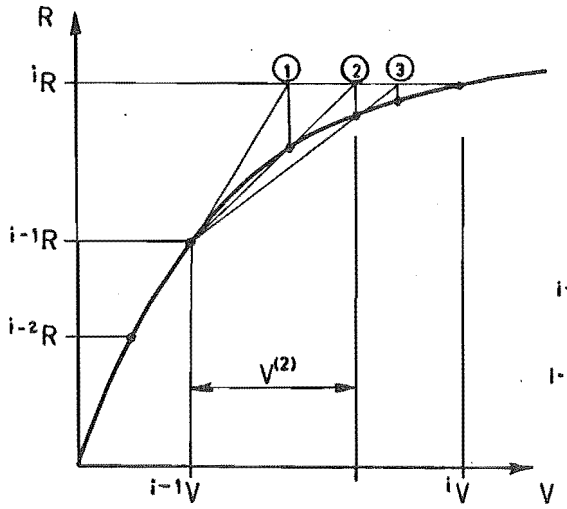

(a) Single degree of freedom (SDOF) structure.

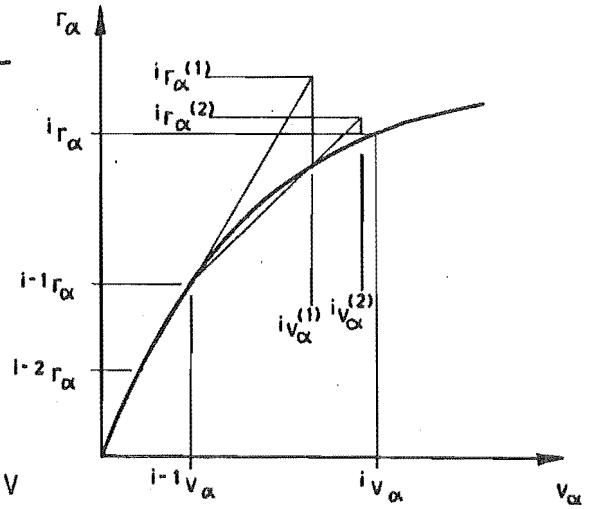

(b) Internal element α, of a multi-degree of freedom structure.

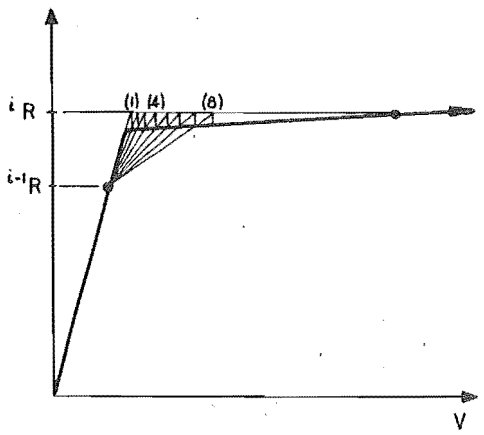

(c) Slow convergence at slope discontinuity (SDOF)

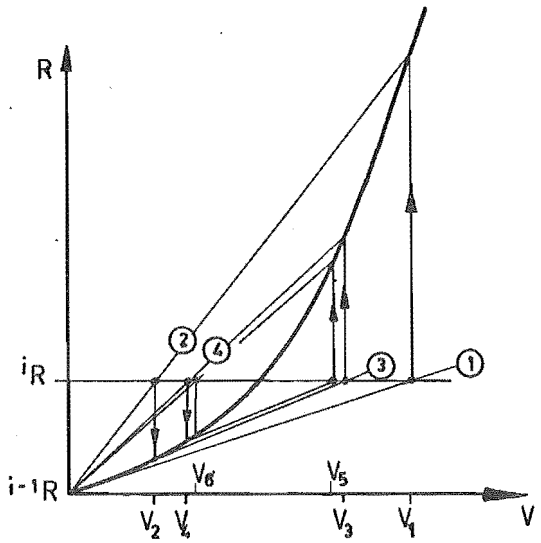

(d) Strain stiffening response (SDOF)

FIGURE 2.11 : INCREMENTAL-PURE ITERATION PROCEDURE

in strain from one iteration to the next is too small, this type of behaviour may not be detected when the solution is tested for convergence, especially if it occurs at only a few locations in a large structure. As a result, the iteration process could be prematurely terminated.

(b) No equilibrium checks are made on the section forces. Consequently, equilibrium errors resulting from false convergence in any increment are carried forward for the remainder of the analysis. This applies whether the errors are due to the type of behaviour described above or to any other cause.

(c) The iteration technique may be incapable of effecting satisfactory solution convergence when the response within the load increment is strain stiffening. This is illustrated in Figure 2.11d for a single degree of freedom (SDOF) structure. As indicated, the rate of convergence reduces with each iteration and the solution rapidly approaches a state of stable oscillation. This effect diminishes with decreasing increment size. However, for practical sizes of load increment, satisfactory convergence could not be assured if there is a large increase in stiffness, e.g. such as can occur when concrete cracks close due to reverse loading, or when sliding shear deformations (Chapter 5) are dominant.

2.5.3 Generalized Newton-Raphson Iteration

The generalized Newton-Raphson (N-R) iteration technique is one of the most powerful general structural analysis solution procedures available. For an incremental loading application, the technique can be characterized by the set of recurrence relations

$$ {}^{*}\mathbf{R}^{(j)} = {}^{i}\mathbf{R} - \mathbf{R}_r({}^{i}\mathbf{V}^{(j-1)}) \qquad \ldots (2.30a) $$

$$ {}^{*}\mathbf{V}^{(j)} = [\mathbf{K}_t({}^{i}\mathbf{V}^{(j-1)})]^{-1} . {}^{*}\mathbf{R}^{(j)} \qquad \ldots (2.30b) $$

$$ {}^{i}\mathbf{V}^{(j)} = {}^{i}\mathbf{V}^{(j-1)} + {}^{*}\mathbf{V}^{(j)} \qquad \ldots (2.30c) $$

where ${}^{*}\mathbf{R}^{(j)}$ are the out-of-balance forces which are equal to the

difference between the applied forces ${}^{i}\mathbf{R}$ and the forces $\mathbf{R}_r$ actually resisted by the structure at displacement ${}^{i}\mathbf{V}^{(j-1)}$, $\mathbf{K}_t({}^{i}\mathbf{V}^{(j-1)})$ is the tangential stiffness matrix of the structure evaluated at displacement ${}^{i}\mathbf{V}^{(j-1)}$, and ${}^{*}\mathbf{V}^{(j)}$ are the changes in displacement which occur when the out-of-balance forces are released, i.e. ${}^{*}\mathbf{V} = \mathbf{K}_t \cdot {}^{*}\mathbf{R}$. These are added to displacements ${}^{i}\mathbf{V}^{(j-1)}$ estimated in the previous iteration (j-1) to yield a new (and usually better) estimate of the structure displacement ${}^{i}\mathbf{V}^{(j)}$. As previously, i and j denote the i^{th} increment and j^{th} iteration respectively.

Starting with an initial estimate of the displacement field ${}^{i}\mathbf{V}^{(o)}$, Eqs. 2.30 are successively applied to obtain improving approximations, ${}^{i}\mathbf{V}^{(j)}$. This process is continued until satisfactory convergence is established (Section 2.5.7). The whole process is then repeated for each remaining increment. In elastic geometrically nonlinear analyses, the out-of-balance nodal forces for each element can be computed directly from the nodal displacements. However, in materially nonlinear analyses, the member responses must initially be solved at a local level before the out-of-balance nodal forces can be computed. The steps required for this are outlined in Section 2.6.1.

In the present application, the converged displacement field at the end of the previous increment is always used as the initial displacement estimate, i.e. ${}^{i}\mathbf{V}^{(o)} = {}^{i-1}\mathbf{V}$ (the absence of the iteration superscript on ${}^{i-1}\mathbf{V}$ indicates a "converged" solution). Under this definition, the initial application of the incremental load $\Delta\mathbf{R}$ is regarded as part of the 1st iteration, i.e. ${}^{*}\mathbf{R}^{(1)} = \Delta\mathbf{R} + {}^{*}\mathbf{R}$, where ${}^{*}\mathbf{R}$ is the residual out-of-balance force from the previous increment. This solution process is illustrated in Figure 2.12a for a single degree of freedom response and in Figure 2.12b for a single internal co-ordinate of a multi-degree of freedom structure.

Although this iteration technique has been widely applied to the solution of geometrically nonlinear structural problems, there have been comparatively few applications to non-conservative materially nonlinear problems. Several investigators cite difficulties with oscillation of the solution between loading and unloading, and have questioned its

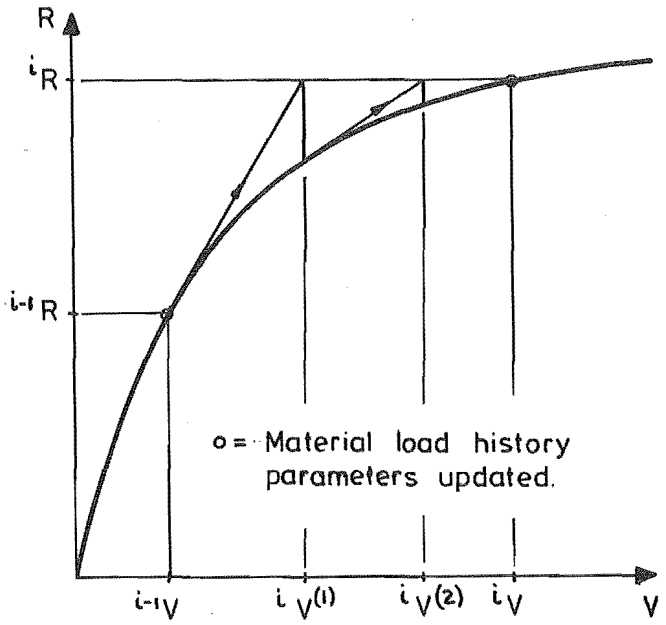

(a) S D O F structure

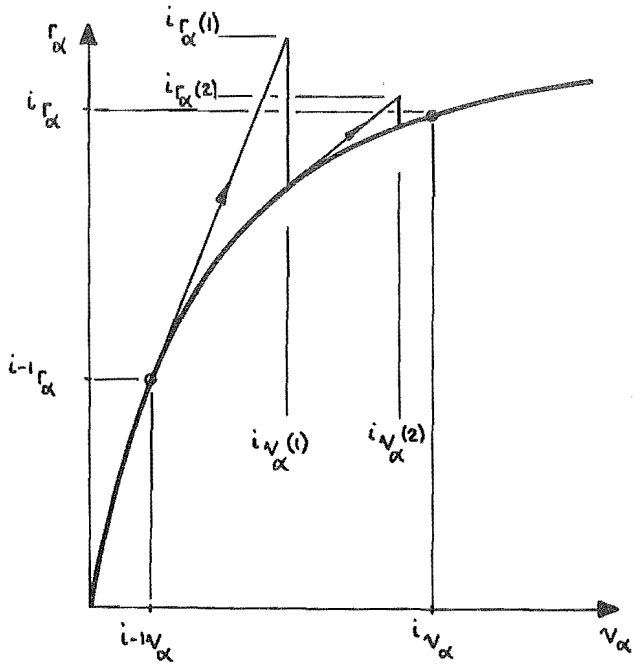

(b) Individual internal co-ordinate (α) of a multi-DOF structure.

FIGURE 2.12 : GENERALIZED NEWTON-RAPHSON ITERATION

applicability to path dependent problems (59). However, the results obtained in this study show that, as long as special precautionary measures are taken (Chapters 3 and 4), the N-R iteration technique can provide a highly effective and efficient means of analysing reinforced concrete structures subjected to high intensity cyclic loading.

2.5.4 Modified Newton-Raphson Procedures

In the generalised N-R procedure described by Eqs. 2.30, the tangent stiffness matrix is recomputed and the force-displacement relationships solved at each iteration. This part of the process is not a necessary requirement for convergence, and most analysts developing geometrically nonlinear formulations have recommended use of modified N-R procedures (Figure 2.13) in which the stiffness matrix is held constant for several iterations and is only updated when the rate of convergence deteriorates. For analyses involving large numbers of degrees of freedom, this type of modification can significantly reduce the overall computational effort, especially if the response is not highly nonlinear.

Modified N-R procedures have also been successfully used for inelastic analyses of reinforced concrete structures. Phillips and Zienkiewicz (60) found that the most efficient approach was to update the stiffness matrix on the first iteration in every load increment. However, they considered only monotonic loading and in the present study, it was found that serious difficulties would be encountered if a modified N-R procedure were used to analyse a structure subjected to large post-yield load reversals. This occurs because of the complexity of the material constitutive relationships, particularly the large slope discontinuities at the onset of steel yielding and unloading. The effects of these discontinuities are discussed in Section 3.9.

2.5.5 Displacement Controlled Iteration

Almost all standard iteration techniques used for static analyses operate under constant applied loading. This type of iteration technique is, however, often difficult to apply in regions of very low stiffness (e.g. yield plateau regions), especially if the load-deflection slope changes sign within the solution interval. If this occurs, it is generally

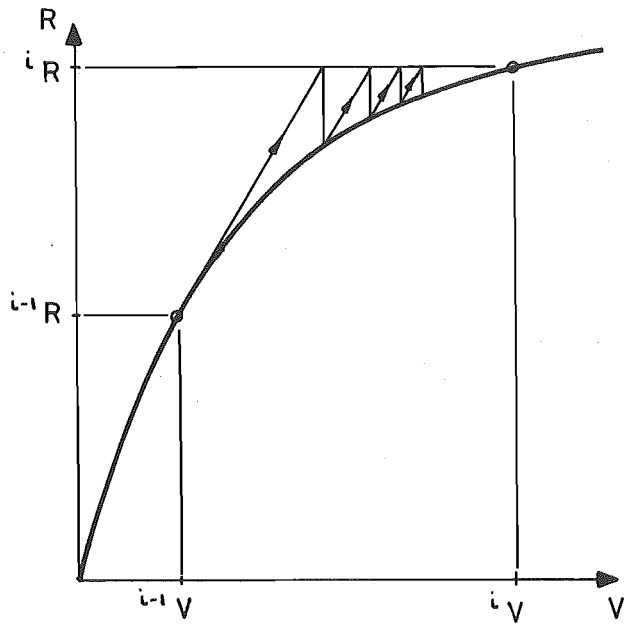

FIGURE 2.13 : MODIFIED NEWTON-RAPHSON ITERATION (SDOF STRUCTURE)

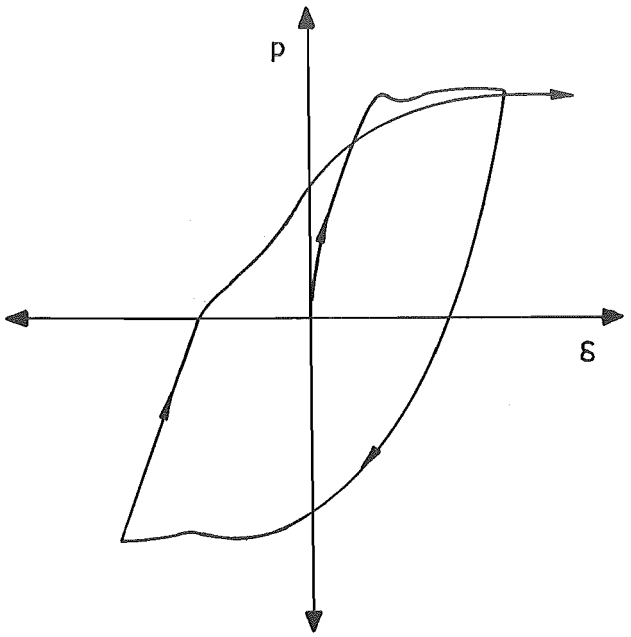

FIGURE 2.14 : EXAMPLE OF AN INELASTIC RESPONSE OF A REINFORCED CONCRETE MEMBER

necessary to abandon iteration until the solution is clear of the slope reversal. As indicated in Figure 2.14, these conditions can apply over a significant portion of the post-elastic response of a reinforced concrete structure. Therefore, in order to permit iterated solutions to be readily obtained over the full range of the response, a displacement controlled iteration procedure was developed and has been incorporated into the computer program. This procedure, which is used in conjunction with the standard N-R iteration technique described in Section 2.5.3, also permits the applied loading to be more effectively controlled.

2.5.5.1 Scalar Displacement Variable

The displacement control procedure operates under the same principle of load incrementation as the standard N-R procedure, i.e. $\mathbf{R} = p.\mathbf{R}_{ref} + \mathbf{R}_o$. However, in this case the loading is specified in fixed increments of the overall magnitude of displacement*, rather than in fixed increments of force ($\Delta p = \bar{p}$). The first requirement is therefore to define a suitable scalar variable, δ, to represent the magnitude of the vector displacement field, $\mathbf{V}$, i.e.

$$\delta = f(\mathbf{V}) = f'(p) \qquad \ldots (2.31)$$

This variable serves as the control variable for the iteration process. Any variable which is a linear function of the displacements** will, in general, be satisfactory provided that there is a continuous equilibrium path $\delta(p)$ having no limit points $\delta_{,p} = 0$ within the solution interval (Figure 2.15). However, to ensure that the range over which displacement control can be applied is not unnecessarily restricted, it is best to select a variable which is representative of the overall response.

In the present study, one of the components of the nodal displacement

---

* There is still only one independent load variable. The resulting pattern of displacement is a function of the load pattern and the response of the structure.

** More precisely, δ is required to be a linear function of the displacements of an equivalent elastic structure with a stiffness matrix equal to $\mathbf{K}_t$ in Equation 2.30b.

vector was always used as the control variable, i.e.

$$i_{\delta}(j) = i_{V_{\overline{\alpha}}}(j) \qquad \ldots (2.32)$$

where $\overline{\alpha}$ is the nodal degree of freedom specified for displacement control. For some complex geometrically nonlinear responses it can be difficult to select a sufficiently representative displacement component without foreknowledge of the form of the response. In these cases, a suitably weighted average of the displacements at the load points would probably be a better control variable. However, in all the materially nonlinear analyses in this study (and the majority of geometrically non-linear analyses), use of a single displacement component as the control variable proved to be completely satisfactory and to provide very effective control over the iteration process. Also, this definition of the control variable was very convenient for specifying load reversal displacement limits, e.g. by using the tip deflection of a cantilever, or the top floor deflection of a frame as the control variable.

2.5.5.2 Iteration Technique

In pure or incremental-pure iteration, the displacements are always directly related to the applied loads, e.g. for pure iteration*, $\mathbf{R}^{(j)} = \mathbf{K}_s^{(j)} \mathbf{V}^{(j)}$ during every iteration j. Displacement control therefore requires only simple scaling of the applied loads to maintain $\delta^{(j)}$ at any prescribed value ($\overline{\delta}$) throughout the iteration process.

In Newton-Raphson (N-R) iteration, the displacements and applied loading are not directly related and consequently a simple scaling procedure cannot be used. In this case, the procedure that has been developed is shown in Figure 2.15. This procedure is governed by the set of recurrence relations:

---

* Note that in displacement controlled solution processes, the total applied load $\mathbf{R}^{(j)}$ will, in general, vary from iteration to iteration.

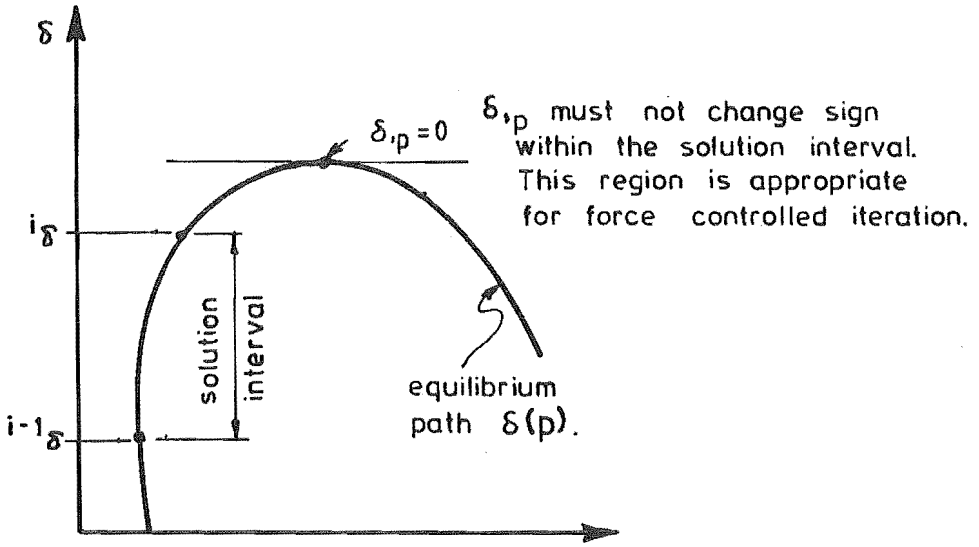

FIGURE 2.15 : EQUILIBRIUM PATH $\delta(p)$

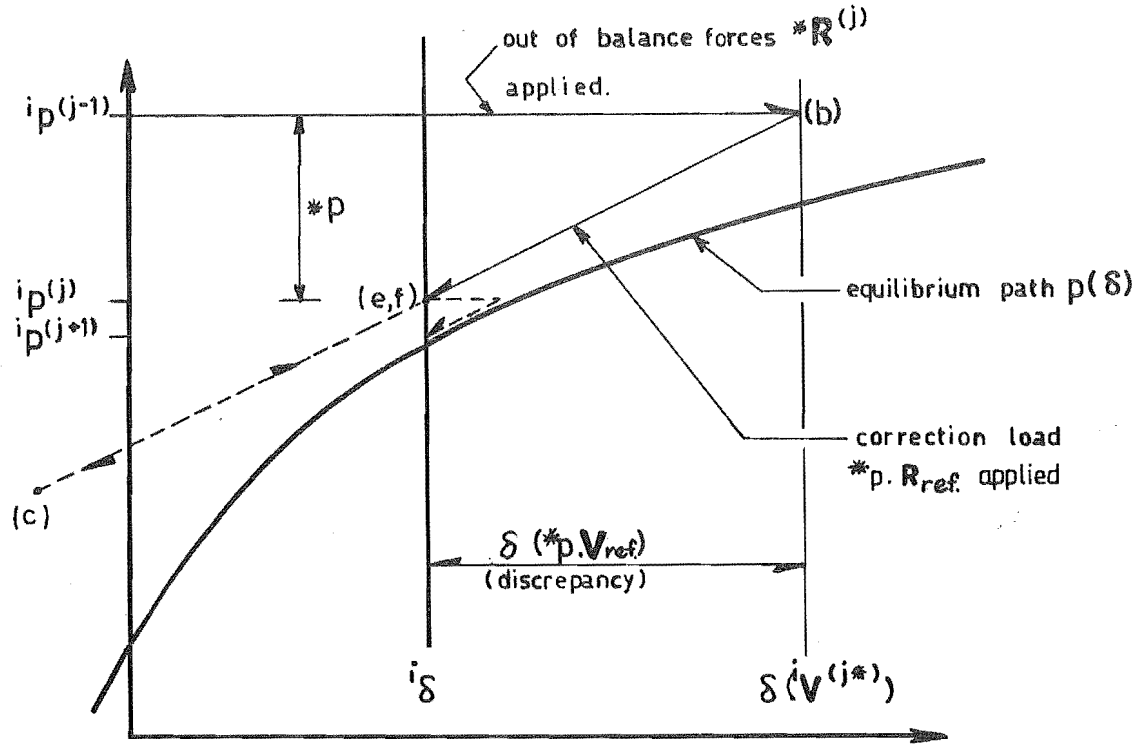

FIGURE 2.16 : DISPLACEMENT CONTROL PROCEDURE FOR NEWTON-RAPHSON ITERATION

$$ {}^{*}\mathbf{R}^{(j)} = {}^{i}\mathbf{R}^{(j)} - \mathbf{R}_r({}^{i}\mathbf{V}^{(j-1)}) \qquad \ldots (2.33a) $$

$$ {}^{i}\mathbf{V}^{(j*)} = [\mathbf{K}_t({}^{i}\mathbf{V}^{(j-1)})]^{-1}.{}^{*}\mathbf{R}^{(j)} + {}^{i}\mathbf{V}^{(j-1)} \qquad \ldots (2.33b) $$

$$ \mathbf{V}_{ref} = [\mathbf{K}_t({}^{i}\mathbf{V}^{(j-1)})]^{-1}.\mathbf{R}_{ref} \qquad \ldots (2.33c) $$

$$ {}^{*}p = [{}^{i}\delta - \delta({}^{i}\mathbf{V}^{(j*)})]/\delta(\mathbf{V}_{ref}) \qquad \ldots (2.33d) $$

$$ {}^{i}\mathbf{V}^{(j)} = {}^{i}\mathbf{V}^{(j*)} + {}^{*}p.\mathbf{V}_{ref} \qquad \ldots (2.33e) $$

$$ {}^{i}\mathbf{R}^{(j+1)} = {}^{i}\mathbf{R}^{(j)} + {}^{*}p.\mathbf{R}_{ref} \qquad \ldots (2.33f) $$

The first two equations in this set are similar to Eqs. 2.30. They are applied in the same manner, excepting that the total applied load ${}^{i}\mathbf{R}^{(j)}$ no longer remains constant during iteration. These two equations yield ${}^{i}\mathbf{V}^{(j*)}$, the displacements consistent with ${}^{i}\mathbf{R}^{(j)}$, i.e. the displacements determined by standard N-R iteration prior to applying displacement control. This is shown as point b in Figure 2.16. In the case shown, this has caused the displacement δ to overshoot the limit (${}^{i}\delta$) prescribed for increment i. The third step (Eq. 2.33c) is to compute the displacements $\mathbf{V}_{ref}$ that would be induced if the full reference load vector $\mathbf{R}_{ref}$ were applied to the structure assuming it responded in accordance with its tangential stiffness matrix. If these displacements (i.e. $\mathbf{V}_{ref}$) were subtracted in full from the structure displacement field, the solution would move to point c in Figure 2.16. In the example shown, this would cause δ to overshoot ${}^{i}\delta$ in the other direction. The fourth step (Eq. 2.33d) is therefore to determine what proportion (${}^{*}p$) of $\mathbf{V}_{ref}$ has to be subtracted to ensure that ${}^{i}\delta^{(j)} \equiv {}^{i}\delta$, i.e. such that ${}^{i}\delta({}^{i}\mathbf{V}^{(j*)}) + {}^{*}p.\delta(\mathbf{V}_{ref}) = {}^{i}\delta$. The required displacement correction is therefore ${}^{*}p.\mathbf{V}_{ref}$ and since $\mathbf{R}_{ref} = \mathbf{K}_t.\mathbf{V}_{ref}$ (Eq. 2.33c), the adjustment to the applied loading necessary to make this correction is ${}^{*}p.\mathbf{R}_{inc}$. These adjustments are made in Eqs. 2.33e and 2.33f, i.e. point (e,f) in Figure 2.16. These yield the new vectors ${}^{i}\mathbf{R}^{(j+1)}$ and ${}^{i}\mathbf{V}^{(j)}$ for the applied loading and the displacement field. These are used as the starting point for the next iteration. The process is then repeated until satisfactory convergence of the solution is established.

The above displacement control technique is used in conjunction with the standard N-R iteration procedure. Each increment starts off under force controlled iteration, but the solution changes automatically to displacement control if the prescribed displacement limit is exceeded. This can occur at any stage, including during the initial application of the load increment in the first iteration. In the formulation used in this study, the solution process is prevented from reverting back to force control until the start of the next increment. Once under displacement control, it must remain so until the solution has converged. This was necessary to prevent solution oscillation in regions where the slope of the response ($\delta_{,p}$) changes sign.

The differences between force and displacement control can be viewed as follows: In the standard force iteration techniques, a scalar load variable ^{i}p is prescribed and the solution process iterates to obtain the N displacement components (V_1, V_2, ..., V_N). In the displacement procedure, one of the displacement components is prescribed, and the solution process iterates to obtain the load ^{i}p and the remaining N-1 displacement components. This iteration process extends to the overall structure, the facility for force redistribution which occurs at an element level in a statically indeterminate structure subjected to standard force iteration, e.g., if an element is overloaded, the excess above yield load will be removed from the element and transferred to the surrounding structure (assuming that the element is weak compared with the structure as a whole). Under displacement controlled iteration, any overload is removed from the structure by adjusting the applied load.

2.5.5.3 Advantages of Displacement Control

There are three main advantages of using displacement control in conjunction with standard force iteration.

(a) Solution Stability

The stability of solution convergence is enhanced in two ways. First, structure overload no longer presents any significant

problems (e.g. Figure 2.17) as the iteration procedure automatically reduces the loads applied without interrupting the solution convergence. Secondly, the rigid control over displacements prevents solution oscillation in the vicinity of limit and bifurcation points. As shown in Figure 2.18, the procedure consistently maintains ${}^{i}\delta^{(j)} \equiv {}^{i}\delta$, regardless of whether the stiffness is positive or negative.

Because of the greater stability of the solution procedure, contingent provision for abandoning a partly iterated increment and the retention of back-up storage for restarting the iteration process, are no longer necessary. By selective use of either displacement control or standard force iteration, as appropriate, it will generally be possible to effect convergence at any desired point on a response.

(b) Control Over Loading

The usual approach to displacement incrementation is to scale the load vector only on the basis of the deflections computed when the load increment is first applied (61). Because there is no control over the displacements during subsequent iteration, the resulting displacement increments can become erratic in regions where the response is highly nonlinear. The displacement control procedure described in Eq. 2.33 operates during all iterations and thus ensures that the solution converges to the specified displacement increment. This ensures uniform displacement increments and makes it possible to converge directly to the specified displacement limit for each load reversal (Figure 2.19).

(c) Rate of Convergence

The Newton-Raphson procedure operates by making successively improving approximations to the equilibrium displacement vector ${}^{i}\mathbf{V}$. The accuracy of the estimated displacement vector ${}^{i}\mathbf{V}^{(j)}$ in the j^{th} iteration considerably influences the number of subsequent iteration cycles required for convergence. In general, the prescription ${}^{i}\delta^{(j)} \equiv {}^{i}\delta$ provides a better approximation to ${}^{i}\mathbf{V}$ than is obtained by prescribing ${}^{i}p^{(j)} \equiv {}^{i}p$. The

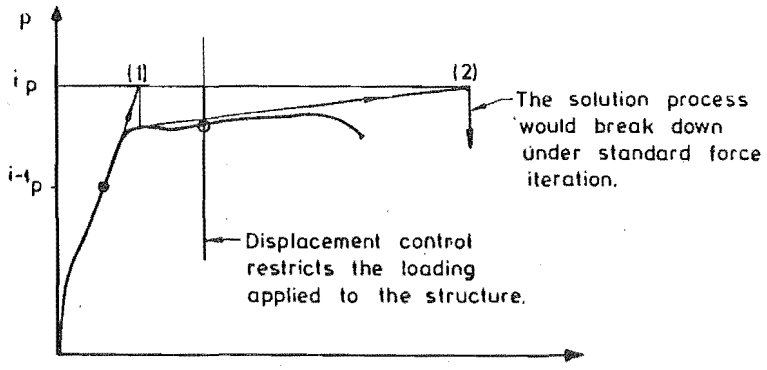

FIGURE 2.17 : PREVENTION OF SOLUTION FAILURE DUE TO OVERLOADING

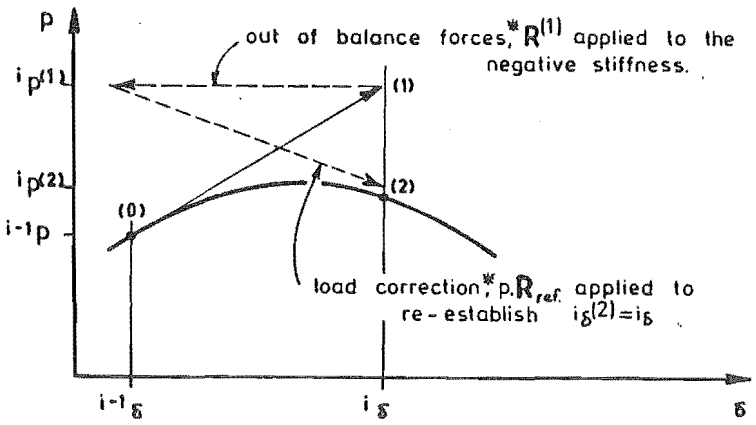

FIGURE 2.18 : SOLUTION CONVERGENCE FOR AN INCREMENT WHICH CROSSES A LIMIT POINT

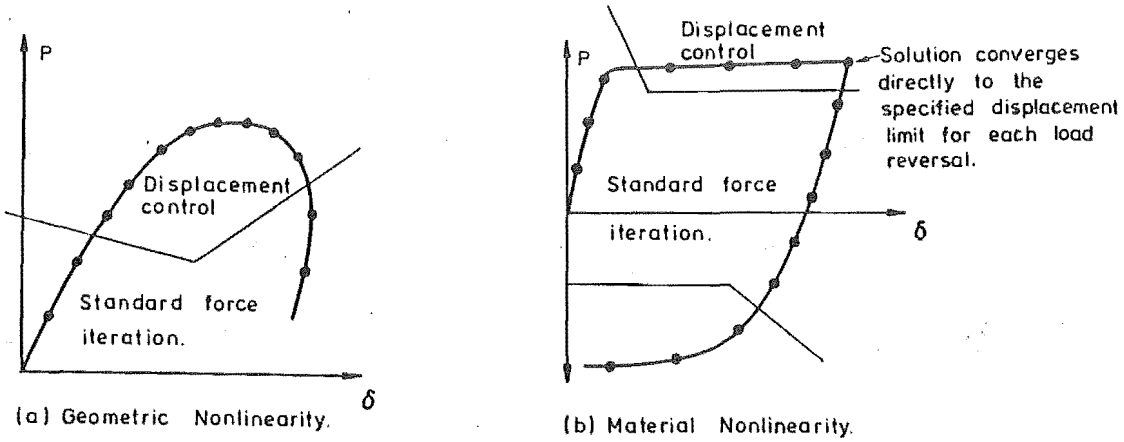

FIGURE 2.19 : COMBINED FORCE AND DISPLACEMENT CONTROL

accuracy of the approximation, and thus the number of iterations required, is also far less sensitive to increment size. Consequently, the improvement in convergence rate increases as the size of increment increases. These effects are, however, more pronounced in geometrically nonlinear analyses. The size of increment in a materially nonlinear analysis will usually be limited by the material constitutive relationships and consequently the improvements in convergence rate will be less pronounced.

2.5.6 Solution of the Force-Displacement Equations

The equation solver used in the computer program for solving the force-displacement equations (Eqs. 2.30b and 2.33b) is based on the Gaussian column elimination algorithm shown in Figure 2.20. For this procedure, the stiffness matrix is separated into columns, and only the elements between the first non-zero element and the diagonal are stored or operated on. The operations performed on each element are the same as in the more common Gaussian band elimination scheme. However, because of the rearranged sequence of elimination, almost all unnecessary operations are eliminated without specific checking for zero elements. As a result, the computation time depends more on the storage area of the stiffness matrix than on the maximum bandwidth. This can substantially reduce the time required to solve the force-displacement equations, particularly if the bandwidth varies considerably.

To further reduce the cost of solving the force-displacement equations, the equation solver subroutine was coded in VECTORMODE ALGOL. This coding was found to be up to 3½ times faster than the equivalent standard FORTRAN code.

2.5.7 Convergence Criterion

For the majority of analyses it is not necessary to establish convergence at each response component independently, and consequently an overall evaluation of convergence is generally used. Probably the most common approach is to use either a force or displacement criterion of the form

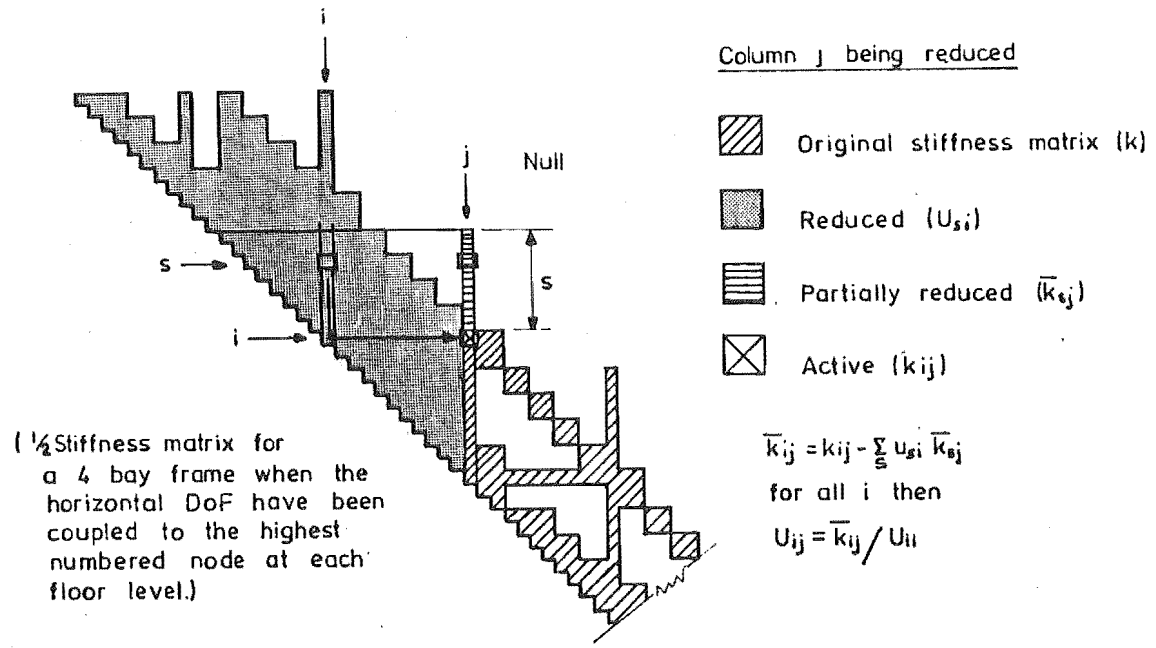

FIGURE 2.20 : COLUMN ELIMINATION ALGORITHM FOR GAUSSIAN DECOMPOSITION

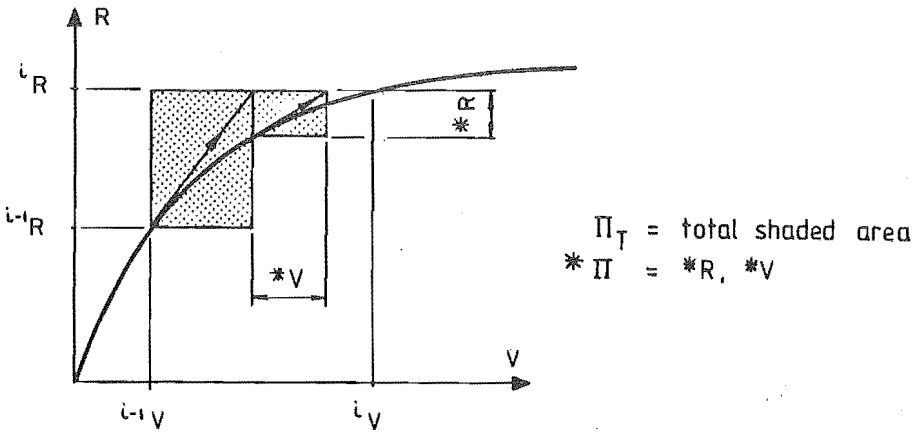

FIGURE 2.21 : ENERGY SUMMATION FOR CONVERGENCE CRITERION (CHARACTERIZATION)

$$||{}^{*}\mathbf{R}|| \,/\, ||{}^{i}\mathbf{R}|| \leq {}^{*}\Delta \qquad \ldots (2.34a)$$

where $||{}^{*}\mathbf{R}||$ and $||{}^{i}\mathbf{R}||$ are the Euclidian norms of the out-of-balance forces and the applied loading respectively; or

$$||{}^{*}\mathbf{V}|| \,/\, ||{}^{i}\mathbf{V}|| \leq {}^{*}\Delta \qquad \ldots (2.34b)$$

where $||{}^{*}\mathbf{V}||$ and $||{}^{i}\mathbf{V}||$ are the Euclidian norms of the correction and total displacement vectors respectively, and ${}^{*}\Delta$ is the prescribed convergence tolerance.

One disadvantage of these criteria is that, due to dimensional inconsistency, the rotational force (i.e. moment) and translational displacement degrees of freedom will generally be heavily weighted in comparison with the other force and displacement degrees of freedom. In many applications this weighting is not important as the convergence of the rotational and translational responses are unlikely to be significantly out of phase. Nevertheless, to avoid any bias, some analysts have preferred to use modified norms based on nondimensionalized forces or displacements (61, 62). In this study, an energy based criterion has been adopted, i.e.

$${}^{*}\pi/\pi_{T} < {}^{*}\Delta \qquad \ldots (2.35)$$

where ${}^{*}\pi = {}^{*}\mathbf{R}.\ {}^{*}\mathbf{V}$, and $\pi_{T} = \Sigma\ {}^{*}\pi$ (shaded area, Figure 2.21).

This criterion takes account of both forces and displacements, and, as the response at each degree of freedom is weighted in accordance with its energy participation, it directly reflects the degree of internal energy redistribution. A value of ${}^{*}\Delta = 0.01$ was normally used for geometrically nonlinear analyses and analyses of individual reinforced concrete sections. However, to minimise the risk of the solution being prematurely assessed as converged, ${}^{*}\Delta$ was normally reduced to 0.001 for materially nonlinear analyses of reinforced concrete frames.

2.6 GENERAL DETAILS OF PROGRAM

This section examines several general aspects related to the computer program. The basic solution steps for a combined materially and geometrically nonlinear analysis are summarised and details related to coupling of horizontal floor displacements and computation times requirements for materially nonlinear analyses are discussed.

2.6.1 Program Structure

The basic program steps performed in a combined materially and geometrically nonlinear analysis are summarised in Table 2.2. The description given is for the Newton-Raphson iteration and recursive geometric nonlinearity options, and excludes details of peripheral operations (e.g., base reactions, input-output details) and of the section analysis procedure. Furthermore, the ordering of the individual operations is not, in all cases, identical with that in the computer code.

2.6.2 Coupling of Degrees of Freedom

For a large frame with comparatively flexible beams, the high cost of decomposing the stiffness matrix at every iteration can be partially offset by coupling all the horizontal degrees of freedom at each floor level.

However, coupling the horizontal degrees of freedom constrains the frame behaviour, and would not normally be regarded as valid for an analysis which accounts for inelastic axial expansion of the beam plastic hinge zones. Two effects need to be considered:

(a) The restraint against expansion of the beam hinge zones would normally induce large axial compressive forces in the beams, which would subsequently modify the moment-curvature response of the plastic hinge zone. The induced axial forces can, however, be avoided by specifying real hinges at the member axial degrees of freedom (= slots). This uncouples the member axial degree of freedom (r_1, v_1) from the joint node displacements, permitting unrestrained elongation of the beams, while still maintaining

slope continuity between the beam and column node rotations. This does not model the true behaviour, as, in general, some axial force will be induced in the beams due to slab restraint, frame interaction and transmition of forces between the slabs and columns. However, due to the inadequate treatment of the effect of the slabs, specifying independent horizontal displacement degrees of freedom at each column will not necessarily improve the results. It would probably be more realistic to attempt to model the slab restraint at the section level, possibly by including a small area of non-yielding steel in the flange.

(b) Coupling the horizontal degrees of freedoms means that equal horizontal displacements are imposed on each column, whereas, in the real structure, there would be some differential displacement due to expansion of the beam-slab system. However, the differential displacements in the real structure are likely to remain small in comparison with the total displacements imposed, and consequently they should not significantly affect the response.

2.6.3 Efficiency of the Program Code

Coding efficiency is often one of the more neglected areas in the development of computer programs. However, because of the large computation time requirements anticipated for the present computer program, it was important that considerable attention be given to the efficiency of the coding used in the critical member and section analysis subroutines. Generally, Central Processor Unit (CPU) time was used as the main criterion of efficiency, and this has resulted in the code being somewhat more bulky than is usual. Some of the steps taken to improve the efficiency were to keep the critical subroutine sizes as large as practicable so as to avoid data transfer costs, to minimise use of functions such as sine, log and exponentiation in critical parts of the code, and to replace small arrays by scalars.

The extent to which the computation time can be affected by the coding used is illustrated by the example given in Table 2.3. This comparison

of identical matrix transformations from the present computer program and from Sharpe's program (53) shows that a 40 fold reduction in computer time was obtained by using scalar arithmetic and only evaluating the 10 independent elements of the element stiffness matrix. The FORTRAN DO loops alone take 7 times as long as the scalar transformation. Possibly a more appropriate measure is that the absolute reduction in CPU time of almost 8000 microseconds is approximately equal to the average CPU time required for analysing a reinforced concrete beam or column section subjected to post-elastic cyclic loading (one iteration). For a coarse member idealization with only one segment at each end, the savings on the various transformations and in other areas of the code, would probably more than offset the cost of the nonlinear section analyses.

TABLE 2.2 : BASIC SOLUTION ALGORITHM

Initialization:

(1) Input and echo all data.

(2) Initialize and store:

(a) per section; ${}^{o}f_t$ (section flexibility matrices)

(b) per member; ${}^{o}S_t$, $T({}^{o}C_e)$ (member stiffness and transformation matrices)

(c) for the structure; ${}^{o}K_t$ (structural stiffness matrix).

Start New Load Reversal: (Note 1)

(3) Compute new direction of force and displacement loading; LR = LR + 1.

(4) Compute the maximum force and displacement increments, $\Delta p_{LR} = p_{LR} - p_{LR-1}$ and $\Delta\delta_{LR} = \delta_{LR} - \delta_{LR-1}$, to be applied during the load reversal.

Start New Load Increment:

(5) Set: $i = i + 1$ (increment count)
$j = 0$ (iteration count)
$\pi = 0$ (incremental energy)
$NUPD = 0$

(6) Compute maximum increments of force and displacement, Δp and $\Delta\delta$, consistent with specified maximum increments, $\overline{p}$ and $\overline{\delta}$, and with Δp_{LR} and $\Delta\delta_{LR}$.

(7) Set: ${}^{*}R^{(1)} = \Delta p \cdot R_{ref} + {}^{*}R$ (${}^{*}R$, are the residual out-of-balance nodal forces from the previous increment)
${}^{i}\delta = {}^{i-1}\delta + \Delta\delta$

Start New Iteration:

(8) Set: $j = j+1$

for the overall structure:

(9) Solve: ${}^{*}V^{(j)} = ({}^{i}K^{(j-1)})^{-1} \cdot {}^{*}R^{(j)}$

(10) Compute: ${}^{*}\pi = [{}^{*}R^{(j)}]^T \cdot {}^{*}V^{(j)}$

(11) ${}^{i}\delta^{(j)} = {}^{i}\delta^{(j-1)} + \delta({}^{*}V^{(j)})$

(12) Check: $|{}^{i}\delta^{(j)}| \leq |{}^{i}\delta|$?

(13) ${}^{*}\pi/\pi_T^{(j-1)} \leq 0$? If so, horizontal tangent?

(14) If (12) or (13) affirmative, place iteration under displacement control, which is maintained for the remainder of the current increment.

(15) If under displacement control, compute $\Delta p^{(j)} = p(\Delta\delta)$. Adjust ${}^{*}\pi$ and ${}^{*}V$ accordingly (Section 2.5.5).

(16) Set: $\pi_T^{(j)} = \pi_T^{(j-1)} + {}^{*}\pi$

(17) If ${}^{*}\pi/\pi_T^{(j)} < {}^{*}\Delta$, $NUPD = 2$ (solution converged, Eq. 2.35).

(18) If $j \geq j_{max}$, $NUPD = 2$

(19) Set: ${}^{i}K^{(j-1)} = 0$ (null matrix)

(20) ${}^{i}p^{(j)} = {}^{i-1}p + p^{(j)} + \Delta p^{(j)}$

(21) ${}^{i}R^{(j)} = {}^{i}p^{(j)} \cdot R_{ref} + R_o$ (total load on structure)

(22) ${}^{i}V^{(j)} = {}^{i}V^{(j-1)} + {}^{*}V^{(j)}$

for each element:

(23) Extract: ${}^{*}\mathbf{V}_e$ from ${}^{*}\mathbf{V}^{(j)}$ (element nodal displacement)

(24) Set: $\mathbf{V}_e^{(j)} = \mathbf{V}_e^{(j-1)} + {}^{*}\mathbf{V}_e$ (element displacement during current increment)

(25) Compute: ${}^{*}v = {}^{i}\mathbf{T}^{(j-1)} \cdot {}^{*}\mathbf{V}_e$ (member displacements due to ${}^{*}\mathbf{R}^{(j)}$)

(26) $v^{(j)} = v^{(j-1)} + {}^{*}v$ (member displacement during current increment, assuming $C_e = {}^{i}C_e^{(j-1)}$)

(27) ${}^{*}r = {}^{i}\mathbf{S}_t^{(j-1)} \cdot {}^{*}v$ (member forces due to ${}^{*}\mathbf{R}^{(j)}$)

(28) ${}^{i}r^{(j)} = {}^{i}r^{(j-1)} + {}^{*}r$ (total applied member force)

(29) $\Delta r^{(j)} = {}^{*}r - {}^{*}r^{(j-1)}$ (change in applied member force since previous iteration due to force redistribution within the structure and loading/unloading by the global solution procedure. ${}^{*}r^{(j-1)}$ computed step 52)

for each section:

(30) If member elastic, go directly to step 42.

(31) Compute: ${}^{i}q^{(j)} = fn({}^{i}r^{(j)})$ (total force applied to section)

(32) $\Delta q^{(j)} = fn(\Delta r^{(j)})$ (change in applied section force since previous iteration)

(33) Compute: ${}^{i}\epsilon^{(j)} = {}^{i}f_t^{(j-1)} \cdot \Delta q^{(j)} + {}^{i}\epsilon^{(j-1)}$ (total section strain)

(34) Consistent with the material constitutive relationships and the strain history, analyse the section for ${}^{i}\epsilon^{(j)}$, and obtain ${}^{i}f_t^{(j)}$, the new section flexibility matrix, and q_r, the forces resisted by the section at a strain of ${}^{i}\epsilon^{(j)}$. Update the strain history terms only if NUPD = 2.

(35) Compute: ${}^{*}m_q^{(j)} = {}^{i}q^{(j)} - q_r$ (out of balance section forces due to material nonlinearities)

(36) ${}^{*}m_\epsilon = {}^{i}f_t^{(j)} \cdot {}^{*}m_q^{(j)}$ (additional strain required for the section to resist the out of balance force = section strain incompatibility)

(37) ${}^{i}\epsilon^{(j)} = {}^{i}\epsilon^{(j)} + {}^{*}m_\epsilon$ (total section strain consistent with the force ${}^{i}q^{(j)}$ acting on the section, Note 2)

for each element:

(38) Compute: ${}^{i}\mathbf{A}_t^{(j)} = \int_0^L {}^{i}f_t^{(j)}.ds$ (member flexibility - includes anchorage flexibility components)

(39) ${}^{*}m_v = \int_0^L {}^{*}m_\epsilon.ds$ (section strain incompatibilities integrated over member length to yield member displacement incompatibility - includes anchorage components. Note 3)

(40) ${}^{i}\mathbf{S}_t^{(j)} = [{}^{i}\mathbf{A}_t^{(j)}]^{-1}$ (new member tangential stiffness matrix)

(41) Adjust: ${}^{i}\mathbf{S}_t^{(j)}$ for real hinges (if any), and store. Note 4.

(42) Compute: ${}^{i}C_e^{(j)} = C_e({}^{i-1}C_e, \mathbf{V}_e^{(j)})$ (updated configuration parameters - store only if NUPD = 2)

(44) ${}^{i}\mathbf{T}^{(j)} = \mathbf{T}({}^{i}C_e^{(j)})$ (new transformation matrix; store)

(45) ${}^{i}\mathbf{F}^{(j)} = \mathbf{F}({}^{i}C_e^{(j)}, {}^{i}(j))$ (initial stress stiffness matrix)

(46) ${}^{i}\mathbf{K}_{et}^{(j)} = [{}^{i}\mathbf{T}^{(j)}]^T.{}^{i}\mathbf{S}^{(j)}.[{}^{i}\mathbf{T}^{(j)}] + {}^{i}\mathbf{F}^{(j)}$ (nodal stiffness matrix of the element)

(47) $\mathbf{C}^{(j)} = \frac{1}{2}[{}^{i}\mathbf{T}^{(j)} + {}^{i-1}\mathbf{T}]$ (compatibility transformation matrix)

(48) ${}^{c}v = \mathbf{C}^{(j)}.\mathbf{V}_e^{(j)}$ (incremental member displacements compatible with the incremental nodal displacements, $\mathbf{V}_e^{(j)}$)

(49) $^{*}g_{v} = v^{(j)} - c_{v}$ (geometric component of member displacement incompatibility - $v^{(j)}$ from step 26)

(50) $^{*}v = {}^{*m}v + {}^{*g}v$ (total member displacement incompatibility)

(51) $v^{(j)} = c_{v}$ (except, if NUPD = 2, $v^{(j)} = 0$ - store)

(52) $^{*}r^{(j)} = {}^{i}S_{t} \cdot {}^{*}v$ (member forces required to eliminate the member displacement incompatibility. Store)

(53) $^{i}r^{(j)} = {}^{i}r^{(j)} - {}^{*}r^{(j)}$ (total member force consistent with the nodal displacements, $^{i}V^{(j)}$, the constitutive material responses, and the strain history)

(54) $^{i}K_{t}^{(j)} = \sum_{e} {}^{i}K_{et}^{(j)}$ (new structural tangential stiffness matrix. Σ over all elements)

(55) $^{*}R^{(j+1)} = {}^{i}R^{(j)} - \sum_{e} [{}^{i}T^{(j)}]^{T} \cdot {}^{i}r^{(j)}$ (equivalent nodal out of balance force = force to be applied during next iteration. Σ over all elements)

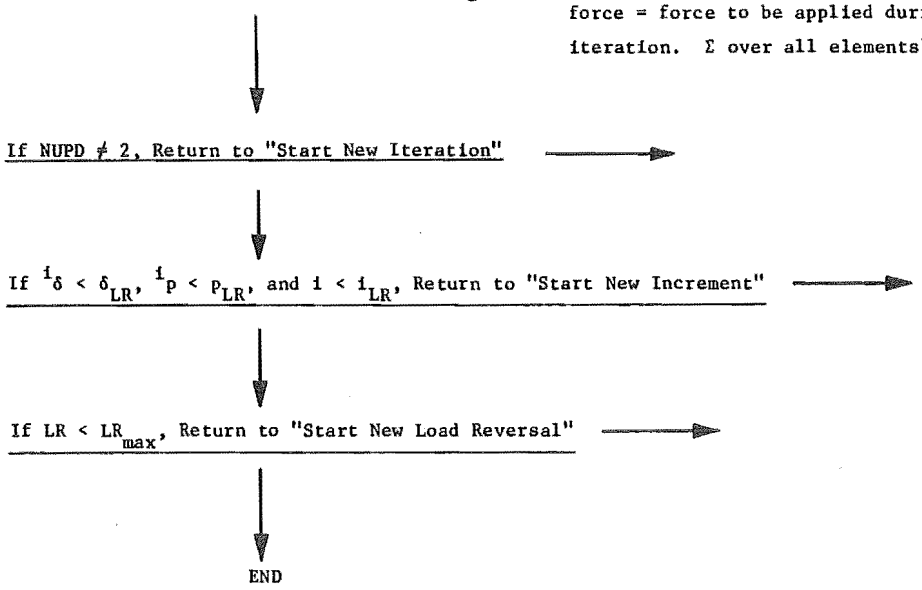

Note 1. To avoid complicating the summary, the application of the initial fixed load component, R_{o}, is not indicated.

Note 2. The operations performed during Steps 33 to 37 are illustrated in Figure 2.22 for a typical section, n, and degree of freedom, α (e.g., α = 1 = section axial strain degree of freedom.

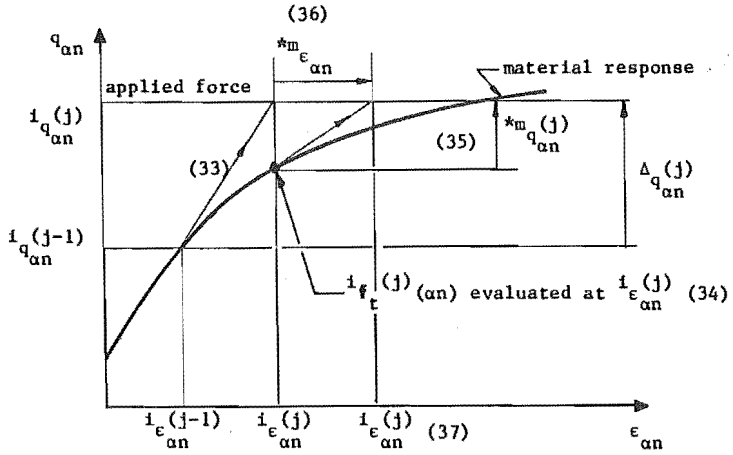

FIGURE 2.22 : EVALUATION OF MATERIAL COMPONENT OF OUT-OF-BALANCE FORCE

Note 3. The axial and flexural strain distributions required for this integration are unknown, and consequently assumed distributions must be used. Ideally, the strain distribution assumed for ${}^{*m}\boldsymbol{\epsilon}^{(j)}$ should be similar to the (unknown) distribution of strains associated with the correction forces ${}^{\Delta}\mathbf{r}^{(j+1)}$ in the next iteration, particularly in situations where the latter are, in part, an adjustment for overshoot of the solution caused by the former. This type of situation could cause difficulties with the solution procedure if the section integration points are not at the mid-points of the segments and the components of $({}^{*m}\mathbf{q}^{(j)} - {}^{\Delta}\mathbf{q}^{(j+1)})$ are small compared to the corresponding components of ${}^{*m}\mathbf{q}^{(j)}$. However, it is not possible to estimate the distribution of ${}^{\Delta}\mathbf{q}^{(j+1)}$ along a segment in advance, and in the program, the distributions of ${}^{*m}\epsilon_1{}^{(j)}$ and ${}^{*m}\epsilon_2{}^{(j)}$ are based on the distribution of the total section forces, ${}^{i}\mathbf{q}^{(j)}$. The approximation used, is to separate both ${}^{*m}\epsilon_1{}^{(j)}$ and ${}^{*m}\epsilon_2{}^{(j)}$ into axial force and moment related components according to the energy ratios $\phi_1 = {}^{*}\pi_{11}/({}^{*}\pi_{11} + {}^{*}\pi_{22})$ and $\phi_2 = {}^{*}\pi_{22}/({}^{*}\pi_{11} + {}^{*}\pi_{22})$, where ${}^{*}\pi_{11} = {}^{i}q_1{}^{(j)}.{}^{*m}\epsilon_1{}^{(j)}$ and ${}^{*}\pi_{22} = {}^{i}q_2{}^{(j)}.{}^{*m}\epsilon_2{}^{(j)}$. The axial force related components, $\phi_1.{}^{*m}\epsilon_1{}^{(j)}$ and $\phi_1.{}^{*m}\epsilon_2{}^{(j)}$ are integrated along each segment according to the axial force distribution (≡ uniform) and the moment related components, $\phi_2.{}^{*m}\epsilon_1{}^{(j)}$ and $\phi_2.{}^{*m}\epsilon_2{}^{(j)}$, are integrated according to the moment distribution.

Note 4. Real hinges can be specified at any one, or at any combination of the three member degrees of freedom, including the axial degree of freedom (= slot).

TABLE 2.3 : COMPUTATION TIMES FOR MATRIX TRANSFORMATION USING SCALAR AND ARRAY CODING

Program	Code	CPU time* (microseconds)
Author	SM11 = T11*P11 + T21*P12 + T31*P13 SM12 = T11*P21 + T21*P22 + T31*P23 . . . SM66 = T14*P41 + T24*P42 + T34*P43 (only 10 independent elements evaluated)	200
Sharpe (53)	DO 11 I = 1,6 DO 11 J = 1,6 SM(I,J) = 0.0 DO 11 K = 1,3 11 SM(I,J) = SM(I,J) + TRANS(K,I)*A(K,J)	8160
	DO 11 I = 1,6 DO 11 J = 1,6 DO 11 K = 1,3 11 CONTINUE	1500

* Times for the University of Canterbury's Burrough's B6718 computer (1977)

3. MODEL FOR PREDICTING STEEL RESPONSE

SUMMARY

This chapter describes the model developed for predicting the inelastic response of the reinforcing steel. The model uses the Ramberg-Osgood function for representing the Bauschinger effect in reversed post-elastic load paths, but its method of employment differs from the approach normally used. Existing models of reasonable accuracy were available, but these were found to be too inefficient for use in a frame analysis program where often hundreds of bar responses would have to be evaluated at every iteration. The proposed model is 10 to 20 times faster than the existing models for which codes were available, while still maintaining equal, and in some cases, better accuracy.

Another important aspect of this work was the development of special stabilizing procedures which made it possible to use the powerful Newton-Raphson solution procedure in the frame program.

3.1 INTRODUCTION

Because of the strong influence of the steel reinforcement on the behaviour of reinforced concrete members, past investigations have placed considerable emphasis on realistic representation of the steel response. As a result, a number of comparatively accurate models have been developed (12, 44, 48, 50, 63).

The original intention in this study was to directly incorporate an existing steel model into the frame analysis program. Attention was initially confined to models developed by Thompson (44) and, to a lesser extent, Kent (48), as the computer codes for these were readily available. Both models are based on the Ramberg-Osgood function (64) which has been shown to be particularly suited to modelling the behaviour of steel subjected to inelastic load reversals.

However, after investigation, it was found that the strain history storage and particularly the computation time requirements of these

models were well in excess of the limits that could be tolerated in the frame analysis program. Other models were available which offered some improvement, but the computation times still appeared to be excessive for the proposed use.

Because of the importance of the steel model to the success of the frame analysis program, it was necessary to develop a new model with particular emphasis on reducing the computation time. Fortunately this proved to be possible without sacrificing the quality of the predicted responses. Thompson's model, which is a development of Kent's work, has been used as a basis for evaluating the proposed model as results from it were available from the initial stages of the present investigation.

3.2 MONOTONIC LOADING CURVES

A typical stress-strain* response for a reinforcing bar loaded in tension consists of three well defined regions (Figure 3.1); an initial elastic region, the yield plateau, and the strain hardening branch. The relationships adopted to model these regions are discussed below:

(a) Elastic Region ($\varepsilon_s < \varepsilon_{sy}$): The response is assumed to be linerarly elastic up to a well defined yield point at $\varepsilon_s = \varepsilon_{sy}$, i.e.

$$\sigma_s = E_o \varepsilon_s \qquad \ldots (3.1a)$$

where σ_s is the steel stress, E_o is the initial elastic modulus, ε_s is the imposed steel strain, and ε_{sy} is the steel yield strain.

In practice, most reinforcing bars start to soften just before reaching their yield stress (Figure 3.1). This softening is largely a result of residual rolling stresses and variations in yield strength over the bar area. It is usually of little consequence and was therefore ignored.

---

*Except where explicitly stated otherwise, the terms 'stress' and 'strain' are used in their engineering sense as the nominal stress and strain based on the undeformed bar geometry.

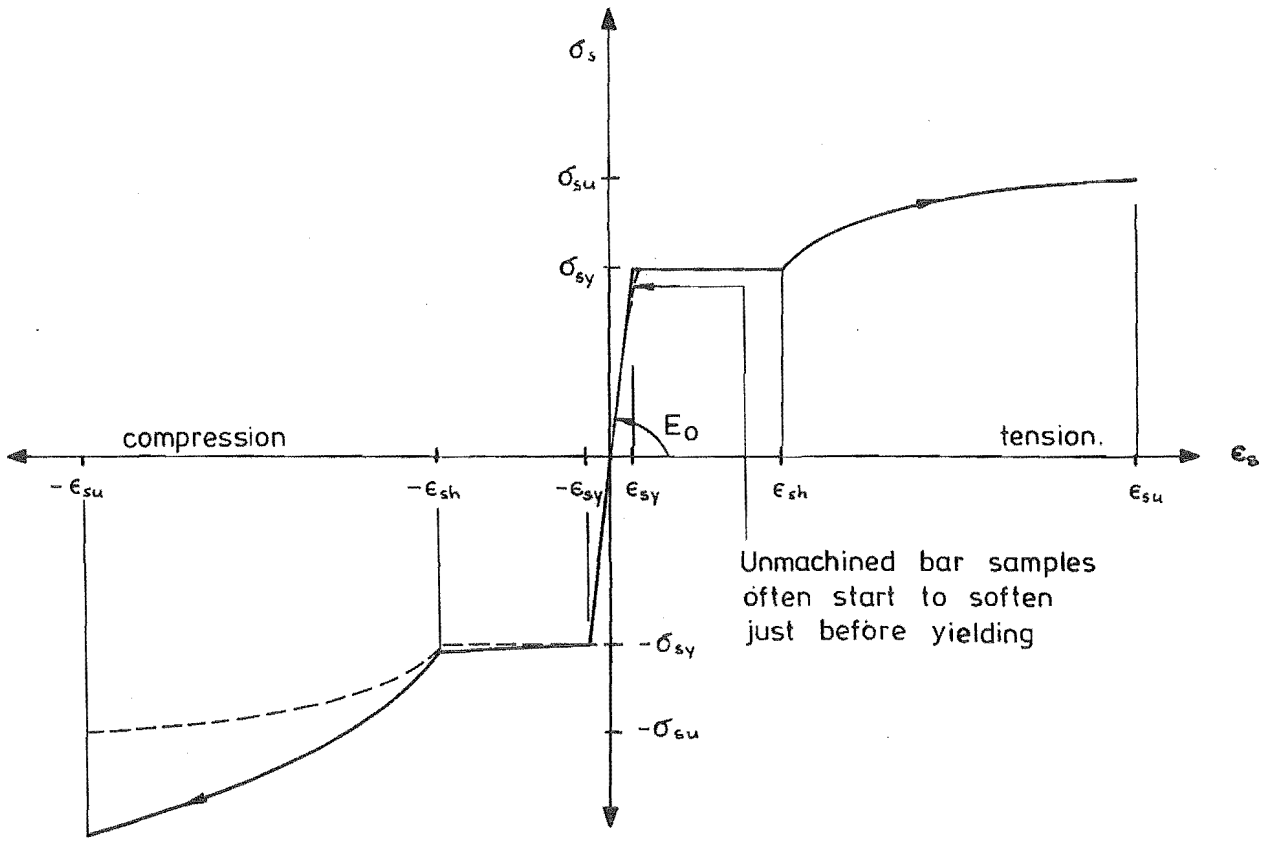

FIGURE 3.1 : TYPICAL MONOTONIC STRESS-STRAIN RELATIONSHIP FOR STEEL

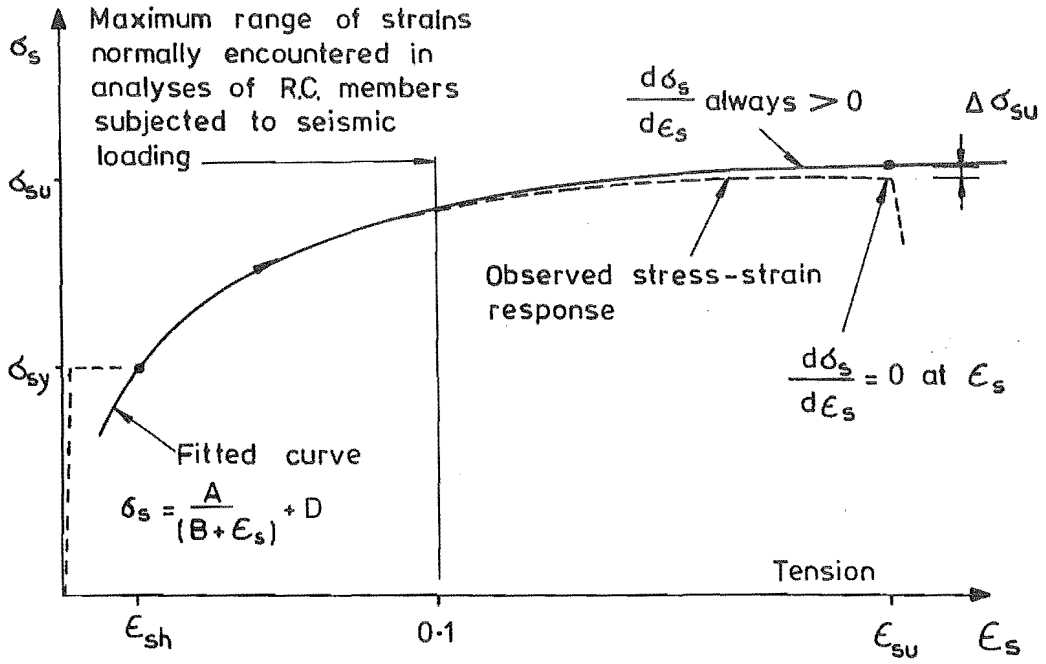

FIGURE 3.2 : COMPARISON BETWEEN OBSERVED AND ASSUMED STRAIN HARDENING BRANCH OF STEEL RESPONSE

(b) Yield Plateau ($\varepsilon_{sy} \leq \varepsilon_s < \varepsilon_{sh}$): Modelled as constant steel stress, i.e.

$$\sigma_s = \sigma_{sy} \qquad \ldots (3.1b)$$

where σ_{sy} is the steel yield strength and ε_{sh} is the strain at the onset of strain hardening (Figure 3.1).

(c) Strain Hardening Branch ($\varepsilon_{sh} \leq \varepsilon_s < \varepsilon_{su}$): This region is modelled using the relationship:

$$\sigma_s = A/(B + \varepsilon_s) + D \qquad \ldots (3.1c)$$

where A, B and D are model constants fitted to the measured stress-strain response of the steel, and ε_{su} is the ultimate strain of the steel.

A non-linear least squares computer program was written to evaluate the constants A, B and D from the measured stress-strain responses of the bars used in the experimental part of this study. However, it was later found that the strain hardening branches for most reinforcing bars could be modelled to within the accuracy of the bar tests using a fixed value of $A \simeq -7$ MPa. Only two constants (B and D) are then unknown and these can be found directly from the stress and strain at any two points on the strain hardening branch, i.e.

$$A = -7 \text{ MPa} \qquad \ldots (3.2a)$$

$$B = (\bar{\varepsilon}_s^{\,2} - A.\Delta\varepsilon_s/\Delta\sigma_s - \varepsilon_{s_1}.\varepsilon_{s_2})^{\frac{1}{2}} - \bar{\varepsilon}_s \qquad \ldots (3.2b)$$

$$D = -A/(\varepsilon_{s_2} + B) + \sigma_{s_2} \qquad \ldots (3.2c)$$

where σ_{s_1}, σ_{s_2} and ε_{s_1}, ε_{s_2} are respectively the stresses and strains at the two selected points on the strain hardening branch, $\Delta\varepsilon_s = \varepsilon_{s_1} - \varepsilon_{s_2}$, $\Delta\sigma_s = \sigma_{s_1} - \sigma_{s_2}$, and $\bar{\varepsilon}_s = (\varepsilon_{s_1} + \varepsilon_{s_2})/2$. In this study, values of $\varepsilon_{s_1} \simeq \varepsilon_{sh} + 0.01$ and $\varepsilon_{s_2} \simeq \varepsilon_{sh} + 0.04$ were normally used for the two points when suitable stress-strain data was available. Where detailed stress-strain measurements are not available, the onset of strain hardening

and ultimate bar strain* can be used to evaluate B. Estimates of these properties will generally be available for most types of steel.

As indicated in Figure 3.2, Eq. 3.1c cannot be made to accurately fit the full strain hardening branch as it does not satisfy the condition $d\sigma_s/d\varepsilon_s = 0$ at ultimate ($\varepsilon_s = \varepsilon_{su}$). Because of this, some analysts (48, 65) have used more general relationships of the form

$$\sigma_s = A/(B + \varepsilon_s) + C\varepsilon_s + D \qquad ...(3.3)$$

This form of relationship was initially investigated for use in the proposed steel model. However, it was found that the simpler relationship (Eq. 3.1c) gave just as good a fit to the experimental data over the full range of strains which were of interest in this study, i.e. ε_s generally less than 0.06 to 0.10.

The relationships given in Eq.3.1, with strain limits suitably adjusted, are also used as a basis for the compression loading curve. In this case the stresses computed in accordance with Eqs. 3.1b and c are also multiplied by $(1-2\varepsilon_s)$. This scaling factor makes allowance for the theoretical difference between the deformed bar areas at equivalent tensile and compressive strains (Poisson's ratio $\nu \simeq 0.5$ for plastic straining). The magnitude of this factor is consistent with the behaviour exhibited by machined bar specimens tested by Aktan et al. (63). Note that since ε_s is negative for compression, the factor $(1-2\varepsilon_s)$ is always greater than 1.

3.3 STRESS ENVELOPES FOR CYCLIC LOADING

The stress-strain response for monotonic loading has been shown by several investigators (44, 65) to approximately describe the envelope curve for reversed cyclic loading in which the net plastic strains

---

* When these points were used, the stress at ultimate was increased by a small amount $\Delta\sigma_{su}$ (generally about 5 MPa) as this usually gave a better fit of the stresses at the start of the strain hardening branch (see Figure 3.2).

imposed remain either entirely tensile or entirely compressive. By suitably displacing the curve origins (Figure 3.3), the same basic curves can also be used to stress envelope for general cyclic loading situations where both net tension and compression strains are imposed (44)*.

This approach has been adopted for the proposed model. As described later, these envelope curves form an integral part of the method of modelling softening of the steel response.

3.4 BAUSCHINGER EFFECT

The strain-softening behaviour of steel under reversed plastic loading is known as the Bauschinger effect (Figure 3.3). This effect becomes more pronounced with increasing magnitude of maximum plastic strain imposed in preceding load reversals.

In the proposed model, this softening behaviour is simulated using stress-strain load curves based on the Ramberg-Osgood function. The general form of this function can be written as:

$$C = X + X^r \qquad \ldots (3.4)$$

where $C = E_{xo}(\varepsilon_s - \varepsilon_{xo})/\sigma_{ch}$ and $X = (\sigma_s - \sigma_{xo})/\sigma_{ch}$ are the non-dimensional strain and stress on the theoretical curve; σ_{xo}, ε_{xo} are the stress and strain state at the beginning of the curve (Figure 3.4); σ_{ch} is the characteristic stress (Section 3.5.3), the sense of which is such that C and X are always positive; E_{xo} is the unloading modulus at the beginning of the curve; and r , the Ramberg-Osgood function exponent, is the parameter which determines the basic shape of the curve.

---

* Theoretically some scaling of both the tensile and compressive stress response would be expected because of the changed area of the bar at the new curve origins. However, this behaviour is not evident in the responses measured by Aktan et al. (63).

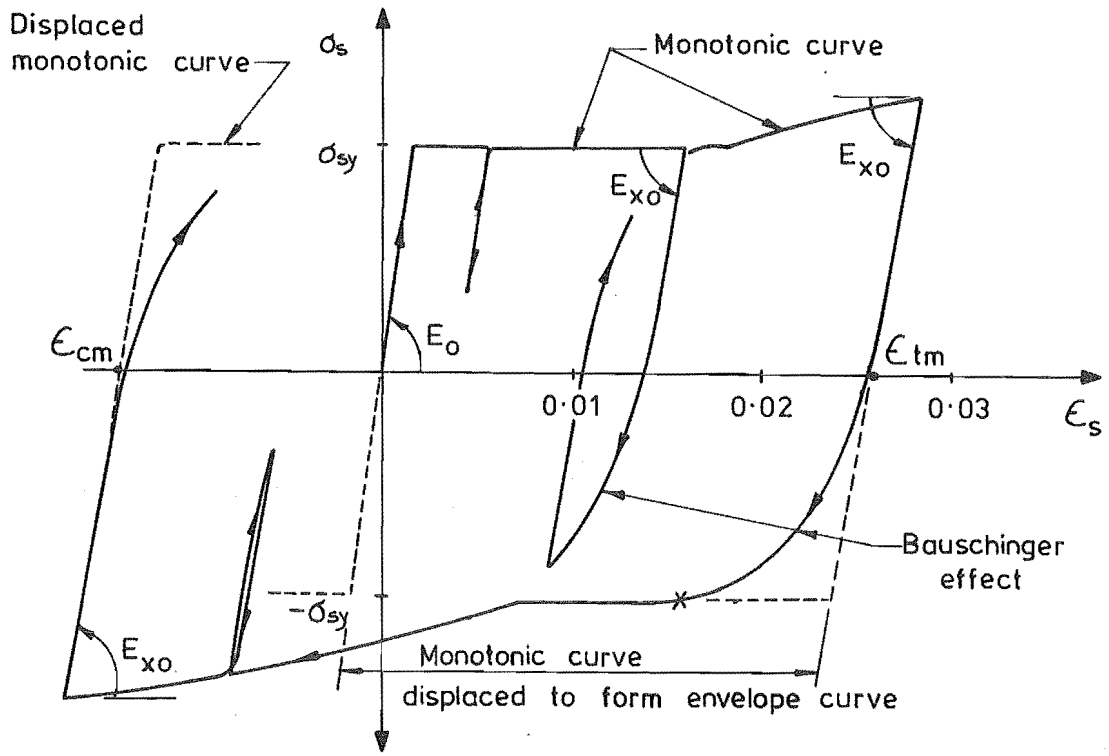

FIGURE 3.3 : TYPICAL STRESS-STRAIN RESPONSE OF GRADE 275 REINFORCING BAR SUBJECTED TO INELASTIC STRAIN REVERSALS

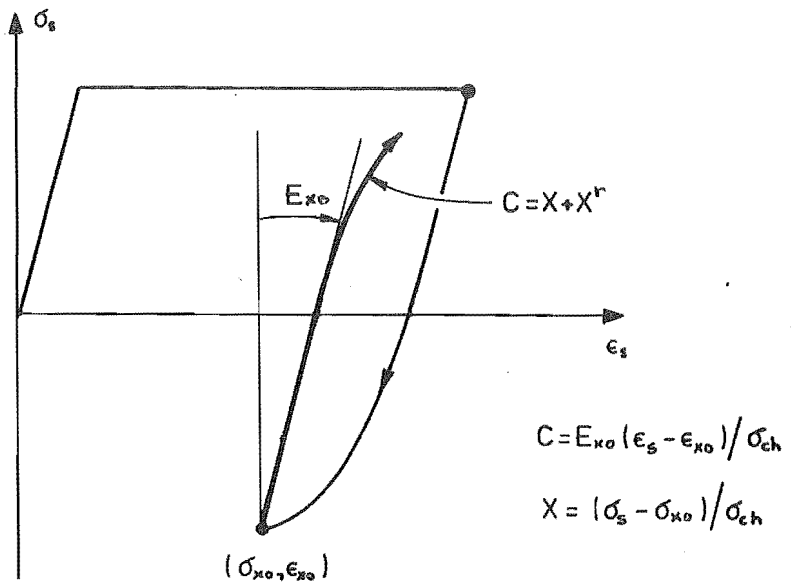

FIGURE 3.4 : RAMBERG-OSGOOD LOADING CURVE

Various forms of this relationship have been used by a number of analysts (12, 44, 48) to represent the inelastic response of steel subjected to plastic strain reversals. Other similar functions have also been used (50, 67). The main attraction of the Ramberg-Osgood (R-O) function has usually been the ability to generate curve shapes representing a wide range of states of softening, simply by varying the exponent, r (Figure 3.5). Most existing Ramberg-Osgood based procedures use this approach to model the extent of softening.

In contrast, the steel model proposed in this study uses only a single value of r for all responses in the one straining direction. This model assumes that there is only one basic curve for reverse loading, and, instead of varying r, the state of softening is determined by a combination of interaction with the envelope curves, the load curve origin (σ_{xo}, ε_{xo}), and the values of E_{xo} and σ_{ch} (see Figure 3.6).

With this approach to modelling the steel response it was possible to obtain a very good fit of the experimental loading curves, except over a small transition zone at the junction of the Ramberg-Osgood and envelope curves. However, the main advantage of the fixed shape Ramberg-Osgood curve was that a finite difference procedure could be used to solve for X in Eq. 3.4, thereby substantially reducing the computation time required for the steel analysis. Variable exponent Ramberg-Osgood formulations are heavily disadvantaged by the high cost of real exponentiation* and by the fact that an iterative procedure must be used to solve Eq. 3.4. The iteration procedure used in Thompson's steel model, for example, was measured as taking an average of approximately 8 iterations and 7200 microseconds of central processor unit (CPU) time for each evaluation of the Ramberg-Osgood function. Even when recoded with an efficient Newton-Raphson iteration procedure

---

* Timing checks made on the B6718 computer showed that each real exponentiation operation (e.g. A = B**Z) took approximately 600 microseconds of CPU time, as compared to only 10-12 microseconds of CPU time for simple multiplication (e.g. A = B*C).

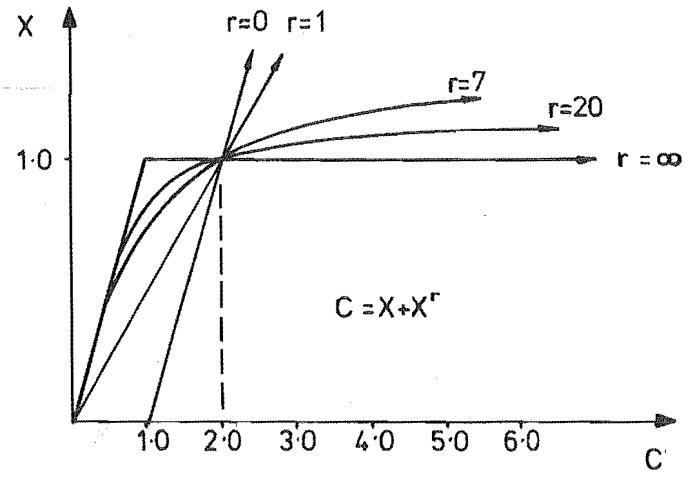

FIGURE 3.5 : EFFECT OF r ON CURVE SHAPE

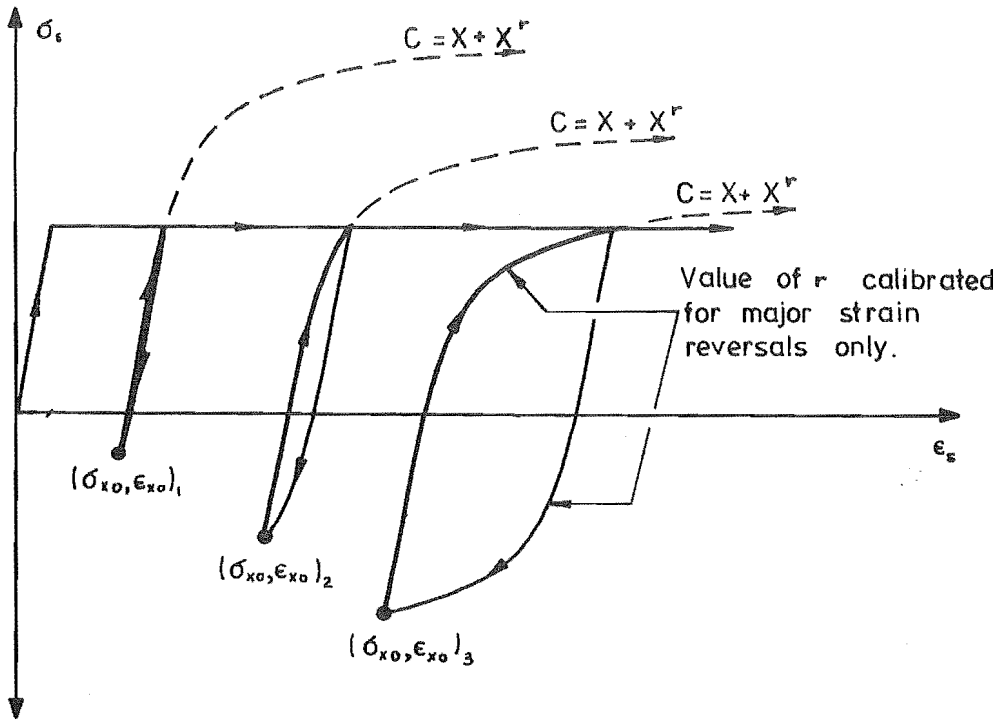

FIGURE 3.6 : INTERACTION BETWEEN RAMBERG-OSGOOD AND ENVELOPE LOAD CURVES FOR r = CONSTANT

requiring a maximum of only 2 to 3 iterations to solve for X, the computation time was still of the order of 1200-1800 microseconds. By comparison, the first order finite difference procedure used in the proposed model took approximately only 50 microseconds of CPU time to solve for X and compute the steel stress $\sigma_s = \sigma_{ch} X - \sigma_{xo}$.

3.5 EVALUATION OF RAMBERG-OSGOOD FUNCTION CONSTANTS

The size and shape of the Ramberg-Osgood loading curves are determined by three parameters, E_{xo}, r, and σ_{ch}. The task of calibrating these parameters was simplified by the form of the model which made it possible to calibrate them sequentially. First, the relationship of E_{xo} to strain history was assessed from the slopes of the unloading curves. Values for r (tension and compression straining) were then determined based on the shapes of the load curves for major strain reversals only, taking into account appropriate values of E_{xo}. These values were then used to assess the influence of the strain history on σ_{ch} by examining a typical range of load curves.

Only integer values of r were considered in the calibrations and all curve fitting was carried out graphically. Because of the limited range of experimental data available, a more precise fitting of the experimental loading curves using a least squares analysis was not considered to be warranted. Emphasis was instead placed on the basic form of the model and on ensuring that the effect of the strain history proceeding each load reversal was correctly modelled.

The data used to calibrate the Ramberg-Osgood curve parameters were largely obtained from tests carried out by Kent (48) and by Aktan et al. (63). In both cases the tests were performed on small steel coupons machined out of reinforcing bars. Kent's specimens were obtained from bars with a nominal yield strength of 275 MPa, while those tested by Aktan et al. were from bars with a yield strength of approximately 460 MPa. The unloading branches of Kent's experimental stress-strain responses were not recorded. After the tests, the full stress-strain load histories for the specimens were reconstructed by joining the

various individual load reversals with assumed linear unloading branches with slopes equal to the initial elastic modulin (E_o). Kent's data could therefore not be used for assessing the effect of the strain history on E_{xo}.

3.5.1 Unloading Modulus, E_{xo}

In many existing analytical models of the steel response, E_{xo} is assumed to remain constant and equal to the initial elastic modulus of the unstrained steel, E_o (Figure 3.3). However, this is not consistent either with the behaviour observed in the majority of experimental stress-strain responses or with that expected from a theoretical point of view. A more realistic theoretical approach would be to assume that the natural elastic modulus, relating true stress and strain, remained constant. Allowing for changes in bar length and area ($\nu = 0.5$ for plastic strain) and expressing in terms of engineering strain results in the theoretical relationship:

$$E_{xo} = (1 - 2\varepsilon_{xp}).E_o \qquad \ldots (3.5)$$

where E_{xo} is the unloading modulus based on the original bar area and ε_{xp} is the plastic strain at the curve origin (i.e. at the start of unloading).

This relationship shows reasonably good agreement with the experimental unloading behaviour of most of the steel specimens tested by Aktan et al. (63). However, machined steel coupons were used for these tests. The limited amount of experimental data available for unmachined samples indicated that, at least for moderate net plastic tensile strains, the reduction in unloading modulus for reinforcing bars in their natural state is even larger than predicted by Eq. 3.5. Two examples illustrating this behaviour are shown in Figure 3.7. Thompson's experimentally derived relationship is based on the stress-strain response of 7mm (.276") diameter high tensile stress relieved prestressing tendons. This predicts 2 to 2.5 times greater reduction of the unloading modulus than is indicated by the theoretical relationship (Eq. 3.5). The two values measured in the present study indicate an even larger reduction. These

latter values were measured in an investigation into strain ageing effects on reloading responses (Appendix A). The remaining bars in this series were strain aged before reloading and there were not sufficient measurements of the unloading response to enable an accurate determination of the unloading moduli. However, those measurements taken indicated that the reduction in unloading moduli was of the order of 20% for all bars.

Although both sets of data are for small diameter bars, the results indicate that reductions in the unloading modulus of normal reinforcing bars may be considerable. However, insufficient data was available to enable a reliable calibration to be made. Consequently, as a temporary measure, both a modified version of Thompson's relationship for prestressing tendons and the theoretical relationship of Eq. 3.5 have been included as options in the computer program. The modifications made to Thompson's relationship affect only insignificantly the predicted unloading moduli. They were, however, necessary to ensure compatibility with the behaviour apparent in the experimental responses measured by Aktan et al., i.e. that the unloading modulus E_{xo} is related to ε_{xo} rather than to the maximum imposed strain, and also to make allowance for the lower yield strength of ordinary reinforcing bars*. The relationship used is:

$$E_{xo} = (58.27\ \varepsilon_{xo}^{2} - 6.946\ \varepsilon_{xo} + 1.008).E_o \leq E_o \qquad \ldots (3.6)$$

In respect of this relationship, it should be noted that the effect of these values of E_{xo} on the other Ramberg-Osgood parameters was not investigated as only repeated loads (i.e. no load reversals) were imposed in Thompson's tests. Corresponding strain-softening data was therefore not available. However, in view of the magnitude of the reduction in unloading observed for unmachined samples, Eq. 3.6 should still give a better fit to the overall stress-strain relationship than Eq. 3.5.

---

* Thompson's relationship was specifically developed for prestressing tendons.

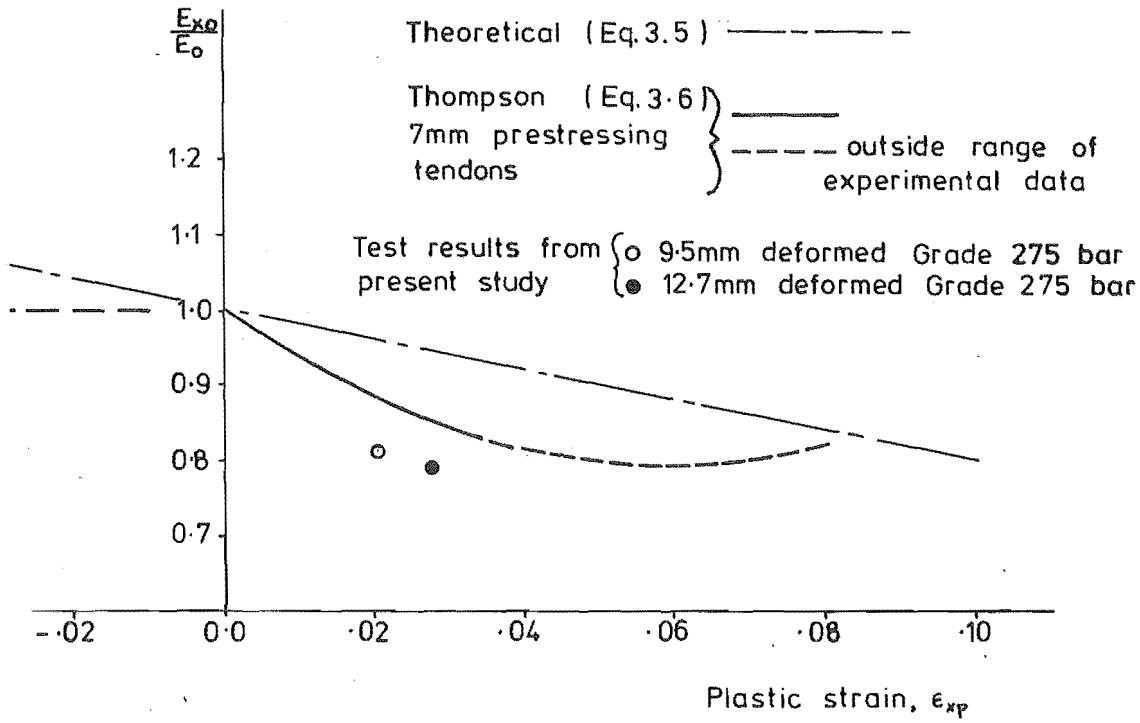

FIGURE 3.7 : RELATIVE CHANGE IN UNLOADING MODULUS, E_{xo}, WITH PLASTIC STRAIN

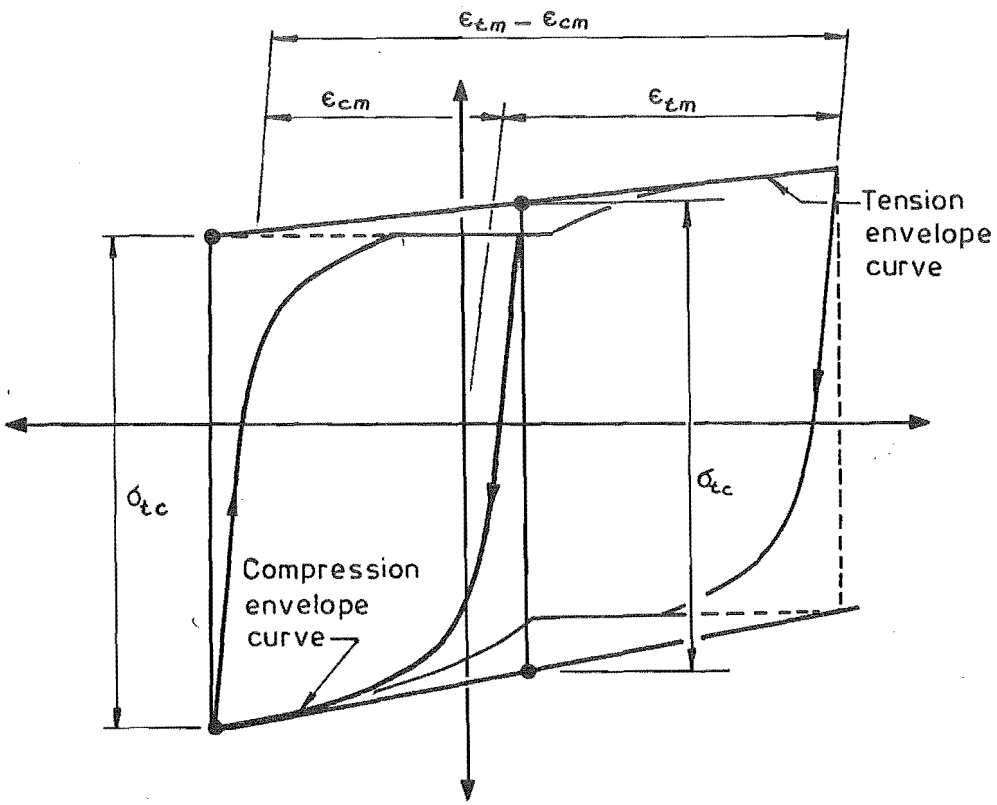

FIGURE 3.8 : EVALUATION OF σ_{tc}

Further investigation of the behaviour of unmachined bar samples is needed to obtain a more realistic relationship for E_{xo} for normal reinforcing bars.

3.5.2 Ramberg-Osgood Exponent, r

Values of r = 8 and r = 7 were found to give the best fit for the major tension and compression loading responses of the steel specimens tested by Aktan et al., while for Kent's data (48) a value of r = 8 was obtained for both loading directions. The limited range of the data used for these calibrations makes it impossible to assess how generally applicable these values are for normal reinforcing steels.

At present, the steel model used in the frame analysis program is coded for fixed values of r = 8 for tension loading and r = 7 for compression loading. More reliance has been placed on the data obtained by Aktan et al. because of the absence of data for the unloading response for Kent's specimens. Also, the strain sequences imposed by Kent included comparatively few major compression load reversals.

3.5.3 Characteristic Stress, σ_{ch}

The definitions of characteristic stress employed in the proposed steel model are given by the relationships:

$$\sigma_{ch} \text{ (tension)} = \phi_{ch} \cdot \sigma_{tc} \quad \text{and} \qquad \ldots (3.7a)$$

$$\sigma_{ch} \text{ (compression)} = -\phi_{ch} \cdot \sigma_{tc} \qquad \ldots (3.7b)$$

where σ_{tc} is based on the stress difference between the tension and compression envelope curves as shown in Figure 3.8, and ϕ_{ch} is the characteristic stress scaling factor.

Values of ϕ_{ch} were obtained for typical loading curves from the data of both Kent and Aktan et al. and compared with corresponding values for the maximum plastic strain difference $\varepsilon_{tm} - \varepsilon_{cm}$ (see Figure 3.8). These values are shown in Figure 3.9, together with the interrelationship

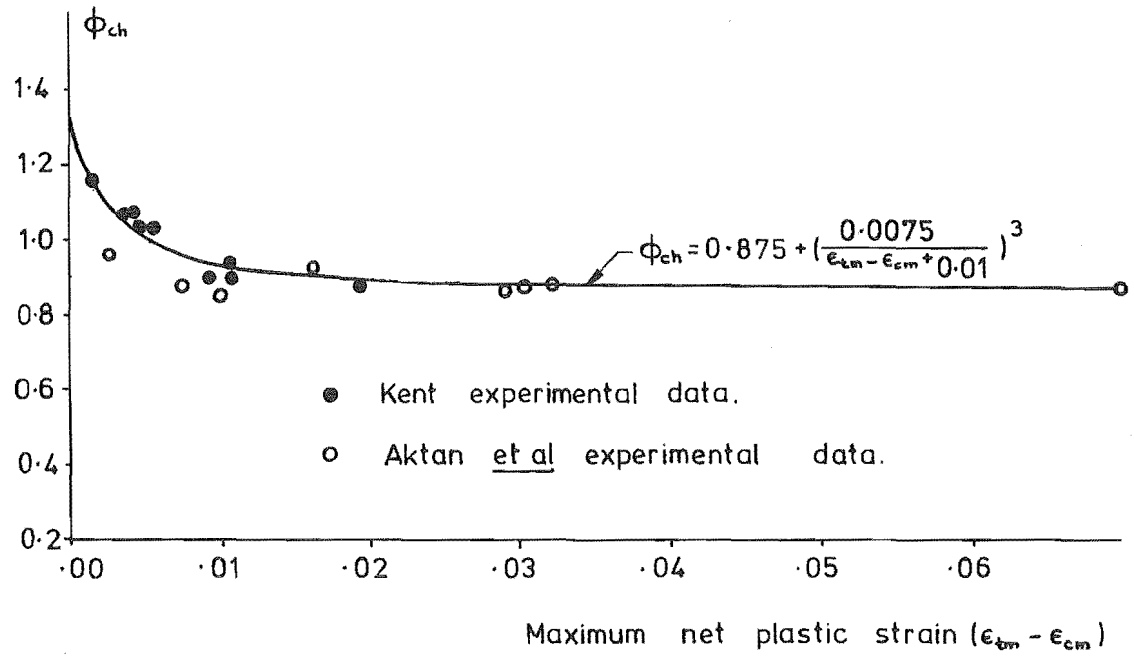

FIGURE 3.9 : RELATIONSHIP BETWEEN ϕ_{ch} AND $(\varepsilon_{tm} - \varepsilon_{cm})$

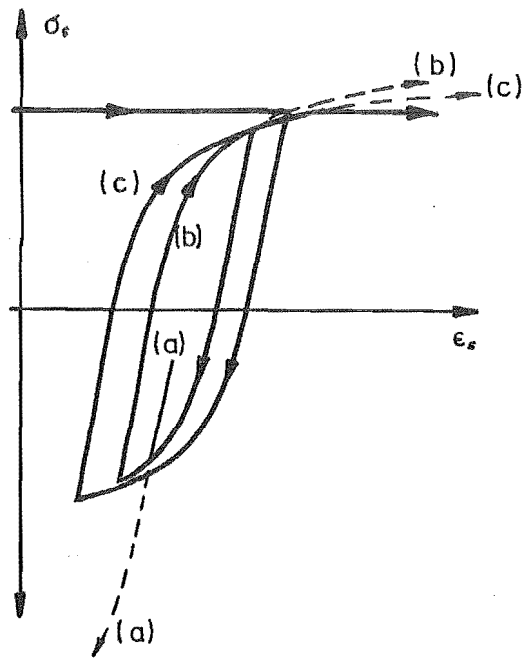

FIGURE 3.10 : BEHAVIOUR MODELLED FOR INTERSECTING CURVES

assumed in the model, i.e.

$$\phi_{ch} = 0.875 + \left[0.0075/(\varepsilon_{tm} - \varepsilon_{cm} + 0.01)\right]^{3} \quad \ldots (3.8)$$

There is some discrepancy between the two sets of data at low values of $(\varepsilon_{tm} - \varepsilon_{cm})$, and as is indicated, the assumed relationship has been weighted in favour of Kent's data in this region. There were two reasons for this: first, Kent's data included a greater number of load reversals at low values of $(\varepsilon_{tm} - \varepsilon_{cm})$, and secondly, as $(\varepsilon_{tm} - \varepsilon_{cm})$ tends to zero, the reversed loading curve would be expected to tend towards the initial elastic loading curve. The value of $\phi_{ch} \simeq 1.3$ predicted by Eq. 3.8 for $(\varepsilon_{tm} - \varepsilon_{cm}) = 0$ is close to the minimum that would realistically model this behaviour.

3.6 RETAINED STRAIN HISTORY

The inelastic response of steel is strongly influenced by its past loading. In addition to modelling the basic curve shapes, it is necessary to give consideration to the treatment of intersecting load paths in situations where two or more levels of decreasing size strain reversals develop. This is one aspect where existing steel models tend to be fairly limited and was one of the reasons for developing a new model.

The treatment of intersecting responses adopted for the proposed model is indicated in Figure 3.10, i.e. when an "inner" and an "outer" load path intersect, the subsequent response is made to follow the outer path as this offers least resistance to further loading. The procedure used allows up to 3 or 4 levels of curves in each load direction to be retained in memory at any one time (Figure 3.11). Although this may seem a high degree of refinement, the computation time and the number of strain history terms required have been kept significantly less than for less refined models such as those of Thompson and Kent, e.g. 17* strain history terms were required per bar as compared with 48 for Thompson's model.

---

* Excluding 2 terms required solely for adaption of the N-R solution procedure (Section 3.8).

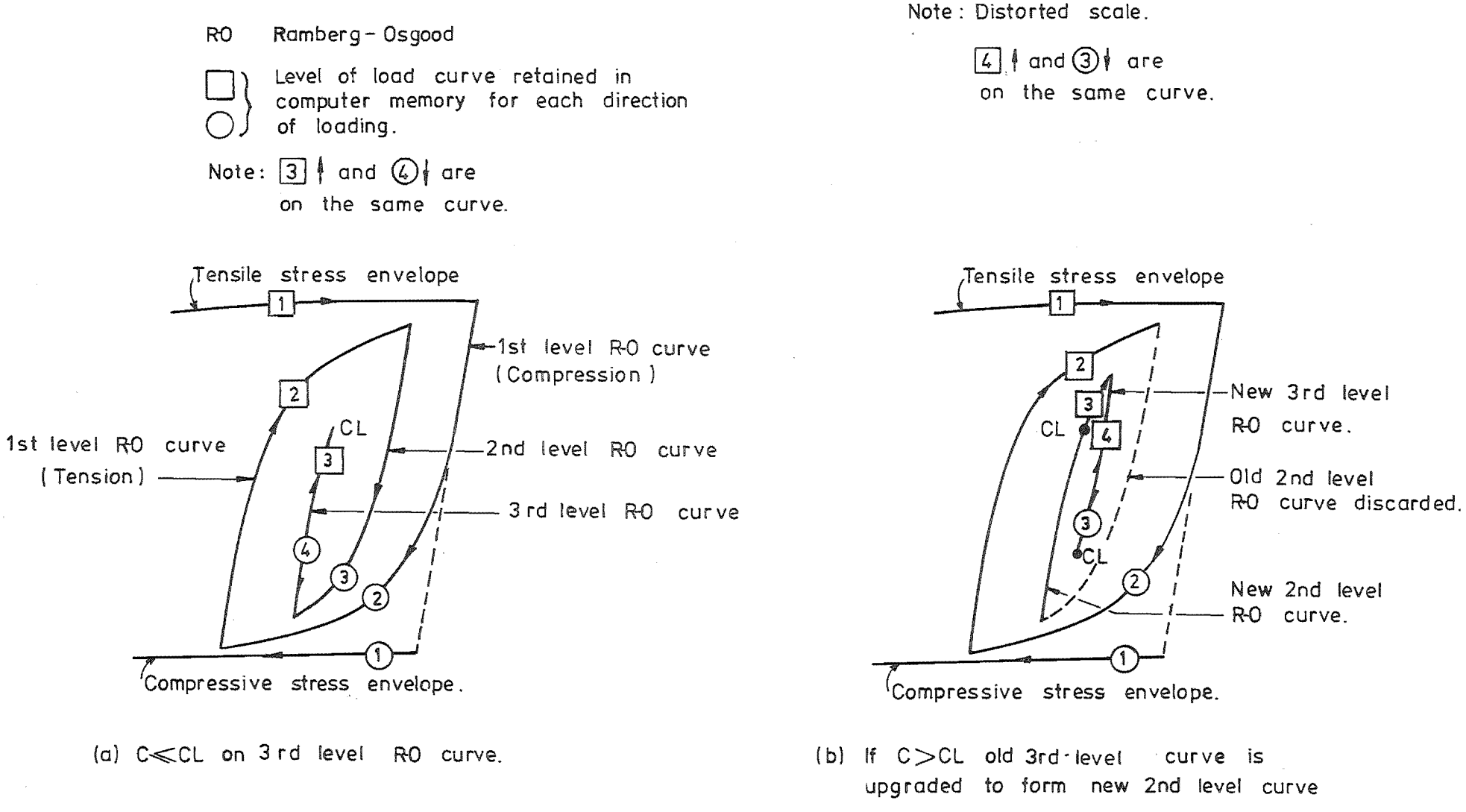

FIGURE 3.11 : LOAD CURVES RETAINED IN COMPUTER MEMORY

The system used operates on a defined hierarchy of curves as follows (refer Figure 3.12):

(a) Envelope Curves (KN = 0): These take precedence over all other curves. Once on the envelope curve, the response continues to follow it until the straining direction reverses.

(b) First Level R-O Curves (KN = 2 or KN = 1): These curves are subordinate to only the envelope curve of the same straining direction and are generated by either unloading off an envelope curve (then KN = 2), or unloading off a first level R-O curve with KN = 2 or second level curve with KN = 4 (then KN = 1). The difference in code number has significance only for the purpose of classifying curves that unload from the first level R-O curves, i.e. KN = 2 (or 4) curves generate new first level curves with KN = 1, whereas KN = 1 curves generate KN = 3 curves - see paragraph (c). A curve with priority KN = 1 changes to priority KN = 2 for all $C \geq CU$. As presently coded, a value of CU = 2.0 is used.

(c) Second Level R-O Curve (KN = 3 or KN = 4): This is subordinate to both the envelope and first level R-O curves of the same straining direction and is generated by a strain reversal off a KN = 1 curve, or as described subsequently, by a strain reversal off a KN = 3 curve in the reverse straining direction. In this latter case, the Ramberg-Osgood function parameters are retained in storage for the new KN = 3 curve only. If a KN = 3 curve crosses the first level R-O curve in the reverse straining direction, then it is upgraded to KN = 4 (Figure 3.12). Any curve unloading off this is then established as the new first level curve in the reverse direction with a priority of KN = 1.

(d) Third Level R-O Curve: (KN = 5 for tension straining direction and KN = 7 for compression straining direction): This is subordinate to all other curves and is generated by a strain reversal off a KN = 3 curve. The storage areas normally used for the stress and strain of the previous increment are used for storing the origin stress

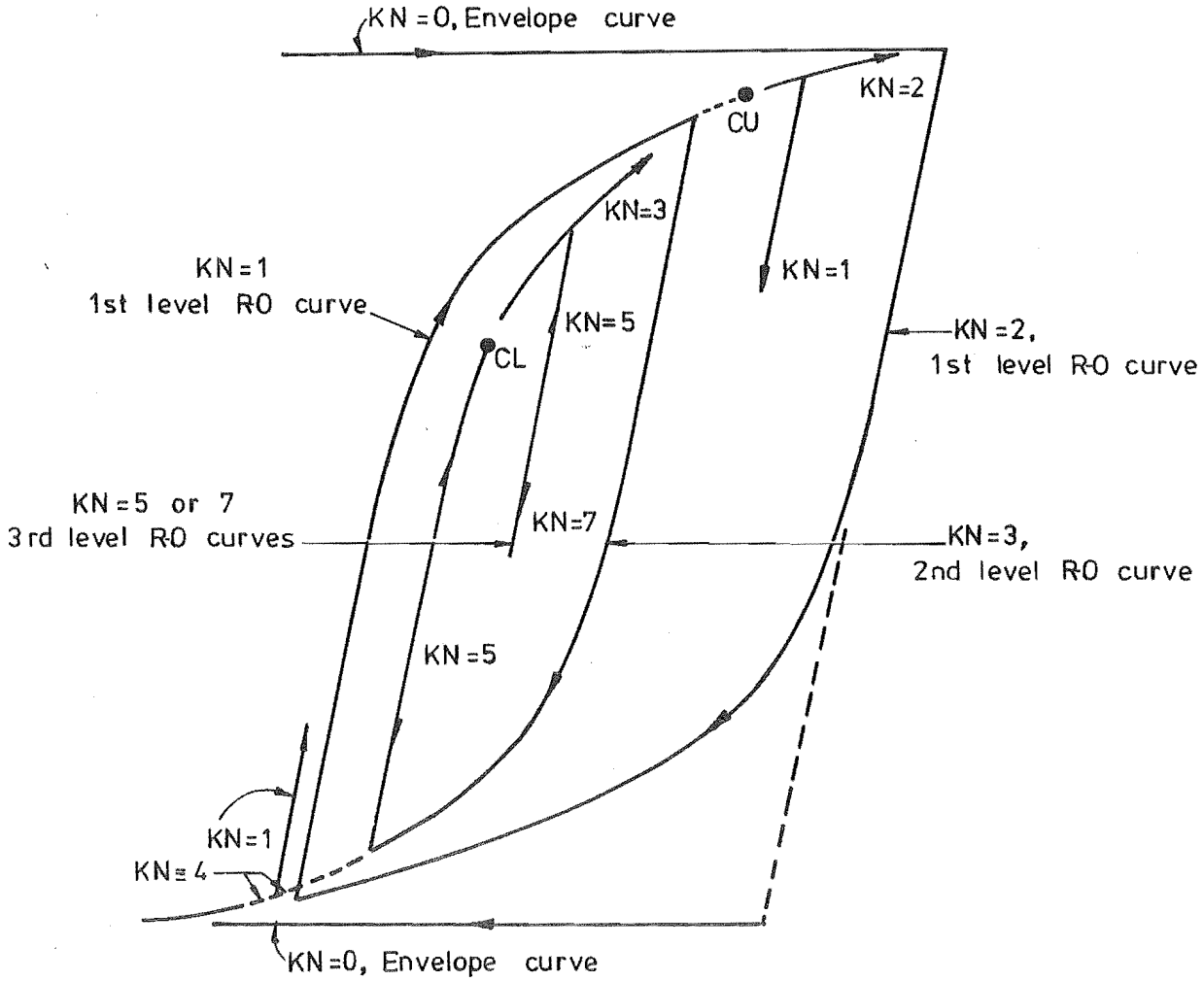

FIGURE 3.12 : CODE NUMBERING SYSTEM USED FOR ORDERING STEEL RESPONSE CURVES

and strain for this curve. This means that the last stress and strain cannot be stored while on this curve and consequently that "loading" and "unloading" responses follow the same path. Once a value of C = CL has been exceeded, this curve is upgraded to form a new KN = 3 curve. If, however, the response reverses back past the origin before reaching C = CL, then it will revert to following the old KN = 3 curve. As presently coded a value of CL = 0.7 is used. Because no additional storage terms are required, the inclusion of this curve adds only minimally to the cost of the steel analysis.

The curve code numbers (KN) used are not ranked in strict order of priority, but have been designed to ensure optimal stacking of curves (i.e. each curve assigned its highest permissible priority) and to allow efficient use of combined numeric and Boolean logic. Despite the complexity of the system, the computation time required for management of the various curve types and interrelationships still constitutes only a small portion (approximately 15%) of the total steel analysis time. This cost is more than offset by the reduction in the number of checks made against curves of higher priority.

The values of the strain limits CL (= 0.7) and CU (= 2.0) were selected to minimise the two types of path error indicated in Figure 3.13. The maximum path error of this type is of the order of 0.05 σ_{ch} ($\simeq$ 10% of σ_{sy}), but the probability of an error exceeding even 0.02 σ_{ch} is very small.

3.7 COMPARISON BETWEEN OBSERVED AND PREDICTED RESPONSES

The measured stress-strain responses of three steel coupons tested by Kent are compared in Figures 3.14 to 3.16 with corresponding analytic responses predicted by both Thompson's and the proposed models. The predicted responses shown for the proposed model were computed using r = 8 for both tension and compression loading curves, and assuming a constant unloading modulus $E_{xo} \equiv E_o$ (see section 3.5). Thompson's model for ordinary reinforcing steel was based on Kent's experimental responses and already assumed a constant unloading modulus.

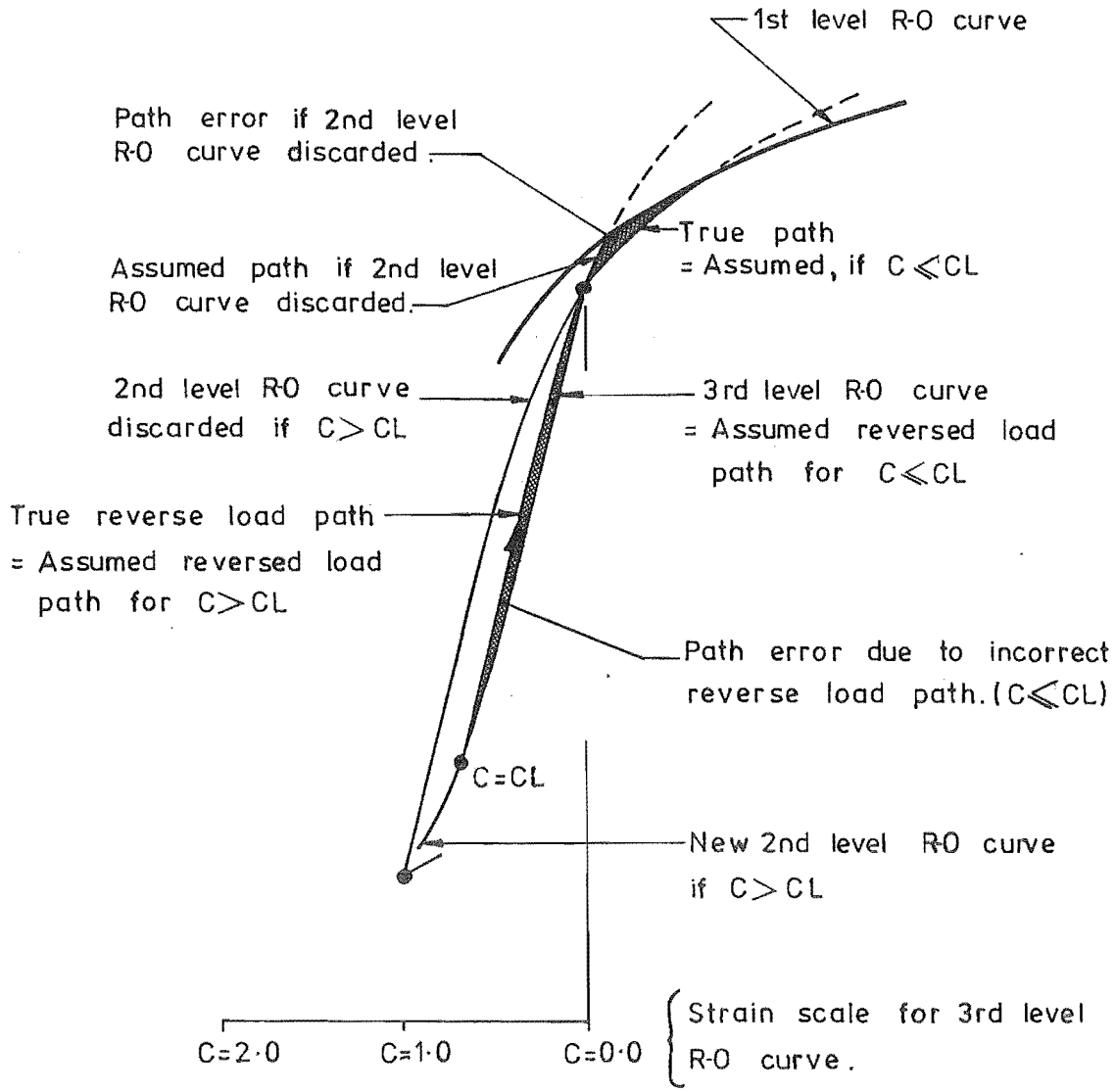

Note: (1) Approx. to scale.
(2) Approx. maximum path errors indicated.
(3) All references to C refer to 3rd level curve values
(4) ● denotes strain reversal.

FIGURE 3.13 : PATH ERRORS ASSOCIATED WITH THE THIRD LEVEL R-O CURVES

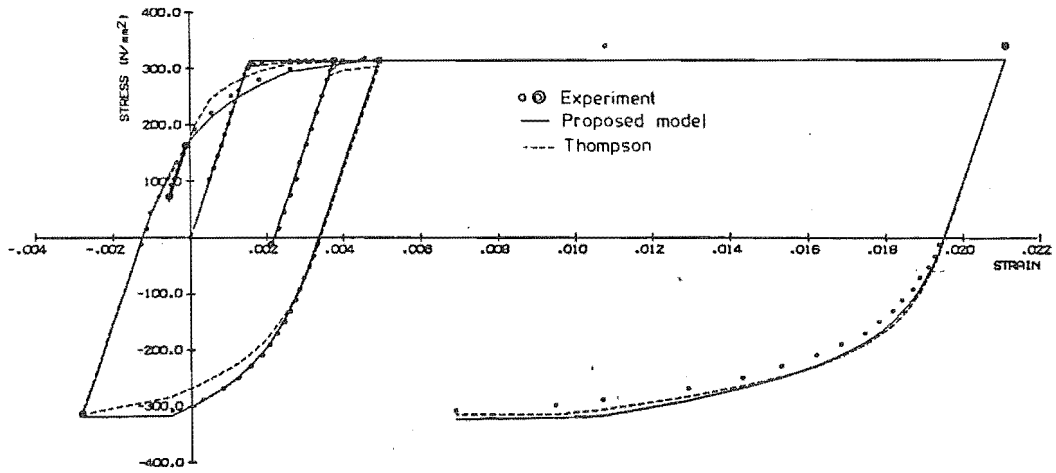

FIGURE 3.14 : STRESS-STRAIN RESPONSES FOR BAR SPECIMEN NO. 8 TESTED BY KENT (48)

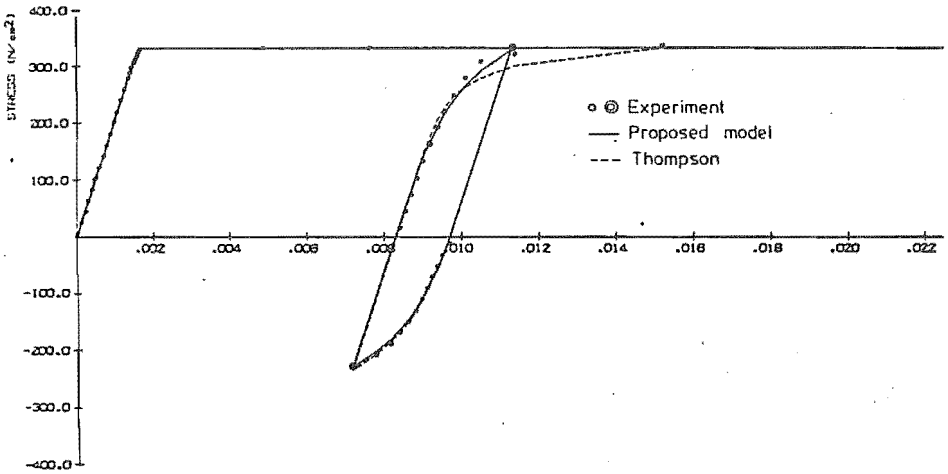

FIGURE 3.15 : STRESS-STRAIN RESPONSES FOR BAR SPECIMEN NO. 12 TESTED BY KENT (48)

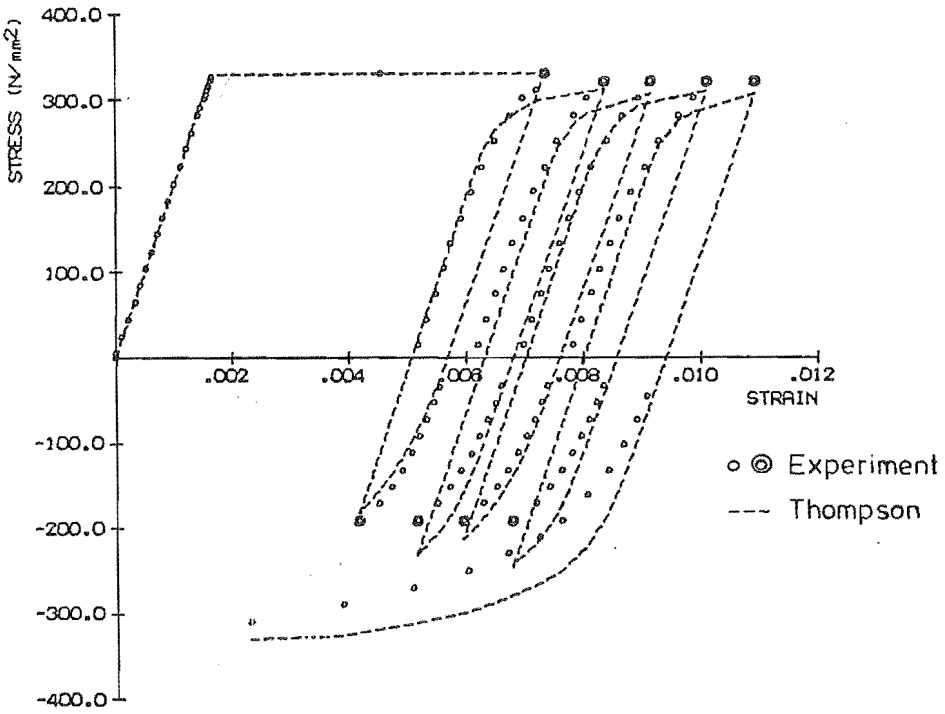

(a) Analytic response for Thompson's steel model

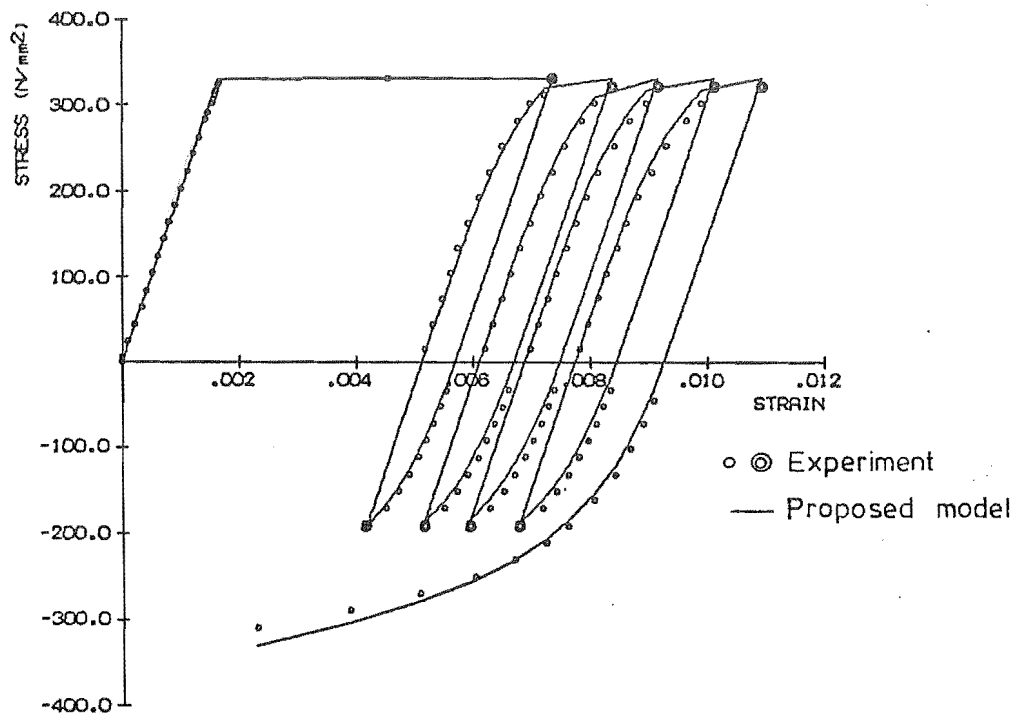

(b) Analytic response for proposed steel model

FIGURE 3.16 : STRESS-STRAIN RESPONSES FOR BAR SPECIMEN NO. 20 TESTED BY KENT (48)

As indicated, both models predicted the responses of the three specimens reasonably accurately, with the present model showing the slightly better overall agreement. The greatest difference between the two predicted responses occurs for specimen 20. In this case, Thompson's model significantly underestimates the softening in the last four compression load reversals. The main reason for this is that, in Thompson's model, the degree of softening is related to the incremental plastic strains in the preceding load reversal, rather than to the maximum plastic strains ε_{tm} and ε_{cm} .

As indicated in Figure 3.17, the proposed model also satisfactorily predicted the higher strength steel specimens tested by Aktan et al. (63). Thompson's model was not used for analysing this specimen because the magnitude of the strains, and the extent to which strain hardening influenced the response were outside the scope of his model. The analytic response given for the proposed model was computed using $r = 8$ and $r = 7$ respectively for the tension and compression loading curves, and with the unloading modulus adjusted for the deformed geometry of the bar in accordance with Eq. 3.5. The only significant discrepancy between the observed and predicted responses occurred during the first compression load reversal. In all subsequent load reversals, the steel response was predicted accurately (including the compression branches). The predicted behaviour during the first compression load reversal did, however, indicate the possibility of the Ramberg-Osgood curve not intersecting the envelope curve. This occurred because the Ramberg-Osgood curve stresses are not increased for change in the bar area, while the compression envelope is (Section 3.3). If it were not for a subsequent load cycle, this could have resulted in a significant underestimate of the compression stress at large compression strains. In the present study, the problem did not arise, however, as most of the analyses performed involved only Grade 275 steel reinforcement. The greater length of yield plateau for these bars ensures that the branch and envelope curves intersect.

3.8 STABILIZING PROCEDURES REQUIRED FOR NEWTON-RAPHSON ITERATION

One of the main advantages of using the Newton-Raphson solution procedure

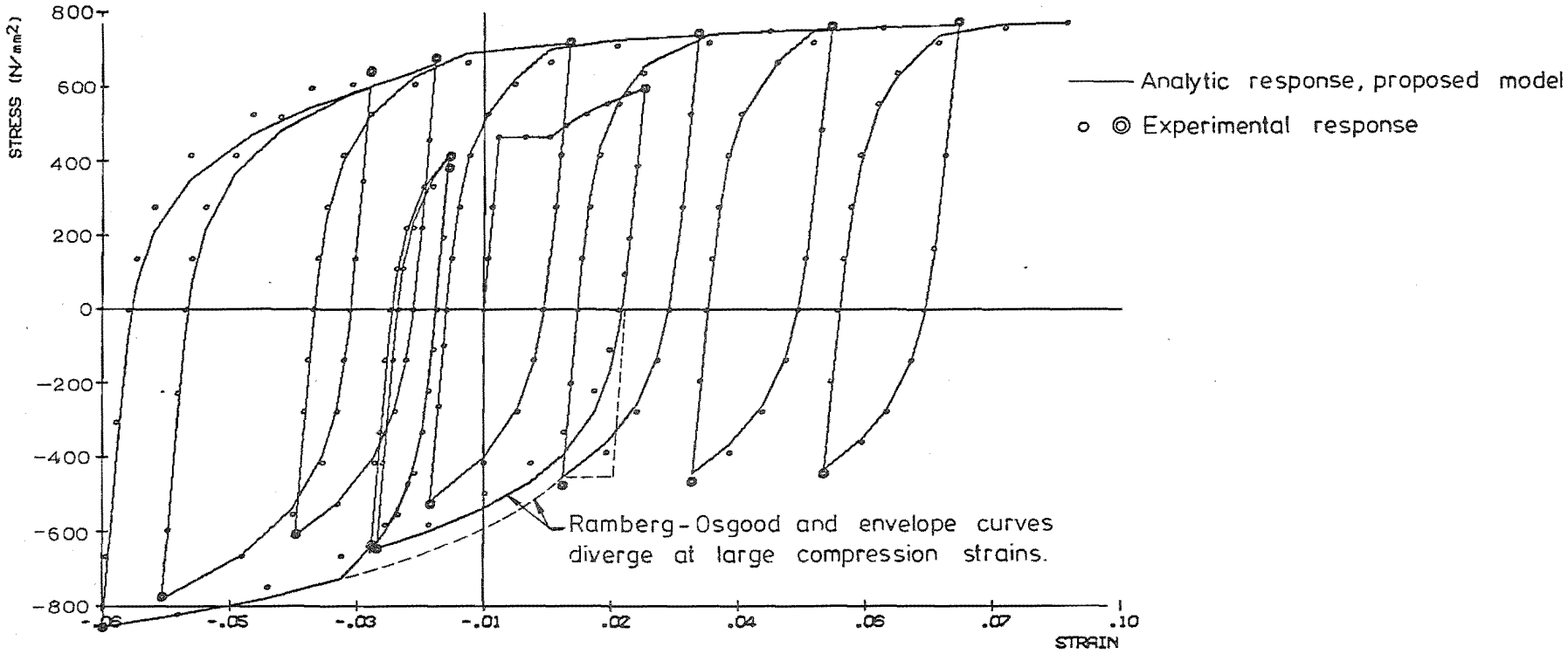

FIGURE 3.17 : STRESS-STRAIN RESPONSES FOR BAR SPECIMEN NO. 6 TESTED BY AKTAN ET AL (63)

for materially non-linear analysis problems is its ability to adjust to sudden changes in state,such as occur at the onset of steel yielding or unloading from yield. However, because of the form of the inelastic response of steel, this sensitivity can also seriously destabilize the solution convergence. These problems were investigated in detail in this study and it was only after special stabilizing procedures had been built into the steel model that the Newton-Raphson procedure could be used successfully to analyse beams or frames subjected to reversed post-elastic loading.

Three main problem areas were encountered and are discussed in the following subsections. In dealing with these, the approach taken was that the corrective action should be directed at the local source of disruption in the steel model and not applied globally. In all three cases, the effect on the solution convergence is greatest in situations where all the flexural reinforcement is placed in only two distinct groups of bars (e.g. as in many beams). Most of the illustrative examples given in the following subsections are based on the iteration behaviour at one of two modelled bar groups in this type of member. However, similar solution instabilities can also develop in members with more distributed reinforcement.

Because of the direct control exercised by the global solution procedure, the types of problem discussed in the following subsections generally have little effect on the analysis of individual sections or of beams where only one segment is yielded at any one time. Serious instability problems and complete breakdown of the solution were only encountered in analyses involving several simultaneously yielding segments and particularly when the analysis of a full frame was attempted.

3.8.1 Yield Plateau

Problems occur in this region because of the zero tangential modulus of the constant stress yield plateau. In situations where the applied moment is resisted solely by two rows of bars, use of a zero modulus for one of the rows in an analysis would make the solution indeterminate and would cause the equation solver to fail.

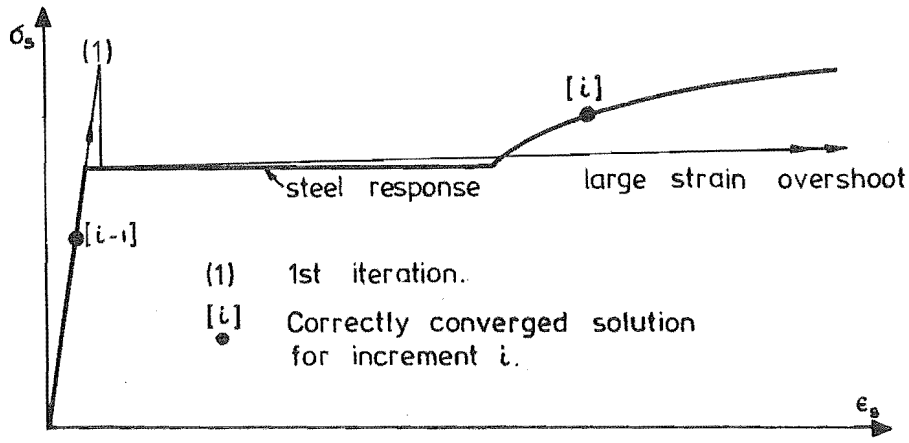

(a) Strain overshoot due to low yield modulus.

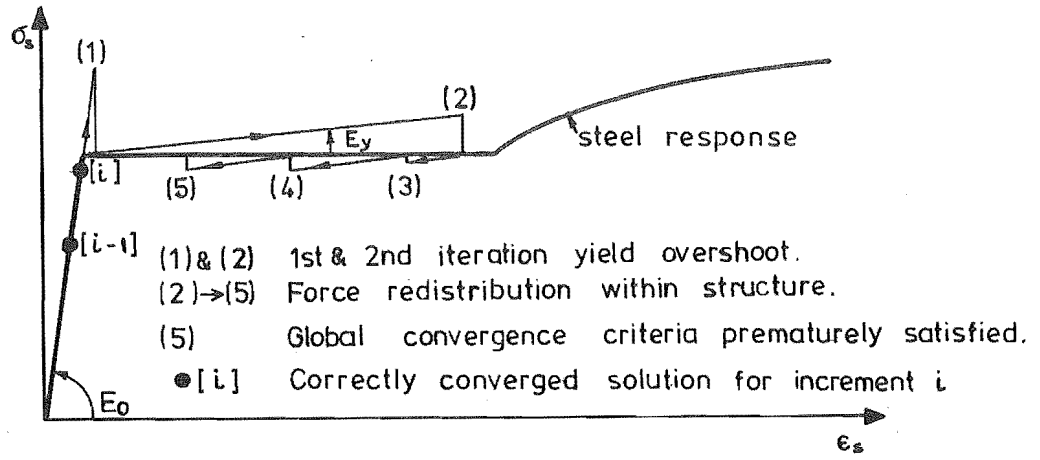

(b) False yield due to slowed local convergence.

FIGURE 3.18 : EFFECT OF USING A FICTITIOUS YIELD MODULUS ON THE YIELD PLATEAU

The usual corrective action for this type of situation is to introduce a fictitious finite yield modulus $E_y = \phi_y . E_o$. This approach was initially adopted (successfully) for the proposed steel model. Because of the direct control exercised over the section strains by the global solution procedure, very low values of ϕ_y (0.0001 or smaller) could be used for individual section analyses. The convergence rate continued to improve with decreasing values of ϕ_y.

More care was necessary in choosing a suitable value of ϕ_y for analyses of beams, although use of a value of $\phi_y = 0.001$ appeared to give satisfactory results. Use of smaller values increased the risk of a large overshoot of the true solution (Figure 3.18a) which could initiate adverse interaction with other components of the section, while larger values slowed the convergence rate and consequently increased the risk of the global convergence criteria being prematurely satisfied (Figure 3.18b).

These problems became more pronounced in analyses of full frames. Although analyses were able to be performed using a value of $\phi_y = 0.001$, there was evidence of disturbed convergence during some increments, and the accuracy of the predicted strains for some member segments was doubtful.

To help alleviate these problems, a modification was introduced to allow the value of ϕ_y to be varied during the iteration process. This modification is shown in Figure 3.19 and was designed to restrict overshoot of the correct solution. In effect, the value of ϕ_y is adjusted in accordance with the magnitude of the initial yield overshoot, and attempts to restrict the change in strain during any iteration. This permits use of a lower minimum value of ϕ_y and hence improves solution convergence with less risk of a large solution overshoot. The modified procedure is also more robust, permitting larger initial overshoot of yield stress and hence larger load increments can be applied to a structure.

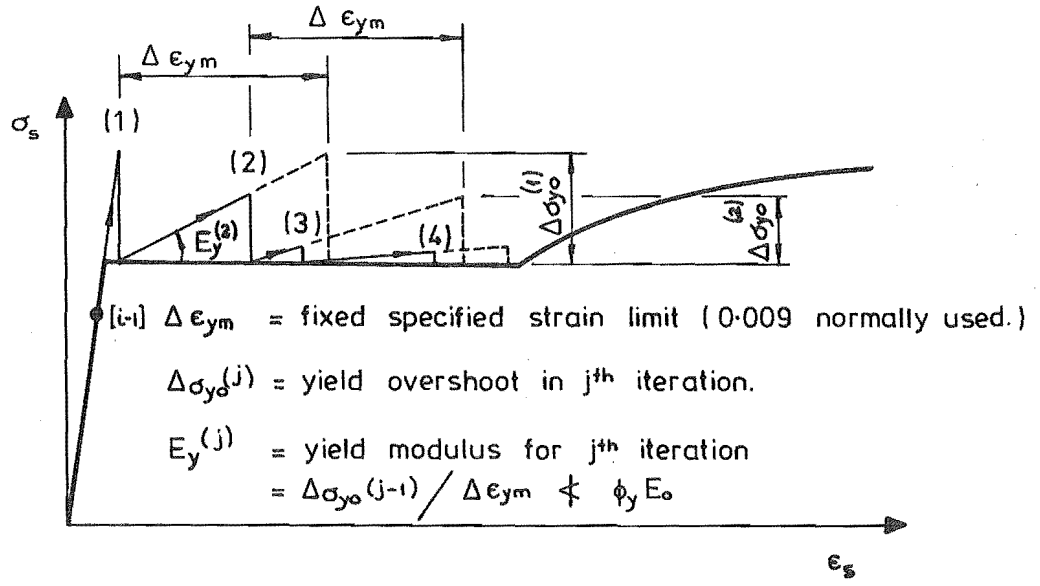

FIGURE 3.19 : ITERATION BEHAVIOUR USING VARIABLE YIELD MODULUS

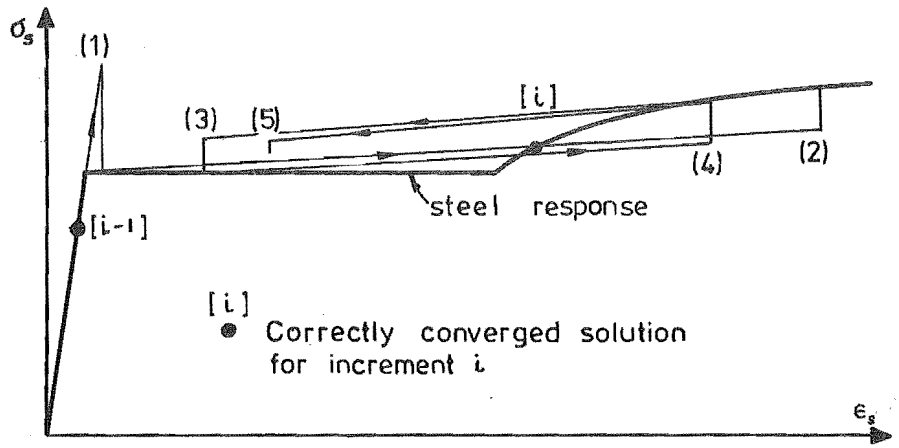

FIGURE 3.20 : SOLUTION OSCILLATION IN THE YIELD PLATEAU-STRAIN HARDENING REGION OF THE STEEL RESPONSE

3.8.2 Onset of Strain Hardening

The type of problem encountered in this region of the response is illustrated in Figure 3.20. This behaviour is caused by the slope of the response first increasing then decreasing (i.e. stepped shape response) within the solution space. Whether the oscillation that develops is divergent, stable, or slowly convergent, depends largely upon the extent and nature of interaction with the surrounding structure, the particular constitutive properties of the bar group, and on the size of the load increment. For a beam section which has not previously yielded, the stabilizing influence of the concrete compression block is generally sufficient to ensure solution convergence, although the rate of convergence can still be considerably slowed. However, in subsequent load reversals when only the steel couple is effective in resisting moment, solution convergence cannot be assured, even if relatively large values of fictitious yield modulus, e.g. $0.02\ E_o$, are used to reduce the extent of overshoot into the strain hardening range.

Two approaches were considered for overcoming this difficulty. The first of these was found to be unsatisfactory for general application, but is described here in order to demonstrate an important feature of the iteration behaviour. The procedure envisaged is shown in Figure 3.21, and involves temporarily inserting a fictitious linear strain hardening branch as an intermediate solution step. The fictitious branch is tangential to the start of the true strain hardening branch, and is employed only for the iteration in which strain hardening is first encountered. This establishes a temporary bilinear response which is used to guide the solution onto the appropriate portion of the true strain hardening branch. The solution can then converge normally to the true equilibrium position.

This procedure has the advantages that the tangent modulus is retained throughout and that the steep fictitious branch actively forces the solution back to the vicinity of the equilibrium position. However, because the fictitious branch is used only temporarily, the procedure will not function satisfactorily if there is strong interaction with

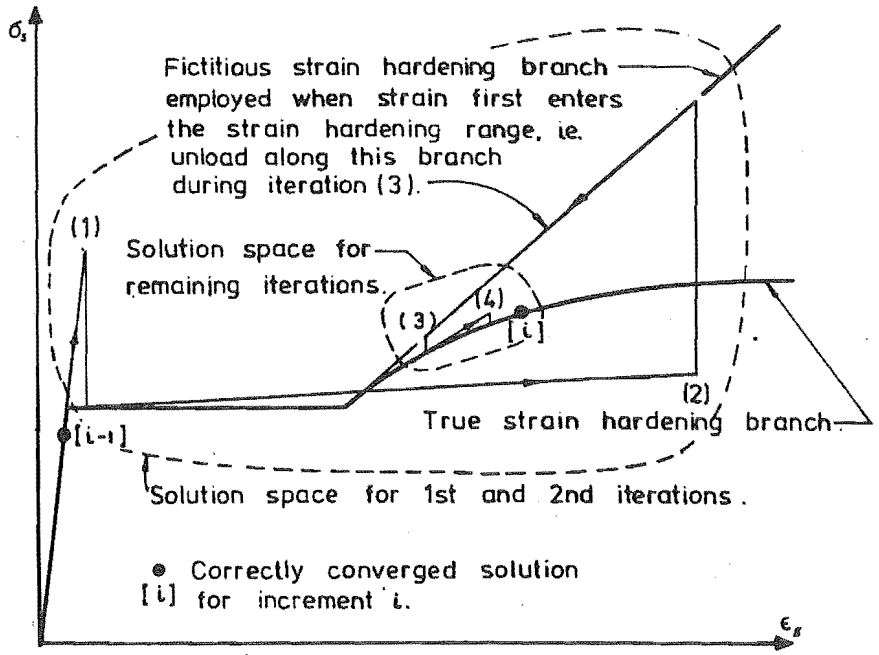

FIGURE 3.21 : TEMPORARY USE OF A FICTITIOUS STRAIN HARDENING BRANCH TO ENSURE SOLUTION CONVERGENCE

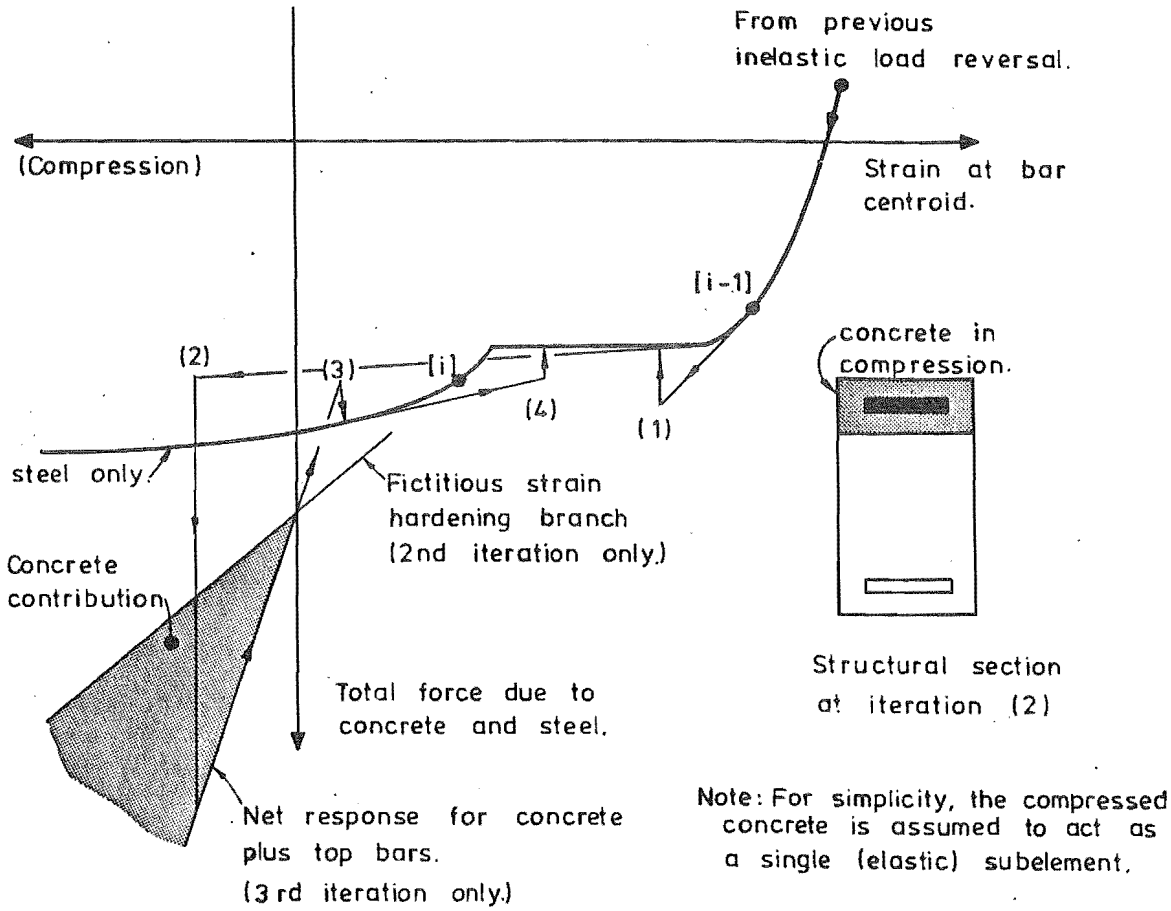

FIGURE 3.22 : SOLUTION OSCILLATION DUE TO THE TEMPORARY NATURE OF THE FICTITIOUS STRAIN HARDENING RESPONSE

other elements, especially at the local section level. The effect of this type of interaction is illustrated in Figure 3.22 for a case where the initial overshoot has induced compression in the concrete surrounding the bar group. In this case, the added rigidity provided by the concrete delays recovery of the solution to the vicinity of the true equilibrium position. Because the fictitious branch is not used for the next iteration, the solution reverts back to an oscillatory behaviour. Unfortunately, there is a reasonably high probability of this or similar types of interaction with other steel or concrete subelements and it is therefore essential that any stabilizing procedure take account of this type of effect.

To overcome these problems it was necessary to use a stabilizing procedure which remained effective for all remaining iterations in the increment in which the solution first encounters the strain hardening. The procedure adopted is illustrated in Figure 3.23. As indicated, this requires abandoning use of the tangential modulus for the remainder of the current increment, and substituting in its place a secant modulus which pivots about the start of the strain hardening branch. Since the secant modulus is used for all remaining iterations during the increment, this effectively establishes a sequence of fictitious linear branches. These converge such that the solution on the fictitious branch is eventually coincident with the equilibrium point on the true strain hardening branch. The analysed response in the yield plateau - (fictitious) strain hardening region therefore remains single curvatured during all stages of the iteration process and consequently the procedure is not susceptible to the type of disruption illustrated in Figure 3.22.

The solution can, of course, still back off onto the yield plateau again. Such a "back off" could either be permanent, i.e. because of general force redistributions in the overall structure, or temporary, i.e. due to disturbed convergence in other parts of the section or structure. In the former case, the solution process simply reverts to the type of iterative behaviour described in Figure 3.19 without causing any problems.

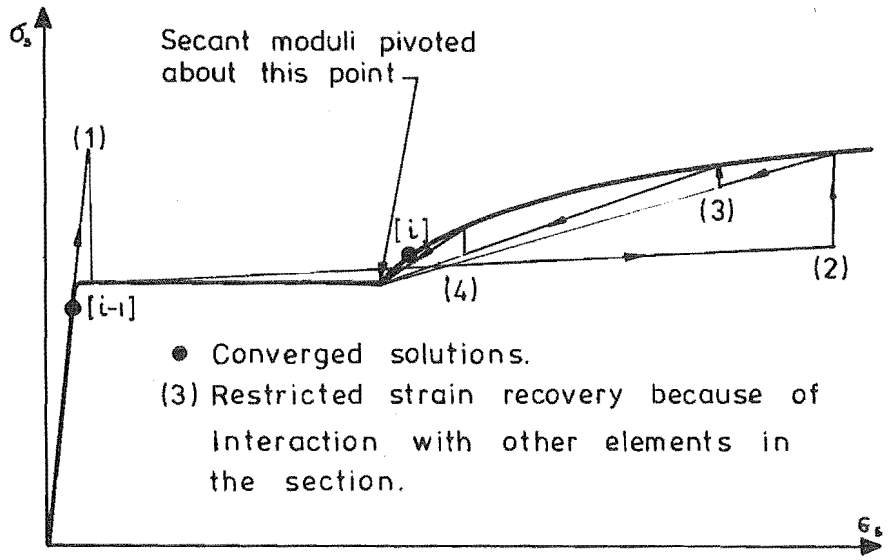

FIGURE 3.23 : USE OF SECANT MODULUS IN ORDER TO INHIBIT THE SOLUTION FROM OSCILLATING BETWEEN THE YIELD PLATEAU AND STRAIN HARDENING BRANCHES

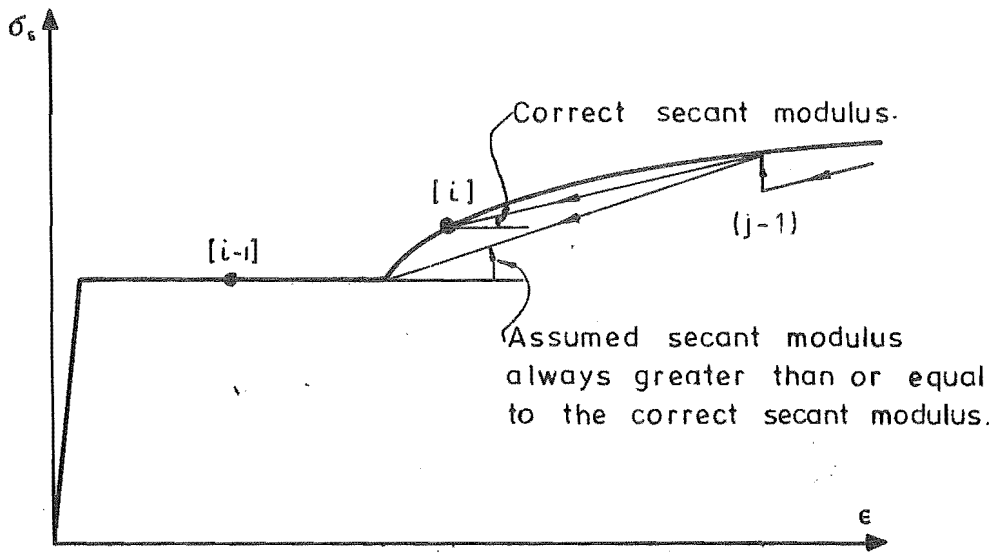

FIGURE 3.24 : CORRECT AND ASSUMED SECANT MODULI FOR j^{th} ITERATION

The latter case usually results in a new overshoot of the true solution on the strain hardening branch, and the secant modulus is again introduced. This process should, in general, settle down and not continue to oscillate. The secant moduli used are always greater than or equal to the "correct" moduli (see Figure 3.24). This acts as a damper* and has a stabilizing influence on the solution convergence.

The use of secant, rather than tangential, moduli inevitably causes some slowing of the convergence rate, especially as the solution approaches equilibrium. This effect should, however, be comparatively moderate, providing the converged solution is reasonably close to the start of the strain hardening branch. The difference between the secant and tangential moduli only becomes pronounced further away from the start of the curve.

Once the solution has converged, the procedure reverts back to using tangential moduli for subsequent increments on the strain hardening branch.

3.8.3 Unloading After Yielding or Softening of the Steel

Two examples of the type of problem associated with the steel unloading response are illustrated in Figure 3.25. Both of these are caused by the "stepped shape" of the response within the solution space. Figure 3.25a shows the type of behaviour that develops when the stress at first overshoots yield and then, in later iterations, tries to drop back below yield because of force redistribution in the overall structure. In the second example (Figure 3.25b), the behaviour shown is a result of reversal of the direction of loading. If, on unloading, the strain remains within the "elastic" portion of the unloading branch, then in both cases no problems arise and the solution rapidly converges. However, because of the small range of the "elastic" region and the low initial

---

* In contrast, secant moduli less than the correct value (e.g. Figure 3.22), tend to destabilize the convergence process by actively forcing the solution to overshoot.

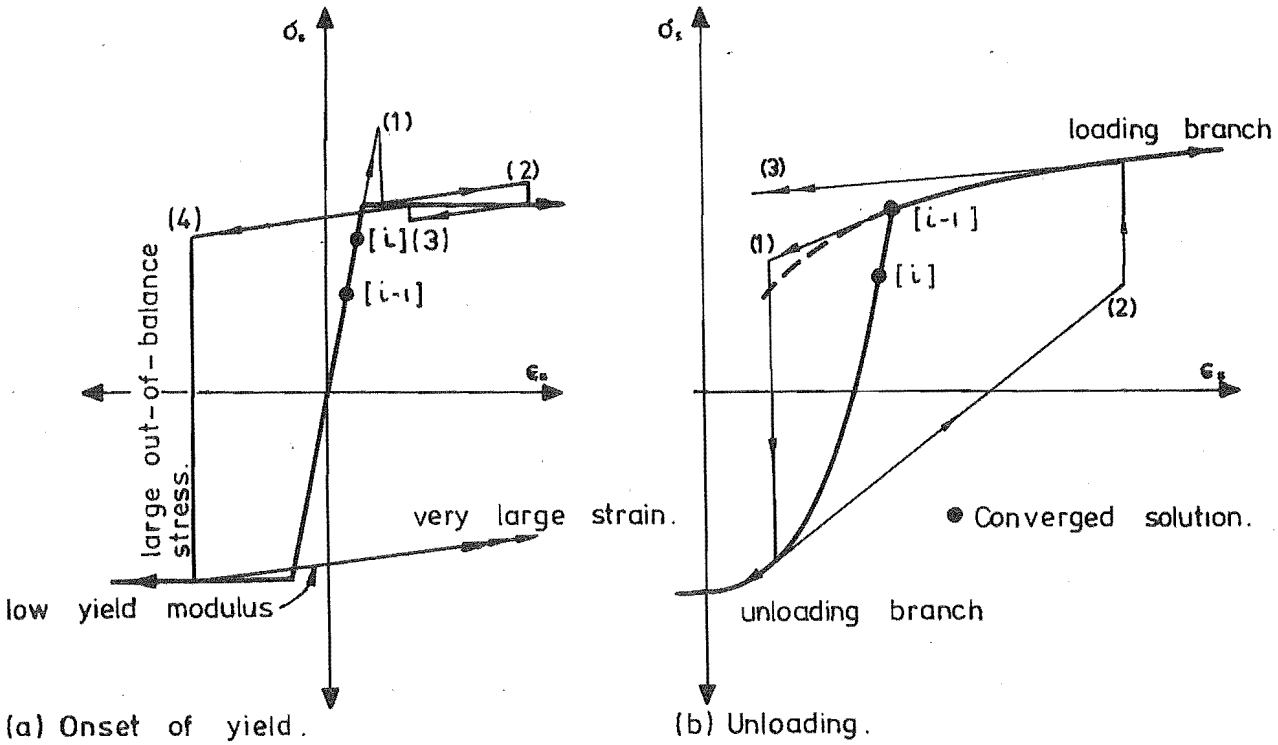

FIGURE 3.25 : DISRUPTION OF SOLUTION CONVERGENCE DUE TO SOLUTION REVERSING OFF YIELD PLATEAU

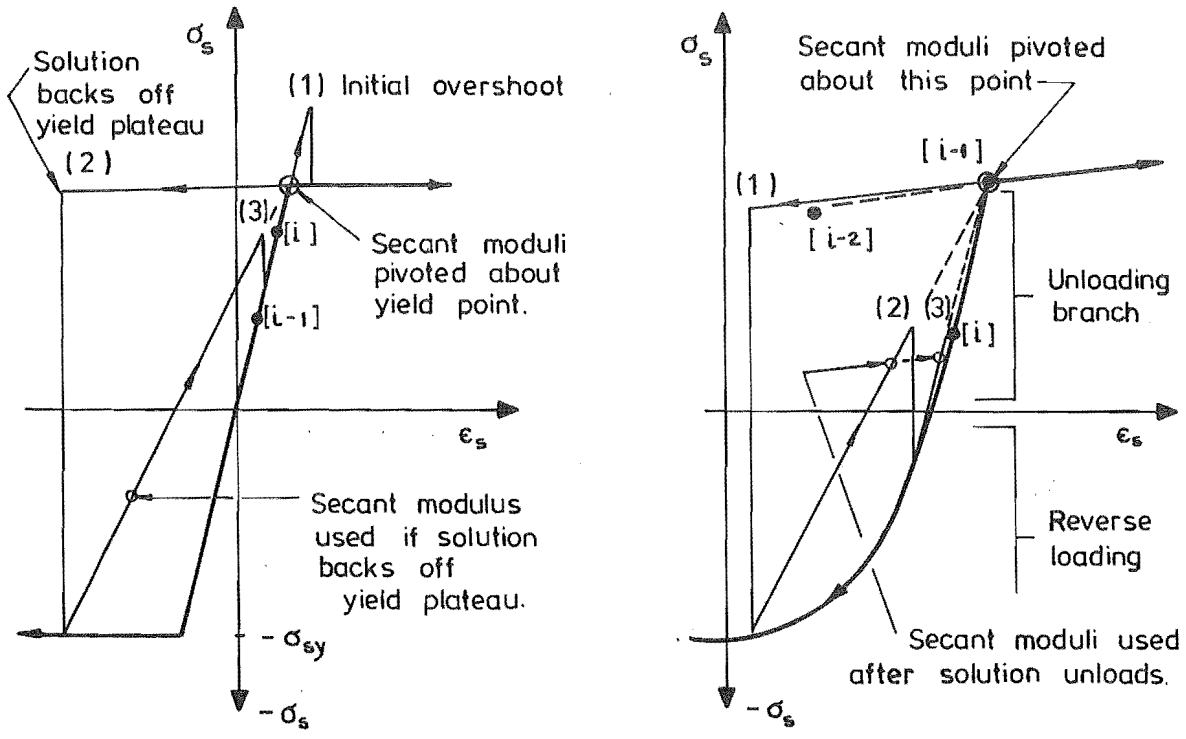

FIGURE 3.26 : USE OF SECANT MODULI TO PREVENT SOLUTION INSTABILITY AFTER UNLOADING FROM YIELD PLATEAU OF REVERSAL OF STRAINING DIRECTION

modulus, it is almost impossible to ensure that the solution does not overshoot back onto the softening or yield portion of the reversed loading curve, thereby resulting in the type of behaviour illustrated in Figure 3.25b.

The approach used to counter this type of behaviour is basically the same as that used at the onset of strain hardening, i.e. using secant moduli rather than tangent moduli for all subsequent iterations in which the solution remains on the unloading branch. This behaviour is indicated in Figure 3.26. In these cases, the solution convergence rate is only marginally affected by the use of secant moduli as the converged solution should always lie on the almost linear unloading branch, rather than on the reverse loading branch (Figure 3.26). In analyses performed in this study, no difficulties were experienced in directly unloading to as little as a quarter of the stress in the preceding load increment.

Problems may occur if the solution only unloads from the yield or softened response path in the final iteration cycle of an increment. In this situation, the load history parameters for the integration point involved are not updated as usual (Table 2.2-34), as otherwise the solution convergence and steel response in subsequent increments could be adversely affected.

Another important point in relation to the unloading response concerns the use of purely incremental procedures and particularly the initial value self-correcting procedure. Tillitson et al. (59) have suggested that this type of solution is inherently more reliable than an iteration procedure for analysing materially non-linear responses. In fact, this type of solution procedure does not prevent problems similar to that shown in Figure 3.25b. Initial value self-correcting incrementation is an available option in the frame analysis program but the only time it was used for a materially non-linear analysis of a frame, the solution failed on attempting to unload after the first post-elastic load reversal. This problem was not further investigated.

3.9 MODIFIED NEWTON-RAPHSON ITERATION

As stated in Section 2.5.4, Modified Newton-Raphson iteration was not considered to be suitable for analyses of complex loading-unloading responses. The reason for this is largely that solution convergence can be assured only if the stiffness matrix is updated immediately unloading occurs. If the stiffness matrix is not updated, an iteration behaviour similar to that shown in Figure 3.27 will develop. Similar difficulties are also likely to occur in the yield plateau-strain hardening transition region.

Suitable preventative updating criteria could probably be built in, but it is questionable whether such a procedure would offer any advantage over the generalized Newton-Raphson procedure. For most analyses of this type, the cost of solving the global force-displacement equations is considerably less than the cost of analysing the non-linear material responses. The potential advantage of the modified procedure would therefore probably be eliminated by the slower convergence rate.

3.10 COMPUTATION TIME

The average times taken to compute the responses shown in Figures 3.17 to 3.20 were approximately 500 and 8,300 microseconds per iteration* for the proposed and Thompson's model respectively. These times may be compared with approximately 600 microseconds required for a single evaluation of A = B**Z. For some of Kent's specimens (responses not shown), the computation times taken by the proposed model were as low as 350 microseconds per iteration. However, a relatively high proportion of the data points were on the envelope curve and consequently the smaller computation times are probably unrepresentative.

---

* Iteration was not required for these analyses, but in order to simulate more realistically the normal structural analysis situation, 3 non-updating and 1 updating analyses were performed for each strain increment and the measured computation times averaged.

The times quoted above are for all operations required to evaluate the steel stress at a given strain, i.e. recalling strain history terms from storage, solution of Ramberg-Osgood function, checking for the correct loading branch, etc. The times quoted for the proposed model also allow for computing the tangent modulus and operating the stabilizing procedures required for the Newton-Raphson solution procedure.

3.11 DISCUSSION

As indicated in the preceding sections, the basic objectives of developing an accurate analytic steel model which is economical enough to be operated as part of a general frame analysis program, have largely been achieved. Special stabilizing procedures have also been incorporated into the model to allow the use of the generalized Newton-Raphson solution procedure for materially non-linear analyses.

In this study, only a limited range of experimental data was evaluated. The model still requires further calibration and detailed adjustment to improve its generality. In particular, more extensive calibration is required for the response of unmachined deformed bars typical of the types used in reinforced concrete construction.

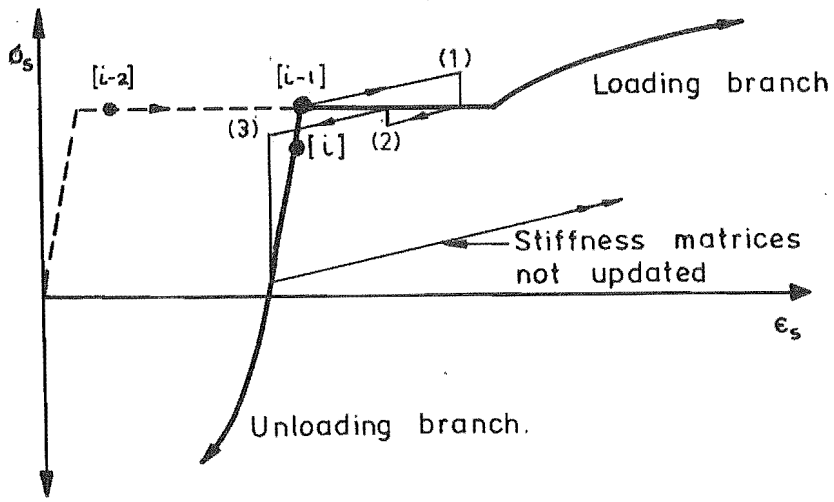

FIGURE 3.27 : BEHAVIOUR OF MODIFIED NEWTON-RAPHSON SOLUTION PROCEDURE WHEN THE SOLUTION UNLOADS FROM THE YIELD PLATEAU

4. MODELS FOR PREDICTING THE RESPONSE OF CONCRETE SUBJECTED TO UNIAXIAL LOADING

SUMMARY

This chapter describes the models used to predict the stress-strain responses of the concrete layers in the inelastic section analysis subroutines. The general model is largely based on an earlier concrete model developed by Kent (48) and subsequently modified by Blakeley (68). Only minor adaptions were made in this study. A simplified model has also been provided for uses in special situations.

The descriptions given in this chapter relate purely to the behaviour of the concrete under uniaxial loading. Modifications to the axial stress-strain relationships to account for the effect of shear displacements in plastic hinge zones are discussed in Chapter 5.

As in the case of the steel model (Chapter 3), stabilizing procedures were incorporated to ensure compatibility of the model with the Newton-Raphson solution procedure.

4.1 INTRODUCTION

Less emphasis was placed on developing a model for the concrete behaviour in this study as a number of existing models were available which were suitable. Also, in general, the normal stress-strain response of the concrete has less influence than the steel on the inelastic behaviour of the plastic hinge zones in reinforced concrete members, particularly beams.

The Kent/Blakeley model was chosen as the basis for modelling the concrete behaviour as it was sophisticated enough to take account of the effect of confinement and softening of the unloading and reloading responses at large strains, while still using simple linear relationships for defining most of the load paths. This latter aspect was important because of the number of concrete layers (at least 10) required to be

used to satisfactorily model a section. The model had also been used successfully by both Blakeley (68) and Thompson (44) for predicting the inelastic moment-curvature responses of prestressed concrete members to large post-elastic load reversals.

More sophisticated concrete models have been published, but those that were available at the time the computer program was developed (eg 69,70) were based on unconfined concrete.

4.2 GENERAL ANALYTIC MODEL

The general analytic model used to predict behaviour of the concrete under cyclic loading is shown in Figure 4.1* Details of this model, and the modifications made to the Kent (48) and Blakeley (68) models are discussed in the following subsections.

4.2.1 Envelope Curve

The general model for the envelope curve, which also defines the behaviour under monotonic loading, is divided into three regions. The relationships governing the behaviour are the same as proposed by Kent except in the first region, where a variable cubic relationship developed by Lampert et al. (71) was adopted in place of the parabolic relationship used by Kent. The relationships for each of the three regions are as follows:-

Region OA: $\varepsilon_c \leq \varepsilon_o$

$$\sigma_c = \rho f_c' \{\varepsilon_c/\varepsilon_o - (2-3/\rho)(\varepsilon_c/\varepsilon_o)^2 + (1-2/\rho)(\varepsilon_c/\varepsilon_o)^3\} \quad \ldots (4.1a)$$

where $\rho = \varepsilon_o E_c/f_c'$, σ_c is the concrete stress for the strain currently imposed on the concrete (ε_c), ε_o is the strain at the maximum

---

* In order to be consistent with conventional notation, the descriptions of the concrete models in this chapter are given in terms of positive stresses and strains. In all other chapters, the reverse sign convention of tension positive, compression negative, is used.

compressive stress (f_c'), and E_c is the initial tangent modulus of elasticity of the concrete (Figure 4.1).

This relationship defines a curve which varies in shape from cubic ($\rho = 1.5$) to parabolic ($\rho = 2$), and was adopted in preference to Kent's parabolic relationship because it showed better agreement with concrete stress-strain relationships measured* for the specimens tested in the experimental part of this study (Chapter 7). For most analyses $\rho = 1.5$ was used, with f_c' as the measured compressive strength** and E_c either calculated from $E_c = 0.043w^{1.5}\sqrt{f_c'}$ (MPa) (20) or measured (w = concrete density).

Region AB: $\varepsilon_o < \varepsilon_c \leq \varepsilon_{20}$

$$\sigma_c = f_c' \{1 - Z (\varepsilon_c - \varepsilon_o)\} \qquad \ldots (4.1b)$$

where Z is the parameter defining the slope of the falling branch (AB). In the computer program, the value of Z is inputted as data and consequently any desired value can be used. However, for most analyses performed in this study, the value of Z used was calculated in accordance with Kent's model for the effect of confinement, i.e.

$$Z = 0.5/(\varepsilon_{50h} + \varepsilon_{50u} - \varepsilon_o)$$

where: $\varepsilon_{50u} = (2f_c' + 20.7)/(1000f_c' + 6900)$ for f_c' in MPa units, and

$\varepsilon_{50h} = 0.75\rho'' (b''/s)^{0.5}$

ρ'' = confining steel ratio = $2(b'' + d'')A''_s/ (b'' d'' s)$

b'' = width of the confined concrete to the outside of the ties

d'' = depth of the confined concrete to the outside of the ties

---

* Strain measurements taken from opposite sides of standard 305mm x 152mm diameter concrete test cylinders using 102mm Demec strain gauges.

** If appropriate, the value of f_c' can be increased to allow for the strength enhancement effect of the confining steel, e.g. as suggested by Scott (72).

A''_s = cross-sectional area of one leg of the confining hoops

s = spacing of the hoops

For unconfined, e.g. cover, concrete $Z = 0.5/(\varepsilon_{50u} - \varepsilon_o)$, and the stress drops to zero when the imposed strain reaches the crushing strain ε_{cr}.

Region BC: $\varepsilon_c > \varepsilon_{20}$

$$\sigma_c = 0.2\, f'_c \qquad \ldots (4.1c)$$

In the case of unconfined concrete, if $\varepsilon_{20} < \varepsilon_{cr}$, the stress developed will remain at this level up to a strain of ε_{cr} then drop to zero. For confined concrete the stress developed under monotonic straining is assumed to remain at this level for all strains greater than ε_{20}.

4.2.2 Unloading and Reloading

The relationships for modelling the unloading and reloading behaviour are shown in Figure 4.1. These idealizations are based on the model proposed by Blakeley (68) and are discussed below:

Region OA:

During unloading and reloading in this region, the concrete is assumed to respond linearly, with the slope of the response curve equal to the initial elastic modulus, E_c. In practice, some energy is dissipated during load cycling in this region. However, there was not sufficient data available to be able to model this behaviour and consequently the assumed linear response used by Blakeley was adopted without modification.

Region AB:

The model for unloading from, and reloading to this part of the envelope curve is shown in Figure 4.1. In Blakeley's model, unloading from curve AB causes an initial instantaneous 50% loss in stress for no decrease in compressive strain. After this, the response follows a linear unloading path with a slope of $0.5R_c$, where R_c is a reduced elastic modulus as

defined in Figure 4.1. The value of R_c varies linearly from $0.8E_c$ at $\varepsilon_m = \varepsilon_o$ to $0.1E_c$ at $\varepsilon_m = \varepsilon_{20}$. Reloading from zero concrete stress occurs along a linear path with a slope of R_c, so that the envelope curve is eventually reached at the same point (stress and strain) as the origin of the unloading branch. The response then continues to follow the envelope curve until a further strain reversal occurs. Reversals of strain while still on the unloading branch cause the stress to immediately double, after which the response follows the reloading curve (Figure 4.1). Similarly, unloading from the reloading branch reverses the behaviour, with an immediate halving of the stress to bring the response onto the unloading branch.

While this behaviour was acceptable for the section analyses performed by Blakeley and Thompson, the instantaneous changes in stress of up to $0.5f'_c$ were a serious potential threat to the solution convergence process in analyses of multi-degree of freedom structural assemblages. Blakeley's model was therefore modified to include initial unloading and reloading transition branches with a slope of E_c (see Figure 4.1). Although made primarily to facilitate the convergence process, the modifications should also more accurately model the changes in stress and the energy dissipation associated with small magnitude strain reversals.

Region BC:

The model for unloading and reloading is the same as for Region AB, except that the value of R_c is fixed at $0.1E_c$ regardless of the value of ε_m.

4.2.3 Behaviour of Concrete in Tension

As indicated in Figure 4.1, the response of the concrete in tension is assumed to follow a linear path with a slope of E_c up to the tensile capacity of the concrete, f'_t. At this stage, the concrete is assumed to crack with total loss of tensile capacity. In Blakeley's model, pre-loading in compression was assumed not to affect either the tensile

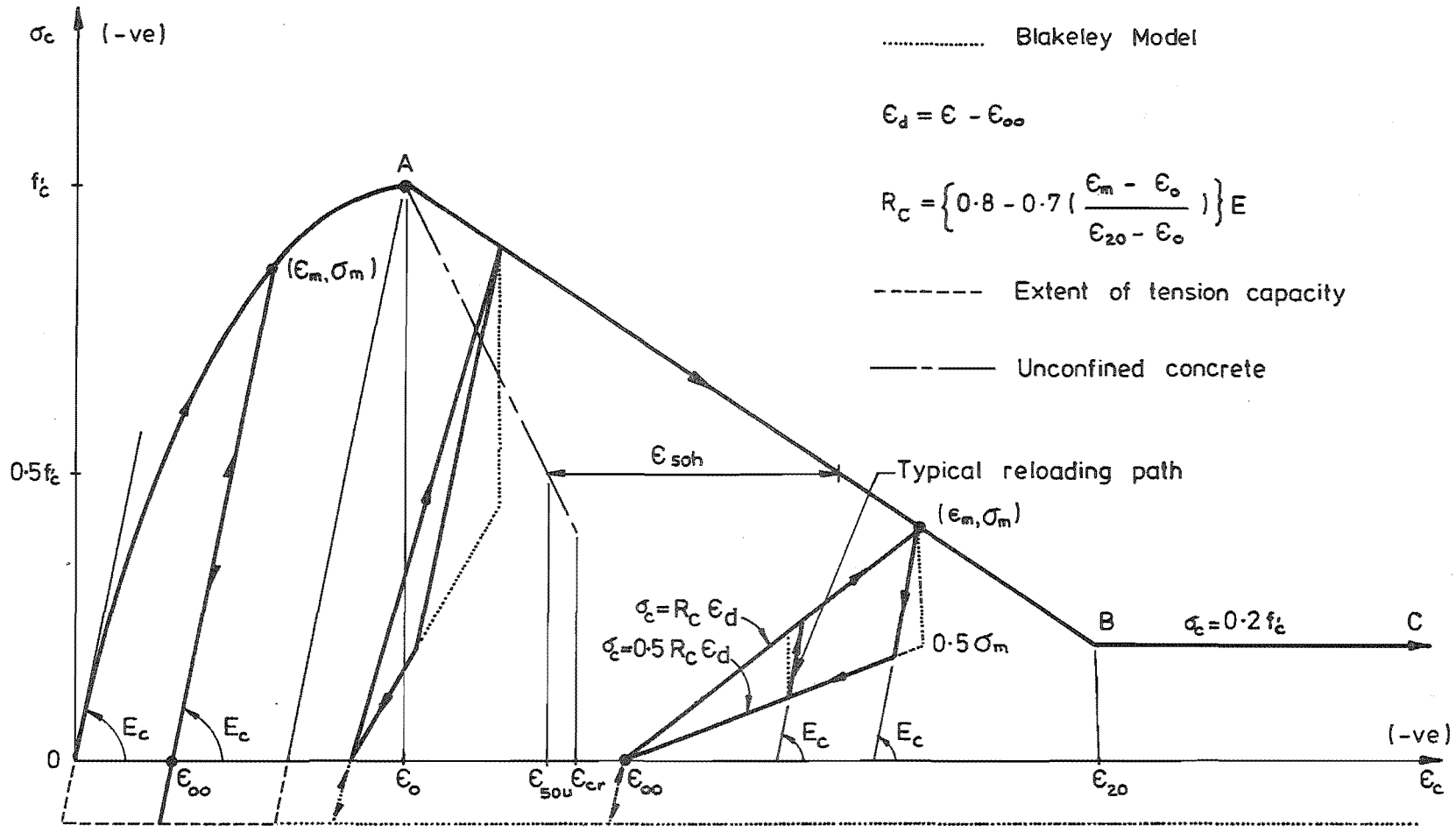

FIGURE 4.1 : GENERAL MODEL FOR THE RESPONSE OF CONCRETE SUBJECTED TO CYCLIC LOADING

capacity or the elastic modulus for tension loading, regardless of the maximum compressive strain imposed (except where the predicted strain exceeded the crushing strain of modelled unconfined concrete).

This has been modified in the proposed model so that the tensile capacity of the concrete is lost if the maximum compressive strain exceeds ε_o. Although this intuitively seems more realistic than assuming that even very large compressive strains have no affect on the tensile response, the modification was made mainly in order to reduce the number of strain history terms required.

4.3 SIMPLIFIED ANALYTIC MODEL FOR TYPE C SECTIONS

The simplified concrete model used in the Type C section analysis procedure (Section 2.3.4), is shown in Figure 4.2. As indiciated, the modelled response is the same as for the general concrete model (Section 4.2) for compressive strains of up to ε_o. This is followed by a constant stress envelope branch ($\sigma_c = f'_c$), with unloading and reloading occurring along the same straight line path which has a slope of E_c.

No maximum strain limit has been imposed. However, this section analysis procedure considers only the concrete to be inelastic and consequently it should not be used in situations where the compression strains are likely to exceed about 0.004.

4.4 EFFECT ON SOLUTION CONVERGENCE

This section considers only the general concrete model, two features of which were identified as potentially causing problems with the solution convergences. Similar problems do not arise in the simplified model, partly because of the form of the model, and also because of rigidity provided by the steel, which is assumed to always be elastic in Type C sections.

4.4.1 Unloading and Reloading Paths

The problems encountered here are caused by 'steps' in the response involving first an increase, and then a decrease in the slope of the load

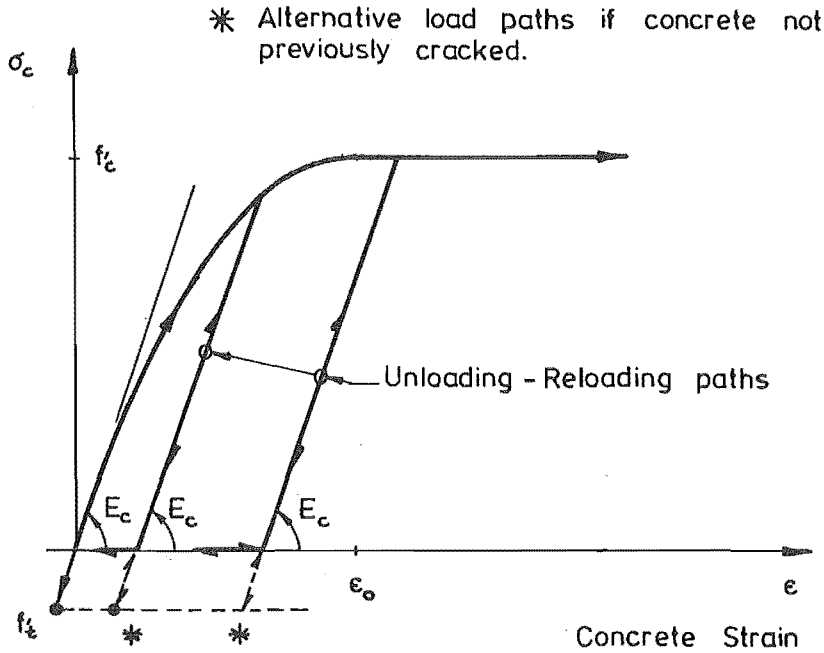

FIGURE 4.2 : SIMPLIFIED CONCRETE MODEL FOR TYPE C SECTION ANALYSES

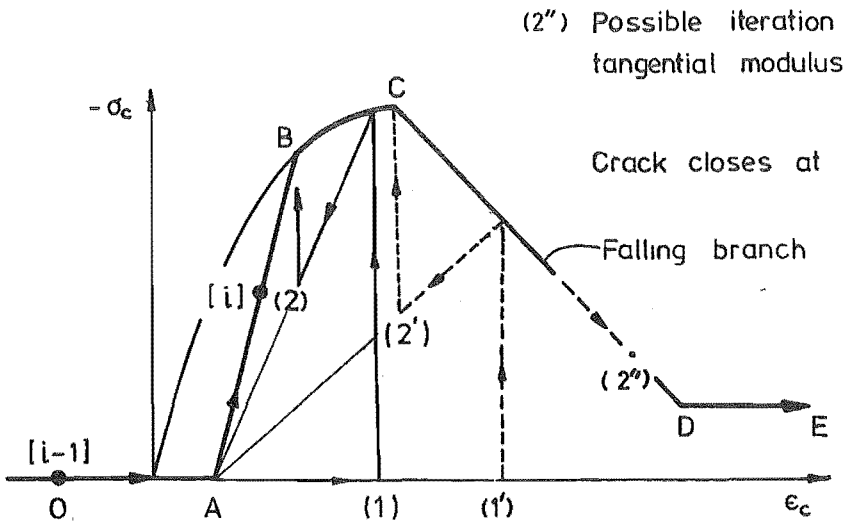

Note: Secant moduli are used for all iterations in which the solution is in the region BCDE.

FIGURE 4.3 : USE OF SECANT MODULI WHEN CRACKS FIRST CLOSE

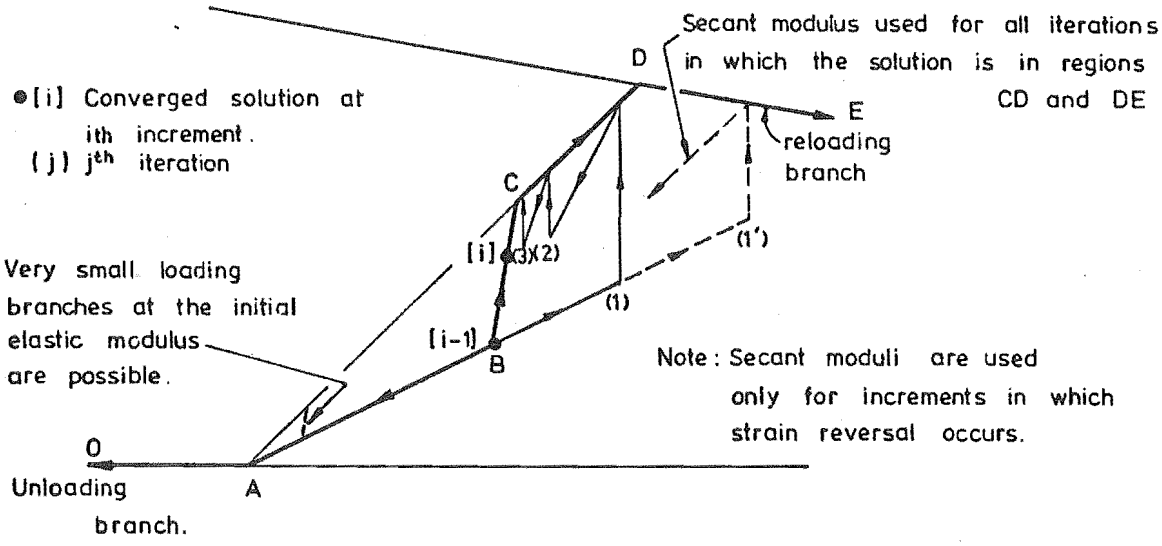

(a) Reloading.

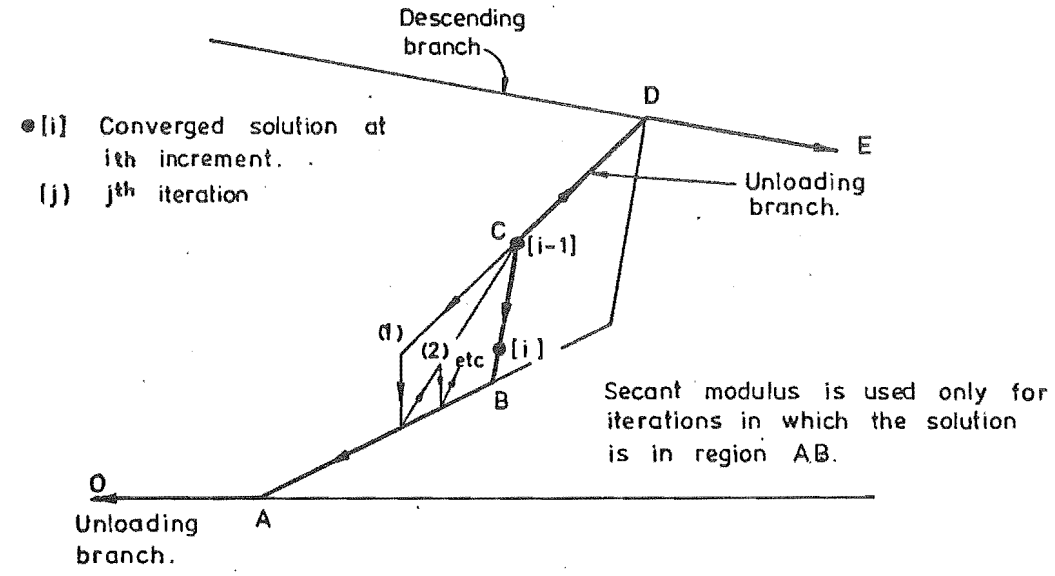

(b) Unloading.

FIGURE 4.4 : USE OF SECANT MODULI FOR STRAIN REVERSALS WHICH OCCUR WHILE THE CONCRETE IS UNLOADING OR RELOADING

curves. As in similar situations in the steel model (Sections 3.8.2 and 3.8.3), substitute secant moduli are used to inhibit solution oscillation (Figures 4.3 and 4.4). Secant moduli are also used if the solution overshoots on to the falling branch.

As in the case of the onset of strain hardening in the steel model, the use of secant moduli at these locations in the concrete model can retard the solution convergence rate. However, in the analyses performed in this study, the average convergence rates over several load increments appeared to be little affected.

4.4.2 Descending Branch

As shown in Figure 4.5, the presence of both ascending and descending branches on the load curve means that non-unique solutions exist in the local concrete response. A similar situation can also occur on reloading (Figure 4.5). No direct action was taken in respect of this type of problem.

The use of the secant moduli as in Figures 4.3 and 4.4 generally helps to return the solution to the correct branch, as does displacement control, whether this is provided by the solution procedure or by interaction with other parts of the structure. However, the effectiveness of these stabilizing factors diminishes as the true solution approaches the junction between the ascending and descending branches and in members where two or more segments are predicted to yield at the same time. In these situations, probably the only effective method of reducing the risk of the analysis converging to the wrong solution is to reduce the size of load increments applied.

Despite the inability to fully guard against incorrect solutions in these situations, no problems of this type were actually detected in the analyses performed. Neither is this problem likely to significantly affect the overall response of the structure.

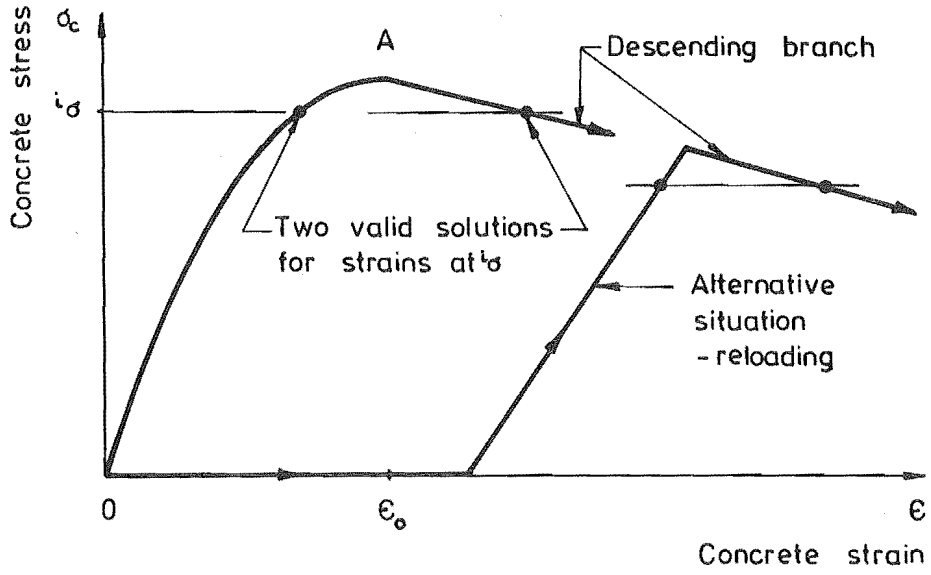

FIGURE 4.5 : NON-UNIQUE SOLUTIONS ASSOCIATED WITH THE DESCENDING BRANCH OF THE CONCRETE STRESS-STRAIN ENVELOPE CURVE

5. MODEL FOR PREDICTING SLIDING SHEAR RESPONSE

SUMMARY

This chapter reviews the basic mechanisms of shear resistance in plastic hinge zones in reinforced concrete members and describes the inelastic sliding shear model developed for the frame analysis computer program. The emphasis in this model has been placed on modelling the shear deformations resulting from sliding between crack faces and the effect of the resulting mismatched crack surfaces on crack closure.

5.1 INTRODUCTION

There is now considerable experimental evidence showing that the post-elastic response of cyclically loaded ductile beams and walls with conventional reinforcing can be significantly affected by shear deformation in the plastic hinge zones, e.g. (10, 11, 12, 22). The shear deformation developed under these conditions is largely due to sliding along wide full depth cracks opened up by the large plastic tensile strains induced in the longitudinal bars, and can be significant even when the maximum nominal shear stress is quite moderate, e.g. less than 1 MPa.

Modelling of these shear deformations was considered important in this study as there appeared little justification in carrying out expensive refined analyses of the flexural responses if significant components of the total deformations were ignored. As far as is known, no other detailed models of this type of shear response were available which would have been suitable for use in a general frame analysis computer program. The model developed in this study was therefore intended to provide a more realistic and balanced procedure for analysing the post-elastic response of reinforced concrete structures subjected to seismic loading.

Because of the complexity of the behaviour and the lack of detailed measurements, only a preliminary investigation of several aspects of the

shear behaviour has been made in this study. Nevertheless it was found that for the types of structure considered (Section 2.2), the shear deformations predicted by the model for large displacement reversed loading were generally in reasonably good agreement with observed results, and the predicted total deflections were considerably more accurate than could have been obtained otherwise.

5.2 SHEAR TRANSFER MECHANISMS

A large number of studies of the shear behaviour of reinforced concrete members have been made. Several detailed reviews of this work are available (73, 74), and therefore only a general review of the basic mechanisms of shear transfer is made in this section. This is largely restricted to studies of shear response due to monotonic loading as very few studies have evaluated the shear response of flexural members subjected to post-elastic reversed cyclic loading. However, many of the mechanisms that influence the monotonic response are also relevant to the sliding shear response and consequently serve as useful background to the analytic model developed in subsequent sections.

Four basic mechanisms of shear transfer are considered: direct concrete shear stresses, interlock shear transfer, dowel action and shear reinforcement.

5.2.1 Direct Shear Stresses

Most experimental studies of biaxial stress states in concrete have concentrated on establishing the biaxial fracture and crushing behaviour, rather than on the stress-strain response. In only a few studies, such as that of Kupfer et al. (75), have comprehensive strain measurements been made, and consequently, many aspects of modelling the biaxial response remain speculative.

In many finite element applications where biaxial stress states have been considered (e.g. 58, 76), the principal normal stress-strain responses have been assumed given by the unaltered uniaxial response,

and the Mohr-Coulomb law has been used as the failure criterion. More sophisticated idealizations have been developed, such as that used by Phillips and Zienkiewicz (60), based on hydrostatic and deviatoric components of stress and strain and on a linear form of the octahedral shear stress failure criterion. These have shown good agreement with the limited experimental biaxial response data available. However, none of these models has been verified, or are likely to apply for highly fractured concrete with mismatched crack surfaces.

5.2.2 Interlock Shear Transfer

Interlocking of aggregate and concrete irregularities between crack surfaces has only been recognised as a reliable shear transfer mechanism within the last 20 to 30 years. The behaviour of this mechanism has been examined in a number of recent studies, and the review of this work given below considers the main parameters which influence the interlock response.

(a) Crack Width

This is the most significant parameter influencing the rigidity of the interlock mechanism. Quantitative assessment of this influence has been made in several studies using small scale test specimens with preformed cracks, the widths of which were held constant during each test run.

Fenwick (73) used 102 mm x 102 mm x 356 mm plain concrete specimens (Figure 5.2) to examine the aggregate interlock response for crack widths ranging from 0.063 mm to 0.38 mm. Typical observed responses for these specimens are shown in Figure 5.1. Failure of the test blocks was caused by the formation of either diagonal or flexural cracks (Figure 5.2), and did not involve breakdown of the interlock mechanism. For the range of crack widths considered, the relationship between interlock rigidity and crack width was found to be given by:-

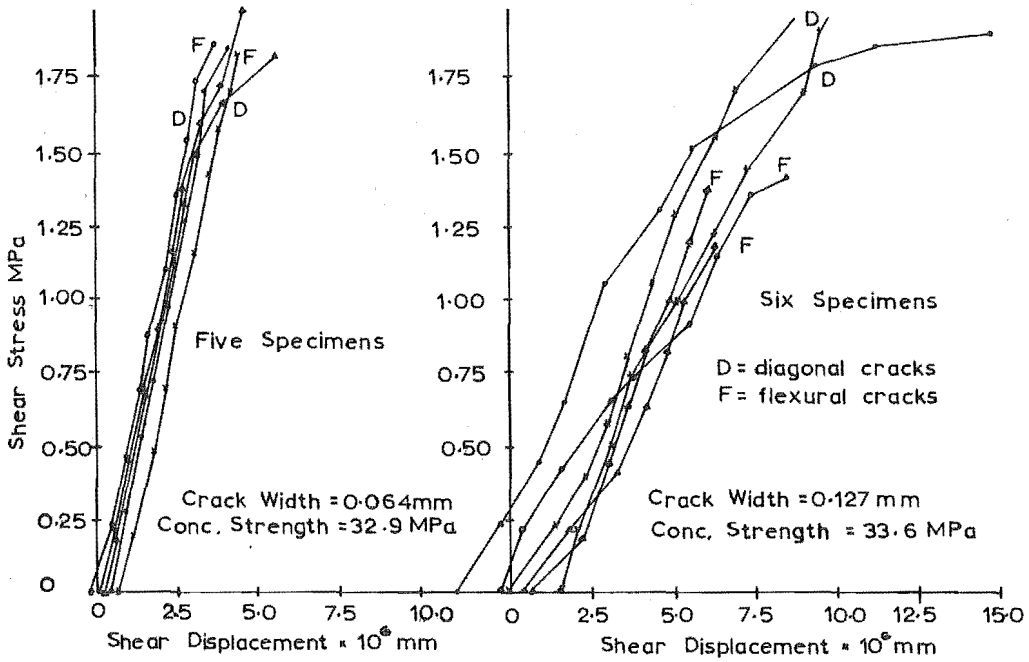

FIGURE 5.1 : TYPICAL INTERLOCK RESPONSES MEASURED BY FENWICK (73)

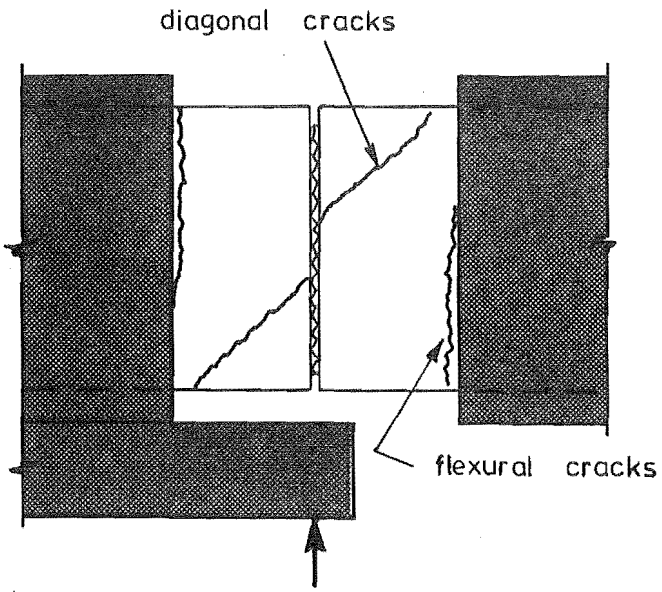

FIGURE 5.2 : INTERLOCK TEST SPECIMEN USED BY FENWICK (73) SHOWING DIAGONAL AND FLEXURAL CRACKING PATTERNS

$$A_{int} = 2113/c - 1561 \quad (N/mm)^* \qquad \ldots (5.1)$$

where A_{int} is the interlock rigidity, and c is the crack width in millimeters.

Houde and Mirza (76), using a test specimen with similar geometry, carried out tests for crack widths ranging from 0.05 mm to 0.5 mm. They observed similar response and failure modes, but found that for their results, the relationship between interlock rigidity and crack width could best be given by:-

$$A_{int} = 767/c^{1.5} \quad (N/mm)^* \qquad \ldots (5.2)$$

Both this, and the relationship suggested by Fenwick, give similar values of interlock rigidity for crack widths in the range 0.1 mm to 0.9 mm.

Paulay and Loeber (77) also investigated the response of the interlock mechanism, but with a test specimen designed to avoid the diagonal and flexural cracking failures of Fenwick's tests. They were able to impose substantially larger shear loads (up to 7 MPa) and, as can be seen in Figure 5.3, the stiffness measured in these tests did not remain constant with increasing sliding displacement. However, transverse restraining forces of up to 4.2 MPa were required to maintain the "crack width" constant, and over much of the upper portion of the response, the cracks would have been effectively closed, since restraining stresses of this magnitude would be provided only in the compression block. Below a shear stress of approximately 1 MPa, the interlock rigidities measured in these tests were in good agreement with the relationship proposed by Fenwick (Eq. 5.1).

---

* The relationships have been adjusted to correspond with a concrete 152 mm cube strength of 35 MPa.

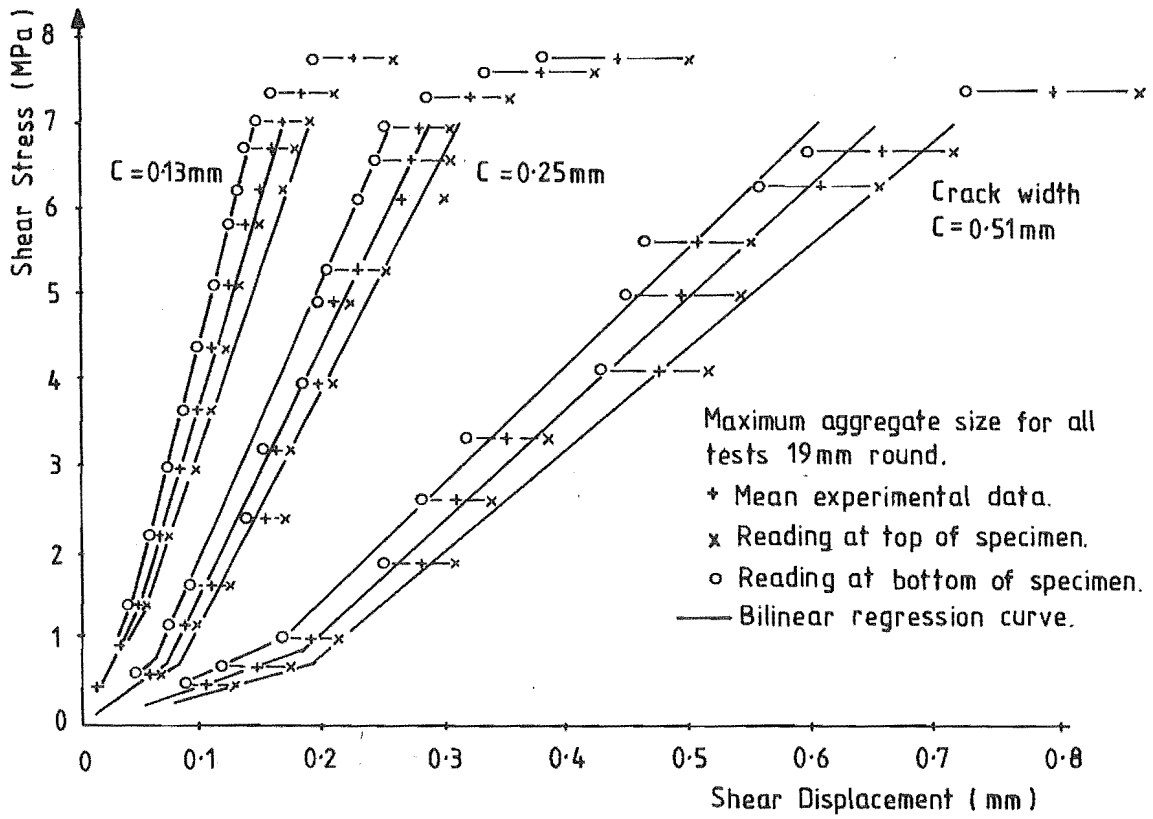

FIGURE 5.3 : SHEAR STRESS-SHEAR DISPLACEMENT RELATIONSHIPS MEASURED BY PAULAY AND LOEBER (77)

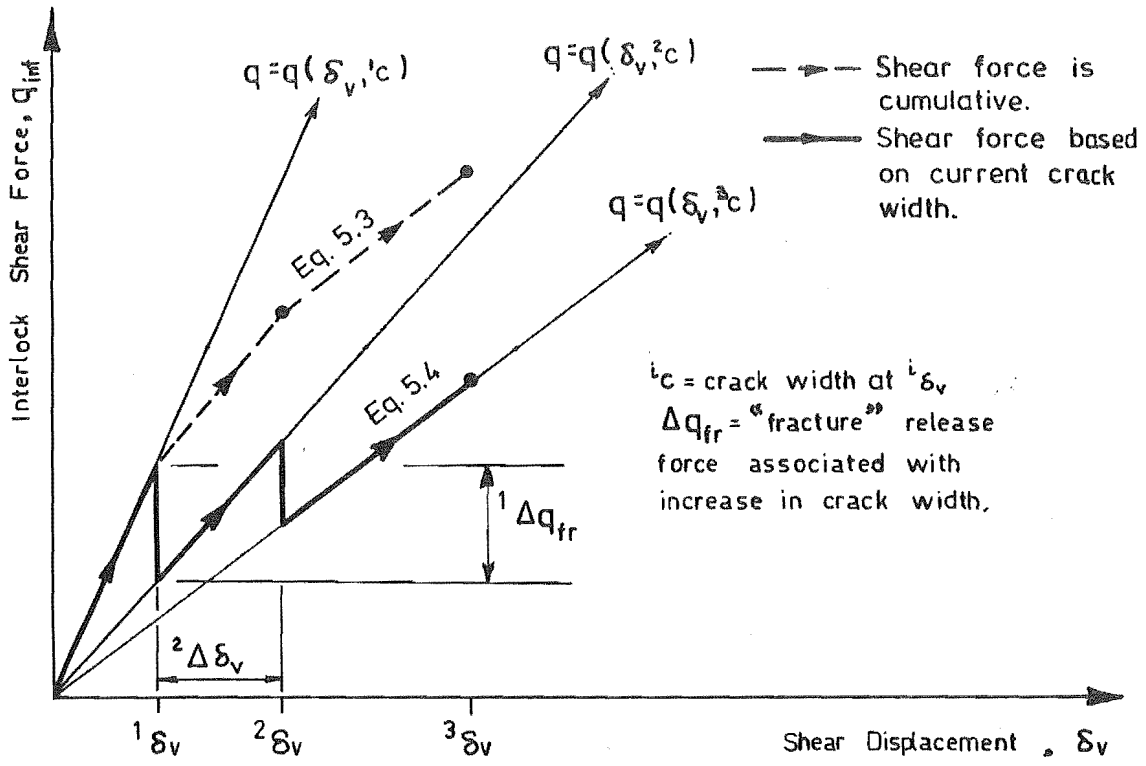

FIGURE 5.4 : ALTERNATIVE SHEAR AGGREGATION PROCEDURES FOR SITUATIONS WHERE CRACK WIDTHS INCREASE WITH INCREASING SLIDING

(b) Concrete Strength

Fenwick and Houde & Mirza both found the rigidity of the interlock mechanism to be directly proportional to $(f_c')^{\frac{1}{2}}$. This is consistent with the usually accepted variation in concrete elastic modulus (20).

(c) Maximum Aggregate Size

Most test results, including those obtained in the above three investigations, have indicated that the maximum aggregate size has only negligible influence on the rigidity of the interlock mechanism, provided that it is large in comparison with the crack width.

(d) Reloading

Paulay and Loeber subjected nine interlock shear test specimens to repeated loads of up to 6.2 MPa shear stress in one direction. Prominent features of the responses of these specimens were an increase in stiffness on reloading and accumulation of residual sliding displacements. After testing, the crack surfaces were found to be heavily striated, with considerable loose material evident.

Similar deterioration of the interlock response has also been observed in tests involving low intensity cyclic fatigue loading of pavement slabs (78, 79).

(e) Shear Force Aggregation

For constant crack widths, the interlock shear stress-displacement responses measured by Houde & Mirza and by Fenwick were found to be linear, while those measured by Paulay & Loeber were bi-linear. In the latter two studies, small "no load" displacements were also evident. However, in practice crack widths do not generally remain constant and it is therefore necessary to ascertain the laws governing aggregation of the interlock shear resistance under

variable crack width conditions. Two possible laws for cracks opening with increasing shear strain are shown in Figure 5.4. The relationships governing these are

$$q_{int} = \Sigma_i \Delta q_{int} \quad (^i\Delta\delta_v, {}^ic) \qquad \ldots (5.3)$$

which is path dependent, i.e. the interlock shear resisted is cumulative, and

$$q_{int} = q_{int} \quad (\delta_v, c) \qquad \ldots (5.4)$$

which is path independent, i.e. the shear at any stage is defined by only the current values of δ_v and c.

In order to account for variations of crack width directly, Taylor (80) carried out tests in which the ratio of increment in crack width, Δc, to incremental shear displacement, $\Delta\delta_v$, was held constant during loading, i.e. crack width not constant. Shear responses were obtained for a realistic range of values of the ratio $\Delta c/\Delta\delta_v$ which had previously been determined from extensive measurements of both normal and sliding components of crack displacements in beams. However the information available from tests of this type has relatively restricted applicability. The ratio $\Delta c/\Delta\delta_v$ does not, in general, remain constant, and consequently a general analysis procedure must be capable of treating variations in crack width and sliding displacement independently. Only by comparing responses from both variable and constant crack width interlock tests is it possible to establish the necessary global laws governing shear aggregation.

One such comparison has been made by Paulay & Loeber (Figure 5.5), and the results of this indicate that in situations where the crack width is increasing, the aggregation of shear stress is in close agreement with Eq. 5.4. This behaviour is also consistent with the physical mechanism, i.e. an opening crack can be conceptualized as a partial fracture of the interlocking mechanism and is likely to be associated with fracture release stresses (Figure 5.4), comparable to those for concrete cracking under uniaxial tension. Nevertheless, further comparisons, both with

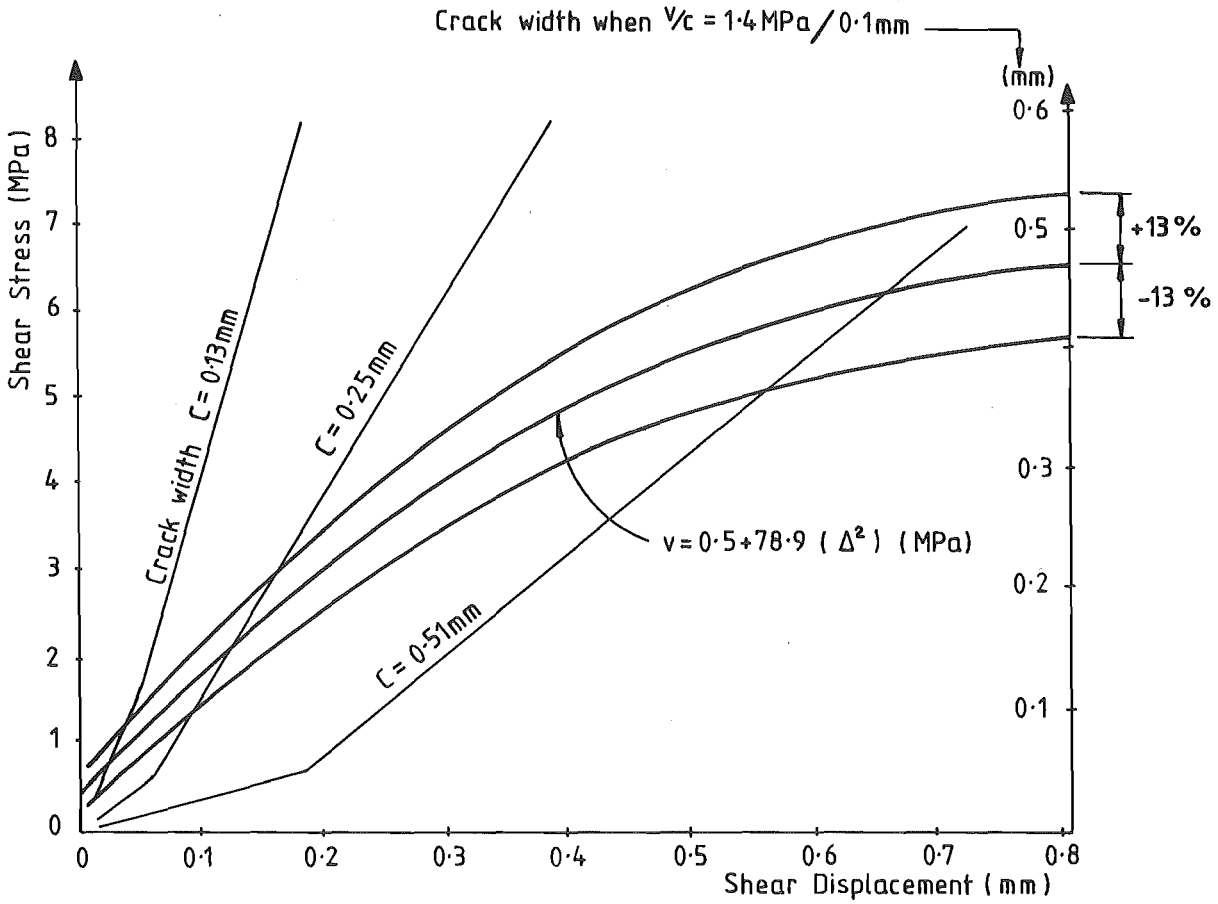

FIGURE 5.5 : SHEAR STRESS-SHEAR DISPLACEMENT RELATIONSHIP FOR CONSTANT SHEAR STRESS TO CRACK WIDTH RATIO, FROM PAULAY AND LOEBER (77)

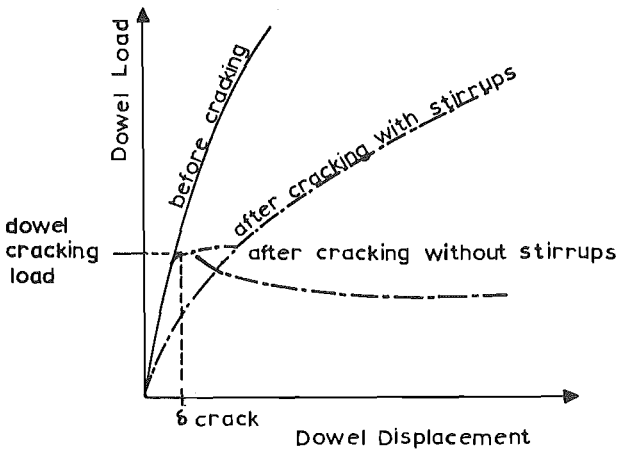

FIGURE 5.6 : TYPICAL DOWEL LOAD-DISPLACEMENT RESPONSES, FROM HOUDE AND MIRSA (76)

different variations in Δc and $\Delta\delta_v$ and with loading and unloading responses, are still required, first to verify, and if necessary modify this aggregation law, and secondly, to ascertain the laws applicable for other types of response. It is, for instance, unlikely that the same aggregation law applies in the case where the crack width decreases with increasing sliding displacement.

(f) Restraining Forces

On the basis of measurements of the normal restraining forces necessary to maintain crack widths constant, Paulay & Loeber concluded that the relationship between the interlock shear force and the restraining force was approximately linear and had a slope corresponding to a coefficient of friction $\mu = 1.7$. Neither the crack width nor the maximum aggregate size significantly affected this relationship. Similar results have also been obtained in "push-off" tests where reinforcement was used to provide passive restraint to preformed crack slip planes (81, 82).

It is significant, however, that in the tests conducted by Paulay & Loeber, much of the restraining force was imposed while making corrections to the crack widths at the end of every second to third increment. For increments of shear loading, when only the passive restraint of the test rig was available and the cracks were able to expand slightly, the change in restraining force was much less. Similarly, in the variable crack width tests conducted by Taylor (83), the normal restraining forces were estimated not to have exceeded 20% of the applied shear force (i.e. $\mu \gtrsim 5$).

The above results indicate that the relationship between the shear and restraining forces is substantially influenced by the relative displacements along and normal to the crack surface. However, considerably more detailed experimental data, including measurements of the complete biaxial force-displacement behaviour of the crack zone under varying loading conditions, are required before it will be possible to ascertain the precise nature of the relationship.

5.2.3 Dowel Action

Typical stages of a dowel load-displacement response are shown in Figure 5.6.

Due to the differing nature of many of the tests and varying interpretations placed on the measured responses, there have been substantial differences in the relative importance accorded to parameters which affect the dowel cracking load and displacement (Figure 5.6). Parameters that have been considered to be of significance include bar size, number of layers of bars, position of bar group (i.e. top or bottom), longitudinal stress in bars, depth of beam, distance to support or spacing of main cracks at the level of the dowel reinforcement, depth of concrete cover, and most commonly, the net width of the concrete section at the level of the dowel reinforcement (b_n in Figure 5.7) and the concrete tensile strength (f'_t or $\sqrt{f'_c}$). In most instances the dowel load-displacement response prior to dowel cracking has been approximated as being linear, although there are large differences, i.e. up to a factor of 10, in the stiffness assumed for this response by various investigators (76).

For a beam with stirrups, the most significant controllable parameters influencing the dowel post-cracked shear-displacement response have been found to be the strength and spacing of individual stirrup groups and the number of layers of dowel bars (84 , 85, 86). These parameters directly affect the length, stiffness and strength of the dowel acting as a beam (Figure 5.8) and the strength of the "fixed end" support, i.e. the strength of individual stirrup groups. Unless it yields, only the stirrup group closest to the tension face of the main crack participates effectively in resisting the dowel shear. The dowel flexural strength is also affected by the net tension induced in the reinforcement by flexure in the reinforced concrete member. On the other hand, the cover concrete contributes little to the dowel shear-displacement response because of the high bond stresses required for composite action.

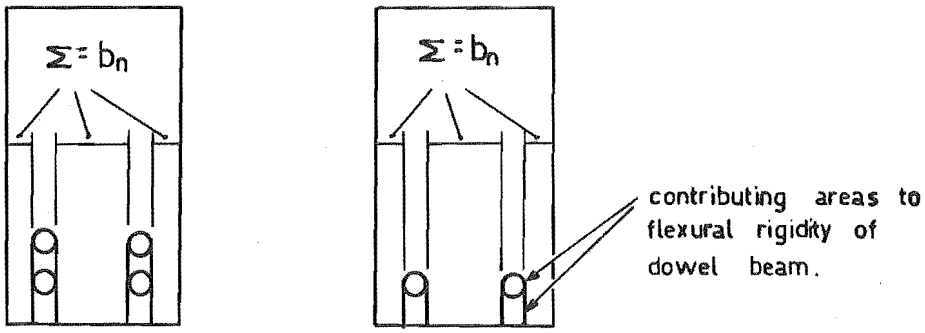

FIGURE 5.7 : AREA OF THE DOWEL BEAM AFTER CRACKING

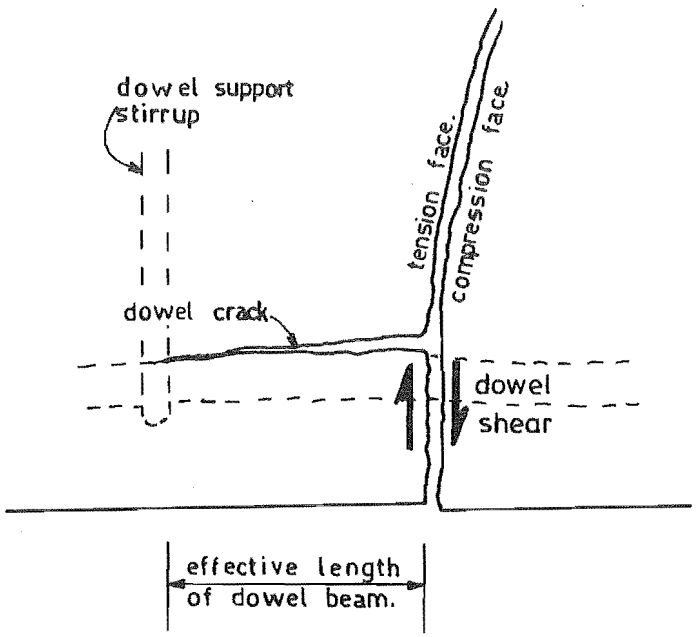

FIGURE 5.8 : IDEALIZED DOWEL BEHAVIOUR

5.2.4 Shear Reinforcement

It is now recognised that the customary view that shear reinforcement acts only as a part of a truss mechanism significantly over-simplifies the true situation (87). The shear reinforcement can also aid the interface shear transfer by restricting the widening of the cracks, and as discussed in Section 5.2.3, the strength and spacing of stirrup groups can substantially influence the dowel response. Bent-up bars have been found to be slightly less effective than stirrups largely because they do not provide support for the main reinforcement acting as dowels (88).

5.3 PLASTIC HINGE ZONE SHEAR DEFORMATIONS

In recent years several researchers have made measurements of the shear deformations in the plastic hinge zones of reinforced concrete members (11, 12, 31). The qualitative evaluation of the plastic hinge zone behaviour given in this section is largely based on the behaviour observed in these tests and in those conducted in the present study (Chapters 7 to 9).

5.3.1 Sliding Shear Mechanism

An idealization of the sliding shear mechanism for a doubly reinforced beam member is illustrated in Figure 5.9. The behaviour illustrated is for a beam which is subjected to moderate to high intensity pre-yield load reversals before being loaded into the post-elastic range. However the pre-yield loading is not a prerequisite for the formation of a sliding shear mechanism. The main features of the mechanism illustrated are:-

(a) The formation of full depth slip planes as a result of the interconnection of flexural (or flexural-shear) cracks originating from opposite faces of the member. The crack spacing and widths are smaller, and hence the interlock rigidity larger in the vicinity of the main reinforcement (Figures 5.9 c and d).

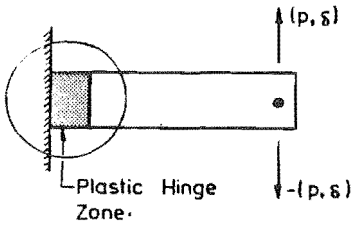

(a) Member Loading

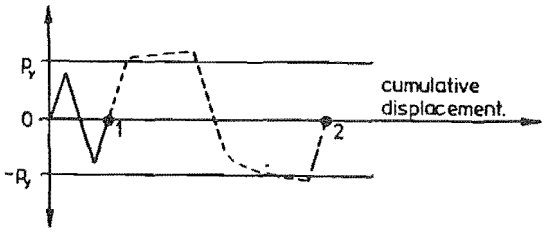

(b) Loading Sequence

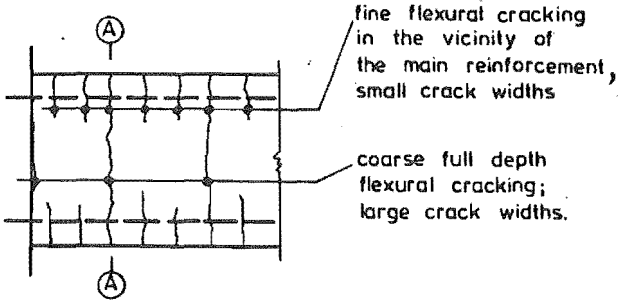

(c) Detail of Plastic Hinge Zone at Load 1

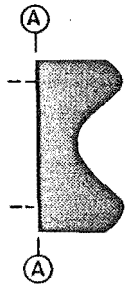

(d) Approximate Distribution Interlock Rigidity Along Slip Line A-A

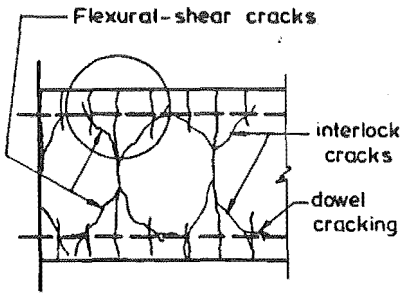

(e) Detail of Plastic Hinge Zone at Load 2

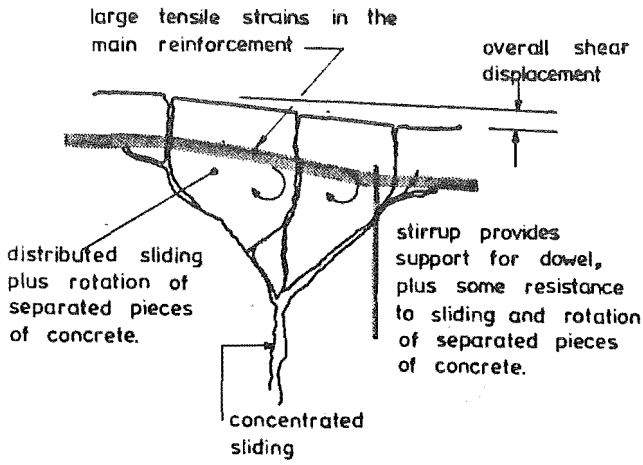

(f) Detail B

FIGURE 5.9 : IDEALIZED SLIDING SHEAR MECHANISM

(b) At high load intensities and particularly during post-elastic loading, inclined shear, interlock and dowel cracks form due to the concentration of shear stress in the vicinity of the bars (Figure 5.9 e). These cracks, both in their own right and by linking with the smaller flexural cracks, reduce the effective shear rigidity in the vicinity of the main flexural reinforcement. This results in a more even distribution of interlock shear resistance over the depth of the member. Both rotational and sliding displacements of the loosened pieces of concrete contribute to the overall shear displacement. Resistance to displacement (rotation and sliding) is provided by concrete interlock, which is a function of the crack widths, and by dowel action of the longitudinal and transverse reinforcement (Figure 5.9 f).

(c) After the first main post-elastic load reversal there are large residual plastic strains in the bars which have yielded in tension. Consequently on reversal of loading the cracks in the compression face are fully open. On further loading these open over the full depth of the section, and shear slip can occur along the crack faces. This slip occurs at low load intensities before the applied moment closes the cracks in the compression face.

(d) The sliding causes the rough surfaces of the crack to come into contact before the axial strain at the compression face reaches zero (Figure 5.10). This both restricts the magnitude of the shear deformations and prevents the cracks from fully closing. The resulting residual tensile strain at the compression face results in an increased elongation of the plastic hinge zone as larger plastic strains have to be developed in the tension bars at the opposite face in order to attain the same curvature.

Typical sliding shear deformation response curves for a reinforced concrete beam are shown in Figure 5.10. The pinched shape of the

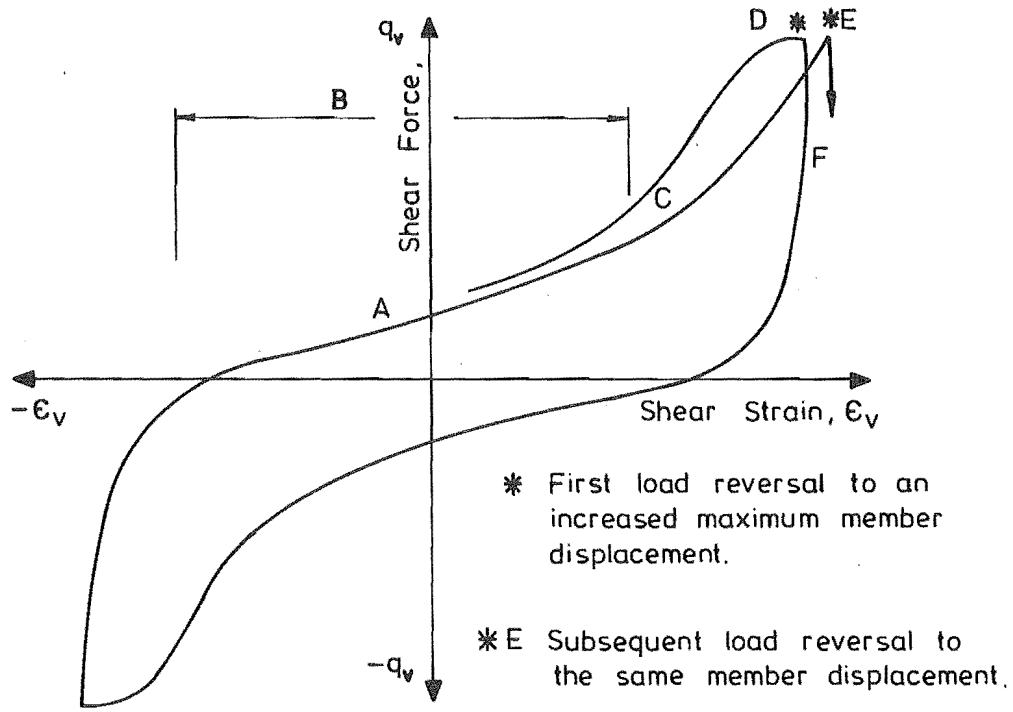

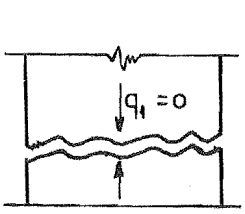

Open crack. (A)

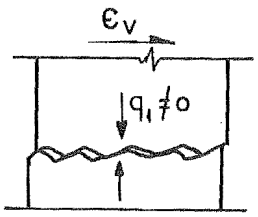

"Closed crack" (C)

For $\epsilon_v \neq 0$ the crack is unable to fully close, resulting in significant residual tensile strains. As indicated the magnitude of sliding is limited by the crack roughness and the axial strain.

q_1 = normal force

FIGURE 5.10 : TYPICAL SLIDING SHEAR FORCE STRAIN RESPONSE FOR A REINFORCED CONCRETE PLASTIC HINGE ZONE

hysteresis loop develops only after the first full post-elastic load cycle. Region A is the soft central region of the response where sliding occurs at low loads along open full depth cracks. The extent of this region is indicated by B. After the cracks close, there is a sharp increase in the shear rigidity (C). This may be followed by a region of strain softening at high load intensities (D), although as indicated, the softening is usually significant only during the first load reversal to a larger displacement. This softening is probably largely caused by opening up of the main inclined flexural-shear cracks in the plastic hinge region due to increased plastic strain in the tension bars, crushing (or spalling) of cover concrete may also contribute to the shear deformations in this region of the response. The shear response for subsequent load reversals to the same maximum member displacement exhibits less softening at high loads and normally a small increase in the peak shear strain (E). This is largely due to increased residual elongation of the plastic hinge zone (see point (d) above) and deterioration of the concrete caused by the sliding along the rough crack surfaces.

The effective shear rigidity during the initial stages of unloading from a high load intensity is usually much higher (F) than in any other region of the response. The corresponding behaviour during unloading from the soft central region (A), or from the region where the cracks start to close (A to C), is not accurately known and the writer is unaware of any detailed measurements of the shear response under these conditions.

5.3.2 Factors Influencing the Sliding Shear Response

The main controllable factors affecting the sliding shear response are:

(a) The distribution of flexural reinforcement over the section depth. A more even distribution of reinforcement, such as may exist in a shear wall, would result in less variation in flexural crack spacing, and hence interlock rigidity, over the section depth. This would be likely to affect the interlock cracking behaviour and should improve the dowel resistance.

(b) The shear reinforcement content and spacing. The effect in this case will be similar to that on the dowel response under monotonic loading (c.f. Figures 5.8 and 5.9 f). The shear reinforcement also controls the extent of deformation due to truss action and may influence the shear deformation component due to opening of the inclined flexural-shear cracks (Section 5.3.1).

(c) The relationship between the axial, flexural and shear load sequences applied to the plastic hinge zone. This influences the pattern and severity of cracking, the magnitude of residual elongation of the plastic hinge zones, and the relationship between the crack widths and the applied shear force.

5.3.3 Previous Analytic Model

The only detailed analytic model of the sliding shear mechanism known to the writer, is that developed by Ma (89) and subsequently revised by Ma et al. (12). This model was developed after a detailed evaluation of the observed shear behaviour of the plastic hinge zones in several beams tested by Ma. The model includes separate elements for representing interlock, stirrup and dowel shear resistance mechanisms, and also takes account of the restriction on sliding due to the slope and roughness of the crack surfaces.

However, Ma developed the model for evaluating shear resistance along specific cracks in a beam, and it could not be used for a general analysis. The shear response is analysed in isolation from the flexural response and foreknowledge of the crack width, shape and position relative to the stirrups is required. Good correlation between observed and predicted responses was evident only for cyclic loading to a member ductility (DF) of $\pm$ 1 and for the first cycle to DF = $\pm$ 2.

5.4 ANALYTIC MODEL

It is neither practical nor economic to model in its full complexity the shear behaviour described in the preceding sections. Practical limitations

are imposed by the scope of the basic frame element idealization used to represent the member and by the lack of quantitative information about the constituent material (severely cracked concrete) responses under post-elastic load reversals. Furthermore, for the type of member considered in the present study, the shear response is generally secondary to the flexural response and consequently the same degree of accuracy is not required for the model.

The proposed shear model for general inelastic section analyses is primarily directed at representing the interlock behaviour and the effect of shear strains on crack opening and closing. The model assumes the total shear force resisted by a section to be divided into two components; one resisted by interlock action and the other by direct shear stresses in the concrete compression block, i.e.

$$q_v = q_{int} + q_{conc} \qquad \ldots (5.5)$$

where q_v is the total shear forces and q_{int} and q_{conc} are the components of shear force resisted by interlock action and direct concrete shear stresses respectively.

Dowel action of the flexural bars and the contribution of the stirrups to the shear rigidity have not been explicitly considered. However, some allowance for these factors is incorporated by virtue of the fact that the model constants were calibrated against measured values of total shear displacements within the plastic hinge zone which include components due to dowel and stirrup deformations (Section 5.5). Also, the model has been developed specifically for analysing the response of plastic hinge zones with adequate shear reinforcement to prevent diagonal tension failure. Consequently the component of deformation due to truss action of the stirrups will be small compared with the total shear displacements developed during post-elastic load cycles.

5.4.1 Interlock Response

Simplifying assumptions were made in modelling the interlock response. In particular, the modelled interlock shear rigidity is related to the

average axial strain for the section and the effect of the longitudinal and transverse reinforcement on the interlock response are not accounted for.

The model is based on an assumed average interlock shear modulus for a section which is given by:-

$$G_{int} = K_{int} / \varepsilon_{ave} \; \dagger \; (G_{int})_{max} \qquad \ldots (5.6)$$

where G_{int} is the average interlock shear modulus for the concrete section

$(G_{int})_{max}$ is a prescribed maximum value for G_{int}

K_{int} is an experimental constant, and

ε_{ave} is the average effective axial strain (see Section 5.4.3).

The governing differential force-strain relationship for the section is given by:-

$$dq_{int} = G_{int} \cdot A_{vi} \cdot d\varepsilon_v \qquad \ldots (5.7)$$

where q_{int} is the interlock component of the section shear force

A_{vi} is the shear area of the concrete section, and

ε_v is the section shear strain.

This equation must be evaluated incrementally as it is not possible to describe the response as a closed form relationship equivalent to those used in the steel and concrete models. In these latter cases, the entire response path can be defined for any load reversal as soon as the origin stress and strain are known. However, the shear developed by interlock action will vary depending on the relationship between the axial and shear strains occuring during the load reversal.

The validity of using the average strain ε_{ave} to define the shear modulus may be questioned, especially in view of the variation in concrete strain, strain rate and type of interlock response (sliding-only

to sliding plus rotation of loosened pieces of concrete) over the section depth. Nevertheless, the behaviour indicated by the sliding shear responses evaluated in this study suggests that the influence of the axial strain can be satisfactorily represented by ε_{ave}.

By using the axial strain, ε_{ave}, as the independent variable, both crack widths and spacing* are considered simultaneously, thereby avoiding the necessity for a detailed assessment of the cracking behaviour. The fact that loose pieces of concrete are free to rotate as well as slide means that the rigidity of the post-elastic sliding shear mechanism will be considerably lower than would be predicted from the behaviour of special interlock specimens of the types used by Fenwick (73), Houde and Mirsa (76), and Paulay and Loeber (77). Also, unlike for the relationships derived by the above investigators, the value of G_{int} obtained from Eq. 5.6 is scale independant, i.e. the inverse of ε_{ave} is scale independant.

As currently formulated, the model ignores any normal restraining force generated by the shear displacements. The reasons for this are first that the true behaviour of the restraining mechanism is yet to be fully resolved (Section 5.2.2f) and secondly, that to include restraining forces would introduce direct coupling between the section axial and shear force responses. This would have required modification of the basic member formulation (Section 2.3.2).

As discussed in Section 2.3.3 , different values of K_{int} can be specified for web and flange areas of a section, or for confined and unconfined concrete.

5.4.2 Shear Aggregation

The most realistic approach to interlock shear force aggregation would have been to use a dual procedure, with Eq. 5.4 being used in situations

---

* Both variables are required in order to determine the shear modulus, as opposed to the rigidity of the interlock mechanism along an individual crack.

where crack widths decrease with increasing shear strain and Eq. 5.3 in situations where crack widths increase with increasing strain (Section 5.2.2e). However, this approach would have required a complex multi-stage evaluation of the shear force similar to that indicated in Figure 5.11. This requires the axial and shear strain and the shear force values for a large (and varying) number of preceding increments to be retained for assessing the fracture release forces associated with crack opening. Such a procedure was considered to be too complex and costly for use in a general frame program and consequently a simple cumulative shear aggregation procedure similar to Eq. 5.3 was adopted.

This procedure was adequate for the type of loading analysed in this study, i.e. pseudo-static large displacement load reversals, since the average tension strain (ε_{ave}) generally increased only after the cracks closed. Consequently, in the real situation, any decrease in the interlock shear resisted would be compensated for by an increase in the shear resisted by the compression block. This situation would also normally apply for members subjected to real earthquake loading unless substantial axial tensions were induced in the members.

5.4.3 Coupling Between Axial and Shear Strain

One of the most important aspects of the inelastic shear model is the provision for simulating the effect of mismatched crack surfaces. This phenomenon occurs because of shear slip along full depth cracks in the concrete section and is important because of its effect on the axial strain at which the cracks close, and particularly because of the resulting limitation on the amount of free sliding that can occur (Figure 5.10).

The effect of mismatched crack surfaces is modelled by introducing the concept of an effective axial strain ε_e, such that, at any concrete layer

$$\varepsilon_e = \varepsilon_c - \varepsilon_{oo} - \varepsilon_{xv} \qquad \ldots (5.8)$$

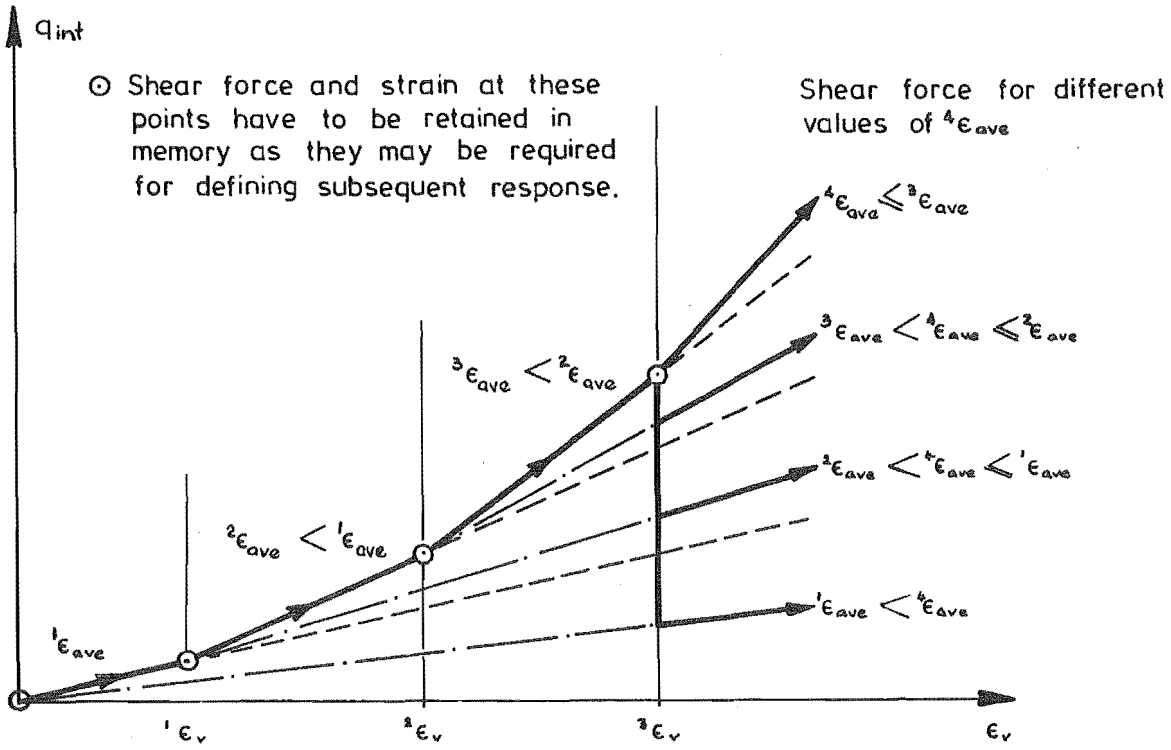

Note: The response shown assumes that ϵ_{ave} remains constant during each strain increment. In the real situations, where ϵ_{ave} varies continuously, the aggregation procedure would be more complex.

FIGURE 5.11 : EVALUATION OF SHEAR RESISTANCE USING DIFFERENT AGGREGATION RESISTANCE RELATIONSHIPS FOR CRACK OPENING AND CLOSING RESPONSES

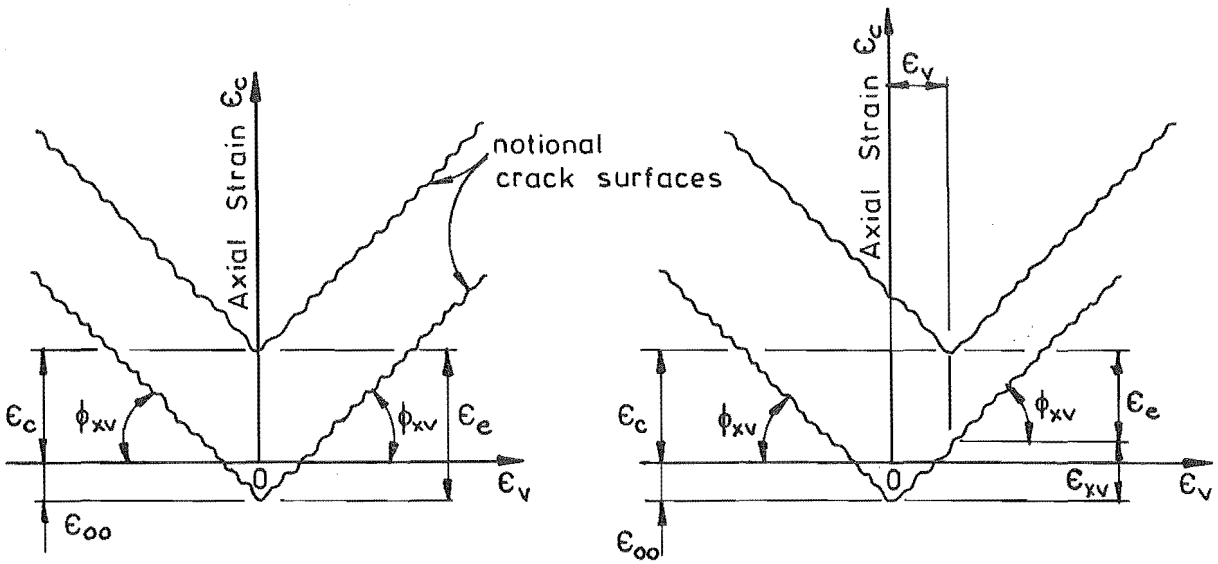

FIGURE 5.12 : EFFECTIVE CONCRETE STRAIN, ϵ_e

where ε_c is the absolute axial strain, ε_{oo} is the residual plastic compression strain in the concrete layer (Figure 4.1), and ε_{xv} is a coupling term which measures the reduction in effective axial strain due to the shear strain (Figure 5.12). This is obtained from

$$\varepsilon_{xv} = \phi_{xv} \cdot \int_o^{\varepsilon_v} J.d\varepsilon_v \geq 0 \qquad \ldots (5.9)$$

where ϕ_{xv} is the coupling constant which defines an assumed effective slope of the crack surfaces (Figure 5.12), ε_v is the shear strain, and $J = 0$ if any layer of concrete in a section is in compression or, if ε_e is positive for every layer (full depth cracking), equals 1 for ε_v positive and -1 for ε_v negative. Since ε_{xv} is evaluated on an overall section basis (e.g. cracks have to be open over the full depth of the section for $J \neq 0$), the same value of ε_{xv} applies to all concrete layers in a section.

The assumption of a fixed effective crack slope, ϕ_{xv} in Eq. 5.9, is very much an approximation. However, comparisons made with experimental sliding shear responses in this study (Chapters 6, 8 and 9) indicate that the model sensitivity to imposed plastic hinge rotation and axial load intensity is in reasonable agreement with the observed behaviour.

As noted in Section 5.4.1, the effective axial strain is used to evaluate ε_{ave}. This means that q_{int} is in part a function of ε_v^2. There is an apparent conflict with the results obtained by Fenwick (73) and Loeber and Paulay (77). However, the main cracks in their specimens were artificially formed on a flat plane and consequently the shear resistance was largely provided by aggregate interlock. By comparison, the coupling term ε_{xv} in Eq. 5.8 accounts for surface irregularities and shape (e.g. slope) as well as aggregate interlock.

5.4.4 Evaluation of ε_{xv}

Over two-thirds of the computer time required for the inelastic shear analyses is consumed in evaluating the coupling strain ε_{xv}. Most of this time is required for delineating the boundaries between the

different values of J required in Eq. 5.9.

The basic boundary situations which occur during crack opening and closing are shown in Figure 5.13. These become even more complex when the shear strain changes sign during an increment, because of boundaries at $\varepsilon_v = 0$ and at $\varepsilon_{xv} = 0$. The large amount of computer time required to evaluate ε_{xv} occurs because the extent of strain coupling has to be checked at every concrete layer in a section in order to determine the strain at which the cracks first open or close. This cannot be assessed solely from the top and bottom layers because the residual plastic compressive strain (ε_{oo} in Figure 4.1) in each layer will generally be different.

5.4.5 Effect of Coupling on Concrete Normal Stress Response

The effect of the coupling strain ε_{xv} on the modelled concrete normal stress response is indicated in Figure 5.14. This shows the concrete stress-strain relationship defined in terms of the absolute strain ε_c and, as indicated, significant residual tensile strains may be predicted as a result of mismatching of crack surfaces (Figure 5.10).

In practice, the stiffness on reloading would be expected to be reduced by the coupling effect because of the smaller area of contact associated with the mismatched crack surfaces. However, no allowance was made for this in the model for the core concrete response, mainly because of the absence of suitable experimental data. It was also thought that the effect on the overall response would be relatively small because the shear strains would be likely to be small in situations where there was significant net axial compression. On the other hand, where the net compression was small, the concrete would have comparatively little influence on the overall response (cf. the use of relatively simple concrete models in moment-curvature analyses, Chapter 4). However, subsequent comparisons with measured responses showed that the early closing of cracks due to the modelled strain coupling (Eq. 5.8) significantly increased the effect of the concrete on the normal strain response and that the model was overestimating the residual tensile strains resulting from mismatched crack surfaces.

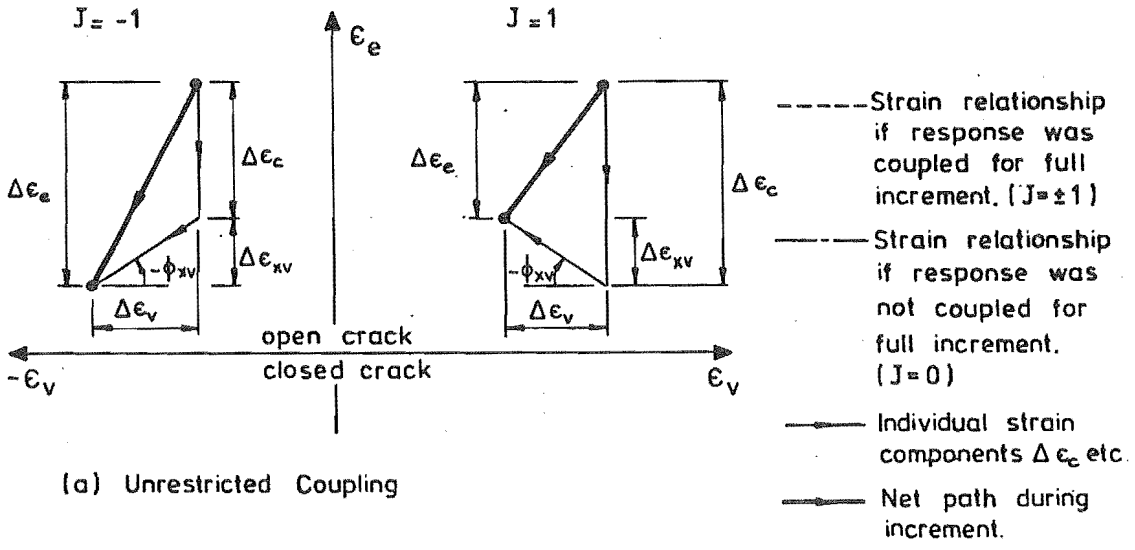

(a) Unrestricted Coupling

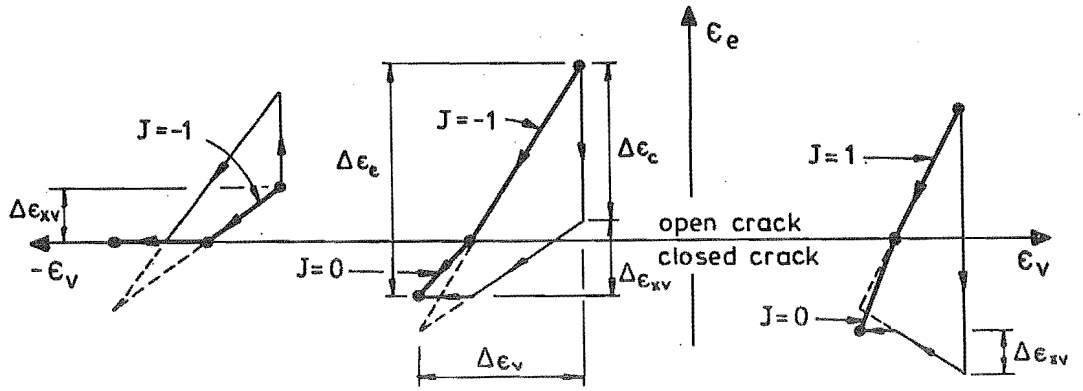

(b) Restricted Coupling, Cracks Closing

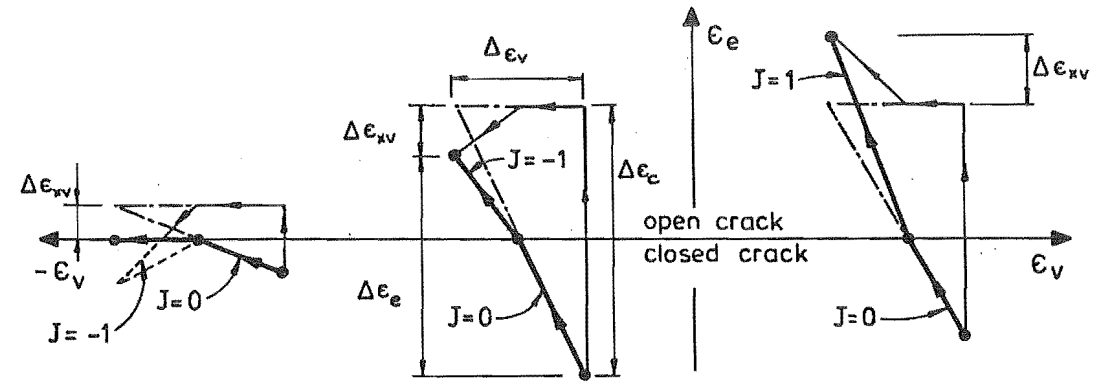

(c) Restricted Coupling, Cracks Opening

FIGURE 5.13 : EVALUATION OF INCREMENT IN ϵ_{xv} FOR DIFFERENT BOUNDARY CONDITIONS

This in turn caused the shear strains in subsequent load reversals to be overestimated.

An attempt was made to take account of the reduced contact area by reducing the slopes of the reloading and unloading branches in the model for the normal response of the concrete, while still retaining the same basic shape of hysteresis loop (Figure 4.1). This modification was not successful as the increase in strain required to unload the concrete resulted in situations where the cracks were not predicted to open until there was a large reversal of load on the section.

No further attempts were made to model softening of core concrete resulting from mismatched crack surfaces as a sufficiently detailed evaluation of the behaviour of the concrete under these conditions was beyond the scope of this investigation. However, to make some allowance for the softening, the reloading and unloading moduli for areas of cover concrete have been modelled such that they reduce as the magnitude of ε_{xv} increases. This has been done solely by reducing the effective strength of the cover concrete and consequently the increment in strain required to unload the concrete from any point on the response curve has not been affected.

5.4.6 Shear Resisted by Concrete

After cracks close, part of the subsequent increase in shear force is assumed to be resisted by direct shear stresses in the previously cracked concrete. The model for this component is based on the area of concrete in contact and the elastic modulus of the concrete appropriate to the current strain state. At any load point, the response is defined by

$$dq_{conc} = \phi_g . EA_{conc} . d\varepsilon_v \qquad \text{.....(5.10)}$$

where q_{conc} is the shear force component resisted by the concrete,

EA_{conc} is the axial rigidity of the concrete in compression determined in accordance with the imposed normal strains only, i.e., the strains induced by the shear stresses are ignored for determining the strain in the concrete,

and

ϕ_g is an experimental constant.

In the computer program, the increase in q_{conc} during any load increment (Δq_{conc}) is computed only approximately using the average of the values of EA_{conc} applicable at the beginning and end of the load increment.

Although this component of the shear response has been treated only very cursorily, it is essential for modelling the sharp increase in shear rigidity observed after cracks close (Figure 5.10). A more precise evaluation was not considered warranted in view of other limitations in the concrete model currently used in the computer program.

5.4.7 Unloading Response

The modelled shear rigidity during unloading was originally based solely on the interlock and compression block response models described in the preceding sections. However, it was found that this did not satisfactorily model the differences between the shear rigidities for loading and unloading (cf. C and E in Figure 5.10). This was partly because the reduction in reloading modulus of the concrete caused by mismatched crack surfaces had been ignored, with the result that an artificially low value of ϕ_g was being used. To compensate for this, a scaling factor ϕ_{unl} was introduced to increase the unloading rigidity. This scaling factor was applied to both the interlock and compression block components of the response.

5.5 CALIBRATION OF MODEL CONSTANTS

Four main experimental constants, K_{int}, ϕ_{xv}, ϕ_g and ϕ_{unl}, are used in the inelastic shear model. Calibration of these constants was largely carried out on a 'trial and error' basis using shear responses measured for three beams tested by Celebi and Penzien (refer Section 6.3) and one beam tested in this study (TB1, Chapters 7 and 8).

The main features relating to the sliding shear response, considered in these calibrations were as follows:

(a) Slope of the soft central region of the sliding shear response (A in Figure 5.10). This is largely determined by K_{int}, although ϕ_{xv} also has some influence by virtue of its effect on the axial strain response, see (f) below.

(b) Extent of the soft central region of the response (B in Figure 5.10). This is largely determined by ϕ_{xv}, although K_{int} may also be significant in some cases.

(c) Slope of the stiff loading portion of the response (C in Figure 5.10). This is determined by ϕ_g and to a lesser extent, K_{int} (refer Section 5.4.7 regarding the effect of the modelled axial rigidity of the concrete on ϕ_g).

(d) Strain softening behaviour at the peaks of the initial load reversals preceding an increased member displacement (D in Figure 5.10). No specific provision has been made for modelling this behaviour and none of the constants has any significant control over it.

(e) Unloading initiated at high load intensities (E in Figure 5.10). This is influenced by K_{int}, ϕ_g and ϕ_{unl}. No suitable observed data was available for evaluating the shear response during unloading initiated at low load intensities, and it is not known how valid the modelled scaling of K_{int} by ϕ_{unl} is in these situations.

(f) The effect of strain coupling on the normal strain response. Smaller values of K_{int} and larger values of ϕ_{xv} reduce the load at which predicted crack closure occurs. This increases the tensile strains developed in the flexural reinforcement, which in turn affects both (a) and (b) above.

(g) Sensitivity to load state and history. This is largely dependent on the interrelationship between the interlock modulus ($G_{int} = K_{int}/\varepsilon_{ave}$), the degree of strain coupling (ϕ_{xv}) and the modelled axial strain response - see point (f) above.

Priority was given to modelling the slope (a) and extent (b) of the soft central portion of the shear response, the effect of strain coupling on the external axial response (f) and the sensitivity to load state and history (g). Because of the interdependence of these

factors and the approximations in the analytic model, some degree of trade-off was necessary in arriving at suitable values for K_{int} and ϕ_{xv}. The predicted responses were, however, not highly dependent upon the values of these constants and satisfactory agreement with the observed shear responses was obtained for values of K_{int} = 0.14 MPa to 0.21 MPa and ϕ_{xv} = 0.8 to 1.0. The values of ϕ_g and ϕ_{unl} were simply adjusted to give reasonable shapes for the shear load-displacement response curves, without attempting to exactly match the slopes of the observed curves, which varied considerably. Values of ϕ_g = 0.1 to 0.16 and ϕ_{unl} = 5.0 were used for almost all analyses performed subsequent to the initial calibration runs.

A more accurate calibration of the shear models was not considered to be warranted because of both the limitations of the model and the lack of a sufficiently wide range of accurate measurements of this type of shear response.

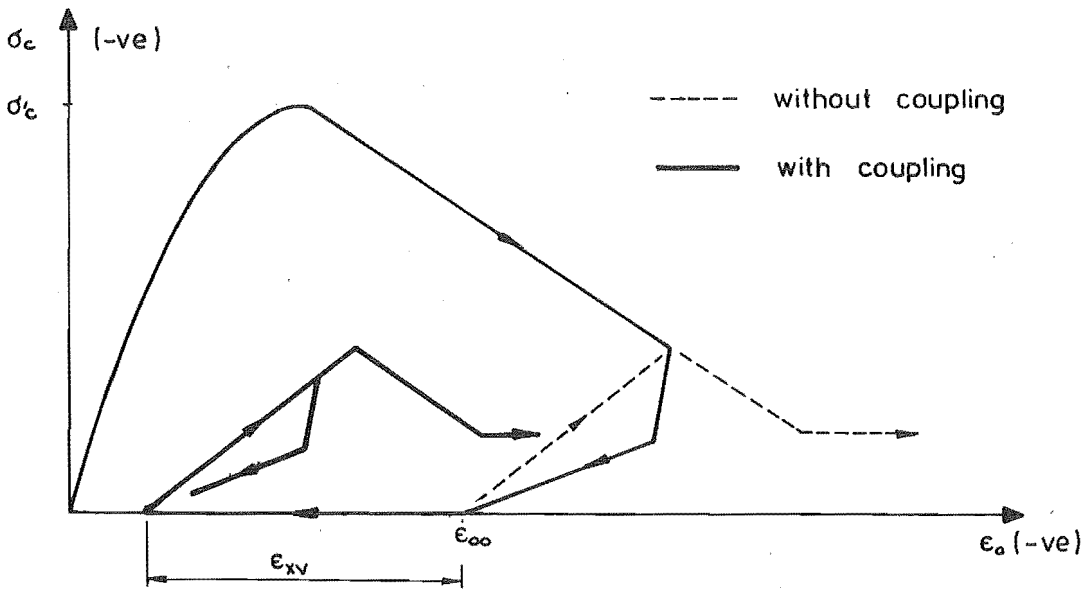

FIGURE 5.14 : EFFECT OF ε_{xv} ON CONCRETE NORMAL STRESS-STRAIN RESPONSE

6. EVALUATION OF FRAME ANALYSIS COMPUTER PROGRAM

SUMMARY

This chapter presents results from a number of analyses which were used to evaluate different aspects of the frame analysis computer program. In the first section, four elastic, geometrically non-linear structures are analysed and the computed responses compared with previously published solutions. The remaining sections are related to analyses of reinforced concrete specimens subjected to post-elastic load reversals. Aspects covered in these analyses include the effect of the size of inelastic segment used to model plastic hinge zones (mesh refinement), calibration of the inelastic shear model constants and subsequent evaluation of the computer program, and particularly the shear model, under a variety of structural conditions. Specific variables considered in these analyses include member shear span to depth ratio, maximum shear stress intensity, inclined cracking and the effect of axial compression. In the final two sections the performance of the Newton-Raphson solution procedure adapted for use in the computer program, is investigated and an assessment made of the computation times required for some of the analyses.

6.1 ELASTIC GEOMETRICALLY NONLINEAR RESPONSES

Four elastic, geometrically nonlinear structures were analysed in order to assess the second order analysis formulations (Section 2.4) under different structural and loading conditions. All the structures analysed were represented as a series of straight elastic elements with linear member displacement responses. The analyses were also used for initial debugging and evaluation of the solution procedures used in the materially nonlinear analyses.

The first three examples considered were taken from a series of structures analysed by Ebner & Ucciferro (90) as part of a comparison of elastic geometrically nonlinear finite element formulations presented by several analysts. These structures had earlier been analysed by a

number of other analysts. The arch structure analysed in the fourth example is one of a family of arches analysed by Sabir & Lock (91).

6.1.1 Cantilever Beam

A flexible cantilever beam with two lateral loads (Figure 6.1) was analysed using the second order recursive formulation without iteration (initial value self-correcting solution procedure). The computed deflections are compared in Table 6.1 with results given by Ebner & Ucciferro for analyses of the same beam using formulations developed by Jennings (56), Powell (92), and Manuel & Lee (93). The magnitude of the displacements in this example is well outside the range encountered in reinforced concrete structures, but the problem serves as a useful test of the formulation under extreme conditions.

Because of the large displacements imposed on the beam, the present formulation could not be used to obtain a direct solution. However, the results obtained using the recursive formulation showed reasonably good convergence with both element and increment refinement, and were considerably closer to the iterated direct solutions for Jennings' formulation and that of Manuel and Lee, than the incremental solutions given by Ebner and Ucciferro.

6.1.2 Column with Initial Eccentricity

The column analysed (Figure 6.2) had an initial eccentricity of 0.0003 times its height and represents an example of nonlinearity associated with high axial load and small displacements. An eight element half member idealization of this column was analysed using the 2nd order Lagrangian formulation. The results obtained are compared in Figure 6.2 with those presented by Ebner and Ucciferro for the direct formulations of Mallet and Marcal (94), Jennings (56) and Powell (92). As this comparison shows, the response predicted by the present formulation agrees well with those obtained using Jennings' and Powell's formulations.

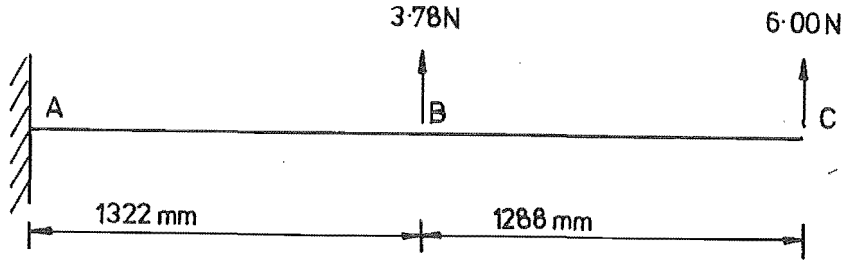

$EI = 14348\ kN.mm^2$

$EA = 26688\ kN$

FIGURE 6.1 : CANTILEVER WITH TWO LATERAL LOADS

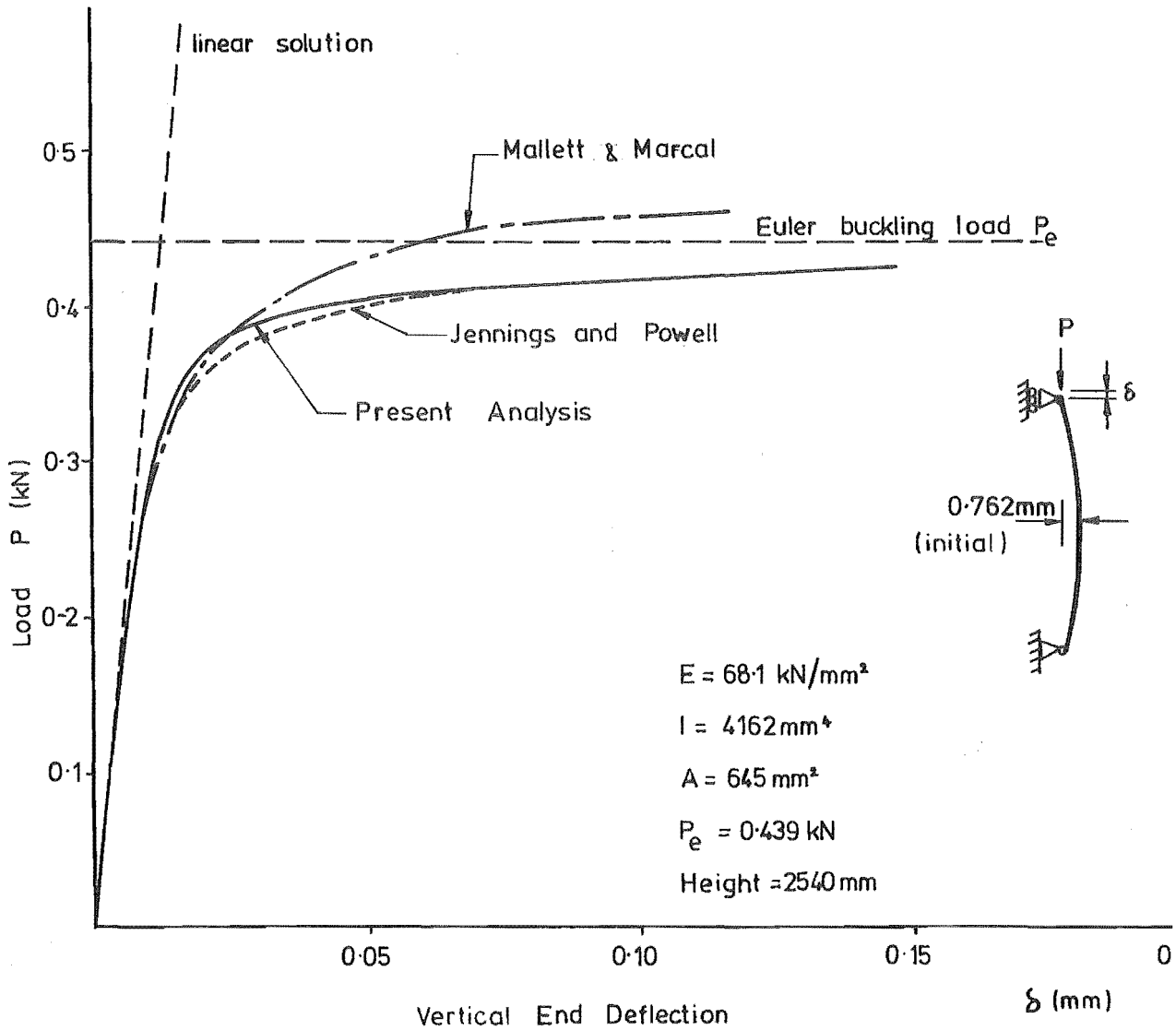

FIGURE 6.2 : LOAD DEFLECTION FOR COLUMN WITH INITIAL ECCENTRICITY

TABLE 6.1 : SOLUTIONS FOR CANTILEVER BEAM WITH TWO LATERAL LOADS

Formulation		Horizontal Deflections at B (mm)	Horizontal Deflections at C (mm)	Vertical Deflections at B (mm)	Vertical Deflections at C (mm)
Iterated Direct Solutions:					
Manuel & Lee*		-206.2	-781.1	640.7	1700.8
Jennings*	4 elements	-206.2	-781.1	630.4	1700.5
	2 elements	-205.2	-778.0	626.9	1695.7
Powell*	20 elements	-142.5	-544.3	542.3	1441.7
Incremental Solutions: (elements, increments)					
Jennings*	(20,100)	-125.5	-381.3	523.2	1299.0
Powell*	(20,100)	- 86.4	-290.3	430.3	1130.0
Present analysis, recursive formulation	(8,20)	-204.6	-781.6	633.0	1705.6
	(8, 4)	-209.4	-813.3	646.4	1753.9
No iteration	(2,20)	-182.0	-789.4	669.4	1763.8
	(2, 4)	-184.4	-820.4	682.2	1812.0

* from Ebner & Ucciferro (90), Refer Figure 6.1

6.1.3 Two Pinned Shallow Circular Arch

This arch (Figure 6.3) was idealized using 5 elements/half arch and was analysed using the 2nd order Lagrangian formulation. The results obtained are compared in Figure 6.3 with those obtained by Ebner and Ucciferro using the formulations of references (56), (92) and (94). The present formulation again shows best agreement with Jennings' and Powell's direct formulations.

Ebner and Ucciferro were able to obtain the entire load-deflection response only for the incremental analyses. With the present formulation, both direct and incremental solutions could be obtained for any point on the load-deflection curve. An example of such a direct solution onto the falling branch section of the response curve is shown in Figure 6.3 together with the iterative adjustments made to the crown load and deflection during the convergence process. This solution required only 4 iterations. Although such a large increment would not be reliable for a more complex structure, the example does illustrate the advantages of being able to specify either force or displacement control of the solution process.

6.1.4 Shallow Circular Arch Exhibiting Bifurcation and Looping

Arches which are slightly deeper than the one analysed in the preceding example, or which have a lower ratio of flexural to axial rigidity, can exhibit both bifurcation and looping in their responses. The arch analysed here (Figure 6.4) exhibits these characteristics. It has the same span and section properties as the arch shown in Figure 6.3, but a smaller radius of curvature. The arch was analysed primarily in order to verify the ability of the solution procedure (combined force and displacement control) to follow complex load-displacement paths. Various aspects related to the behaviour of this type of arch are discussed by Sabir and Lock (91).

Results obtained from analyses (recursive formulation) with both 5 and 10 elements per half arch are compared in Figure 6.4 with the analytical load-deflection response given by Sabir and Lock. As indicated, the form of the response was predicted accurately and particularly good

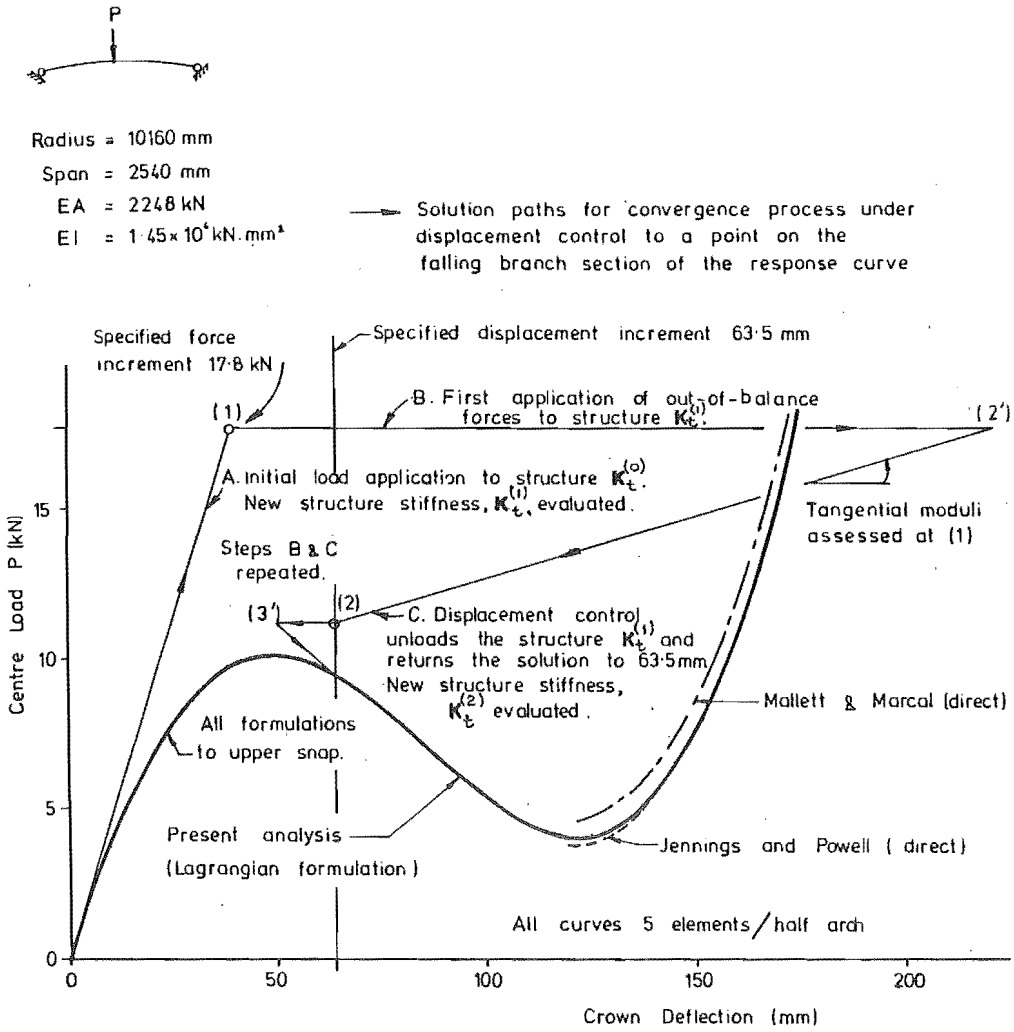

FIGURE 6.3 : THIN CIRCULAR ARCH WITH RADIUS TO SPAN RATIO OF 4

agreement was obtained for the displacement limits of the vertical tangents and the displacements at which the curve intersects the zero load axis.

The only difficulties with the solution procedure were the natural tendency of the Newton-Raphson solution procedure to follow the symmetric load path, despite it being unstable in region A-B (Figure 6.4), and the necessity of using very small increment steps (approximately 0.89 kN, 5 mm) in the vicinity of point D marked on the response. In order to get the solution to follow the anti-symmetric path, a small anti-symmetric load* must be temporarily applied to the arch when the solution is in the vicinity of the bifurcation at point A. Once on the anti-symmetric path, however, the solution continues to follow it without difficulty. Fully converged solutions were obtained (2-3 iterations) for every point analysed. This includes all increments where the solution traversed bifurcation and horizontal tangent points (under displacement control) or vertical tangent points (under force control).

6.2 INVESTIGATION OF MESH REFINEMENT IN ANALYSES OF REINFORCED CONCRETE BEAMS

Because of the potentially high cost of materially nonlinear analyses of reinforced concrete structures, it is important to assess the effect of mesh size on the computed responses. This section discusses results obtained from a series of analyses which were performed in order to investigate different aspects related to the representation of beam plastic hinge zones. The first subsection briefly considers the effect of the number of concrete layers on the computed section response (section representation), and the remaining subsections consider various factors related to the size of segment used to model plastic hinge zones (member representation).

The analyses used to investigate member representation were performed on two cantilever beam test specimens. The first beam considered was

---

* On the basis of the experience with these analyses, provision has been made for a small asymmetric load to be applied for the first iteration of each load increment.

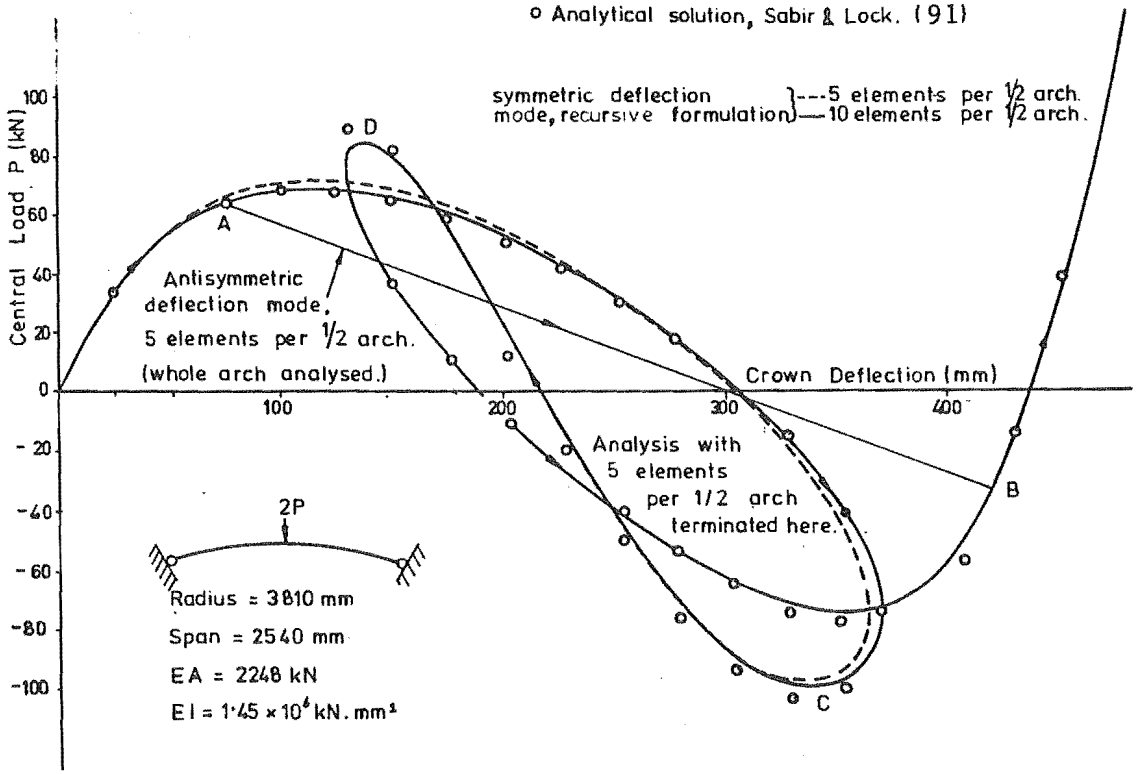

FIGURE 6.4 : THIN CIRCULAR ARCH WITH RADIUS TO SPAN RATIO OF 1.5

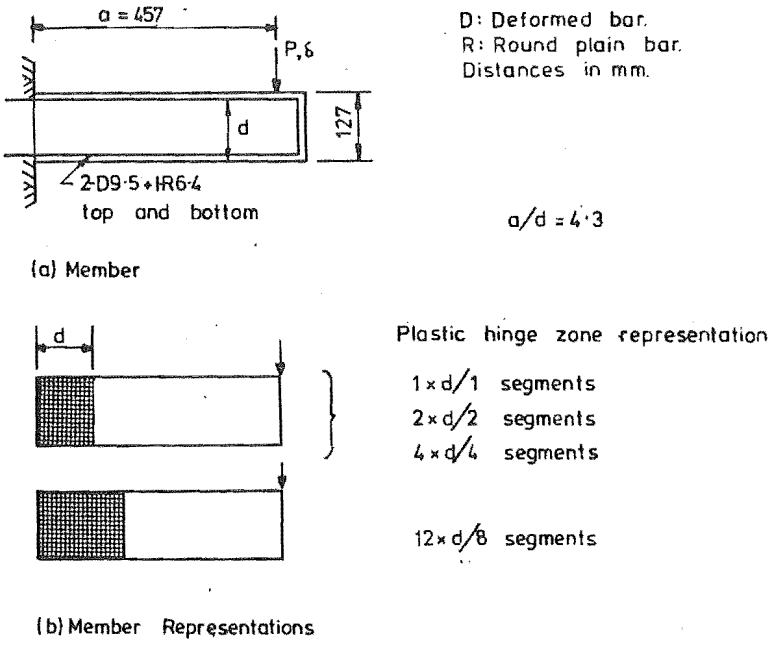

FIGURE 6.5 : MEDIUM SPAN CANTILEVER BEAM USED FOR MESH REFINEMENT ANALYSES (SPECIMEN TB1, CHAPTERS 7 AND 8)

one of four small scale beam-wall specimens tested in the experimental part of this study (see Chapters 7 and 8). Four sets of analyses were performed on this specimen in order to investigate the effects of mesh size and their interaction with the modelled idealizations for crushing or spalling of cover concrete (ε_{cr}), shear induced stresses in the flexural reinforcement* (e_v) and inelastic sliding shear deformations. Four different meshes, with segment lengths ranging from d/8 to d, were used to represent the plastic hinge zone in these analyses (Figure 6.5).

In the case of the second specimen (Section 6.2.5), the analyses were restricted to consideration of the relationship between the effects of mesh size and the value of e_v.

6.2.1 Section Representation

Most analysts appear to use meshes of between 10 and 20 concrete layers per section, although some have used much finer meshes, e.g. Kent (48) used 100 layers per section for his moment-curvature analyses. In the present study, the number of concrete layers used varied depending on the complexity and importance of the section, but was generally between 10 and 14 for beam or column sections and 14-18 for wall sections.

Several moment-curvature analyses were performed using meshes with 10 to 50** concrete layers per section. The results obtained from these showed that, excepting for the local effect of crushing occurring at different curvatures, the maximum error in the predicted peak cycle moments for sections modelled with 10 concrete layers was less than 1% for a beam section and less than 2% for a section acted on by a net axial stress of 2.76 MPa. With 14 layers, the maximum error in the computed moment at any point on the beam moment-curvature response

---

* Only the effect of e_v on the computed response is considered in this investigation. The question of how realistic this allowance is for cyclic load conditions is considered in later sections.

** In this discussion, the response computed for the 50 concrete layer idealization is considered to be "exact". Also for any given number of concrete layers, the representation will generally be improved by concentrating them towards the top and bottom of the section. However, for these analyses, only uniform distributions of layers were considered.

(local crushing effects excluded) was less than 1% of the yield moment.

6.2.2 Basic Member Representation

The load-deflection responses obtained for the first set of analyses are compared in Figure 6.6, and the corresponding curvature distributions at several load intensities, in Figure 6.7. These analyses were performed with crushing of the cover concrete suppressed, with no allowance for shear induced stresses in the flexural reinforcement, and with only elastic shear deformations considered.

As indicated, both the curvature distributions and particularly the load-displacement responses show rapid convergence with mesh refinement. The portions of the reverse loading curves controlled by the Bauschinger softening of the steel were very similar for all member representations, despite obvious differences in the plastic strain distributions. Several analysts (47, 48 , 52) have suggested that failure to correctly model the actual distribution of plastic strains along the reinforcement will result in an incorrect assessment of the softening of the reversed loading curves. In fact, the relationships which govern the degree of softening of the steel loading curves, i.e. Eqs. 3.4 to 3.8, are such that, for the greater part of the inelastic strain range, the effects due to under- and overestimating the bar strain largely compensate one another. Since the net plastic elongation of the bars in the plastic hinge zone is approximately the same for all representations, the degree of softening of the load-deflection responses will also be similar for each case.

The largest representation errors in the load-deflection response generally occurred at the onset of yielding. Even then, it was only in the analysis with largest segments, i.e. segment length of d, that the "error" in the computed response (approx. 6-7%) was significant in comparison with experimental variability. The differences between the curvature distributions are of little practical significance.

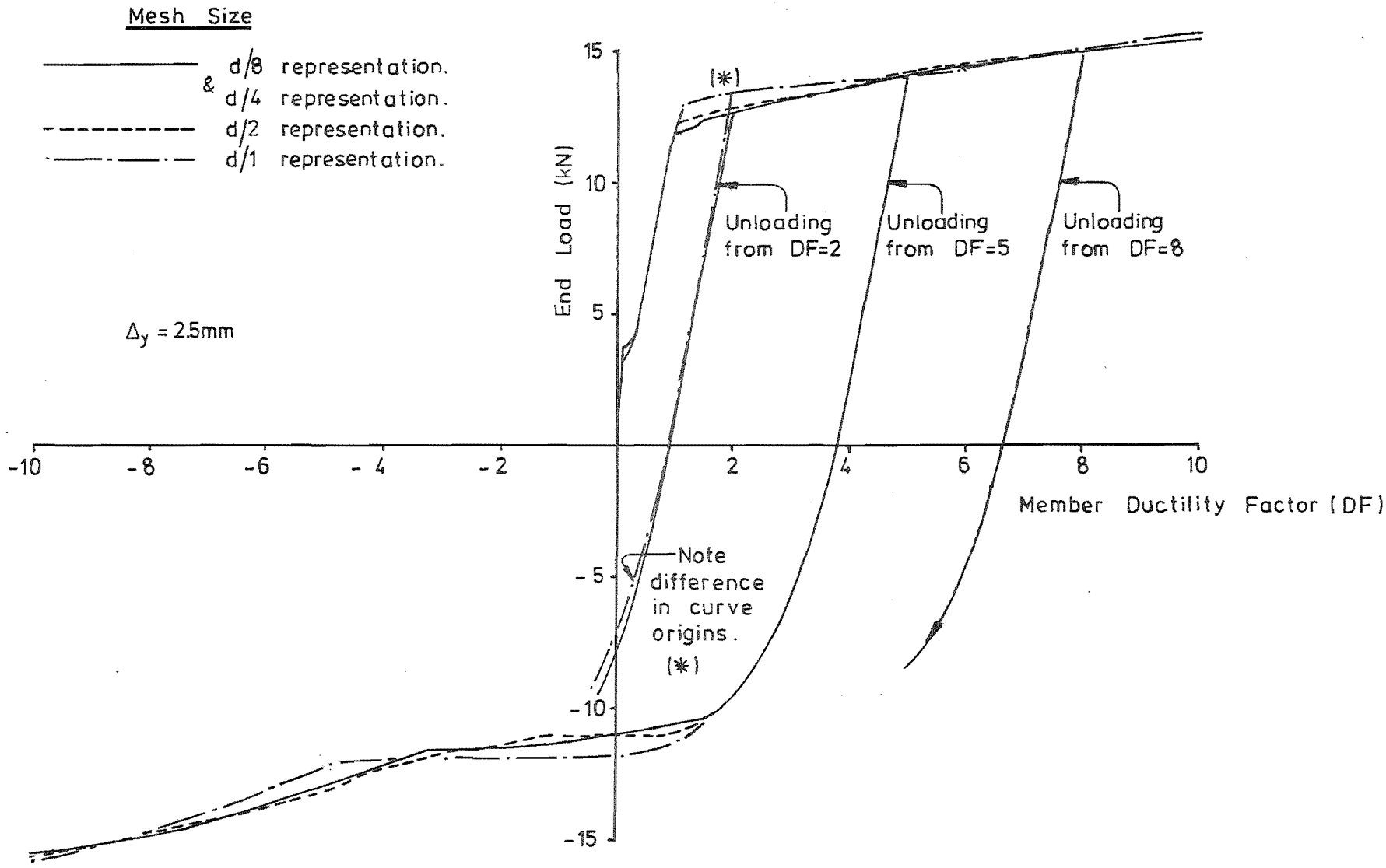

FIGURE 6.6 : EFFECT OF MESH REFINEMENT, ONLY FLEXURAL DEFORMATIONS

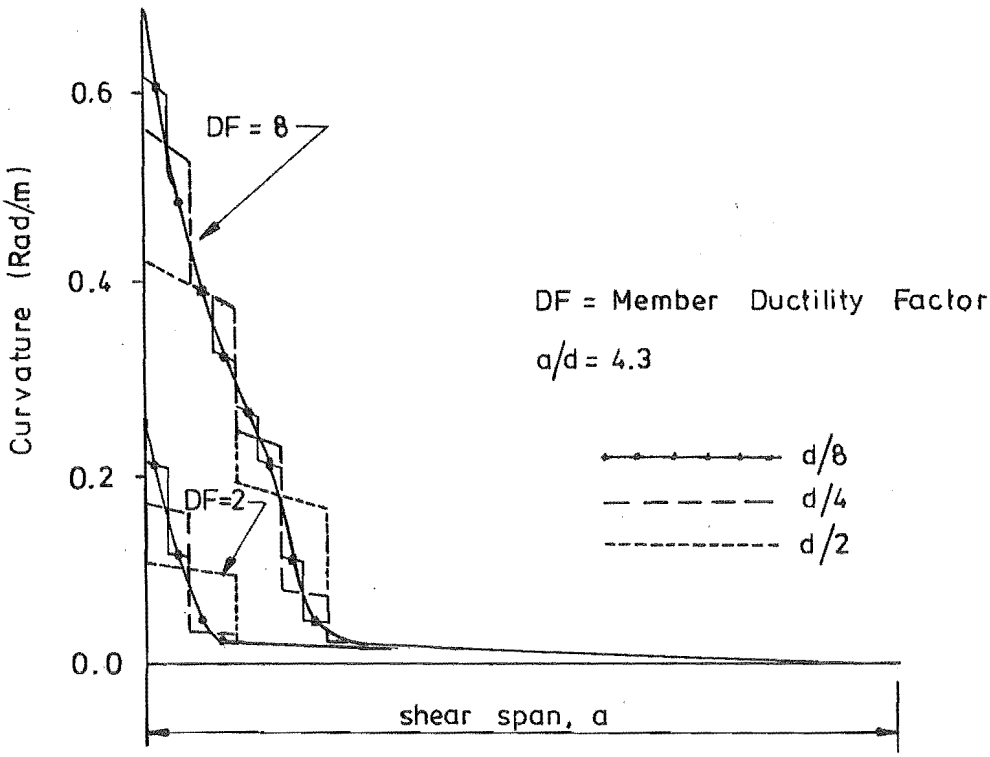

(a) Curvature distributions at ductiles of 2 and 8

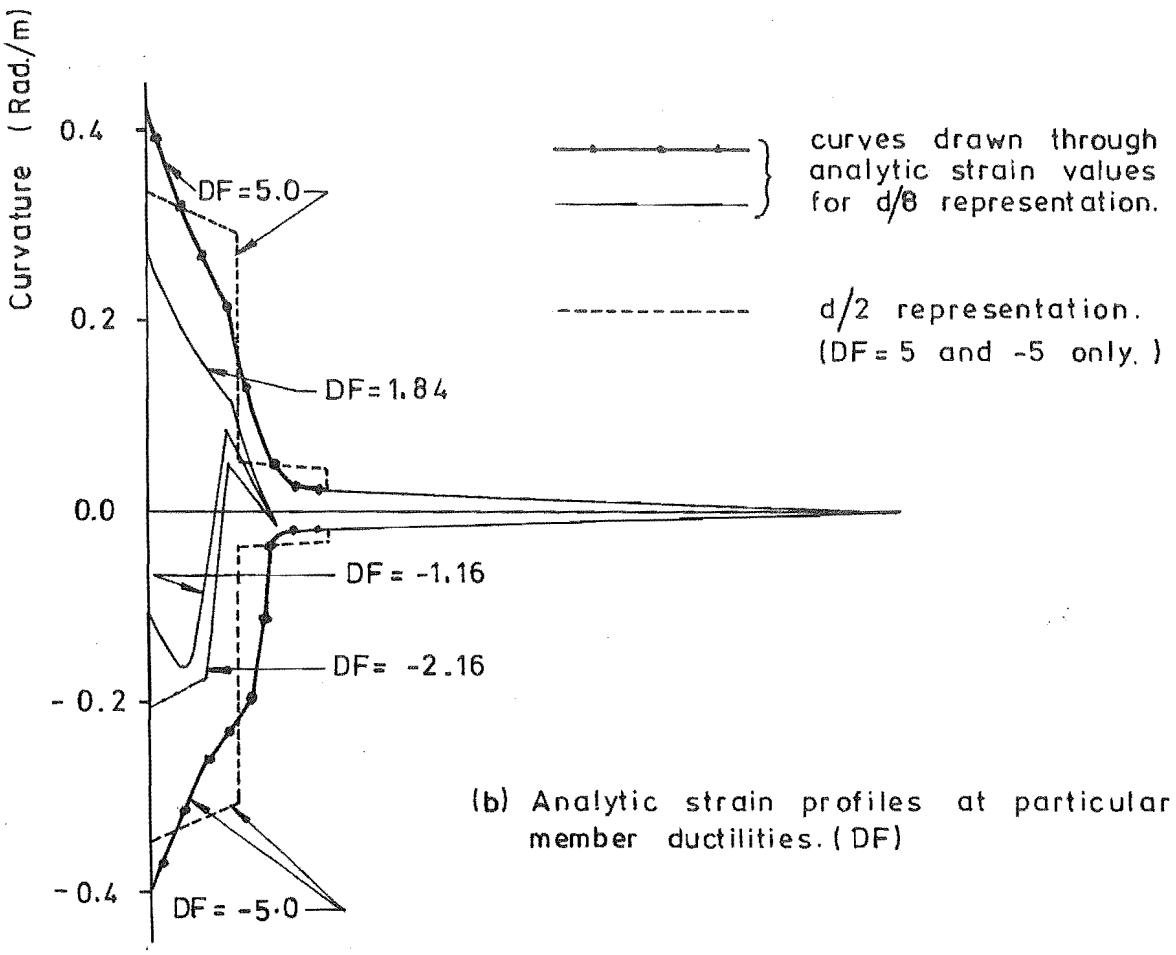

(b) Analytic strain profiles at particular member ductilities. (DF)

FIGURE 6.7 : CURVATURE DISTRIBUTIONS FOR ANALYSES SHOWN IN FIGURE 6.6

6.2.3 Effect on Crushing of Cover Concrete

As seen in Figure 6.8, the effect of mesh size is greater when crushing of the concrete is considered ($\varepsilon_{cr} = -0.004$). However, the differences are still within the range of experimental variability, especially for segment lengths d/2 or shorter. Also, one aspect which became apparent during these analyses was that very small segments do not necessarily give the most accurate representation. Because each segment responds independently, generally only one segment crushes at a time. The loss in strength that accompanies crushing means that this segment must undergo substantial further straining before sufficient strength is regained to be able to crush an adjoining segment. With fine member representations, this results in large curvatures developing in localized regions of the member (see Figure 6.9).

The actual crushing/spalling behaviour of real beams can vary considerably, depending on a number of factors. However, for most rectangular beams, a segment length of d/4 to d/2 should give a reasonable representation of the extent of spalling and crushing of the cover concrete.

6.2.4 Effect of Shear Induced Stresses in the Flexural Reinforcement (TB1, a/d = 4.3)

Figure 6.10 shows the load-displacement relationships computed for the d/1, d/2 and d/4 representations, allowing for both crushing ($\varepsilon_{cr} = -.004$) and shear induced stresses in the flexural reinforcement ($e_v = 0.5$ jd).+ The curvature distributions along the member computed in the last increment prior to yield and at a member ductility* of DF ≈ 5 are shown in Figure 6.11. Several observations can be made regarding the effect of e_v.

(a) The gain in strength after the beam yields is smaller than for the case where $e_v = 0$. This is due to the lower stress gradient in the tension steel in the plastic hinge zone (Figure 6.11). As a result, the plastic deformations are spread over a greater length, thereby reducing the maximum stresses developed in the

---

+ Refer Section 2.2.4 for definition of e_v.
* See Figure 8.2.

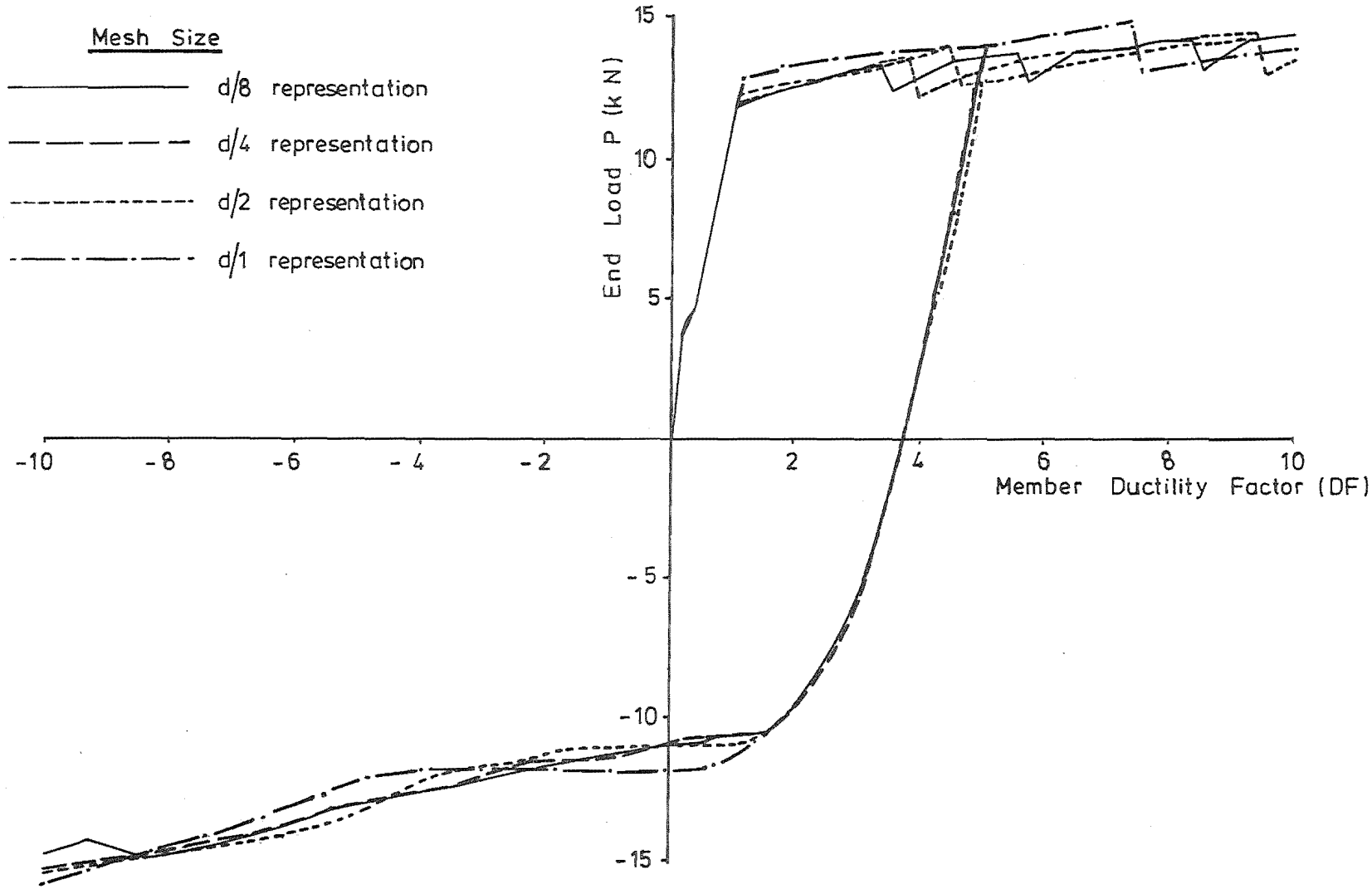

FIGURE 6.8 : EFFECT OF CONCRETE CRUSHING ON MESH REFINEMENT
(TB1, e_v = o)

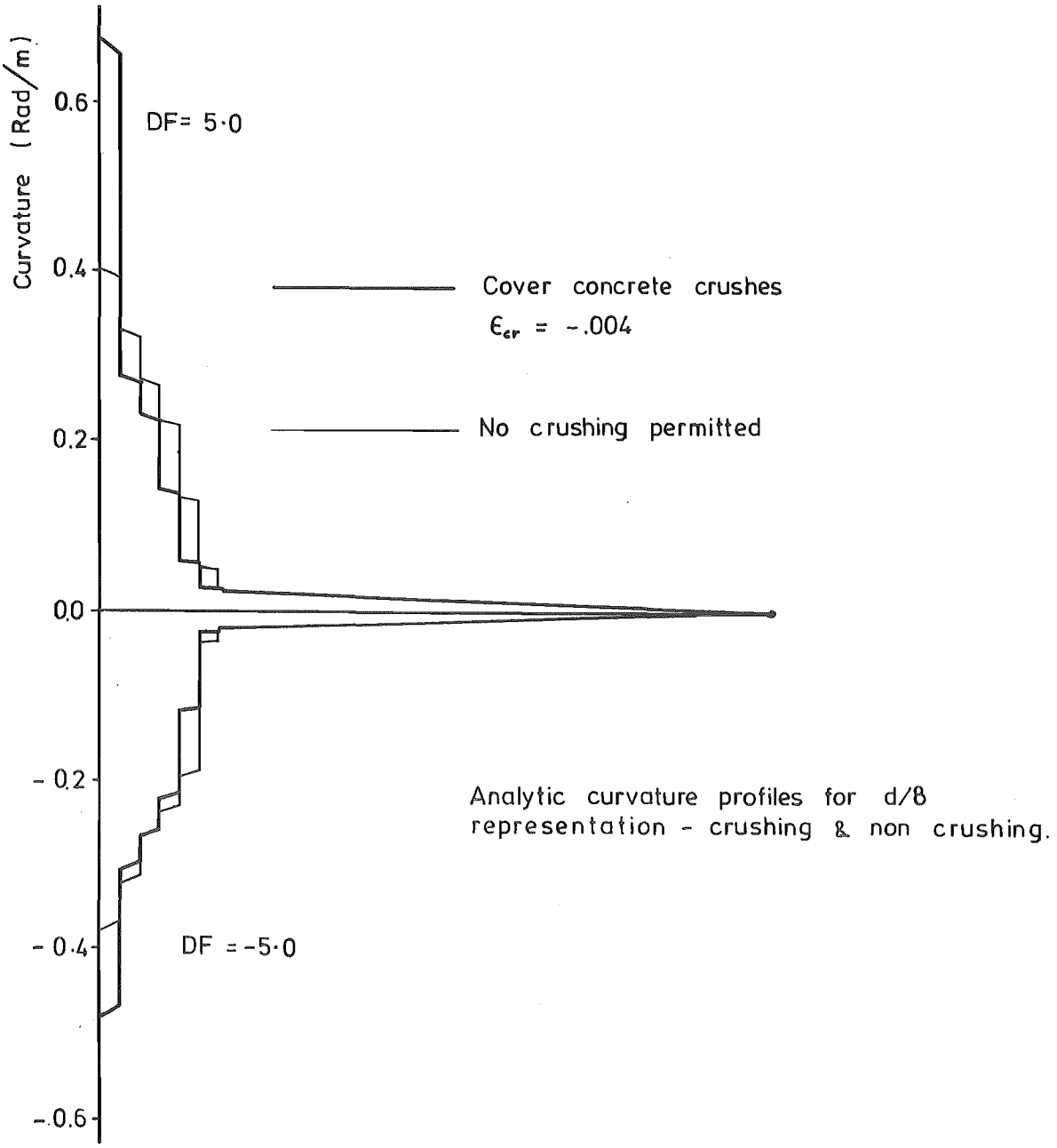

FIGURE 6.9 : CURVATURE DISTRIBUTIONS, AFFECTED BY CONCRETE CRUSHING (REFER FIGURE 6.8)

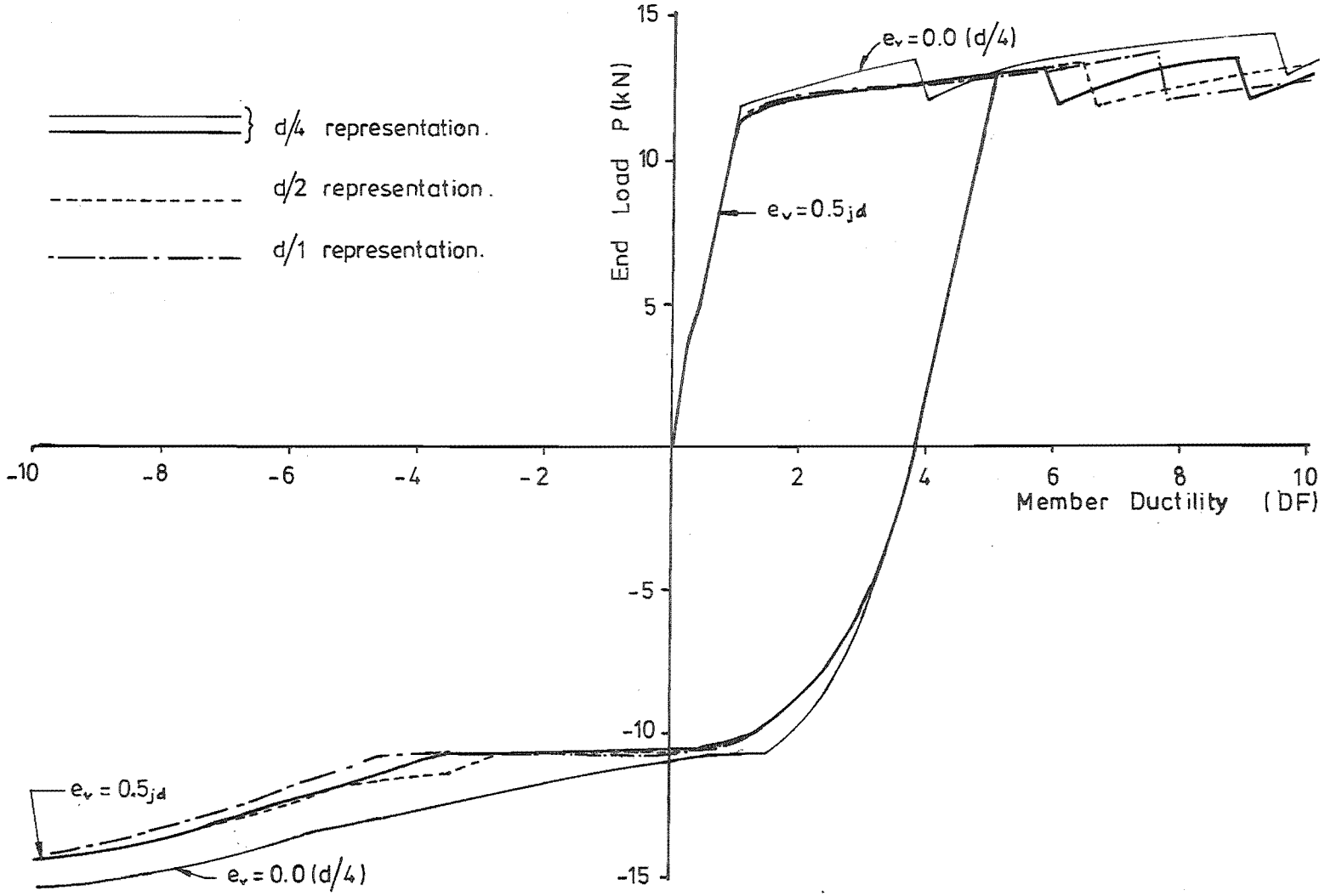

FIGURE 6.10 : LOAD-DEFLECTION RESPONSES FOR e_v = 0.5 jd

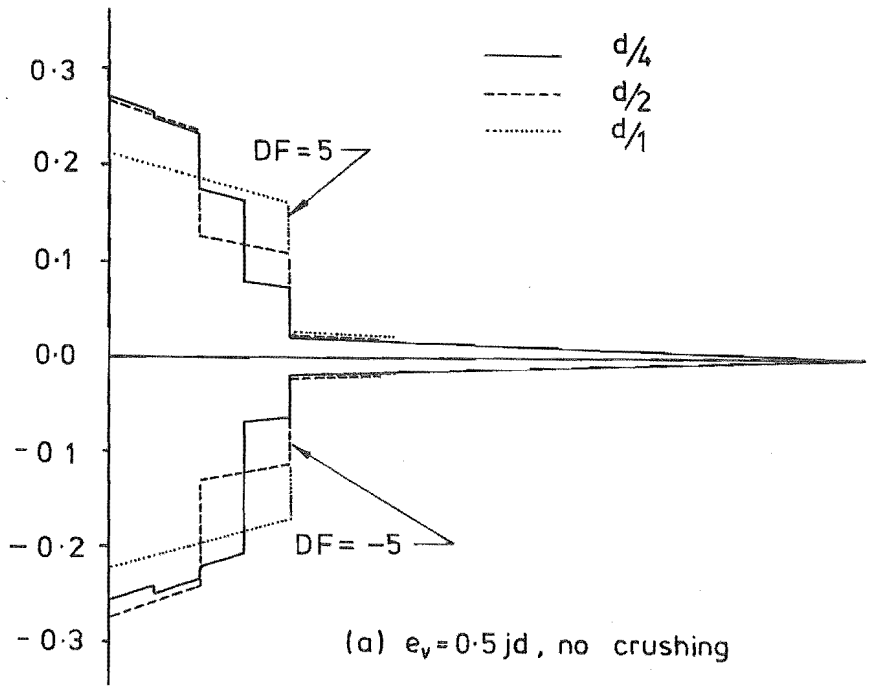

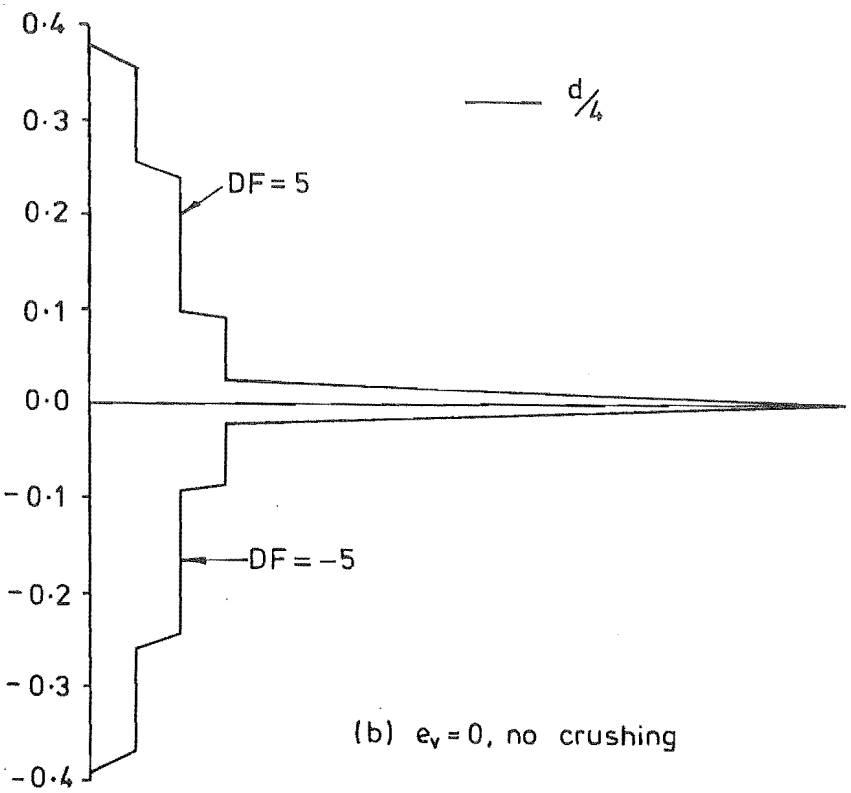

FIGURE 6.11 : EFFECT OF MESH REFINEMENT ON RESPONSES PREDICTED WITH ALLOWANCE FOR INELASTIC SHEAR DEFORMATION

tension bars.

(b) The differences between the responses predicted for the three representations are considerably reduced. In particular, the yield load of the member is less affected by the degree of mesh refinement, because the low stress gradient in the tension steel means that all points within a distance of d/2 from the end of the member will yield at similar load. Also, the greater spread of plastic strains means that the plastic strain distribution computed for the d/1 representation agrees more closely with the distributions predicted for the more refined meshes.

(c) Because of the lower tension force developed in the reinforcement, the onset of crushing occurs at a larger displacement than is predicted when $e_v = 0$ is used. Comparisons made with the observed response for this specimen (Section 8.2.1) indicate that the crushing behaviour predicted in the $e_v = 0$ analysis is probably* the more accurate of the two.

6.2.5 Effect of Shear Induced Stresses in the Flexural Reinforcement (a/d = 2.3)

A second set of analyses was performed to establish whether the results obtained in Section 6.2.4 also held true for beams with smaller shear span to depth ratios. The beam used in these analyses (Figure 6.12) had a shear span to depth ratio (a/d) approximately half of that of the beam considered in the previous example. Segment sizes of approximately 0.2d and 0.4d were used to represent the plastic hinge zone and analyses were performed both with and without allowance for the effect of shear induced stresses in the flexural reinforcement. This beam was one of three tested by Celebi and Penzien (11) which were used for calibrating the inelastic shear model. The member representations used were chosen in accordance with the location of instrumentation used in the tests.

Only monotonic responses are considered in the analyses of this specimen.

---

* The predicted crushing behaviour is dependent on the value of crushing strain modelled. All analyses in this study assumed a standard value of $\varepsilon_{cr} = -0.004$.

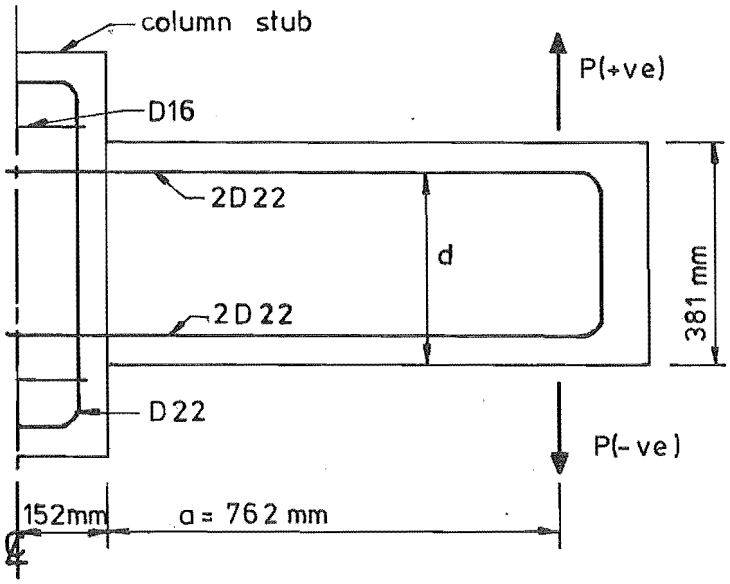

b = 229 mm
d = 330 mm
a/d = 2.31
σ_{sy} = 345 MPa
σ'_c = -31.6 MPa
P_t = 108 kN
= calculated capacity
P_y = 104 kN
= theoretical yield load

(a) Half test specimen.

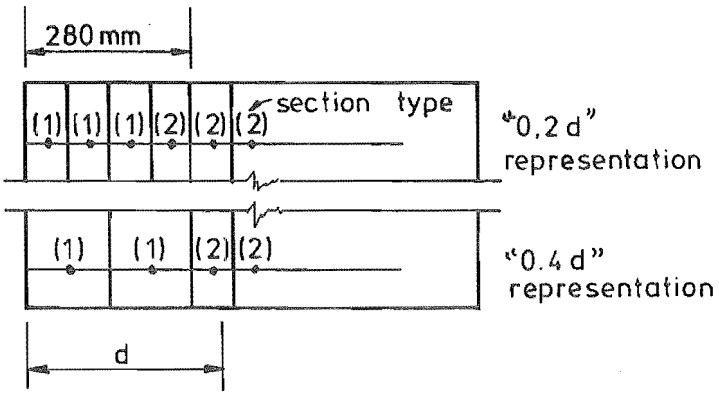

(b) Member representation.

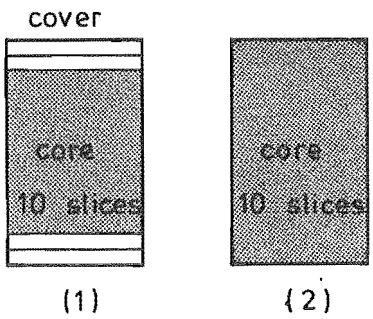

(c) Concrete section types used in analysing be

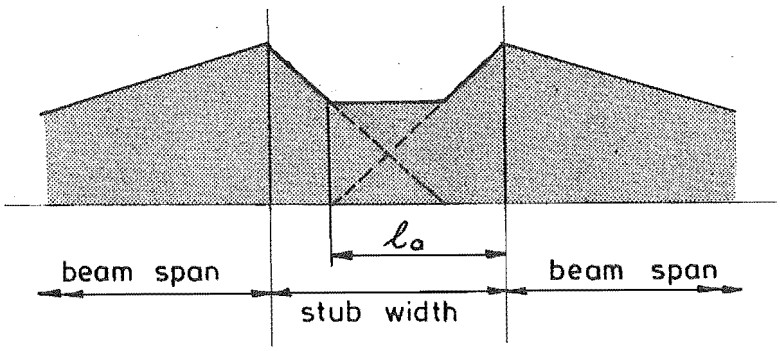

(d) Effective curvature distribution within stub due to overlap of anchorage lengths.

FIGURE 6.12 : CELEBI AND PENZIEN TEST SPECIMEN NO. 12

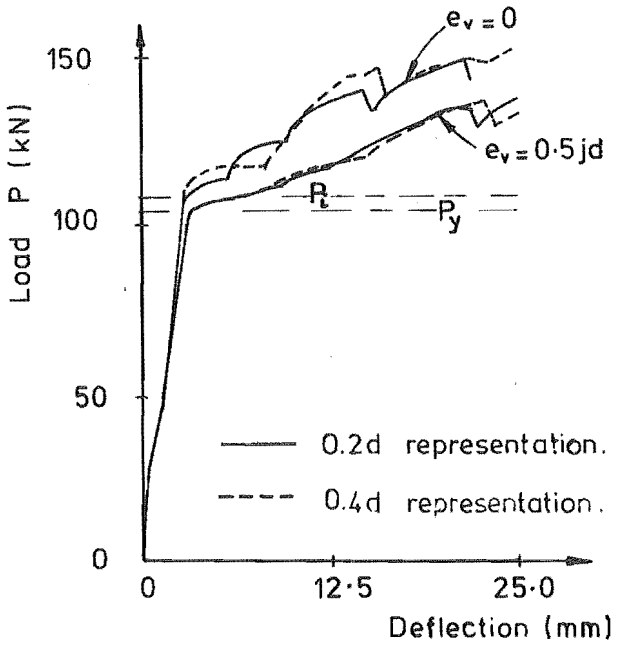

FIGURE 6.13 : LOAD DISPLACEMENT RESPONSES FOR CP 12

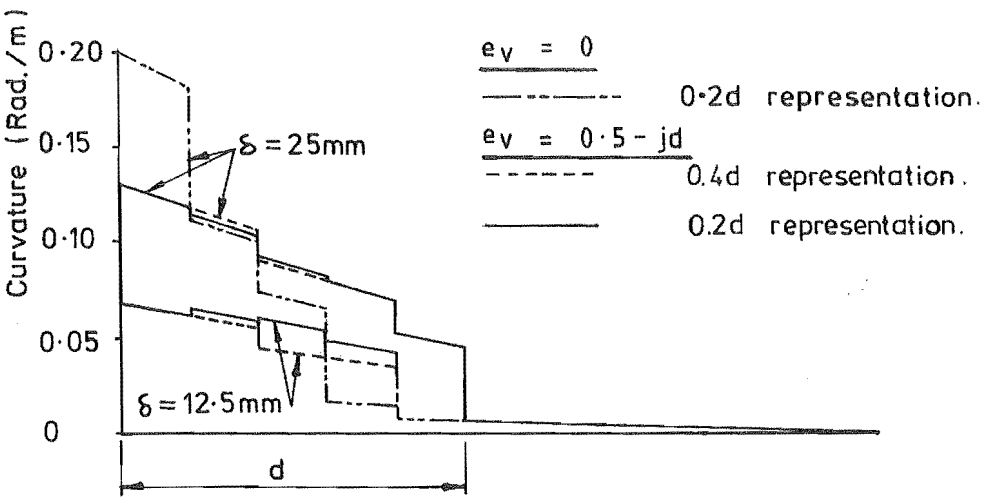

FIGURE 6.14 : INELASTIC CURVATURE DISTRIBUTION

As seen in Figures 6.6 and 6.8, the difference between the responses computed for different member representations during the initial inelastic load reversal are generally representative of those occurring during subsequent load reversals..

The load-deflection responses obtained from analyses with e_v = 0.0 and e_v = 0.5 jd for both member representations are compared in Figure 6.13. Corresponding curvature distributions at three load intensities are shown in Figure 6.14. As these results show, the reduction in the post-yield strength gain due to the shear induced stresses in the flexural reinforcement was larger for this beam than for the previous beam, reflecting the greater influence of the shear forces. As in the previous case, the discrepancy between the computed responses for the coarse and fine meshes was considerably smaller for the analyses performed with e_v = 0.5 jd. Again, as shown by the inelastic curvature distributions, it would be possible to use only a single 0.8d (= 0.35a) segment to represent the hinge zone without introducing significant representation errors due to mesh size. Thus, even for comparatively short members, the depth of the section, rather than the shear span, controls the theoretical yield penetration (i.e. for e_v = 0.5 jd). This is consistent with most experimental results for beams with small aspect ratios.

6.2.6 Effect of Segment Size on the Computed Inelastic Shear Response

Load-deflection and shear force-shear displacement responses obtained from three analyses of specimen TB1 (Figure 6.5) are compared in Figure 6.15. The results presented are for segment sizes of d/1, d/2 and d/4, and were computed using the full inelastic section model with e_v = 0.5 jd. The cycle displacement limits used are the same as for the initial post-elastic stages of the test load sequence (Figure 8.1). The values of the shear model constants* used in these analyses were

K_{int} = 0.138 MPa,
ϕ_g = 0.12,
ϕ_{xv} = 1.0, and
ϕ_{unl} = 5.0 .

---

* Refer Section 5.4 for definitions of the shear model constants.

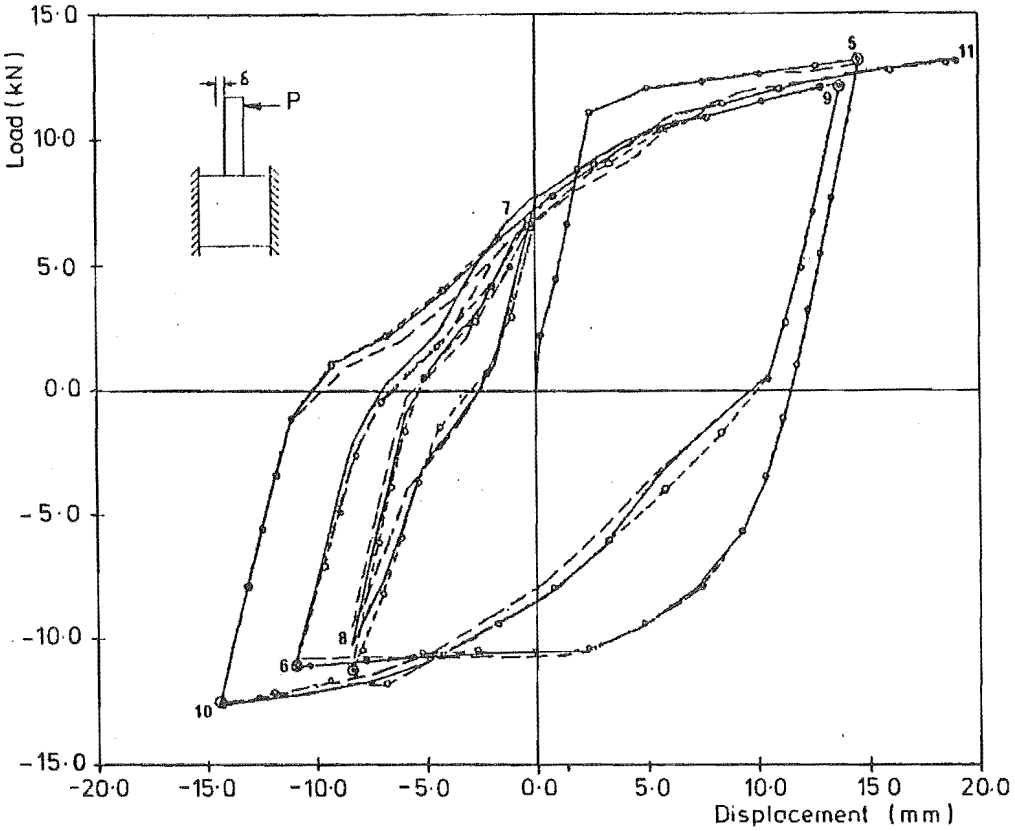

(a) Load - Deflection response

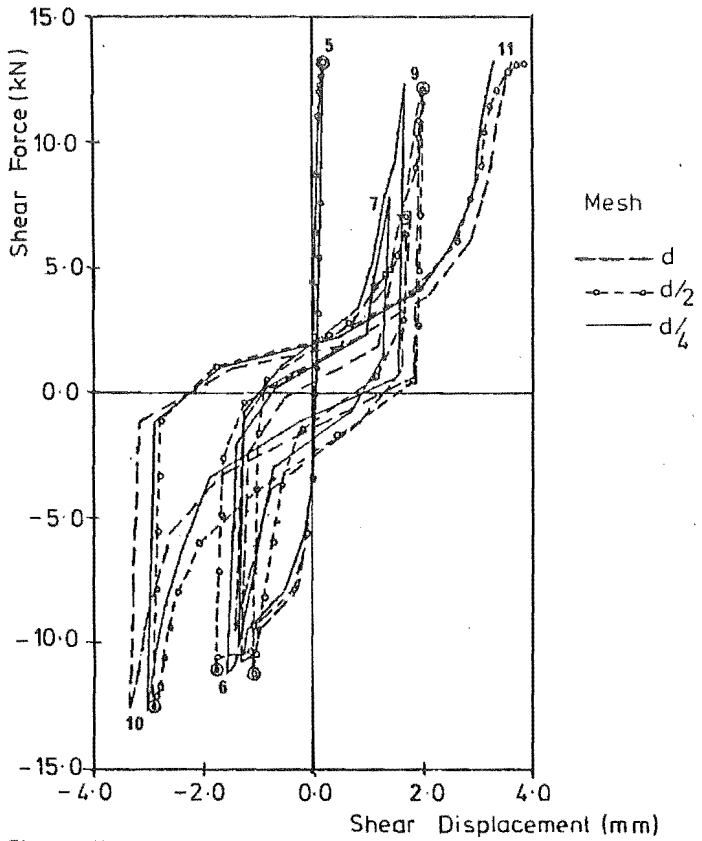

(b) Shear Force - Shear displacement response

FIGURE 6.15 : EFFECT OF MESH REFINEMENT ON RESPONSES PREDICTED WITH ALLOWANCE FOR INELASTIC SHEAR DEFORMATION

Attempts were made at using a d/8 segment representation, but in each case solution failure prevented completion of the analysis.

As in the earlier analyses (Section 6.2.4), the predicted maximum loads resisted by the beam were similar for all three mesh sizes. However, as indicated in Figure 6.15b, there were discrepancies of up to 0.5 mm in the predicted shear deformations at the peaks of the main load reversals (cf. maximum predicted shear deformation of 3 mm to 4 mm). These discrepancies did not show any consistent trend and there is no indication that the d/1 representation is necessarily less accurate than the other two, or vice versa.

The discrepancies in the shear deformations largely originate because of the sensitivity of the model to the timing of the predicted opening and closing of cracks and are not primarily a function of the segment size, i.e. the predicted shear deformation during any increment are to some extent affected by whether the cracks are just open or just closed.

As seen in Figure 6.15a, the effects on overall load-deflection responses are comparatively small. The results also show that segments as coarse as d/1 can be used without inherently affecting the accuracy of the computed shear deformations.

6.2.7 Overall Evaluation

The results obtained from this investigation do not support the view that the number of segments used to represent a plastic hinge zone is likely to have a marked influence on the computed load-deflection response (cf. Section 6.2.2.). Generally, it was found that the plastic hinge zones could be adequately represented with as few as two segments, or even one when e_v = 0.5 jd was used. In other analyses performed in this study, generally 2 or 3 segments were used, except in cases where a more refined representation was required for comparing observed and predicted curvature distributions.

6.3 CELEBI AND PENZIEN TEST BEAMS

This section presents results from analyses of three of a series of twelve reinforced concrete beam specimens tested by Celebi and Penzien (11) and comparisons are made with the corresponding experimental responses. The three beams, designated 5, 9 and 12, had shear span to depth ratios (a/d) of 5.10, 3.70 and 2.31 respectively. Each was subjected to a series of quasi-static large displacement load reversals, with displacement ductility (DF) cycle limits progressively increasing from DF = ±2 to DF ±5.

These three beams, together with one of the small scale beam-wall specimens tested in this study (TB1, Chapter 7), were used for initial calibration of the inelastic shear model constants (Chapter 5). They were chosen for this purpose because experimental responses had been obtained for both shear deformations and strains in the flexural reinforcement, in addition to the member displacements. This permitted a reasonably comprehensive evaluation of the performance of the theoretical model.

6.3.1 Test Specimens and Loading Sequence

Details of the test specimen and the member idealization used for Beam 12 are shown in Figure 6.12. Only the '0.4d' representation was used for these analyses. Beams 5 and 9 differed from Beam 12 only in the lengths of their shear spans, i.e. for Beam 5, a = 1676 mm, and for Beam 9, a = 1219 mm. The maximum nominal shear stresses imposed were 0.145, 0.187 and 0.311 $\sqrt{f'_c}$ (MPa) respectively for Beams 5, 9 and 12.

Due to both the symmetrical loading arrangement and the column stub reinforcing detail used, it is unlikely that there was a significant reduction in the stresses in the beam flexural reinforcement between the faces and the centre of the stub. To model this behaviour, an anchorage length of 3/4 of the stub width was used. The interaction of the anchorages from either face of the stub results in an effective elastic bar strain distribution in the anchorage stub as shown in Figure 6.12d.

Bar strains measured during test loading of a preliminary test specimen showed that yield had penetrated to the centre of the stub at a member displacement ductility of between 4 and 5. Because of the possible significance of this parameter, analyses were performed with both $\phi_{pa} = 0.2$ and $\phi_{pa} = 0.4$ (ϕ_{pa} is the ratio of the inelastic anchorage rotation to the plastic hinge rotation, Section 2.2.3).

The test loading sequence, which was the same for all specimens, is shown in Figure 6.16. The ductility values shown correspond with the definition used by Celebi and Penzien. They are used in this study only in the sense of being a title for each set of load cycles, as the theoretical yield displacements for Beams 9 and 12 were considerably less than the experimental values*. Since the actual experimental cycle displacement limits were used for the analyses, the ductilities for the predicted responses are larger than those shown in Figure 6.16.

6.3.2 Measured Deformations

Celebi and Penzien used two approaches for measuring shear deformations in their tests. In the first, used for Beams 5 and 9, diagonal displacement gauges crossing the hinge zone were used. One assumption made when computing the shear deformations from the displacement readings, was that the curvature over the gauge length is constant. This condition is not generally satisfied, and consequently the computed shear deformations are likely to contain some flexural component. Another complication is likely to develop if there is a difference between the transverse expansions of the beam at either end of the gauge. However, these factors should have only a comparatively small effect on the shear strains at low loads when there are only small changes in curvature. In the comparisons made in this study, deformations based on differential diagonal displacement measurements are compared directly with theoretical shear strains.

In the second approach, used for Beam 12, the deformations were based on the lateral displacement a short distance from the fixed end of the cantilever. In this case, it was possible to make a direct comparison between identical experimental and predicted values. However, the value

* The cause of this discrepancy is not known, although it is possibly due in part to inadequate allowance for shear deformations resulting from inclined cracking.

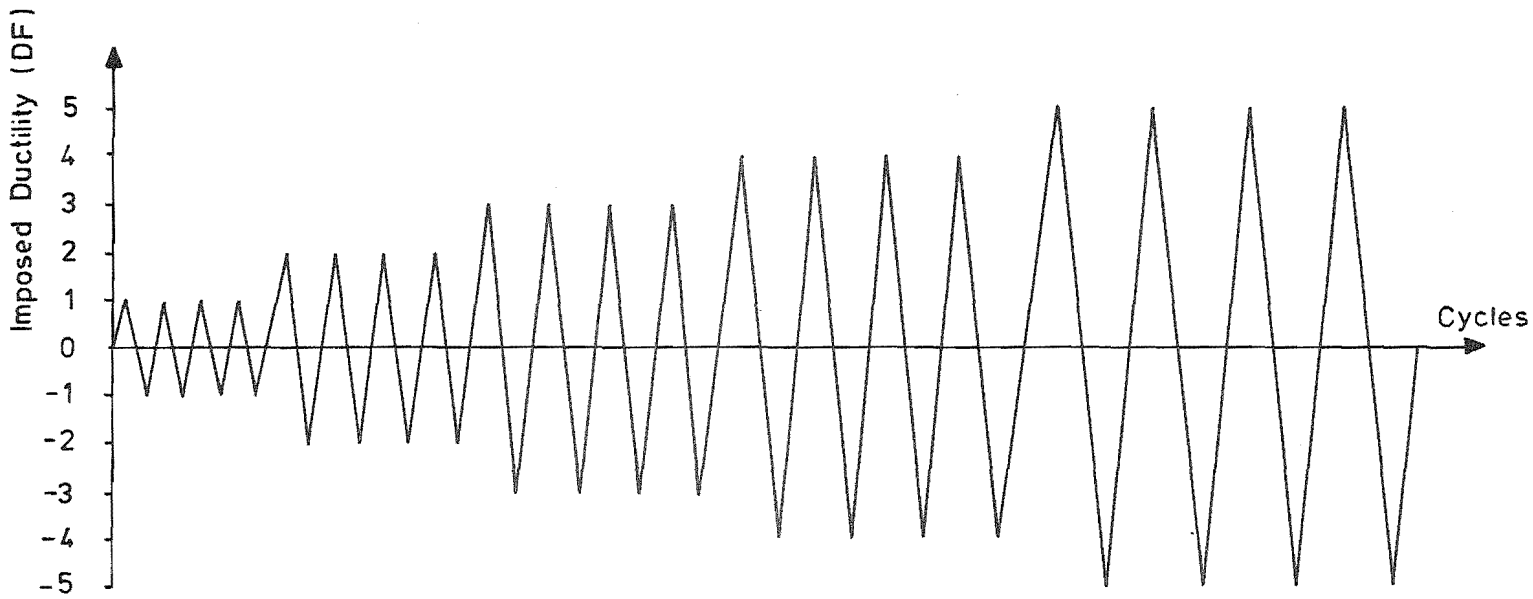

FIGURE 6.16 : DISPLACEMENT LOAD SEQUENCE FOR BEAMS 5, 9 AND 12 TESTED BY CELEBI AND PENZIEN

predicted is more sensitive to the modelled anchorage deformations.

Because of the above approximations, Celebi and Penzien used the term "shear deformation index" to describe the computed experimental deformations. In this section, the term "(shear) strain index" is used. To avoid complicating the description, this term is applied to both experimental and theoretical values, regardless of the fact that the values predicted for Beams 5 and 9 are true shear strains.

6.3.3 Calibration Procedure

Calibration of the shear model constants was carried out in two stages. The first consisted of an initial series of trial and error analyses. These analyses were first carried out for Beam 5, and then, for reduced ranges of values, were repeated for Beam 12. To further reduce the computer time required, only the four load cycles to DF = ±4 were analysed during this stage. The errors caused by missing out the initial stages of the load sequence were minimised by only evaluating the final two load cycles of the predicted response. In the second stage of the calibration, all three beams (i.e. 5, 9 and 12) were analysed for the full experimental load sequence. These analyses were used to verify both the inherent sensitivity of the model to load intensity and the accuracy of the values obtained for the model parameters based on consideration of only part of the experimental load sequence.

The values for ϕ_g (0.1 used for these beams) and ϕ_{unl} (5.0)* were determined first based largely on the pre-yield response and the loading and unloading shear deformation responses at high load intensities. These values were subsequently used in all analyses to determine the remaining model constants K_{int} and ϕ_{xv}.* In calibrating these constants, account also had to be taken of the allowance for shear induced stresses in the flexural reinforcement and the allowance made for softening of the cover concrete due to mismatched crack surfaces.

To rationalize the selection process, five readily quantifiable characteristics were used for assessing the performance of the theoretical model. These were:

---

* Model constants defined and discussed in Sections 5.4 and 5.5.

(a) The difference between the peak loads for the positive and negative load reversals.

(b) Peak-to-peak value of shear strain index. Both experimental and predicted values were averaged over a 279mm gauge length starting from the face of the column stub.

(c) Strains in flexural reinforcement at maximum positive and negative displacements. The experimental values were measured over a 127 mm gauge length and the theoretical values over a 140 mm gauge length. Because of the discrepancies introduced by errors in the predicted curvature distributions (unrelated to the shear model), emphasis was placed on assessment of the tension strain residuals when the bars were loaded in compression, and on the progressive increase in bar strains during the four cycles analysed.

(d) Amount of "pinching" of the total load displacement loops. This was taken as the ratio of the load differences (positive-negative load reversal value) at zero displacement and at the cycle maximum displacements. This value gives an indication of the softening of the member response.

(e) Amount of "pinching" of the shear force-strain index hysteresis loops.

These analyses indicated that best correlation with the experimental responses could be obtained using values of K_{int} = 0.14 MPa to 0.21 MPa and ϕ_{xv} = 0.8 to 1.0.

The predicted responses for Beams 5 and 12 subjected to the full load sequence computed using values of K_{int} = 0.17 and ϕ_{xv} = 1.0 are compared in Figures 6.17 to 6.22 with the equivalent experimental responses.

Particular aspects related to the performance of the theoretical analysis procedure in these analyses are discussed in the following subsections.

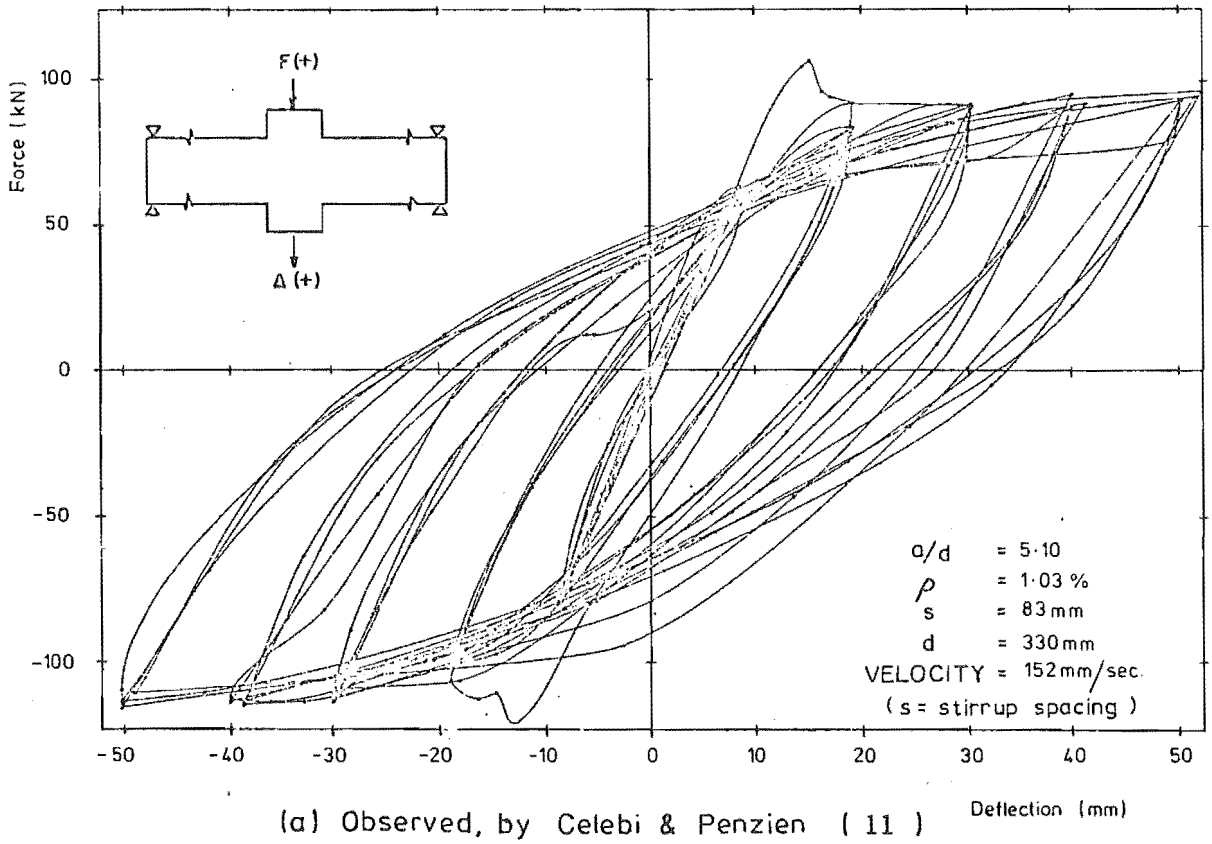

(a) Observed, by Celebi & Penzien (11)

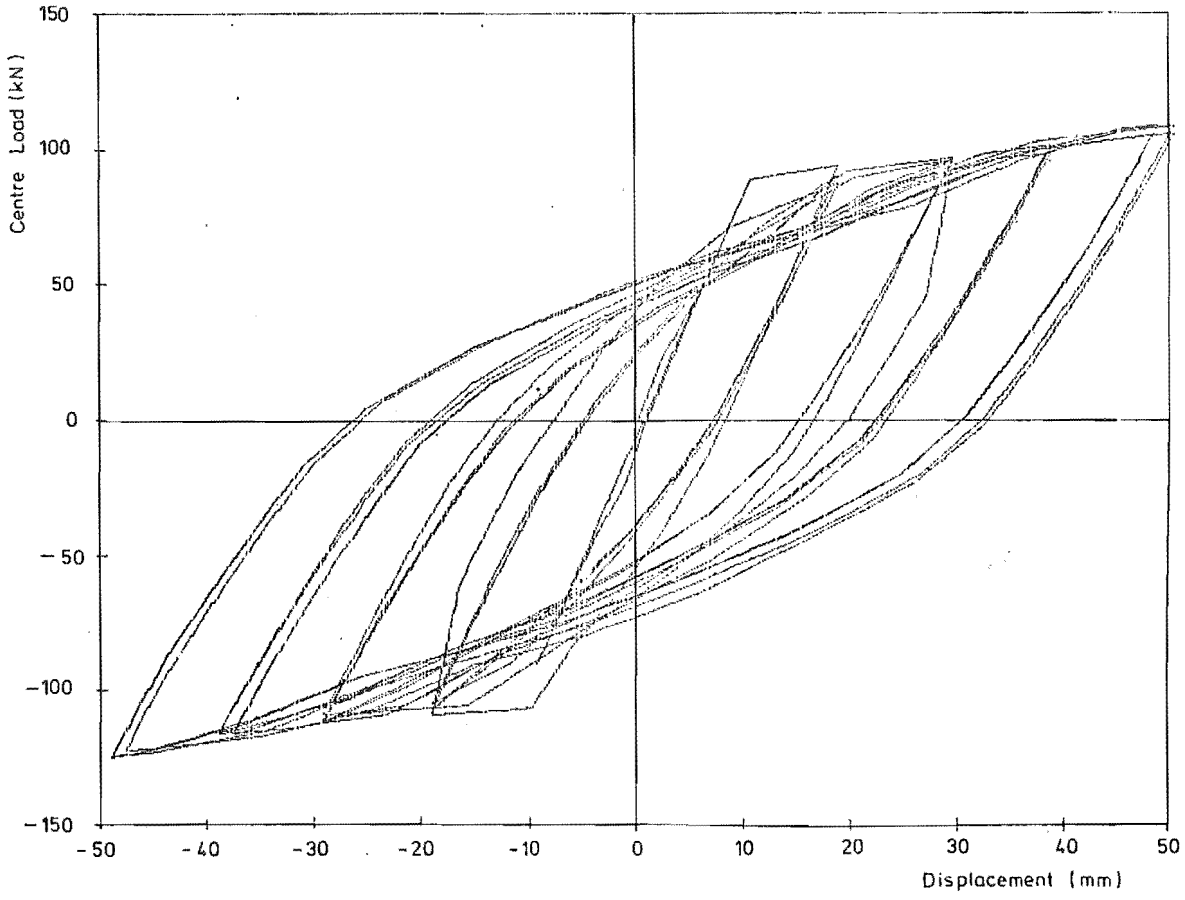

(b) Predicted

FIGURE 6.17 : LOAD-DEFLECTION RESPONSES, BEAM 5

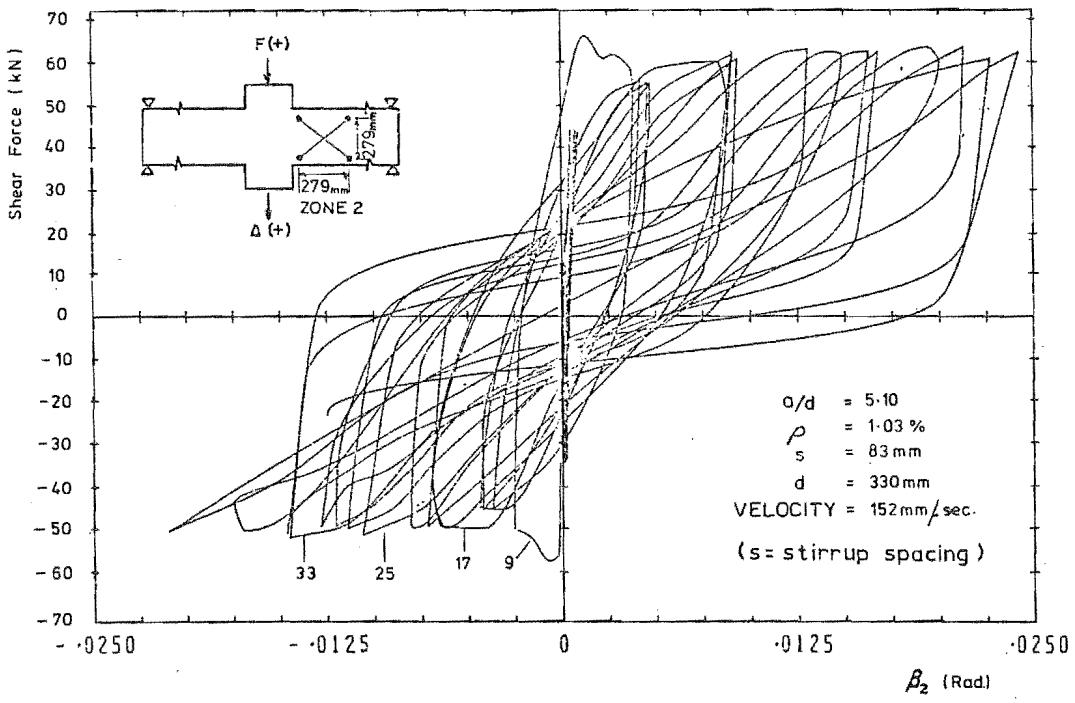

(a) Observed, by Celebi & Penzien (11)

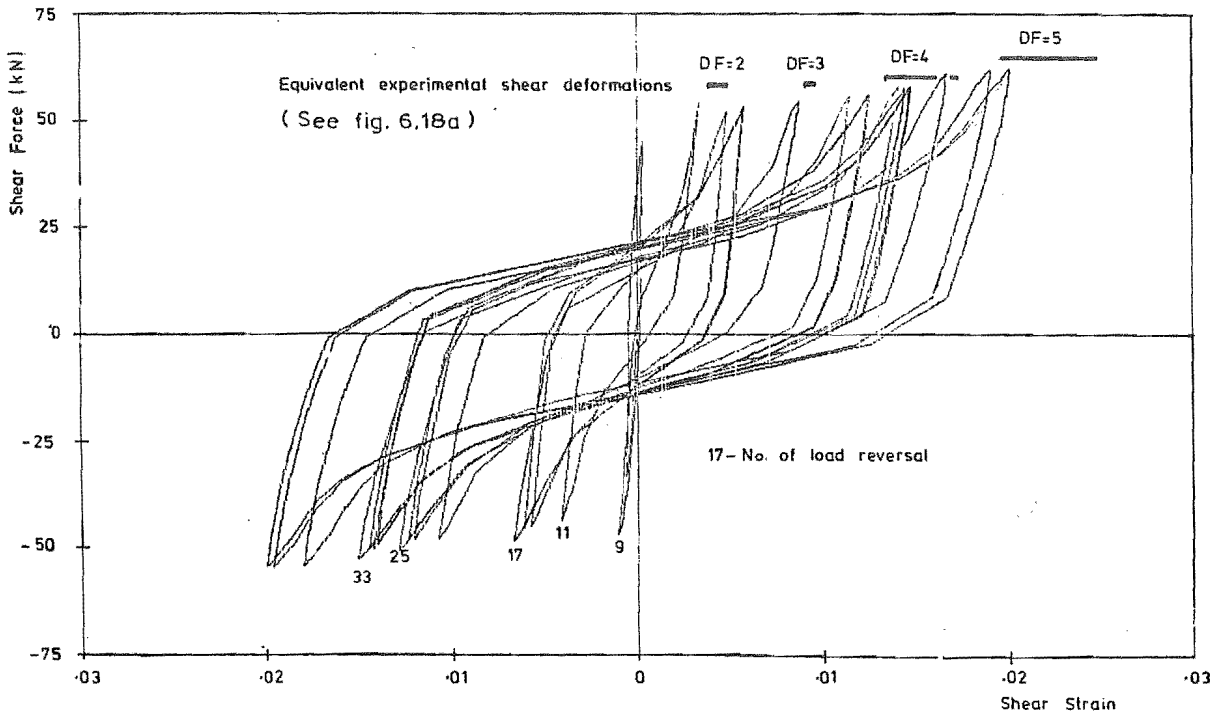

(b) Predicted

FIGURE 6.18 : SHEAR FORCE-SHEAR STRAIN INDEX, BEAM 5

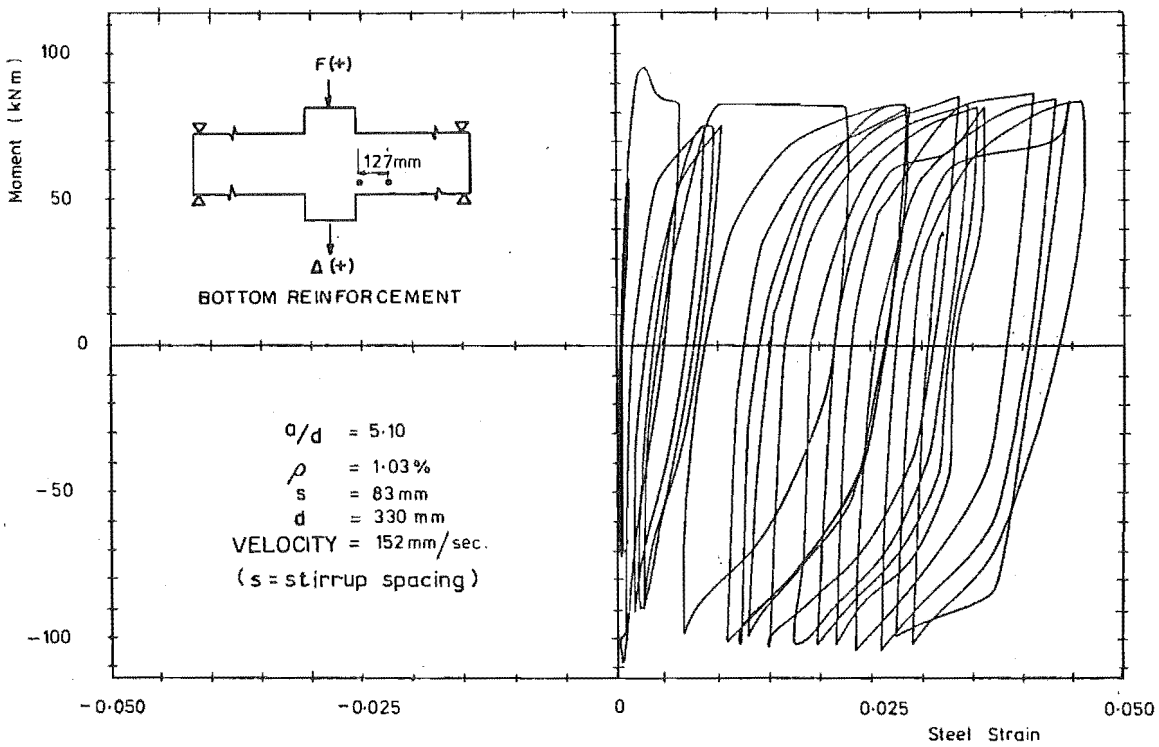

(a) Observed, by Celebi & Penzien (11)

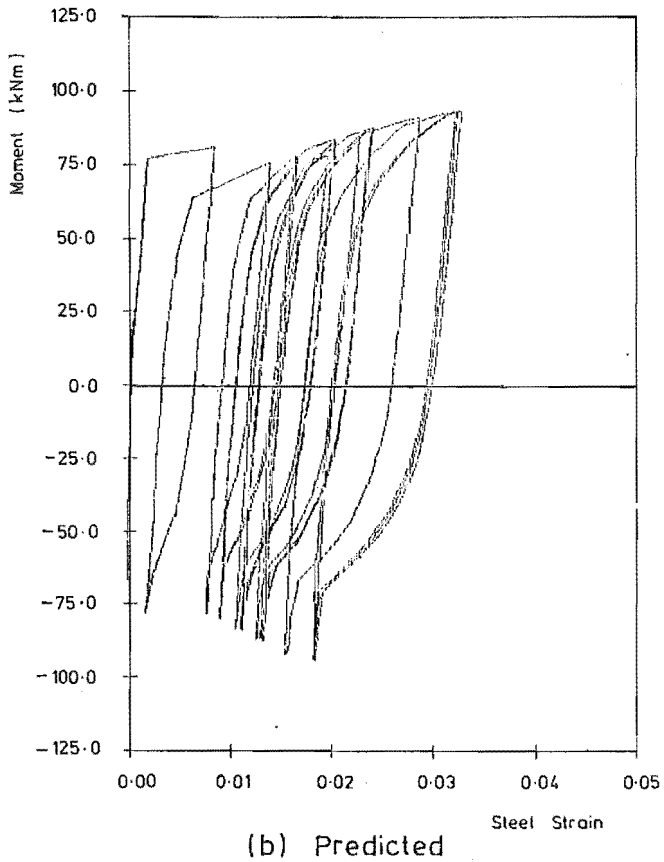

(b) Predicted

FIGURE 6.19 : STEEL STRESS-STRAIN RESPONSE, BEAM 5

6.3.4 Shear Deformation under Monotonic Loading

Inelastic shear behaviour under monotonic loading is not specifically considered in the shear model. However, the results of the analyses performed to calibrate the shear model show that the monotonic shear behaviour is an integral part of the more general inelastic shear behaviour, and should be incorporated into the cyclic shear model. The model fails to predict the shear deformations occurring at high load intensities when a structure is first loaded to a larger displacement ductility, i.e. load reversals 9, 17, 25 and 33 in Figure 6.18. This has little immediate effect on the load-deflection response, but it does affect the plastic hinge rotations which increase to compensate for the underestimated shear deformations. The effect of this on the computed responses for Beams 5, 9 and 12 is comparatively small because the peak displacement ductilities were never increased by more than one in any load cycle.

Although it was not realized at the time the shear model was developed, much of shear deformation occurring under monotonic load is due to the widening of inclined flexural-shear cracks as a result of the plastic strains in the tension bars (e.g., see Section 9.3.8). This behaviour is also indicated by the fact that the measured shear deformations during the first load reversal to a higher ductility increased roughly in proportion to the imposed end displacement, and were also similar to the shear deformations measured during subsequent load reversals to the same displacement limit (Figures 6.18 and 6.22). Both types of shear deformation are related to the plastic strains developed in the tension bars; the initial shear deformations being developed at high load intensities when the tension bars yield while the shear deformation during the subsequent load reversals is largely due to sliding between cracks at low load intensities.

Modelling this type of behaviour should not be difficult, and would significantly improve the quality of the predicted responses.

6.3.5 Concrete Softening due to Mismatched Crack Surfaces

The failure to model softening of the core concrete due to mismatched crack surfaces is probably the most important source of error affecting

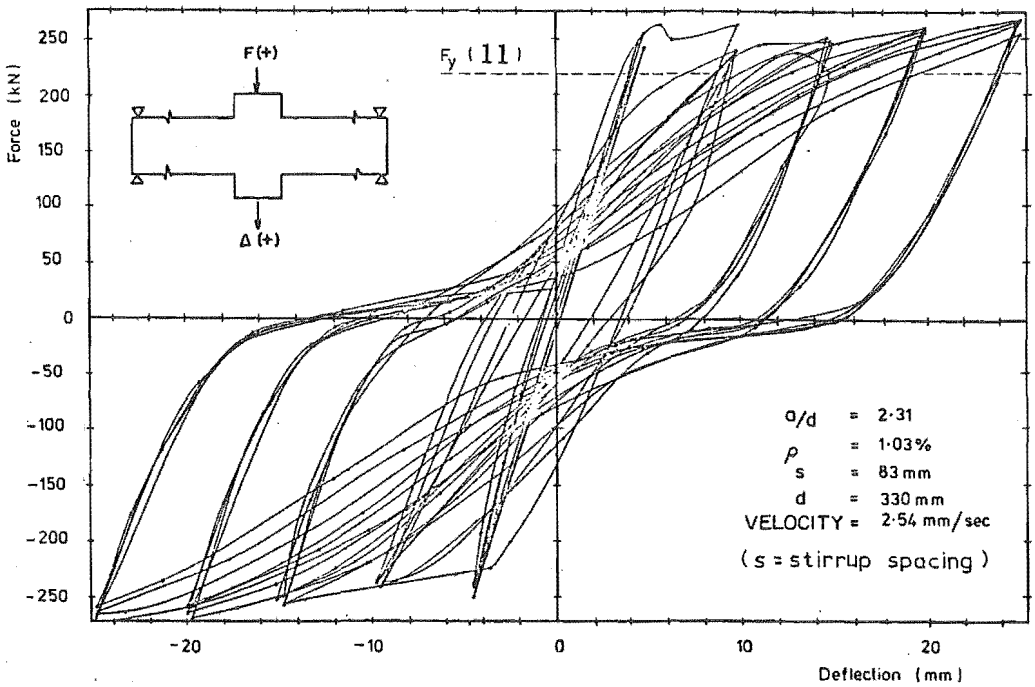

(a) Observed, by Celebi & Penzien (11)

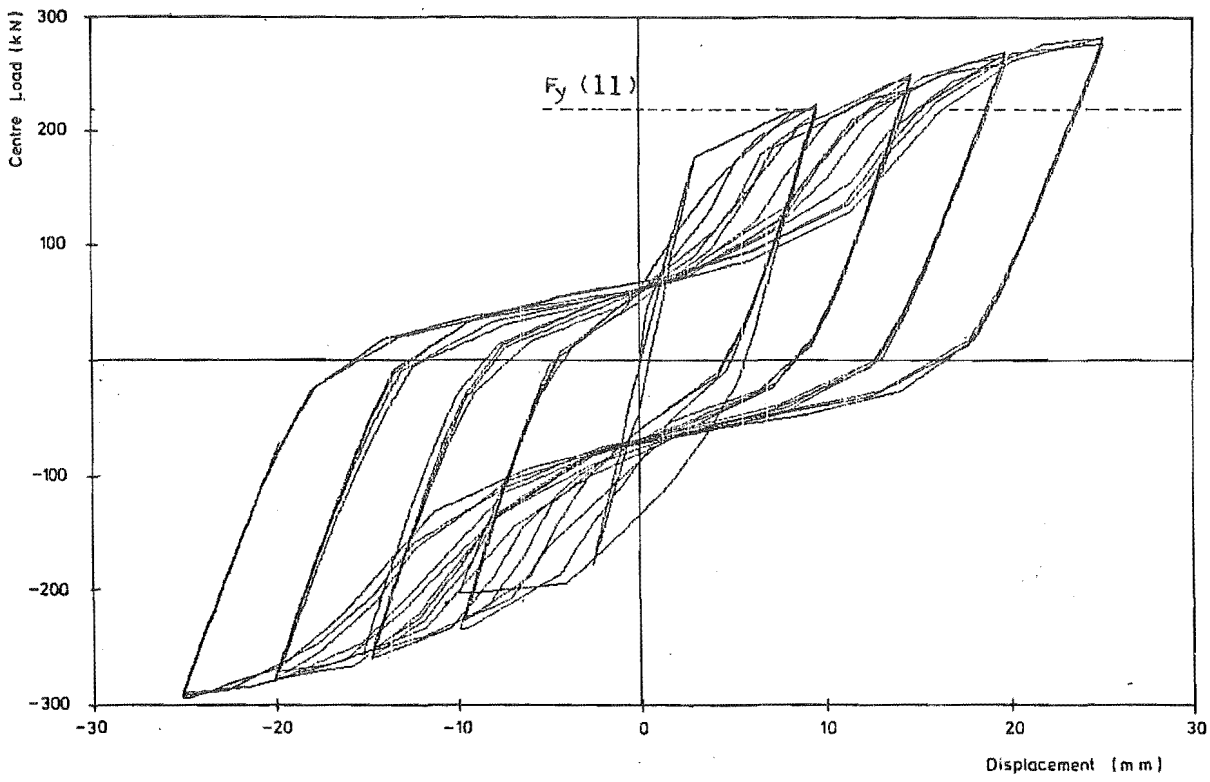

(b) Predicted

FIGURE 6.20 : LOAD-DEFLECTION RESPONSE, BEAM 12

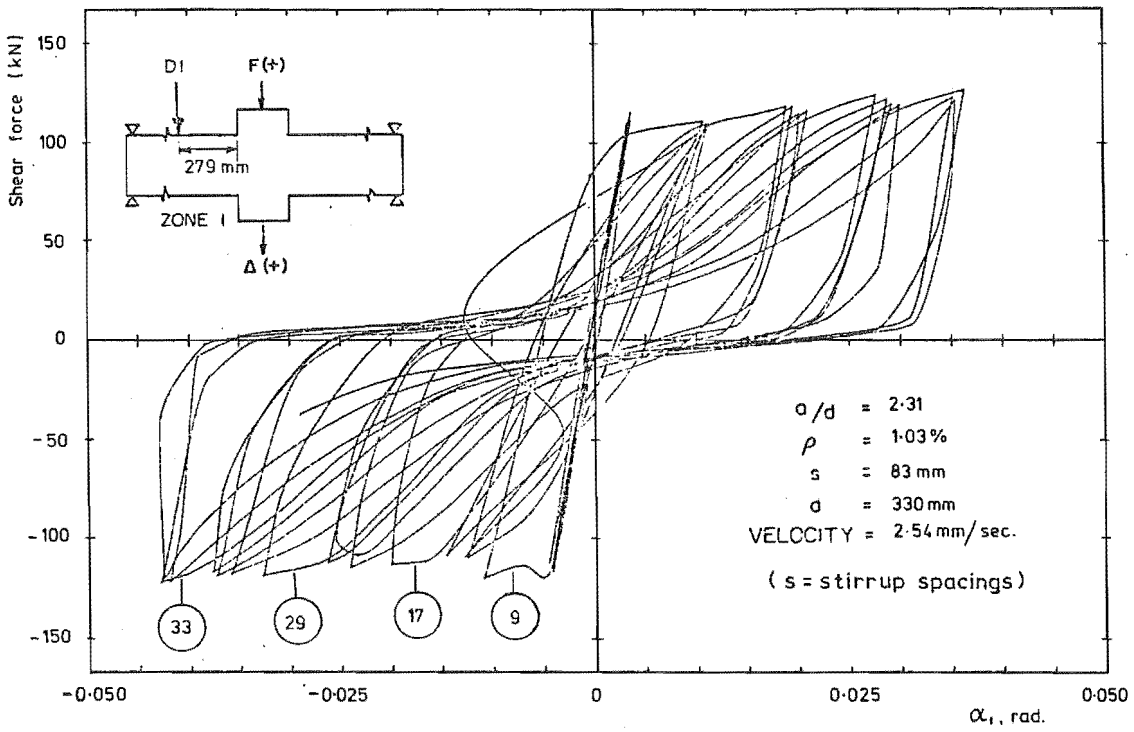

(a) Observed, by Celebi & Penzien (11)

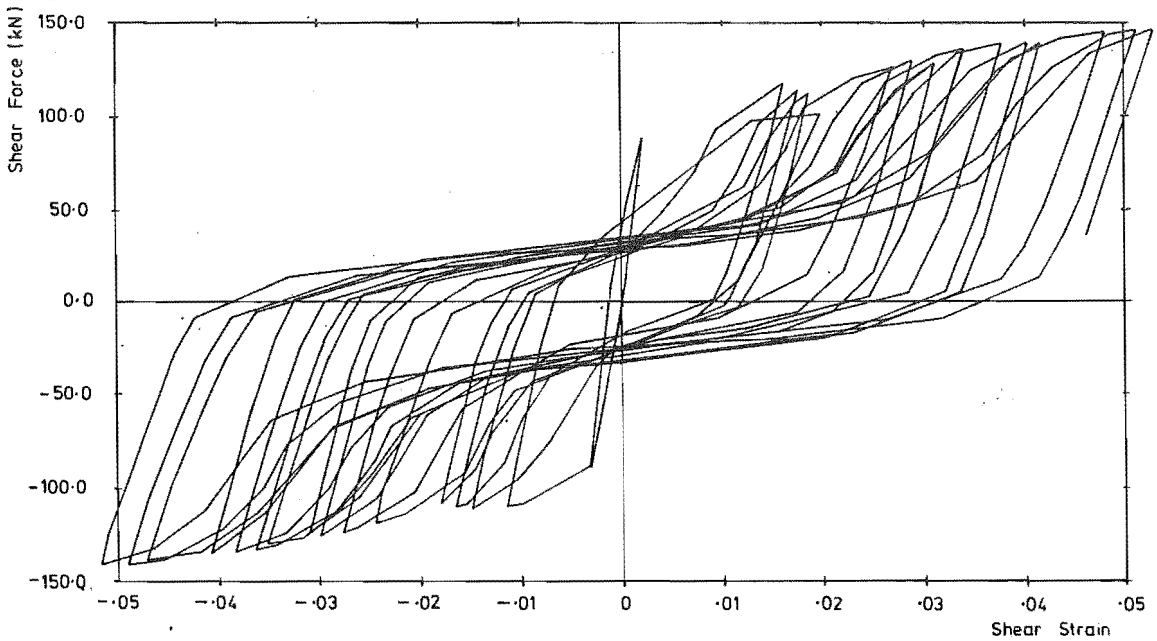

(b) Predicted

FIGURE 6.21 : SHEAR FORCE-SHEAR STRAIN INDEX, BEAM 12

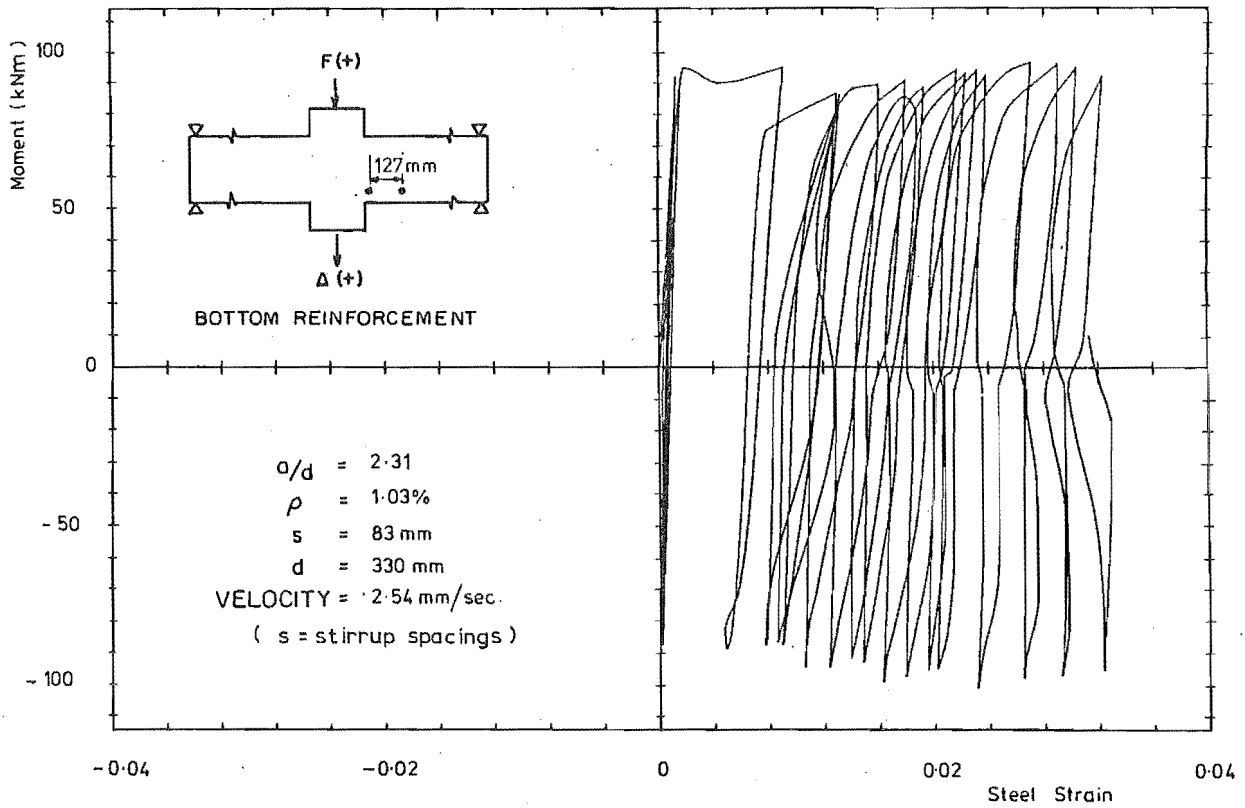

(a) Observed, by Celebi & Penzien (11)

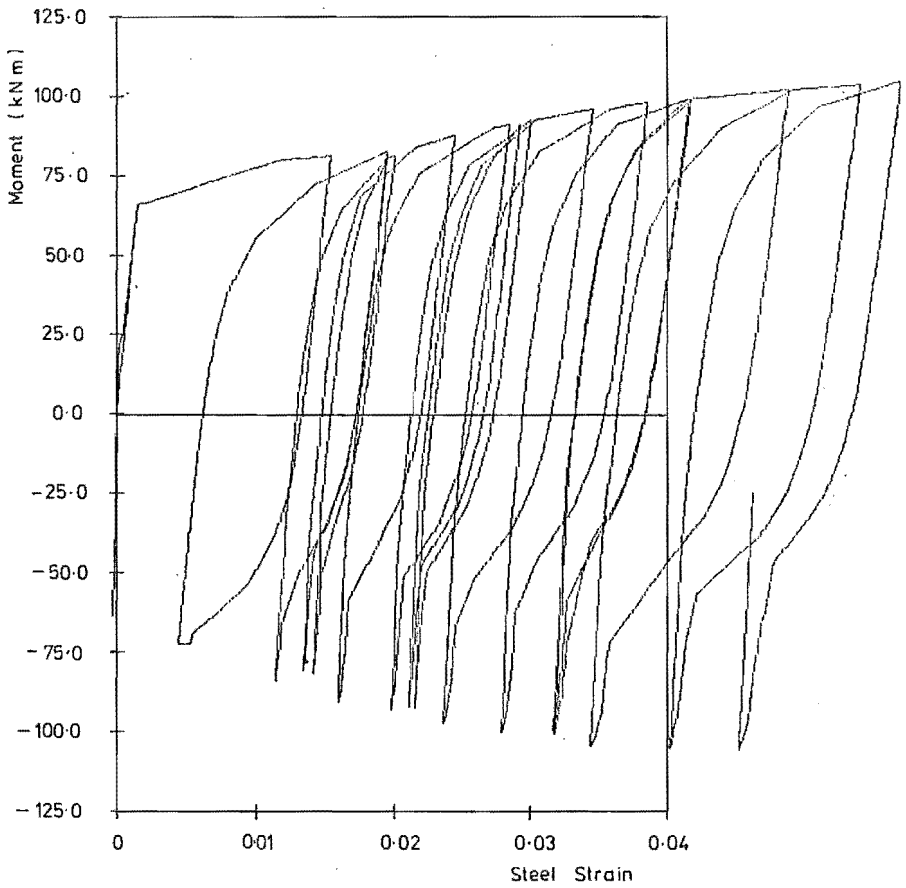

(b) Predicted

FIGURE 6.22 : STEEL STRESS-STRAIN RESPONSE, BEAM 12

the ability to match the observed and predicted responses.

The two most noticeable effects are the sudden increase in the predicted stiffness of the beam immediately after the cracks close, and over-estimation of the peak moments (Figure 6.20).

However, the excessive rigidity of the concrete also means that larger strains have to be developed in the tension bars in order to attain the same curvature (Figure 6.22). This causes the axial elongation of the plastic hinge zone to be overestimated, and in turn allows larger shear strains to develop (Figure 6.21).

The total elongation of the plastic hinge zone was not measured and consequently it was not possible to accurately check how closely the error in the predicted shear strains for Beam 12 related to the over-estimation of the axial strains.

Despite the overestimation of shear strain and member strength for Beam 12, the overall load-deflection response is still considerably more accurate than could be predicted without allowing for the inelastic shear deformations.

6.3.6 Effect of Shear Induced Stresses in the Flexural Reinforcement (e_v)

As in the analyses described in Section 6.2.5, this parameter had a significant influence on the cycle peak loads. It was generally found that a value of $e_v = 0.5$ jd resulted in best agreement between the predicted and experimental peak loads. This is consistent with the value suggested by Park and Paulay (95) for a beam which the shear reinforcement in the hinge zone is designed to carry the full shear load by truss action. However, the results obtained from these analyses were not sufficiently conclusive to establish whether this factor accurately modelled the real behaviour in the member. The cycle peak loads were sensitive to a number of model parameters. In particular, with the core concrete normal stress response not being modified for the effect of mismatched crack surfaces, the question of the extent to which the improved correlation with the experimental

results was due to compensating errors, could not be resolved. For the analyses with e_v = 0.5 jd, the predicted bar strains underestimated in the case of Beam 5 and overestimated in the case of Beam 12. Since these bar strains were measured over only part of the hinge zone, they are not necessarily representative of the strain distribution along the member.

6.3.7 Yield Penetration into Anchorage Zone (ϕ_{pa})

Surprisingly, the value used for ϕ_{pa} did not appear to have a very significant influence on the response, e.g., increasing ϕ_{pa} from 20% to 40% caused a decrease of only 3 to 4% in the computed peak loads for Beam 5, and had little influence on the other response characteristics.

6.3.8 Strain Coupling Ratio, ϕ_{xv}, and Interlock Rigidity Constant, K_{int}

There is considerable interaction between the effects of these parameters. The same peak to peak shear displacements can be obtained using a lower value of ϕ_{xv} and higher value of K_{int}, and vice versa. Higher values of ϕ_{xv} increase the pinching effect, but they also increase the load overestimation due to the effect of coupling. The values for these parameters were chosen as a compromise between these effects. This compromise was to a large extent necessary because of the failure to model softening of the core concrete normal stress response caused by mismatching of crack surfaces. If this had been done, different values of ϕ_{xv} and K_{int} would probably have been obtained.

6.3.9 Onset of Sliding Shear Deformations

During unloading from the peaks of the post-elastic load reversals, the shear rigidity of the specimens generally started to decrease earlier than predicted. Similarly, the large shear displacements which developed once reverse loading was applied, generally occurred at a lower load than indicated by the model, e.g. the model generally overestimated the shear force required to return to zero shear strain in the plastic hinge zones.

These discrepancies suggest that effective crack opening was occurring earlier than predicted. The main factors influencing this behaviour in

the analytic model are the strain interval over which unloading occurs* in the concrete and steel models and the fact that the model ignores the effect of shear force on the strains induced in the concrete (Section 5.4.6). The strain intervals for unloading used in the concrete model are the same as used by Blakeley (68). However, it became evident that this quantity considerably influences the shapes of the predicted shear force-displacement loops when attempts were made to allow for softening of the core concrete due to mismatched crack surfaces (Section 5.4.5). The steel unloading response affects the change in strain required to unload the section as a whole, i.e. rather than to unload the concrete. Reducing the steel unloading modulus (see Section 3.5.1) would therefore result in the model predicting cracks to open earlier. Including shear induced strains in the concrete would also be likely to result in the model predicting earlier opening of cracks.

6.4 BEAM-COLUMN SUBASSEMBLAGE

The beam-column subassemblage is the basic structural component in a moment resisting frame structure. A considerable number of experimental studies have been carried out in an effort to assess, and where possible improve, the performance of beam-column subassemblages under seismic loading (3 , 4 , 6 , 7 , 10). In many of these tests, however, the joint shear and/or beam reinforcement anchorage mechanisms have severely deteriorated, even at moderate load intensities. This type of behaviour is undesirable and is not modelled in the present analysis procedure. The subassemblage analysed here (Figure 6.23a) is one of a series of beam-column specimens tested by Beckingsale (6) at the University of Canterbury. A comparatively high axial compression load (13.8 MPa) was applied to the column and this was effective in largely suppressing both deterioration of the joint shear response and overall slip of the beam reinforcement within the column.

---

* The difference between the normal strains at the peak of load reversal and at zero stress.

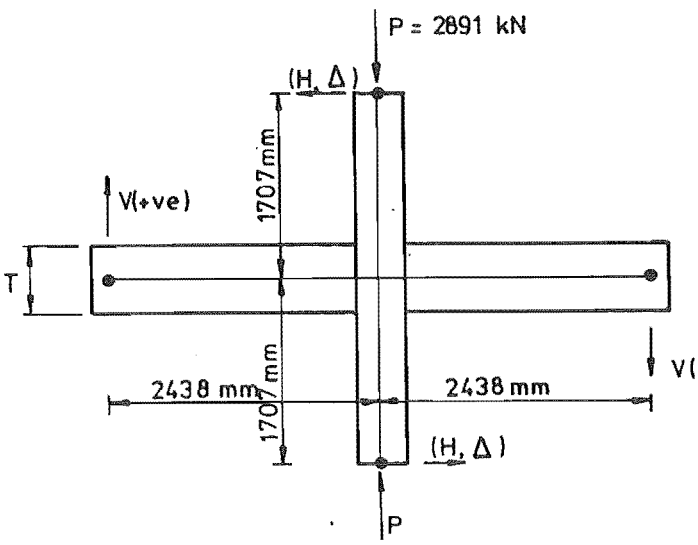

f_c' = 34·7 MPa.

Beam.
b = 356 mm
T = 610mm
d = 556mm
$\rho s = \rho' s$ = 0.0087
a/d = 3.98

Column
b = 457 mm
T = 457 mm.
ρs (total) = 0.022

(a) Test Specimen B13A

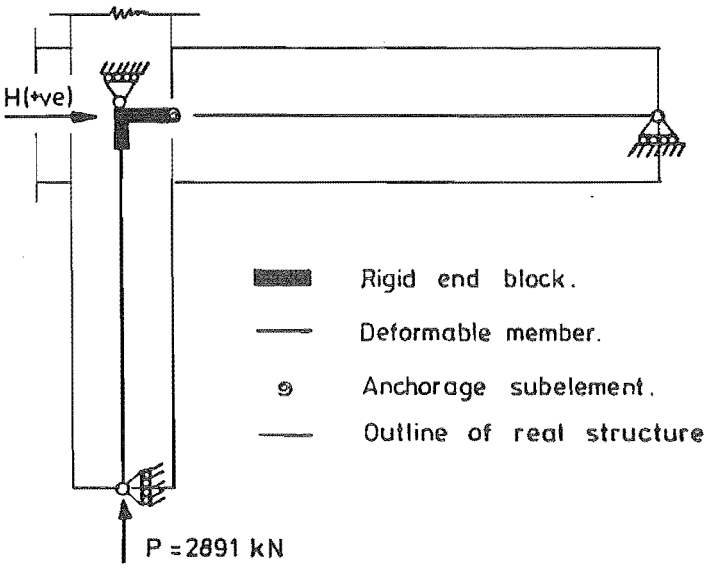

Anchorage Subelement.
ℓ_a = 216 mm ϕ_{pa} = 0·25

Inelastic shear model parameters·
K_{int} = 0·172 MPa
ϕ_{xv} = 1·0
ϕ_g = 0·1
ϕ_{uml} = 5·0

Beam hinge zone segmentation
(3 × 0.32d)

Correction for shear cracking (beam only) e_v = 0.5jd

(b) Half Structure Idealization of Beam - Column Subassemblage

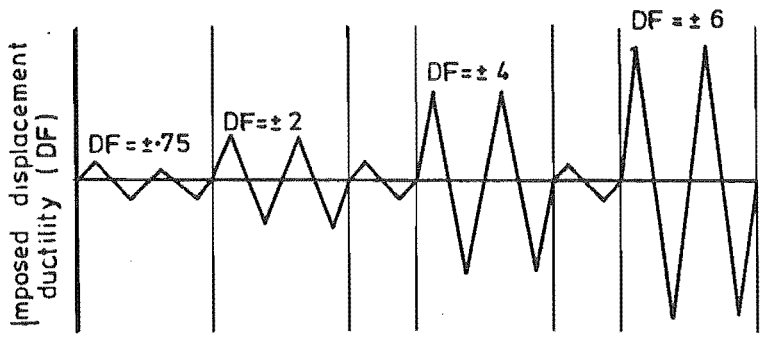

$$DF = \frac{\Delta (total)}{\Delta (at\ yield)}$$

(c) Test Loading Sequence B13A

FIGURE 6.23 : BEAM COLUMN SUBASSEMBLAGE TESTED BY BECKINGSALE (6)

As shown in Figure 6.23b, half structure idealization of the beam-column subassemblage was used for the present analysis. Both material and geometric nonlinearities were considered as the test results obtained from Beckingsale had been corrected for P-Δ effect. The various model parameters and the beam and column member segmentation used are given in Figure 6.23b. Further details of this specimen are given in Reference (6).

The beam anchorage length used, i.e. half the column width, was based on the beam reinforcement strain distributions measured in the test. These showed the bar strains decreasing to zero near the centre of the column for both directions of loading. No allowance was made for the self weight of the beams as this would have resulted in a non-symmetric structure. The effects of these weights on the column shear-displacement response should be approximately self compensating.

The predicted column shear-displacement response obtained when allowing for both inelastic sliding shear deformations in the beam hinge zone and the effect of shear cracking (e_v = 0.5 jd) on the beam flexural strain distributions is compared in Figure 6.24a with the equivalent experimental response. As indicated, the predicted response shows good overall agreement with experiment response, particularly as far as the general shape of the large displacement hysteresis loops and the cycle peak loads are concerned. Much of the discrepancy that did occur was due to the tendency of the theoretical procedure to underestimate the softening occurring during unloading (note rotation of the beam zero load axis due to the P-Δ effect). This characteristic was previously noted in Section 6.3.9.

In order to illustrate the extent to which the beam shear deformation affects the response of the subassemblage, an analysis was performed with inelasticity restricted to the normal stress actions. All other

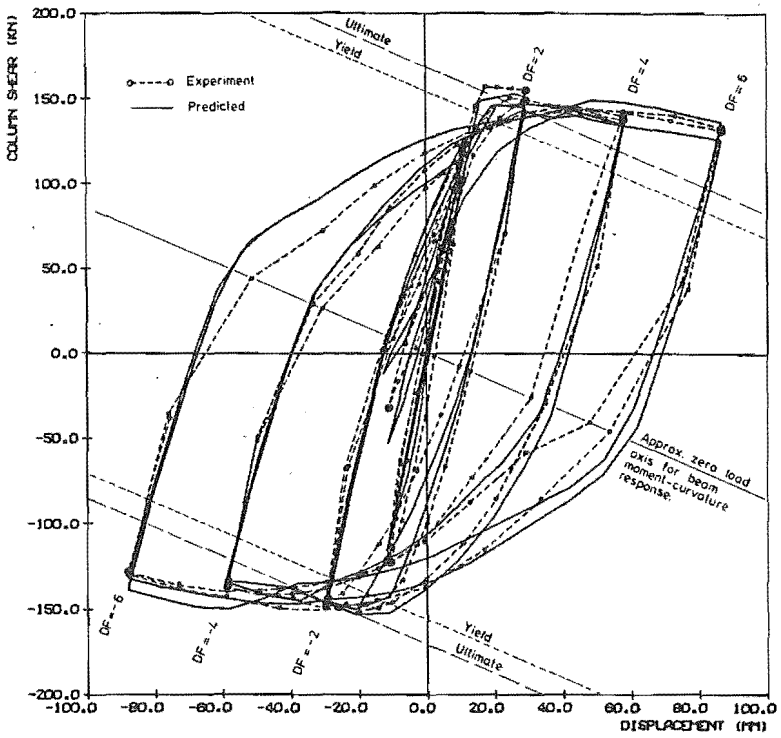

(a) Comparison with response predicted using inelastic shear model

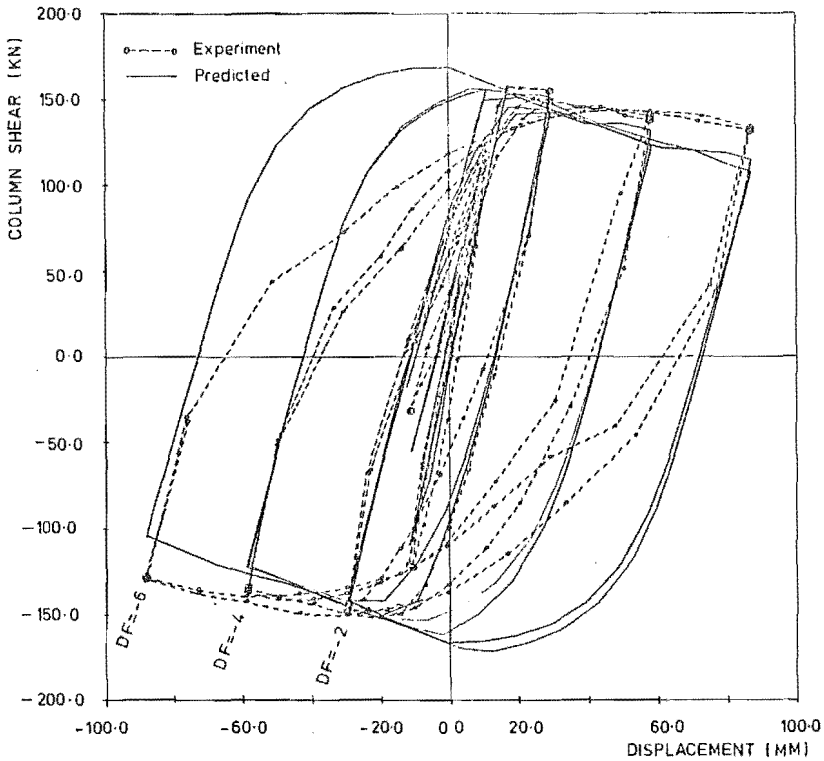

(b) Comparison with response predicted using elastic shear model.

FIGURE 6.24 : COMPARISON BETWEEN OBSERVED AND PREDICTED LOAD-DEFLECTION RESPONSE TESTED BY BECKINGSALE

parameters were the same as used for computing the analytic response shown in Figure 6.23b. The obtained predicted and the observed column shear-displacement are compared in Figure 6.24b. As indicated, the theoretical model with elastic shear deformations substantially underestimates the degree to which the response softens. Also, the resulting form of the load curves at large ductilities differs considerably from that of the experimental curves.

6.5 FLEXURAL WALL SPECIMENS

The analyses performed in the preceding two sections tested the analytical procedure under conditions where only flexural and shear forces acted on the plastic hinge zones. In the case of a wall, however, the inelastic behaviour is also influenced by the net axial load accumulating at the base of the wall. Because of the influence of the section axial strains, the inelastic shear deformations in particular, are sensitive to the axial load. Finally, walls differ from beams also because they normally have some flexural reinforcement distributed through their webs.

Several analyses were therefore performed on wall specimens to check what effect these factors had on the responses predicted by the computer program and whether the values for the shear model parameters were still valid. Two framed walls (SW1 and SW2) tested by Wang, Bertero and Popov (31) were chosen for these analyses. In the tests on these walls, particular attention had been given to correctly simulating the critical loading conditions, including axial stresses, expected at the base of the wall. Moreover, the specimens were extensively instrumented, permitting evaluation of a number of response characteristics. The specimens were also of interest because of the very high nominal shear stress* of $0.94\sqrt{f'_c}$ MPa imposed. This is in excess of the maximum nominal design shear stress allowed by most building codes, and thus represents an upper limit of shear stress intensity likely to be encountered in practice.

---

* The specimens were designed for a maximum nominal shear stress of $0.83\sqrt{f'_c}$ MPa, which was the maximum permitted by the 1973 Uniform Building Code (96).

6.5.1 Test Specimens, Analytic Idealization, and Applied Loading

The two test specimens consisted of one-third scale models of the first three storeys of a typical wall in a prototype ten storey frame-wall building. The basic geometry and reinforcing details were the same for both specimens (see Figure 6.25).

The actual material strengths, which were used in the analyses, were approximately 503 MPa for the steel yield stress and 36.5 MPa for the concrete on the day of testing. The specimens were cast vertically, floor by floor, to simulate actual construction practice, but were tested in a horizontal position. Loading was applied to the top of the specimens by 3 double acting jacks, set out as shown in Figure 6.26. The two jacks acting on the edge columns applied both a constant net axial compression force and a moment which was varied in proportion to the transverse force applied by the third jack. This arrangement of moment and transverse loading was equivalent to a single transverse load applied at 4420 mm from the base of the wall.

The analytic section, member and structure idealizations used to model the test specimens are shown in Figure 6.27. Important details related to these idealizations are as follows:

(a) The arrangement used for the axial loading jacks, meant that they imposed a small transverse load component associated with the transverse displacement at the top of the specimen, i.e., a "P-Δ" component due to inclination of the axial jack assemblages. All the experimental responses given for the specimens are corrected for this component. To allow for it in the analyses, the axial load was applied through a pin-ended elastic loading strut of the same length as the axial jack assemblage's, and the combined structure analysed for both material and geometric nonlinearities.

(b) The segmentation used for the wall is considerably finer than necessary. The segment locations shown in Figure 6.27 correspond approximately with the location of curvature gauges used in the tests.

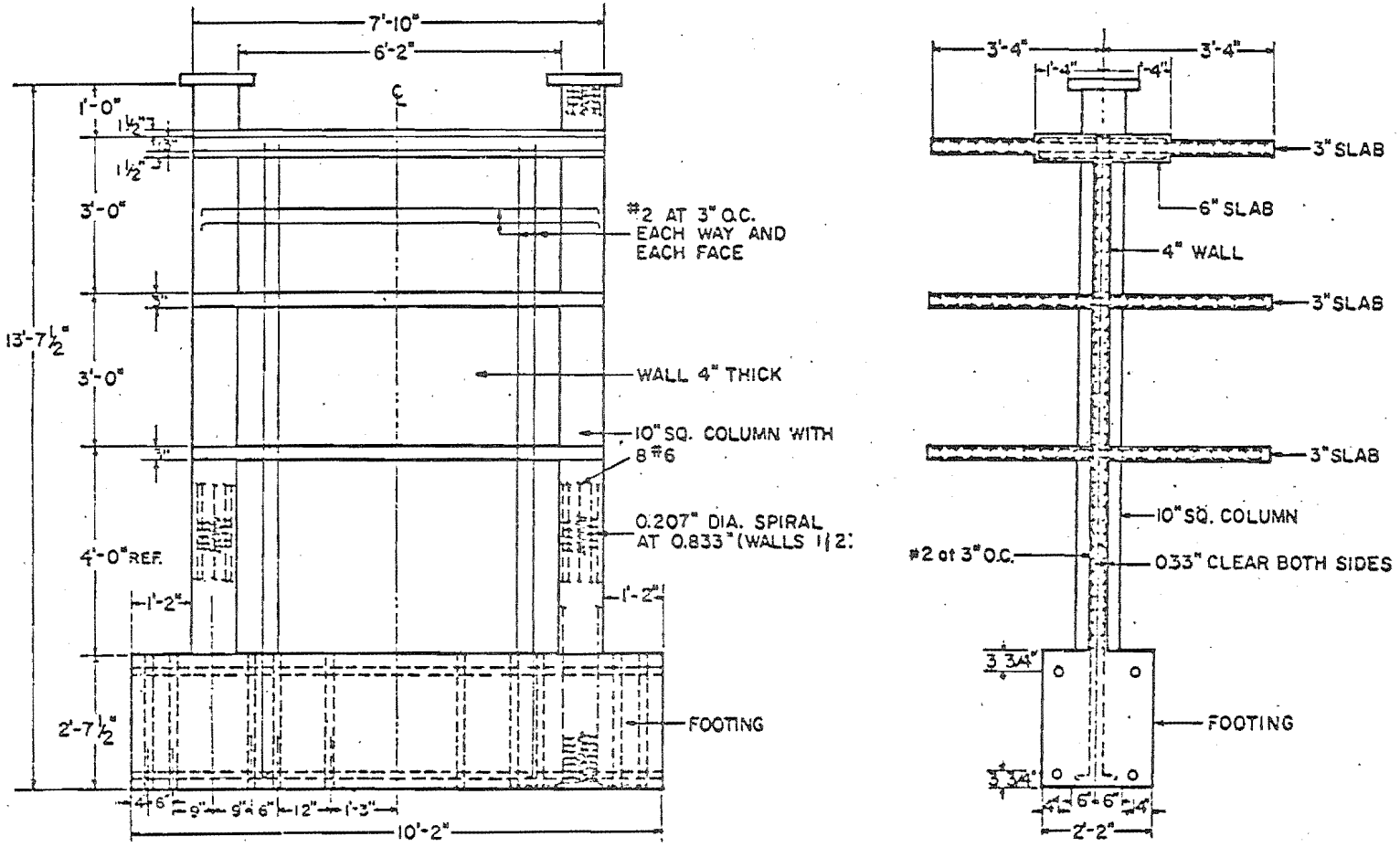

FIGURE 6.25 : DIMENSIONS AND DETAILS OF WALL SPECIMENS FROM WANG ET AL (31)

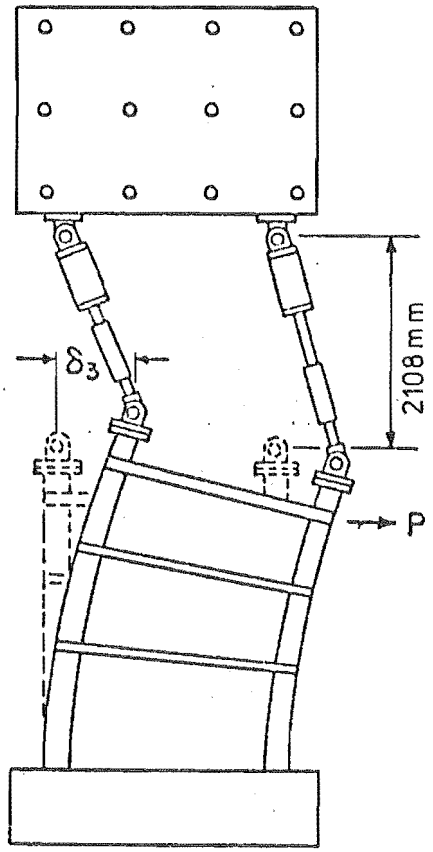

$P_1 + P_2 = 867\ kN$

$\Delta P_1 + \Delta P_2 = \Delta P$

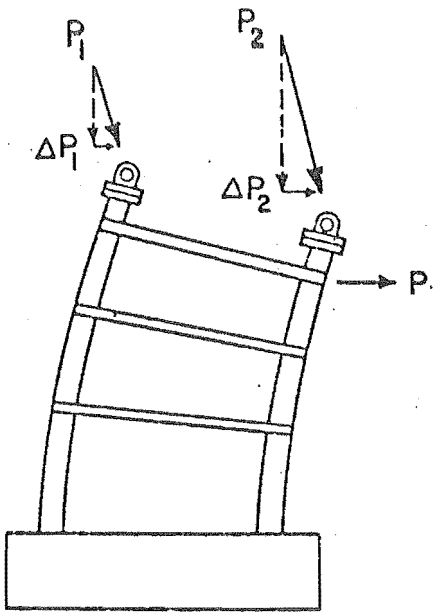

FIGURE 6.26 : HORIZONTAL COMPONENT OF NET AXIAL FORCE, BY WANG ET AL (31)

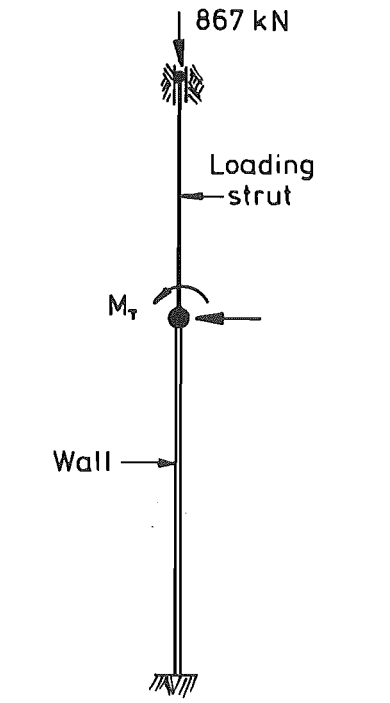

(a) Structure Idealization

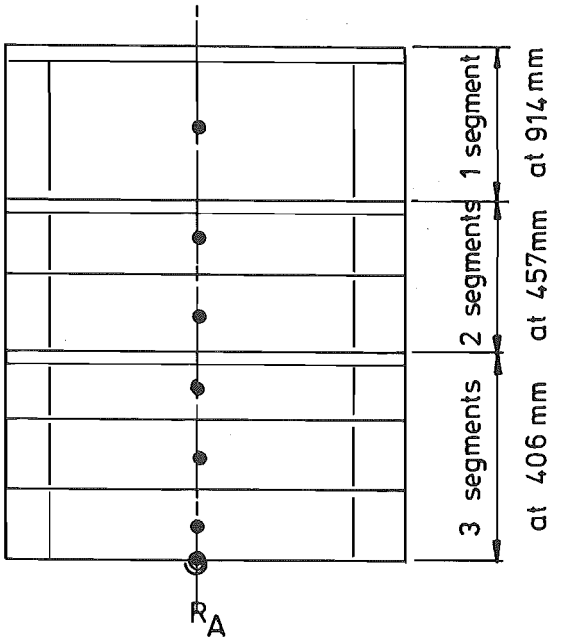

(b) Member Idealization

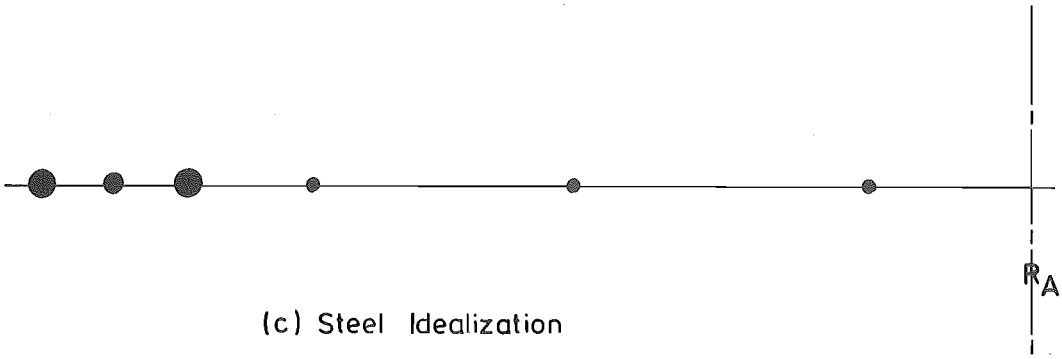

(c) Steel Idealization

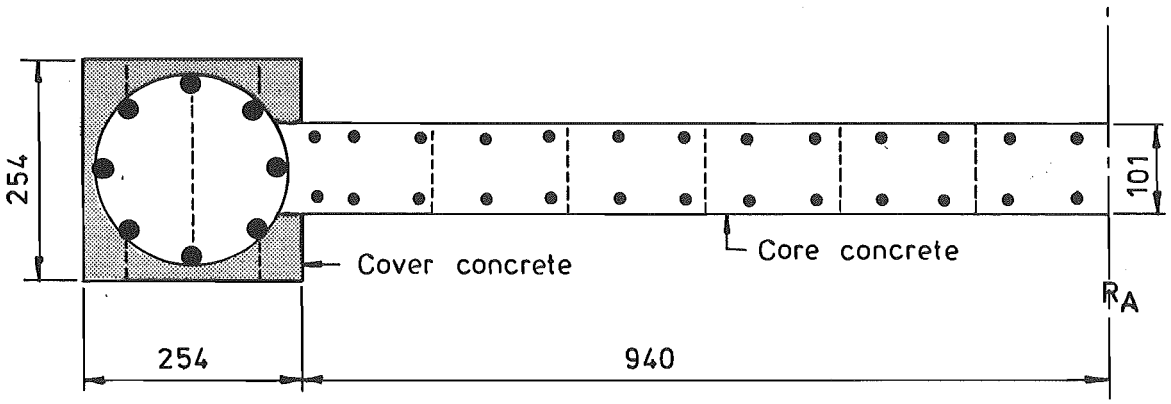

(d) Concrete Idealization

FIGURE 6.27 : STRUCTURAL IDEALIZATION OF WALL FOR COMPUTER ANALYSIS

(c) The value used for the anchorage parameter ϕ_{pa} (= 0.11) was obtained from the observed responses. The total anchorage length was assumed to be equal to the full length of (straight) column reinforcement embedded in the footing, i.e. 749 mm.

(d) The test results indicated that the slabs acted as heavy shear strengthening elements, and provided considerable restraint against the diagonal shear cracks opening in the wall in the vicinity of the slabs. To investigate this behaviour, two approaches were used for computing the effect of inclined cracking (e_v = 0.5 jd) on the flexural steel stresses. In the first, it was assumed that the slabs had no effect on the steel area reduction factors (Section 2.2.4), and in the second, it was assumed that no inclined cracks crossed the slabs, i.e. the reduction factors were computed for each storey as if the floor slab for that storey was the fixed end support for the remainder of the cantilever. To differentiate between these approaches, the responses computed for each are labelled "e_v = 0.5 jd, no slabs" and "e_v = 0.5 jd, with slab effect" respectively.

The displacement load sequences used for each of the specimens is shown in Figure 6.28. Specimen SW1 was analysed only for the first 3 post-elastic load reversals, but SW2 was analysed for the full experimental (post-elastic) load sequence. After the initial load sequences to failure (Figure 6.28), both specimens were repaired and retested. These were not analysed.

6.5.2 Inelastic Shear Model Parameters

At first yielding of the flexural reinforcement, the cracking pattern in the wall panels of both specimens differed considerably from that which develops in a conventionally reinforced concrete beam. Uniform and closely (76 mm) spaced diagonal cracks had formed over the full height of the wall. On loading up to yield in the reverse direction, similar cracks developed in the opposite direction. Other than at the junction of the wall and end block, no full depth flexural cracks developed.

This type of cracking, which is partly due to the distributed flexural

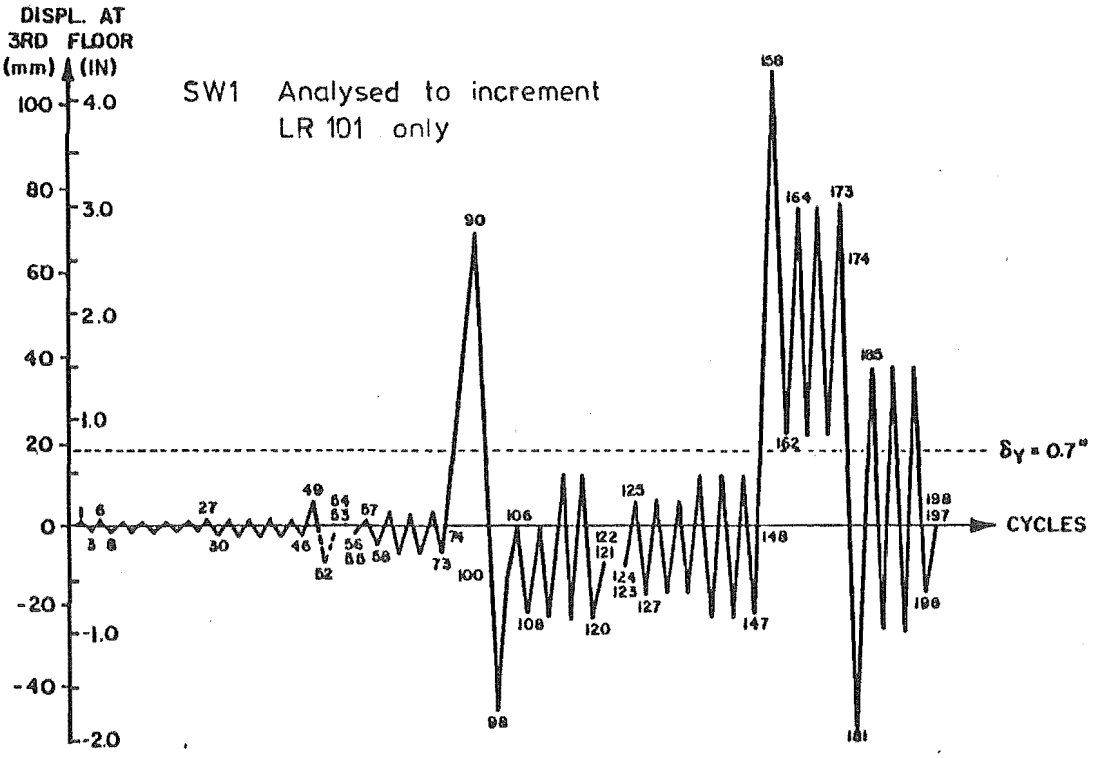

(a) SW1

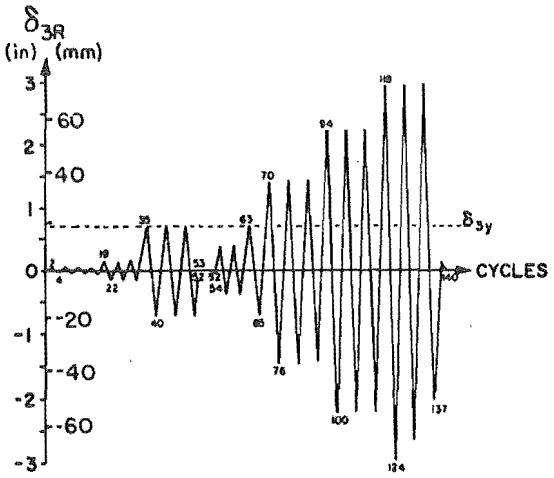

(b) SW2

FIGURE 6.28 : DISPLACEMENT HISTORY USED BY WANG ET AL (31)

reinforcement in the web, is likely to result in improved interlock and dowel rigidities. However, the effect of the distribution of flexural reinforcement is not specifically taken into account in the shear model, and it was found that the predicted shear force-deformation responses could be improved by increasing the value of K_{int} from 0.172 MPa, as used for plastic hinge zones in beam specimens, to 0.276 MPa. However, the values for all other parameters, obtained for the response of conventionally reinforced beams, were found to be satisfactory for predicting the wall behaviour.

6.5.3 Load-Deflection Responses

The observed and predicted load-displacement responses for SW1 and SW2 are compared in Figures 6.29 and 6.30. As indicated, the overall agreement is reasonable, although the predicted response for SW2 exhibits many of the faults apparent in the response for Beam 12 (Section 6.3.5). The most noticeable of these are the overestimation of rigidity after crack closure and peak load resistance.

6.5.4 Shear Force-Shear Strain Responses

The observed and predicted shear force-strain hysteresis loops for specimen SW2 are compared in Figure 6.31. As in the case of Beam 12 in Section 6.3, the predicted shear force-strain loops are significantly more "hooked" than the observed loops, although the net shear strain for all repeated cycles agree reasonably closely with the experimental results. A direct comparison is shown in Figure 6.32.

Because of the combination of high axial compression and high shear stresses, the cracks in the walls close at a relatively low lateral load, and as a result the compression concrete plays a more dominant role in resisting the shear forces. Because of the combined actions of the axial load, axial-shear coupling and the compression concrete rigidity, the shear strains developed in the walls are smaller than those in Beam 12 (Section 6.3), despite the imposed nominal shear stresses being approximately three times larger. Considering the large difference in the structural and loading environment between the

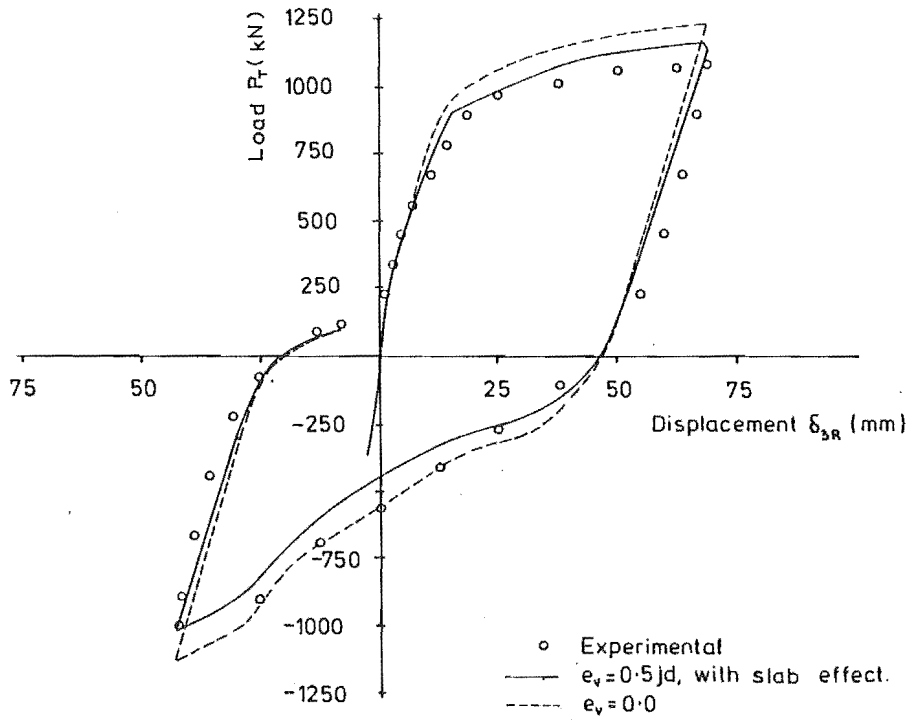

(a) Comparison between observed and predicted response.
(First two main post-elastic load reversals.)

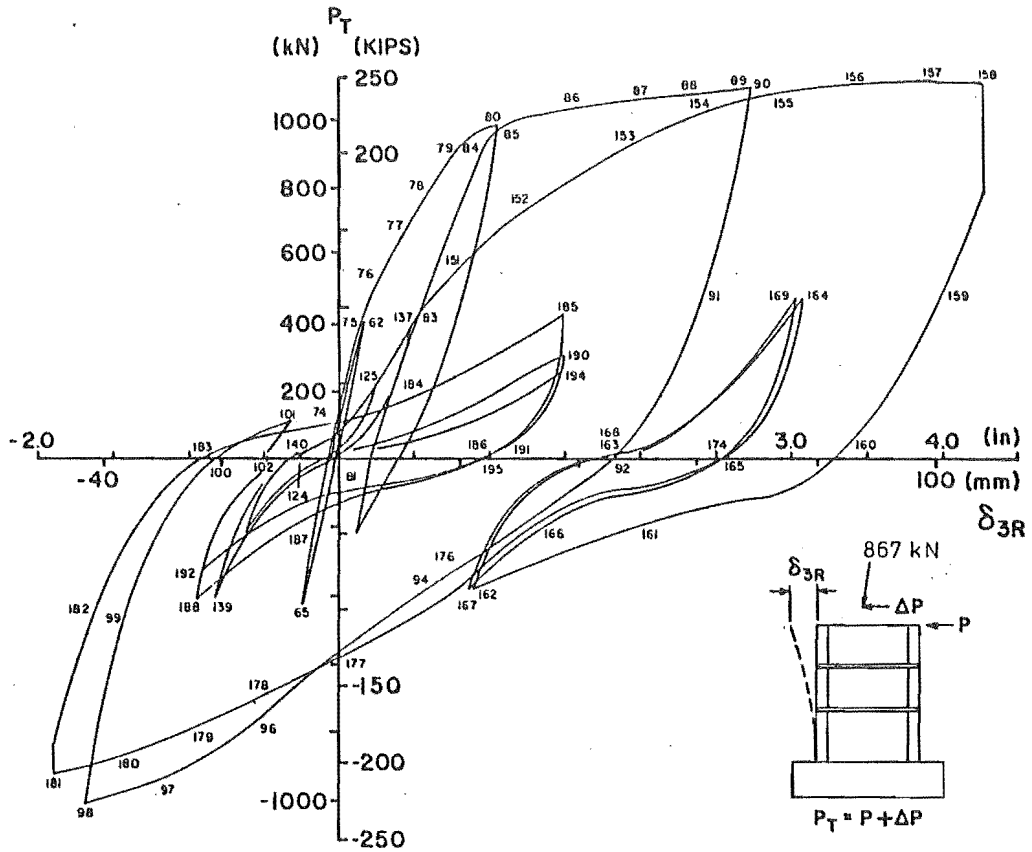

(b) Full observed response, by Wang et al (31)

FIGURE 6.29 : LOAD-DEFLECTION RESPONSES, SW1

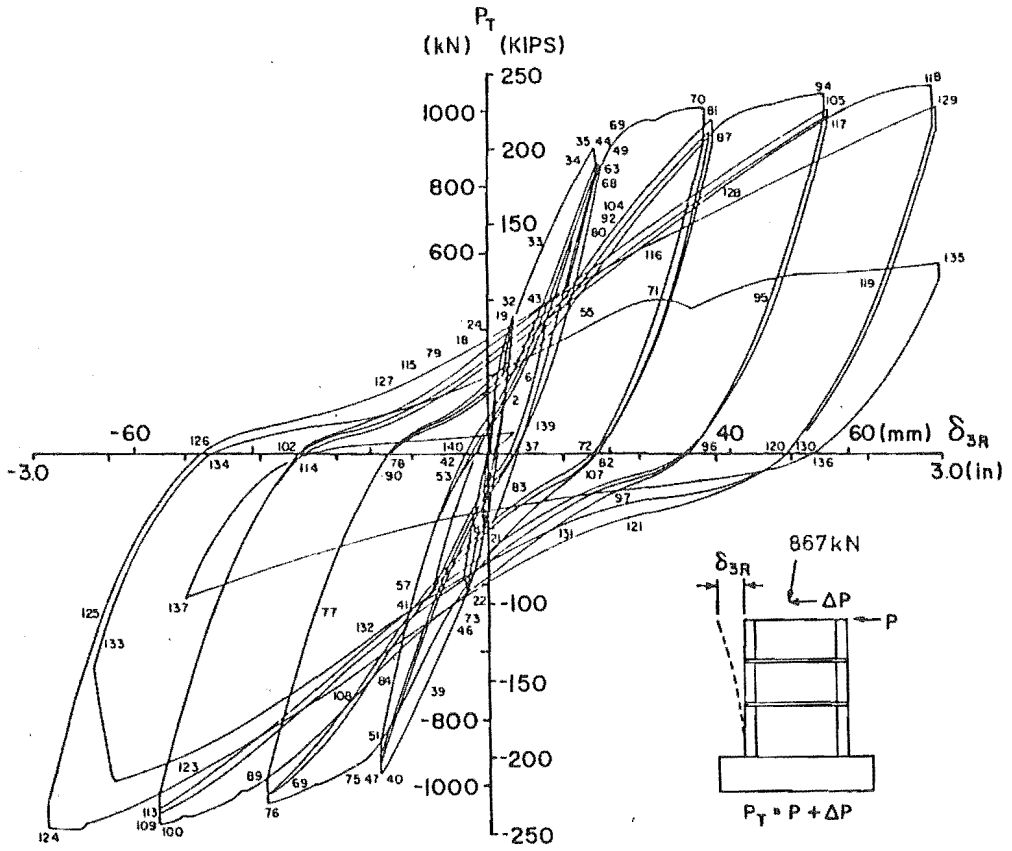

(a) Observed, by Wang et al (31)

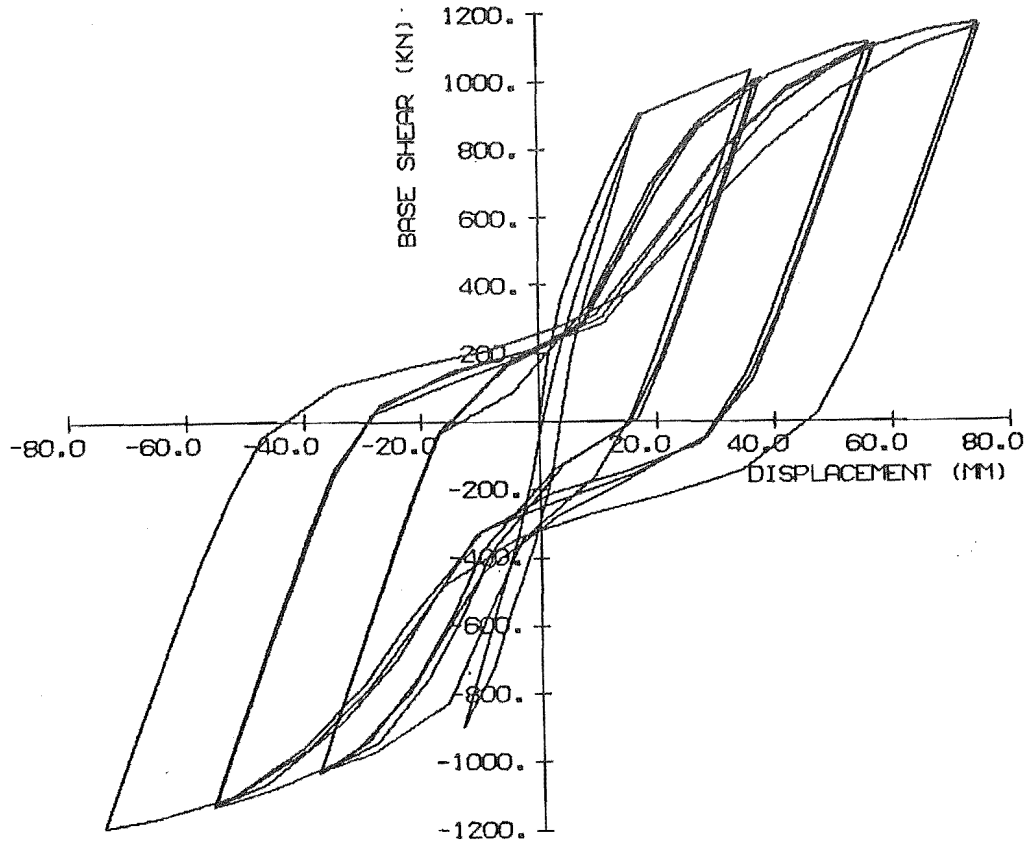

(b) Predicted

FIGURE 6.30 : LOAD-DEFLECTION RESPONSES, SW2

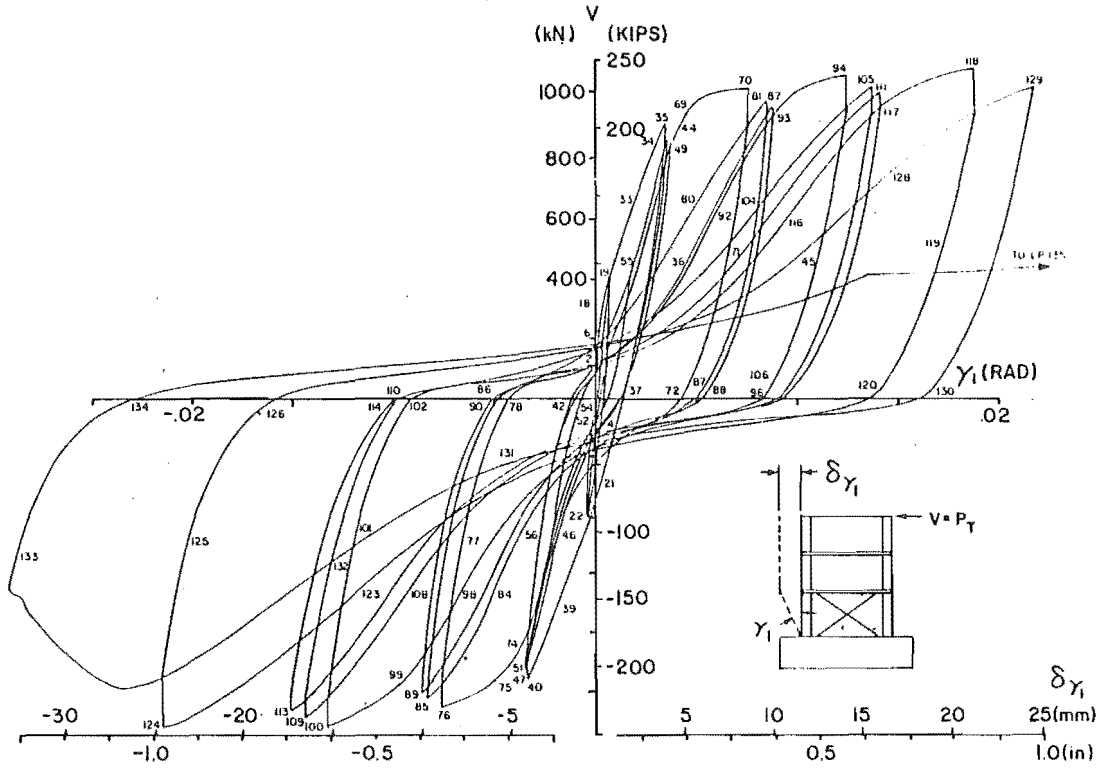

(a) Observed, by Wang et al (31)

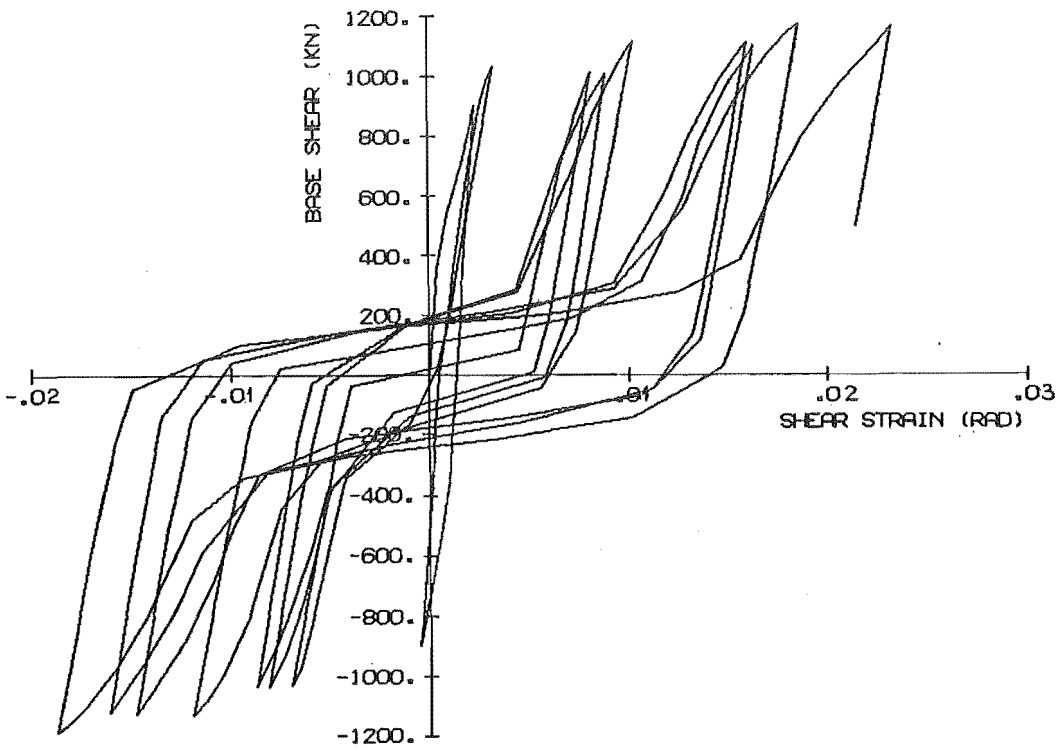

(b) Predicted

FIGURE 6.31 : SHEAR FORCE-STRAIN RESPONSES, SW2

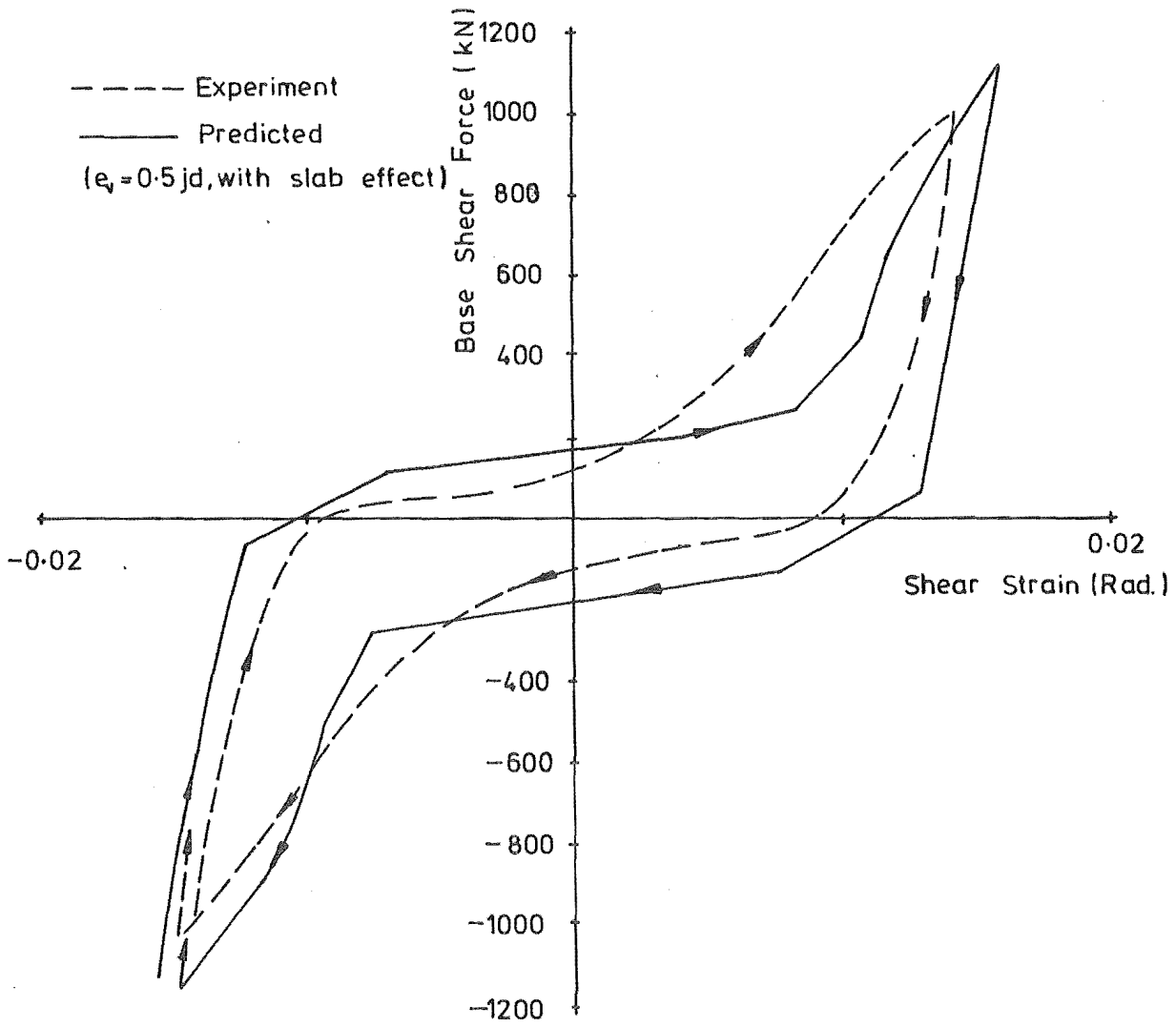

FIGURE 6.32 : DIRECT COMPARISON BETWEEN EXPERIMENTAL AND THEORETICAL SHEAR FORCE-STRAIN LOOP FOR AN INTERMEDIATE DUCTILITY LOAD CYCLE

beam and wall specimens, the accuracy of the predicted shear deformations suggest that the sensitivity of the model to these factors is quite reasonable, even considering the fact that a higher value of K_{int} was used for these analyses (Section 6.5.2).

6.5.5 Curvature Distributions

Figures 6.33 and 6.34 compare observed and predicted curvature distributions obtained for the two walls at different load stages. The most noticeable feature of the observed distributions is the general tendency for the curvature within each storey to increase up the height of the wall. This trend is evident in both the pre- and post-yield distributions. The curvature gauges were mounted on small pins embedded in the concrete, and it appears that the curvature measurements have been affected by slip between the concrete and the reinforcement due to the high shear stresses. This can be seen from the observed curvatures for region 3 at increment 79 (Figure 6.33), which exceed the theoretical yield curvature, even though the moment applied to this region was well below the yield moment. Most of the input energy is dissipated by the reinforcement, and it would probably be more relevant to compare the distribution of either strain in the tension bars or curvature obtained from gauges attached to the bars. Curvature region 1 was the first to yield in both test specimens which suggests that, as predicted by theory, the strains in the tension bars decreased up the height of the wall.

Several features of the predicted curvature distributions are as follows:

(a) The effect of allowing for the slabs can be seen most clearly in the curvature distribution at low load intensities (Figure 6.33). These show a large decrease in curvature between regions 3 and 4, i.e. the regions immediately below and above the level 1 slab. Within each storey, the agreement between the observed and predicted curvatures was closest in the bottom curvature region, i.e. regions 1 and 4.

(b) As indicated in Figure 6.33, the observed curvature in region 4 after yielding, was generally between that predicted assuming the slab

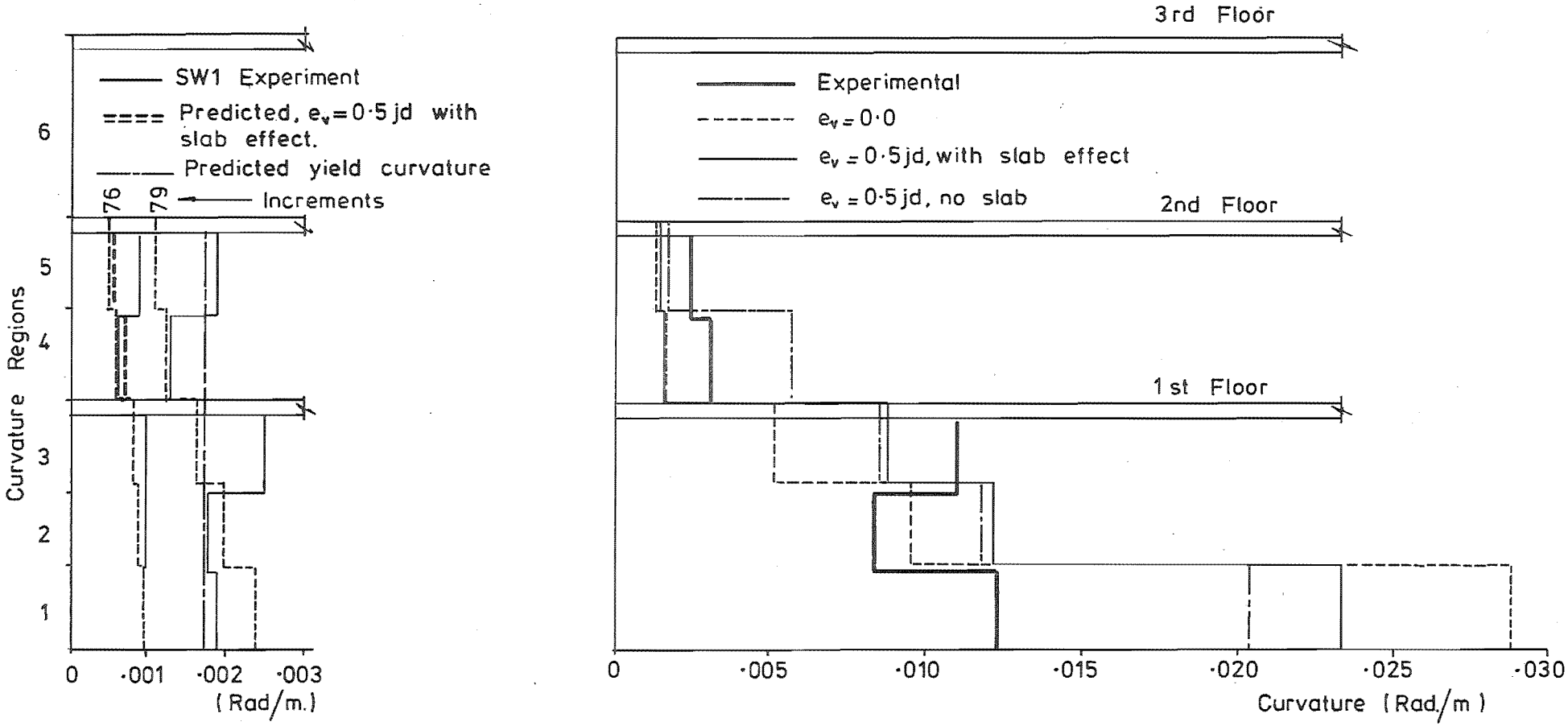

(a) Pre-yield curvatures

(b) Curvatures at DF=4

FIGURE 6.33 : EXPERIMENTAL AND THEORETICAL CURVATURE DISTRIBUTIONS FOR SW1

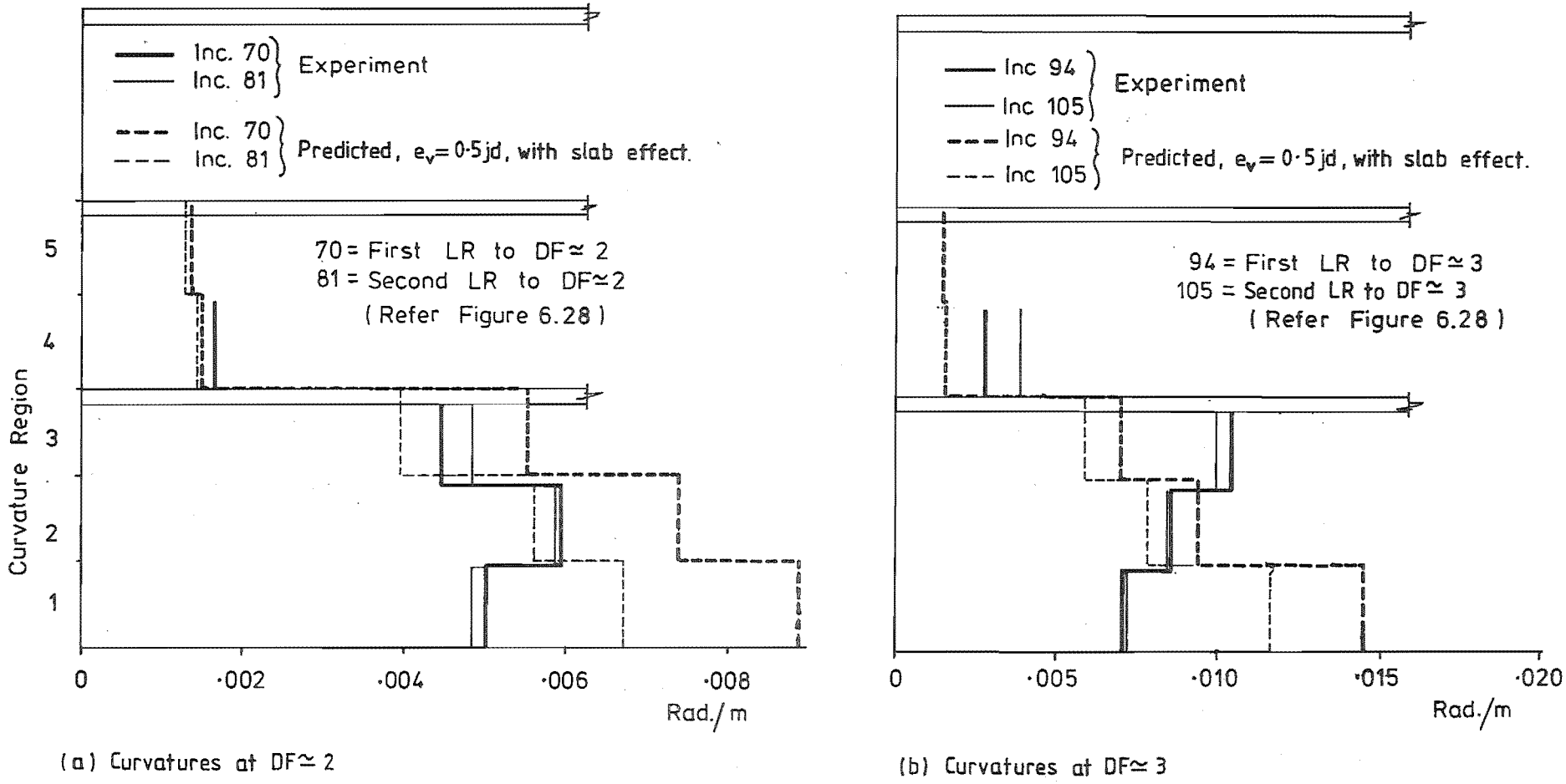

(a) Curvatures at DF ≃ 2

(b) Curvatures at DF ≃ 3

FIGURE 6.34 : EXPERIMENTAL AND THEORETICAL CURVATURE DISTRIBUTIONS FOR SW2

provided full restraint against transfer of shear effects and that predicted assuming that the slab had no effect on the behaviour. In the tests several cracks crossed the slab, but were restrained by the slab from opening up. The curvature distributions computed for $e_v = 0.0$ generally showed poorest agreement with the experimental distributions.

(c) The effect of underestimating the shear deformations under high intensity monotonic loading can be seen in Figures 6.33 and 6.34. These show the curvature distributions for each specimen at the peak of the first main post-elastic load reversal. In both cases, the predicted total rotation* of the plastic hinge zone was considerably larger than the experimental value. However, for a subsequent load reversal to the same displacement limit, the observed and predicted values are in much closer agreement (increments 81 and 105 in Figure 6.34), indicating that the shear deformations are being predicted reasonably accurately for these load reversals.

(d) Although the curvatures computed for the individual curvature regions often did not show close agreement with the experimental values, the overall prediction of curvature distribution (e.g., depth of yield penetration) was generally good. Better agreement for the individual curvature regions would possibly have been obtained if the observed curvatures had been determined from the strains in the flexural reinforcement.

6.5.6 Moment-Curvature Responses

Figures 6.35 and 6.36 compare observed and predicted moment-curvature responses for curvature regions 1 to 3 of SW2. The predicted response shown in Figure 6.35b for region 2 was obtained directly from the wall analysis, while those shown in Figure 6.36 were computed from separate section analyses of the three curvature regions using the measured peak curvatures for the load reversal displacement limits**.

---

* The area to the left of the curvature distribution curves.

** To allow the loading branches to be compared directly, the curves shown in Figure 6.36 have been adjusted so that the observed and predicted curvatures at zero load are coincident.

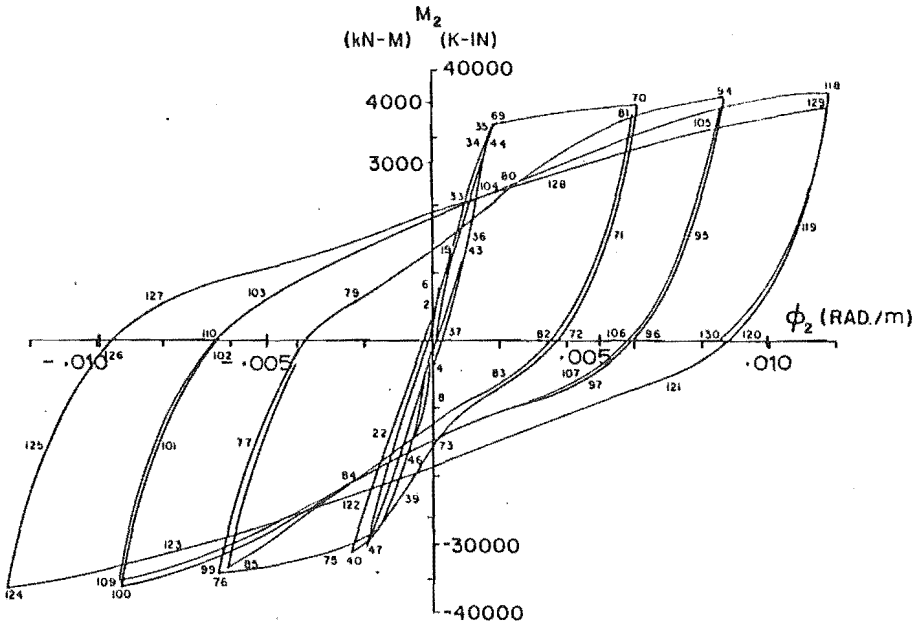

(a) Observed, by Wang et al (31)

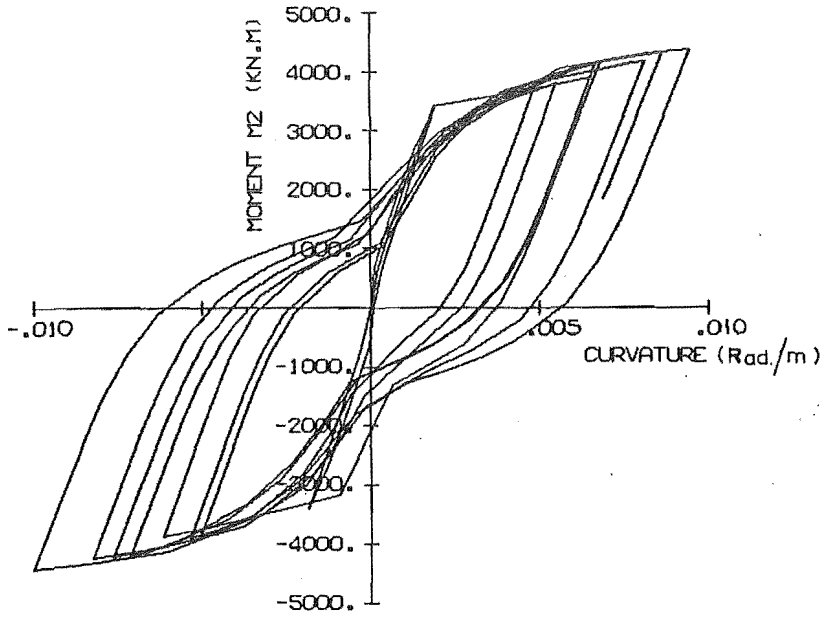

(b) Predicted

FIGURE 6.35 : MOMENT-CURVATURE RESPONSE, SHEAR WALL SW2

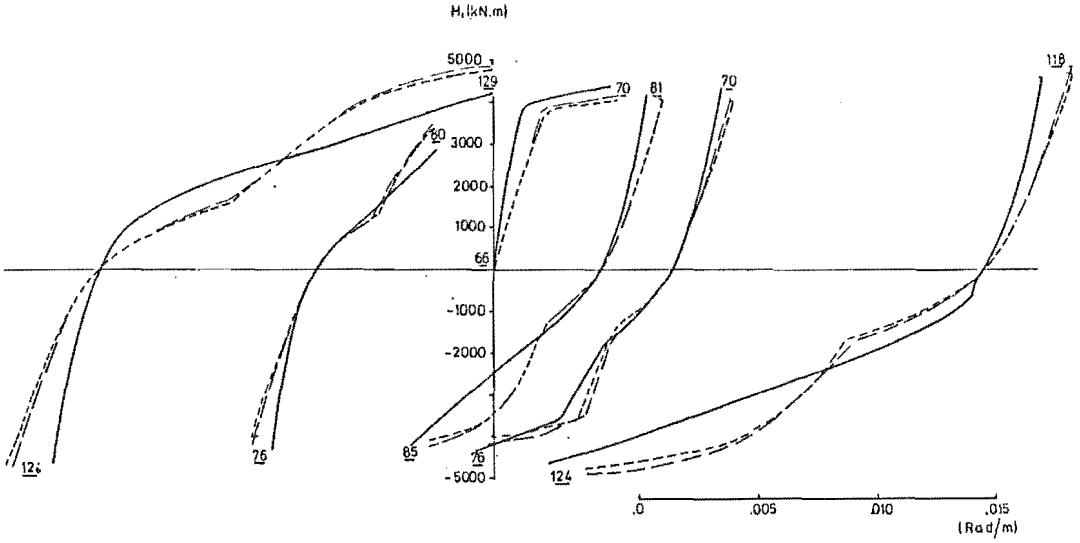

(a) Curvature Region 1

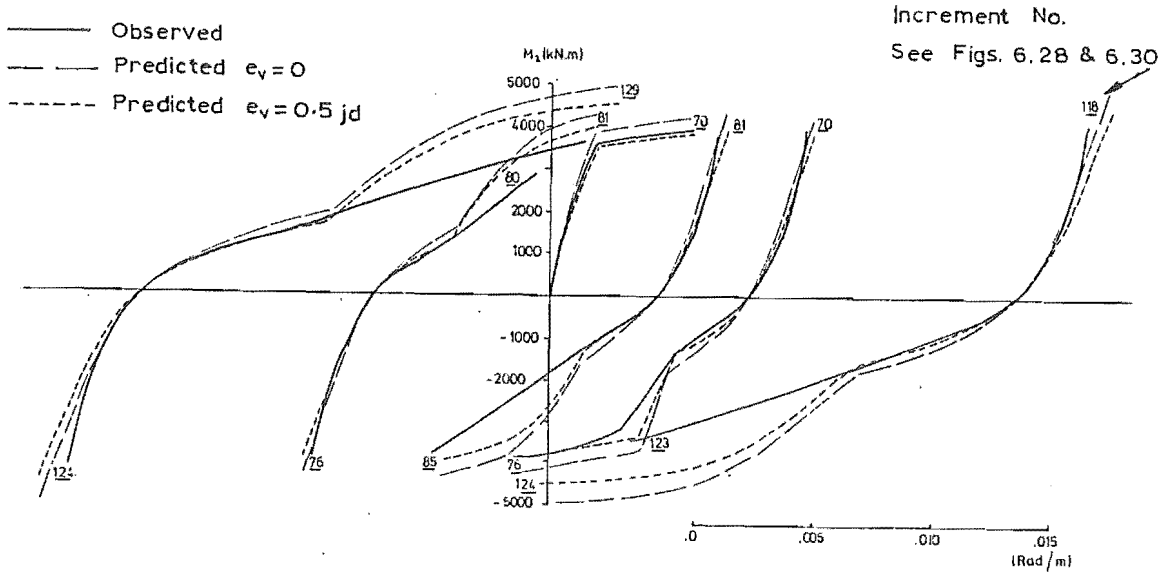

(b) Curvature Region 2

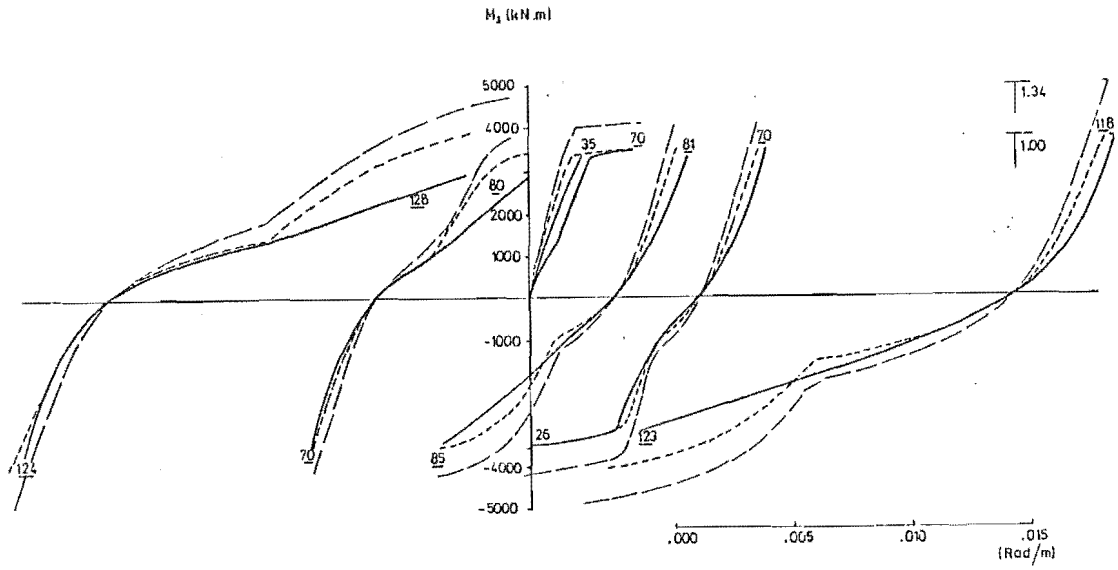

(c) Curvature Region 3

FIGURE 6.36 : MOMENT-CURVATURE RESPONSES OBTAINED FROM SECTION ANALYSES OF CURVATURE REGIONS 1 TO 3, SHEAR WALL SW2

These comparisons were made in order to study two aspects of the moment-curvature response; the effect of e_v, and the effect of the concrete normal stress response. These are discussed below:

(a) As indicated, the yield loads computed for all three regions using e_v = 0.5 jd show good agreement with the experimental values.

(b) Generally both the initial stage of loading up to crack closure and the curvature at which the cracks closed were generally predicted satisfactorily (Figure 6.36). However, as occurred for Beam 12 tested by Celebi and Penzien (Section 6.3), the subsequent rate of increase in moment was considerably over-estimated because of failure to model softening of the concrete normal stress response.

6.5.7 Discussion

It had been expected that these specimens would be outside the scope of the computer program because of their short shear spans (a/d ≃ 2) and the very high nominal shear stresses (0.94 $\sqrt{f'_c}$ MPa) imposed. The loads resisted were significantly overestimated because of failure to model softening of the concrete. However, the overall load-deflection response and particularly the shear deformations were predicted with reasonable accuracy. The main factors giving better correlation than had been expected were the net axial compression, the moderate maximum ductilities imposed*, and the presence of the slabs which substantially reduced the effects of inclined cracking.

6.6 PERFORMANCE OF THE NEWTON-RAPHSON SOLUTION PROCEDURE

The two most important aspects relating to a solution procedure are rate of convergence and reliability. In both respects, the performance of the Newton-Raphson procedure used in the frame analysis program was generally excellent. Average rates of convergence for the materially non-linear analyses ranged from approximately 2.5 (initial guess +1.5

---

* This is probably not an unrealistic maximum ductility for a wall, since the value of 4 is based on the measured deflection at yield rather than the deflection at nominal design strength (see footnote in Section 8.1).

subsequent iterations) to 4 iterations per increment. Two important factors influencing the successful application of the Newton-Raphson procedure to these analyses were the special precautionary measures taken to suppress solution instabilities (Chapters 3 and 4) and the displacement control procedure developed for use in conjunction with the standard Newton-Raphson force iteration procedure.

6.6.1 Section Analyses

For individual section analyses, the displacement control procedure was normally operated on the flexural degree of freedom and this generally prevented any large overshoot of the correct solution strains during iteration. This dominating control, together with the form of the constitutive relationships used, resulted in a very rapid decay of the force and strain residuals in most increments. Two typical examples illustrating the rapid decay of strain residual are shown in Figures 6.37a and b for a beam section. Generally, the decay of force residual slows significantly only when the concrete first cracks or when cracks previously open over the full depth of the section partial (or fully) close during an increment (Figure 6.37c). Because of the small number of such increments, this has little effect on the total cost of the analysis.

6.6.2 General Frame and Member Analyses

For a general frame or member analysis, there are usually a much larger number of internal degrees of freedom than for a section analysis. The displacement control procedure operates only on one degree of freedom, and consequently its control over the local iteration behaviour is reduced. This, in practice, affects only a few increments for which the response is highly nonlinear. As indicated by the average iterations per increment of between 2.7 and 4.0 for general frame or member analyses, the solution still converges rapidly for the great majority of increments.

However, although the total solution time is not affected to any large extent, those increments where interaction between components of the response does develop due to highly non-linear response, can seriously

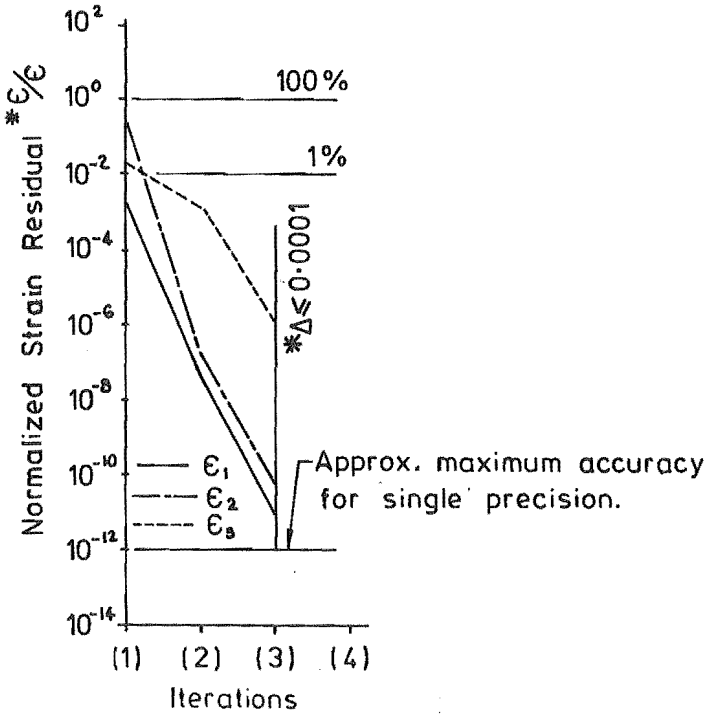

(a) Example 1 : Moment resisted by steel only.

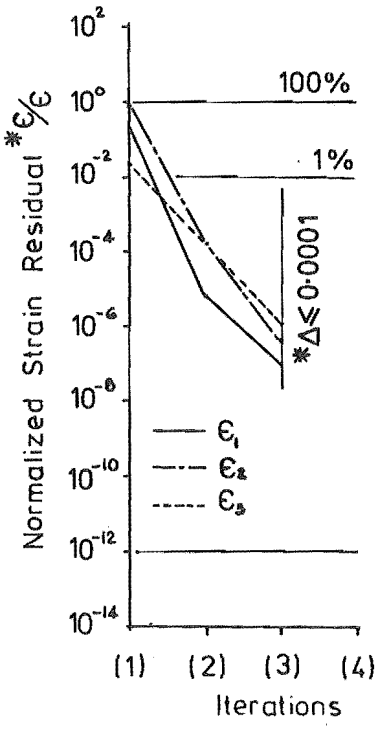

(b) Example 2 : Steel 'yields'

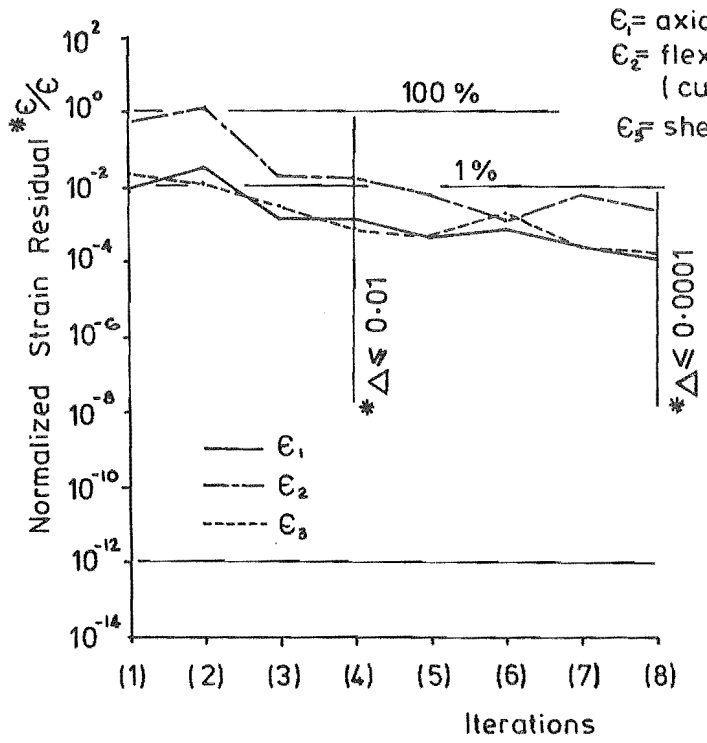

(c) Example 3: Cracks close

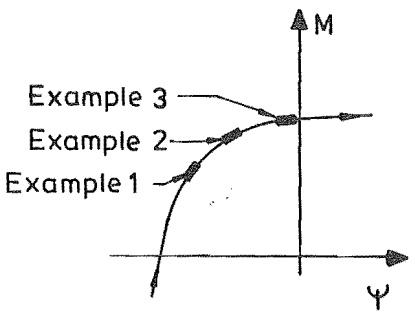

Selected Regions Of Moment – Curvature Response

FIGURE 6.37 : TYPICAL RESIDUAL DECAY RATES FOR AN INDIVIDUAL SECTION ANALYSED UNDER COMBINED FORCE AND DISPLACEMENT CONTROL

test the ability of the solution procedure to obtain a correctly converged solution. This applies particularly to analyses where several segments are used to represent each plastic hinge. Occasional (<< 1% of increments) instances of the solution failing to converge correctly under these conditions occurred in this study. However, in most cases where interaction developed, the iteration procedure was able to converge the solution with less than 9 iterations (a maximum of 9 iterations was specified for most analyses). Most cases of solution failure are believed to have been connected with the sliding shear model which was not as rigorously protected against sources of instability as was the steel model.

Two examples of iteration behaviour taken from analyses of one of the beams used in the mesh refinement investigation (Figure 6.5) are given here to illustrate the ability of the solution procedure to cope with highly nonlinear response situations. Both examples are taken from in the vicinity of the region of the load-displacement response shown in Figure 6.38b. The member segmentations and the magnitude of the displacement imposed in the initial inelastic load reversals were different, however.

Example 1

The situation considered for this example is shown in Figure 6.38c. Figure 6.39 shows the convergence of the moment applied to and resisted by the beam. Although this is taken from an analysis of an individual cantilever, the same type of iteration behaviour could readily develop in an individual member of a frame or frame-wall assemblage.

In the first iteration, when the beam was still comparatively stiff, the full force increment was applied, resulting in force overload which caused segments 1 to 4 to be loaded above their yield moment. The solution came under displacement control in the second iteration, and the force acting on the beam was reduced as the yielding became more concentrated in the sections nearest the fixed end (beam tip displacement being held constant). Sections 3 and 4 were loaded past yield curvature in the first two iterations, but as a result of the reduction in force on the beam as a whole, the moments at these sections dropped back below

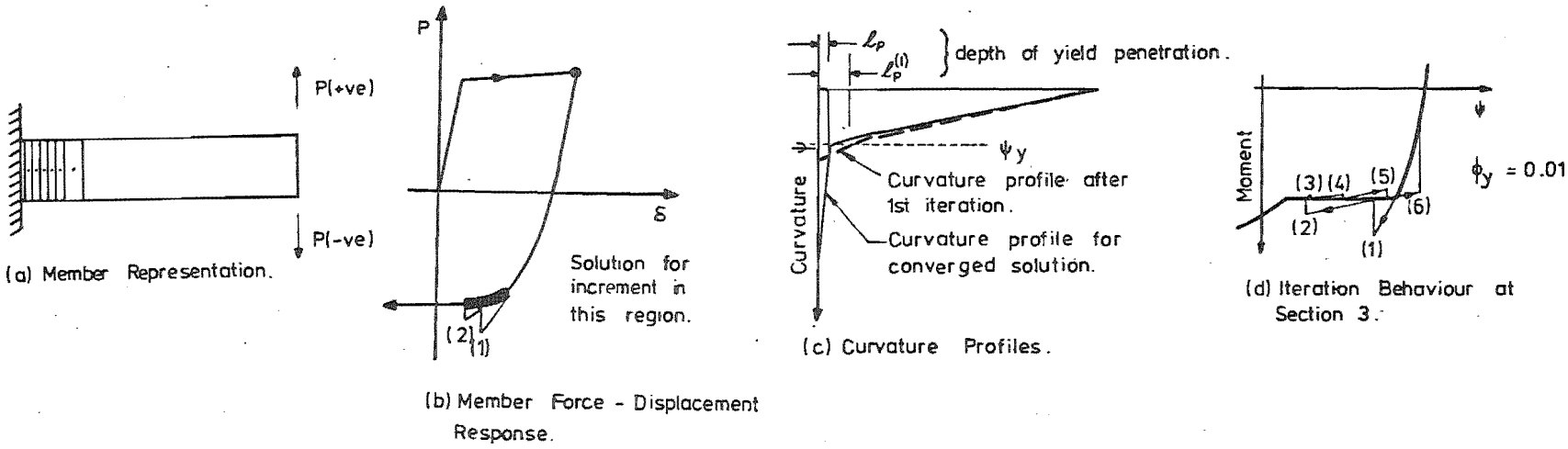

FIGURE 6.38 : MEMBER RESPONSES FOR EXAMPLE 1

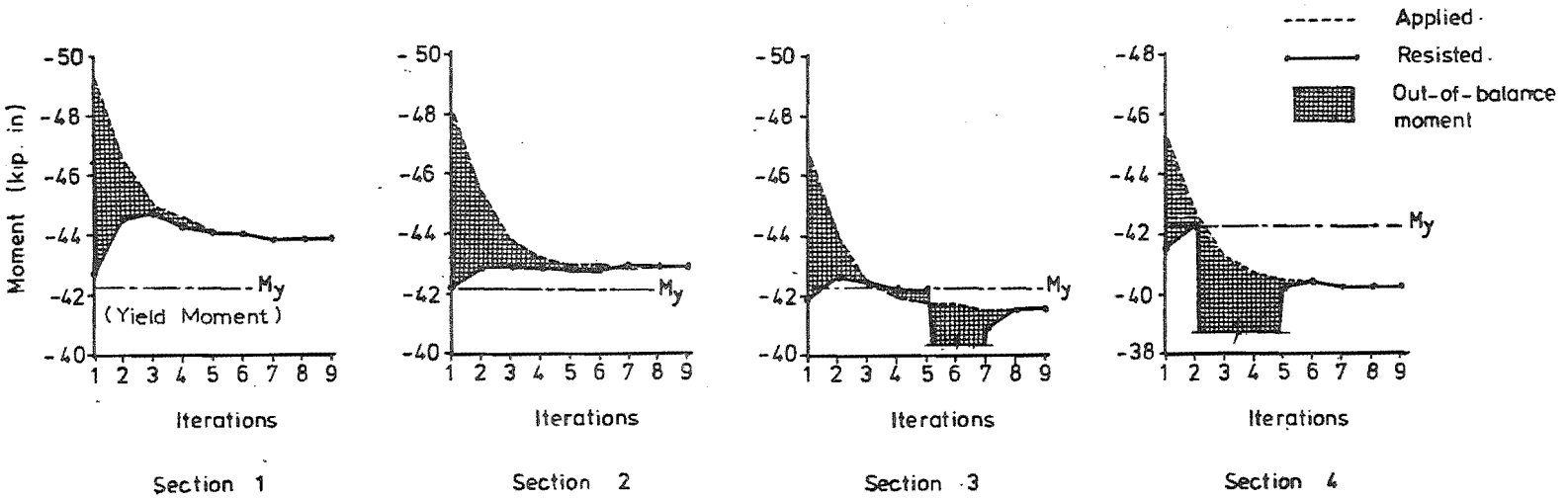

FIGURE 6.39 : ITERATION BEHAVIOUR OF FIRST FOUR SECTIONS, EXAMPLE 1

yield in later iterations. As shown in Figure 6.39, the solution procedure had little difficulty in returning these sections to an "unyielded" state, despite the large out of balance moments caused by the solution backing off the yield plateau, i.e. the presence of alternative loading and unloading paths did not cause any problems.

Example 2

This example illustrates the type of interaction that can develop locally between various parts of the same section. In the description given below, the listed numbers refer to the iteration numbers shown in Figure 6.40.

(1) The initial application of the full increment load to the softened compression bars caused the concrete cracks in the vicinity of the bars to just close. Only a small strain increment was imposed on the partially unyielded tension steel.

(2) With the concrete in contact, the section was very stiff and there was only a small change in the section strains to just open the concrete cracks. This type of behaviour can lead to the solution being prematurely assessed as converged. However, it was found that a value of $^{*}\Delta = 0.001$ was sufficient to reduce the likelihood of this occurring to an acceptable level.

(3) With the total section moment being resisted only by the two sets of bars, the application of the out-of-balance section forces to the low fictitious modulus, $\phi_y.E_o$, of the tension steel resulted in a large strain overshoot to $\varepsilon_s = 0.39$. This caused an overshoot of the prescribed displacement at the tip of the cantilever, and the displacement control procedure reduced the load on the cantilever sufficiently to return the tip displacement to the prescribed value. In doing this, the strain in the tension steel was returned to point (3) in Figure 6.40a. The strain was not immediately returned to its correct value because of interaction between the various segments of the cantilever; i.e. compensating strain errors in the other segments. Nevertheless, as illustrated, the displacement control procedure had a marked stabilizing influence on the iteration behaviour.

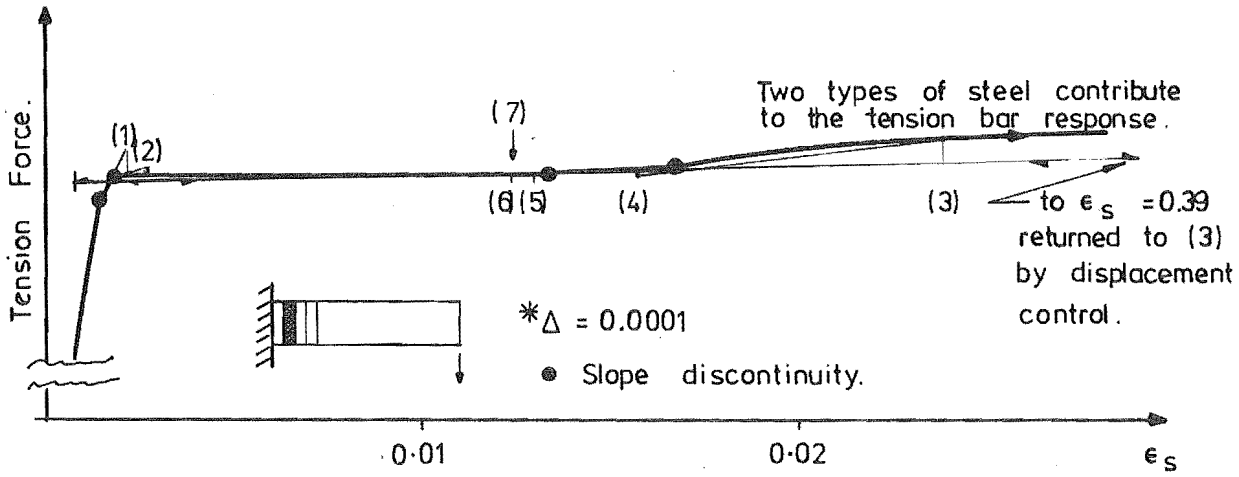

(a) Tension Bars.

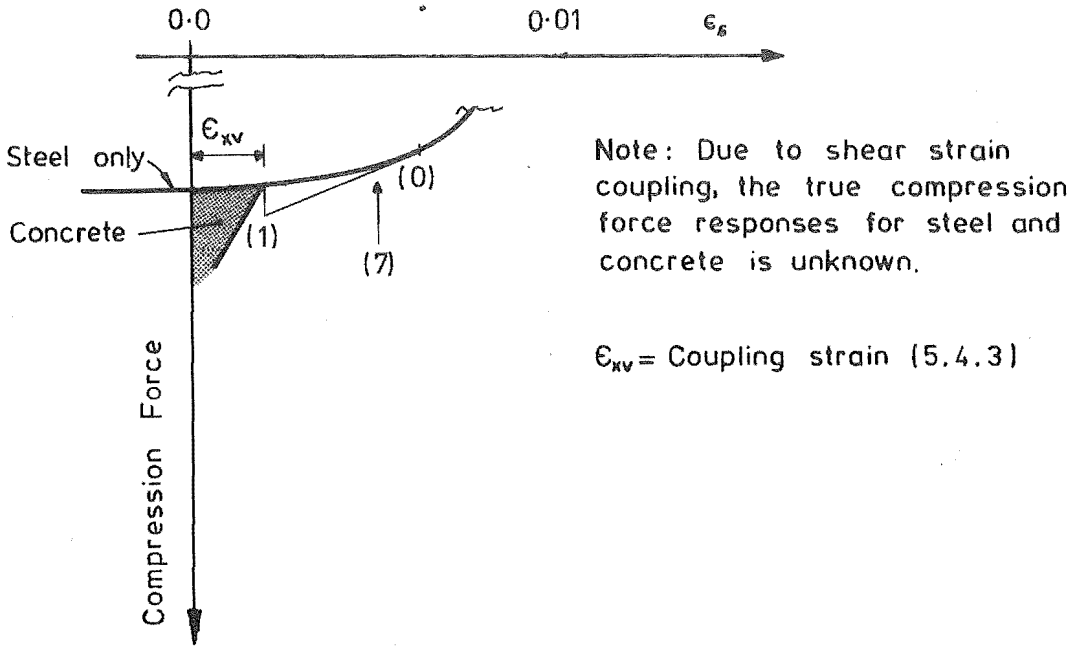

(b) Compression Bars

FIGURE 6.40 : ITERATION BEHAVIOUR FOR EXAMPLE 2

(3)-(5) Because the two types of steel contributing to the response of the tension (and compression) bar group had different strain hardening values, a further two iterations were required to return the solution strain to the yield plateau.

(6)-(7) The initial strain overshoot during iteration (6) was a consequence of the slope discontinuity between the strain hardening branch and the yield plateau. However, because the responses of the other segments had nearly converged, the displacement control returned the solution strain to near its correct value. The solution was assessed as being converged at iteration (7).

6.7 COMPUTATION TIMES

Table 6.2 gives a breakdown of computation times* (CPU only) taken for three of the structures analysed in this study. It should be noted, however, that the time taken for any given analysis can vary by as much as 20-30%, depending on the operating conditions in the computer at the time of the analysis.

The average computation time per iteration per inelastic section analysis (inelastic shear model) ranged from approximately 6500 microsec. to 10,000 microsec. for sections with 2-4 bar groups and 10-14 concrete layers, cf. approximately 8000 microsec. to perform the matrix transformation in Table 2.3. For section analyses where only elastic shear deformations were considered, the computation times ranged from approximately 5000 microsec. to 7500 microsec. This gives as average time per increment (2.6 iterations) for an "elastic shear" section analysis of the order of 0.02 sec. By comparison, Taylor (52) estimated that Thompson's (44) section analysis procedure (no shear deformation) required approximately 0.87 sec. per increment (B6718 computer).

No direct comparisons were made with other computer programs. However, judging from the coding in some computer programs and the total analysis

---

* Burrough's B6718 computer, at University of Canterbury Computer Centre.

TABLE 6.2 : BREAKDOWN OF COMPUTATION TIMES FOR INELASTIC ANALYSES

Structure	Beckingsale Beam 13A		Celebi & Penzien Beam 12		Author FSW-1**	
Reference to analysis	Figure 6.23		Figure 6.12		Figure 7.24	
Details	4DØF, 2M, 20ØP 4IS, 4ES 264 Inc., 810 It.		6DØF, 2M, 24ØP 3IS, 2ES 427 Inc., 1536 It.		42DØF, 21M, 154ØP 57IS, 42ES 57 Inc., 226 It.	
	Seconds	%+	Seconds	%+	Seconds	%+
Initialization:	1.83	-	1.53	-	3.58	-
Analysis =	48.71	100.0	80.94	100.0	199.13	100.0
- All structural response subroutines	39.46	81.0	54.61	67.5	165.25	83.0
IS only	22.76	46.7	36.60	45.2	115.83	58.2
ES only	3.28	6.7	1.56	1.9	9.85	4.9
- Equation Solving	2.61	5.4	11.47	14.2	23.32	11.7
- Output	5.15	10.6	10.98	13.6	7.00	3.5

Notation: DØF = external degrees of freedom; M = members; ØP = number of variables outputted each increment; IS = inelastic sections; ES = elastic cracked concrete sections; Inc. = increments; It. = total iterations

Comparative time basis: A = B*C took approximately 10 microseconds
A = B**C took approximately 600 microseconds

** 7 storey × 1 bay frame-wall assemblage

+ percentage of analysis time only

times required*, it appears that the present computer program would be as fast, if not faster, than some much simpler programs currently being used for dynamic analyses of buildings.

---

* e.g., 3300 seconds (B6718) CPU time to analyse a 12 storey × 1 bay frame for 1000 time steps (97).

7. EXPERIMENTAL PROGRAMME

SUMMARY

Simulated seismic load tests were carried on four beam-wall specimens and two 7 storey x 1 bay frame-wall assemblages. Both sets of specimens were approximately quarter scale. This chapter discusses various aspects related to the modelling and the type of loading used, and describes details of the specimens and the test procedure. Results of the beam-wall tests are given in Chapter 8, and of the frame-wall tests, in Chapter 9.

7.1 INTRODUCTION

The experimental programme for this study was carried out in two parts; the first involved testing four reinforced concrete beam-wall specimens (TB series) and the second, two 7 storey x 1 bay reinforced concrete frame-wall assemblages (FSW series). The beam-wall specimens were approximately the same geometry as the beam-wall junctions of the frame-wall assemblages and both sets of specimens were to the same scale (approximately quarter-scale). High intensity pseudo-static cyclic loading was used in both series to simulate seismic loading.

The main objectives of these tests were to provide experimental data for direct assessment of the response characteristics and for evaluating the analytic computer model developed in the preceding chapters.

7.2 IDEALISATION OF STRUCTURE

The economics and practical requirements of testing reinforced concrete components and assemblages generally necessitate considerable simplification of the real structural complexities. The main specimens tested in this study were 1 bay x 7 storey frame-wall assemblages and the structure of these specimens was kept as simple as possible, consistent with the aims of assessing interaction between the frame and wall elements, and of obtaining data suitable for evaluating the frame analysis program. A reduced scale was necessary because of the 7 storey height.

This section discusses the most important aspects of structural idealisation and examines the effect of scale reduction on the specimen responses and construction details.

7.2.1 Model

Four main simplifications were made in idealising the test specimens:

(a) No floor slabs were modelled, partly because of the limitations imposed by the existing test rig and also because the slab effects were outside the planned scope of the frame analysis program. Most pseudo-static cyclic load tests on reinforced concrete beams have not modelled floor slabs. Results from these tests have been accepted as demonstrating the ability of the beams to sustain large plastic deformations without significant loss of strength. Nevertheless, slabs which are integrally connected to beams can significantly affect the beam responses and recognition of such effects must be given when interpreting results obtained from the present tests.

(b) The frame-wall specimens were two-dimensional and were subjected to only in-plane loads.

(c) Passive lateral restraint was provided for the frame-wall specimens, but it is difficult to compare its effectiveness with that provided in a real building. Not only is the effectiveness of "lateral" restraint provided in real buildings very variable, but individual components will also be actively subjected to "out-of-plane" deformations (refer Section 9.3.10).

(d) The specimens were modelled as idealised 1 bay x 7 storey frame-wall assemblages and their geometry was not typical of real frame-wall buildings. This will, however, have a greater effect on the actual response than on the response characteristics which were under investigation in this study, e.g., the effect of frame-induced axial load variation on the behaviour of the wall plastic hinge zone; if the walls (aspect ratio 7:1) had been made less slender then frame

action would have had a diminished effect on the wall response characteristics.

7.2.2 Scale Effects

Reduced scale models provide a relatively economic, and in many cases the only feasible means of testing complete structural assemblages. Most data relating to pseudo-static loading of reinforced concrete flexural members indicate that scale effects are generally significant only for very small scale models, e.g., beams with a depth of the order of 10 mm or less (98, 99,100). For larger models with scale ratios of say 1:5 or larger and constructed of materials similar in behaviour to normal building materials, most response characteristics show good agreement with the prototype behaviour (101). A 1:4 scale ratio was used in this study.

One exception, where it appeared that agreement may not have been good, was the sliding shear response. Results obtained from interlock shear tests conducted by Fenwick (73), Loeber (102), and Houde and Mirza (76), suggest that the effective shear flexibility due to sliding along cracks should reduce as specimen size reduces (Section 5.4.1). In contrast, the formulation for the sliding shear model developed in this study is scale-independent, i.e., shear flexibility is independent of specimen size. One point of interest in the present tests was therefore whether the sliding shear responses would be affected by the specimen scale, or whether they would support the assumptions made in the analytic sliding shear model.

7.2.3 Effect of Scale on Materials and Detailing

The effects of reduced scale on the design of the specimens were largely confined to the selection and detailing of the reinforcement, instrumentation and to a lesser extent, the concrete mix.

Three main similitude requirements governed the selection of suitable reinforcement:

(a) The stress-strain relationships of the model reinforcement should be typical of those possessed by normal structural grades of reinforcement.

(b) All main flexural reinforcement in potential plastic hinge zones should be deformed bars.

(c) Bar sizes should be approximately to scale.

Unfortunately, no reinforcement was available which complied with all three criteria, which would have required use of deformed bars of 5 mm to 8 mm diameter. The only bars readily available, which appeared to be close to satisfying the requirements, were 6.4 mm diameter plain bars and 9.5 mm diameter deformed bars. Both these types of bars were used for flexural reinforcement for the first two beam-wall specimens. However, the plain bars did not perform satisfactorily and were not used for main flexural reinforcement in regions susceptible to yielding in any of the remaining specimens. Samples of deformed 6.4 mm diameter bar were obtained from United Kingdom, but on testing these were found to be unsatisfactory also, with a yield strength of over 600 MPa and an ultimate strain of only 0.025.

Detailing of the reinforcement was largely based on the provisions of the ACI 318-71 Building Code (103). The main exceptions were that plain bars were used for flexural reinforcement in some cases, that the fixed minimum cover and spacing requirements were reduced in accordance with the specimen scale ratio, and that the requirement for a minimum anchorage length of 305 mm was generally disregarded. In addition, the specified minimum radii of curvature for bends in the reinforcement were not adhered to in the beam-column joint regions of the frame-wall specimens. A strength reduction factor of $\phi = 1$ was used because all dimensions and material properties were measured.

The similitude requirements for the concrete mix are generally less critical than for the reinforcement, and in these tests maximum aggregate sizes of 9.5 mm and 12.7 mm were used for the beam-wall and frame-wall specimens respectively. Provided that aggregates of similar material and roughness are used and that the crack widths remain small compared with the crack roughness, varying the maximum aggregate size by a factor of two to three generally has little affect on the shear deformation response (77,101).

The small size of the specimens also caused some problems in relation to instrumentation, particularly for measurement of bar strains. This was mainly because the mechanical strain gauges used and the studs and concrete penetrations required to give access to the reinforcement were larger, relative to the size of the specimens than is normally the case. As a result, the effect of the studs and concrete penetrations (Figure 7.7) was probably greater than normal, and it was also not possible to obtain detailed measurements of the distribution of bar strains in the plastic hinge zones.

7.3 REPRESENTATION OF EARTHQUAKE LOADING

Both the beam-wall and frame-wall specimens were subjected to high intensity pseudo-static load reversals. This section describes general details of the loading used and discusses the validity of using this type of loading for assessing structural behaviour under real earthquake excitation.

7.3.1 Distribution of Loading

The inertia forces generated in a structure during an earthquake vary with time and position according to the interaction between the structure and the base excitation. In representing these forces by pseudo-static loads, it is not intended (nor is it feasible) to exactly duplicate any real earthquake loading pattern.

The usual approach, and that adopted in these tests, is to represent the inertia forces by a fixed distribution of lateral loads, and to vary only the load intensity. The distribution of loads used for the frame-wall assemblages was based on the lateral force distribution specified by the then (1973) current New Zealand loadings code (104). For a lateral load resisting system with a height to width ratio greater than or equal to 3, this required 10% of the code base shear to be applied at the top and the remainder to be applied in an inverted triangular distribution. It is now recognised that this will not generally represent the critical shear loading condition at the base of the wall (105) and the current New Zealand concrete design code NZS 3101:1982 (19) requires separate load distributions to be considered for the moment and shear design of walls.

However, while the unconservative nature of the inverted triangular load distribution is significant from the point of view of a building subjected to real earthquake loading, it is of less relevance to these tests. In the first instance, the distribution of loads to be imposed was known and consequently the specimen could be reinforced accordingly to enforce the desired type of response. Regardless of what distribution had been adopted, the specimen reinforcement would have been designed to prevent a shear failure at the base of the wall. In the second instance, the purpose of testing the assemblages was to evaluate the interaction between the various structural components and the effect of this interaction on the component and overall assemblage responses. The behaviour of particular elements of a structure under critical load conditions, e.g., maximum shear forces, would generally be obtained more economically from tests on the element or sub-assemblage concerned.

7.3.2 Loading Sequence

A number of different types of loading sequences have been used to represent earthquake loading, each having its own advantages and disadvantages.

Probably the most common type of load sequence currently in use involves imposing several cycles of loading to a ductility of approximately ±2, then gradually increasing the cycle displacement limits in steps, with two or three cycles of loading applied at each step. Generally equal positive and negative displacement limits have been used for each set of load cycles. This type of loading sequence has become particularly popular with the availability of automatic loading devices and data collection, which have permitted larger numbers of load cycles to be imposed. The standardised nature of this type of load sequence is very useful from the point of comparing responses. However, it is important not to lose sight of the fact that any one load sequence can only reveal a limited amount of information and that in many cases, other load sequences may be more critical (106). More results are also needed for specimens subjected to different types of loading sequence to provide a wider range of data for developing analytic models.

The loading sequences used for the specimens tested in this study generally followed the pattern indicated in Figure 7.1, i.e., an initial post-elastic cycle to a ductility of approximately ±4, followed by several cycles of generally increasing post-elastic deformations.* Specific details of the sequences used for each specimen are given in Chapters 8 and 9. The magnitude of the deformations imposed in the initial cycles of these tests were intended to reflect the maximum severity of loading expected under design earthquake conditions. Because of the manually operated loading equipment and instrumentation used, no attempt was made to precisely control deformations, or to impose repeated cycles, between each set of displacement limits.

In retrospect, it would have been more useful if the load sequences used for some of the beam-wall specimens had contained a more varied mixture of large and small load reversals.
However, the computer program had not been developed at the time the experimental work was carried out and the need for this type of information was not recognised.

7.3.3 Rate of Loading

Studies of both monotonic and cyclic loading reviewed by Blakeley (68) show that rate of loading has little effect on the stiffness, damping or ultimate section curvature of a reinforced concrete member. The only significant effect of dynamic loading noted was an increase in strength resulting from an increase in the initial yield strength of the reinforcement. In the case of prestressed concrete members, where the concrete properties have a greater influence on the response, there was also a slight increase in the initial flexural stiffness. This is likely to apply also to columns which are subjected to significant axial compression.

More recent research carried out by Mahin and Bertero (107) and by Celebi and Penzien (11) supports the above findings for reinforced concrete members, and is particularly relevant to seismic load simulation. Mahin and Bertero tested six simply-supported, doubly

* The definitions of ductility factor, relevant to these tests are found in Figures 8.2 and 9.2.

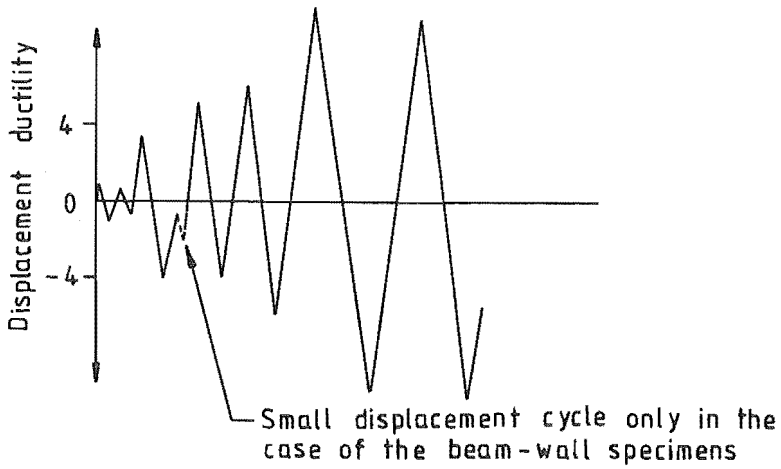

FIGURE 7.1 : TYPICAL LOADING SEQUENCE USED IN TESTS

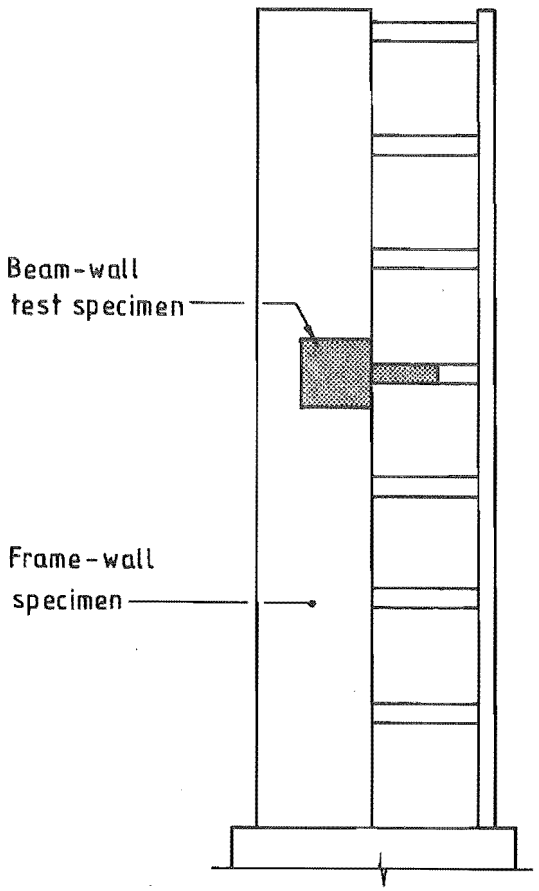

FIGURE 7.2 : RELATIONSHIP BETWEEN BEAM-WALL AND FRAME-WALL SPECIMENS

reinforced concrete beams, each being subjected to alternating sequences of low velocity (2.5 mm/sec) and high velocity (254 mm/sec) load reversals. In the second set of tests, Celebi and Penzien subjected six sets of beam specimens (Section 6.3) to high intensity load reversals. Each set consisted of two identical specimens. During the post-elastic cycles one was loaded at 2.5 mm/sec, and the other at 152/mm sec. The shear span to depth ratio these beams ranged from 2.31 to 5.10. The results obtained from both the Mahin and Bertero, and the Celebi and Penzien tests were very similar and showed that the only significant effect of dynamic loading is an increase in the initial yield strength. After the first post-elastic cycle, the faster rates of loading had negligible affect on the hysteresis loops.

One effect not covered by the preceding discussion, is the drop in load that often occurs when the loading is held "stationary" for a period of time, to allow strain and displacement measurements to be taken. This drop in load usually occurs because creep in the specimen causes the comparatively rigid loading system to partially unload, not because the creep affects the strength of the specimen. It is therefore important that the loads be measured as soon as possible after each displacement increment has been imposed.

7.3.4 Strain Ageing

One rate of loading effect that was not recognised at the start of the experimental work, was strain ageing of the reinforcing steel. Strain ageing can noticeably affect the steel response within one or two days of initial plastic straining and after 5 to 10 days can start to increase the ultimate strength of the steel.

Because of the large number of readings taken, and the use of manually operated load equipment and instrumentation, each test took a considerable time to complete, typically a week in the case of the beam-wall specimens and two to three months in the case of the frame-wall specimens. The potential for problems resulting from strain ageing was not recognised until after the third beam-wall

specimen had been tested, and by that stage only one beam-wall and the frame-wall specimens remained to be tested. To minimise any strain ageing effects, testing on the last of the beam-wall specimens was accelerated by omitting most of the planned steel strain measurements.

A more detailed discussion on strain ageing and on the extent to which the specimen responses were affected, is given in Appendix A.

7.4 BEAM-WALL TESTS

The specimens used in these tests were modelled on a typical beam-wall junction in the frame-wall specimens (see Figure 7.2). The beam reinforcing and the loading imposed were similar to, and the model scale the same as for the frame-wall specimens. However, due to a change in design, the beam shear spans were longer than in the frame-wall specimens, i.e., 457 mm as compared with approximately 350 mm in the frame-wall specimens.

The main reasons for testing these specimens were:

(a) To assess the response characteristics of the scale beams used in the frame-wall specimens, and the ability of the frame analysis program to model these responses. Since the frame-wall assemblages were statically indeterminate, the beam responses could not be determined directly from the frame-wall tests. At the time these tests were carried out (1972-73), very few detailed studies had been made of sliding shear displacements in plastic hinge zones of reinforced concrete members.

(b) To check the suitability of the beam reinforcing details planned for the frame-wall specimens.

(c) To assist planning the instrumentation for the main test series.

The beam-wall, rather than beam-column junction, was chosen for these tests because a suitable test rig already existed, and the anchorage deformations could be more readily measured. The beam dimensions and reinforcing details are shown in Figures 7.3 and 7.4, and the properties of the reinforcing bars are summarised in Table 7.1.

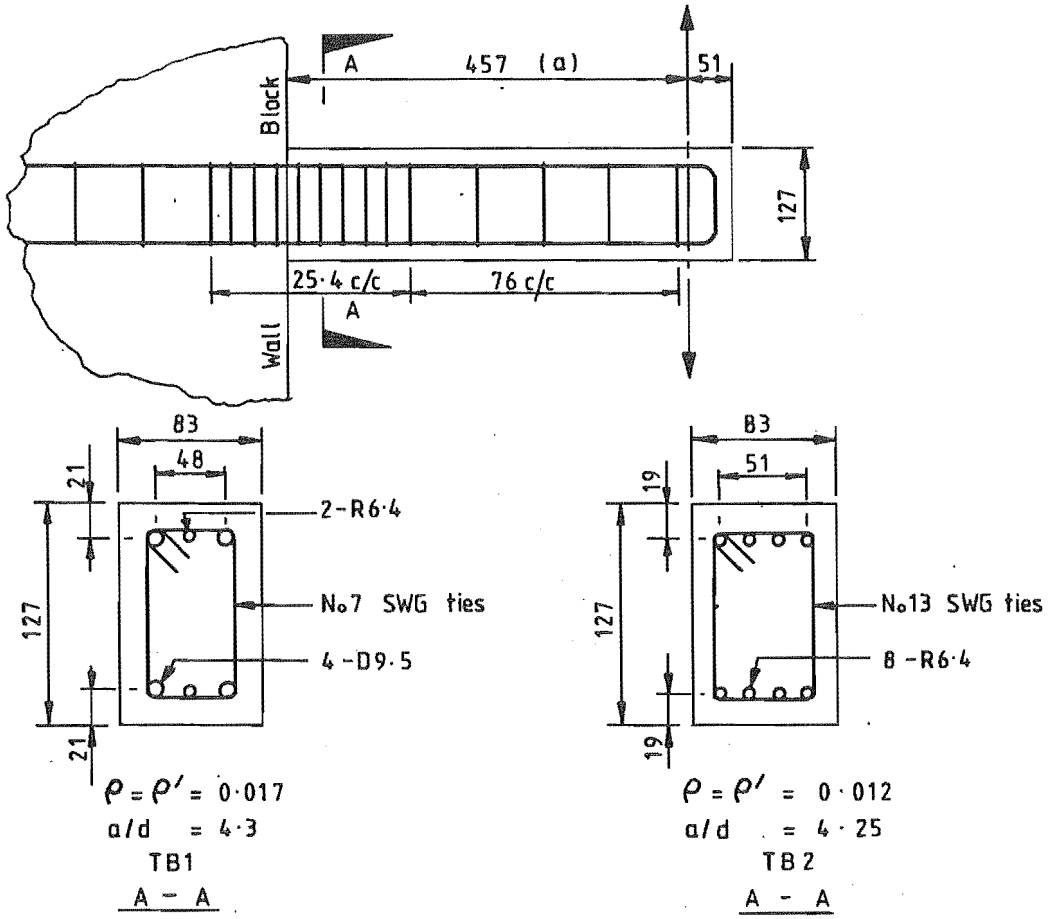

FIGURE 7.3 : CONVENTIONALLY REINFORCED SPECIMENS TB1 AND TB2

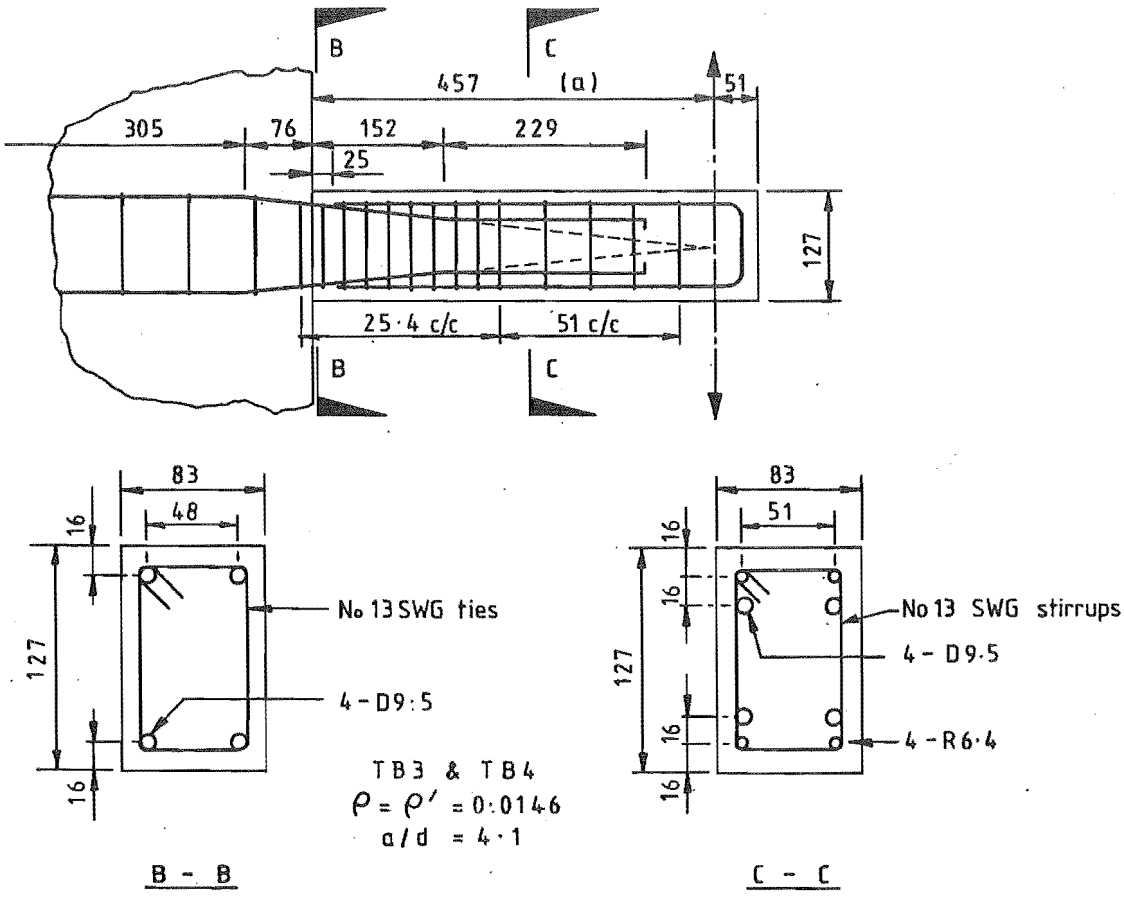

FIGURE 7.4 : DIAGONALLY REINFORCED SPECIMENS TB3 AND TB4

TABLE 7.1 : PROPERTIES OF BEAM REINFORCING BARS USED IN BEAM-WALL SPECIMENS

	f_y (MPa)	E_o (GPa)	ε_{sh}	f_{su} (MPa)
6.4 mm diameter plain bars				
TB1, TB2	363	233	0.0098	518
TB3, TB4	368	223	0.0153	501
9.5 mm diameter deformed bars				
TB1	307	208	0.0125	433
TB3, TB4	300	210	0.0161	429

NOTES

(1) ε_{sh} = strain at onset of strain hardening.

(2) All strengths and moduli are based on nominal area of bars.

TABLE 7.2 : PROPERTIES OF CONCRETE USED IN BEAM-WALL SPECIMENS

UNIT	AGE AT TESTING (DAYS)	COMPRESSIVE STRENGTH f'_c (MPa)	INITIAL ELASTIC MODULUS E_c (GPa)	DENSITY ρ (kg/m^3)
TB1	34	53.0	-	2411
TB2	29	46.3	35.5	2399
TB3	48	57.6	38.6	2417
TB4	50	54.0	33.6	2415

NOTES

(1) All concrete was mixed in the laboratory.

(2) Maximum aggregate size = 9.5 mm.

(3) Water/Cement Ratio = 0.48.

7.4.1 Beam Reinforcement : Conventionally Reinforced Specimens, TB1 and TB2

The beams in the first two specimens (TB1 and TB2) were conventionally reinforced with flexural bars parallel to the beam axes (Figure 7.3). Different flexural steel contents were used in each of these specimens as it had originally been intended to reinforce the beams in one of the frame-wall specimens to match the distribution of beam end moments obtained from an elastic frame analysis (refer Section 7.5.2). This would have required the beams at different levels to have different steel contents.

The flexural reinforcement for these two specimens was provided by a combination of 9.5 mm diameter deformed bars (D9.5) and 6.4 mm diameter plain bars (R6.4). As explained previously, neither of these types of bar fully satisfied similitude. Subsequent premature failure of the bar anchorages in TB2 clearly demonstrated that the use of plain bars was not satisfactory for this type of testing, and therefore only deformed bars were used for main flexural reinforcement in the remaining specimens.

The stirrups provided in the potential plastic hinge regions of each of these specimens were designed to resist the full applied shear at 1.25 times the ideal strength calculated from the measured properties of the concrete and flexural reinforcement. The stirrup spacing (25 mm) in this region was approximately d/4.

Outside the plastic hinge region, allowance was made for the shear strength of the concrete in accordance with the ACI 318-71 Code (103), and the stirrup spacing was increased to 75 mm (approximately 0.75d).

7.4.2 Beam Reinforcement : Diagonally Reinforced Specimens, TB3 and TB4

The reinforcement arrangement used in these specimens (Figure 7.4) was modelled on the diagonal bar arrangement first proposed by Paulay (22) for low aspect ratio coupling beams in coupled shear walls. This arrangement of reinforcement effectively provides a triangulated steel

truss which primarily relies on the concrete only for the stability of the bars. After yielding, the total applied load (moment and shear) is capable of being directly resisted by the axial forces in the main diagonal reinforcing bars, and consequently the inelastic shear deformations and associated damage are substantially reduced.

The coupling beams tested by Paulay (108) and others (23, 30) had bars placed along the two diagonals, crossing at the centre of the beam. In addition, nominal ties and conventional parallel reinforcement were provided over the central length of the beams to contain the concrete.

This detail was modified for the larger aspect ratio beams in TB3 and TB4 so that the bars were only inclined over the potential plastic hinge zone (see Figure 7.4). Outside this region, the concrete was considered capable of adequately resisting the applied shear forces and the bars were bent parallel to the beam axis to avoid congestion near the free end* of the beams and to restrict the spread of yielding. Additional parallel bars were provided outside of the bent up bars to cater for gravity loads and, again, to minimise the spread of yielding. Near the free end of the beam, advantage was taken of the greater lever arm of these latter bars, and the bent bars were therefore terminated at the point where they were no longer required.

Within the plastic hinge zone, the diagonal bars were capable of resisting the full applied shear force, i.e., the bar centre lines crossed at the point of loading. The ties indicated in Figure 7.4 in this region were provided solely to prevent local buckling of the bars and to confine the core concrete. The stirrups outside the plastic hinge zone were, however, provided for shear resistance, and were designed as for a conventionally reinforced beam.

7.4.3 Concrete

The concrete used in all specimens was prepared in the laboratory and had a compressive cylinder strength of between 46 MPa and 57 MPa. The maximum aggregate size was 9.5 mm.

---

* Equivalent to the centre region of a full length frame member subjected to yielding at both ends.

For casting, the moulds were placed with the wall block lying horizontally and the concrete compacted with an immersion vibrator. Each specimen was cured for 7 days under wet hessian covered with polythene, and then air dried in the laboratory until they were tested. Standard 152 mm diameter x 305 mm cylinders were taken from the concrete mix for each specimen, and were cured in the same environment as the specimens. These cylinders were tested just before the specimens were first loaded into the post-elastic range. The concrete properties obtained from these tests are given in Table 7.2.

7.4.4 Test Rig and Load Application

Figure 7.5 shows a schematic view of the test rig with a specimen positioned ready for testing. Load was applied at the end of the beam by a hand operated jack through tension bars and was resisted by reaction between the wall block and the test rig. For loading in the reverse direction the tension bars, jack and load cell were moved to the other end of the rig.

7.4.5 Instrumentation and Measurements

The following measurements were made during the tests:

(a) Applied Load

The load applied by the jack was measured every increment using a 50 kN Philips load cell (Type PR 9226/5) which was read using a manually operated Budd strain bridge. On average, approximately 12 load increments were applied in every load reversal.

(b) Beam Deflections

Deflections were measured every increment at several points along the length of the beams, using dial gauges reading to 0.025 mm and 0.0025 mm. These gauges were arranged as shown in Figure 7.6. The B and C dial gauges indicated in these diagrams were used for assessing overall rotation and translation of the wall blocks. The base translations were not measured in the first two tests and it was assumed in

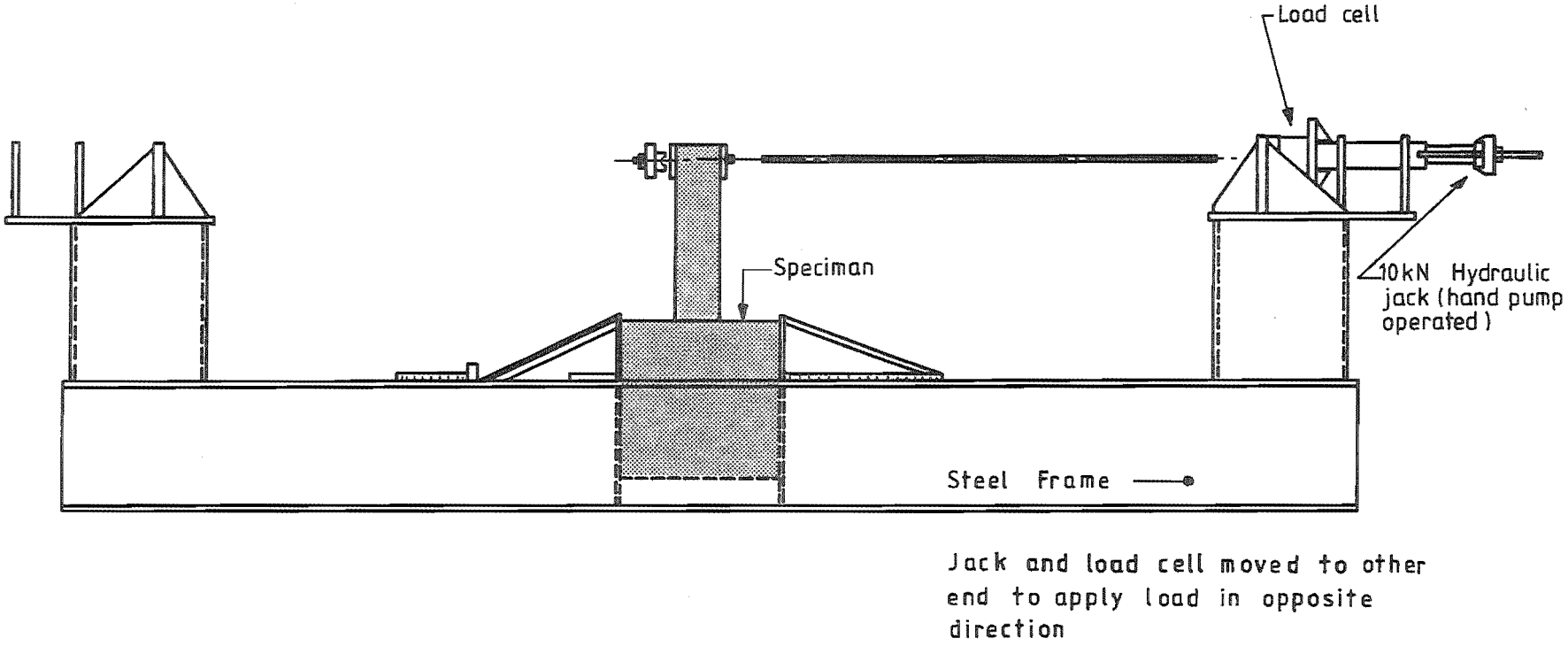

FIGURE 7.5 : TEST RIG FOR BEAM-WALL SPECIMENS

these cases that the wall blocks rotated about their centres. The measurements obtained for TB3 and TB4 confirmed that the displacement of the centre of the wall blocks was very small and that the assumption made for TB1 and TB2 would have introduced only minor errors.

(c) Steel Strains

Strains developed in the flexural reinforcement were measured using BAM mechanical contact strain gauges for the first two specimens (TB1 and TB2) and using Demec demountable mechanical strain gauges for the third and fourth specimens (TB3 and TB4). These gauges are discussed in the following section (7.4.6).

The locations at which strains were measured are shown in Figure 7.6. At each location, readings were taken on both sides of the specimen and the results averaged. For the tests on TB1 and TB3, these readings were generally taken between 3 and 8 times per load reversal, until the start of the final two load cycles when the maximum bar strains exceeded the range of the gauges (at a strain of approximately 0.04). These strain readings were very time consuming and in order to speed up testing and minimise strain ageing effects, considerably fewer sets of readings were taken for TB4.

The strain measurements obtained from these tests were used to determine the following information:

(i) Imposed steel strains.

(ii) Curvatures and elongations at various points in the beam and anchorage region.

(iii) Component of beam deflection due to flexure; subtracting this from the total deflection measured with the dial gauges gave an assessment of the beam shear displacement reponse.

(iv) Component of beam end deflection resulting from the strains developed in the bars anchored in the wall blocks.

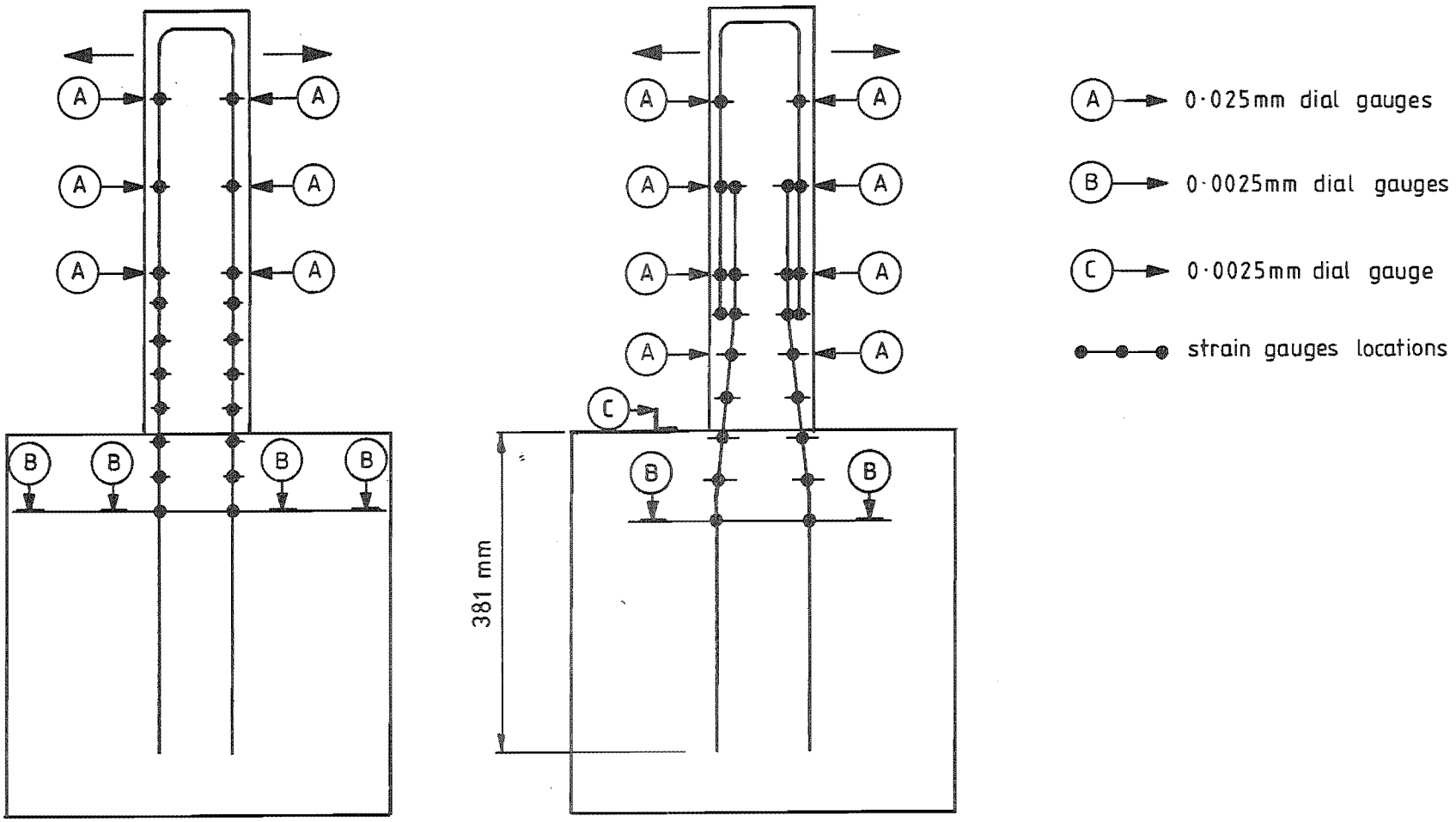

FIGURE 7.6 : INSTRUMENTATION FOR BEAM-WALL SPECIMENS

(d) Crack Observations

The specimens were painted white and during the tests, the propagation of cracks was marked on the specimens and photographed at regular intervals.

7.4.6 Strain Gauges

In previous tests on reinforced concrete components at the University of Canterbury, Demec (109) gauges have generally been used to measure bar strains (Figure 7.7a). However, two features of the operation of these gauges can adversely affect their accuracy.

(a) The studs extending from the bars to the concrete surface magnify any buckling or twisting of the bars. This introduces additional errors into the readings which are only partly overcome by measuring strains on both sides of the specimens.

(b) For the small bar diameters used in these tests, the tack welds used to fix the studs to the reinforcement were large enough to increase the strength of the bars in the vicinity of the weld. The greater strength of these regions was clearly visible in sample lengths of bar loaded to failure in tension. Because of the holes provided in the concrete (Figure 7.7a), cracks often formed at the stud locations, where the reinforcing bars were strongest.

One of the objectives of the beam-wall specimen test was to evaluate the suitability of an alternative type of mechanical strain gauge supplied by Fritz Staeger (110). These gauges, which were used on TB1 and TB2, measure the bar elongation (or contraction) between two small ball bearings punched directly into the bar surface as indicated in Figure 7.7b. This overcomes both the above deficiencies of the Demec system. However, the gauges were found to be even slower to operate than the Demec gauges. In addition, the surrounding cover concrete restricted vision and it was often difficult to place the gauge correctly over the ball bearings. This made it difficult to obtain consistent readings for some gauge locations. Access would have been even more of a problem for the

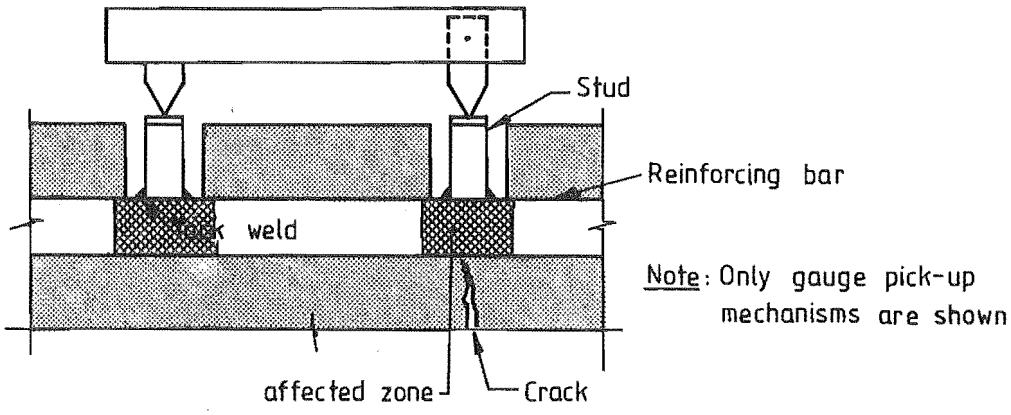

(a) Demec strain gauge (109)

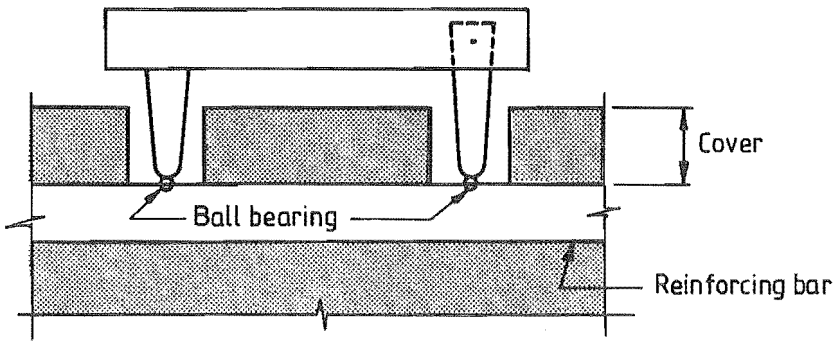

(b) BAM strain gauge Fritz Staeger (110)

FIGURE 7.7 : SCHEMATIC VIEW OF PICK-UP MECHANISMS ON DEMEC AND BAM MECHANICAL CONTACT STRAIN GAUGES

frame-wall specimens and consequently it was decided to use the Demec gauges for the remaining specimens (i.e., TB3 and TB4, as well as the frame-wall specimens).

7.5 FRAME-WALL TESTS

The geometry of the two frame-wall test specimens (FSW-1 and FSW-2) is shown in Figure 7.8. This geometry was chosen to represent a general frame-wall assemblage, and was not based on a particular prototype structure.

The main criteria influencing the choice of specimen geometry and reinforcing details were:

(a) That the limitations imposed by the capacity of the existing test rig be not exceeded.

(b) That the assemblage have a reasonable degree of indeterminacy.

(c) That as large a scale as practicable be used, so as to minimise scale effects and, if possible, to allow ordinary structural grade reinforcing bars to be used for the flexural steel.

(d) That the frame carry a reasonable portion of the total over-turning moment in order that the wall would not excessively dominate the overall behaviour of the specimens.

(e) That the stiffness of the assemblage be realistic in terms of code limitations on inter-storey deflection.

(f) That the behaviour of the specimens be consistent with the planned scope of the frame analysis computer program.

The specimen adopted was a quarter scale 7 storey x 1 bay frame-wall assemblage, with overall dimensions of 5.486 m x 1.588 m. The beams had shear span to depth ratios of $a/d = 3.14$ and by frame action, contributed approximately one third of the total overturning moment capacity of each specimen (Table 7.4). The walls, which had an aspect ratio of 7:1, were probably more flexible than would normally be used in a building of this size (i.e., 7 storeys). However, the specimens were stiff enough to comply with limitations

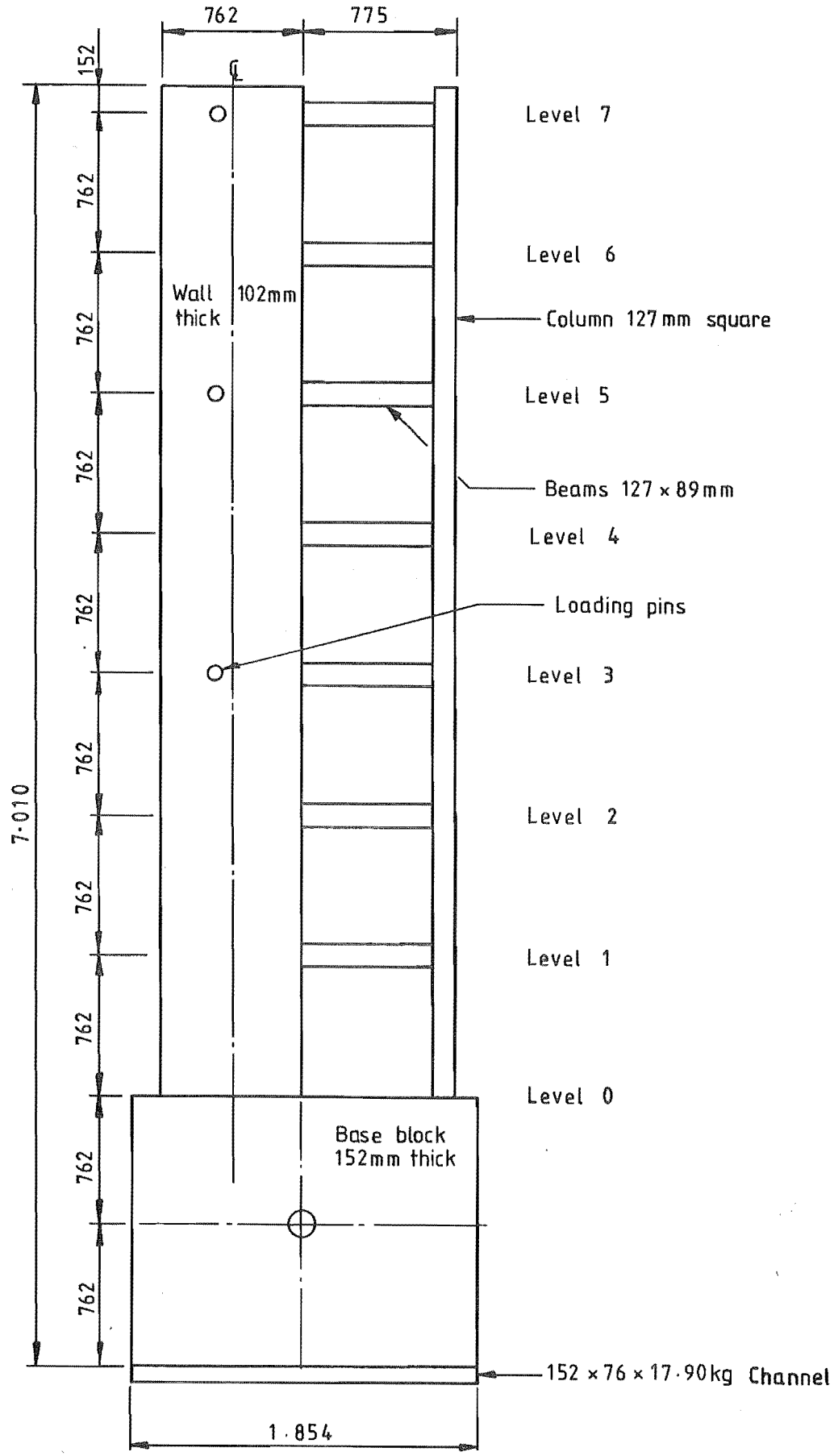

FIGURE 7.8 : GEOMETRY OF FRAME-WALL SPECIMENS FSW-1 AND FSW-2

on inter-storey deflection specified in the New Zealand Loadings Code NZS 4203:1976 (111).

7.5.1 Specimen Reinforcement

The arrangement of the reinforcement in the two specimens is shown in Figures 7.9 to 7.14, and the properties of the reinforcing bars are summarised in Table 7.3.

The two specimens differed in only three details:

(a) Beam reinforcement. The beams in the first specimen (FSW-1) were conventionally reinforced while those in the second specimen (FSW-2) were diagonally reinforced similar to the beams in TB3 and TB4 (cf Figures 7.4 and 7.10b). Both the conventionally and diagonally reinforced beams were detailed to have approximately the same flexural strength.

(b) Additional transverse reinforcement was provided in the wall plastic hinge zone of the second specimen to improve confinement of the main flexural reinforcement (refer Section 7.5.6).

(c) The cut-off point for the wall vertical reinforcement at the frame side of the wall was raised by one storey height in the second specimen.

Specific details relating to design of the reinforcement are discussed in Sections 7.5.2 to 7.5.7.

7.5.2 Beam Reinforcement

The plastic hinge regions of all beams had equal top and bottom steel contents of $\rho_s = \rho'_s = 0.016$ (two 9.5 mm diameter deformed bars top and bottom, Figure 7.10).

One of the specimens had originally been intended to be reinforced to match the distribution of beam end moments obtained from an elastic frame analysis based on gross concrete section properties. This was to be achieved by varying the beam steel content provided at each level, and the first two beam-wall test specimens were constructed to

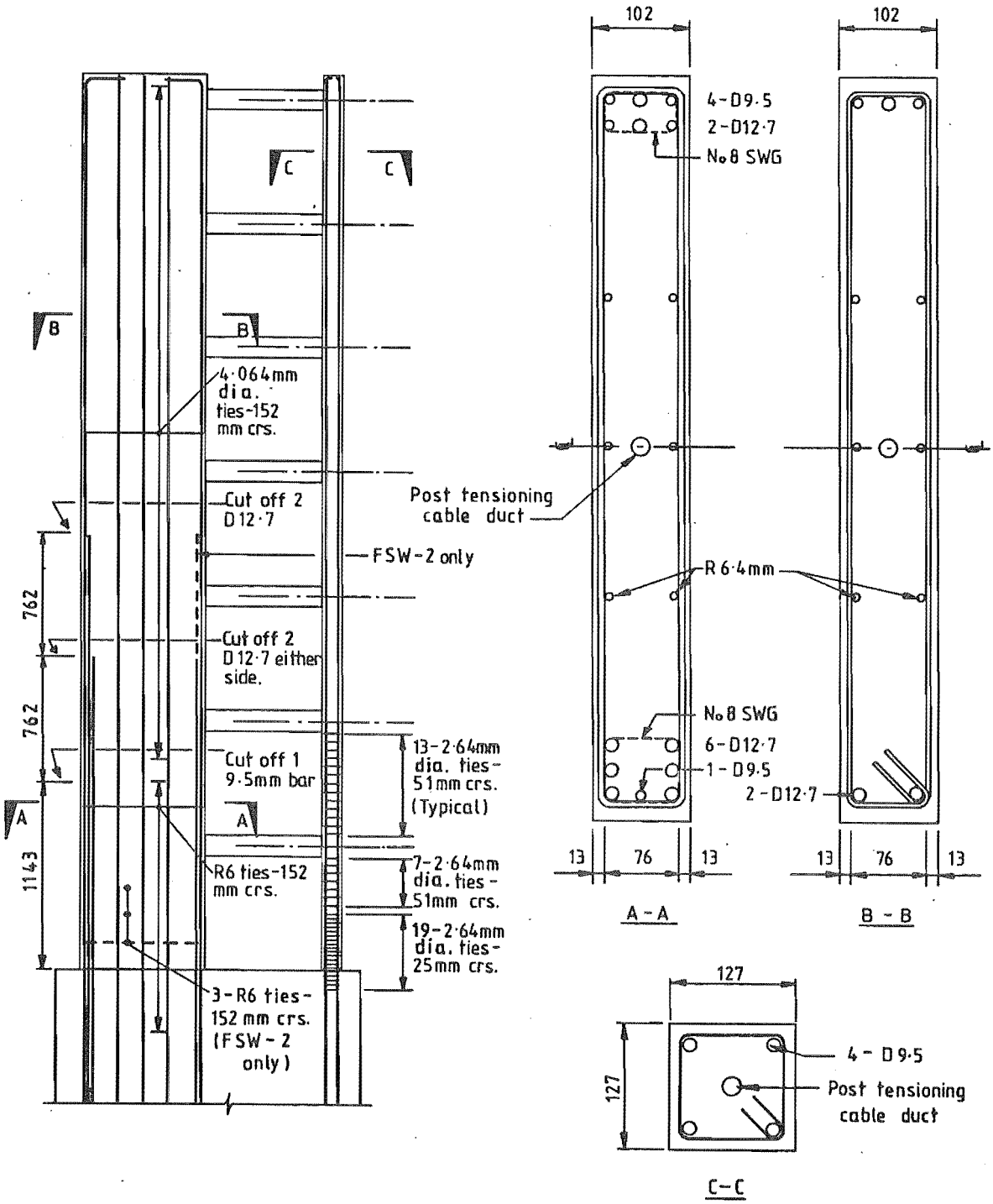

FIGURE 7.9 : WALL AND COLUMN REINFORCEMENT, FSW-1 AND FSW-2

TABLE 7.3 : PROPERTIES OF REINFORCING BARS USED IN FRAME-WALL SPECIMENS

BAR TYPE	f_y (MPa)	E_o (GPa)	ε_{sh}*	f_{su} (MPa)
BEAM FLEXURAL STEEL				
D9.5, FSW-1	304.8	208.7	0.01770	431.2
D9.5, FSW-2	303.7	218.8	0.01734	431.3
R6.4, FSW-2	345	208.9	-	568.9
WALL FLEXURAL STEEL				
R6.4, FSW-1 (·)	382.0	226.5	0.0110	555.2
R6.4, FSW-2 (·)	392.3	217.0	0.0120	565.4
D9.5, FSW-1 (●)	299.4	202.0	0.0176	421.8
(○)	374.0	214.2	0.0206	488.6
D9.5, FSW-2 (●)	310.3	217.5	0.0156	443.2
(○)	386.1	217.5	0.0262	477.5
D12.7, FSW-1 and FSW-2 (□)	331.6	211.7	0.0242	481.5
(■)	339.2	215.1	0.0154	459.0
WALL SHEAR STEEL				
R6.4, FSW-1	395.1	221.2	0.0136	563.3
R6.4, FSW-2	392.3	217.0	0.0120	565.4
COLUMN FLEXURAL STEEL				
D9.5, FSW-1 and FSW-2	375.8	206.9	0.0206	492.9

NOTES

(1) *ε_{sh} = strain at onset of strain hardening.

(2) R6.4 = 6.4 mm diameter plain bars, D9.5 and D12.7 = 9.5 mm and 12.7 mm diameter deformed bars respectively.

(3) All strengths and moduli based on nominal bar areas.

(4) Location of wall flexural steel

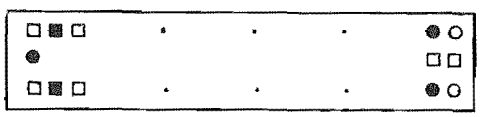

evaluate the behaviour of beams with two different arrangements of reinforcing bars. However, after further analysis, it was realised that simply varying the steel contents to match the elastic moment distribution would not ensure the intended simultaneous onset of yielding of all beams. The reason for this is that because of the large relative stiffness of the wall, the strengths of the beams have little influence on the beam deformations imposed. Consequently, it is the yield displacements rather than the strengths of the beams that determine the hinging sequence. Steel content alone has little influence on the beam yield displacement.

7.5.3 Curtailment of Diagonal Reinforcement (FSW-2 Beams)

In designing the beam reinforcement for FSW-2, the cut-off points for the diagonal bars were scaled from the detail used for the beam-wall specimens (Figure 7.4), in proportion to the beam shear spans, i.e., 349 mm* for FSW-2 versus 457 mm for TB3 and TB4. This detail generally satisfied the requirements of Chapter 12 of ACI 318-71 for the cut-off of the diagonal bars, but did not perform well during the test. On checking, it was found that the original calculations had made no allowance for strain hardening of the bars in the plastic hinge regions. With the effect of strain hardening considered, the continuing parallel reinforcement did not provide adequate strength to resist the moments developed at the cut-off points.

The current New Zealand concrete code (19) requires over-strength of the plastic hinge to be allowed for when determining cut-off lengths and under its provisions, the diagonal bars in FSW-2 should not have been terminated before the centre of the beams.

7.5.4 Beam-Column Joint Detail

The reinforcing detail used for the beam-column joint regions is shown in Figure 7.13. The joint ties provided were designed to resist the total joint shear imposed, assuming over-strength moments developed at the ends of the beams. As additional protection, the

---

* Half the clear span of the beams (refer Section 7.6.3 for comment).

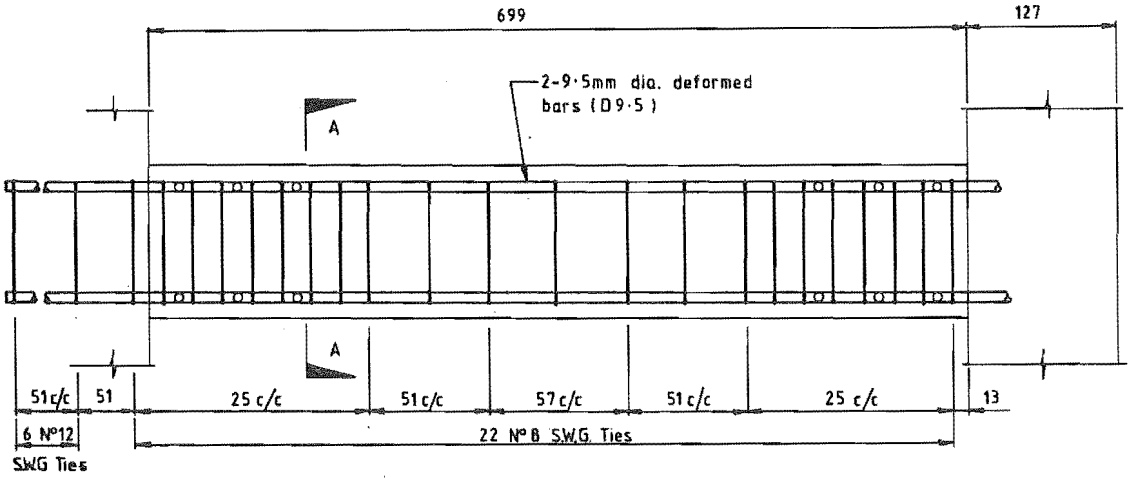

(a) FSW-1

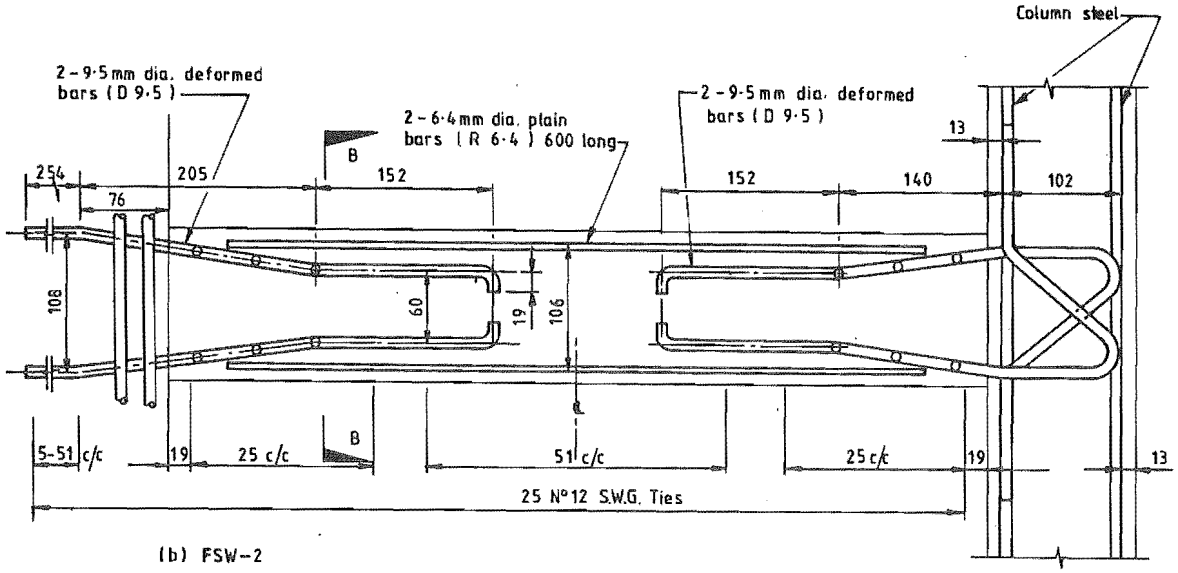

(b) FSW-2

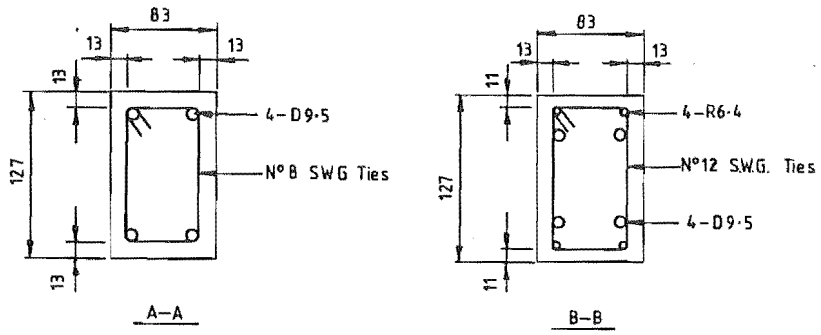

FIGURE 7.10 : BEAM REINFORCING DETAILS FOR FRAME-WALL SPECIMENS

ends of the beam reinforcement were bent back diagonally through the joint region as shown.

The reason for using this unusual detail was that serious degradation of beam-column joints had been observed previously, even though apparently adequate conventional hoop reinforcement had been provided (4, 44). In order to ensure compatibility with the planned scope of the frame-analysis program, it was essential that this type of behaviour be suppressed (refer Section 2.2.3). The diagonally crossed anchorage bars ensured proper anchorage and significantly reduced the risk of joint degradation, without affecting the validity of the responses of the specimens.

7.5.5 Wall Flexural Reinforcement

The walls of the specimens were reinforced to provide approximately equal moment strengths for both positive and negative loading (Table 7.4). Because of the different axial loads on the walls for the two directions of loading, an asymmetric reinforcing pattern was required with less steel at the frame edge of the wall (Figure 7.9).

The cut-off points for the wall flexural reinforcement were designed to ensure that plastic hinging in the walls was confined to the base region. In the case of FSW-1, these locations were determined from an elastic analysis of the specimen subjected to the planned lateral load distribution discussed in Section 7.5.10.2. However, strain measurements taken during the test indicated that the continuing reinforcement at the frame edge of the wall between Levels 2 and 3 was close to yielding at peak loads. The second row of bars at this edge were therefore extended a further storey up the wall in FSW-2 (Figure 7.9).

7.5.6 Transverse Reinforcement in the Wall Plastic Hinge Zones

The transverse reinforcement provided in the wall plastic hinge zone of FSW-1 consisted of full depth closed rectangular ties (6.4 mm

TABLE 7.4 : STRENGTH OF SPECIMEN FSW-1

LOAD CASE	FRAME		WALL		COLUMN		M_B
	P_x (kN)	$P_x.\ell$ (kNm)	P (kN)	M_w (kNm)	P (kN)	M_c (kNm)	(kNm)
POSITIVE LOAD							
ideal strength	±20.34	915.5	44.34	1842.8	- 5.34	39.1	2797.4
over strength	±25.43	1144.4	49.43	2382.8	-10.34	29.4	3556.6
NEGATIVE LOAD							
ideal	±20.34	915.5	3.66	1931.0	35.34	106.6*	2953.1
over strength	±25.43	1144.4	-1.43	2284.2	40.43	111.4*	3540.0

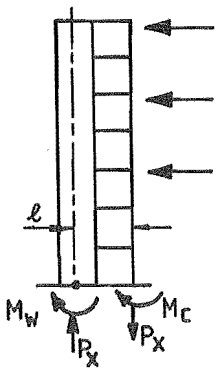

(Positive load case indicated)

Total base moment
$M_B = M_w + M_c + P_x.\ell$

P_g = gravity load

P_x = axial load due to frame action

P = net axial load

= $P_g + P_x$

NOTES

(1) All strengths computed in accordance with NZS 3101 (19), using measured properties of steel (Table 7.5) and concrete (Table 7.6)

(2) Column moments marked '*' were computed assuming that cover was still intact (ε_c = 0.003). In the test, the cover concrete spalled before peak displacement was reached in the first negative post-elastic load reversal.

(3) FSW-2 strengths were very similar.

plain bars) at 150 mm centres (approximately d/4) with local supplementary confining ties around the main flexural reinforcement (Figures 7.11 and 7.12). The main ties had adequate strength to resist the total design shear applied at the base of the specimen (Table 7.5), and the supplementary ties were provided to reduce the unsupported length of the flexural reinforcement to less than 6 bar diameters (19,112).

The supplementary ties proved to be inadequate to prevent local buckling of the flexural bar group at the frame edge of the wall in FSW-1. The number of full depth ties provided in the wall plastic hinge zone was therefore doubled for the second specimen* in order to reduce the risk of similar buckling. Where possible, the additional ties were placed centrally between the existing ones, giving a new spacing of approximately 75 mm, except between the first stirrup and the wall base block where there was a gap of nearly 100 mm (10.5 times the minimum flexural bar diameter).

The original local confining ties were left in the same position as for the first specimen.

7.5.7 Base Block Reinforcement

As indicated in Figure 7.14, all wall and column vertical reinforcement was carried to the full depth of the base block (1.448 m) and welded to the steel channel, to which the reaction truss was fixed. Additional 19 mm diameter bars were welded to the channel to provide flexural reinforcement for the base block. This reinforcement needed to be strong enough to keep the base block flexural deformations well within the elastic range in order to obtain satisfactory measurements of the wall anchorage deformations. However, because of the proximity of these heavier bars, it is likely that the anchorage conditions for some of the wall bars were in fact somewhat more favourable than normal.

---

* The reinforcing cage for this specimen had already been made up and placed in the mould ready for pouring. Dismantling and re-making the cage would have caused significant delays.

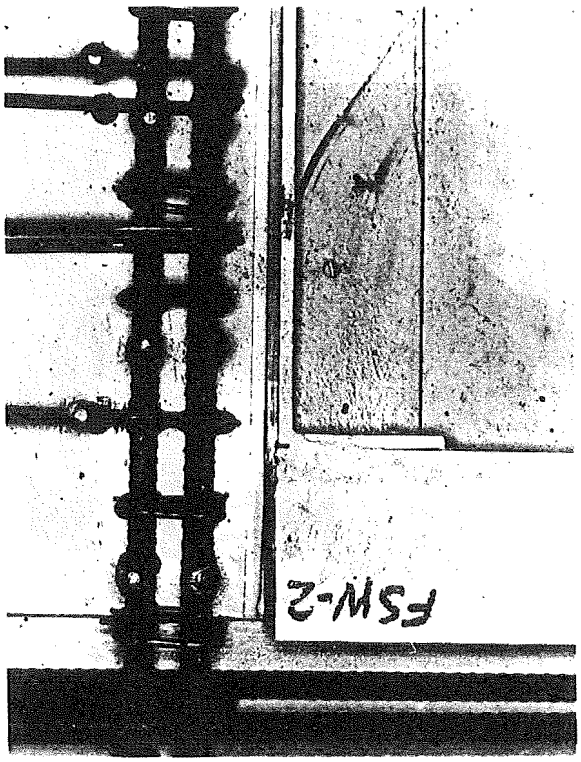

FIGURE 7.11 : LOCAL CONFINING TIES, FRAME EDGE OF WALL (FSW-2)

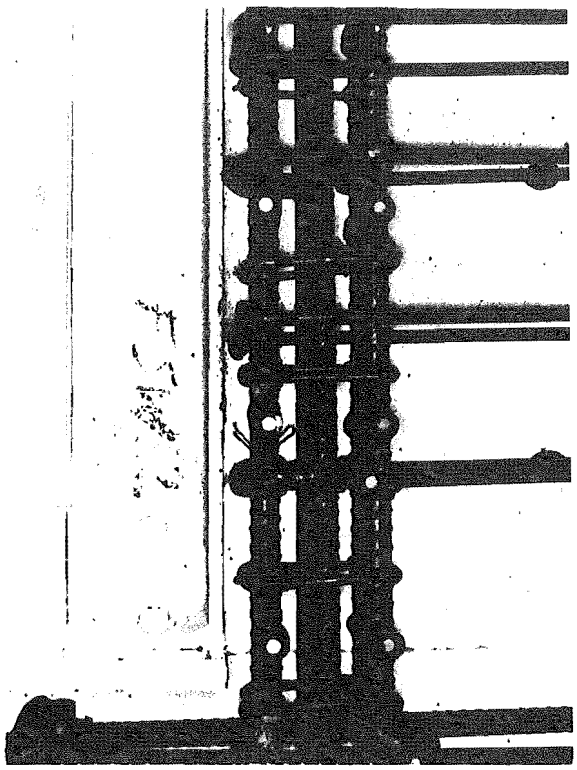

FIGURE 7.12 : LOCAL CONFINING TIES, FAR EDGE OF WALL (FSW-2)

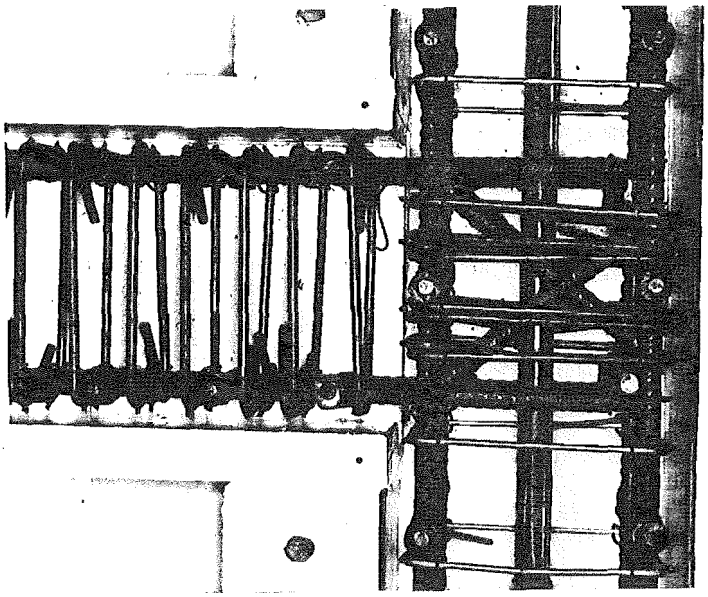

FIGURE 7.13 : BEAM-COLUMN JOINT DETAIL (FSW-1)

Note: Beam bars are bent back through the joint in addition to provision of conventional joint ties. A plastic pre-stressing duct passes through the centre of the joint.

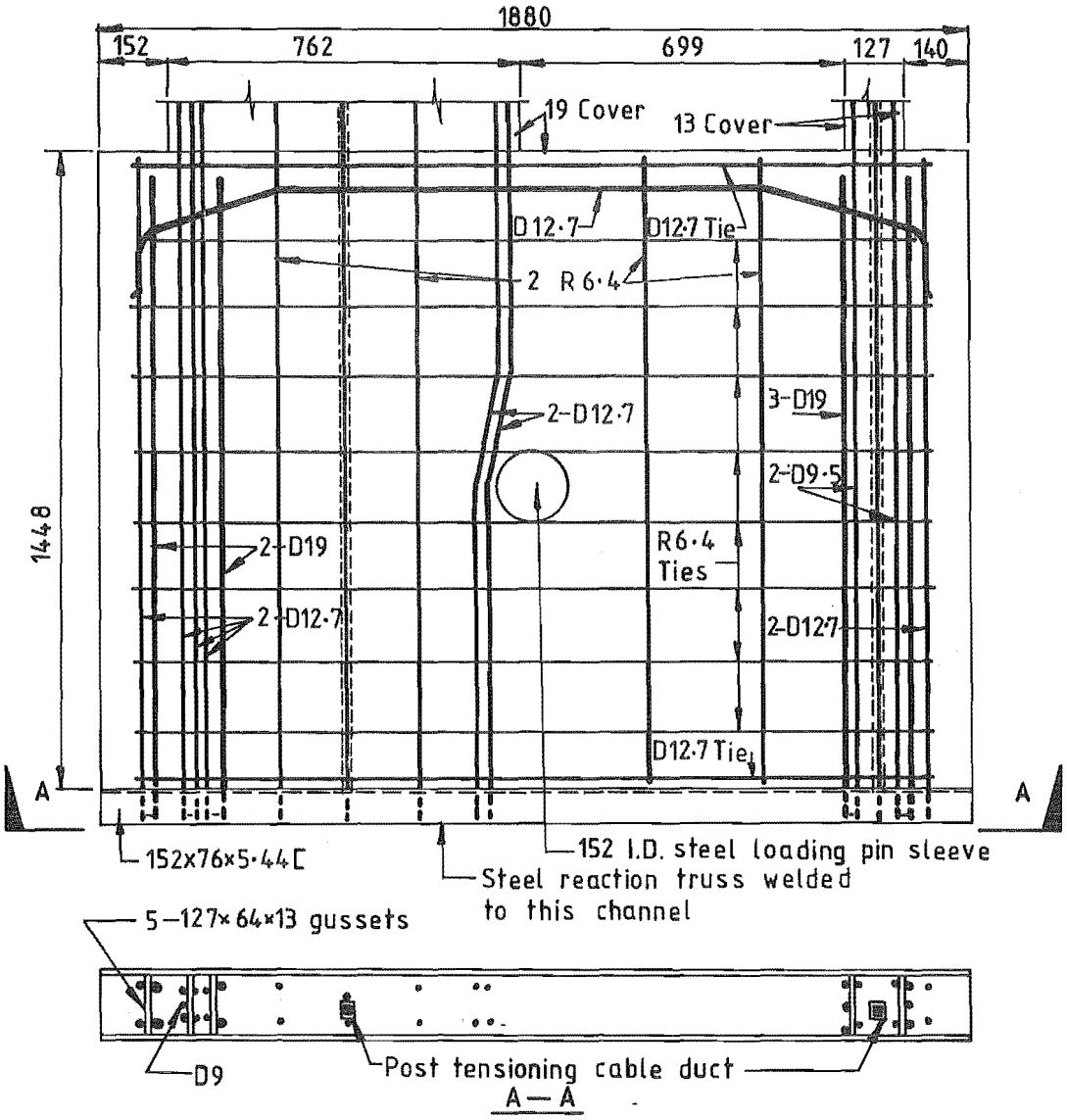

FIGURE 7.14 : BASE BLOCK REINFORCEMENT, FRAME-WALL SPECIMEN

TABLE 7.5 : COMPUTED BASE SHEAR CAPACITIES OF SPECIMEN FSW-1

LOAD CASE	BASE MOMENT M_B (kNm)	BASE SHEAR* V_B (kN)	BASE SHEAR** V_B (kN)
POSITIVE LOAD			
ideal strength	2797.4	73.7	83.0
over strength	3556.6	93.8	105.5
NEGATIVE LOAD			
ideal strength	2953.1	77.9	87.6
over strength	3540.0	93.4	105.0

* Base shear based on design lateral load distribution 1.267:1:1, ignoring gravity lateral load component due to horizontal position of specimens during tests (Section 7.5.10.1)

** Base shear based on actual lateral load distribution 1:1:1 (refer Section 7.5.10.2)

NOTES

(1) Shear strength provided by stirrups in wall plastic hinge zone:

$d_w A_v f_y / s$ = 106.8 kN.

(2) Ideal strength is based on measured steel and concrete properties, and overstrength is based on 1.25 f_y and 1.25f'_c

TABLE 7.6 : PROPERTIES OF CONCRETE USED IN FRAME-WALL SPECIMENS

UNIT	AGE AT TESTING	COMPRESSIVE STRENGTH, f'_c (MPa)	MODULUS OF RUPTURE f_r (MPa)	INITIAL ELASTIC MODULUS E_c (GPa)	DENSITY ρ (kg/m^3)
FSW-1	130	37.0	5.43	28.5	2294
FSW-2	162	39.3	6.12	26.7	2319

7.5.8 Concrete

Commercial ready-mix concrete was used for the two frame-wall specimens. The concrete had a specified 28 day compressive cylinder strength of 38 MPa, 13 mm maximum aggregate size and slump of 76 mm (Table 7.6).

Each specimen was cast in a horizontal position in one pour, and was compacted using an immersion vibrator. Curing was carried out for 7 days under wet hessian covered with polythene sheeting, followed by air drying until testing.

Standard 152 mm x 305 mm cylinders and 76 mm x 76 mm x 305 mm prism samples taken from the concrete mix were cured in the same environment as the test specimens. These were tested at the end of the first post-elastic load cycles to determine the compressive strength, elastic modulus and modulus of rupture of the concrete.

7.5.9 Test Rig and Load Apparatus

Figure 7.15 shows a schematic view of one of the specimens in the test rig, and Figure 7.17 shows a photograph of the test set up for the first specimen. The steel truss to the left of the specimen was welded to a channel section cast in the base block, and provided the leverage required to develop the base moment capacity.

The test rig was designed by Santhakumar (30), and only minor modifications were made for this project. The rig originally had seven loading frames (F1 to F7) for applying the lateral loads. These were arranged with frames at the levels of the 7th, 5th and 3rd floors (F1 to F3), one at the centre of the base block (F4) and three at the truss end (F5 to F7). Frames F1, F3, F4 and F7 also provided restraint against out-of-plane buckling. An eighth frame, F8, at the level of the first floor provided only restraint against out-of-plane buckling.

In the present test series, only five frames (F1 to F4, and F6) were used to apply the lateral loads, but restraint against out-of-plane

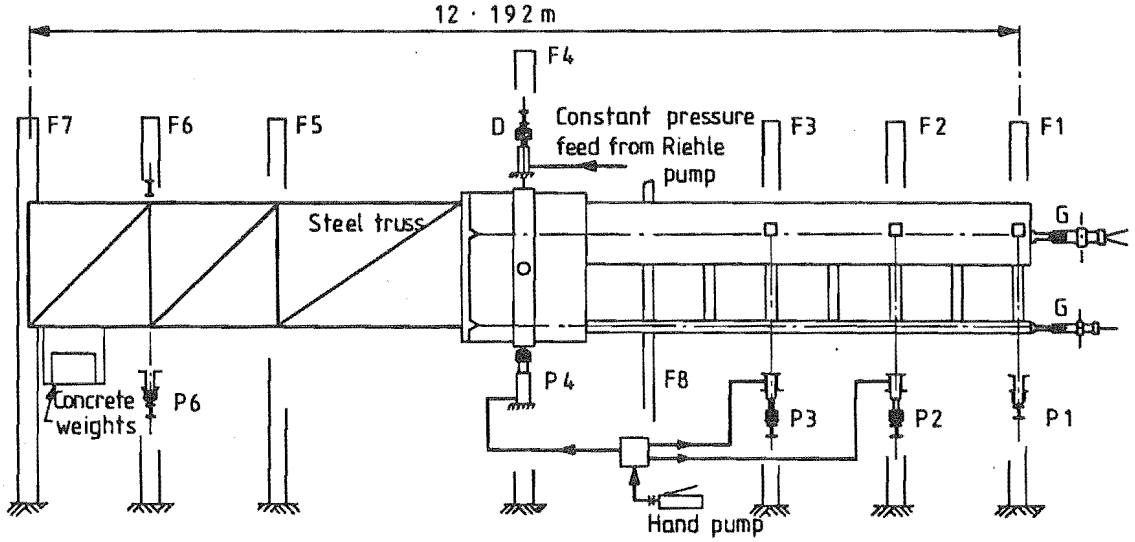

Notes: 1. Jacks at P2 and P3 contract with increasing oil pressure.
2. Jacks, load cells etc not to scale

■ - Load cell

- Hydraulic jack

D = Deadweight counter-balance
G = Prestressing jacks for gravity load simulation.
F = Frame Number

FIGURE 7.15 : SCHEMATIC VIEW OF SPECIMEN IN TEST RIG

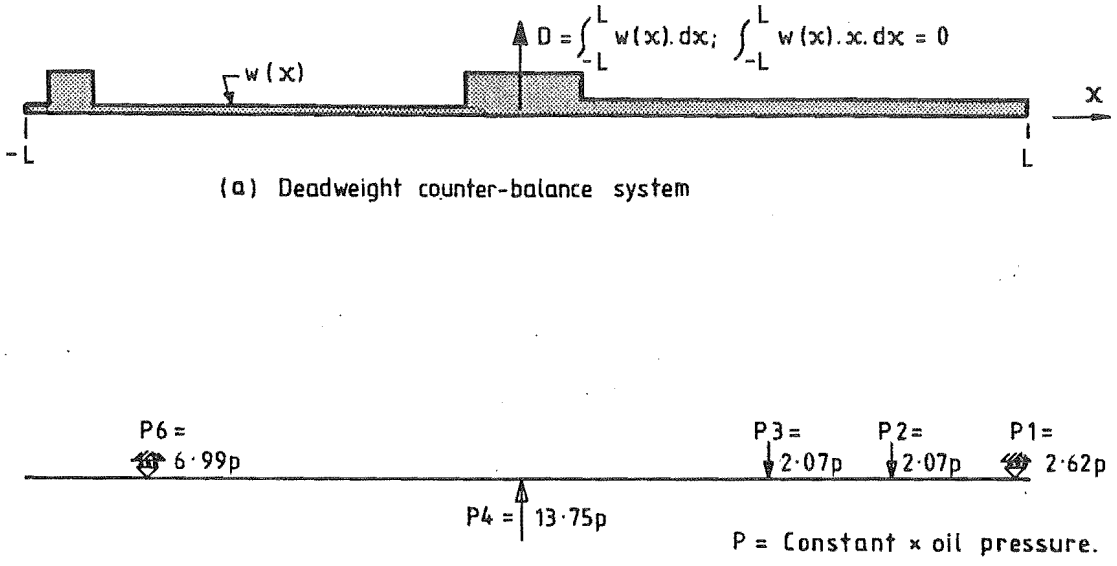

FIGURE 7.16 : LOAD APPLICATION

buckling was provided as in the original rig design. One further modification was to add a second jack (D) at F4 which was used to carry the dead weight of the specimen independently of the reversible lateral loading system.

7.5.10 Lateral Load Application

As indicated in Figure 7.16, the equipment applying lateral load to the frame-wall specimens was separated into two independent self-equilibrating systems.

7.5.10.1 Dead Weight Counterbalance

The full weight of the specimen and attached loading equipment was carried by a 100 kN hydraulic jack (D) acting at the central loading pin. This jack was supplied at constant pressure by a 70 MPa capacity Riehle testing machine, which ensured that the counterbalance for the dead weight was accurately maintained, irrespective of the specimen displacement or of other external loads acting.

Concrete weights were placed at the end of the steel truss to balance the specimen and truss so that the centre of gravity of the combined mass was aligned with the central loading pin. Thus the frame-wall assemblage cantilevered freely on one side and the truss and counterweights, on the other. The resulting cantilever moment induced at the base of the frame-wall assemblage was approximately 10% of the measured strength of the specimen. The effect of these self-weight lateral loads is discussed in the following section (7.5.10.2).

7.5.10.2 Superimposed Lateral Loads

The loading system used to apply the superimposed lateral loads is indicated in Figure 7.16b. In this case, the specimen was regarded as a weightless simply-supported beam with supports at P1 and P6 and active loading with jacks at P2, P3 and P4. Since all three jacks were connected to a common oil pressure system, the loads applied to the specimen were in theory statically determinate, with the oil pressure the only independent load variable. The jacks at

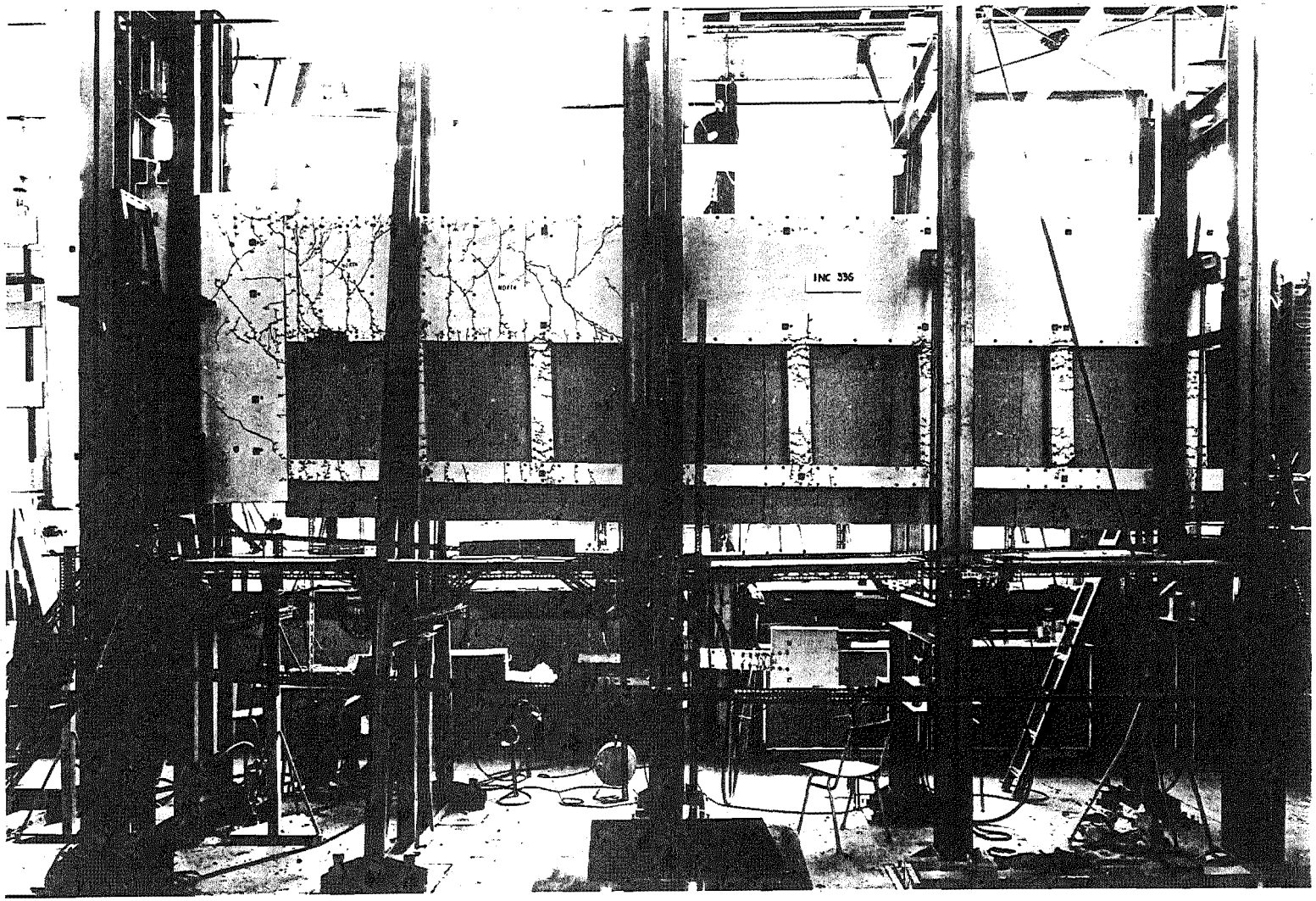

FIGURE 7.17 : TEST RIG WITH SPECIMEN IN POSITION (SPECIMEN FSW-1, AT PEAK OF LOAD REVERSAL 18)

P2 and P3 (1335 mm ram area) acted in the opposite direction to the larger jack at P4 (8871 mm^2 ram area). As a result, the rams of these jacks (P2 and P3) were forced to contract under increasing oil pressure and to extend under decreasing pressure. To reverse the direction of the superimposed loads, the three jacks were simply switched from below (as indicated in Figure 7.15) to above the specimen, or vice versa.

The ram areas of the jacks used should have resulted in a three point loading on the specimen proper of 1.267 p at level 7 (P1), and p at levels 5(P2) and 3(P3), where p = constant x oil pressure. This distribution of loads should have been maintained automatically irrespective of the load intensity (oil pressure). The real situation proved to be not so simple. Because of unexpectedly large internal friction forces in the jacks at P2 and P3, additional adjustments were necessary at each increment to achieve the desired load distribution. In order to reduce the extent of these adjustments, it was found more satisfactory to use a three point loading of P1 = P2 = P3. The effect of this on the specimen moments and shears is indicated in Figure 7.18.

As discussed in the preceding section (7.5.10.1), the self-weight of the wall, columns and beams contributed approximately 10% of the peak base moment. These self-weight loads only acted in one direction and were uniformly distributed over the height of the wall. As a result, the distribution of the net loading on the specimen varied depending on load intensity and direction, e.g., the base moment/shear ratios at peak positive and negative load differed by about 6% (±3% of the moment/shear ratio for the superimposed lateral loads). Although this will have had a small affect on the specimen responses, it was of little relevance to the evaluation of the responses as all test loads, including the self-weight forces, were modelled in the computer analyses.

7.5.11 Gravity Load Simulation

Gravity compression forces in the walls and columns were simulated by prestressing with unbonded cables which were tensioned by adjustable

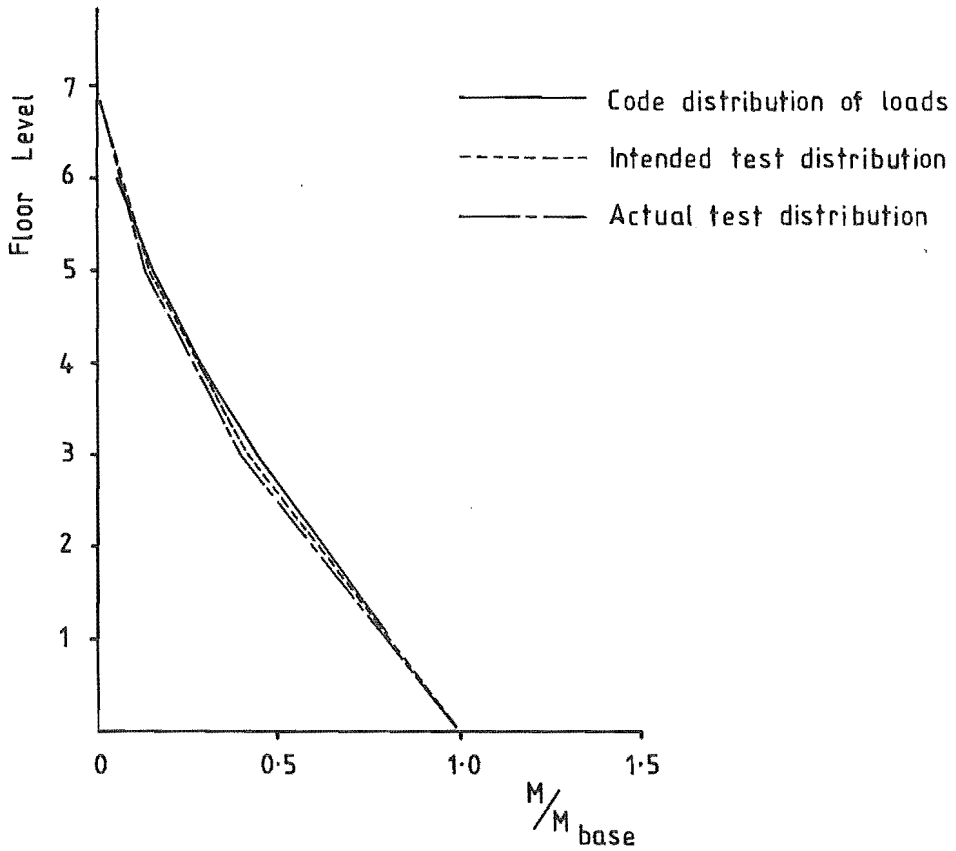

(a) Moment Distribution Up Height Of Specimen

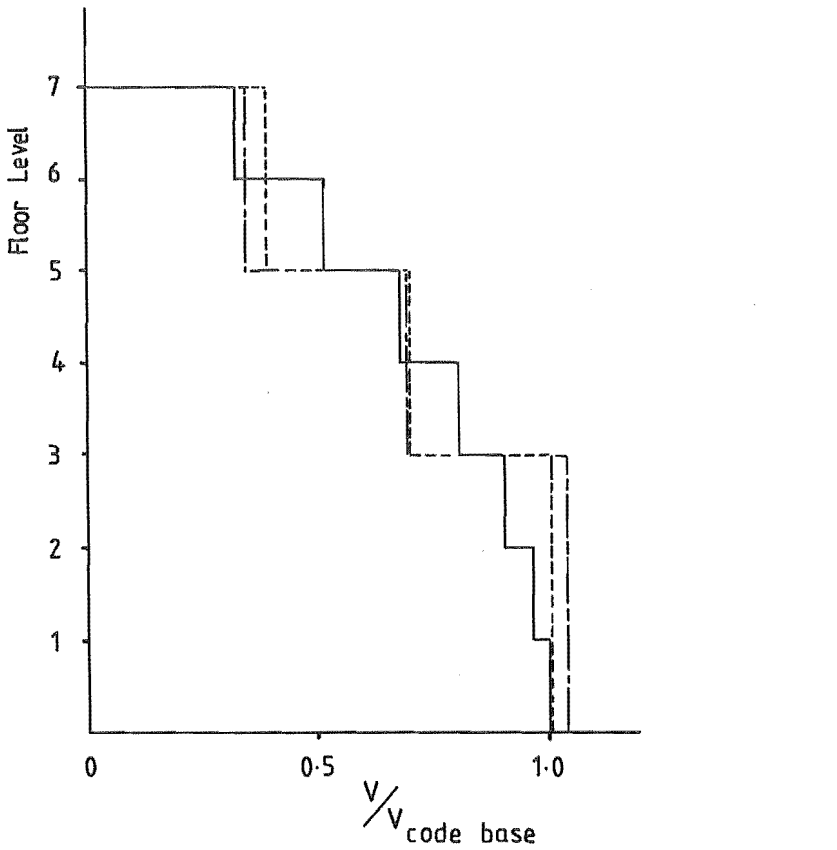

(b) Shear Force Distribution Up Height Of Specimen

FIGURE 7.18 : MOMENT AND SHEAR FORCE DISTRIBUTIONS FOR TEST SPECIMENS

screw jacks (Figure 7.15). The cables passed through ducts running along the wall and column centroids and were anchored at the far side of the base block. Prestress intensities of 1.38 MPa* in the walls and 4.14 MPa* in the columns were applied in both tests. These stress levels were intended to simulate the gravity compression stresses at the bases of the walls and columns and the jacks were regularly adjusted to ensure that these levels were maintained.

The main limitation of the prestressing arrangement was that the intensity of prestress was constant over the full height of the specimen. Varying the compression stresses with height would have been very difficult regardless of the type of loading device used, and in this case, the excess compression in the upper storey regions was of little significance as these regions were designed to remain elastic.

The prestressing system did not (and was not intended to) model P-Δ effects. The net P-Δ forces (i.e., the initial stress components, Section 2.4.3) are mathematically uncoupled from the material responses and can therefore be treated independently. Special gravity load simulators have been used previously to model the P-Δ effect directly. However, this offers no advantage over separate treatment. Moreover, simply applying the vertical loads in a manner which induces P-Δ forces would not model the usual situation, since the distributions of vertical and lateral load resistance are normally different, e.g., P-Δ forces resulting from the axial loads carried by columns as well as walls, have to be resisted predominantly by the walls.

No attempt was made to model gravity loading on the beams. The beams in the specimens were comparatively short and the theoretical gravity load end moments were only 2% to 3% of the moments induced by the lateral loading.

7.5.12 Instrumentation and Measurements

The following measurements were made during the tests on the frame-wall specimens:

---

* Based on gross concrete section.

(a) Loading

All lateral loads applied to the specimens were measured using Philips load cells coupled with manually operated Budd strain bridges. The load cells were located as shown in Figure 7.15, and the readings obtained were checked for equilibrium at each increment. Calibration tests were made on the load cells and strain bridges before and after each specimen was tested and these indicated that the error in the load readings should generally have been less than 0.5% of the maximum applied load.

(b) Reinforcing Bar Strains

As shown in Figure 7.19, the reinforcing bar strains were measured over an extensive network of sampling points. Demec mechanical strain gauges were used and the bar strains at each of the sampling points were measured on both sides of the specimens and then averaged.

The data obtained from these measurements were used to determine the following information:

(i) Steel strains in the beam, column and wall flexural reinforcement and in the wall shear reinforcement.

(ii) Section curvatures and elongations at various points in the beams, columns and walls.

(iii) Flexural components of the deflection and rotation of the wall at each floor level.

(iv) Total elongation of wall at each floor level.

(v) Component of top floor deflection due to deformations within the wall anchorage zone.

(c) Rotation and Deflection Measurements

The vertical and horizontal displacements of a series of grid points established on one side of the test specimens were measured using a Zeiss 010 single second microptic theodilite. In places, the line of sight between the theodolite and a grid point was obstructed by the test rig and the theodolite target had to be slightly offset. The displacements of these grid

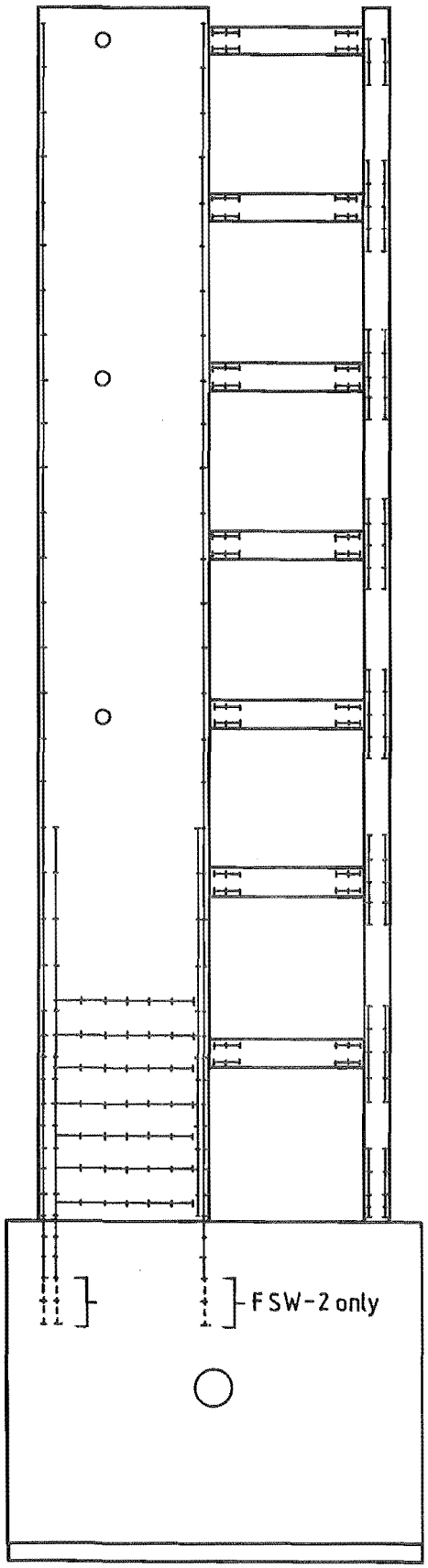

Note: 1 All gauges on both sides of speciman.
2 All gauges measure steel strains

FIGURE 7.19 : STRAIN GAUGE LOCATIONS IN FRAME-WALL SPECIMENS

points were estimated by interpolation. Figure 7.20 shows the location of the targets and grid points.

The grid displacements obtained from these readings were used to determine the following information:

(i) Member elongations and rotations (beams, columns and walls).

(ii) Wall and column displacements and inter-storey drifts.

(iii) Shear component of wall deflection at each floor level.

The displacements derived from the theodolite readings were accurate to approximately 0.2 mm, except for the column and wall lateral deflections where the accuracy ranged from approximately 0.2 mm at level 1 to 0.5 mm at level 7.

The wall shear displacements were calculated from the theodolite measurements of wall displacement and rotation assuming that the curvature was uniform between adjacent pairs of grid points (i.e., uniform over each storey height). The assumption of uniform curvature introduced significant errors into the calculated shear displacements for level 0-1. This was because the rotation at level 0 due to anchorage deformation was not separately measured with the theodolite and also, after yielding, the curvature in the base region was usually far from uniform. An alternative estimate for the wall shear deformation was therefore obtained by subtracting the flexural component of deflection computed from the strain readings from the total deflections measured with the theodolite.

The main advantage of the theodolite measurements was that it was possible to trace both vertical and horizontal displacements of the grid points without obstructing access to the specimen. However, the readings were very time consuming and because of this, the frequency with which readings could be taken had to be limited. To obtain a more detailed record of the lateral deflections, additional readings were taken with dial gauges set up at levels 3, 5 and 7 (Figure 7.20).

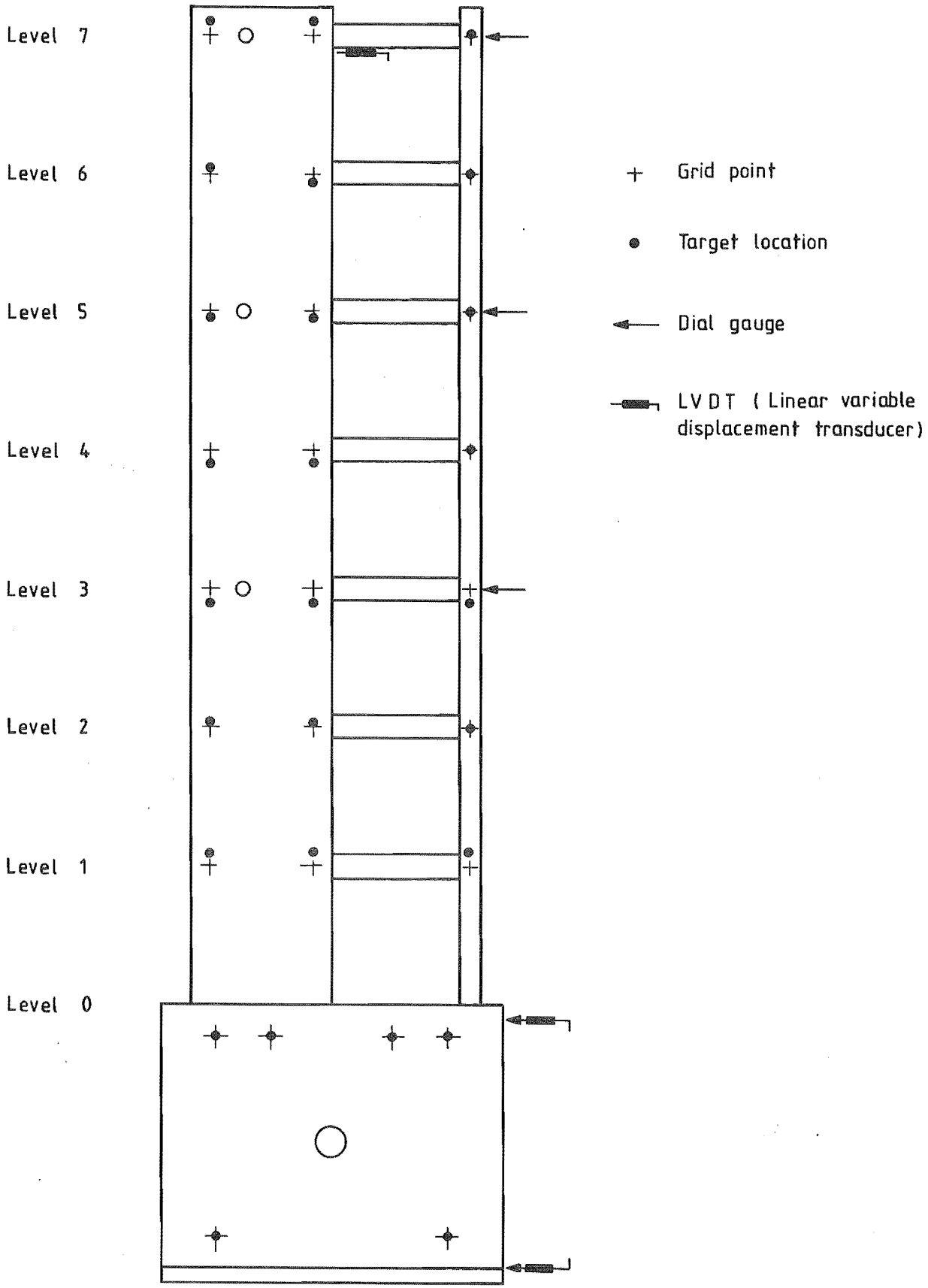

FIGURE 7.20 : LOCATION OF THEODOLITE TARGETS, DIAL GAUGES AND LVDT'S, FOR FRAME-WALL SPECIMENS

(d) Crack Observations

Cracks were located and their development followed with the aid of magnifying glasses. The propogation of the cracks was marked on the specimen and photographed at regular intervals. No systematic measurement of crack widths was attempted, although occasional records were made of both the width and shear slip along a few major cracks.

(e) Load-deflection Control During Test

During the tests a Hewlett-Packard X-Y pen recorder was used to plot a continuous record of the base moment - top floor deflection relationship. The input for the base moment was obtained from the 100 kN load cell reacting against the steel truss at P6 (Figure 7.15). To obtain the input for the top floor deflection, the outputs from three displacement transducers (Figure 7.20) were passed through a simple resistance circuit before being fed to the X-Y recorder. The graphical output obtained was used to observe the general response characteristics and to aid control of the loading during the test.

7.5.13 Test Procedure

Immediately prior to the first load increment, all steel strain, dial gauge and theodolite readings were taken several times to establish their "zero" values. During the tests, the response of the specimen was followed on the X-Y recorder to aid the selection of load increment intervals. After applying a load increment, measurements were generally taken in the following sequence.

At each load increment:

(a) Check gravity load balance and prestressing forces. Adjust if necessary.

(b) Read all load cells and record.

(c) Read all dial gauges and record.

(d) Record time and temperature

At specific load increments: (Note 1)

(e) Record beam strains. (Note 2)

(f) Record column strains.

(g) Record strains in wall flexural reinforcement (102 mm gauges).

(h) Record stirrup strains in wall plastic hinge zones.

(i) Record strains in wall flexural reinforcement (203 mm gauges).

(j) Read bearings and altitudes to the specimen targets with theodolite and record. (Note 3)

(k) Locate and mark cracks. Take photographs if required.

(l) Re-read dial gauges and record.

(m) Record time.

NOTES

(1) Not all readings (e) to (m) were taken with the same frequency.

(2) All strain gauges were read on a standard bar and a temperature control block before and after use.

(3) The bearings and altitudes of three fixed targets located around the laboratory were checked before and after the targets on the specimen were read. These checks indicated that the theodolite moved insignificantly during each test, and consequently these readings were disregarded in the displacement calculations.

7.6 IDEALIZATION OF SPECIMENS FOR COMPUTER ANALYSES

Analytic comparisons were made for all specimens except the second beam-wall unit, TB2, which failed prematurely (Section 8.2.2). This section describes the basic idealizations and model parameters used in the analyses and discusses various aspects related to the models adopted.

Results from the analyses are compared with the corresponding observed responses in Chapters 8 and 9.

Except as specifically noted in this section, all primary steel and concrete model parameters were based on the measured properties of the materials used to construct the specimens. Also, in all cases, the modelled load reversal force* and displacement** limits were matched to the corresponding observed values. For the beam-wall specimens, the forces and displacements at the free ends of the beams were used for load control while for the frame-wall specimens, load control was based on the base moment and the wall displacement at Level 7.

7.6.1 Specimen TB1

A large number of analyses were performed on this specimen. Most of these analyses were for evaluating the mesh refinement characteristics of the computer program (Section 6.2.2) or for calibrating the inelastic shear model (Section 5.5). Only four of the analyses of the full specimen are specifically considered in Chapter 8. These are:

(a) TB1/EV00-I; inelastic shear model with no allowance for inclined cracking ($e_v = 0$),

(b) TB1/EV05-I; inelastic shear model with $e_v = 0.5$ jd,

(c) TB1/EV00-E; elastic shear model with no allowance for inclined cracking ($e_v = 0$),

(d) TB1/EV05-E; elastic shear model with $e_v = 0.5$ jd,

where e_v is the parameter modelling the effect of inclined cracking on the strains induced in the flexural reinforcement (see Section 2.2.4).

The basic specimen idealization and model parameters used in the above analyses are shown in Figure 7.21 and Table 7.7. As indicated, the beam segmentation was based on the gauge layout used for the steel strain readings. This was done to permit comparison of the observed

---

* For load reversals below yield intensity.
** For post-elastic load reversals.

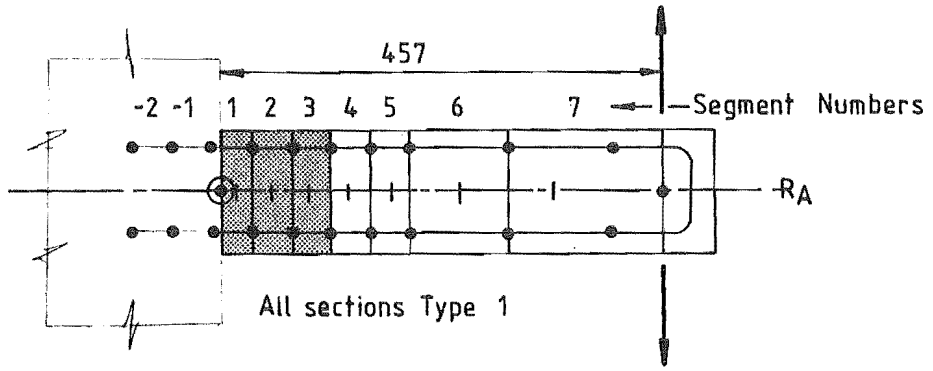

Member Representation

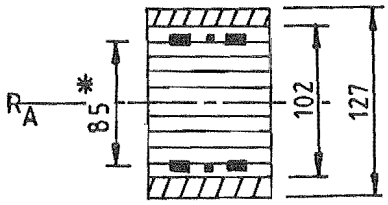

Type 1 Section

Concrete layers for fully inelastic section model. No layering for elastic cracked concrete model.

Modelled concrete and shear parameters given in Table 7.7.

Notation

Fully inelastic section model.

Elastic cracked concrete section model.

Core concrete layer (10 equal size layers per section.)

Cover concrete layer, $\epsilon_{cr} = -0{\cdot}004$

Type 1 steel : $A_s = 32\ mm^2$, $E_o = 199$ GPa, $f_y = 380$ MPa

Type 2 steel $A_s = 143\ mm^2$, $E_o = 208$ GPa, $f_y = 307$ MPa

* Average centre - centre bar spacing measured from photographs of the specimen.

○ Anchorage subelement : $\ell_a = 152$ mm, $\phi_{pa} = 0{\cdot}3$ (Section 2.2.3.3)

Strain gauge locations on beam flexural bars.

FIGURE 7.21 : IDEALIZATION OF SPECIMEN TB1 FOR COMPUTER ANALYSIS

and predicted curvature distributions. It would not normally be necessary to use as many segments to adequately model this type of beam.

The shear model parameters used for the first two analyses were calibrated using the observed responses of TB1 and three beams tested by Celebi and Penzien (Section 6.3). Also, the anchorage model constants ϕ_{pa} and ℓ_a were based on the average measured anchorage deformations in the three beam-wall specimens TB1, TB3 and TB4. The same values were used for these two parameters in the analyses of all three specimens.

In addition to the analyses of the full specimen, analyses were also performed on individual segments in the plastic hinge zone in order to match the observed curvature limits for each load reversal. In these analyses, the segments were treated as short cantilevers with both moment and shear applied at the free ends. Both flexural and shear deformations were modelled using the same model parameters as were used in the analyses of the full specimen. Results for both inelastic and elastic shear model analyses are given in Sections 8.4 and 8.5 for the No. 3 segment shown in Figure 7.21.

TABLE 7.7 : CONCRETE AND SHEAR MODEL PARAMETERS USED FOR ANALYSES OF TB1

Fully Inelastic Section Model

E_c = 36.8 GPa, f'_c = 53 MPa, f'_t = 5.5 MPa
Cover concrete crushing strain, ϵ_{cr} = -0.004

K_{int} = 0.207 MPa, ϕ_{xv} = 0.8, ϕ_g = 0.12
(Refer Chapter 5 for definition of terms)

Elastic Cracked Section Model

E_c = 36.8 GPa, f'_t = 3.7 MPa

TABLE 7.8 : CONCRETE AND SHEAR MODEL PARAMETERS USED FOR ANALYSES OF TB3 AND TB4

Sections Modelled for Inelastic Flexural Deformations

TB3: E_c = 38.5 GPa, f'_c = 57.6 MPa, f'_t = 6.2 MPa

TB4: E_c = 37.3 GPa, f'_c = 54.0 MPa, f'_t = 4.8 MPa

For both specimens cover concrete crushing strain, ε_{cr} = -0.004.

Elastic Cracked Concrete Section Model, Both Specimens

E_c = 38.5 GPa, f'_t = 6.2 MPa

7.6.2 Specimens TB3 and TB4

The basic specimen idealization and model parameters for these specimens are shown in Figure 7.22 and Table 8.8.

The main problem encountered in analysing these specimens was in modelling the part of the lap splice between the diagonal and the parallel flexural reinforcement which extended into the plastic hinge zone. The lap extended part way into No. 1 segment (Figure 7.23) whereas, during the tests, significant yielding in the diagonal bars penetrated as far as No. 3 segment. The parallel bars were only lightly stressed over this region of the lap. As a result, there were large differences between the strains in the diagonal and parallel bars within the No. 1 to No. 3 segments. This could not be directly modelled as the section analysis procedures in the computer program assume linear strain distributions over the depth of the section and no provision was made for modelling slip between reinforcing bars and the surrounding concrete.

In an attempt to overcome this deficiency in the computer program, the analyses were performed with reduced values of E_o and f_y for the parallel reinforcement in the No. 2 and No. 3 segments, and the contribution of the parallel bars extending into the No. 1 segments was ignored. The rationale for this approach was that this would allow the development of large curvatures corresponding to yielding in the diagonal bars, but would restrict the forces developed in the tension bars.

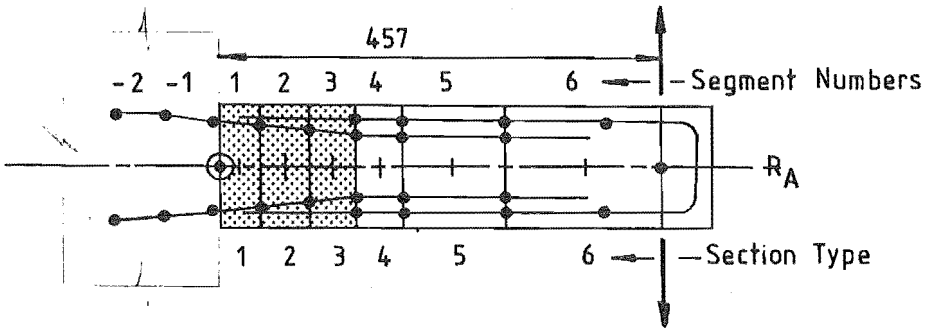

Member Representation

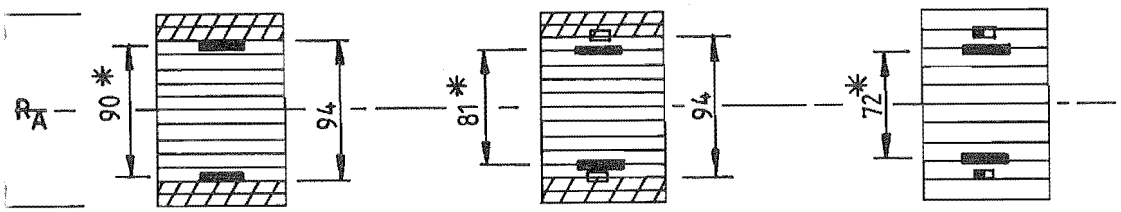

Type 1 Section Type 2 Section Type 3 Section

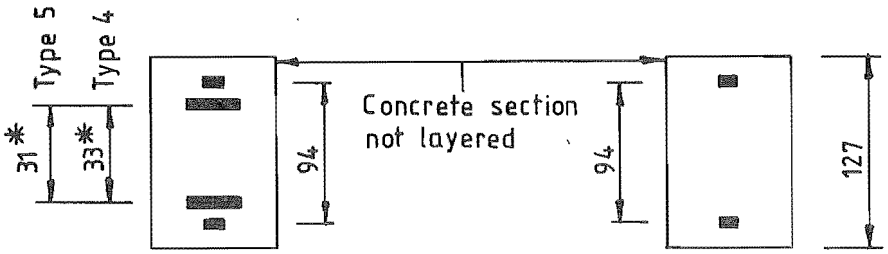

Type 4 & 5 Sections Type 6 Section

Notation

Inelastic flexural deformation only.

Type 1 steel : $A_s = 143\,mm^2$, $E_0 = 210$ GPa, $f_y = 299$ MPa

Type 2 steel : $A_s = 32\,mm^2$, $E_0 = 208$ GPa, $f_y = 366$ MPa

Type 3 steel : $A_s = 32\,mm^2$, $E_0 = 21$ GPa, $f_y = 73$ MPa

Type 4 steel : $A_s = 32\,mm^2$, $E_0 = 69$ GPa, $f_y = 366$ MPa

* Centre-centre bar spacing for TB 3 measured from photographs of specimen. TB 4 values slightly different.

Other notation as for TB 1, Figure 7.21

FIGURE 7.22 : IDEALIZATION OF SPECIMENS TB3 AND TB4 FOR COMPUTER ANALYSIS

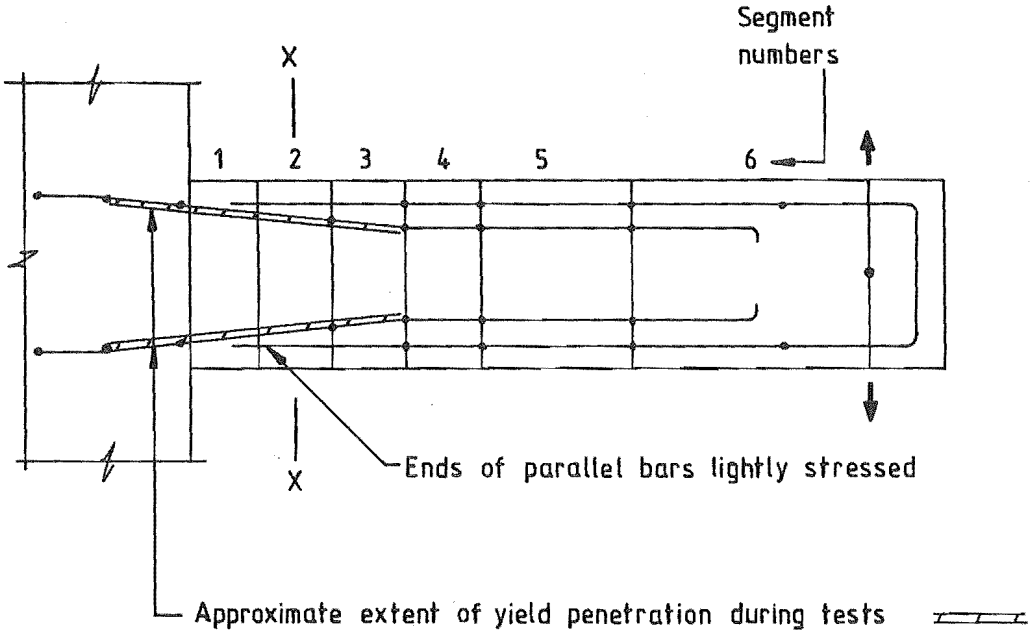

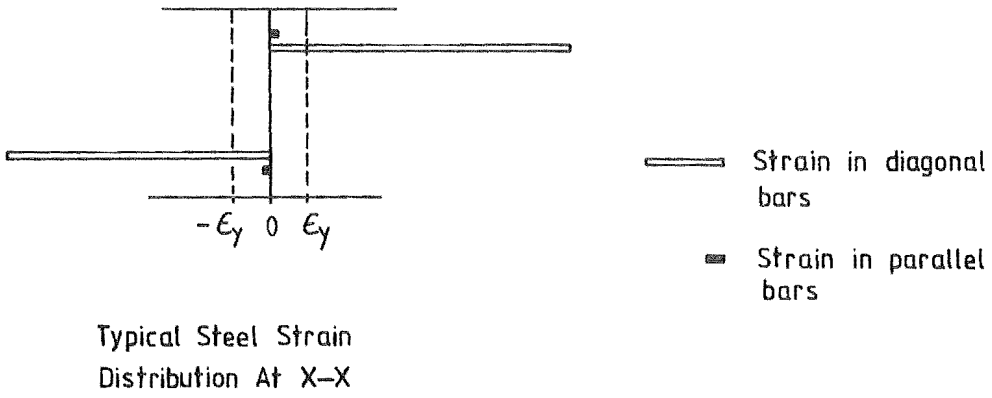

Typical Steel Strain Distribution At X–X

FIGURE 7.23 : EFFECT OF YIELD PENETRATION ON SECTION STRAIN DISTRIBUTION IN REGION OF LAP BETWEEN DIAGONAL AND PARALLEL BARS IN TB3 AND TB4

Trial analyses were performed for TB3 with several different reduction factors, but none of these were completely successful in modelling the observed behaviour. The reduced values of elastic modulus and yield stress used for computing the predicted responses presented in Chapter 8 were 0.1 E_o and 0.2 f_y respectively for the segment No. 2 and 0.33 E_o and f_y respectively for segment No. 3. These values were also adopted for specimen TB4. For both specimens, yielding was predicted in the No. 1 and No. 2 segments, but not in the No. 3 segments.

No allowance was made for inclined cracking in these specimens as the shear rigidity of the diagonal bars ensured that the cracks remained roughly perpendicular to the beam axes.

7.6.3 Specimen FSW-1

Results from a total of six analyses of this specimen are presented in Chapter 9. The analyses concerned are designated as follows:

(a) FSW1/EV00; inelastic shear model with no allowance for inclined cracking ($e_v = 0$), load reversals LR5 to LR19 analysed with force increments of approximately 56 kNm ($\simeq$ 0.18 times the specimen yield strength) and displacement increments of 25 mm (i.e. δ_{7y}, see Figure 9.2). Tensile strength of the concrete was taken as $f'_t = 0.6\sqrt{f'_c} \simeq 3.7$ MPa.

(b) FSW1/EV05; allowance for inclined cracking ($e_v = 0.5$ jd) in the wall and beams only, otherwise as for (a).

(c) FSW1/EV00-S; as for (a), but with the size of the force and displacement increments reduced to 40% of those used in (a) and analysed for load reversals LR5 to LR7 only.

(d) FSW1/EV05-S; as for (b), but with modifications as in (c).

(e) FSW1/EV00-OT; as for (a), except $f'_t = 0$ for column segments and analysed for load reversals LR5 to LR10 only.

(f) FSW1/EV00-EL; as for (a), but with elastic shear model and analysed for load reversals LR3 to LR10.

The structural idealizations and the values of the main model parameters used in the above analyses are shown in Figures 7.24 and 7.25, and in Table 7.9. As for the beam-wall specimens, the member segmentation was based on the gauge layout used for steel strain measurement and was generally more refined than would be necessary for normal use.

In the case of the beam and column members, the segmentation was designed to match exactly the strain gauge locations, except at the column gauge locations which were partly within the beam-column joint regions. For the purpose of analysis, it was necessary to model the joint regions as rigid end blocks with appropriate allowances for anchorage deformation to model strains in the column reinforcement passing through the joints. The end blocks used extended from the beam centrelines to the beam flexural reinforcement (approximately 51 mm) and as a result the modelled end segments of the column members were only half the length of the strain gauges in the joint regions. The analytic results could still be compared with the deformations measured at these gauge locations by combining the predicted end segment and anchorage rotations. However, the large variation in moments over these regions (i.e., normally full moment reversal between the top and bottom of the joints) and the different mechanisms involved (part column, part joint region) would limit the value of the comparisons.

The shortest wall segments used were one-fifth of the length of the wall. No attempt was made to use shorter segments to match exactly the strain gauge locations. The level of representation obtained was quite adequate for the requirements of this investigation and further refinement would have increased the risk of solution instability (Section 6.6.2) and of problems with modelling concrete spalling (Section 6.2.3). Above Level 4, full storey height segments were used as this region remained virtually crack free in the test.

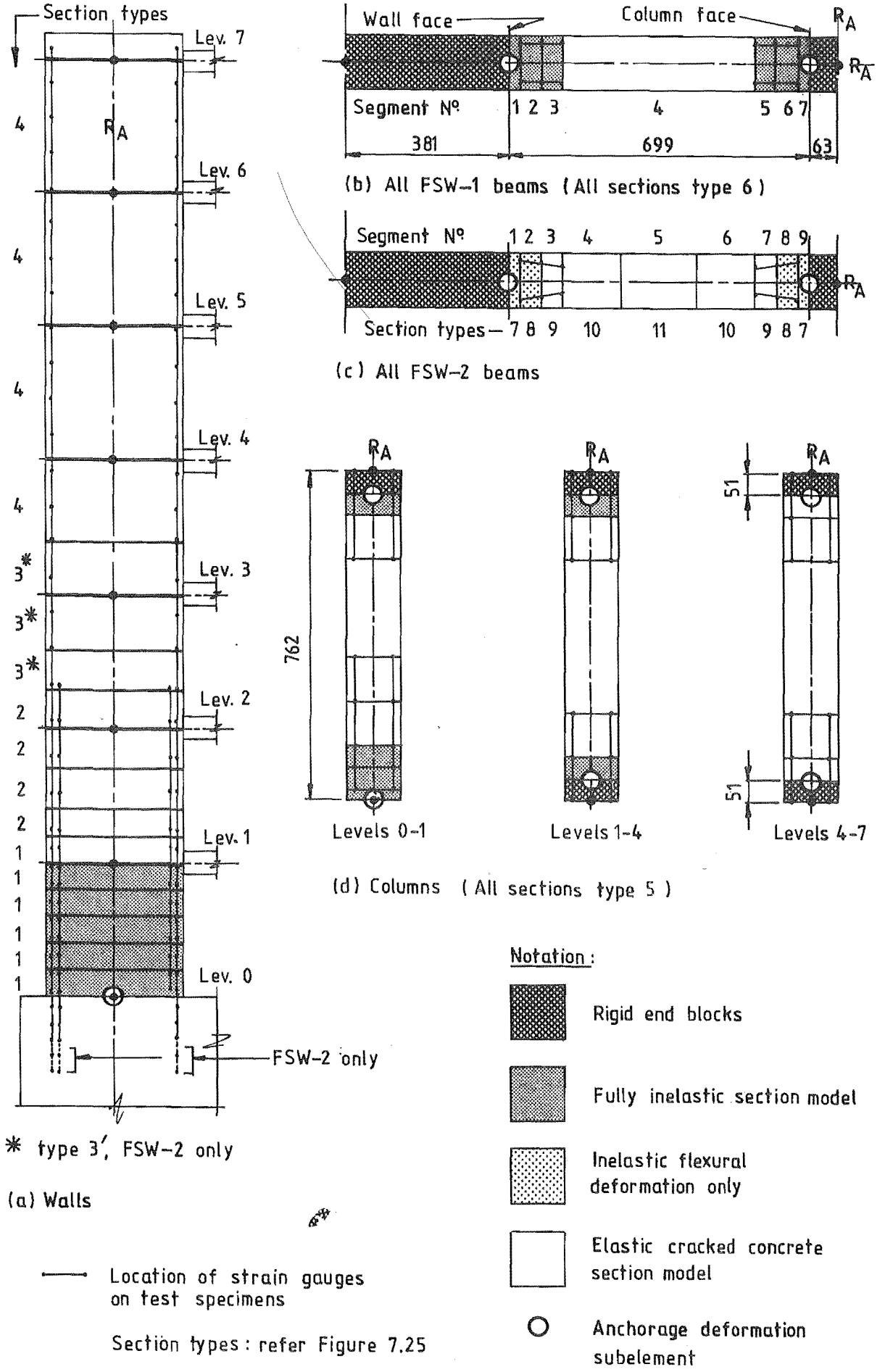

FIGURE 7.24 : MEMBER SEGMENTATION OF FRAME-WALL SPECIMENS FOR COMPUTER ANALYSIS

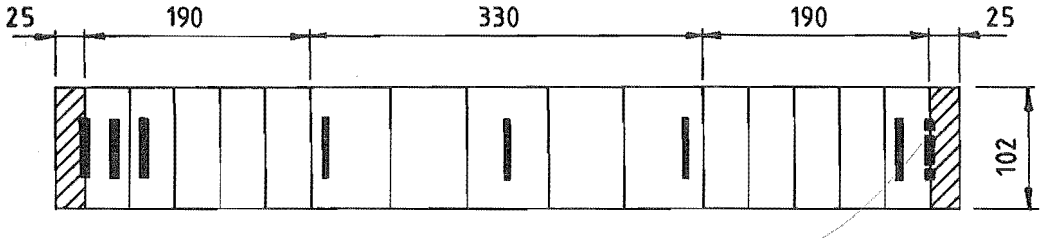

Type 1 Section (Walls)

Properties for type (□) bars substituted for type (○) bars
(Refer Table 7.3 for bar type notation.)

Type 2 to 4 Sections (Walls)

Overall geometry as above, but concrete not layered. Bar areas reduced according to cutoff points indicated in Figure 7.9

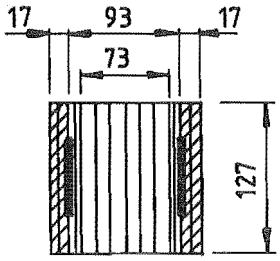

Type 5 Section (Columns)

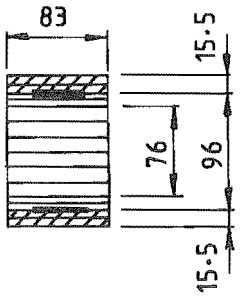

Type 6 Section (FSW-1 Beams)

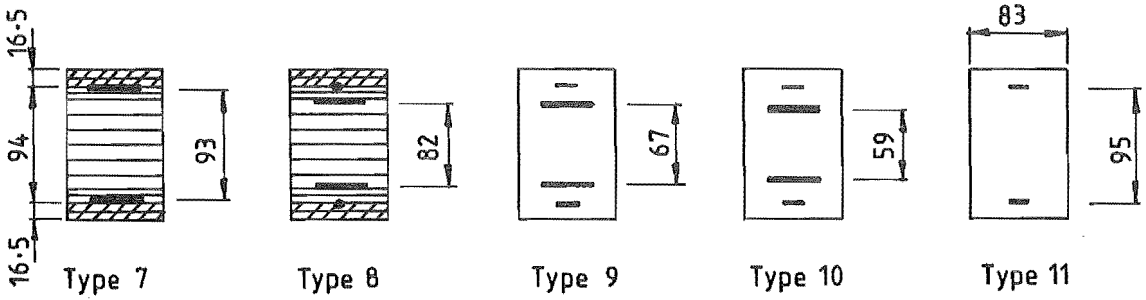

Type 7 Type 8 Type 9 Type 10 Type 11

• Only one tenth of actual bar area allowed for at this location. (Type 8)

Type 7 to 11 Sections (FSW-2 Beams)

Bar areas refer Figs. 7.9 and 7.10. Bar properties refer Table 7.3.

Cover concrete layer, crushing strain -0·004.

Core concrete layer.

Note : Concrete layered only for inelastic segment locations.

FIGURE 7.25 : SECTION TYPES FOR MODELLING SPECIMENS FSW-1 AND FSW-2 (REFER FIGURE 7.24)

TABLE 7.9 : MODEL PARAMETERS USED FOR ANALYSES OF THE FRAME-WALL SPECIMENS

(a) Specimen FSW-1

Concrete properties: E_c = 28.5 GPa, f'_c = 37.0 MPa

Inelastic shear model: K_{int} = 0.207 MPa, ϕ_{xv} = 0.8, ϕ_g = 0.12 (Refer Chapter 5 for definition of terms)

Anchorage model, (Section 2.2.3)

Beams: ℓ_a (wall end) = 152 mm, ℓ_a (column end) = 127 mm, ϕ_{pa} = 0.3

Wall base: ℓ_a = 508 mm, ϕ_{pa} = 0.17

Column base: ℓ_a = 114 mm, ϕ_{pa} = 0.3

Column ends at beam-column joints: ℓ_a = 51 mm, ϕ_{pa} = 0.3

(b) Specimen FSW-2

Concrete properties: E_c = 26.7 GPa, f'_c = 39.3 MPa

Inelastic shear model: as for FSW-1 (wall and columns only)

Elastic shear model (beams): yielding segments, G = 0.08E
elastic segments, G = 0.12E

Anchorage model: as for FSW-1

The inelastic shear model parameters used were the same as those used for specimen TB1 (Section 7.6.1) and were not specifically calibrated for FSW-1. The same values were used for modelling all beam, wall and column plastic hinge zones.

Values for the anchorage model parameters for the walls were calibrated (approximately) against the average deformations measured in the wall anchorage regions in both FSW-1 and FSW-2. The same values were used for the analyses of both specimens. In the case of the beams (Levels 1 to 7), the values used for the anchorage parameters were based on the results from the beam-wall specimens, except that the anchorage length (ℓ_a) at the column end was reduced slightly in acknowledgement of the better anchorage conditions at that end (Figures 7.10 and 7.13). A similar approach was adopted for the anchorage at the base of the column, but in this case the anchorage length was reduced to 75% of the value used at the wall end of the beams. This reduction was made because of the proximity of heavy base block reinforcing bars running parallel to the anchored column reinforcement. At other locations in the columns, i.e., at the beam-column joints, the anchorage lengths were simply taken as half the modelled beam-column joint length. Apart from limited yielding in the vicinity of the bottom two joints, the column bars at these locations remained elastic.

One problem that was experienced in these analyses was in determining the steel area reduction factors to account for the effect of inclined cracking of the beams in the EV05 analyses. These reduction factors are dependant on the member shear spans (Section 2.2.4) which, in non-linear indeterminate structures such as FSW-1, vary with the loading. In the first attempt at these analyses, the shear span was simply taken as half the clear span of the beams. This decision was based on the assumption that the critical loads on the non-yielding segments would be governed by the peak moments developed at the ends of the beams and that, after yielding, the moments at the two ends of each beam would be approximately equal. Also, the results from the EV00 analyses showed that, because yielding softened the beam plastic hinge zones relative

to the columns, the point of contraflexure remained very close to the centre of the beams at high load intensities in the second and subsequent post-elastic load reversals. However, it was found that use of this value, i.e., half the clear span, resulted in yielding being predicted to occur in the No. 2 segments in some beams before in the No. 1 segments. The reason for this was that, just prior to yield in the first post-elastic load reversal, the moments were up to 20% higher at the wall ends of the beams than at the column ends. This resulted in premature yield in the No. 2 segments because the effective shear span was larger than had been allowed for.
The shear span used for computing the reduction factors for the wall ends of the beams were therefore increased by 51 mm (14.5% increase). This was larger than maximum shear spans predicted just before yielding of the beams, and was sufficient to prevent premature yielding of the No. 2 segments.

In the case of the wall, the shear spans used for calculating the reduction factors were based on the maximum shear spans predicted in the EV00 analyses. These gave satisfactory results.

7.6.4 Specimen FSW-2

Four analyses of this specimen are considered in Chapter 9. These are designated as follows:

(a) FSW2/EV00; inelastic shear model (wall and column plastic hinge zones only) with no allowance for inclined cracking ($e_v = 0$), load reversals LR5 to LR17 analysed with force increments of approximately 56 kNm and displacement increments of 25 mm (cf. yield load and displacement, Figure 9.2). $f'_t = 3.5$ MPa ($\simeq 0.6\sqrt{f'_c}$).

(b) FSW2/EV05; allowance for inclined cracking ($e_v = 0.5$ jd) in wall only, otherwise as for (a).

(c) FSW2/EV05-S; as for (b), but with the size of force and displacement increments reduced to 40% of those used in (b), LR5 to LR7 only.

(d) FSW2/EV00-FR; as for (a), except f'_t = 6.1 MPa* = f_r and analysed for load reversals LR5 to LR10 only (* measured rupture strength).

The structural idealizations and the values of the model parameters used were basically the same as for FSW-1, except for modelling of the beams and differences in steel and concrete properties between the specimens (Figures 7.24 and 7.25, and Table 7.9). The anchorage and shear model parameters were the same as those used for the analyses of specimen FSW-1.

Modelling of the beams was based on the analyses of specimens TB3 and TB4 except that, for the second to end segments (No. 2 and No. 8), the area of the parallel bars, rather than the steel elastic modulus, was reduced by a factor of 10 (cf. Figures 7.22 and 7.25). Also, it was apparent, from the results for the beam-wall specimens (TB3 and TB4), that the model would not predict yielding in the third to end segments (No. 3 and No. 7). These were therefore modelled as elastic** segments and no reduction was made in the properties of the parallel bars in them. A check made on the curvatures predicted in the analyses confirmed that yielding would not have been predicted for these segments, even if an inelastic section model had been used.

** Elastic cracked concrete section model.

8. BEAM-WALL SPECIMEN TESTS

SUMMARY

This chapter presents the experimental results for the four isolated beam-wall speciments. To facilitate evaluation of the responses, comparisons are made with the corresponding responses predicted using the theoretical model described in Chapters 2 to 5. Details of the test specimens and the analysis parameters have been given in Chapter 7.

8.1 APPLIED LOADING

The force and displacement loading sequences applied to the four beam-wall specimens are shown in Figure 8.1. For the purpose of discussion in this chapter, these load sequences are subdivided into four categories of load reversals:

(a) pre-yield load reversals;
(b) moderate - displacement load reversals, DF = 1 to 3;
(c) large - displacement load reversals, DF = 3 to 8; and
(d) very large - displacement load reversals, DF > 8

where DF is the member Ductility Factor as defined in Figure 8.2*. Although the above subdivisions are somewhat arbitrary, the upper limit given for the large displacement load reversals is intended to reflect the maximum level of plastic deformation that this type of beam would normally be expected to sustain more than once during a severe earthquake.

---

* The definition of Ductility Factor adopted here follows that commonly used in research work. However, it should be recognised that this is different from the definition usually applying to reinforced concrete design. The yield displacement inferred in most design codes relates to the dependable strength P_{dep}, computed from the nominal material properties with a strength reduction factor of $\phi = 0.9$ for flexure. If the yield displacements had been based on this value rather than on P_i' (see Figure 8.2), the nominal values of Ductility Factor would have been approximately 30% higher. For example, under this latter definition, the Ductility Factors for the large displacement load reversals range from DF = 4 to 10.5.

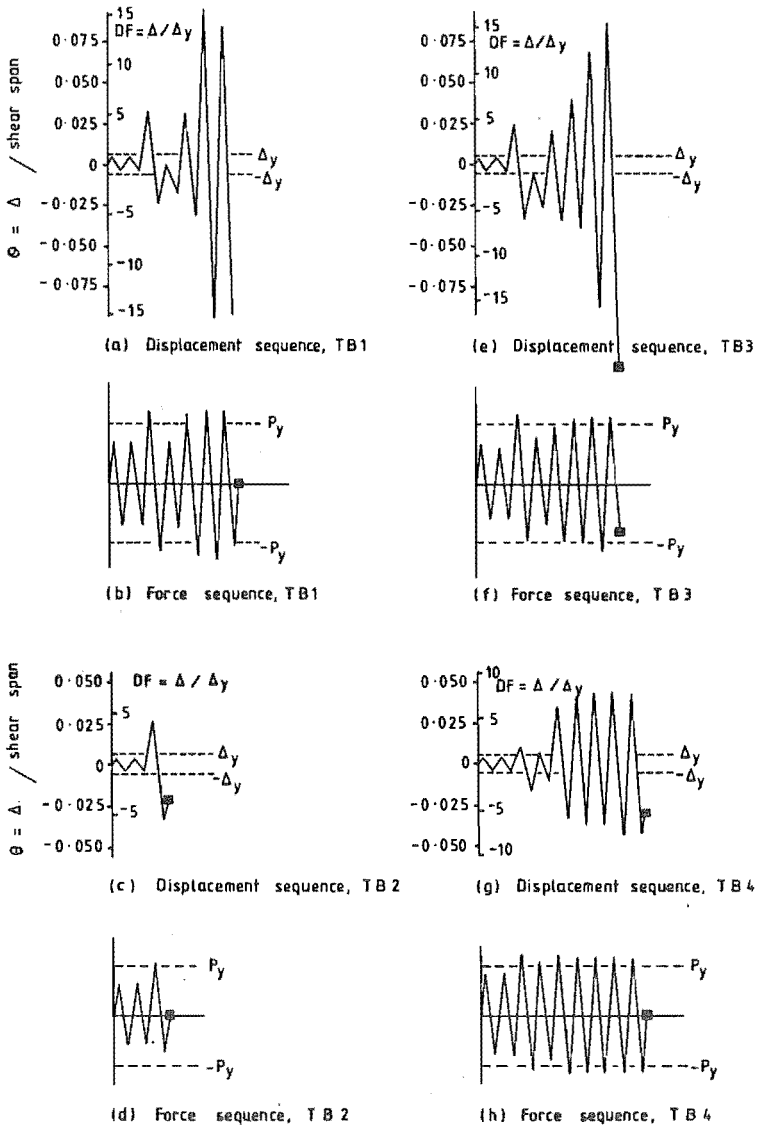

FIGURE 8.1 : LOADING SEQUENCES USED FOR THE BEAM-WALL SPECIMENS

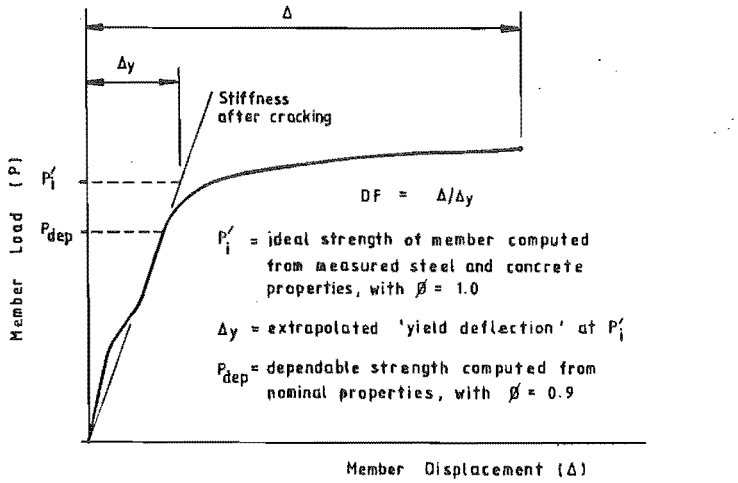

FIGURE 8.2 : DEFINITION OF DUCTILITY FACTOR, DF

As indicated in Figure 8.1, all four specimens were subjected to four load reversals to approximately 70% of their yield strength before being loaded past yield. The subsequent post-yield loading applied to the specimens is discussed below.

(a) The loading sequences for specimens TB1 and TB3 were similar, except that TB3 was subjected to two more large displacement load reversals. Both specimens were subjected to an initial large-displacement load cycle followed by two load reversals to 0.7 - 0.85 times yield strength. This was followed by two (four in the case of TB3) further large-displacement load reversals. Finally, four very large-displacement load reversals were imposed on the specimens in order to observe their behaviour under extreme conditions. The beam deflections were monitored throughout the test. The strains in the reinforcing bars were measured until the range of the gauges was exceeded at the start of the very large-displacement load reversals (maximum strain reading approximately 0.05).

(b) Specimen TB2 was to be subjected to a load sequence similar to that used for TB1. However, because of premature bond failure of the beam reinforcement anchored in the wall block, the loading was terminated after only two post-yield load reversals had been imposed.

(c) Specimen TB4 was subjected to four moderate-displacement load reversals, followed by ten large-displacement load reversals, with a maximum member ductility of approximately ±8. This loading sequence was chosen to provide information on the behaviour of the specimen when subjected to repeated moderate-to-large displacement load reversals. The specimen was not loaded to failure. To reduce the time required for testing this specimen, the bar strains were measured only at the peaks of load reversals 1 and 2 (LR1 and LR2) and during four post-yield load reversals (LR11 to LR14). The beam deflections were measured during all load reversals.

8.2 LOAD-DEFLECTION RESPONSES

Load-deflection responses for the four specimens are shown in Figures 8.3, 8 8.6 and 8.8. The observed values for end deflection were extrapolated from the dial gauge readings in order to obtain the deflection at the load point on the beams (Section 7.4.5). Both the observed and predicted deflections include components due to deformations within the beam anchorage zones.

Details of the model parameters used for computing the theoretical responses have been given in Section 7.6. Only the values of parameters that are relevant to the discussion, or are otherwise important, are referred to here.

8.2.1 Specimen TB1

Three predicted responses are given for this specimen in order to illustrate the effects of various shear parameters. The analyses differed only in the type of shear deformation modelled in the hinge zone (i.e., inelastic sliding shear or elastic shear deformation), and in the allowance made for inclined cracking, e_v. The specific cases modelled in the three analyses are as follows; inelastic sliding shear deformation with $e_v = 0$ (TB1/0.0I) for the response shown in Figure 8.3a; inelastic sliding shear deformation with $e_v = 0.5$ jd (TB1/0.5I) for the response shown in Figure 8.3b; and inelastic shear deformation with $e_v = 0$ (TB1/0.0E) for the response shown in Figure 8.3c.

The main features of the observed and predicted responses are discussed below:

(a) Prior to yielding, the predicted load-deflection curves generally showed good agreement with the observed behaviour. Changing the value of e_v from 0 to 0.5 jd reduced the predicted stiffness by 7%. The second analysis ($e_v = 0.5$ jd) predicted the stiffness most accurately. However, no firm conclusion can be drawn from this as it is possible that results were affected by compensating errors from other sources, e.g., errors in the estimated base translation during the test (Section 7.4.5a), or in the computed anchorage deformation.

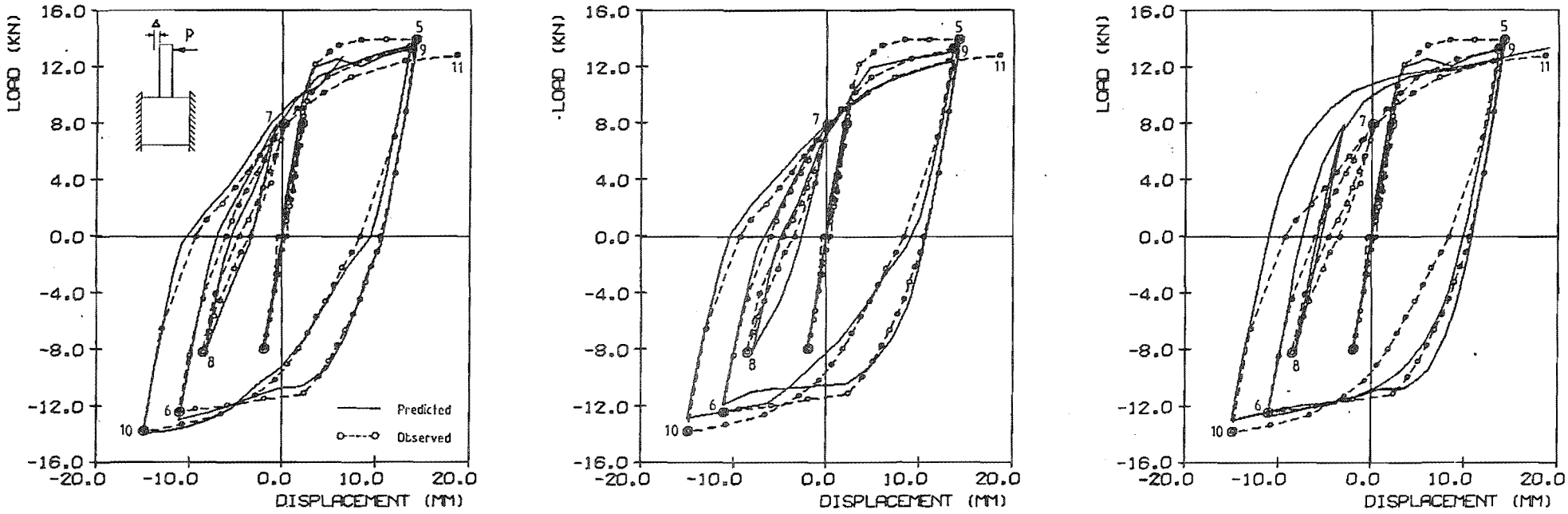

(a) Inelastic shear analysis with $e_v = 0.0$

(b) Inelastic shear analysis with $e_v = 0.5jd$

(c) Elastic shear analysis with $e_v = 0.0$

FIGURE 8.3 : OBSERVED AND PREDICTED LOAD DEFLECTION RESPONSES, SPECIMEN TB1 (CONTINUED NEXT PAGE)

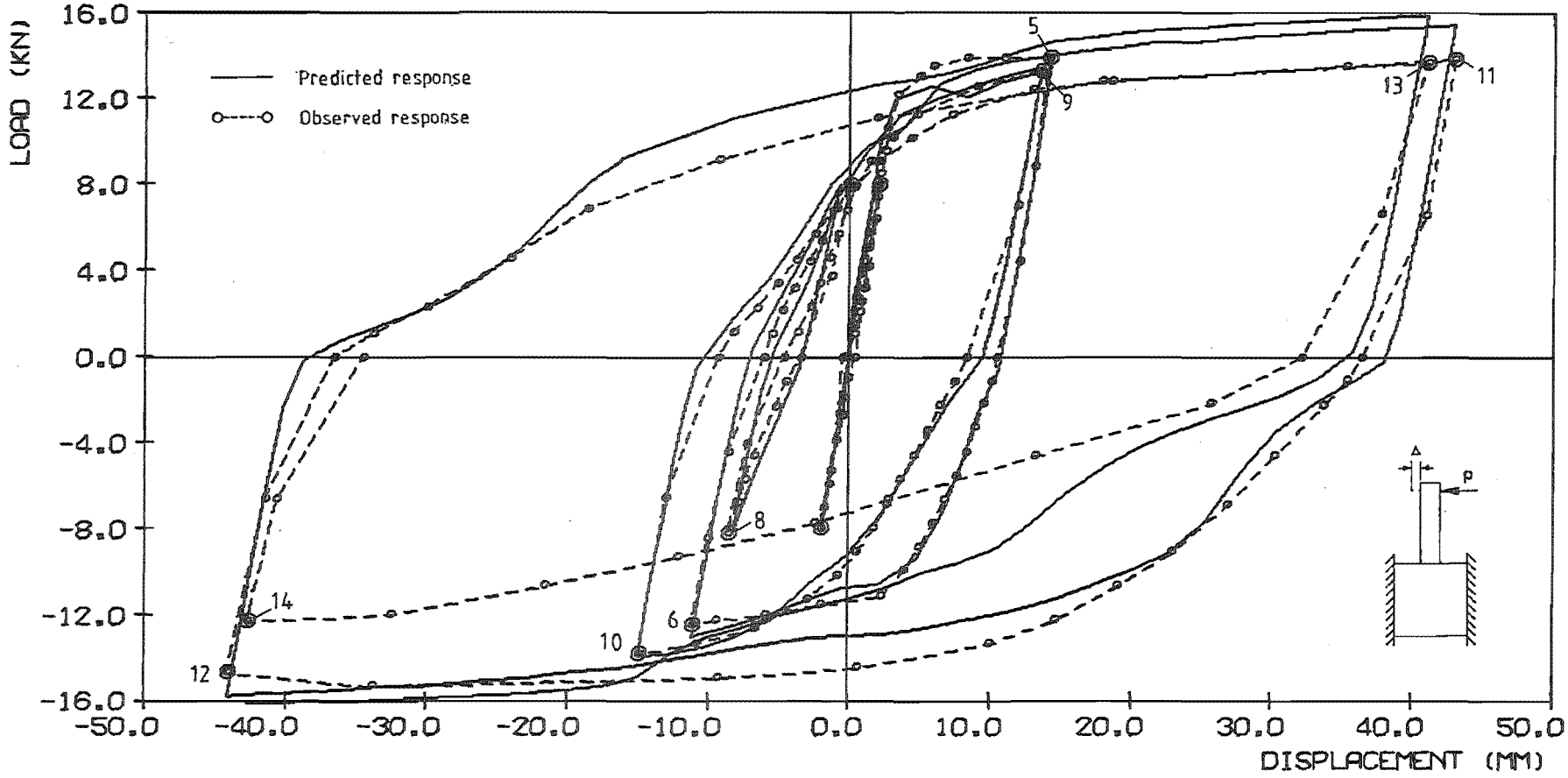

(d) Full load-deflection response, inelastic analysis with $e_v = 0.0$, as for (a)

FIGURE 8.3 : OBSERVED AND PREDICTED LOAD-DEFLECTION RESPONSES, SPECIMEN TB1

(b) Both the initial yield load and the peak loads during the subsequent large-displacement load reversals were predicted most accurately when $e_v = 0$ was used, i.e., with no allowance for inclined cracking.

(c) In the test, the bottom cover concrete crushed just before the peak displacement was reached in load reversal 5. Because of the size of the load increments, the point of crushing does not show on the load-deflection curve. None of the analyses predicted the crushing behaviour correctly; the first analysis ($e_v = 0.0$) predicted crushing at about half the peak displacement in LR5, while the second ($e_v = 0.5$ jd) predicted no crushing in LR5. Both analyses were made assuming a crushing strain of -0.004 (see Section 6.2.3). As evident from Figures 8.3a and 8.3b, the errors in the predicted crushing behaviour had little effect on the accuracy of the predicted responses for subsequent load reversals.

(d) As observed with other similar beams, shear "pinching" of the hysteresis loops developed only after one large-displacement load cycle (LR5 and LR6) had been imposed. As in previous cases (Chapter 6), the analyses usually underestimated the softening of the response during unloading. Also, as indicated in Figure 8.3b (LR8), the shear deformation was not always modelled correctly during small intermediate load reversals. Despite these as yet unresolved problems, the responses predicted using the inelastic sliding shear model (Figures 8.3a and 8.3b) were considerably more accurate than could otherwise be obtained (Figure 8.3c).

(e) The effect of the sliding shear displacements on the moment capacity can be seen from the response of the beam during load reversals 6 and 10. The top* cover concrete was still intact during these load reversals. Because there was little sliding shear during LR6, the compression bars yielded before the cracks closed. This is indicated by the flat plateau on the response

---

* To facilitate description of the behaviour, the faces of the beams in tension when the applied loads are positive (as defined in Figure 8.1) will be referred to as the top faces, and the opposite faces of the beams, as the bottom faces.

curve just after yield load was reached. In LR10, however, there was greater sliding movement which caused the cracks to close earlier, producing a more rounded load curve. As a result, more of the compression load was carried by the cover concrete and, because of the greater effective lever arm, the load carried by the beam was greater than that carried at the same displacements during LR6. This behaviour was evident in the observed response and was predicted accurately in both inelastic shear analyses, but not in the elastic shear analysis. These comparisons clearly illustrate the presence of shear-axial strain coupling in the observed response. Although not particularly significant in terms of the overall behaviour, it is interesting that the model accurately predicted the pattern and extent of this effect.

(f) The load-deflection response during the first two very large-displacement load reversals (LR11 and LR12) was similar to that during load reversals 9 and 10. The top cover concrete did not crush until near the peak displacement in LR12 (i.e., at approximately -40 mm deflection - see Figure 8.3d). Despite some damage to the concrete in earlier load cycles, the maximum strength developed before crushing was about 10% greater than the maximum strength observed under positive loading (i.e., in LR5). The reason for this behaviour is that the compression steel was already carrying some load before the cracks closed in LR12. As a result, the tension bar force (and hence, applied moment) required to overcome the force in the compression bars and crush the cover concrete was greater than required in LR5. After the cover concrete had crushed, most of the remaining support for the reinforcement was lost. This affected the ability of the reinforcement to confine the core concrete and significantly reduced the load capacity when the beam was re-loaded in the same direction (LR14, Figure 8.3d). The behaviour of the beam during these final load reversals is discussed in more detail in Section 8.10.

(g) The deformation imposed on the beam during the very large-displacement load reversals (i.e., DF $\simeq \pm 15$) were well outside the intended scope of the theoretical model. Nevertheless,

even at this intensity of loading (Figure 8.4b), the overall agreement between the observed and predicted responses was still reasonably satisfactory during the first three load reversals. No provision was made for modelling that deterioration in strength that occurred in the final load reversal (LR14), and consequently, the theoretical model was incapable of predicting this behaviour.

8.2.2 Specimen TB2

This specimen failed during the first post-yield load reversal, due to pull out of the beam reinforcement anchored in the wall block. The effect of the anchorage bond slip on the load-deflection response is indicated in Figure 8.5. The mechanism of the bond failure is discussed in Section 8.10.2. Because the failure occurred in the first post-yield load reversal, no other aspects of the performance of this specimen are considered.

8.2.3 Specimen TB3

The observed and predicted load-deflection responses for this specimen are compared in Figure 8.6. In the analyses, the shear deformation in the hinge zone was assumed to be linearly elastic, and no allowance was made for inclined cracking (i.e., $e_v = 0$). As discussed in Section 7.6.2, the stress in the conventional reinforcement in segment 2 was restricted to 0.2 times the steel yield stress to stimulate bond slip at the bar ends.

The main features of the load deflection response for this specimen are as follows:

(a) During the initial "elastic" load reversals, the observed stiffness of this specimen was approximately 33% greater than predicted by the theoretical model. Two main factors appear to have been responsible for the error in the predicted response; firstly, the anchorage deformation during the pre-yeild load reversals was overestimated and secondly, the theoretical model does not account for tensile stresses developed in the concrete between cracks (see (b) below).

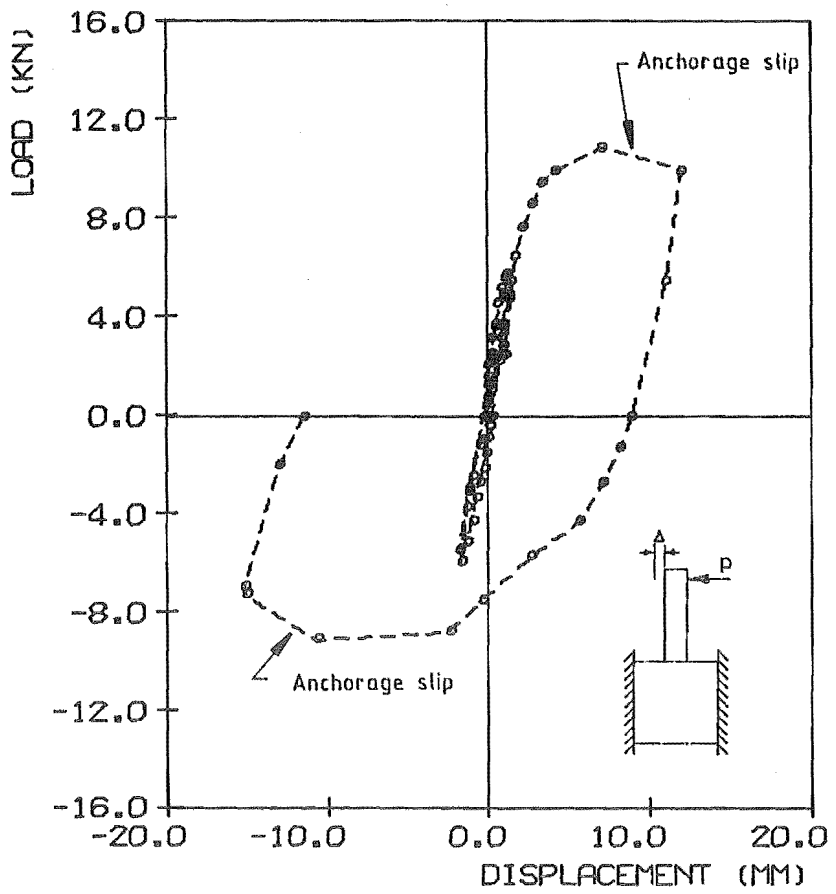

FIGURE 8.4 : OBSERVED LOAD-DEFLECTION RESPONSE, SPECIMEN TB2

(b) The load at first yield in load reversal 5 was approximately 22% higher than the theoretical yield strength computed from the measured strengths of the concrete and steel. This is believed to have been largely due to the effects of the welds used to fix the strain gauge studs to the reinforcement and the residual tension in the concrete between cracks. At this stage of loading (Figure 8.7), only flexural cracks had developed, and almost all of these occurred at positions where studs were located. Therefore, at the position where they crossed the cracks, the bars were oversized due to the welds around the studs. (Refer Section 7.4.6.)

(c) During subsequent load reversals, the response was predicted more accurately. The reason for this is largely that the yielding in the first post-elastic cycle weakened the bond between the steel and concrete which reduced the stresses developed in the concrete between cracks. Consequently, in subsequent load reversals, the response was influenced more by the sections of bar between the stud welds.

(d) During all post-elastic cycles, the load-deflection hysteresis loops show very good energy dissipation by the beam, i.e., very little pinching of the loops. The only softening modelled in the predicted response is that due to the Bauschinger effect in the reinforcement. Although the degree of softening during unloading was usually underestimated slightly, the overall agreement between the observed and predicted responses was still satisfactory. Because of net expansion of the section due to yielding and the inclination of the bars, the hinge zone response during these load reversals was almost completely determined by the steel.

(e) Some of the observed load curves were affected by strain ageing of the reinforcement. This is most noticeable in LR6, where there is a marked change in the slope of the observed response at zero load as a result of the beam being left unloaded for five days. After this was discovered, it was also found that parts of the response of TB1 had also been affected by strain

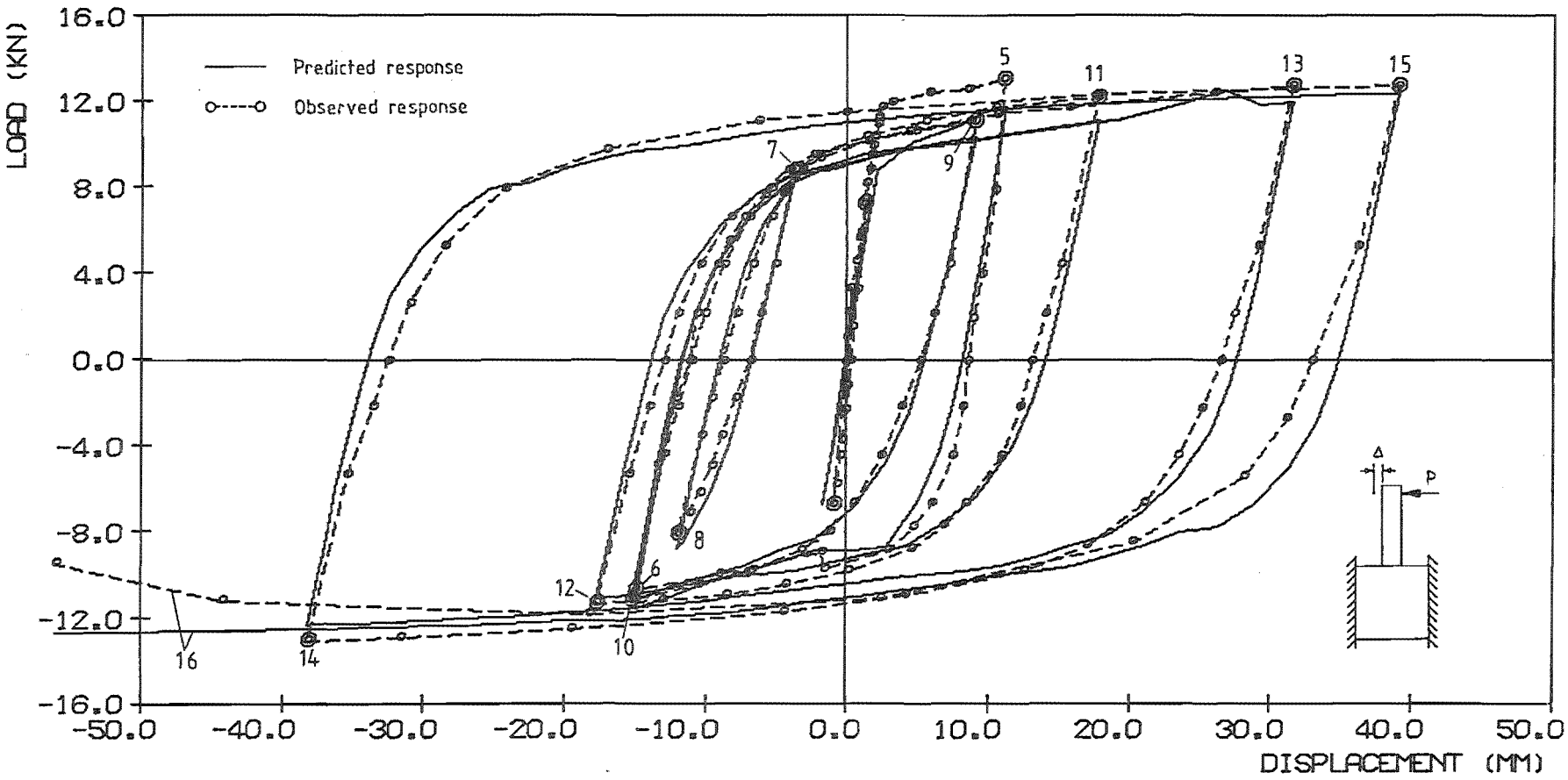

FIGURE 8.5 : OBSERVED AND PREDICTED LOAD-DEFLECTION RESPONSES, SPECIMEN TB3

ageing, although not to the same extent. A fuller description of these effects is given in Appendix A, together with the results of further investigations into the extent of the problems caused by strain ageing.

(f) In the final load reversal (LR16), the compression bars in the hinge zone buckled, causing the beam to twist about its axis (Figure 8.38). The mechanism of this failure is discussed in Section 8.10.3.

8.2.4 Specimen TB4

The observed and predicted load-deflection responses for this specimen are shown in Figure 8.8. In the analysis, the lap region and the shear deformation were treated in the same way as for TB3, i.e., the stresses in the conventional reinforcement in segment 2 were restricted to 0.2 times the yield stress of the steel and the shear deformations in the hinge zone was assumed to be linearly elastic with $e_v = 0$ (Section 7.6).

The following observations are made in respect of the load-deflection responses:

(a) The behaviour of the specimen prior to yielding and during the first post-yield load reversal was similar to that exhibited by TB3, i.e., the specimen was both stiffer (approximately 12%) and stronger (18%) than predicted.

(b) The hysteresis loops for the subsequent moderate- and large-displacement cycles were very stable and indicate a high degree of energy dissipation. The shapes of the hysteresis loops were modelled reasonably accurately, although as in the case of TB3, the unloading and re-loading stiffnesses were generally overestimated during the large-displacement cycles. This is believed to be largely caused by incorrect modelling of the anchorage (Section 8.8) and shear deformations (Section 8.7).

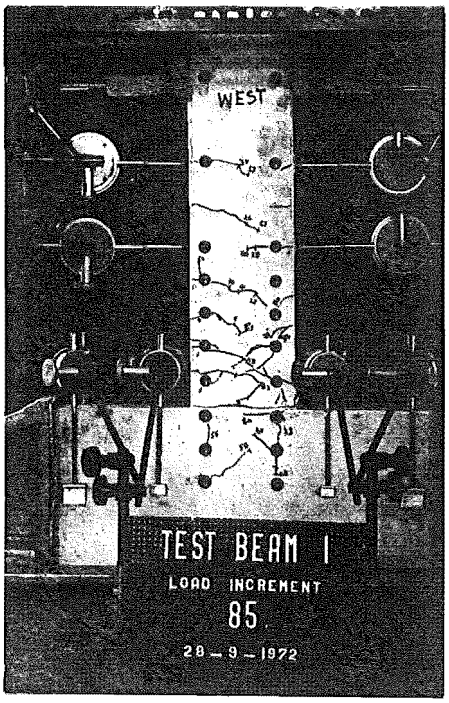

(a) Peak of LR6, DF=-3·5

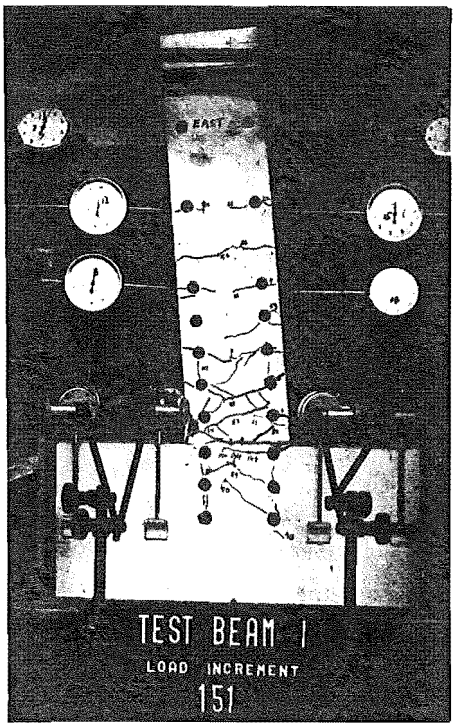

(b) Peak of LR11, DF=15

FIGURE 8.6 : SPECIMEN TB1 DURING TEST

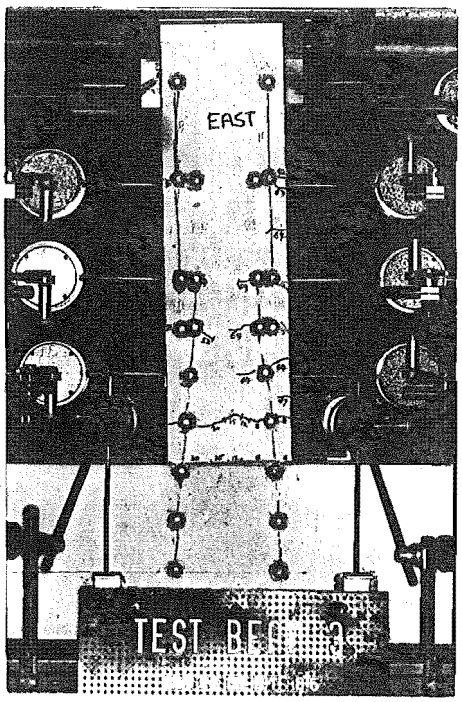

(a) Peak of LR5, DF=4·5

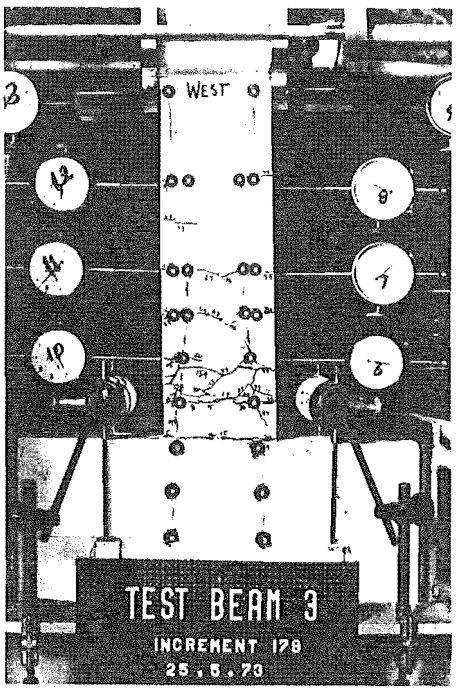

(b) Peak of LR12, DF=-7

FIGURE 8.7 : SPECIMEN TB3 DURING TEST

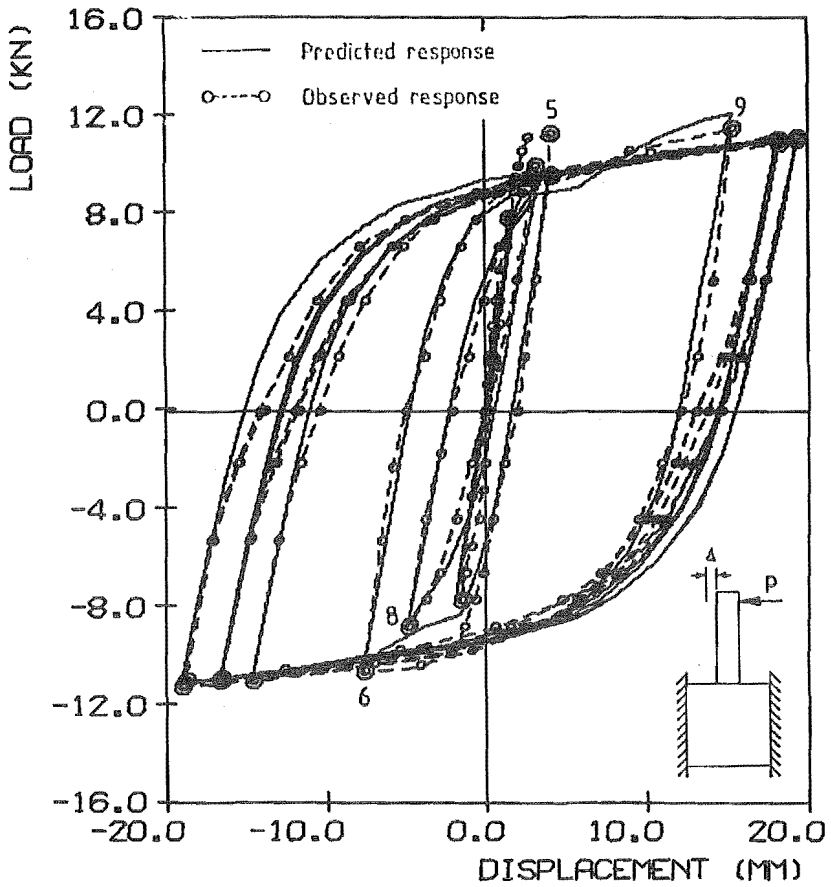

FIGURE 8.8 : OBSERVED AND PREDICTED LOAD-DISPLACEMENT RESPONSES, SPECIMEN TB4

8.3 CURVATURE DISTRIBUTIONS

Figures 8.9 to 8.11 compare the observed and predicted curvature distributions in TB1, TB3, and TB4 at the peaks of several load reversals. The observed distributions shown include "curvatures" determined from the bar strains in the anchorage zones of the specimens. These are discussed separately in Section 8.8. Corresponding predicted curvatures are also shown for the pre-yeild reversals.

For the sake of clarity, both the observed and predicted curvature distributions for the pre-yield load reversals have been shown as continuous curves. In practice, only average curvatures for each segment were measured in the tests, while the predicted values were computed assuming a segmentally linear curvature distribution with discontinuities at the segment boundaries.

8.3.1 Specimen TB1

Predicted distributions from the two inelastic shear analyses, TB1/0.0I and TB1/0.5I, are shown for this specimen in Figure 8.9. In contrast to the load-deflection responses, the curvature distributions were predicted more accurately when a value of e_v = 0.5 jd was assumed. This is particularly noticeable for the post-yield load reversals where the depth of yield penetration was significantly underestimated in the first analysis (e_v = 0.0).

Both analyses predicted cracking over the full length of the beam during the pre-yield load reversals. The measured curvatures also suggest that the end segment was partially cracked, although no cracks were actually detected in this segment until after yielding.

8.3.2 Specimens TB3 and TB4

Figures 8.10 and 8.11 show the curvature distributions in Specimens TB3 and TB4 at the peak displacements in several load reversals. The observed curvatures shown for segments 2 to 4 are based on the strains measured in the diagonal reinforcement while those for segment 6 are

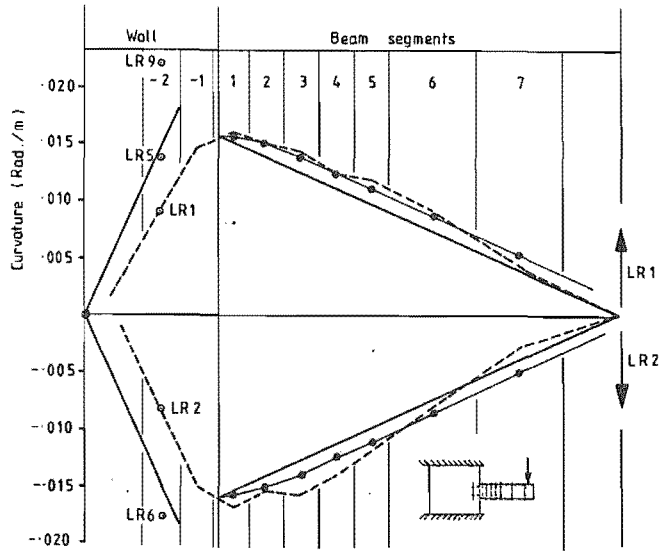

(a). Pre-yield curvature distribution

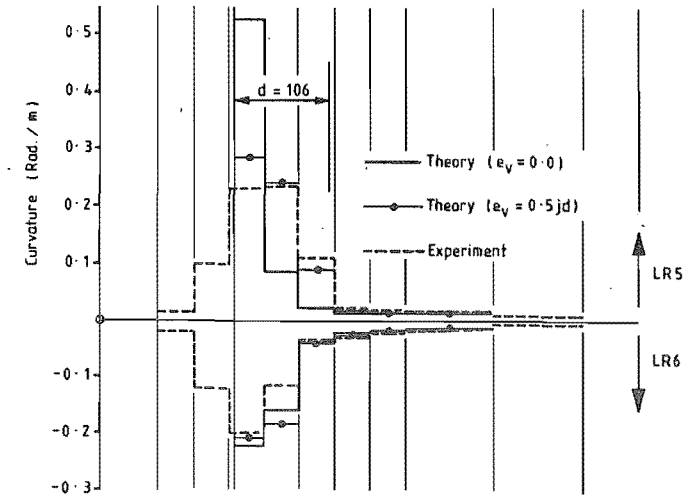

(b) Post yield curvature distribution (LR5 & LR6)

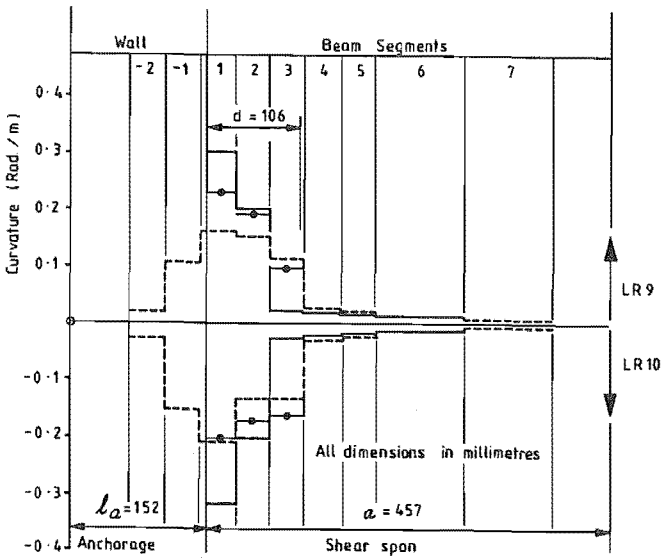

(c) Post-yield curvature distribution (LR9 & LR10)

FIGURE 8.9 : CURVATURE DISTRIBUTIONS, SPECIMEN TB1

based on the strains in the conventional reinforcement. The values shown for segment 5 were averaged from the strain readings for both the diagonal and conventional reinforcement.

Features of the curvature distributions for these specimens are discussed below:

(a) Prior to yielding, the flexibility of those segments of TB3 nearest the beam-wall junction and within the anchorage zone was considerably overestimated by the theoretical model. The flexibilities of the same segments in TB4 were also overestimated, although to a lesser extent. The most plausible explanation for this behaviour is that there were significant residual tensile stresses in the concrete between cracks, as discussed in Section 8.2.3. These stresses are not accounted for in the theoretical model. As shown in Figure 8.7a, there was little cracking in the beam at the end of the pre-yield load reversals.

(b) Concrete cracking penetrated further into the beam during the pre-yield load reversals than was predicted, possibly as a result of concrete shrinkage stresses in the test beams.

(c) During the large displacement cyclic load reversals, yield penetrated as far as the bend in the diagonal bars in the lap region (Figure 7.4). The yield penetration was a result of bond deterioration between the yielded diagonal bars and the surrounding conventionally reinforced concrete which remained elastic. This behaviour is similar to that occurring in the anchorage regions (Figure 8.14).

(d) Because of the strain discontinuities, the post-elastic behaviour of the lap region of the specimens could not be modelled accurately in the theoretical analyses. As a result of bond deterioration, little force was developed in the conventional reinforcement in the plastic hinge zone. An attempt was made to simulate the slip along the diagonal bars by reducing the effectiveness of the conventional bars in the

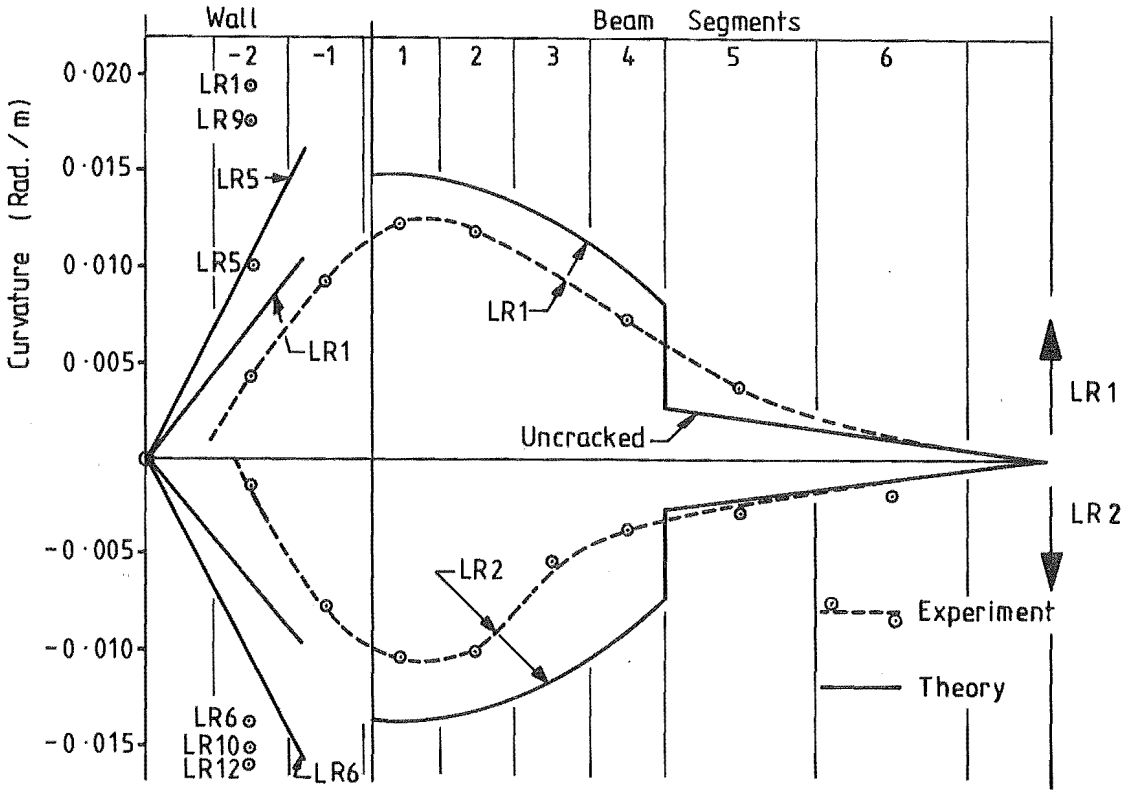

(a) Pre-yield load reversals

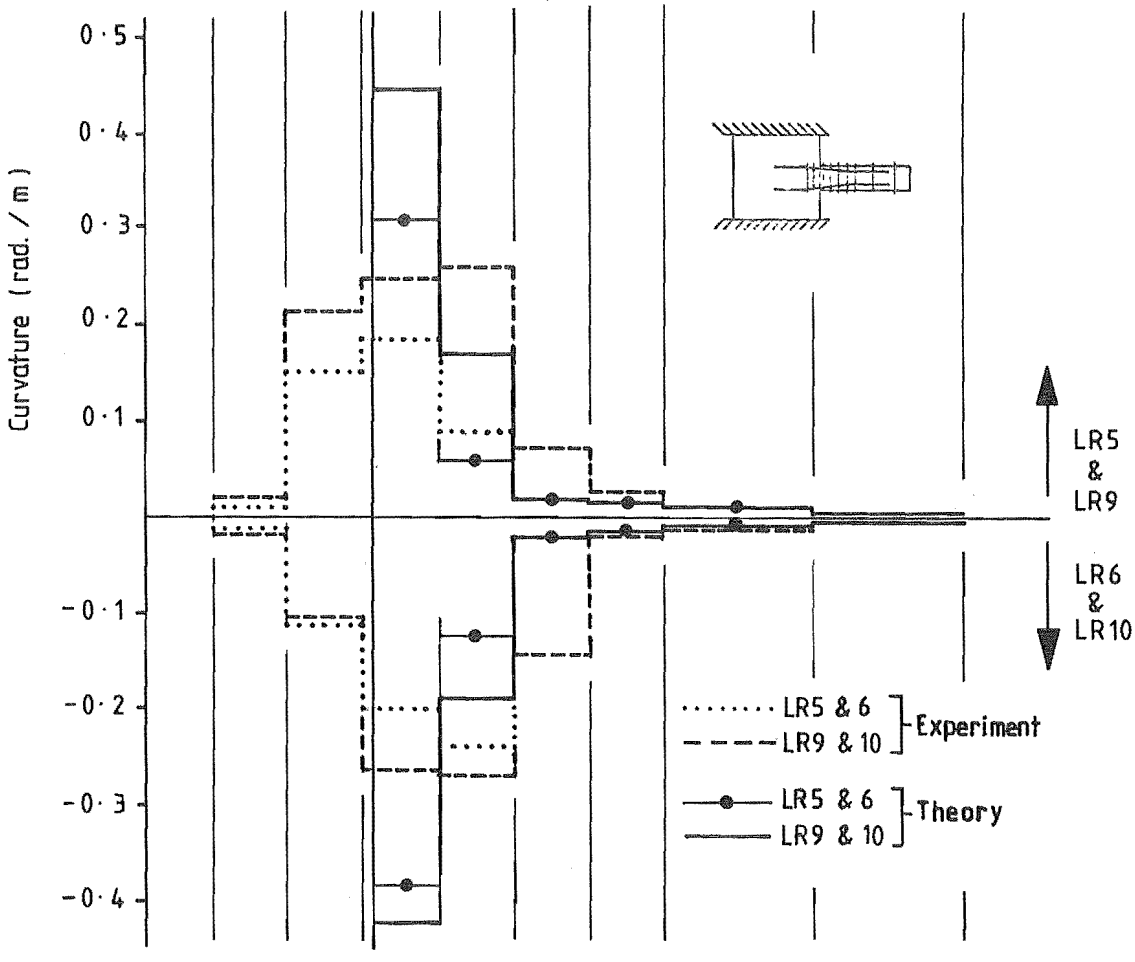

(b) Post-yield load reversals

FIGURE 8.10 : CURVATURE DISTRIBUTIONS, TB3

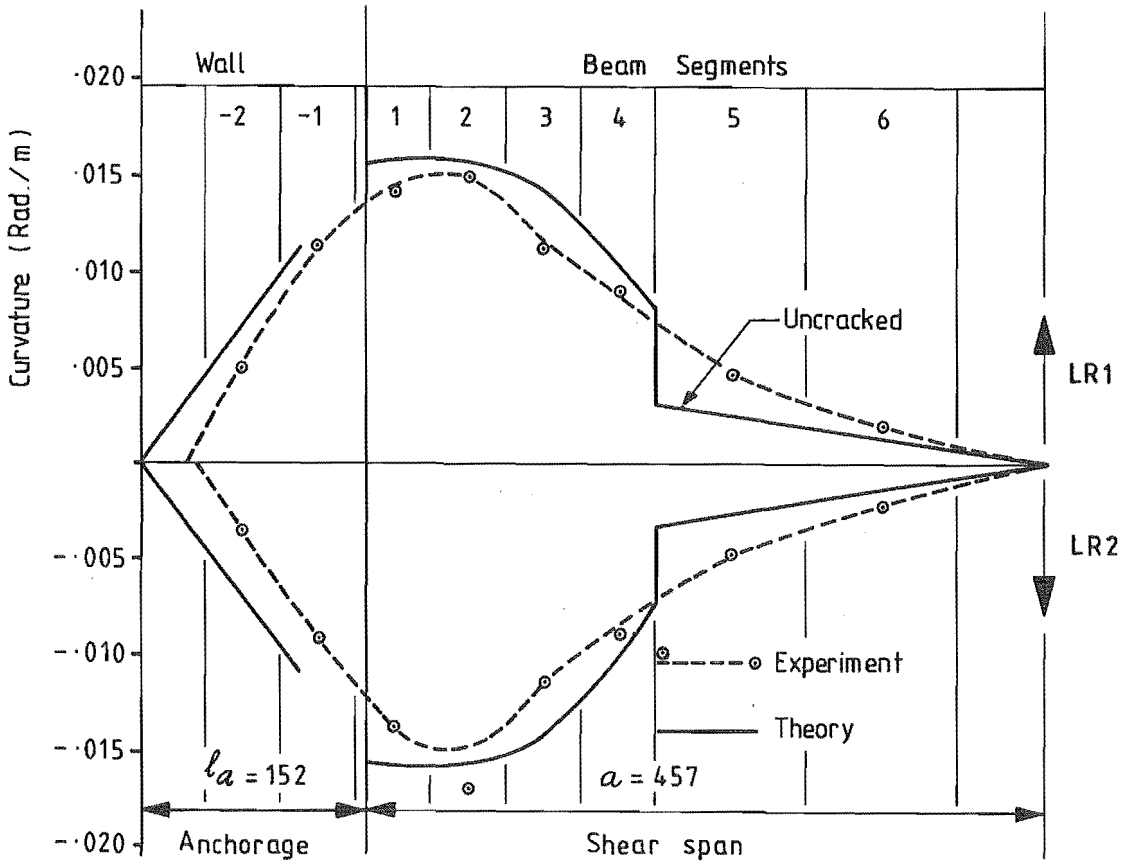

(a) Pre - yield load reversals

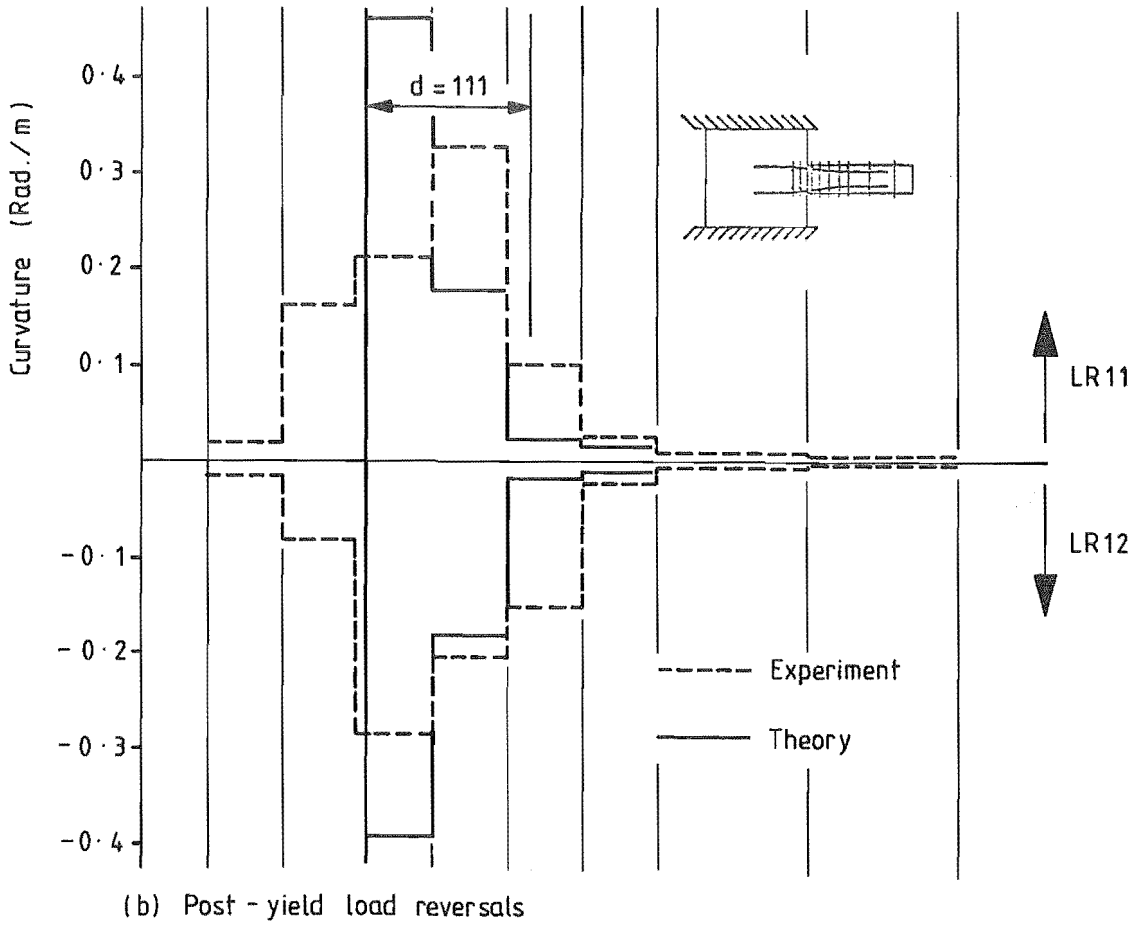

(b) Post - yield load reversals

FIGURE 8.11 : CURVATURE DISTRIBUTIONS, SPECIMEN TB4

lap region (Section 7.6). However, in both analyses (TB3 and TB4), the predicted plastic curvatures were excessively concentrated towards the ends of the beams (Figures 8.10b and 8.11b).

8.4 MOMENT-CURVATURE RESPONSE

Moment-curvature responses for segment 3 of TB1 and segment 1 of TB3 are shown in Figures 8.12 and 8.13.

The predicted responses used in these comparisons were obtained from analyses of the isolated segments using the measured values for the curvature limits of the post-yield load reversals. These analyses used the same material and section parameters as the corresponding load-deflection analyses, and took account of both moment and shear actions on the segments. None of the segments of TB4 were analysed because insufficient readings were taken to determine the complete curvature history.

Two predicted responses are shown in Figure 8.12 for segment 3 of TB1. The first (Figure 8.12a) assumes inelastic shear deformation with e_v = 0.5 jd and the second (Figure 8.12b) assumes elastic shear deformation with e_v = 0. A third analysis was also made assuming inelastic shear deformation with e_v = 0. The response predicted from the third analysis is not shown but was very similar to that predicted in the elastic shear analysis, except that the peak moments in the last three large-displacement load reversals were up to 3% higher.

The following observations are made in respect of these responses:

(a) The moment-curvature response was predicted accurately regardless of whether the sliding shear deformations were allowed for or not. The inclusion of sliding shear slightly increased the modelled flexural strength after the first two large-displacement load reversals, but this effect was insignificant in terms of the overall moment-curvature response.

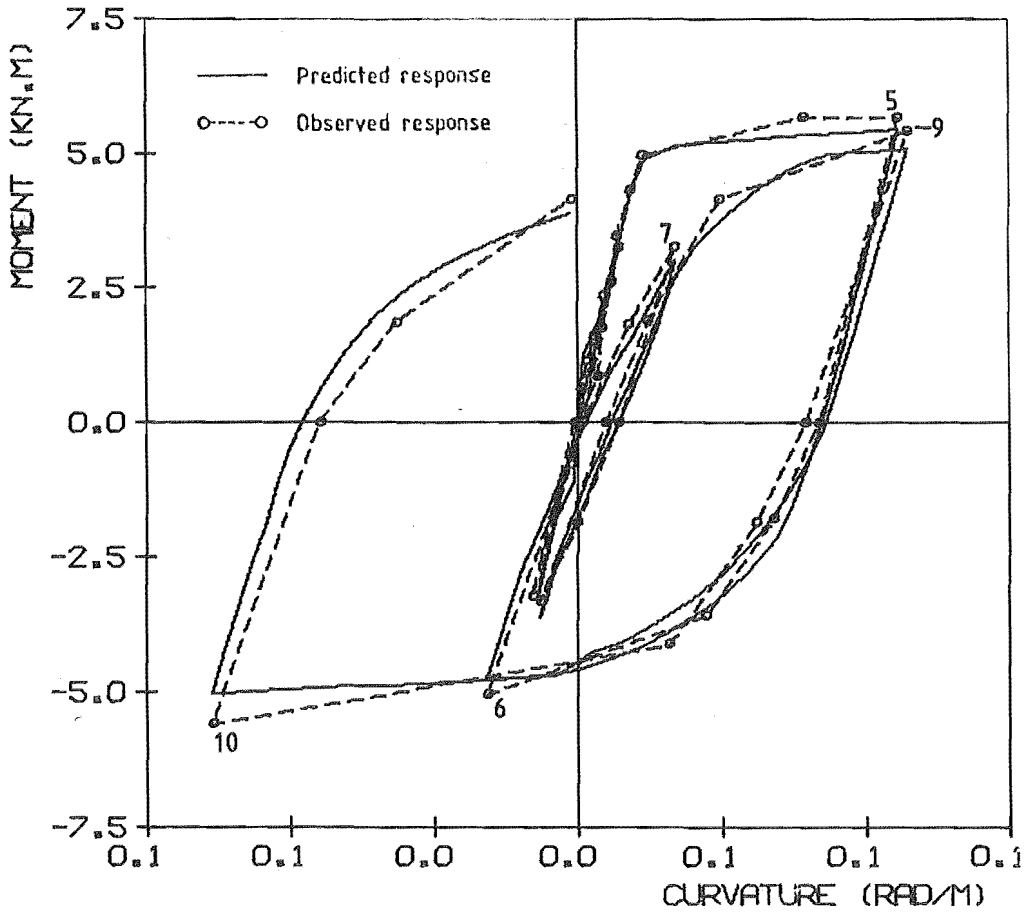

(a) Inelastic shear analysis with $e_v = 0{\cdot}5\ jd$

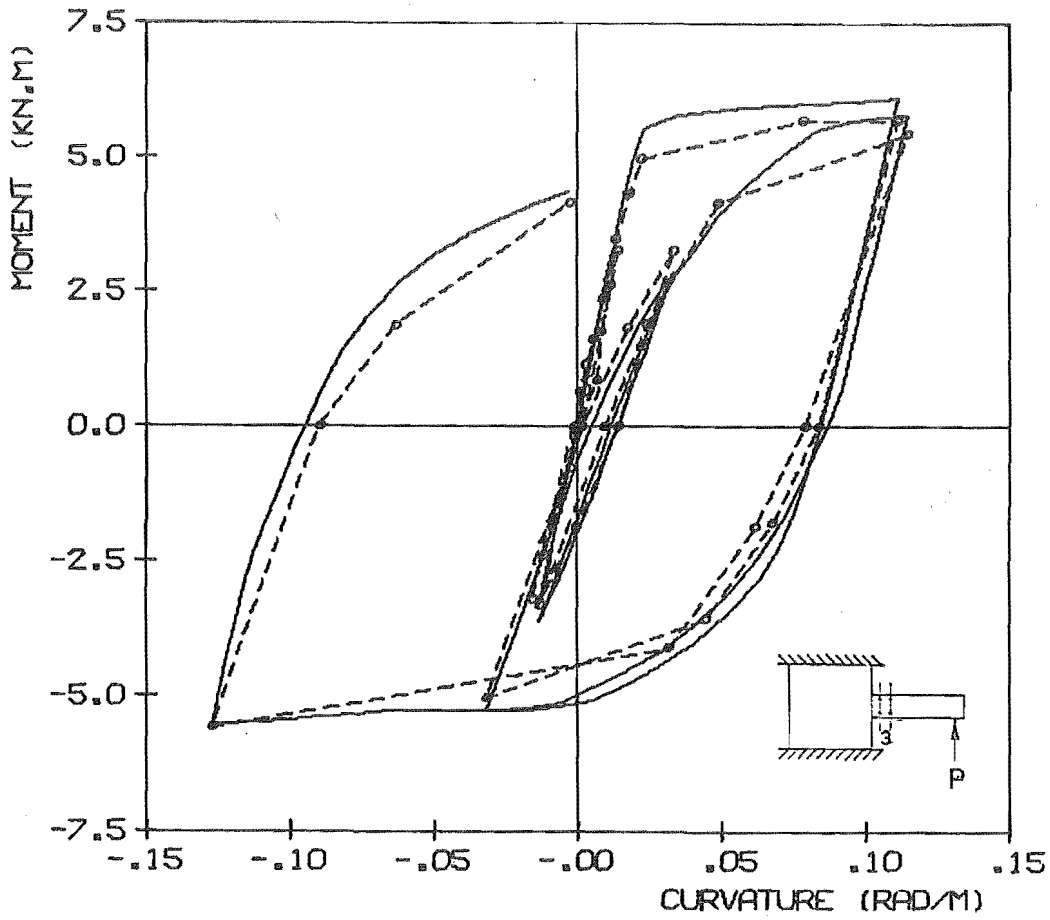

(b) Elastic shear analysis with $e_v = 0{\cdot}0$

FIGURE 8.12 : MOMENT-CURVATURE RESPONSES, SEGMENT 3 OF SPECIMEN TB1

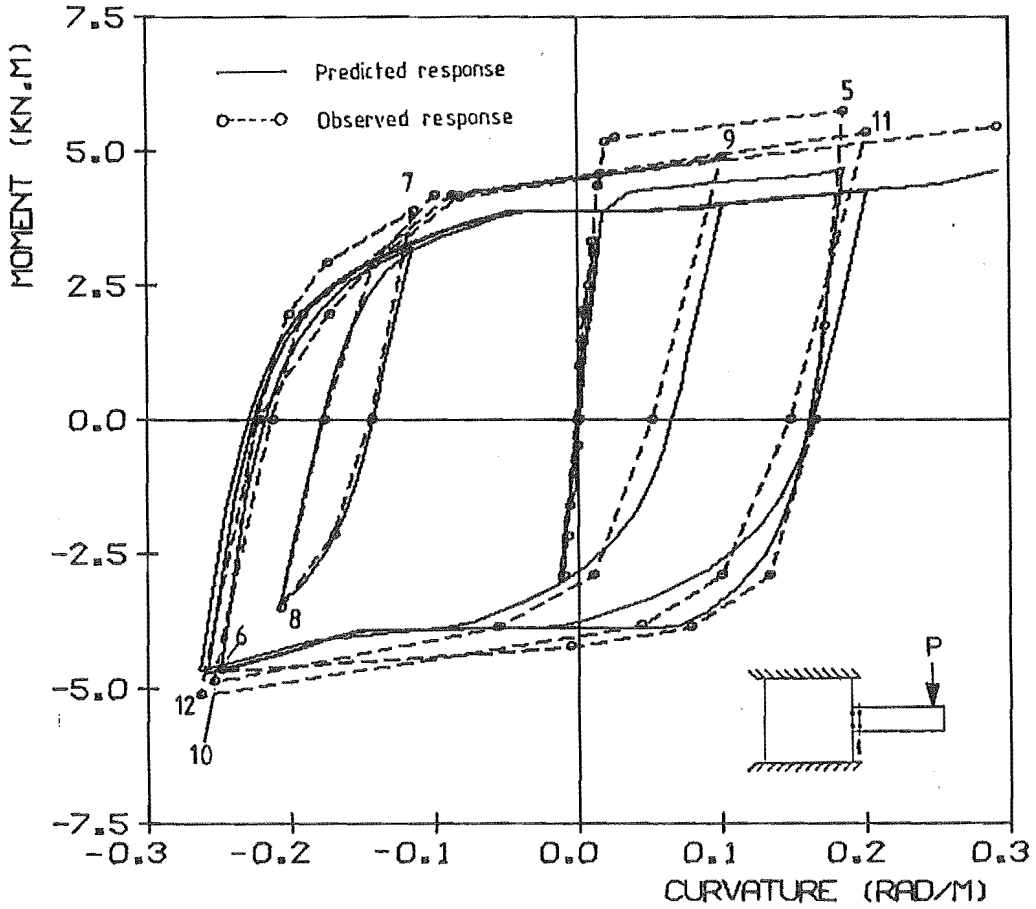

FIGURE 8.13 : MOMENT-CURVATURE RESPONSES, SEGMENT 1 OF SPECIMEN TB3

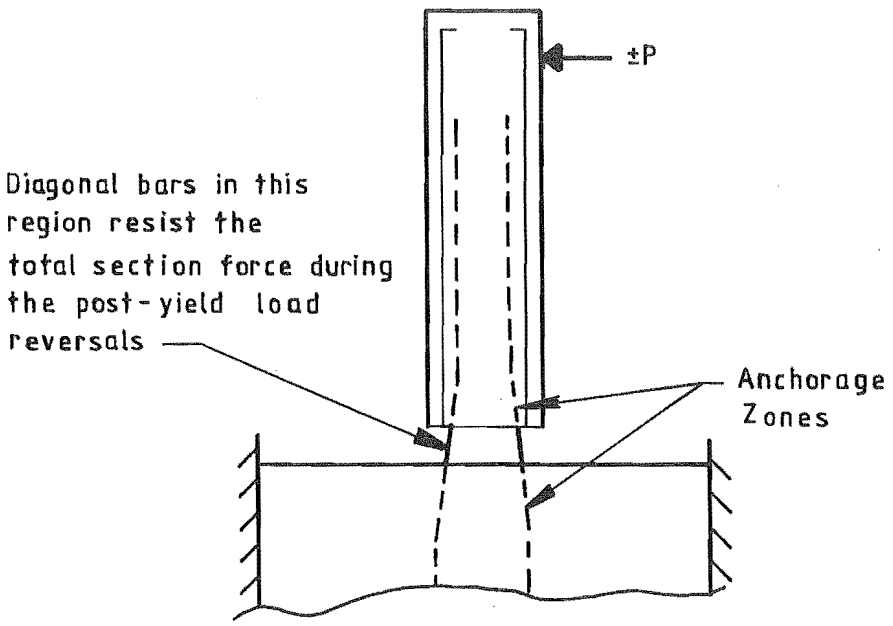

FIGURE 8.14 : IDEALIZATION OF LOAD RESISTANCE IN THE DIAGONALLY REINFORCED SPECIMENS

(b) The initial (pre-yield) slope of the moment-curvature response was predicted most accurately in the analysis assuming e_v = 0.5 jd. In the subsequent load reversals, the observed response was generally somewhere between the responses predicted assuming e_v = 0 and e_v = 0.5 jd. In the case of the segments closer to the wall block (i.e., segments 1 and 2), the distinction was even less clear because these segments are less affected by inclined cracking.

In the case of segment 1 of TB3, the analysis underestimated the moment actually resisted, particularly during the positive load reversals. Two factors possibly contributing to this are errors in assessing the bar strains (Figure 8.16), and the effects of the ends of the conventional reinforcement which penetrated into the segment (Figure 7.4). The predicted load-deflection response of TB3 was less affected because, in that analysis, the curvatures developed in segment 1 were overestimated (Figure 8.10).

8.5 BAR STRAINS

Figures 8.15 and 8.16 show the observed and predicted moment-strain responses for the tension bars* in beam segments analysed in the preceding section. The predicted strain responses used in these comparisons were obtained from the same section analyses as the moment-curvature responses (Figures 8.12 and 8.13).

Unlike the moment-curvature response, the bar strains in the plastic hinge zone of TB1 were significantly affected by the sliding shear deformations. The observed response shows only partial recovery of tensile bar strains during negative loading, with the magnitude of the residual tensile strain increasing significantly between LR6 and LR10. This behaviour was accurately predicted when the sliding shear deformations were modelled (Figure 8.15a). However, in the analysis which did not allow for sliding shear deformation, there was no mis-match between closing crack surfaces. As a result, the predicted residual strains at the peaks of the negative load reversals were much smaller than the observed values (Figure 8.15b).

---

* The term "tension bars" is used here to denote the bars loaded in tension when the applied load is "positive" (refer Figure 8.1).

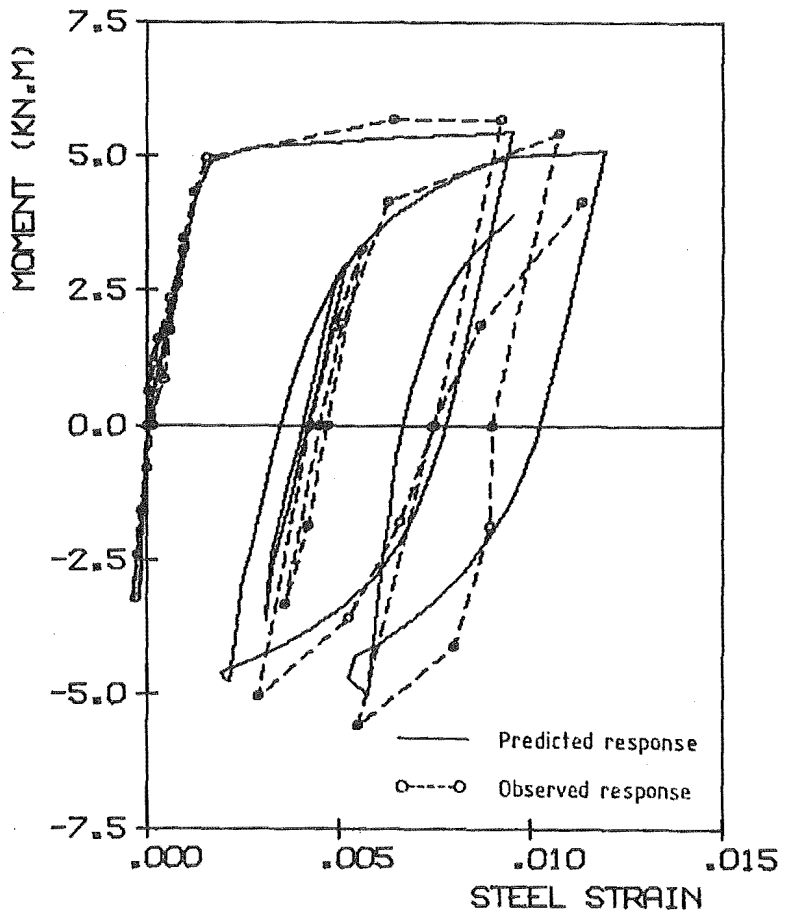

(a) Inelastic shear analysis with $e_v = 0{\cdot}5\,jd$

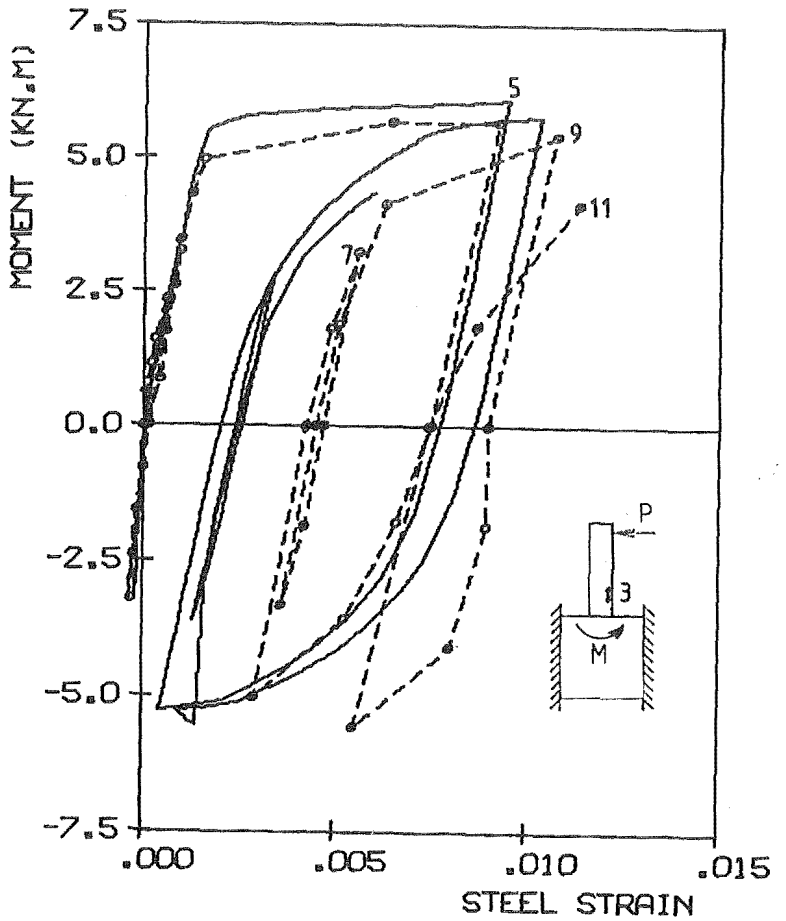

(b) Elastic shear analysis with $e_v = 0{\cdot}0$

FIGURE 8.15 : RESPONSE OF TENSION BARS IN SEGMENT 3 OF TB1

As shown in Figure 8.16, the use of diagonal bars in the hinge zone of TB3 did not result in full recovery of the tensile strains when the bars were loaded in compression. This is evident from the smaller predicted strains, which were computed assuming elastic shear behaviour and hence no mis-match of the closing crack surfaces. Several factors could have contributed to the difference between the observed and predicted behaviour. These include loose chips of concrete between the crack surfaces, a small "sliding shear" component due to imperfect bar alignment, distortion of the bar alignment caused by the imposed plastic deformations, and the effect of the conventional reinforcement protruding into the segment.

8.6 BEAM ELONGATION

Figures 8.17 to 8.19 show the member load-elongation responses for specimens TB1, TB3, and TB4. Both the observed and predicted values shown are the total elongations of the beams, including the elongations of the anchorage zones in the wall blocks. (The predicted values are from the load-deflection analyses, not the moment-curvature analyses referred to in the preceding two sections.)

As shown, the elongation responses exhibit similar characteristics to the local bar strain responses (Section 8.5), particularly the progressive elongation of the beams caused by cracks not closing fully. After four large-displacement load reversals, the net elongations of TB1 and TB3 were 3.1 mm ($\simeq$ 0.03 d) and 2.2 mm ($\simeq$ 0.02 d) respectively.

The elongations predicted for TB1 (using the inelastic shear model) were reasonably accurate, with only a small overestimate of the peak values in the last two load reversals. However, as indicated by the bar strains predicted for TB3, the elongations of the diagonally reinforced beams (TB3 and TB4) were generally underestimated. As discussed in the preceding section, this discrepancy was due to the fact that the theoretical model assumes that the cracks close fully when there is no sliding shear deformation.

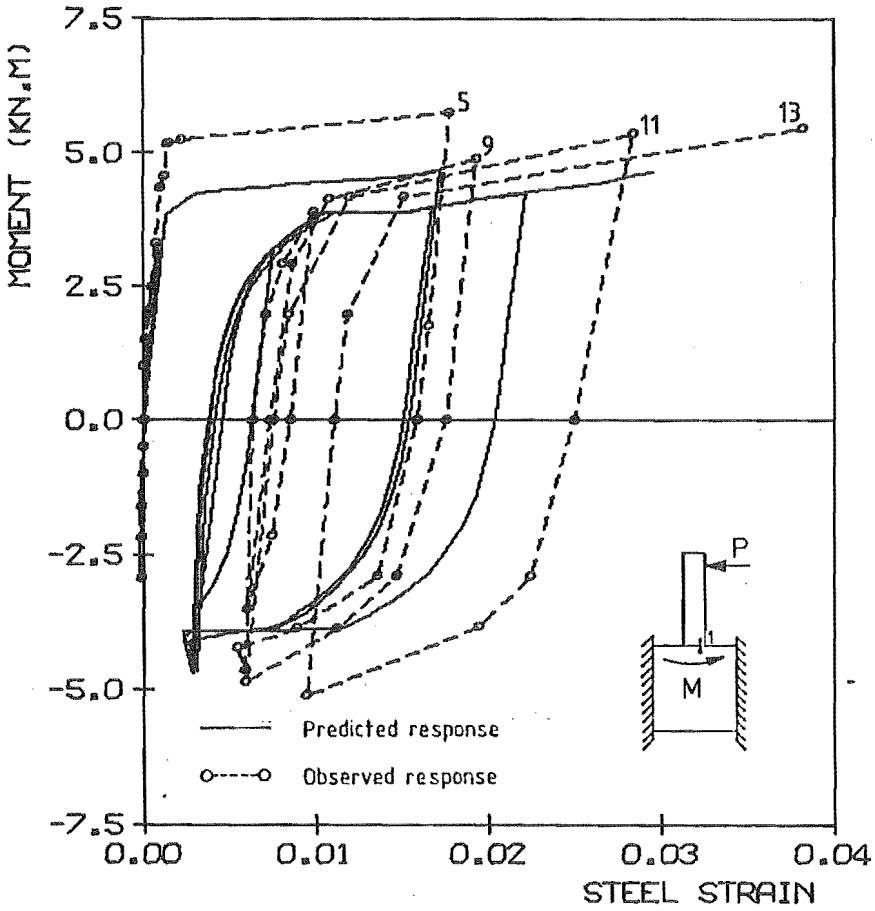

FIGURE 8.16 : RESPONSE OF TENSION BARS IN SEGMENT 1 OF TB3

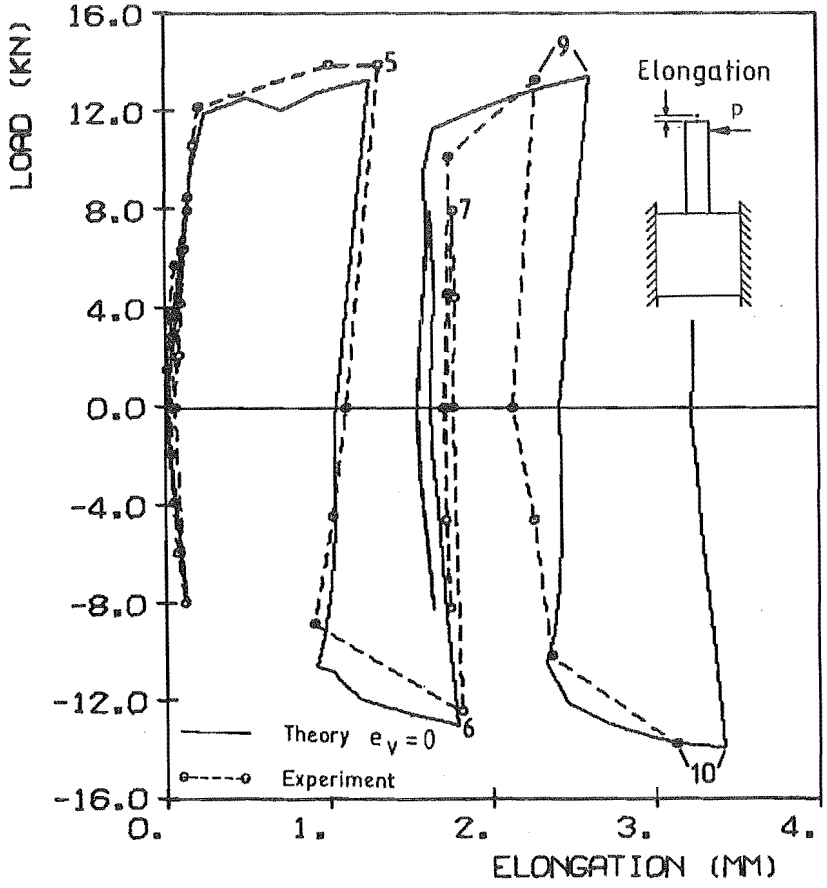

FIGURE 8.17 : BEAM ELONGATIONS, SPECIMEN TB1

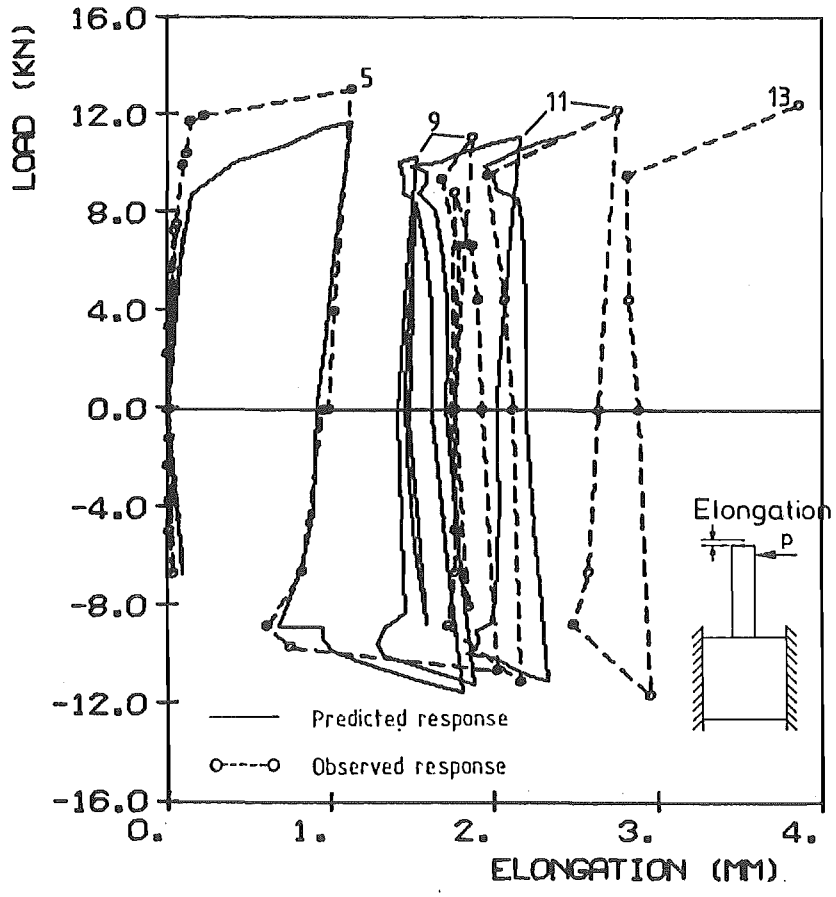

FIGURE 8.18 : BEAM ELONGATION, SPECIMEN TB3

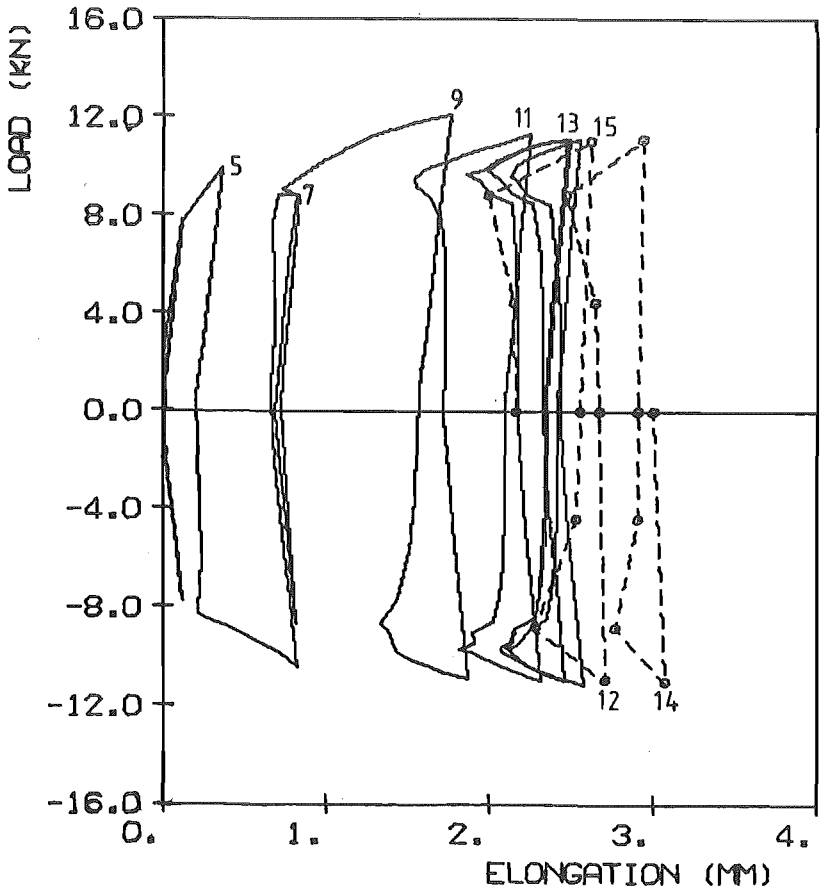

FIGURE 8.19 : BEAM ELONGATION, SPECIMEN TB4

8.7 SHEAR DEFORMATION

The observed and predicted shear force - shear displacement responses for TB1 are shown in Figure 8.20. The observed shear displacements were obtained by first computing the flexural component of end deflection from the steel strain readings and then subtracting this from the total end deflection measured with the dial gauges. Because the resulting shear displacements are the difference of two larger values, the relative experimental error (including unmeasured anchorage components - Section 8.8) will be greater than for the load deflection responses. However, the shape of the obtained shear force - shear displacement response and the small magnitude of measured "shear displacement" for TB3 and TB4 (Figures 8.21 and 8.22), suggest that the observed values in Figure 8.20 are a reasonable indication of the true shear displacements in TB1.

The observed values given in Figure 8.20a indicate that the shear deformation contributed approximately 40% of the total end deflection at low load intensities (i.e., at loads less than one third of ultimate), and approximately 12% of the end deflection of the peaks of load reversals 7 to 10. The overall magnitude of these shear displacements was predicted reasonably well (Figure 8.20b). This is consistent with the analysis results obtained for the beams tested by Celebi and Penzion (see Section 6.3.4), i.e., where the shear deformations were satisfactorily predicted for Beam 5, which had a shear span to depth ratio of $a/d = 5.1$, c.f., $a/d = 4.6$ for TB1.

The observed "shear displacements" for TB3 and TB4 are shown in Figures 8.21 and 8.22. These values are very small (maximum approximately 2½% of the end deflection) and it is probable that they include a large component of experimental error. Some shear deformation will have developed in the hinge zones of these specimens, e.g., that resulting from the component of bar strain perpendicular to the member axis and probably a small "sliding shear" component due to initial mis-alignment of the bars or to subsequent distortion of the bar alignment at high load intensities. The small magnitude of the observed values indicates, however, that these shear displacements are negligible, even at large displacements.

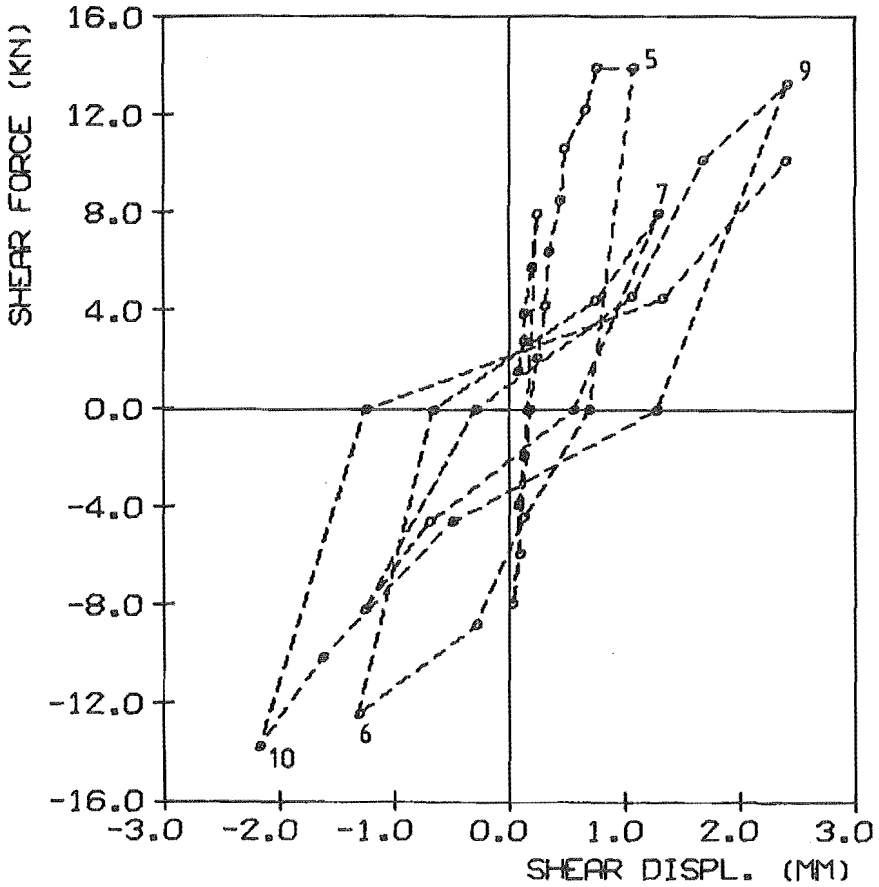

(a) Observed shear response

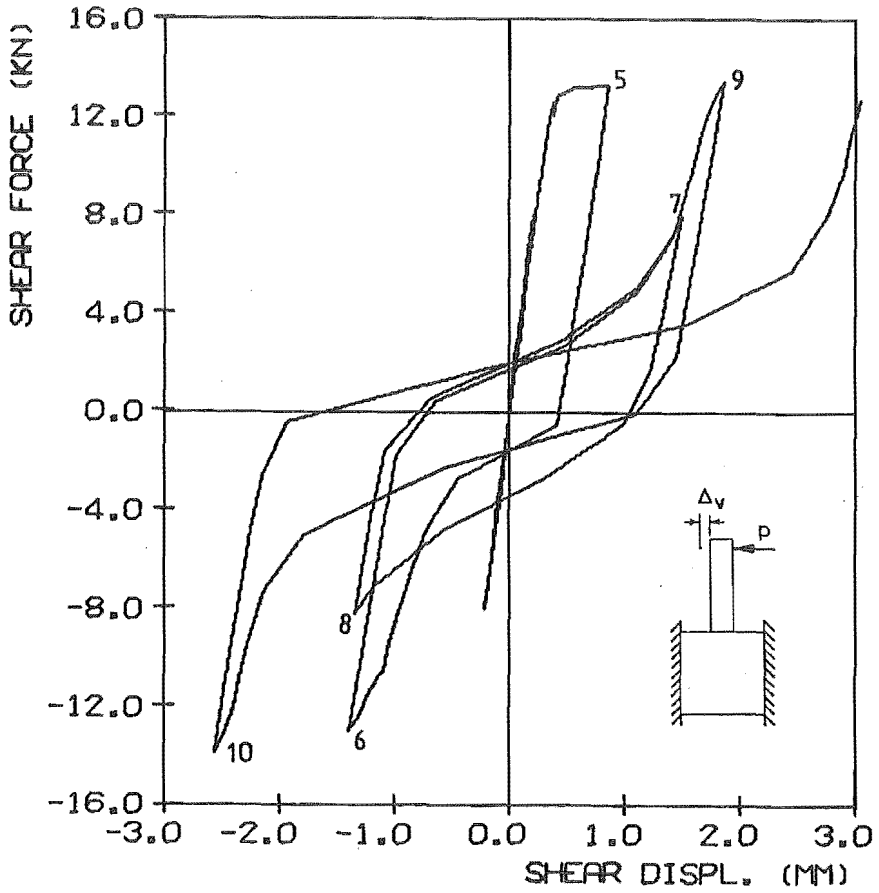

(b) Predicted shear response, $e_v = 0{\cdot}0$

FIGURE 8.20 : OBSERVED AND PREDICTED SHEAR DEFORMATION, SPECIMEN TB1

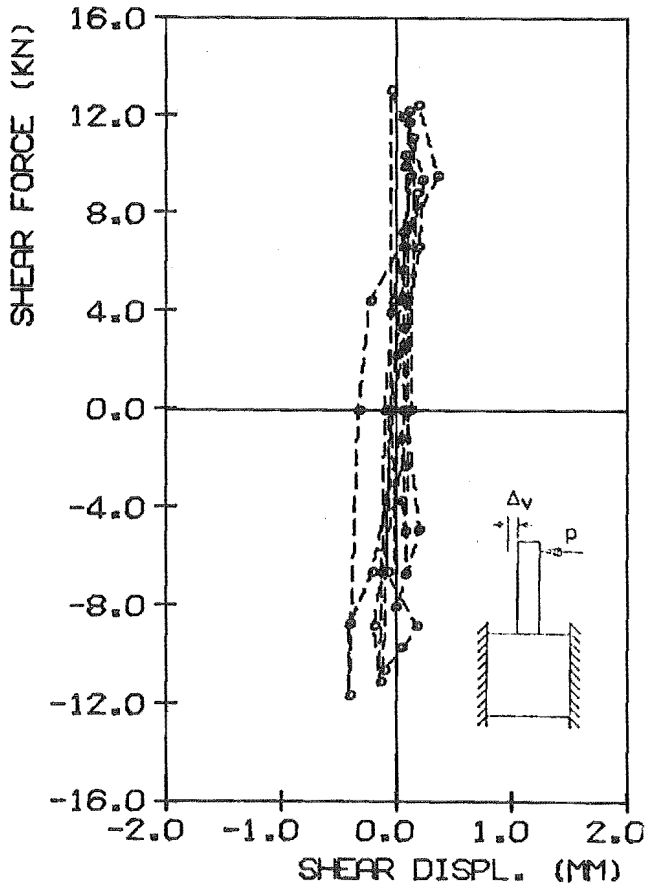

FIGURE 8.21 : OBSERVED " SHEAR" DEFORMATION, SPECIMEN TB3

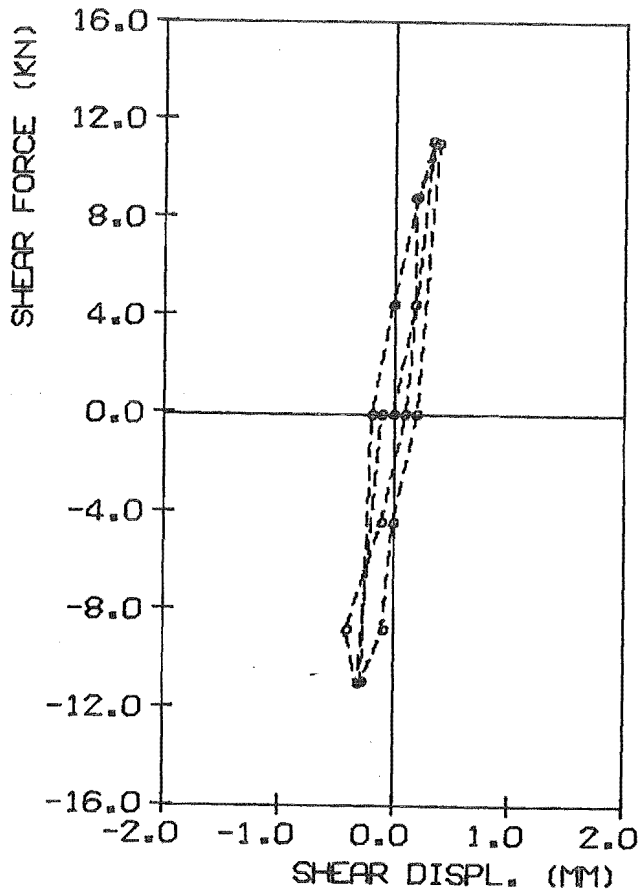

FIGURE 8.22 : OBSERVED "SHEAR" DEFORMATION, SPECIMAN TB4

The difference between the shear behaviour of the conventionally and diagonally reinforced beams during the very large-displacement load reversals can be seen from the deflected shapes of the specimens shown in Figures 8.23 and 8.24. In the case of the conventionally-reinforced specimen, Figure 8.23 indicates that the shear displacement (in TB1) accounted for 70-85% of the end deflection at low load intensities during LR13 and LR14, and to over 30% of the peak end displacements.

8.8 ANCHORAGE DEFORMATION

Figures 8.25 and 8.26 show the observed and predicted anchorage rotation responses for TB1 and TB3. The observed values were computed from the steel strains measured in the anchorage region. Any deformations which occurred outside the gauged area (i.e., further into the wall blocks) are not accounted for.

The predicted and observed responses shown are not entirely independent, as the theoretical model parameters ℓ_a and ϕ_{pa} were calibrated (approximately) from the observed responses (Section 7.6.1). Nevertheless these parameters only define the overall level of anchorage deformations. The shapes of load-rotation curves and the relative magnitude of deformation in each cycle are determined independently by the model. Both these latter factors were predicted as well as could be expected, given the effect of the strain gauge studs (Section 7.4.6) and the fact that small variations in bar yield strength could significantly alter the distribution of plastic rotation between the anchorage and hinge zones. However, as in the case of the beam segments (Section 8.3), the pre-yield flexibility of the anchorage zone of TB3 was considerable overestimated.

Two main assumptions were made in developing the anchorage model. The first was that the anchorage length is independent of load intensity. As Figure 8.27 indicates, the observed anchorage length did vary with load intensity, at least during initial loading in the elastic range. The anchorage length used in the analyses (150 mm) was selected to approximately model the observed anchorage deformations at onset of yielding in the beams. In view of the agreement obtained with the observed anchorage rotations (Figures 8.25 and 8.26), a more sophisticated variable anchorage length model was not considered to be warranted for this investigation.

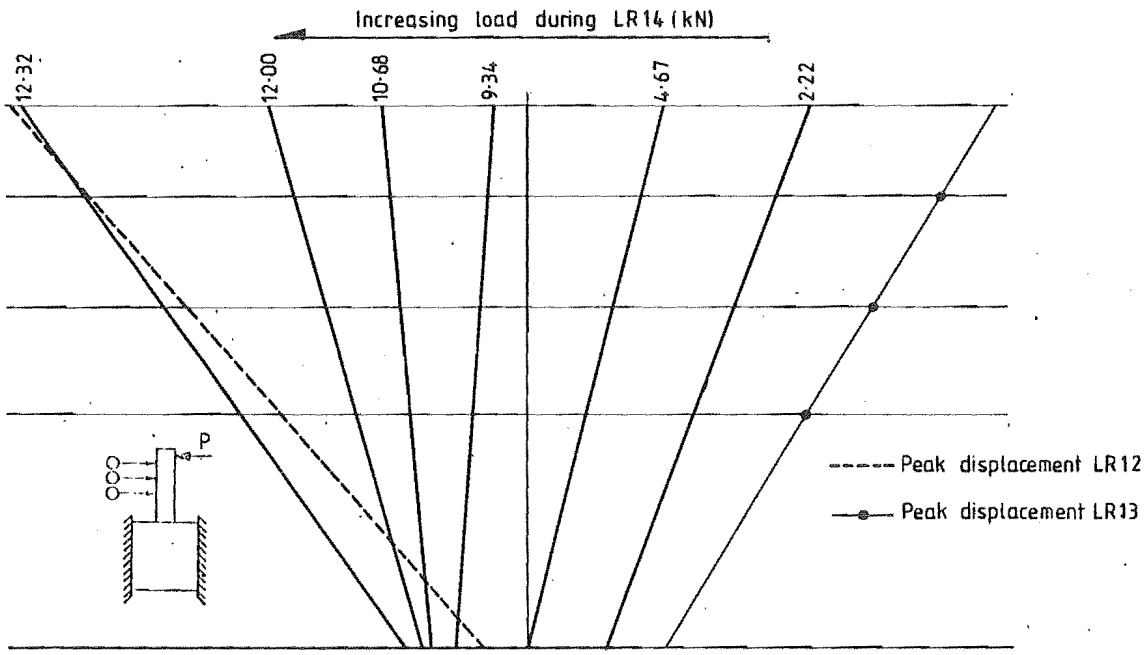

FIGURE 8.23 : DEFLECTED SHAPE OF SPECIMEN TB1 BEAM AT VARIOUS STAGES DURING LR14

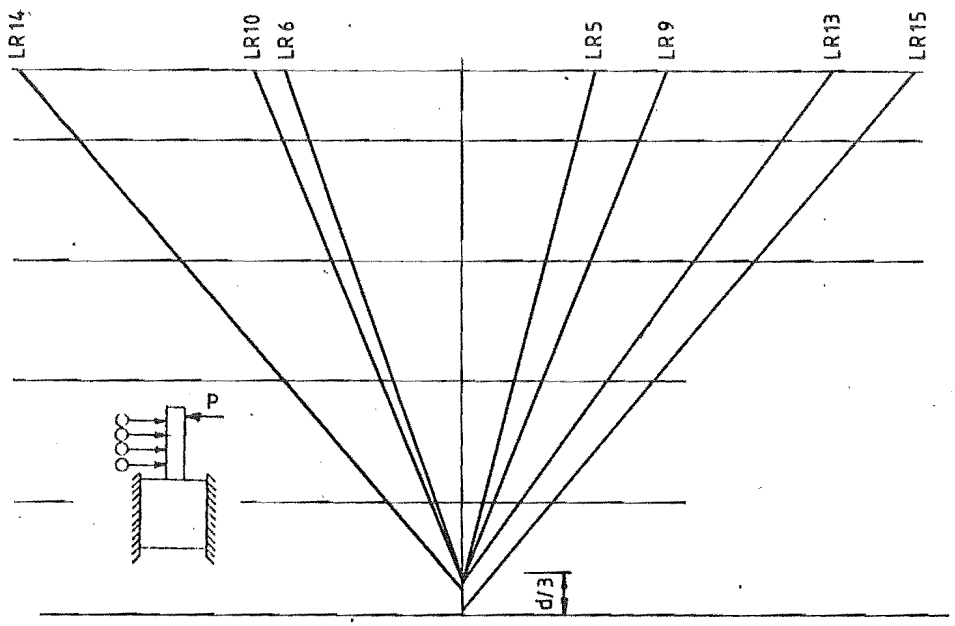

FIGURE 8.24 : DEFLECTED SHAPE OF SPECIMEN TB3 AT THE PEAKS OF DIFFERENT LOAD REVERSALS

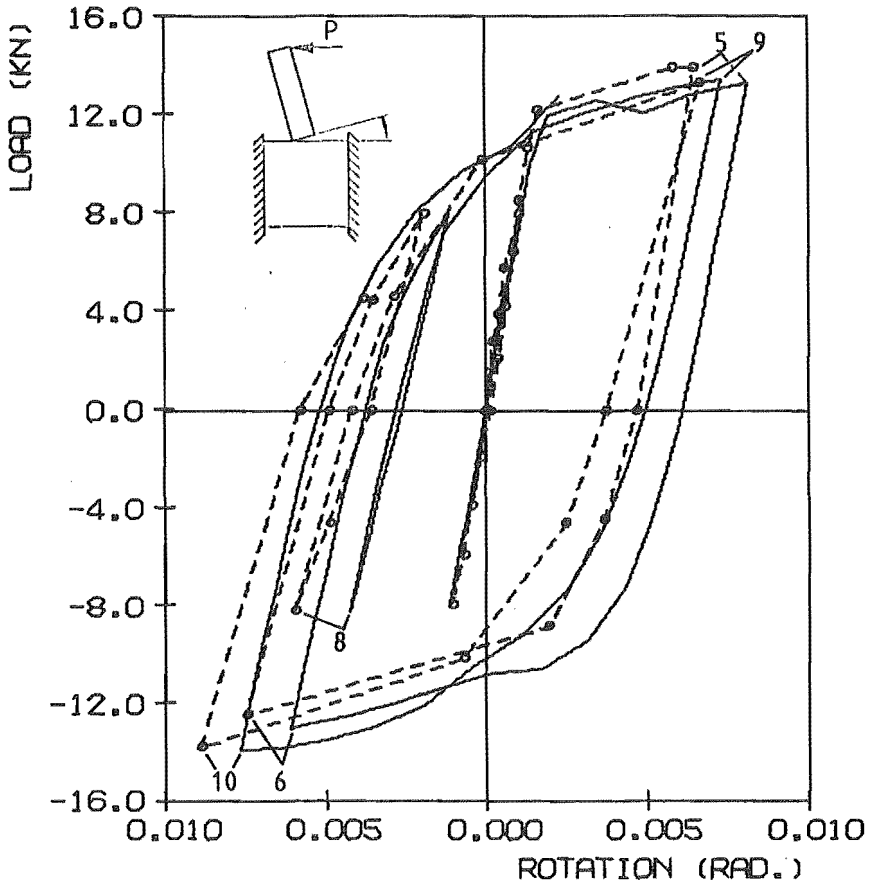

FIGURE 8.25 : ANCHORAGE ROTATION, SPECIMEN TB1

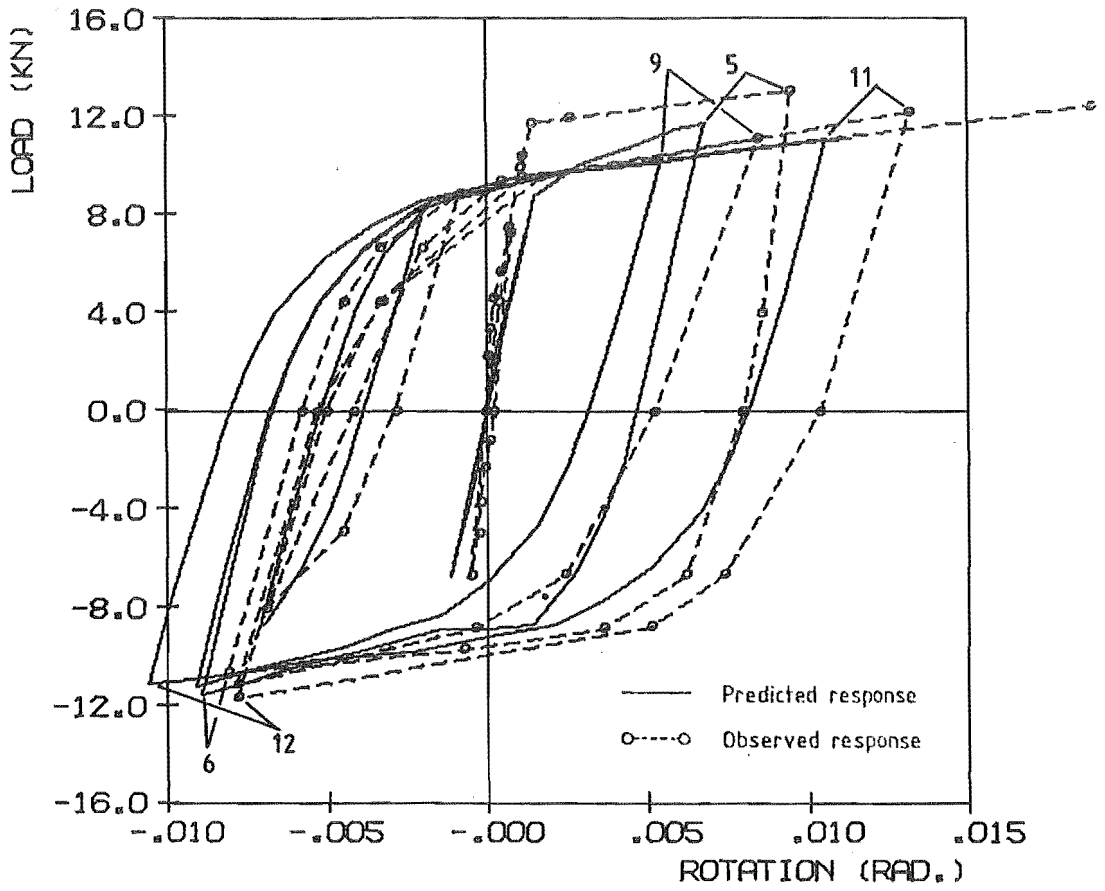

FIGURE 8.26 : ANCHORAGE ROTATION, SPECIMEN TB3

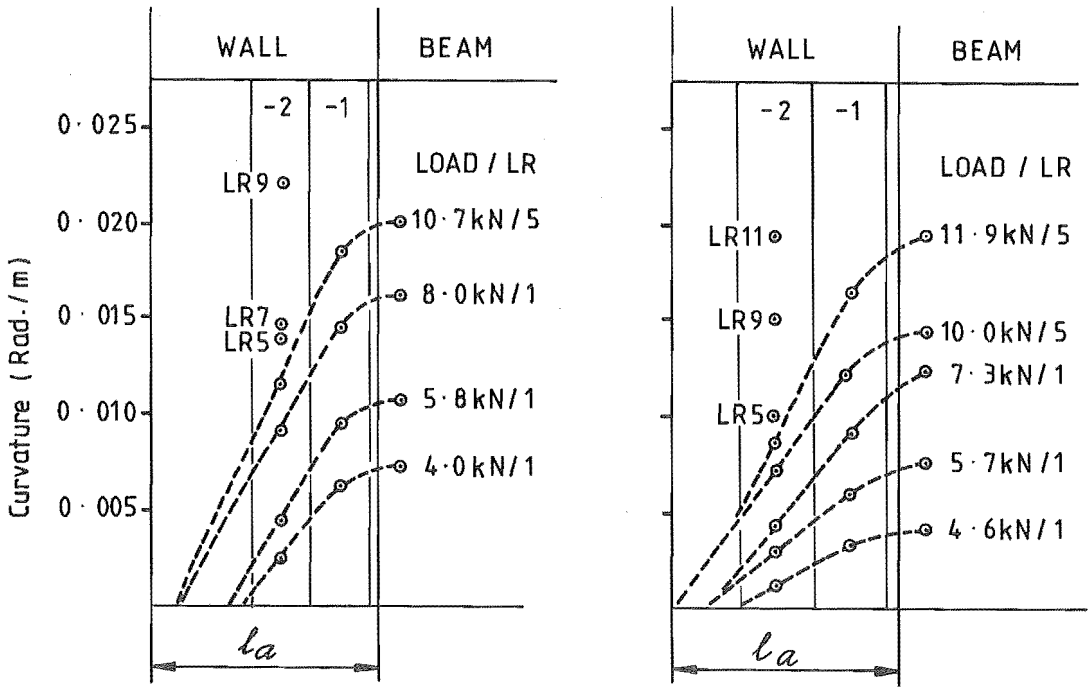

(a) Specimen TB1 (b) Specimen TB3

NOTE: l_a = Anchorage length assumed for analysis

FIGURE 8.27 : OBSERVED "CURVATURE" WITHIN ANCHORAGE ZONES OF TB1 AND TB3

The second assumption was that a constant proportion of the beam end rotation is developed in the anchorage zone. This assumption was based on the observed behaviour shown in Figure 8.28. Although some fluctuation of the anchorage contribution was observed (approximately 28% to 35% for TB1 and TB3), this appeared to be comparatively random in nature. The relative anchorage deformation in TB4 did show a slight dependence on load intensity (Figure 8.28c), but the variation was still only from 24% to 28% of the end rotation (i.e., for both pre and post-yield load reversals). In this case, the maximum curvatures (Figure 8.11) were measured in segment 2, just out from the wall face.

The observed distributions of anchorage deformations during the post-elastic load reversals are shown in Figures 8.9 to 8.11. As indicated, the number of gauge locations in this region was not sufficient to allow the distributions to be determined accurately.

8.9 BEHAVIOUR OF SPLICE REGIONS IN TB3 AND TB4

The reinforcing detail used in TB3 and TB4 relies on satisfactory transfer of forces between the conventional and diagonal bars. The performance of the non-contact lap splice between the two sets of bars was therefore of particular interest in these tests.

Strains in both sets of bars passing through segments 4 and 5, were measured in order to check for bond slip. In addition, the condition of the splice regions was closely observed throughout the tests. Several of the section strain distributions measured in TB3 are shown in Figure 8.29. Very similar strain distributions were obtained for TB4.

The following observations are made:

(a) Segment 4 was the first segment past the bend in the diagonal bars (Figure 7.22). The maximum strains recorded in this segment (840 μs) were well below the yield strain of the bars.

(b) The strain profile in both segments remained approximately linear until after yield in load reversal 5. Even at this stage, however, the observed "neutral axes" were closer to the beam centre line than predicted by theory.

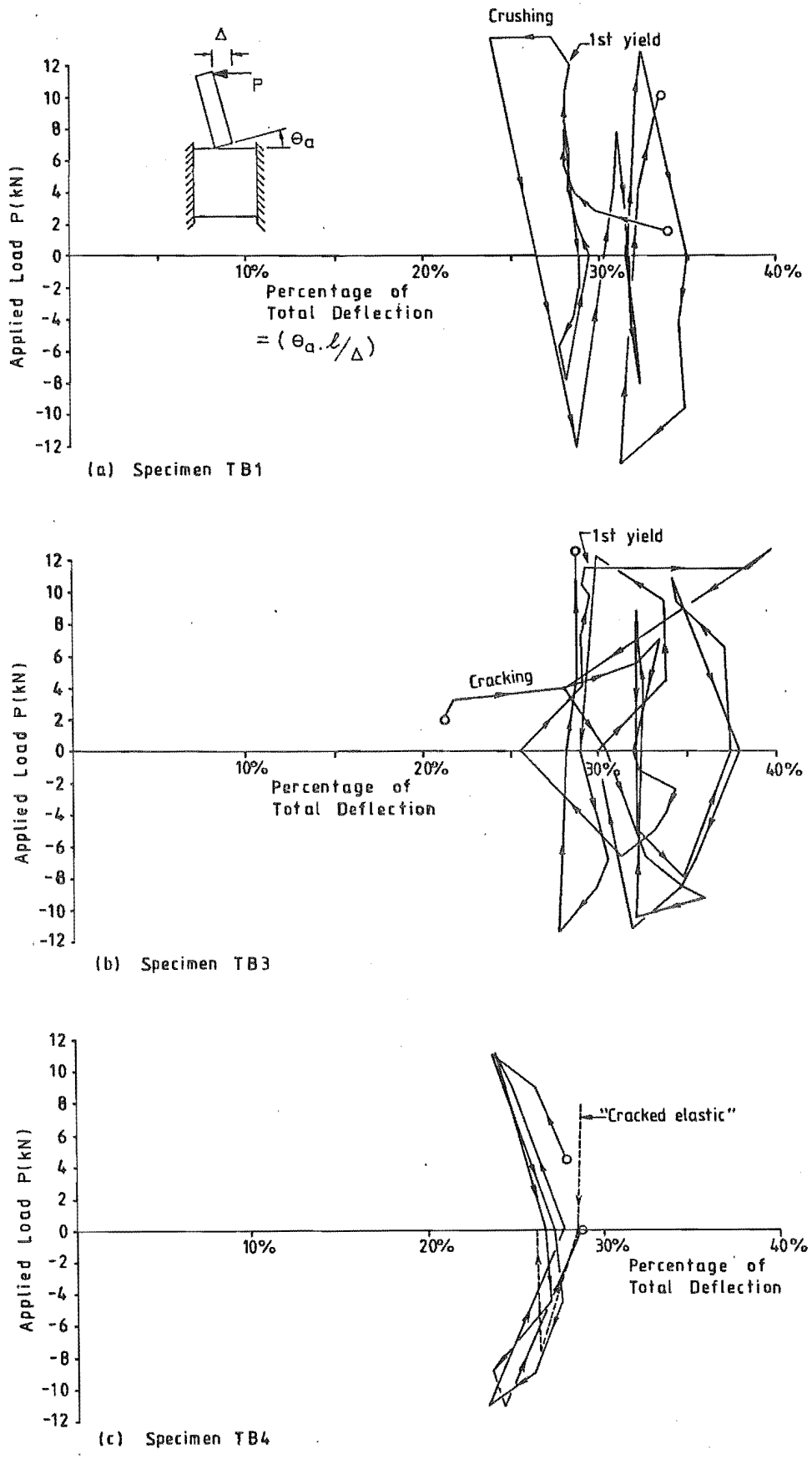

FIGURE 8.28 : MEASURED CONTRIBUTION OF STRAIN IN THE ANCHORAGE REINFORCEMENT TO THE TOTAL END DEFLECTION

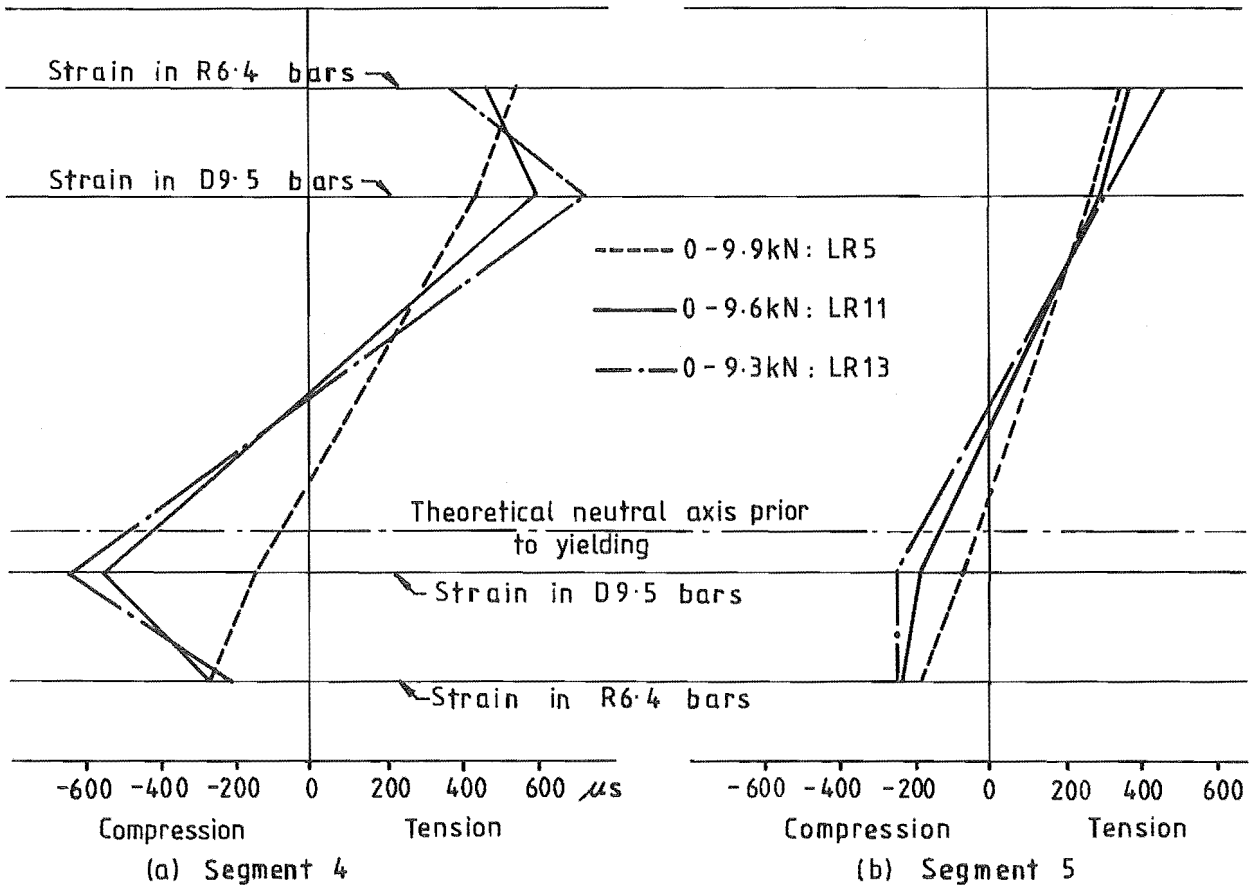

FIGURE 8.29 : MEASURED INCREMENTAL STRAINS IN LAP REGION OF SPECIMEN TB3 : VARIATION IN STRAIN OVER DEPTH OF SEGMENTS 4 AND 5

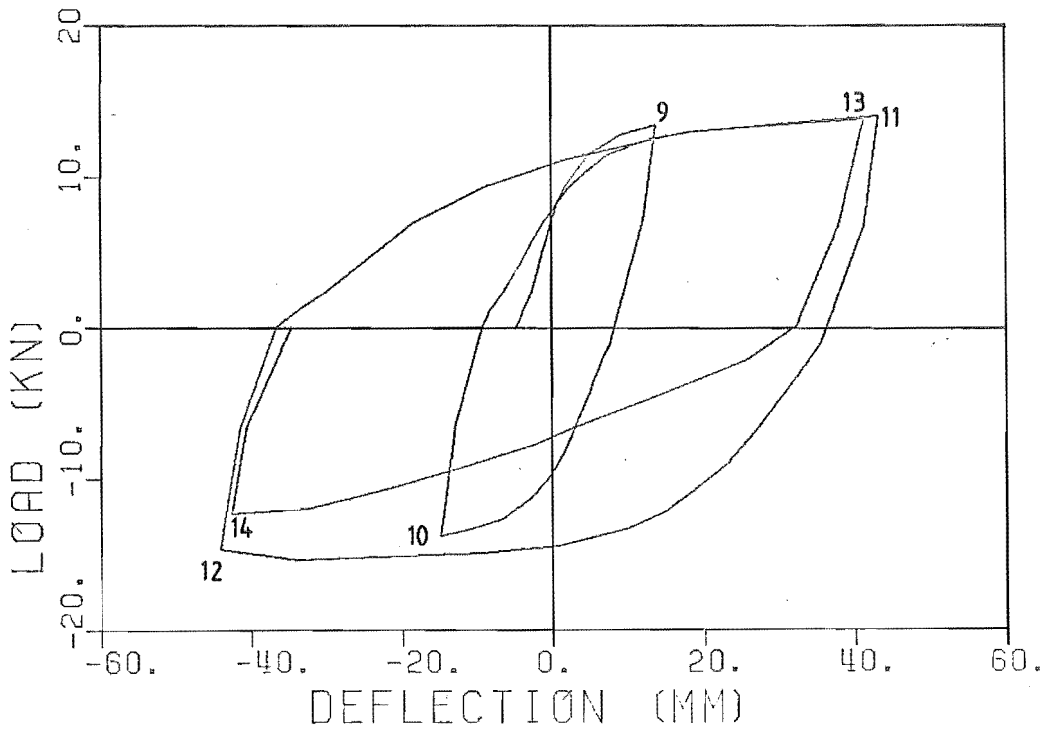

FIGURE 8.30 : OBSERVED LOAD-DEFLECTION RESPONSE FINAL SIX LOAD REVERSALS, TB1

(c) On reversing the load direction (LR6), the strain distribution in segment 4 rapidly became "dog-legged". In subsequent large-displacement load reversals, the strains in the diagonal bars continued to increase relative to those in the conventional bars, and the zero strain point moved very close to the centre of the beam. These results clearly indicate significant deterioration in bond rigidity, at least along part of the length of the diagonal bars in the segment. The symmetry of the tension and compression strains has apparently occurred as a result of the yielding in adjacent segment 3. A large fraction of the moment acting on the plastic hinge side of segment 4 was therefore applied by tension and compression forces in the diagonal bars. As discussed previously, the loading on the splice region was very similar to that imposed on the anchorage zone on the other side of the plastic hinge (Figure 8.14).

(d) The strain distributions measured for segment 5 showed much less change, remaining reasonably linear at least under LR13 when the strain measurements were stopped. These results, together with the comparatively small decrease in the strains in the conventional reinforcement in segment 4, indicate that significant bond forces were still developed in segment 4 despite the increase in flexibility of the bond mechanism.

Overall, the splice appears to have behaved satisfactorily. No sign of distress was detected from the appearance of the splice region, even during the very large-displacement load reversals (DF > ±15).

8.10 FAILURE MECHANISMS

The first three specimens, TB1, TB2, and TB3, were loaded to "failure". The type of failure was different in each case and in this section, the features of the failure mechanisms are discussed.

8.10.1 Specimen TB1

The mechanism of failure for this specimen is best illustrated by reference to the behaviour of the specimen during the last four load reversals. The observed load-deflection response during the latter stages of the test is reproduced in Figure 8.30, and aspects of the behaviour relevant to the failure are discussed below:

LR11 : The large increase in imposed end deflection during this load reversal (to DF ≃ 15) considerably increased the plastic curvature and elongation strains in the hinge zone.

LR12 : Because of the large plastic elongation of the hinge zone in LR11, the interlock rigidity at the start of LR12 was considerably lower than for previous load reversals. However, since the compression face cover concrete was still intact, it provided support for dowel action of the compression bars and also restrained them from buckling. Loading continued up to DF ≃ -15. This caused a further increase in the plastic elongation and towards the end of the load reversal, the cover concrete spalled (although, still remained loosely attached).

LR13 : The very low interlock rigidity and the lack of cover support for either set of bars further increased the sliding shear displacement during this load reversal. This imposed significant kinking deformations on the compression bars. Consequently, at high load intensities in LR13, the bars tended to buckle, resulting in a larger proportion of the compression force having to be resisted by the compression block concrete. The combined effects of the low interlock and dowel rigidities and the kinking/buckling of the compression bars also caused extensive yielding of some of the stirrups in the plastic hinge zone (see Figure 8.31).

LR14 : The behaviour was initially similar to that in the previous load reversal, but the beam was softer because of the deterioration of the concrete in LR13, and because the bars that had buckled had reduced tensile stiffness until they had straightened out. The large sliding shear displacement at the start of this load reversal can be clearly seen from the deflected shapes shown in Figure 8.23. As in LR13, the effectiveness of the compression

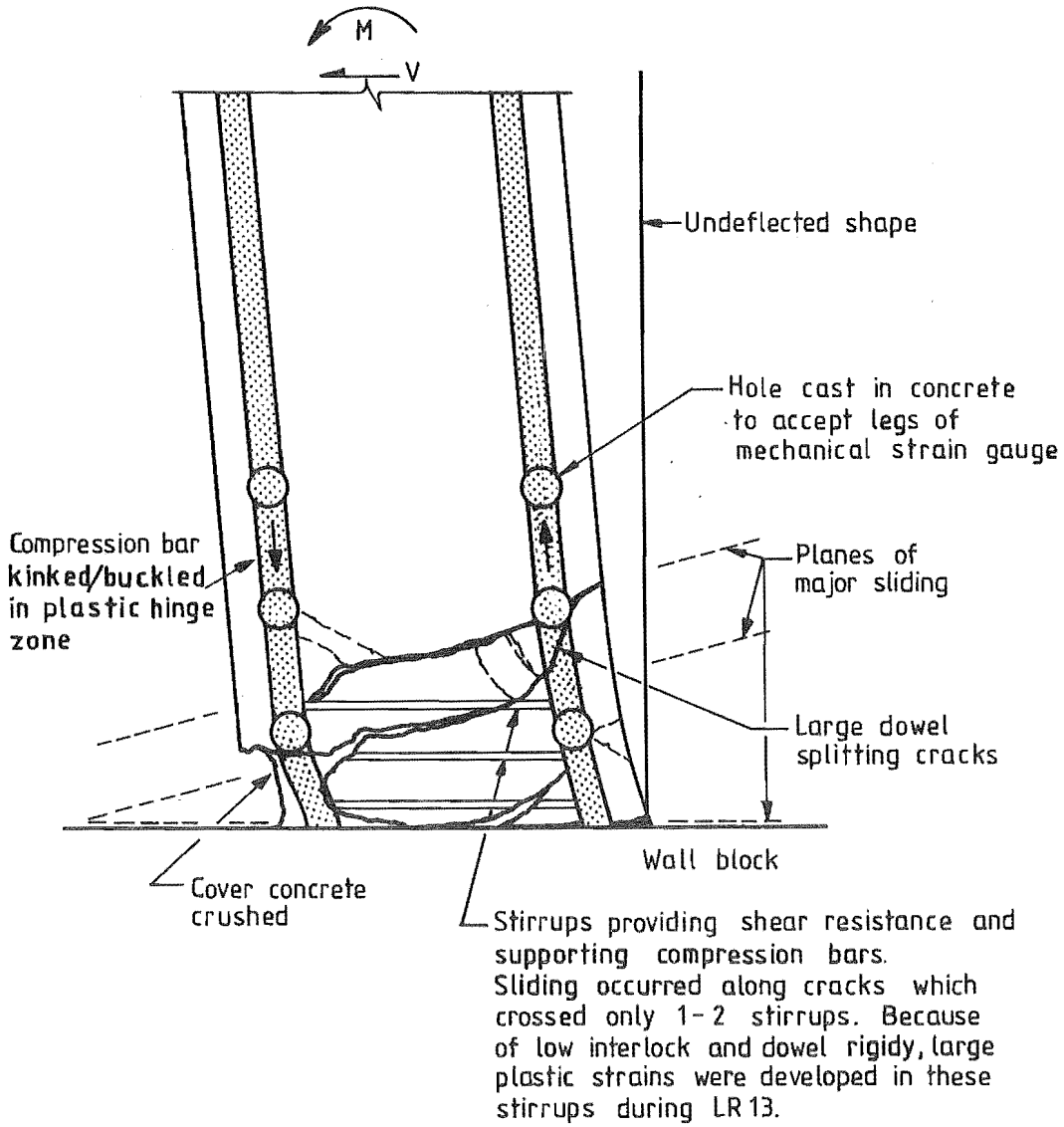

FIGURE 8.31 : CONDITION OF THE PLASTIC HINGE ZONE OF SPECIMEN TB1 AT THE PEAK OF LR13

bars was reduced because of kinking/buckling. This situation was compounded by the loss of confinement due to the stirrups yielding in the previous load reversal. As a result, the core concrete was unable to carry the full compressive and shear forces and the beam did not regain its original strength, even at very large-displacements. The condition of the plastic hinge zone at the end of this load reversal is shown in Figures 8.32a and 8.32b. Further load reversals of a similar magnitude would almost certainly have caused rapid deterioration and loss of core concrete from the plastic hinge region.

As indicated by the above, there were four main stages in the deterioration of the hinge zones:

(a) Initial large flexural deformations, with a substantial reduction in interlock rigidity as a result of the plastic elongation of the hinge zone. The compression face cover concrete would have spalled during this load reversal if it had not already done so.

(b) Loss of effective dowel restraint due to "spalling" of the cover concrete on the opposite face of the beam.

(c) Kinking/buckling of the poorly restrained compression bars leading to increased load on the concrete and yielding of the stirrups in the plastic hinge zone.

(d) Core concrete crushing due to loss of stirrup confinement and kinking of the compression bars.

Although four very large-displacement load reversals were required to induce failure, it should be recognised that the actual ductilities sustained were in part determined by the sequence of loading imposed, i.e., in the test, the loading was increased directly from DF ± 8 to DF ± 15. The beam may still have failed if a smaller ductility had been imposed in the last four load reversals. Failure may also have been induced at a smaller ductility if the cover concrete on the second face had been spalled earlier by increasing the deformation imposed on either LR6 or LR10. The extent to which these factors could affect the failure mechanism can only be determined by further testing.

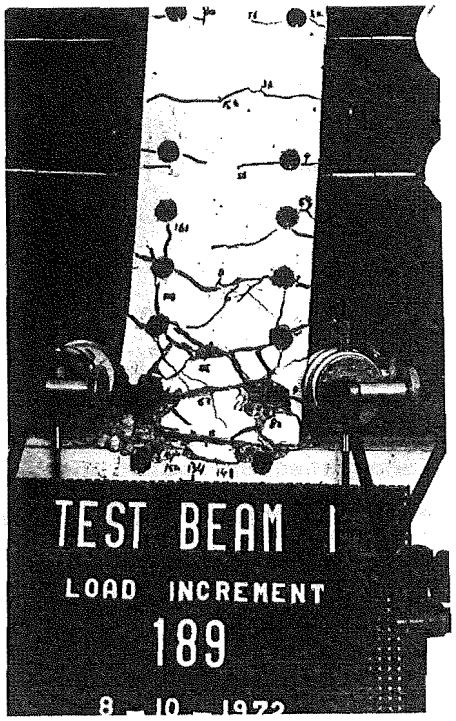

(a) As at end of test (Note open cracks in cover concrete on compression face)

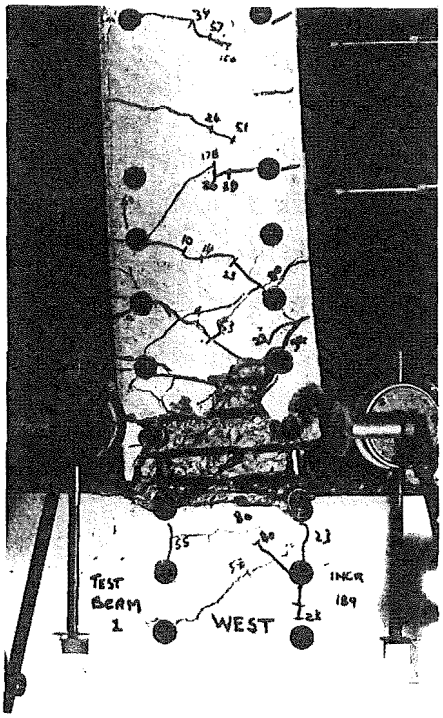

(b) Loose cover concrete removed (Reverse side of beam)

FIGURE 8.32 : CONDITION OF PLASTIC HINGE ZONE IN TB1 AT END TEST

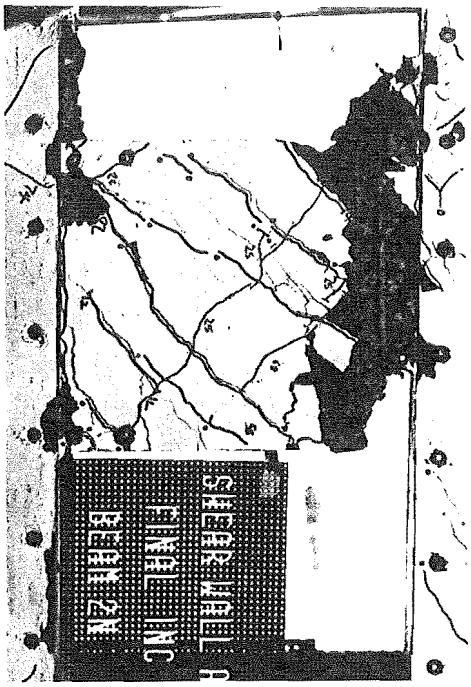

FIGURE 8.33 : SLIDING SHEAR FAILURE OF LEVEL 6 BEAM IN COUPLED SHEAR WALL TESTED BY SANTHAKUMAR (30)

Similar sliding shear failures occurred in the beams of one of the coupled shear wall specimens tested by Santhakumar (30). Despite the much smaller aspect ratios of his specimens (a/d ≃ 0.7), the type of failure observed was similar to that in TB1 (Figure 8.33).

8.10.2 Specimen TB2

The flexural reinforcement in Specimen TB2 consisted of four 6.4 mm diameter plain bars top and bottom. These were anchored without bending in the wall block (Figure 7.3). As indicated in the load-deflection response (Figure 8.5), these anchorages failed at a ductility of only 2 to 3 in the first post-yield load reversal. The slip of the bars relative to the concrete in the anchorage region was clearly visible through the blockouts in the wall used for taking strain readings on the bars (Figure 8.34a).

Following the failure of this specimen, two small pullout specimens were tested to see whether the failure could be duplicated. Each specimen consisted of a length of 6.4 mm diameter plain bar embedded in the full length of a standard 152 mm diameter x 305 mm concrete cylinder. One end of the bar was left protruding from the cylinder and a screw jack was used to apply a pullout force to it (Figure 8.35). Both anchorages failed in a similar manner to the anchorages in TB2 (Figures 8.34 and 8.36). No strain readings were taken in the tests, but on the basis of the dial gauge readings, the strain in the bars must have been in the order of 20,000 μs to 30,000 μs when the far end started to slip. Interestingly, the reduction in pullout strength due to the bars slipping was, in both cases, comparatively small. However, further testing would be needed to establish whether this level of pullout resistance would be sustained under reversed cyclic loading.

The failure of these anchorages is probably initiated when the reduction in bar diameter due to yielding becomes significant in comparision with the surface roughness of the bar. This separates the surface of the bar from the concrete and allows yielding to progressively penetrate the length of the anchorage. Clearly, increasing the length of the anchorages will not prevent this type of failure.

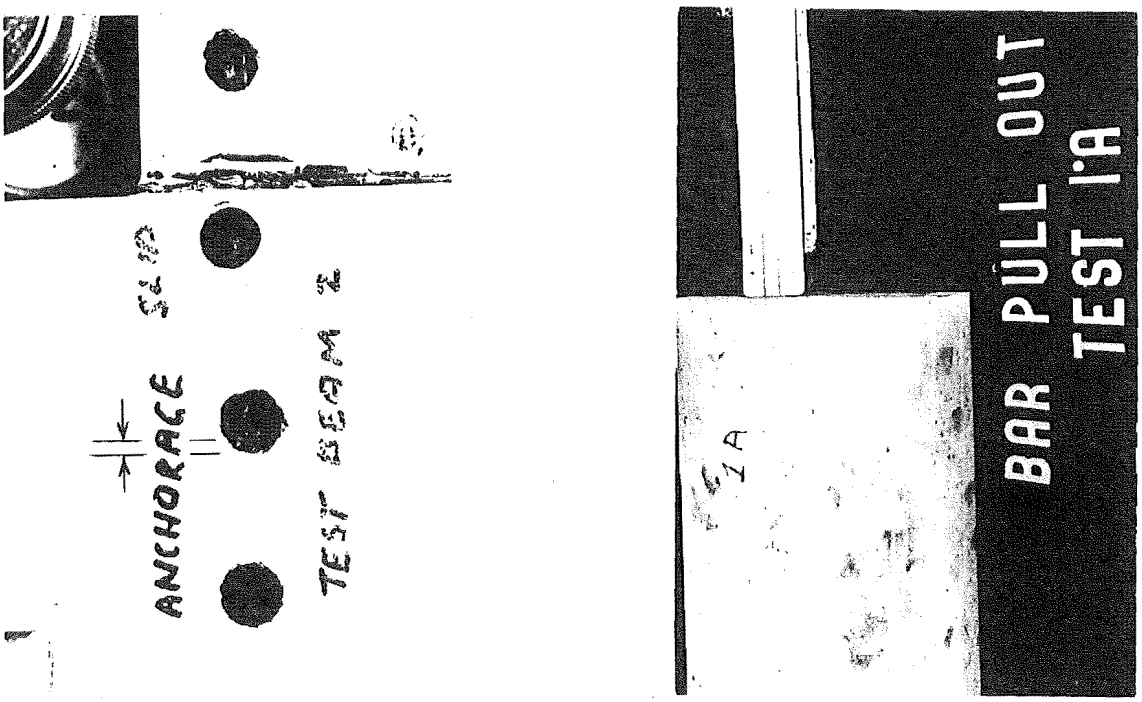

(a) Anchorage zone of TB2 (b) Pull out test specimen

FIGURE 8.34 : BOND FAILURES ALONG 6.3 mm DIAMETER PLAIN BARS SUBJECTED TO POST ELASTIC STRAINS

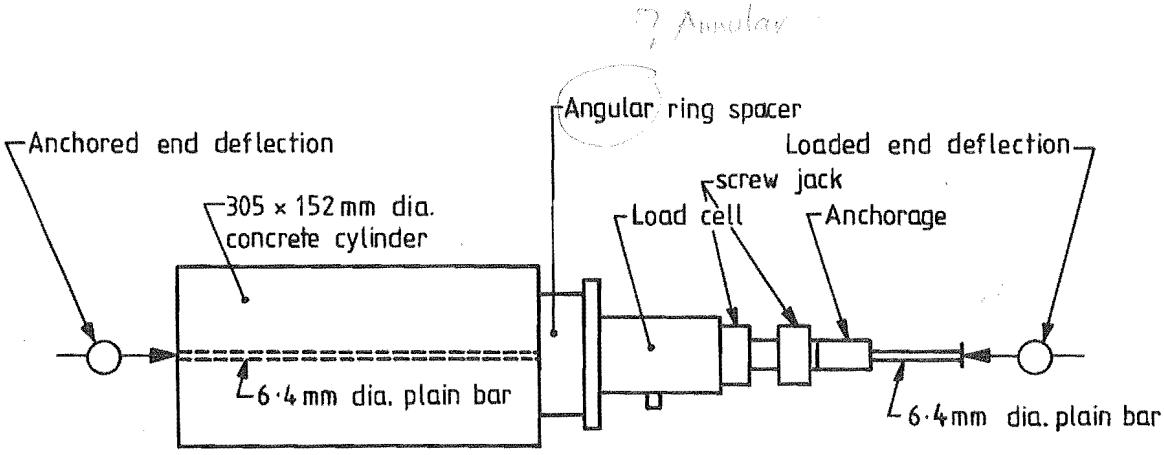

FIGURE 8.35 : TEST SET-UP FOR PULL-OUT SPECIMENS

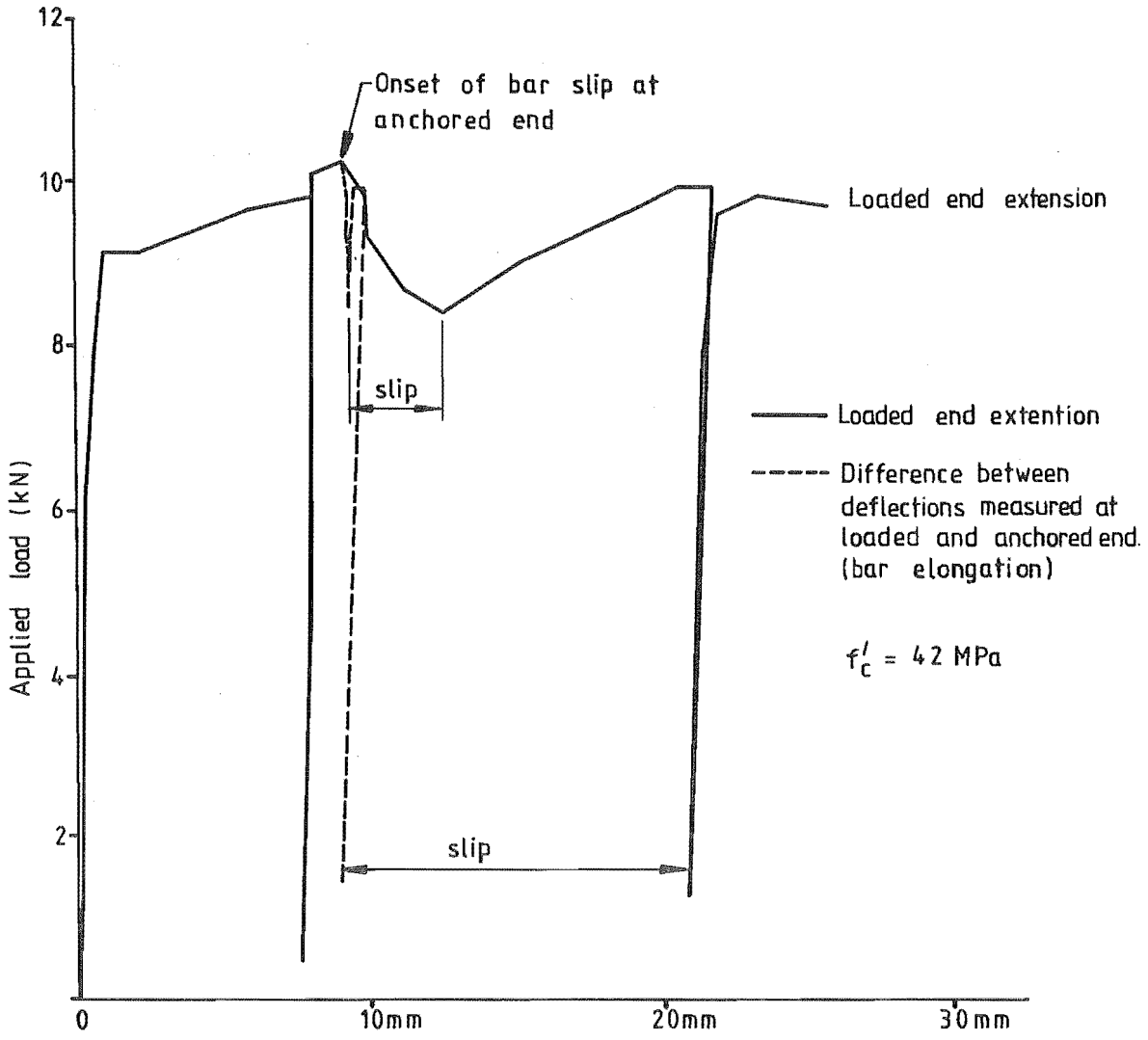

FIGURE 8.36 : LOAD-ELONGATION RESPONSE OF 6.4 mm DIAMETER PLAIN BAR IN SPECIMEN 1A

The behaviour of these anchorages indicates that plain bars are, in general, unsatisfactory for modelling regions of a structure which are subjected to inelastic deformation. Bending the bars would prevent pullout, but would still not satisfactorily model the anchorage behaviour of deformed bars. As a result of the failures of these anchorages, all the subsequent test specimens for this project were designed with only deformed bars for main flexural reinforcement in the plastic hinge regions.

In a previous paper by Paulay and Spurr (113), the reduced strength of TB1 during the final load reversal was mis-interpreted as being caused by pullout of the central plain bars (Figure 7.3). Under closer examination, it was found that the reduction in strength was a result of the large sliding shear displacements in the plastic hinge zone, as described in Section 8.10.1. The plain bars contributed less than one fifth of the total steel area in TB1 and any loss of anchorage strength would have had little effect on the kinking observed in the compression bars or on the core concrete crushing.

8.10.3 Specimen TB3

This specimen failed during the fourth very large-displacement load reversal due to out-of-plane buckling of the compression bars in the plastic hinge zone. This was similar to the type of failure which occurred in the diagonally reinforced deep coupling beams tested by Binney (23). Unlike the case of TB1, there was little degradation of the response in the preceding load reversals and even during the final load reversal, the reduction in strength only became significant at very large ductilities, i.e., DF > 15 (Figure 8.6). At peak displacement in LR16 (DF = 22), the beam was still resisting 95% of its theoretical ideal strength (or 72% of its maximum measured strength).

An important feature of the failure mechanism exhibited by this specimen was that the compression block buckled in an out-of-plane shear mode which caused the whole beam to rotate about its axis.

This is shown in Figure 8.38, and is illustrated in Figure 8.40. The magnitude of twist in the beam was only measured at the end of the test, when it was estimated to be 0.17 radians (10 degrees).

Four main factors which may influence this type of buckling behaviour are discussed below:

(a) Interlock Action The susceptibility of TB3 to torsional buckling was primarily a result of the high resistance to sliding shear provided by the diagonal reinforcing. Because there was little in-plane sliding between crack faces, large compression strains were developed in the reinforcement before the cracks had closed sufficiently to develop interlock action. (Buckling was, however, prevented in the in-plane direction by the high shear rigidity of the main diagonal reinforcing.) By contrast, the cracks in conventionally reinforced beams "close" at relatively low loads because the opposing undulating crack surfaces are mis-matched due to in-plane sliding displacements. Conventionally reinforced beams are therefore much less susceptible to torsional buckling because of their interlock rigidity at high load intensities. In addition, the kinks imposed on the bars by the sliding displacements bias buckling in the in-plane direction.

(b) Dowel Action Before the flexural cracks on the compression side close, most of the lateral restraint for the compression bars is provided by dowel action. The condition of the cover concrete can therefore significantly affect the development of buckling. Unlike for loading in the in-plane direction, stirrups do not contribute to the out-of-plane dowel strength. (See Figure 8.40.) The effect of the cover concrete is indicated by the behaviour during the last three load reversals (LR14 to LR16). The plastic flexural deformations at the start of each of these load reversals were similar. However, large dowel cracks (approximately in the plane of the compression bars) did not open up until shortly before the peak of LR14. At this stage, the flexural cracks in the compression block had already closed. The final load reversal (LR16), which was the next load reversal in the same direction as LR14, was therefore the first in which the compression cover concrete had been ineffective during the

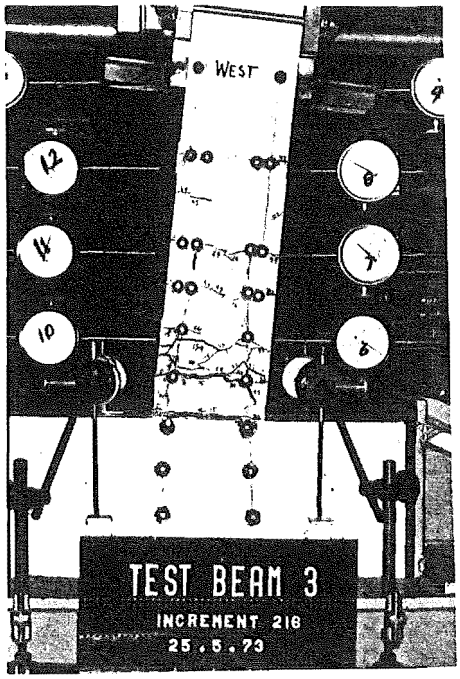

FIGURE 8.37 : SPECIMEN TB3 AT PEAK OF SECOND TO LAST LOAD REVERSAL

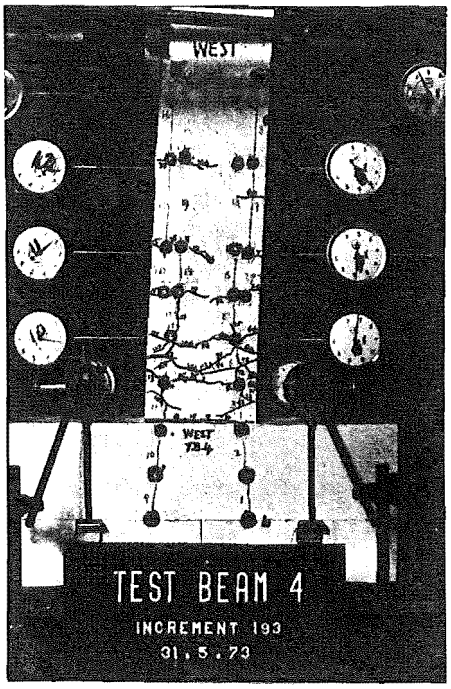

FIGURE 8.39 : SPECIMEN TB4 AT END OF TEST

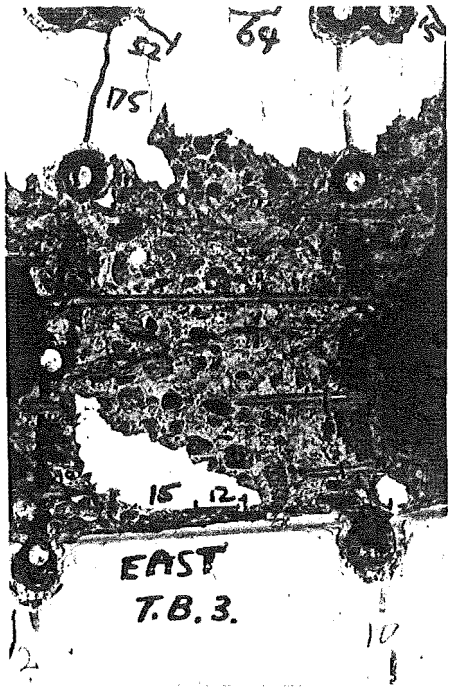

(a) Face on (Reverse side)

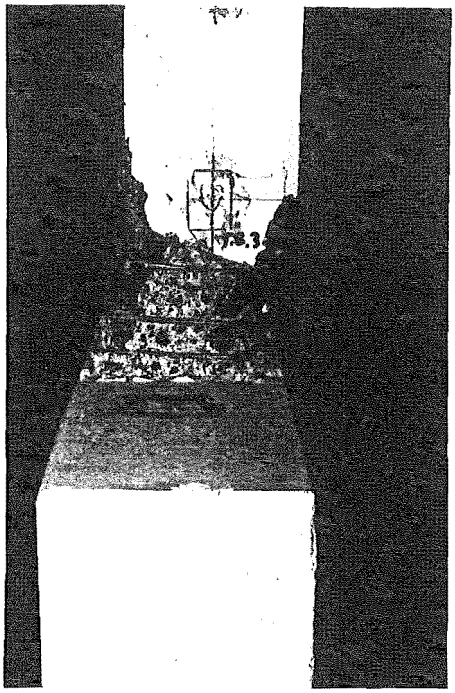

(b) Edge on

FIGURE 8.38 : SPECIMEN TB3 AT END OF TEST, TORSION-BUCKLING FAILURE

critical period before the cracks on the compression side closed. Some dowel action would still have been effective, but it is clear that much of the dowel rigidity was lost when the cover concrete spalled. This suggests that the beam could well have buckled earlier if the deformations imposed during the first few post-yield load reversals had been large enough to spall the cover concrete.

(c) Bar Stability As indicated by the shape of the specimen in Figures 8.38 and 8.40, the bars buckled in parallel. The stability of the compression reinforcement alone (i.e., ignoring the concrete) is therefore governed by the moments of inertia of the individual bars*. This factor is, however, likely to be significant only after the cover concrete has spalled. Therefore, although the oversized bars used in this specimen (Section 7.2.3) may have contributed to the large ductility sustained in LR16, they probably had little effect on the response in the preceding load reversals. Note also that since the bars deform in parallel, the width of the beam has little direct affect on the bar stability, although it will influence cover spalling.

(d) External Restraint The loading system used in the test provided very little restraint against out-of-plane twisting. This models reasonably well, the situation of a beam isolated from the floor system. Premature buckling in this situation must be guarded against. However, usually the beams and floors are cast monolithically. Under these conditions, torsional deformations will actually be imposed on the beams due to the transverse component of the earthquake excitation. Because of the rigidity of the connection between floor and beam, the magnitude of these deformations will be controlled by the deflection of the structure in the transverse** direction and will be much smaller than the maximum twist of 0.17 radians sustained by TB3. The torsional flexibility of the diagonally reinforced beam is then a distinct advantage, i.e., once the cover concrete spalls, the beam can twist "freely" about its axis (restrained by the floor slab) without significant loss of in-plane moment capacity. By contrast,

---

* Binney (23) assumed that the steel parameter influencing buckling of the diagonal bars in his coupling beam specimens was the moment of inertia of the bar group acting compositely. This implies a flexural rather than shear mode of out-of-plane buckling.

** Perpendicular to the beam longitudinal axis.

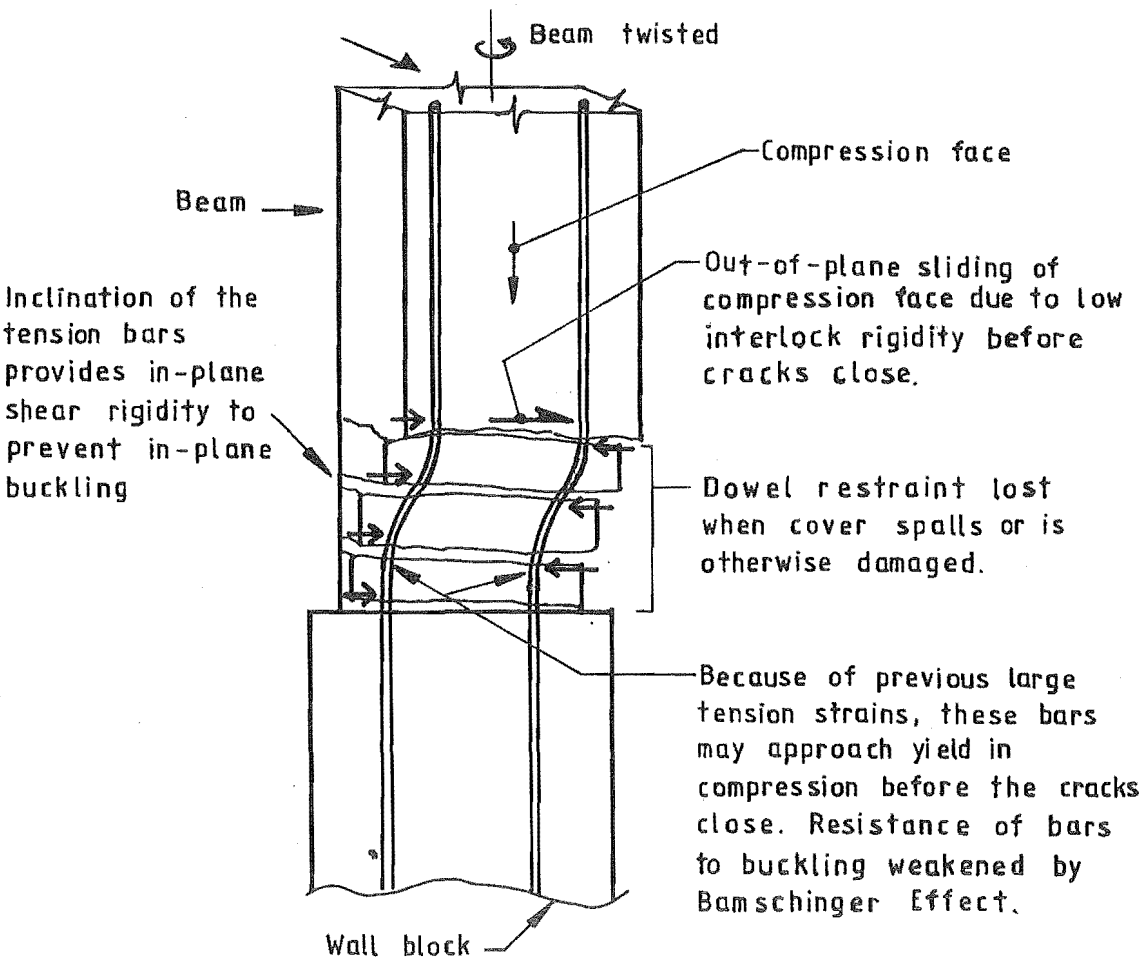

FIGURE 8.40 : IDEALIZATION OF TORSION-BUCKLING FAILURE OF SPECIMEN TB3

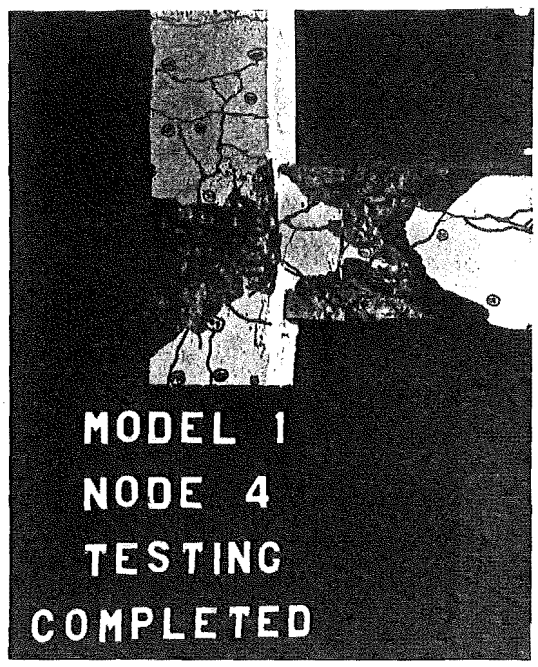

FIGURE 8.41 : COVER CONCRETE IN A SMALL SCALE SIX STOREY FRAME SPALLED DUE TO TORSIONAL DEFORMATIONS IN A BEAM PERPENDICULAR TO THE DIRECTION OF LOADING (100).

conventionally reinforced beams are much more dependent on the integrity of the concrete. The in-plane strength is therefore likely to be considerably affected by torsion-induced damage such as that indicated in Figure 8.41.

8.11 DISCUSSION

All specimens except TB2 behaved well in terms of seismic design expectations, i.e., they were able to sustain four or more cycles of loading to DF > 4 without loss of strength. The two diagonally reinforced specimens exhibited excellent energy dissipation even at very large-displacements. Comparisons with the predicted responses confirm that most of the softening that did occur during post-elastic loading was due to Bauschinger effect in the steel response.

The conventionally reinforced specimen TB1 also exhibited good energy dissipation even though sliding shear contributed a significant component of the post-elastic deformations. The inelastic shear model was as accurate for this specimen as for the larger beams analysed previously and the comparisons made with the observed response again showed the importance of modelling the sliding shear deformations (e.g., Figure 8.3), even in cases where considerable energy is dissipated. It was not possible, however, to confirm the validity of the allowance made for inclined cracking as conflicting answers were obtained for different response components.

The test results also demonstrated the importance of anchorage deformations, with this component contributing 24-35% of the total end deflection. This component would have been even larger if overall slip of the bars or if joint shear deformation had been significant. Under the restricted (but not necessarily unrealistic) conditions applying in the tests, the simple model used proved to be adequate, provided that a realistic "anchorage length" was selected.

The behaviour of TB2 highlighted the susceptibility of plain bars to pullout when loaded into the post-yield range. Although the plain bars were unsuitable for modelling deformed bar reinforced components, it would have been interesting to have continued the loading for several more cycles. The strength after bond slip was only slightly below

yield strength and if maintainable, it is possible that this type of mechanism could be used for energy dissipation under some conditions, e.g., using slightly curved plain bar anchors.

As expected, there was no obvious evidence that scale effects influenced the observed behaviour of these medium scale specimens (Section 7.2.2). No dimensional effects have been incorporated in the theoretical model, and generally the pattern of agreement with the observed responses was very similar to that obtained for larger specimens. Instrumentation did prove more of a problem, especially for measuring steel strains (Section 7.4.6). This is one aspect where particular care needs to be taken with scale tests.

9. FRAME-WALL SPECIMENS

SUMMARY

This chapter presents the results of the tests on the two frame-wall specimens described in Chapter 7. Specific aspects of the wall and frame member responses are evaluated in detail and where appropriate are compared with responses predicted by the computer program (Section 7.6) or with the observed responses of the beam-wall specimens (Chapter 8).

9.1 APPLIED LOADING

The displacement loading sequences applied to the two frame-wall specimens are shown in Figure 9.1. These sequences are given in terms of the specimen ductility factor (DF) which is defined in Figure 9.2.

The same general load sequence was used for both specimens. The direction of loads applied was alternated with approximately equal forces and displacements in each direction. In the first two load reversals (first cycle), the loads were kept below 12% of the specimen yield strength (Figure 9.2) and the specimens remained uncracked. This was followed by a further four pre-yield load reversals in which the specimens were loaded to between 35% and 70% of their yield strength and 15 post-yield load reversals with peak specimen ductilities increasing from approximately 4 to 8.

As indicated in Figure 9.2, first yield in the specimens occurred in the beams at a load (base moment) of $M_b \approx 225$ kNm*. Specimen yield has, however, been taken as the point at which the average strain in the flexural bar group concentrated at the frame edge of the walls**

---

* The loads applied to these specimens have generally been expressed in terms of the total applied base moment (i.e. moment at Level 0); in the first place because the wall flexural response was dominant and secondly, because the loads (displacements) imposed on the beams and columns were largely determined by the wall flexural displacements.

** The loading imposed during the initial post-elastic load reversal (LR7) induced tension in the reinforcement at the frame edge of wall.

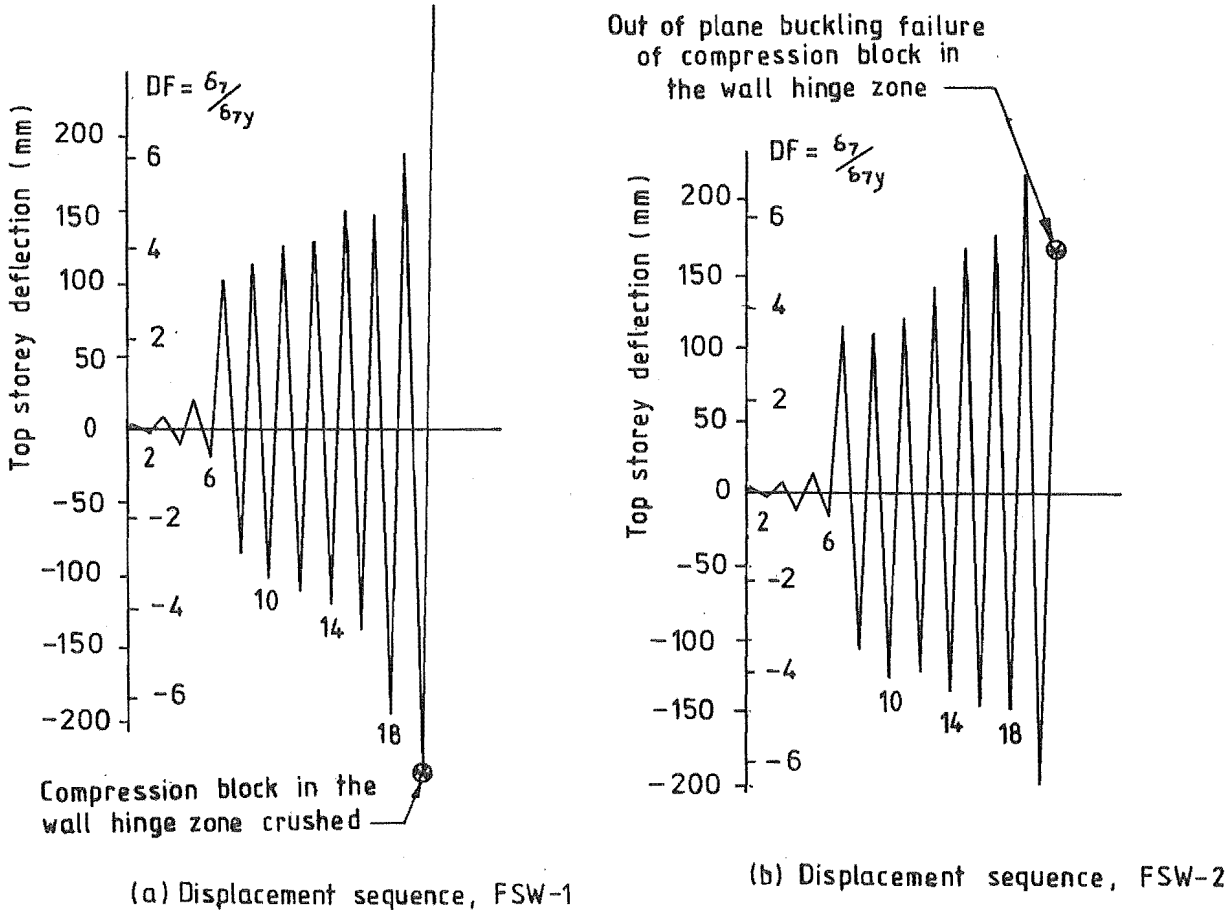

(a) Displacement sequence, FSW-1

(b) Displacement sequence, FSW-2

FIGURE 9.1 : LOAD SEQUENCES APPLIED TO FRAME-WALL SPECIMENS

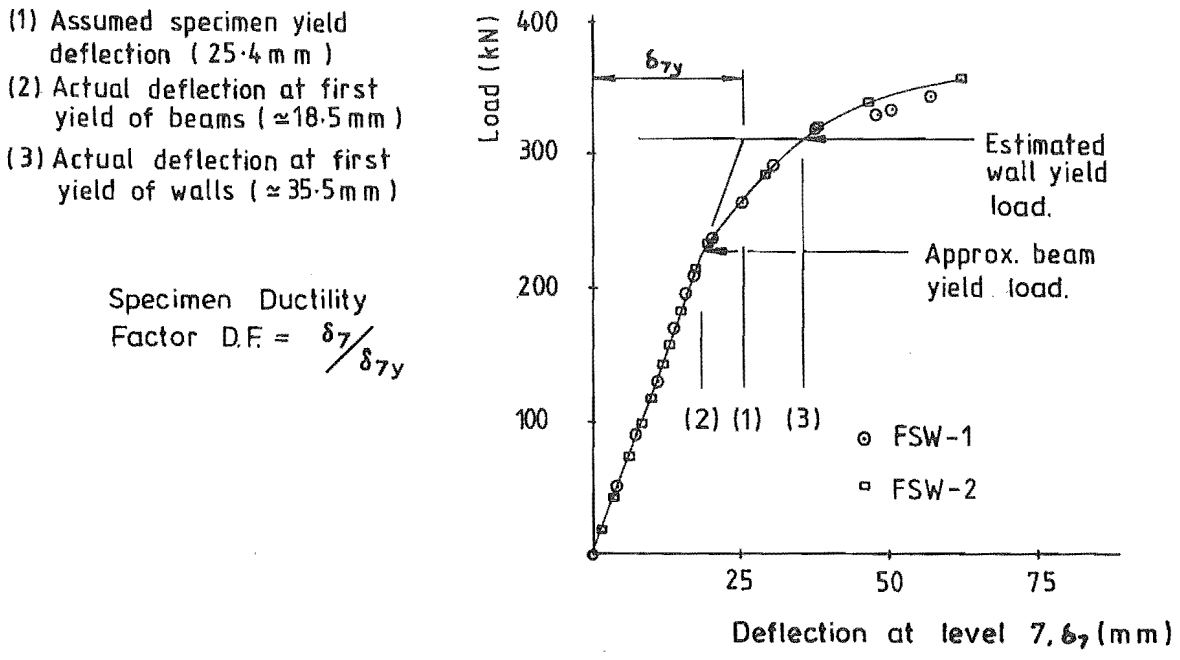

FIGURE 9.2 : DEFINITION OF DUCTILITY FACTOR (DF) FOR FRAME-WALL SPECIMENS

reached yield strain. This occurred at a load of $M_b \simeq 310$ kNm. The main reasons for adopting this criterion, rather than initial (i.e. beam) yield were that the walls contributed about two-thirds of the total base moment resistance and that the load at beam yield was lower than the design strength of the specimens. A beam yield criterion would therefore have given an unconservative indication of the displacement ductilities sustained in comparison with the design situation (See footnote, Section 8.1).

As indicated in Figure 9.2, the nominal yield deflection for the specimen has been taken as the projected deflection at wall yield based on the stiffness of the specimen before onset of beam yield. This value was adopted to give an overall assessment of the ductilities imposed on the specimens, and is consistent with the definition of yield displacement normally adopted in experimental studies of this type. However, the difference between the beam and wall yield deflections does mean that the relative deformations (e.g. ductilities) imposed on the beams and walls were significantly different. For example, the peak displacement imposed on FSW-1 at the peak of LR7 (DF = 3.8) was approximately 5.3* times the deflection at onset of yield in the beams but only 2.7 times the deflection at onset of wall yield.

Because of the large number of manually recorded strain and deflection (theodolite) readings taken, each of the post-elastic loading reversals took about one week to complete. As a result, the effect of strain ageing on the bars in the plastic hinge zones was more significant than that which occurred in the beam-wall specimens. This led to a migration of yielding sections and is further discussed in section 9.3.2.

9.2 OVERALL BEHAVIOUR

This section examines the overall load-deflection responses of the two frame-wall specimens tested under the loading sequences described

---

* This is not equivalent to the beam member ductility, which is the ratio of beam rotation to beam rotation at onset of yield in the beam flexural reinforcement (Section 9.4.2).

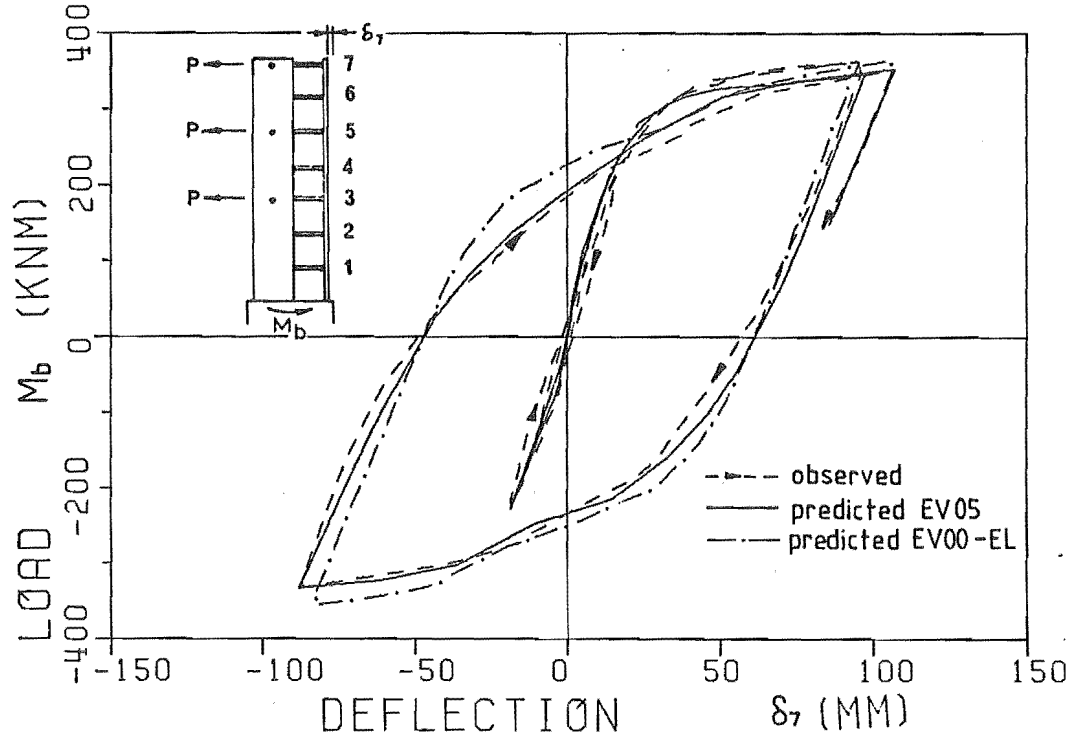

(a) LR 5 to LR 9

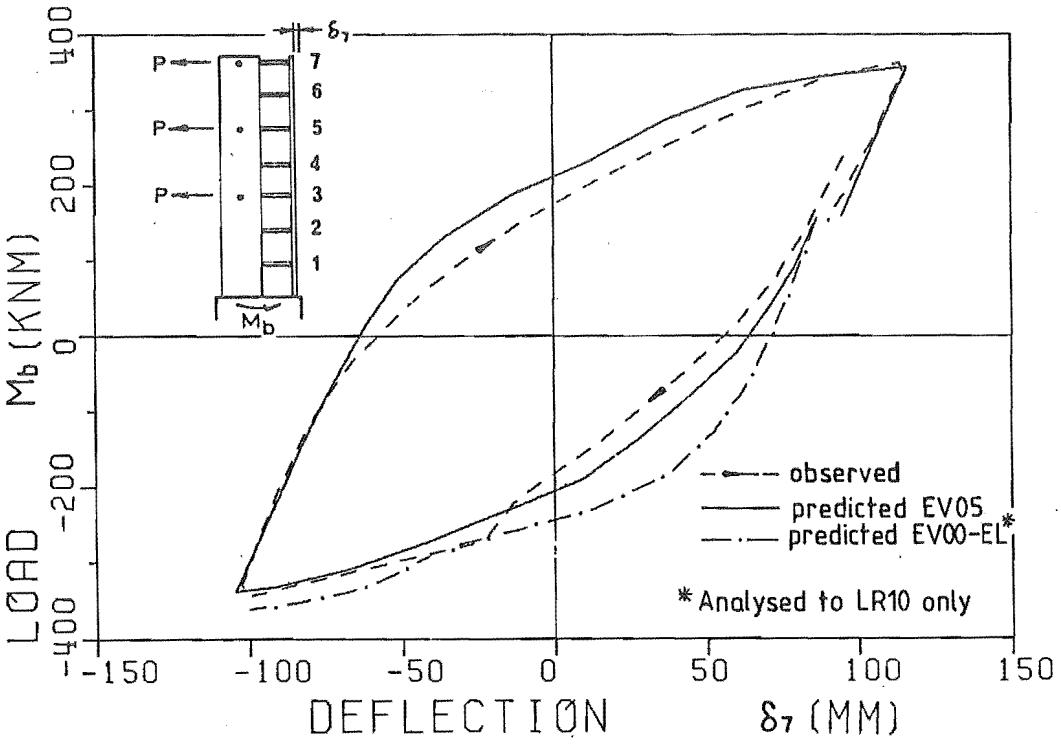

(b) LR 10 and LR 11

FIGURE 9.3 : LOAD-DEFLECTION RESPONSES FOR LOAD REVERSALS 5 TO 11, FSW-1

previously. The hysteresis diagrams for these responses have been plotted in terms of the Level 7 column deflections, measured using the dial gauges, rather than in terms of the wall deflections. These readings were taken more frequently than wall deflections and therefore a more complete record of the responses was obtained.

Other than the results for the elastic shear analysis of FSW-1 (EV00-EL in Figure 9.3), all predicted responses considered in this section were obtained from the EV05 analyses (Section 7.6).

9.2.1 Pre-yield Load-Deflection Responses

As indicated in Figures 9.2 to 9.4, the two specimens behaved very similarly during the pre-yield load reversals, with the stiffness of both specimens being almost identical. The predicted initial load curves (monotonic envelopes) compared well with the observed responses, but under reversed loading the hysteretic energy dissipation was significantly under-estimated (Figures 9.3 and 9.4). The observed curves also indicate significant softening at low loads in LR6 and LR7 whereas the initial parts of the predicted curves for LR6 and LR7 are still similar to the observed envelope curves.

The hysteresis in the observed response could have been due to several factors which were not modelled in the computer program. Prominent among these are the development of residual wall elongations and the factors responsible for them (Section 9.3.3), and hysteresis in the concrete stress-strain response which was not modelled in situations where the maximum stress had not exceeded f'_c (Section 4.2.2).

The first flexural cracks were observed in the beams at a load of approximately 50 kNm and in the walls at approximately 100 kNm. Because of the redundancy of the specimens, these cracks did not cause a distinct change in the specimen load-deflection responses, but rather resulted in a gradual change in slope of the curves as the extent of cracking increased. During the first six load reversals, the cracks in the walls remained primarily flexural, i.e. horizontal*

---

* Although the walls were tested in a horizontal position, for the purposes of description they are treated as being in an upright position.

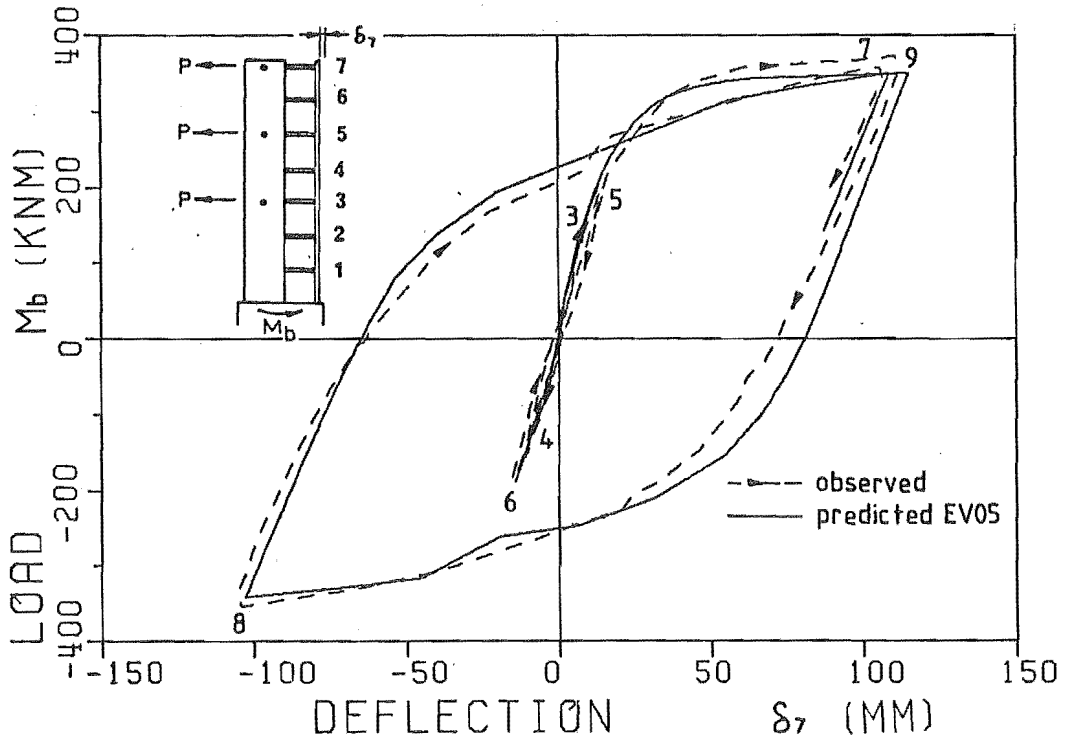

(a) LR5 to LR9

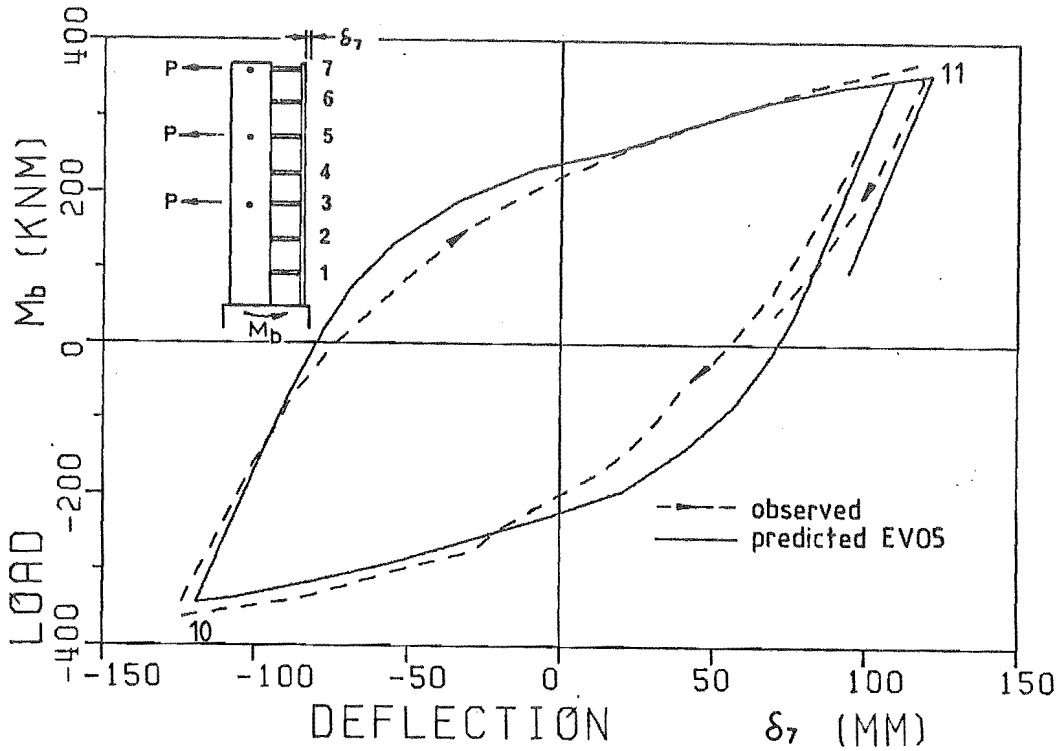

(b) LR10 and LR11

FIGURE 9.4 : LOAD-DEFLECTION RESPONSES FOR LOAD REVERSALS 5 TO 11, FSW-2

(Figures 9.8 and 9.9), and it was not until after the beams yielded and the load had reached approximately 90% of the wall yield strength, that these cracks started to become inclined due to the effects of shear stresses.

9.2.2 Post-yield Load-Deflection Responses

Observed and predicted post-elastic load-deflection responses of the specimens are shown in Figures 9.3 and 9.4 for load reversals 7 to 11, and in Figures 9.5 and 9.6 for the full load sequence. The condition of the specimens at the end of the tests are shown in Figure 9.7.

The responses of both specimens were affected by strain ageing after the second post-elastic load reversal (LR8). The effect of this was obvious at only a few points on the load-deflection curves* (e.g., D in Figures 9.5 and 9.6). However, other aspects of the responses were more noticeably affected. These are discussed in subsequent sections (e.g., Section 9.3.2).

As indicated in Figures 9.5 and 9.6, the observed load deflection responses of the two specimens were reasonably similar during the post-elastic load reversals. The main differences between the specimens were the greater softening of FSW-1 at high load intensities (A in Figures 9.5 and 9.6), presumably due to the effect of sliding shear deformations in the beams, and the effect of local bar buckling in the wall plastic hinge zone in FSW-1 (Section 9.3.9, and B and C in Figure 9.5). Similar local buckling occurred in FSW-2 but this did not develop until the last few load cycles, and was confined to a smaller area. During the final load reversal the wall plastic hinge zone in FSW-2 failed by out-of-plane buckling (Section 9.3.10, and C in Figure 9.6).

Despite the above problems, both FSW-1 and particularly FSW-2 exhibited good overall energy dissipation. The deformations sustained by the

---

* Where possible, weekend or longer delays in the loading programme were arranged to be taken between load reversals, after the specimens had been unloaded.

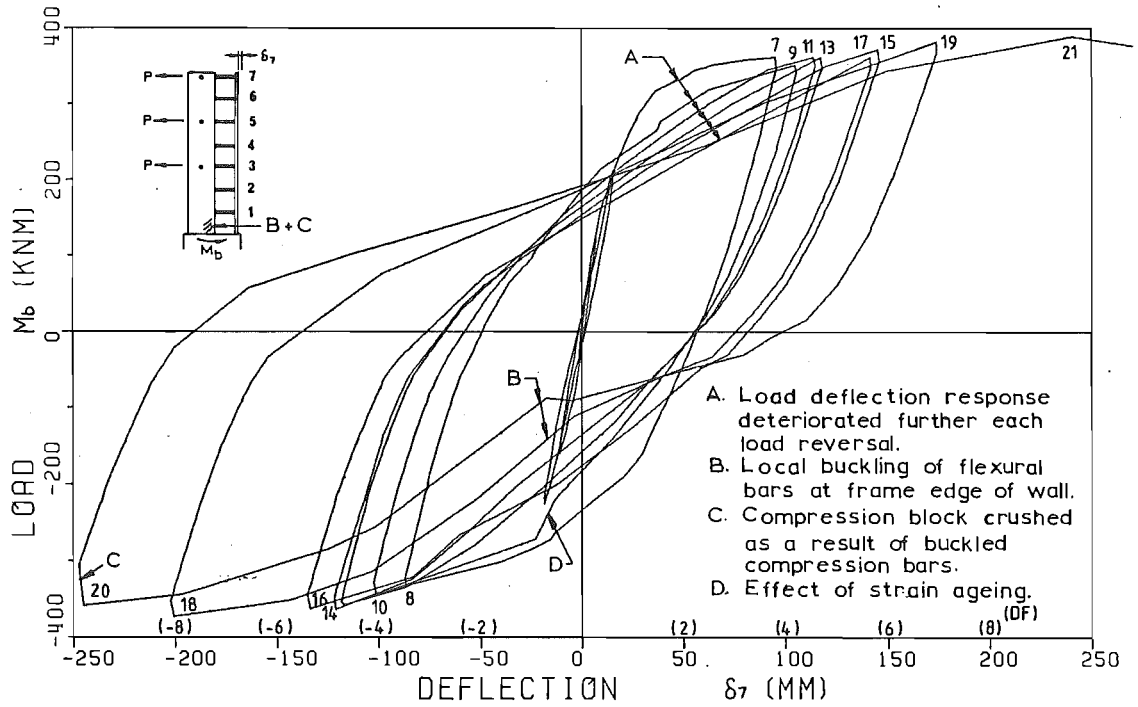

(a) Observed Load-Deflection Response, Full Test Load Sequence, LR1 to LR21

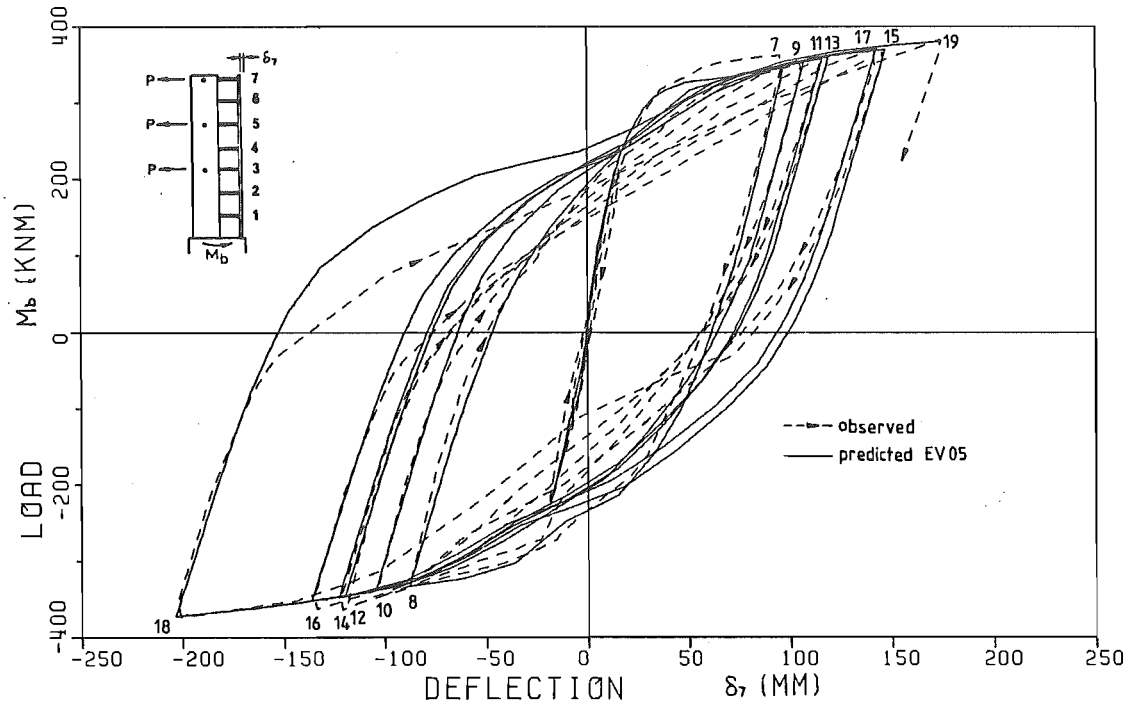

(b) Comparison Between Observed and Predicted Responses, Load Reversals 5 to 19 Only.

FIGURE 9.5 : FULL LOAD-DEFLECTION RESPONSE, FSW-1

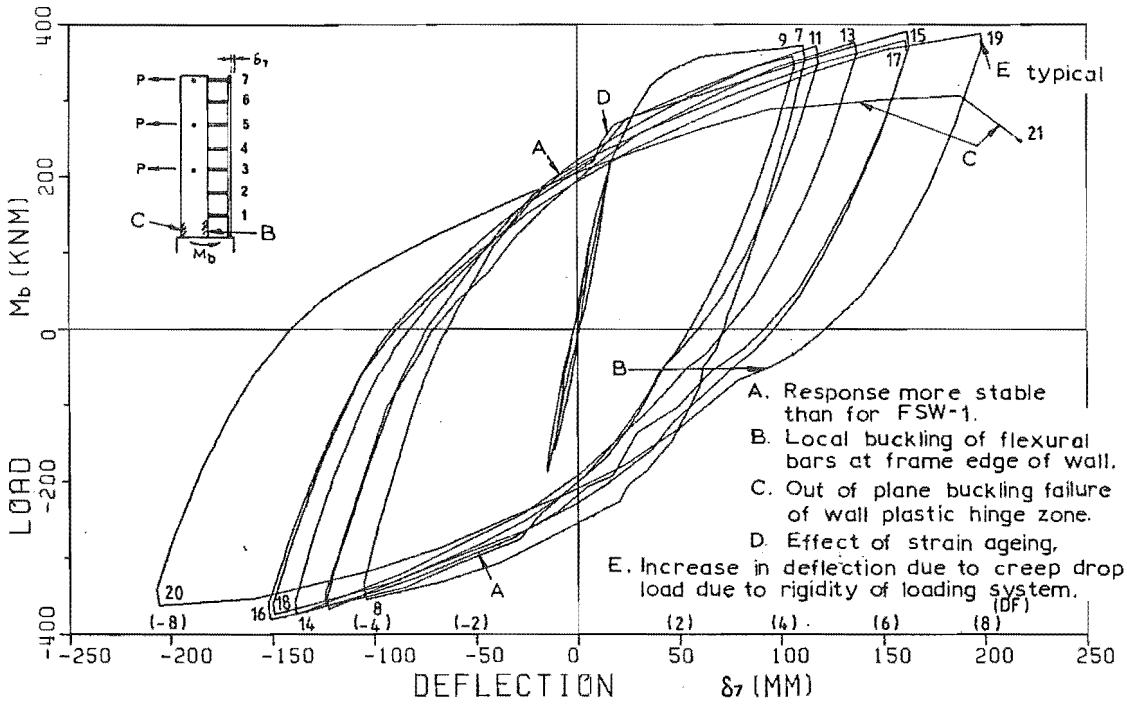

(a) Observed Load - Deflection Response, Full Test Load Sequence LR 1 to LR 21

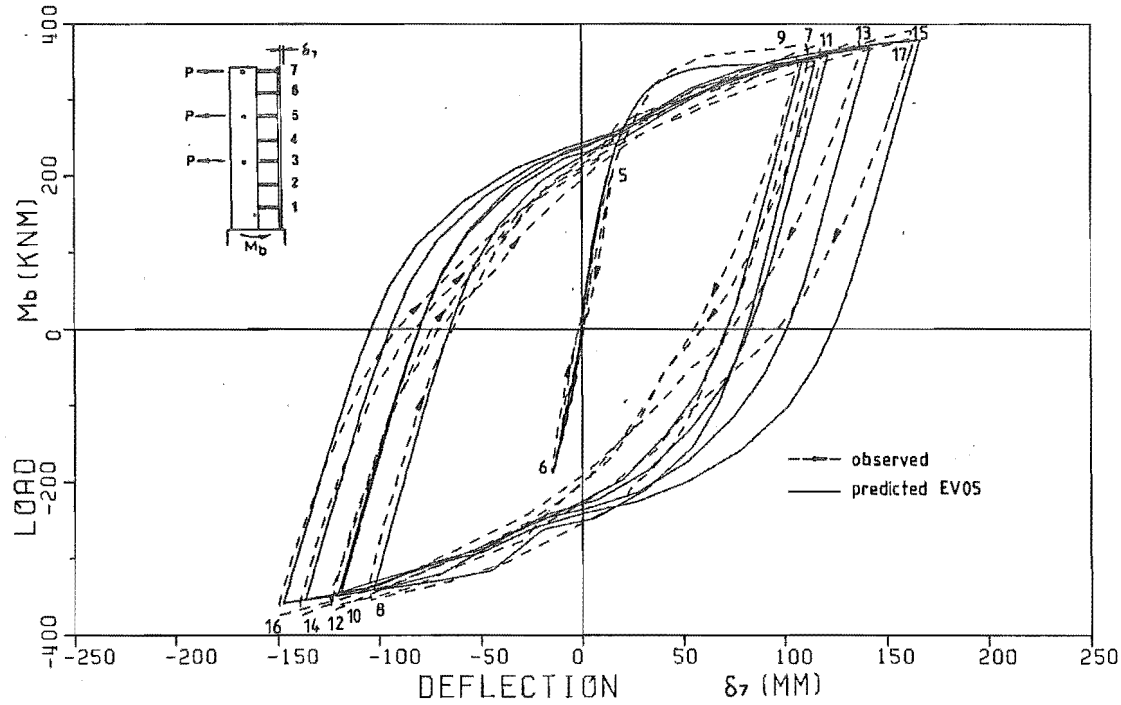

(b) Comparison Between Observed and Predicted Responses, Load Reversals 5 to 17 Only

FIGURE 9.6 : FULL LOAD-DEFLECTION RESPONSE, FSW-2

specimens were in excess of code requirements, i.e., 7 cycles to DF = ±4 to ±8 compared with 4 cycles to DF ±4 required by the code (111). However, as discussed in Section 9.3.10, the susceptibility of the wall plastic hinge zones to out-of-plane buckling needs further investigation.

As indicated in Figures 9.3a and 9.4a, the load-deflection responses were predicted reasonably accurately for the first three post-elastic load reversals (LR7 to LR9). However, in subsequent load reversals, the degree of softening in the last half of the unloading curves and in the reloading curves was significantly underestimated for both specimens (Figures 9.3b to 9.6b). In the case of FSW-2, the largest discrepancies occurred in the first half of the reloading part of the curves. The maximum displacement difference between the observed and predicted curves reached 30 mm or more during LR14 to LR17 (Figure 9.6b). The corresponding discrepancies for FSW-1 were even larger, and in this case the model also failed to predict deterioration of the response of FSW-1 at high load intensities (Figure 9.5b).

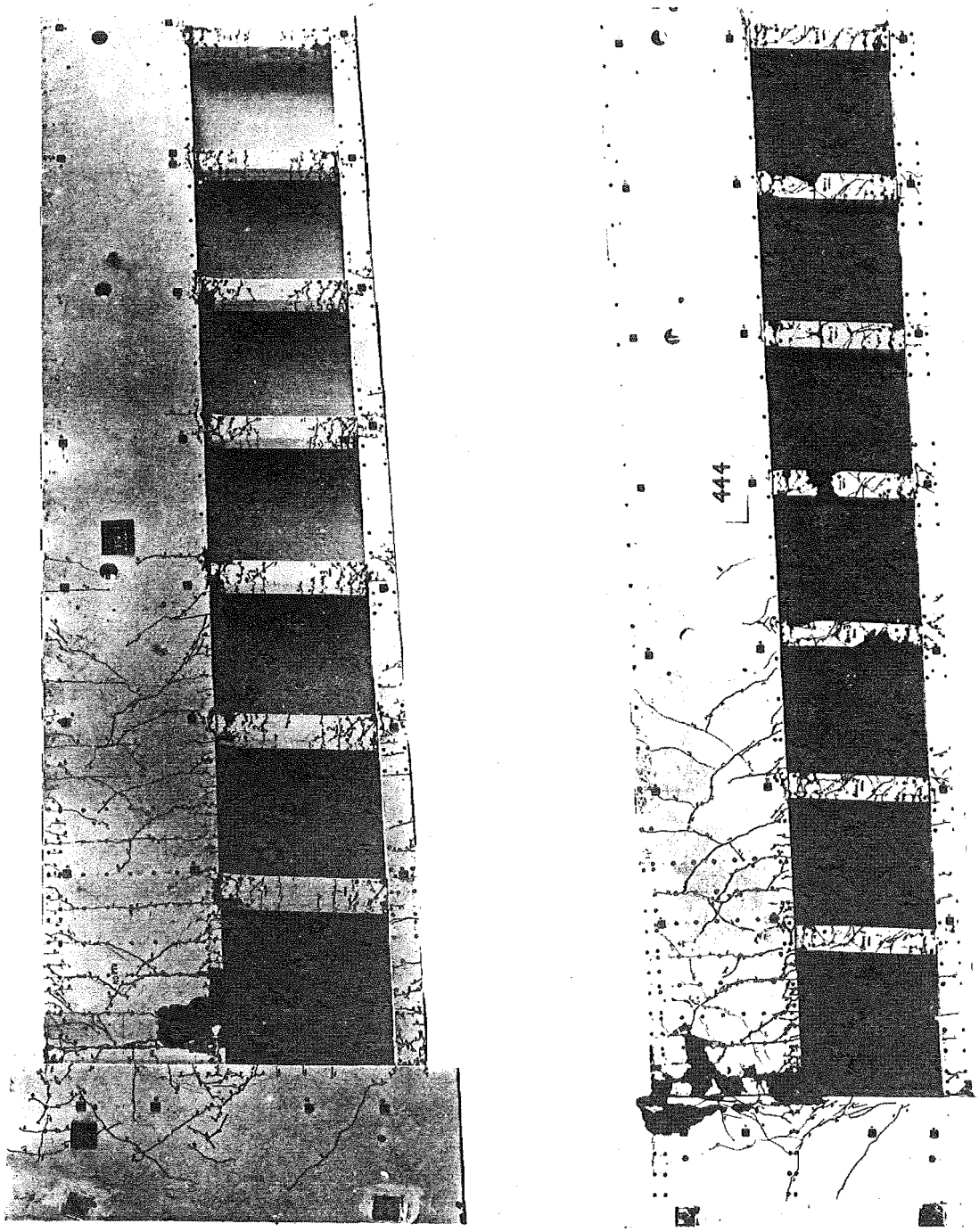

(a) FSW-1 (North side of specimen)

(b) FSW-2 (North side of specimen)

FIGURE 9.7 : GENERAL VIEWS OF FRAME-WALL SPECIMENS AFTER TESTING

9.3 BEHAVIOUR OF WALLS

As indicated in Figure 9.7, very few cracks were developed in the walls above the level 3 beams, in part because of the high simulated gravity compression loading applied in this region (Section 7.5.11). Examination of the behaviour of the walls in this section is therefore largely confined to the bottom halves of the walls, and particularly to the plastic hinge and anchorage regions below the first beam level (See Figures 9.8 to 9.11). Factors investigated in these regions include the flexural, shear and anchorage deformations, wall elongation, stirrup strains and wall failure mechanisms.

9.3.1 Pre-Yield Curvature Distributions

Figures 9.12 and 9.13 compare the observed and predicted pre-yield curvatures of the walls at the peaks of LR5 and LR6, and in the regions outside the plastic hinge zones at the peaks of LR7 and LR8.

The wall curvatures at the peaks of the negative load reversals (LR6 and LR8) were predicted accurately, particularly in the case of FSW-2 and the bottom two sections of wall in FSW-1. However, at the peaks of the positive load reversals LR5 and LR7 (maximum compression on the walls), the theoretical model significantly underestimated the curvatures of the cracked regions of both walls. The cause of this error is not known, although shrinkage and creep due to the prestress may have been contributing factors. Partial relaxation of the shrinkage and creep effects after cracking of the concrete is likely to have increased the flexibility of the walls, especially at low loads. The extent to which the low predicted curvatures are a result of errors in the predicted axial loads and moments on the wall is also not known (see Section 9.4.7).

The allowance made for shear effect on the curvatures in the EV05 analyses (e_v = 0.5 jd_w) partially offset the discrepancy between the predicted (EV00) and observed curvatures. However, it is most unlikely that the discrepancies between the predicted and observed curvatures were primarily due to this type of shear effect, i.e., that the shear effects were much greater than allowed for in

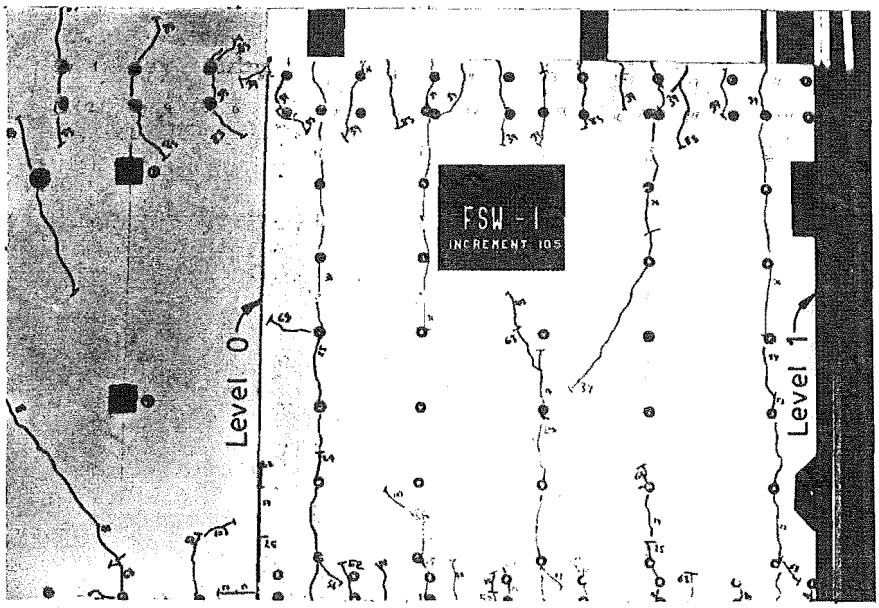

(a) Level 0-1 section

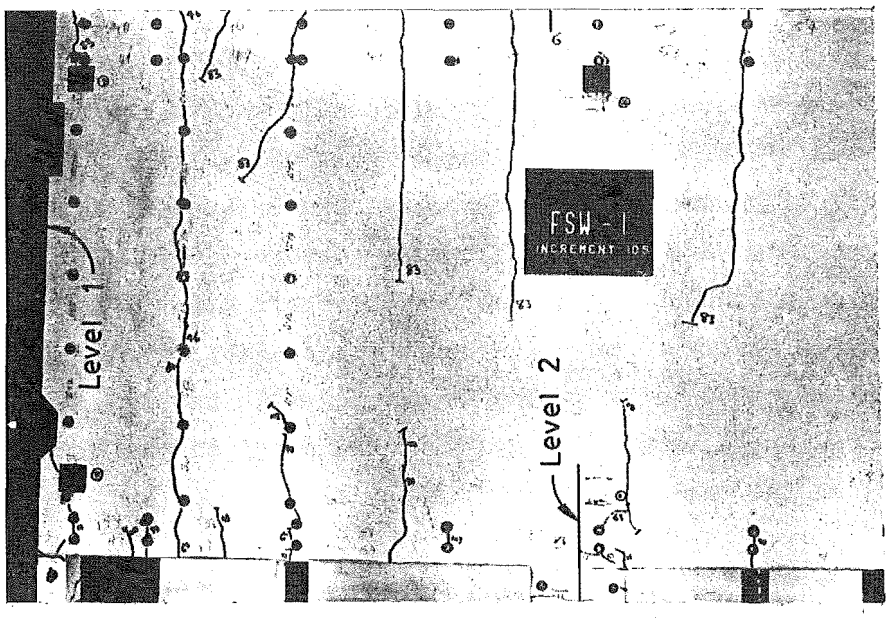

(b) Level 1-2+ section

FIGURE 9.8 : FSW-1 WALL AT BEAM YIELD LOAD IN LR7 (M_b = 226 kN_m)

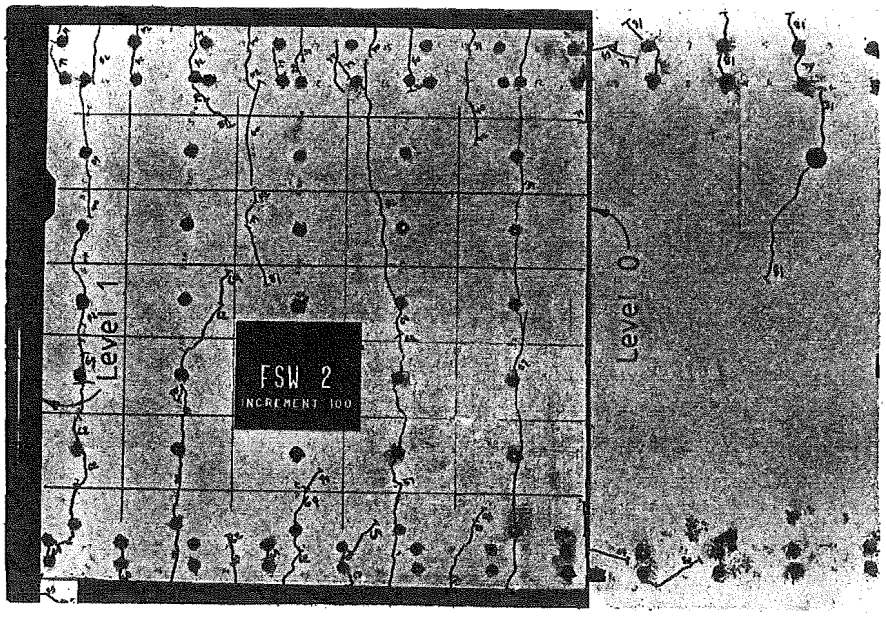

(a) Level 0-1 section

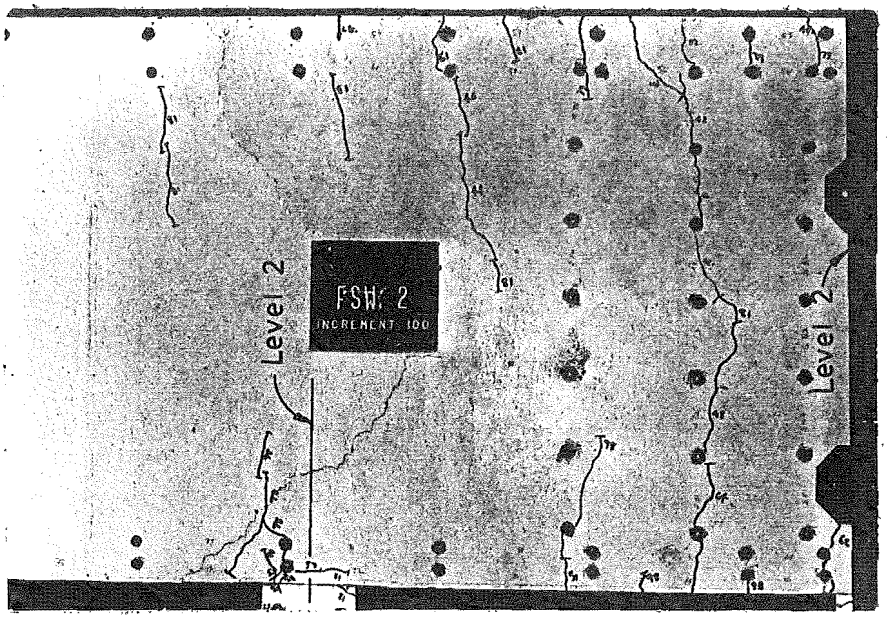

(b) Level 1-2+ section

FIGURE 9.9 : FSW-2 WALL, UNLOADED AFTER LR6

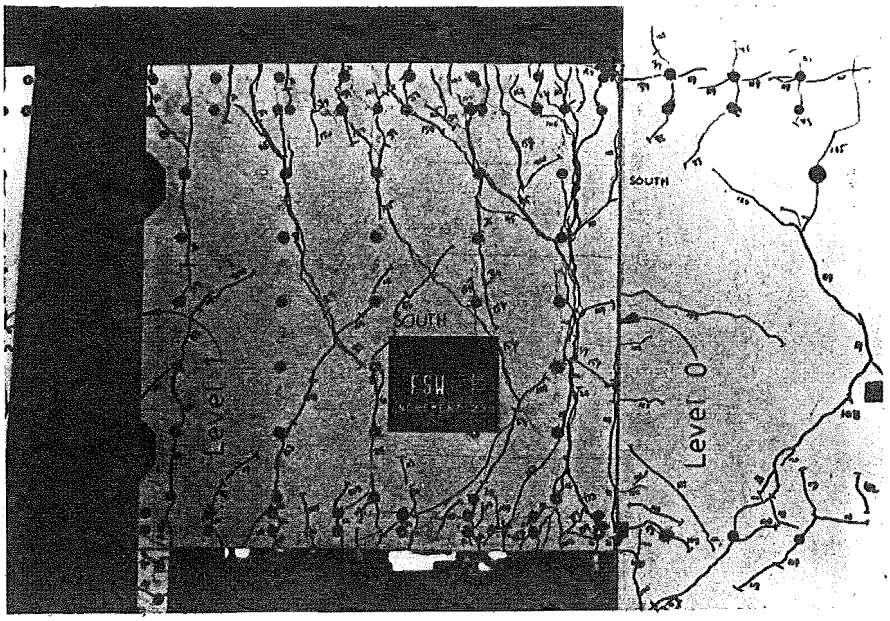

(a) Level 0–1 section

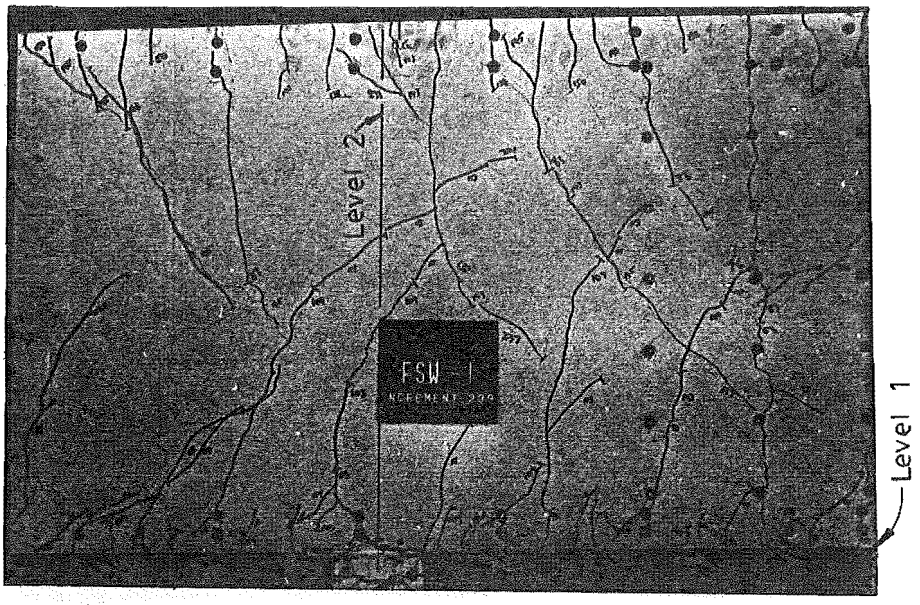

(b) Level 1–2+ section

FIGURE 9.10 : BOTTOM SECTIONS OF FSW-1 WALL AT PEAK OF LR12

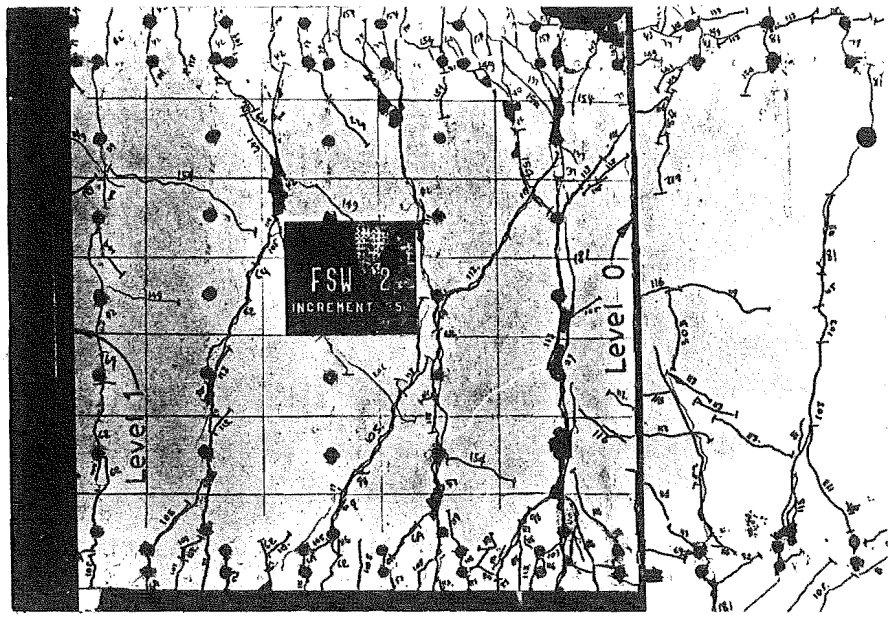

(a) Level 0-1 section

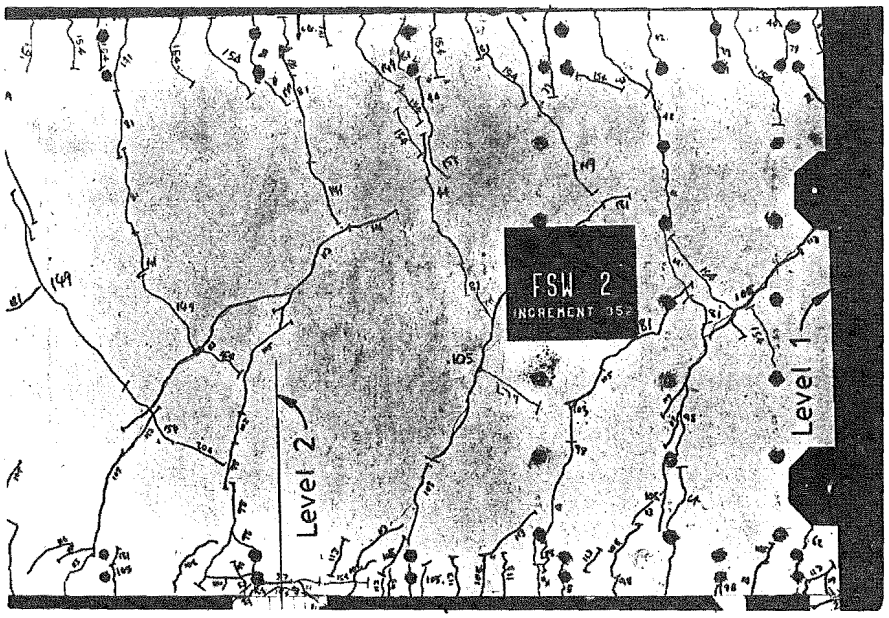

(b) Level 1-2+ section

FIGURE 9.11 : BOTTOM SECTIONS OF FSW-2 WALL AFTER PEAK OF LR17

the EV05 analyses . This is evident from the fact that no inclined cracks were developed in the walls until shortly before reaching yield in LR7, whereas the discrepancies between the curvatures were already apparent at the peaks of the LR5 load reversals (Figures 9.8 and 9.9).

The main analyses made using $f'_t = 0.6 \sqrt{f'_c}$ (MPa) generally showed good agreement with the observed behaviour in terms of the extent of flexural cracking in the walls. A second set of analyses was performed for FSW-2 assuming f'_t equal to the measured modulus of rupture for the concrete. These analyses significantly underestimated the extent of cracking (Figure 9.13). One probable reason for this difference is that in the test, the available tensile capacity of the concrete is likely to have been reduced by the effects of shrinkage and creep.

The bulges in the curvature distributions between levels 2 and 3 in FSW-1 (LR7 and LR8, Figure 9.12) were due to termination of one row of flexural bars on each side of the wall. This behaviour was generally predicted accurately. The maximum measured strain in the remaining row of bars at the inside edge of the wall was approximately 1500 μs and, as a precaution, the cut-off point for the corresponding bars in FSW-2 was increased by one storey height. However, the bars were probably not as close to yielding as originally thought. This is because the measured strains were not corrected to compensate for the initial compressions induced in the bars by either concrete shrinkage or the prestressing forces applied to simulate gravity loading.

9.3.2 Post-Elastic Curvature Distributions

Figures 9.14 and 9.15 compare the observed and predicted curvature distributions over the bottom sections of the walls at the peaks of several post-elastic load reversals. The extent of yielding indicated by the observed curvature distributions at the peaks of LR7 and LR8 are given in Table 9.1.

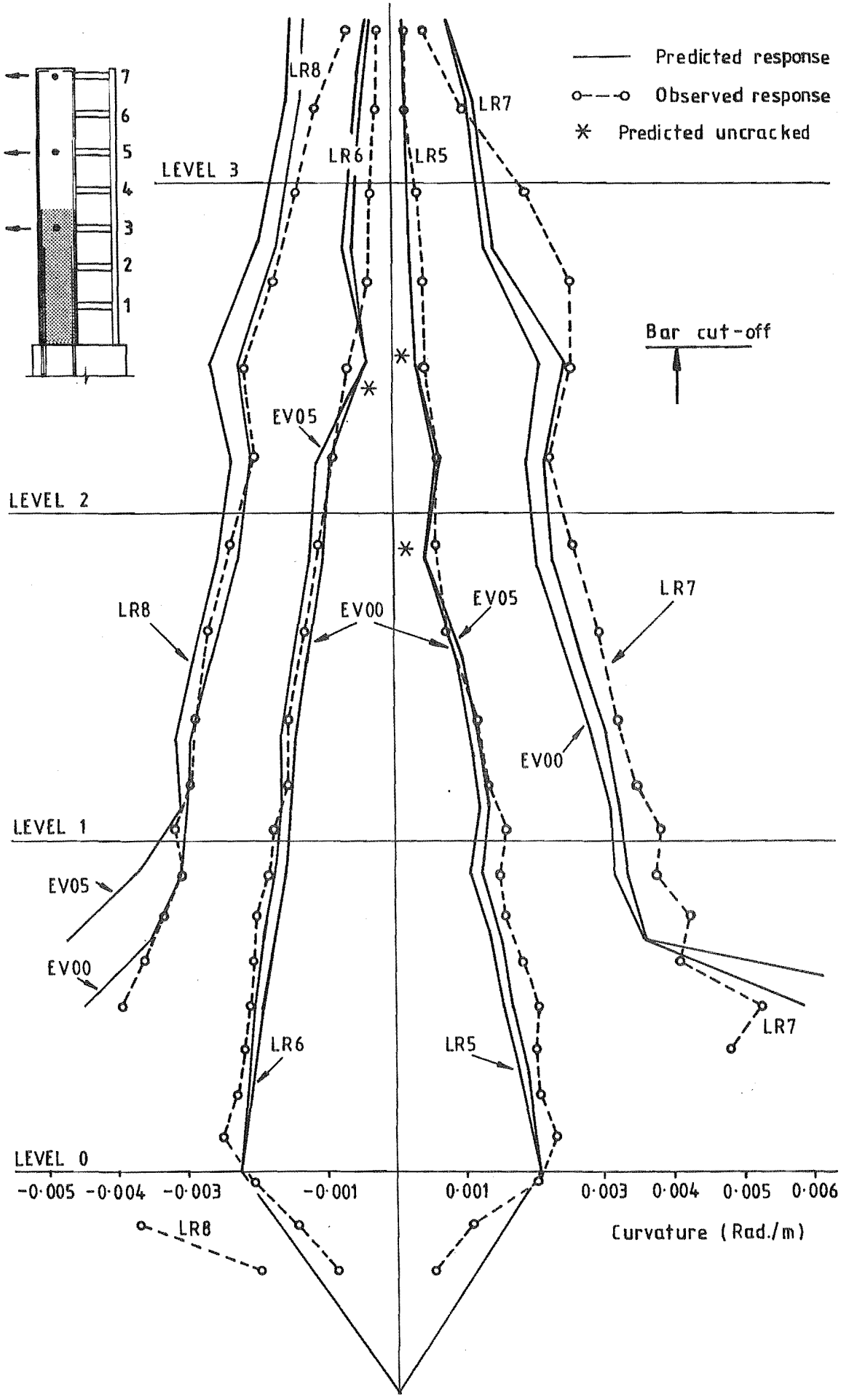

FIGURE 9.12 : PRE-YIELD CURVATURE DISTRIBUTIONS, BOTTOM HALF OF WALL, FSW-1

TABLE 9.1 : OBSERVED EXTENT OF YIELDING IN THE WALL PLASTIC HINGE ZONES

Specimen	Load Reversal	Imposed Ductility (DF)	Height of Yield Penetration	Maximum Curvature Ductility
FSW-1	7	3.9	0.30 ℓ_w	10.3
	8	-3.2	0.43 ℓ_w	- 8.4
FSW-2	7	4.6	0.43 ℓ_w	12.3
	8	-3.9	0.57 ℓ_w	- 9.6

ℓ_w = wall length = 762 mm , ψ_y = 0.00374 Rad/m

The main features of these results are discussed below:

(a) The predicted height of yield penetration (plastic hinge length) at the peaks of LR7 and LR8 agreed well with the observed behaviour. As in previous comparisons, the EVO5 analyses generally gave the better predictions of the curvatures in these regions. However, these analyses did tend to overestimate the curvatures in the areas immediately above the yielding zones.

(b) The maximum section curvature ductilities developed during the first two post-elastic load reversals are given in Table 9.1 . The corresponding curvatures predicted in the analyses were generally in good agreement with the observed values for the negative load reversals (LR8), but were overestimated for the positive load reversals (LR7) - see (c) below.

(c) The total plastic rotations developed in the plastic hinge zones at the peak of LR7 were overestimated in the analyses. This occurred because other components of the wall response, especially the wall shear deformation (Section 9.3.5) and the elastic flexural deformations (Section 9.3.1), were underestimated, while the displacement limits for the analyses were the same as in the tests. The total plastic hinge rotations at the peaks of the LR8 load reversals were predicted much more accurately (see Table 9.2 , also).

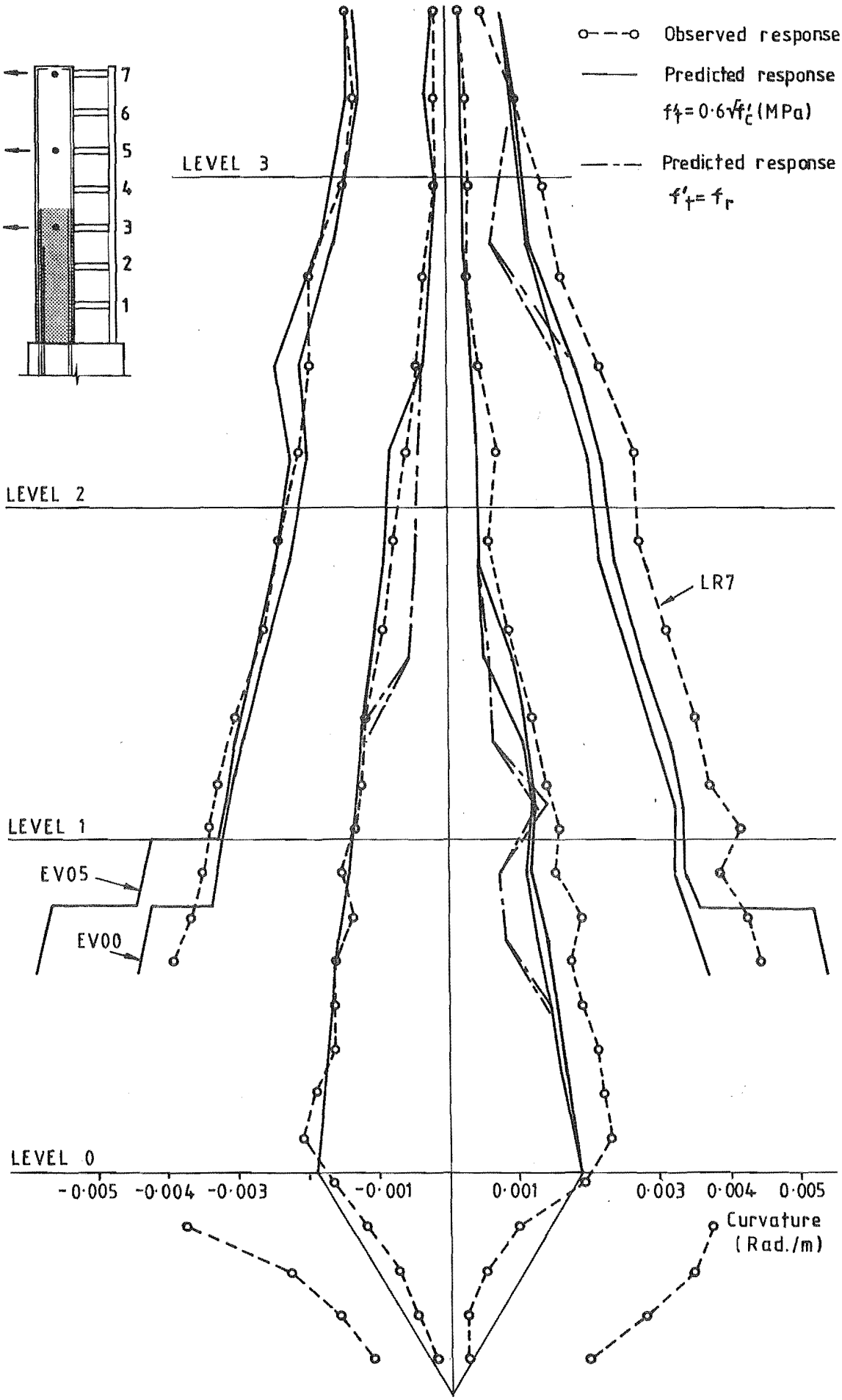

FIGURE 9.13 : PRE-YIELD CURVATURE DISTRIBUTIONS, BOTTOM HALF OF WALL, FSW-2

(d) As indicated in Figures 9.14 and 9.15, and in Table 9.1, yielding was concentrated nearer to the base of the wall at the peaks of the positive load reversals than it was at the peaks of the negative load reversals*. This was mainly due to the fact that the shear force at the base section of the walls was 13% to 14% higher (predicted values) at the peaks of the positive load reversals, although the net axial compression on the wall probably also helped to confine the yielding. The reason for the higher wall shear force, and hence higher moment gradient, was that the base of the column was subjected to a significant net axial tension due to frame action. Because the moment capacity of the column base was low, the column could resist only about 7%** of the total applied base shear, as compared with approximately 21%**, at the peaks of the negative load reversals when there was a large net axial compression acting on the base section of column.

(e) After load reversal 8, the curvatures in the wall plastic hinge zones were considerably affected by strain ageing of the flexural reinforcing bars. This occurred because it took approximately one week to carry out each load reversal (see Appendix A). The effect of the strain ageing can be clearly seen from the observed curvature distributions shown in Figures 9.14 and 9.15. In almost all cases, the maximum curvature of each segment was developed during the load reversal in which the tension bars in the segment first yielded. For example, the average peak curvature of the three wall segments in FSW-1 which yielded in LR7 (DF = 3.9) was approximately 0.035 Rad/m. Under normal short term loading conditions, the peak curvatures of these segments would have been expected to increase in subsequent load reversals if larger displacements had been imposed. However, at the peak of LR9 (DF = 4.2, two weeks later), the average curvature of these three segments reached only 0.021 Rad/m, i.e., only 60% of the peak values in LR7. At the same time, yielding had penetrated into the next two segments higher up the wall, with a maximum curvature of nearly

---

* Especially considering the relative imposed ductilities - see Table 9.1.

** Values predicted by FSW-1/EV00 analysis, but similar values also obtained from the other analyses.

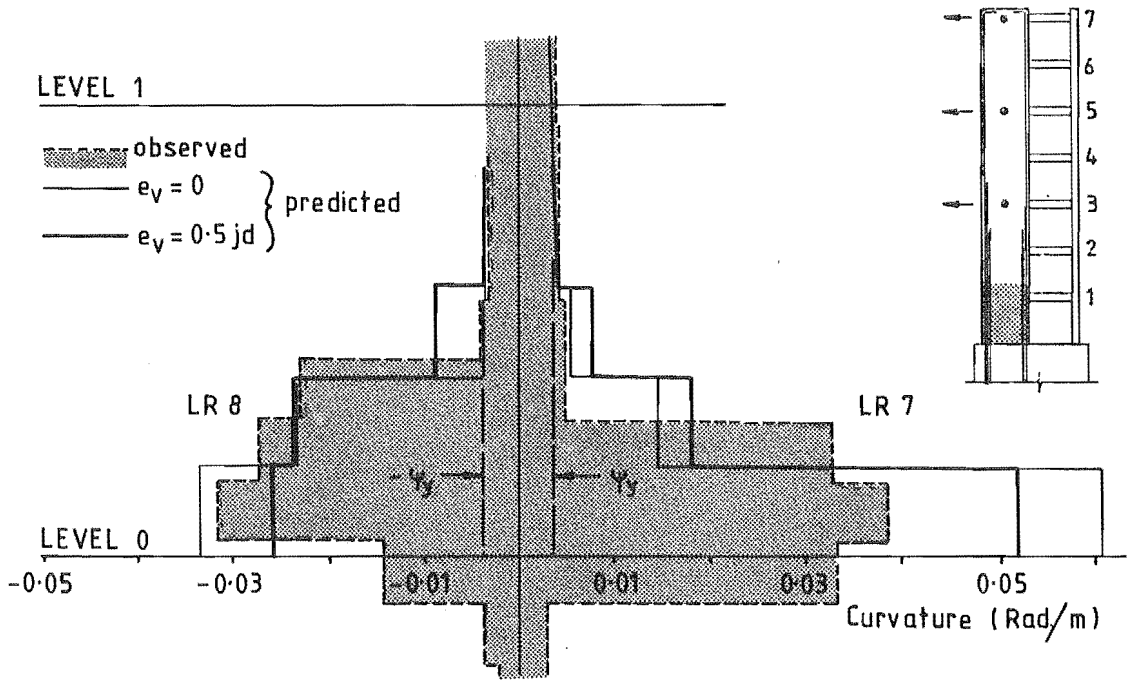

(a) First two post-yield load reversals (LR 7 and LR 8)

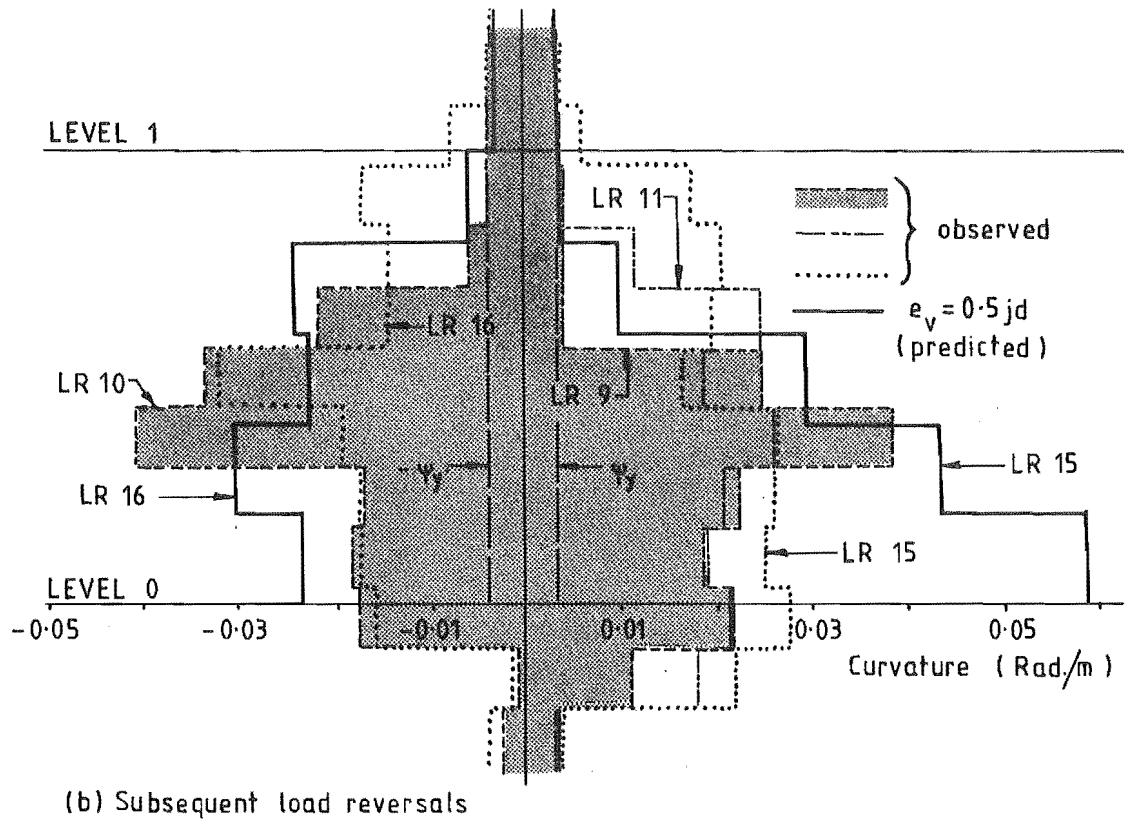

(b) Subsequent load reversals

FIGURE 9.14 : POST-YIELD CURVATURE DISTRIBUTIONS OVER WALL PLASTIC HINGE ZONE, FSW-1

0.04 Rad/m in the first of these (Figure 9.14). In the following positive load reversal (LR11), the peak curvatures of the first three segments were very similar to the values for LR9 (i.e., approximately 0.021 Rad/m), while those of the next two segments had reduced to a similar level. Again, yielding penetrated a further two segments up the wall. The wall curvature distributions for negative loading (FSW-1) and for both positive and negative loading on FSW-2, were very similarly affected.

(f) Apart from the direct effects on the wall curvatures, the strain ageing of the wall flexural reinforcement also affected other aspects of behaviour, such as the strains induced in the wall stirrups (Section 9.3.8) and susceptibility of the walls to buckling (Section 9.3.10). The peak loads resisted by the specimens will also have been increased slightly.

(g) By the end of LR15 and LR16, yielding of the bars had penetrated to 1.1 ℓ_w above the wall base in FSW-1 (DF = +5.9, -5.2), and 1.2 ℓ_w above the wall base in FSW-2 (DF = +6.9, -5.6). Not surprisingly, the maximum extents of yielding predicted by the analyses were smaller, although only by about 20%-30%. Strain measurements continued to be taken until the ends of LR19 for FSW-1 (maximum DF = -7.5, +7.3) and LR18 for FSW-2 (maximum DF = +6.9, -5.7). Yielding did not penetrate any further up the walls during these last few load reversals. However, particularly in the case of FSW-1, the extent of yielding would probably have been larger if the flexural reinforcement at the inside edge of the walls had not buckled (Section 9.3.9).

One aspect highlighted by these tests was the increase in length of the plastic hinge zone caused by strain ageing. This is significant in relation to the repair of structures damaged in an earthquake.

Tension tests carried out on sample bar lengths extracted from the wall plastic hinge zones after the specimens had been tested, indicated that the effect on the bar response depended on the relative directions of loading immediately before and after strain

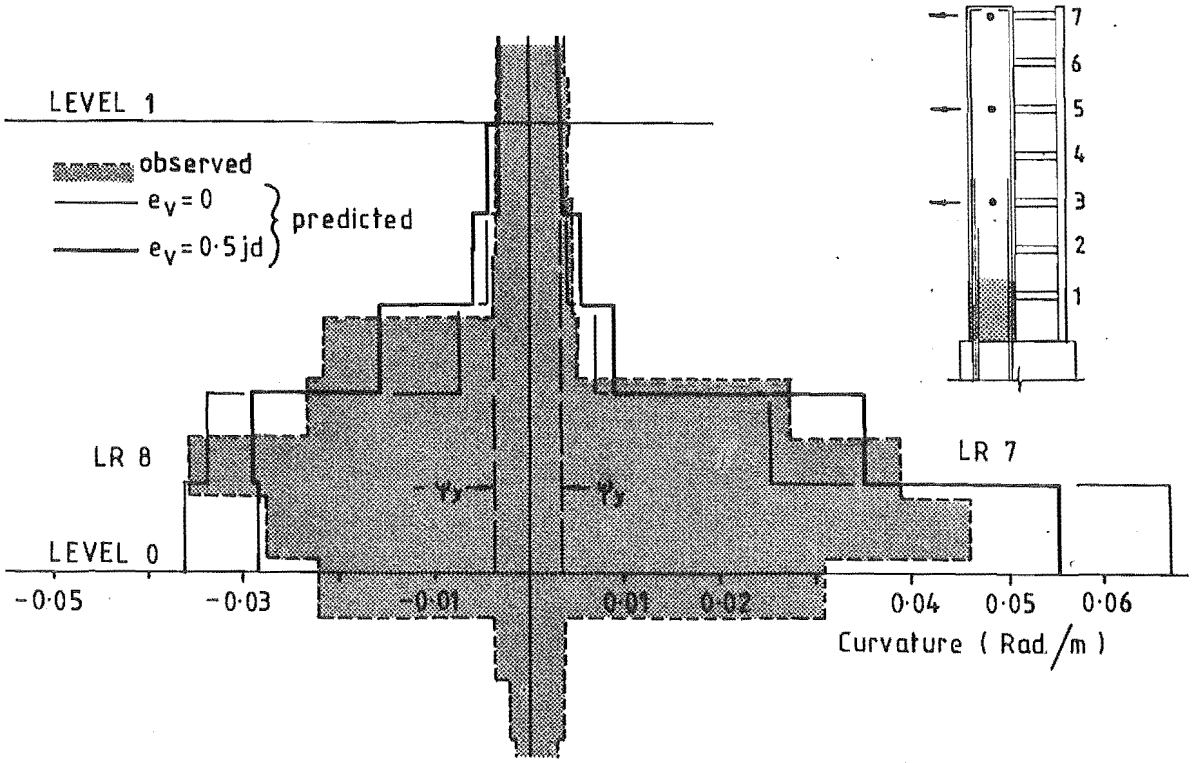

(a) First two post-yield load reversals (LR 7 and LR 8)

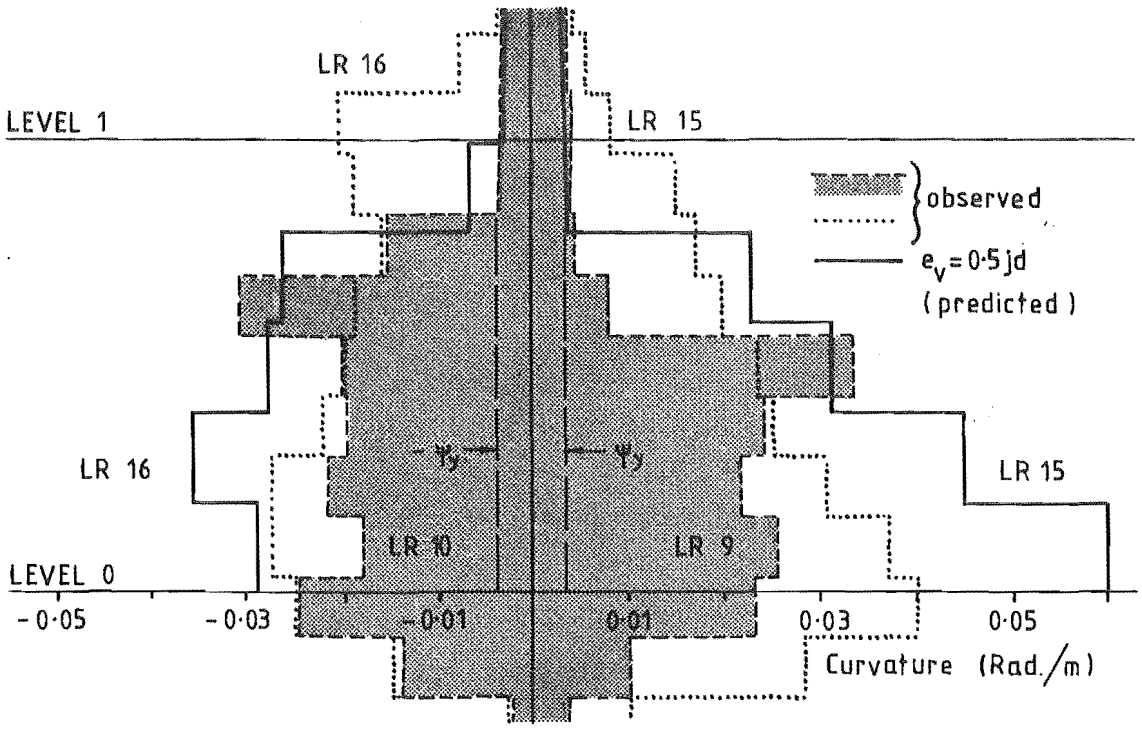

(b) Subsequent load reversals

FIGURE 9.15 : POST-YIELD CURVATURE DISTRIBUTIONS OVER WALL PLASTIC HINGE ZONE, FSW-2

ageing. In the worst case, where loading was continued in the same direction, the combined effects of strain hardening and strain ageing (44 months) resulted in a 42% increase in effective yield stress (Appendix A). In the frame-wall tests, the increases in plastic hinge length were limited because the loading imposed generally involved reversal of straining direction after strain ageing, and because compression 'yielding' of the flexural reinforcing (cracks closing) contributed significantly to the total plastic rotations.

However, reinforced concrete members previously subjected to large plastic deformations are often repaired by resin injection which prevents cracks from closing or by replacing damaged concrete by new concrete. In either case, the repaired member will be similar to the original undamaged member, except that the bars that originally yielded will be stronger than previously. After months or years of ageing, the increase in strength of the original plastic hinge zone may be large enough to force yielding into regions of the structure not detailed for ductility and to significantly increase the maximum shear forces.

9.3.3 Local Section Responses

Figures 9.16 and 9.17 show the observed and predicted load-curvature relationships for a segment of each wall, approximately one-third of a storey height above level 1. These segments remained elastic throughout the tests (yield curvature $\simeq$ 0.0038 Rad/m) and the response curves were initially plotted to assess the variation of the wall moments during each load reversal. For the sake of clarity, most of the unloading sections of the curves are not shown.

During the first two post-yield load reversals (LR7 and LR8), the observed and predicted responses were similar, although as found for the curvature distributions, the theoretical model underestimated the curvatures during LR7 by approximately 15%. The slopes of the response curves for both specimens were approximately constant up to a load of about 200 kNm in LR7. After this, the slope decreased to about half the value below 200 kNm, before increasing again near the

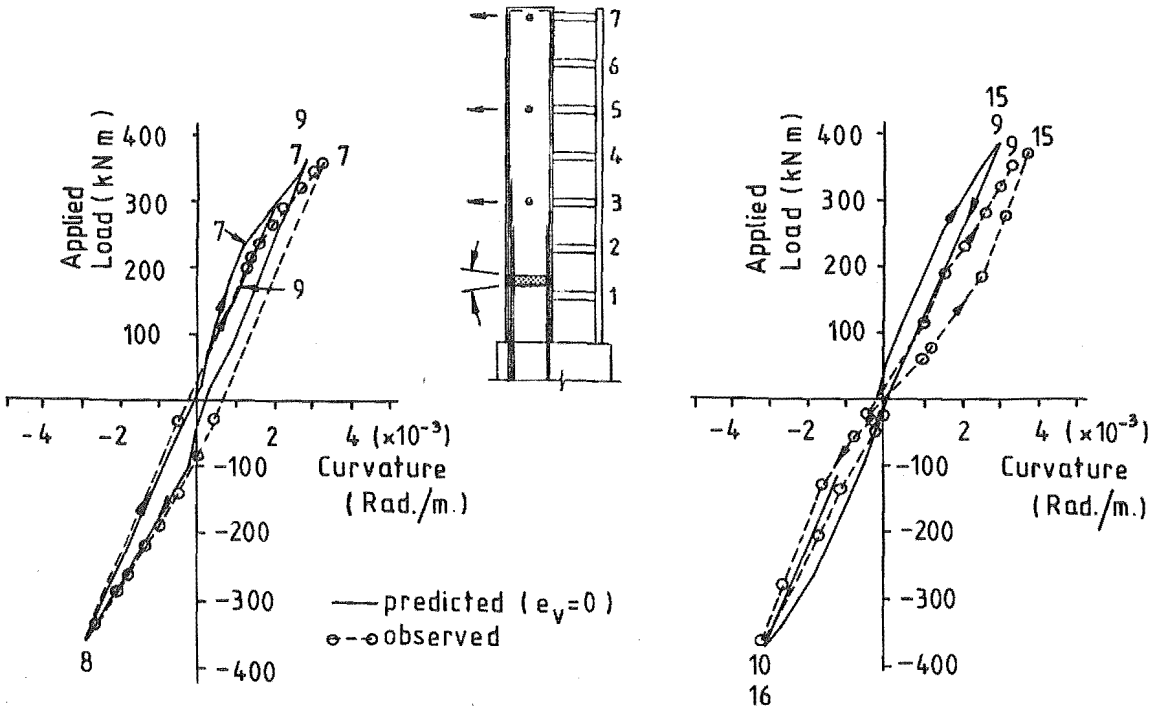

(a) Load reversals 7 to 9

(b) Load reversals 9, 10, 15 and 16

FIGURE 9.16 : LOAD-CURVATURE RESPONSE AT WALL SEGMENT 2-2, FSW-1

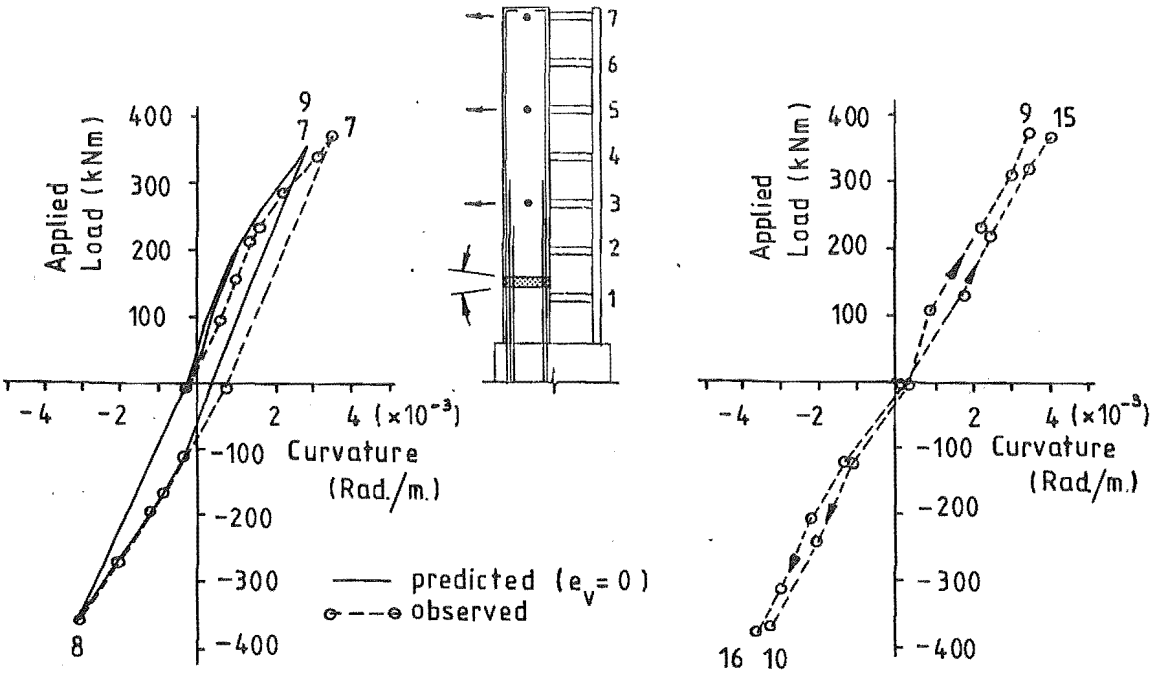

(a) Load reversals 7 to 9

(b) Load reversals 9, 10, 15 and 16

FIGURE 9.17 : LOAD-CURVATURE RESPONSE AT WALL SEGMENT 2-2, FSW-2

peaks of the load reversals (Figs 9.16a and 9.17a). The decrease in slope occurred largely as a result of the beams yielding (see Section 9.4.1) and the consequential increase in the fraction of the subsequent increments of applied load that had to be carried by the walls, which still had not yielded. A similar behaviour was observed during the LR8 load reversals, although in this case the change in slope of the response curves occurred at a lower load and was less distinct, due in part to the Bauschinger effect in the beam steel which had yielded in LR7.

The predicted response curves for subsequent load reversals were similar to those in LR7 and LR8, i.e., decreasing slope above 200 to 250 kNm. However, after LR8, the observed responses changes considerably, with progressively larger curvatures being developed at low loads (Figs 9.16b and 9.17b). The initial slope of the response curves at low loads was reduced to the extent that during LR15 and LR16, it was only 35% (FSW-1) to 50% (FSW-2) of the slope at higher loads.

When the results for FSW-1 were first evaluated, it was assumed that the low initial slopes of the curves were a result of sliding shear deformations in the beams, i.e., at low loads, the beams would have attracted little of the applied load. However, after the predicted responses had been obtained it was realised that this explanation was incorrect, since it is the shapes of the overall load-deflection relationships that govern the beam flexibilities, and hence load attracted by the frame. Unlike the shear displacement response, the overall load-deflection relationship for these beams did not exhibit significant pinching at low loads (e.g., see Fig. 8.3). Therefore, if the force attracted by the frame was the main factor governing the shapes of the load-curvature relationships, curves similar to those obtained for the predicted responses would be expected, i.e., the slope of the response curves decreasing at higher loads after the beams yielded.

It is also clear that the changes in the shapes of the load-curvature relationships for FSW-2 were not caused by sliding shear in the beams.

Some reduction in initial stiffness of these beams would have occurred because of deterioration of the lap regions (Section 9.4.6). However, this effect does not appear to have been enough to have caused such a marked effect on the wall curvatures.

No conclusive explanation of the change in the observed response has been found. However, at least part of the change appears to be caused by a reduction in the rigidity of the segments at low loads because of residual expansion of the walls.

As indicated in Fig. 9.18, the segments in both walls expanded during the tests, such that at zero curvature, there was a net axial tensile strain despite the prestressing applied to simulate vertical gravity loading (see Section 9.3.6a). The average residual expansion after LR8 was of the order of 165 μs* and, until the cracks closed, the wall segments would have been more flexible than considered in the analyses. The segments would also have become more flexible with increasing numbers of load reversals, as deterioration of the flexural bond reduced the stresses carried in the concrete between cracks.

9.3.4 Plastic Hinge Rotations

Table 9.2 compares the observed and predicted rotations of the base of the wall at the peaks of load reversals 7 to 17.

The extent to which the observed anchorage deformations were affected by strain ageing is not known. However, the total rotations at level 1 should not have been significantly affected until about LR13. At about this stage, yielding spread to the segments immediately above level 1, largely because of strain ageing of the bars yielded in earlier load reversals (see Section 9.3.3).

---

* Expansions based on steel strains measured relative to the gauge zero readings, which were taken after the gravity load stressing had been applied.

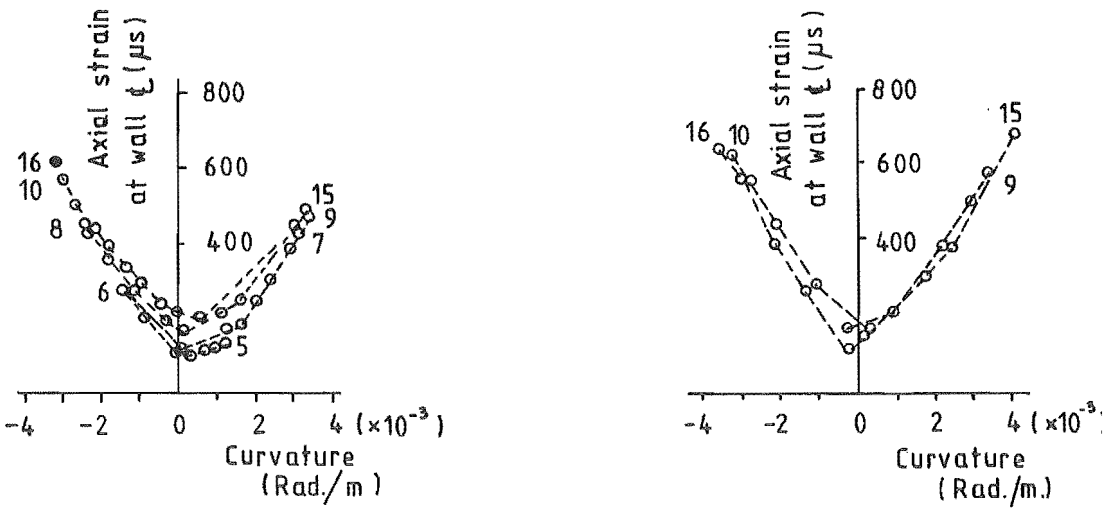

Note:

Axial strains are relative to start of lateral loading, ie. after prestress load was applied to simulate gravity.

FIGURE 9.18 : OBSERVED CURVATURE-AXIAL STRAIN RELATIONSHIP AT SEGMENT 2-

TABLE 9.2 : ROTATIONS AT BASE OF WALL AT PEAKS OF LOAD REVERSALS 7 TO 17

(a) FSW-1

LR	DF	Anchorage Region Only (Rad)		Total Rotation to Level 1 (Rad)	
		Observed*	Predicted**	Observed*	Predicted**
7	3.9	0.0032	0.0028	0.0137	0.0161
8	-3.2	-0.0017	-0.0022	-0.0118	-0.0123
9	4.5	0.0032	0.0031	0.0160	0.0181
10	-3.8	-0.0016	-0.0025	-0.0138	-0.0149
11	4.9	0.0039	0.0033	0.0176	0.0199
12	-4.2	-0.0018	-0.0029	-0.0162	-0.0172
13	5.1	0.0041	0.0034	0.0180	0.0208
14	-4.7	-0.0020	-0.0029	+	-0.0174
15	5.9	0.0048	0.0042	0.0218	0.0263
16	-5.2	-0.0016	-0.0032	+	-0.0193
17	5.8	0.0046	0.0041	0.0209	0.0256

(b) FSW-2

7	4.7	0.0036	0.0033	0.0176	0.0198
8	-3.9	-0.0026	-0.0026	-0.0154	-0.0152
9	4.5	0.0037	0.0031	0.0167	0.0183
10	-4.5	-0.0039	-0.0030	-0.0179	-0.0182
11	5.0	0.0052	0.0035	0.0188	0.0209
12	-4.6	-0.0039	-0.0030	-0.0173	-0.0182
13	5.9	0.0064	0.0040	0.0226	0.0249
14	-5.2	-0.0041	-0.0034	-0.0202	-0.0210
15	6.9	0.0078	0.0047	0.0263	0.0297
16	-5.6	-0.0040	-0.0037	+	-0.0227
17	6.9	0.0077	0.0048	0.0258	0.0298

\+ Observed values were affected by local buckling of flexural bars (Section 9.3.9)

* From steel strain readings.

** From analyses with e_v = 0.5 jd. Analyses with e_v = 0 gave very similar results.

For both specimens, the rotations of the walls at level 1 were predicted accurately for all negative load reversals before local buckling of the compression bars at the base of the walls became significant (Section 9.3.9). However, in the positive load reversals, the analyses significantly overestimated the rotations at level 1. At least part of this discrepancy occurred because the theoretical model underestimated the flexibility of the sections of wall above the plastic hinge zone (Section 9.3.3). In later load reversals, the discrepancy became even larger because of the spread of yielding above level 1. As a result, the observed values include only part of the plastic hinge rotation, whereas in the analyses, all yielding was confined to below level 1.

The accuracy of the predicted wall deformations for positive load reversals was also affected by errors in the predicted distribution of plastic deformation between the wall and anchorage regions, particularly for FSW-2* (see Section 9.3.7). In the case of this specimen, the component of wall rotation actually developed between levels 0 and 1 was overestimated by 30%-40% at the peaks of the positive load reversals LR11 to LR17 inclusive.

9.3.5 Wall Shear Deformations

Figures 9.19 and 9.20 compare the observed and predicted shear responses of the bottom storey of the walls in FSW-1 and FSW-2. The observed shear displacements shown in these diagrams were obtained by comparing the flexural component of the wall deformations (determined from the steel strain readings) with the total deflection measured at level 1 using the theodolite. Because of the limited number of readings taken, the shapes of the observed curves are

---

* The values used for the anchorage model constants in the analyses were the same for both specimens. Because of the differences between the responses of the two specimens and between the responses during the positive and negative load reversals, this resulted in the anchorage rotations for the negative load reversals in FSW-1 being overestimated and those for the positive load reversals in FSW-2 being significantly underestimated (Table 9.2). Further details of the anchorage deformations are discussed in Section 9.3.7.

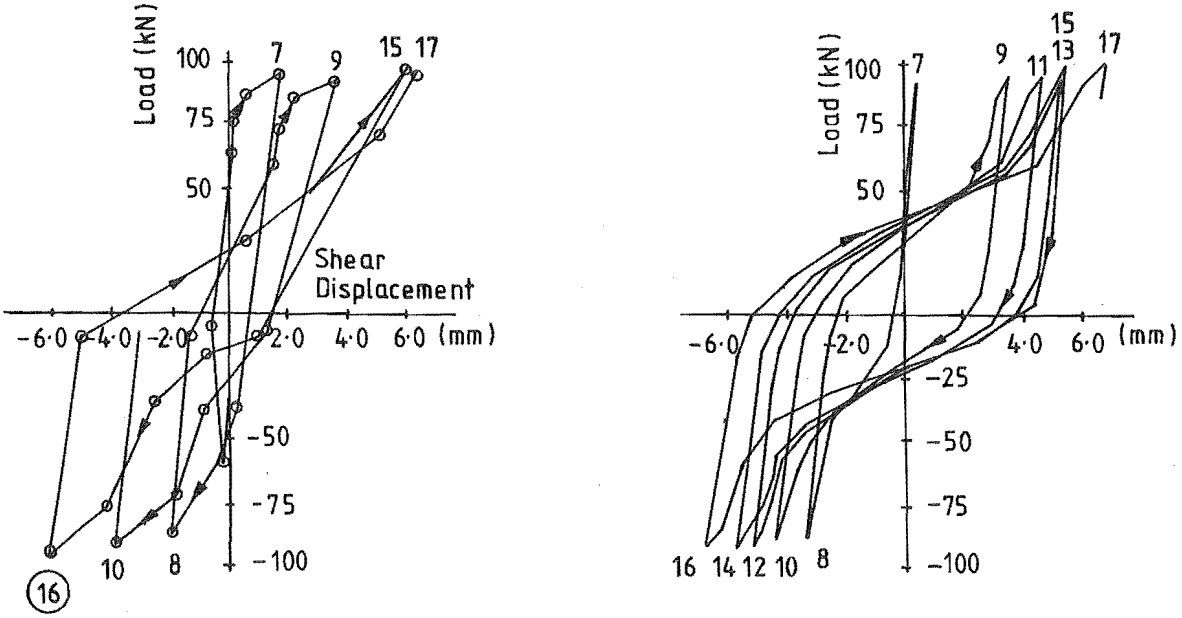

(a) Observed (From theodolite and steel strain readings)

(b) Predicted (EV05 Analysis)

FIGURE 9.19 : LEVEL 0-1 SHEAR DISPLACEMENT, FSW-1

Load = Total base shear force applied to the specimen.

(16) Readings affected by local buckling of the wall flexural reinforcement

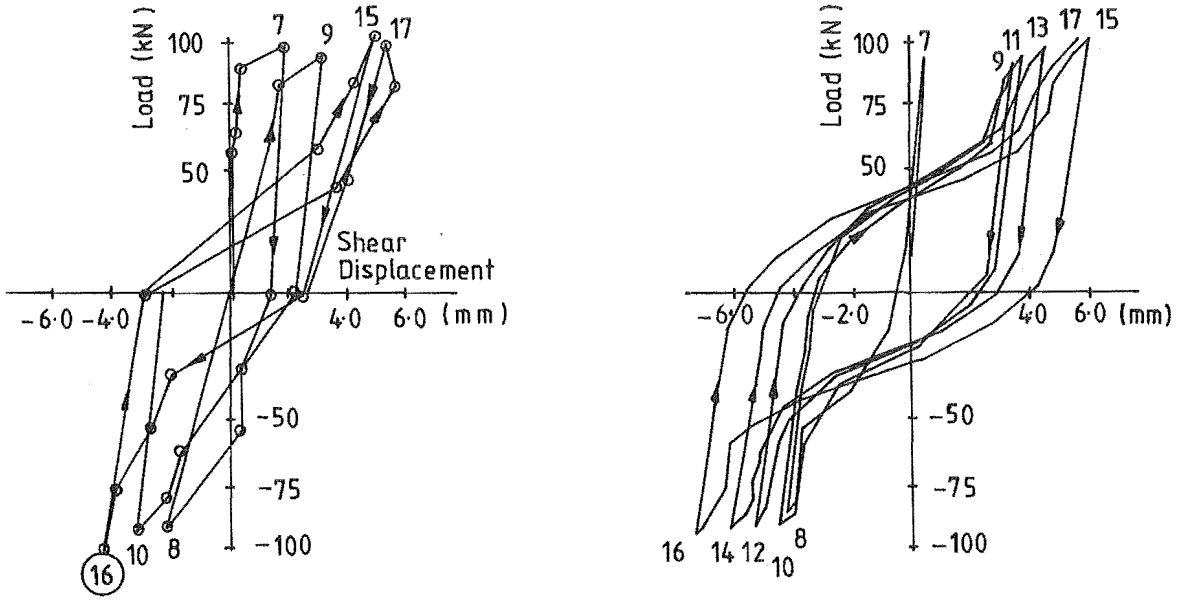

(a) Observed (From theodolite and steel strain readings)

(b) Predicted (EV05 Analysis)

FIGURE 9.20 : LEVEL 0-1 SHEAR DISPLACEMENT, FSW-2

relatively inaccurate, particularly for unloading from the peaks of the positive load reversals.

Values of the shear deformations at the peaks of load reversals 7 to 17 are also given in Table 9.3, together with corresponding values assessed directly from the theodolite readings. The latter values are likely to contain significant components of flexural deformation and are given only to confirm the order of size of shear displacement determined by comparing the theodolite and steel strain readings*.

TABLE 9.3 : SHEAR DEFORMATIONS IN WALL PLASTIC HINGE ZONES AT PEAKS OF LOAD REVERSALS 7 TO 17

(a) FSW-1

LR	DF	Predicted Shear Displacement δ_{v1} (mm)		Observed Shear Displacement			
				Theodolite and Bar Strain Readings			Theodolite Only (mm)
		e_v=0	e_v=0.5 jd	δ_{v1} (mm)	% δ_{w7}	δ_{v1}/d_w	
7	3.9	0.53	0.48	1.8	1.8	0.0025	3.7
8	-3.2	-3.43	-3.38	-2.1	2.6	-0.0029	-3.3
9	4.5	3.56	3.51	3.7	3.2	0.0052	4.8
10	-3.8	-4.60	-4.39	-4.2	4.4	-0.0060	-3.9
11	4.9	5.08	4.62	4.4	3.6	0.0063	5.2
12	-4.2	-5.74	-5.16	-4.8	4.5	-0.0068	-4.0
13	5.1	5.87	5.33	5.0	3.9	0.0070	5.7
14	-4.7	-6.65	-5.77	+	+	+	-4.85
15	5.9	6.27	5.64	6.0	4.0	0.0085	6.6
16	-5.2	-7.90	-6.78	+	+	+	-5.2
17	5.8	7.34	6.76	6.3	4.3	0.008	6.8

(b) FSW-2

7	4.7	0.56	0.53	1.9	1.6	0.0027	4.7
8	-3.9	-4.55	-4.22	-2.2	2.2	-0.0030	-3.7
9	4.5	3.61	3.56	3.1	2.8	0.0044	5.1
10	-4.5	-4.65	-4.39	-3.3	2.9	-0.0046	-4.2
11	5.0		3.86	3.6	2.8	0.0051	5.8
12	-4.6		-5.31	-3.4	2.9	-0.0047	-4.3
13	5.9		4.65	4.7	3.1	0.0066	7.0
14	-5.2		-6.05	-4.3	3.3	-0.0061	-3.4
15	6.9		6.07	5.0	2.9	0.0070	8.2
16	-5.6		-7.24	+	+	+	-5.4
17	6.9		5.70	5.3	3.1	0.0075	8.8

+ Measured flexural deformations used for determining these values contained significant errors because of local buckling of the compression bars at the wall base.

δ_{w7} = wall displacement at level 7.

δ_{v1} = wall shear displacement at level 1.

* The high density of strain gauges provided in the plastic hinge zones permitted a much more accurate determination of the flexural component of deflection than was possible using the theodolite readings alone (Section 7.5.12c).

The observed total shear displacements at level 1 should not have been significantly affected by strain ageing until yielding spread above level 1, around LR13 (cf. Section 9.3.4). It is also unlikely that strain ageing of yielded sections of the bars in the anchorage zones (Section 9.3.7), would have significantly affected the sliding shear response.

Probably the most noticeable feature of the shear response was the relatively small magnitudes of the peak shear displacements. In a number of respects the conditions applying in these walls were similar to, or even more severe than, those in specimen TB1 during the large displacement load reversals (LR5, 6, 9 and 10). The shear span to depth ratio (a/d) at the base of the walls varied from 2-3* at low loads (< 50 kN) to 4.2-4.6* at the peaks of the load reversals, as compared with approximately 4.3 for TB1. Also, as indicated in Table 9.3, the loading applied to the walls was very similar to that applied to TB1 in terms of both ductility (DF_{TB1} = 4.3, -3.4, 4.1 and -4.5 respectively) and maximum nominal shear stress (1.27 MPa for TB1, as compared with 1.12 MPa for the walls). Despite these similarities, the relative magnitudes of the wall shear displacements were considerably smaller than the shear displacements observed for TB1 during LR9 and LR10. This is evident from both the shear contribution to peak end deflections (approximately 16% for TB1) and the maximum nominal shear strains ($\delta_v/d \simeq 0.021$ for TB1). The corresponding average values for the walls during LR9 to LR12 (DF $\simeq$ 4 to 5) were approximately 6.5% of the level 4 deflection (i.e., at a height 'a' above the base of the walls - 3.5% of the level 7 deflection) and $\delta_{v1} \simeq 0.0055$. These results indicate a two to threefold reduction in the sliding shear displacements in the plastic hinge zone. This difference between the wall and beam specimens is due to the effect of an average axial compression of 1.38 MPa on the walls, which is less than 0.04 f'_c. This is less than 40% of the 0.1 f'_c limit, below which the effect of axial compression is ignored in the shear design of plastic hinge regions (19 , 20).

---

* Values from analyses FSW-2/EV05. Note that $a = M_w/V_w$ at level 0.

Despite the variation in axial load on the walls (i.e., approximately 0 to 2.7 MPa), there was no significant asymmetry in the shear response with respect to loading direction. This was largely a result of the unsymmetrical flexural reinforcing which compensated for the axial load differences and ensured that the elongation of the plastic hinge zone was similar for both loading directions.

The shear displacements in FSW-2 (approximately 3% δ_7) were generally smaller than those in FSW-1 (approximately 4% δ_7). The additional wall stirrups provided in FSW-2 (Section 7.5.6) may have been partly responsible for this. However, it is noticeable that the theoretical model, which does not explicitly account for the effect of stirrups, correctly predicted the smaller shear displacements for the positive load reversals, but not for the negative load reversals. As discussed subsequently, this suggests that the larger anchorage deformations in FSW-2 may have contributed to the smaller shear displacements observed for this specimen.

After the first two post-elastic load reversals, the model generally predicted the peak shear deformations reasonably accurately, although the limited data obtained from the tests indicates that the shear displacements at low loads tended to be overestimated (Figures 9.19 and 9.20). This is similar to the results obtained for beam specimens (e.g., Section 6.3) and is due to inadequate modelling of shear deformations occurring after cracks close and the fact that the model was principally calibrated against the shear displacements at the peaks of large displacement load reversals.

The only significant discrepancies between the observed and predicted peak shear deformations occurred in FSW-2, where the values for the negative load reversals were overestimated by up to 56%. At least after LR10, part of this error was due to the fact that the rotations between levels 0 and 1 in FSW-2 were significantly overestimated in the preceding positive load reversals (see Section 9.3.4). For example, the observed rotation of level 0-1 at the peak of LR11 was 0.0136 Rad as compared with the

predicted value of 0.0174 Rad (total rotation to level 1 minus anchorage rotation). The modelled elongation at the start of LR12 would therefore have been larger than in the test, thereby requiring the model to overestimate the shear deformation required to close the cracks.

Despite this discrepancy the overall agreement between the observed and predicted responses was better than that obtained for most of the beam specimens analysed, particularly after several load reversals. This better agreement is, of course, largely a result of the smaller shear strains developed in the walls. The effect of the mismatched crack surfaces on the concrete compression response was therefore not as great as for the beams (Section 6.3).

As stated in Sections 7.6.3 and 7.6.4, the inelastic shear model parameters used in these analyses were basically the same as used for previous beam analyses, and were not specifically calibrated against the response of the frame-wall specimens. The fact that the model accurately predicted the large reductions in shear strain caused by the net compression loads indicates that the inherent sensitivity of the model to axial load was in good agreement with that exhibited by the walls.

The regions of wall above level 1 were modelled in the analyses as having elastic shear responses, with an effective shear modulus of $G = 0.16\ E$ on the gross concrete section. As indicated in Figures 9.21 and 9.22 , this resulted in the shear deformation between levels 1 and 2 being significantly underestimated. Part of the increase in the shear deformations after LR10 was due to yield spreading above level 1. However, even before yielding, these observed shear deformations were up to nearly four times larger than the predicted values. This would suggest that a shear modulus possibly as low as 0.04 E should have been used to model the more highly loaded "elastic" regions of the walls, i.e., regions loaded to between the diagonal cracking and yielding loads.

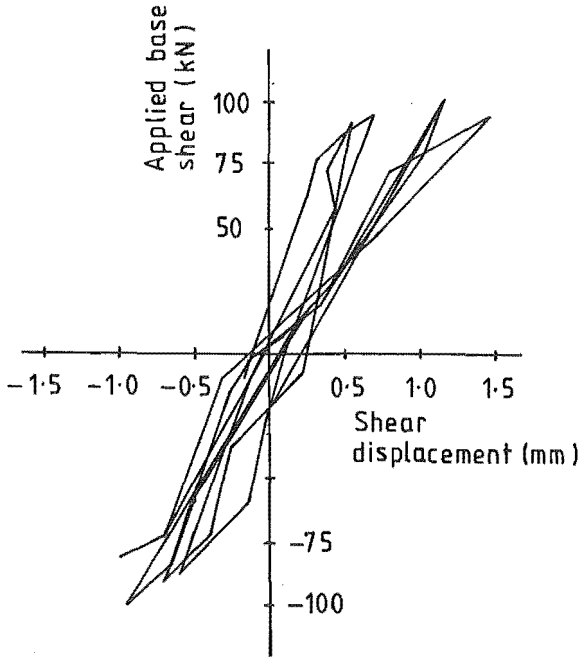

(a) Observed (From theodolite readings only)

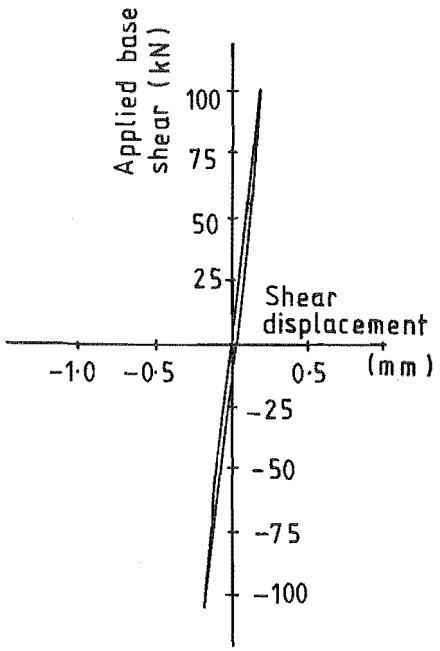

(b) Predicted $e_v = 0$

FIGURE 9.21 : SHEAR DISPLACEMENT LEVEL 1-2, FSW-1

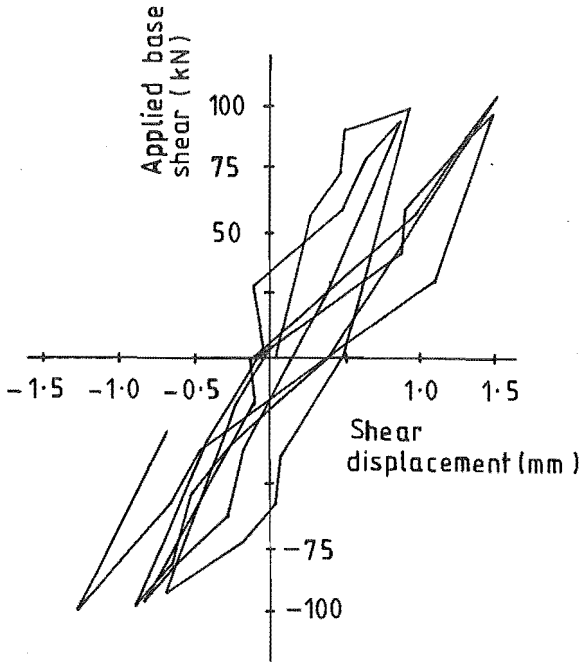

(b) Observed (From theodolite readings only)

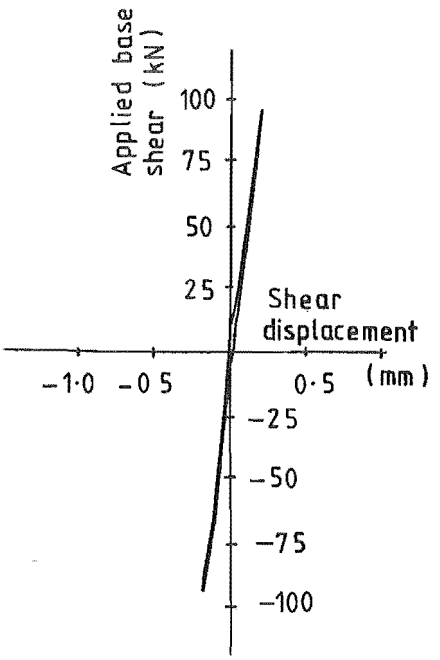

(b) Predicted $e_v = 0$

FIGURE 9.22 : SHEAR DISPLACEMENT LEVEL 1-2, FSW-2

9.3.6 Wall Elongation

Figures 9.23 and 9.24 compare the observed and predicted load-elongation response for the walls of FSW-1 and FSW-2 respectively. The values of elongation plotted are the total expansion along the centrelines of the wall due to lateral loading, and include the "expansion" within the wall anchorage zone. They do not include axial shortening due to initial prestressing (0.25 mm predicted) or concrete shrinkage. The observed values shown were computed from the measured strains in the flexural reinforcement. Both analyses are for $e_v = 0$; in the case of FSW-2, the results are from the standard analysis (FSW-2/EV00), while for FSW-1, they are from a refined analysis using load increments one-fifth the normal size (FSW-1/EV00/5), i.e., $\Delta M_b = 11.3$ kNm, $\Delta\delta_{w7} = 5$ mm as compared with $\Delta M_b = 56.5$ kNm, $\Delta\delta_{w7} = 25$ mm used normally.

Several features of the responses are discussed below:

(a) The elongations predicted during initial loading up to yield were predicted accurately for both specimens. After the initial elastic load cycles (LR1-LR6) the measured strains indicated a small residual elongation at zero load. This behaviour was not predicted and was probably due to a combination of relaxation of initial shrinkage of the concrete, debris between the crack surfaces and hysteresis in the flexural bond-slip response.

(b) The predicted elongations at the peak of the first post-elastic load reversal were slightly larger than the observed values. This is likely to be due to errors in predicting the concrete crushing behaviour in the plastic hinge zones, although there will also be some element of error in the observed values.

(c) In subsequent load reversals, the error in the predicted peak elongations became progressively greater. This is similar to the results obtained for other conventionally reinforced members analysed during the inelastic shear model. Interestingly, the minimum elongations reached before re-expansion in LR8 and LR9 were predicted accurately for both specimens, despite the errors

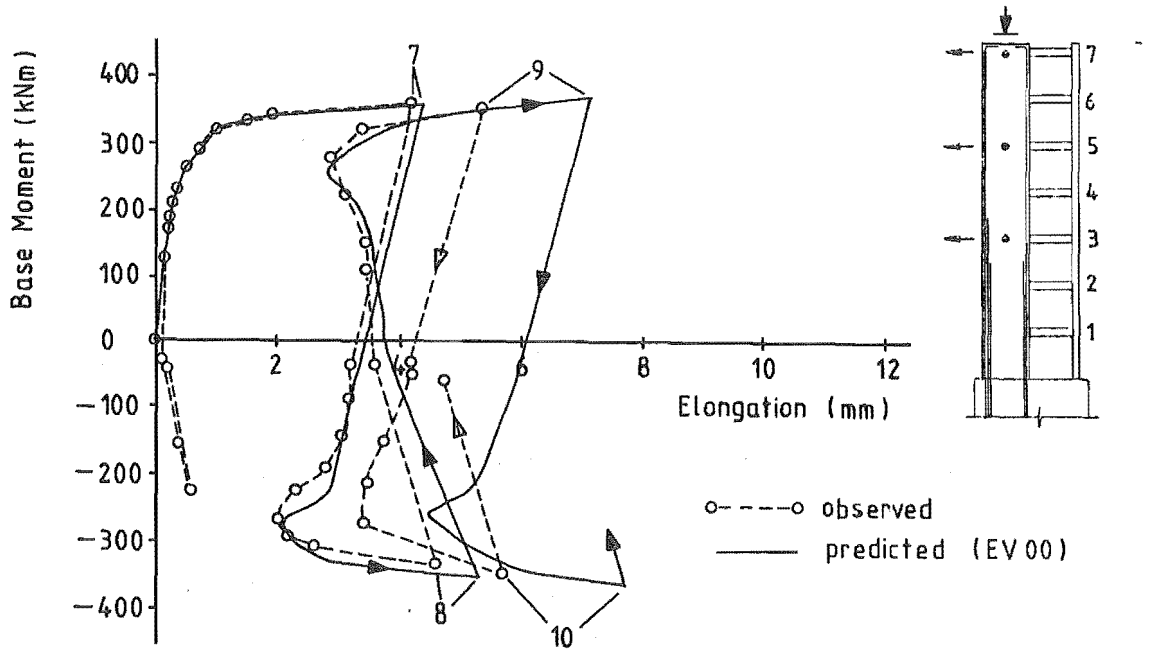

FIGURE 9.23 : TOTAL ELONGATION OF WALL, FSW-1

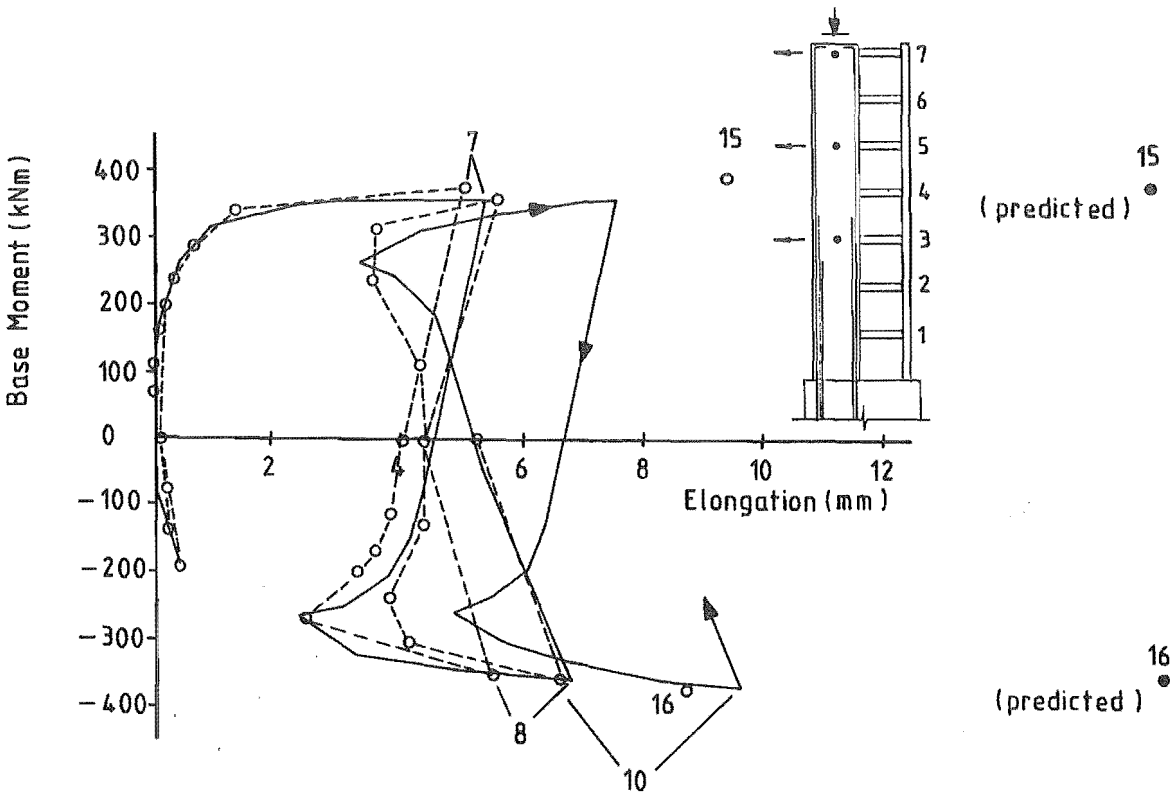

FIGURE 9.24 : TOTAL ELONGATION OF WALL, FSW-2

in the predicted peak elongations. This indicates that the stage at which crack closure occurred was being predicted accurately, and that the errors in the predicted peak elongations are primarily due to failure to adequately allow for softening of the concrete resulting from mismatching of crack surfaces (Section 5.4.5). After LR9, the errors in the peak elongations had become so large that the whole of the subsequent response was affected.

(d) During LR8, predicted softening of the compression steel in the wall plastic hinge zone in FSW-1 occurred at a later stage and more suddenly than was observed in the test. This is indicated by the sharp reduction in predicted wall elongation immediately before crack closure (Figure 9.23). The fact that this occurred at a latter stage than observed in the tests is surprising as the compression bars in the specimen had been affected by strain ageing. Predicted softening of the bars would therefore have been expected to occur at an earlier, rather than later stage. The reason for this discrepancy is not known. A similar behaviour was not evident in the corresponding predicted response for FSW-2.

9.3.7 Deformation of Wall Anchorage Zones

Anchorage deformations similar to those occurring in the beam-wall specimens (Section 8.8), also contributed significantly to the flexibility of the walls in the frame-wall specimens.

As shown in Figure 9.25 , the contributions of the wall anchorage regions as a proportion of the total wall deflections were almost independent of load intensity. In the case of FSW-1, the contribution from the measured anchorage deformations remained in the region of 13% to 17% of the total deflection in all load reversals for which the strains were measured. In FSW-2, the contribution from the measured anchorage deformations was initially about 15%, it increased to around 19% after yielding, and then to about 23% during load reversals 15 to 18. Part of the difference between

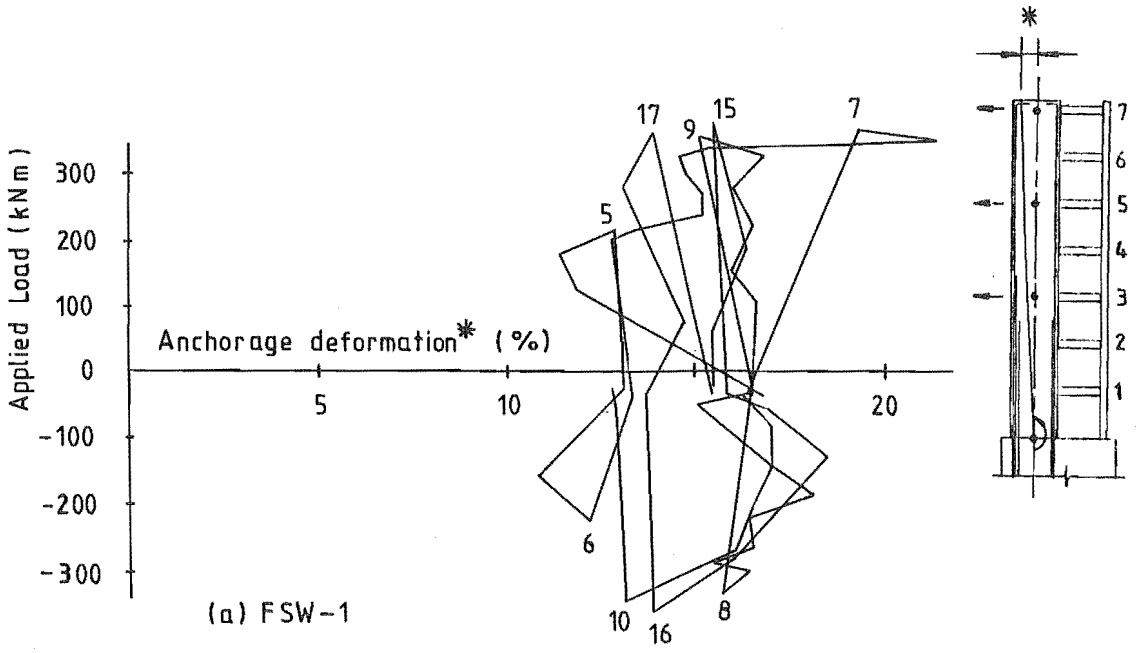

(a) FSW-1

* Percentage of the total flexural component of Level 7 deflection, due to deformations within the wall anchorage region, determined from measured strains in the wall flexural reinforcement.

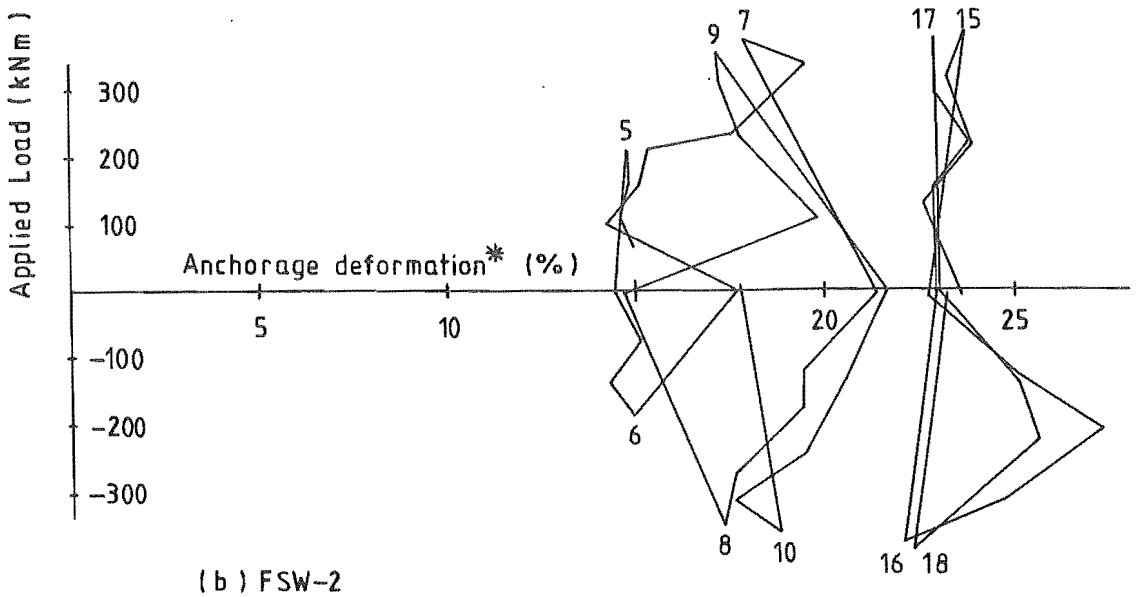

(b) FSW-2

FIGURE 9.25 : CONTRIBUTION OF ANCHORAGE DEFORMATIONS TO FLEXURAL COMPONENT OF LEVEL 7 DEFLECTION

the two specimens was probably due to the more severe local buckling of the bars at the inside edge of the wall plastic hinge zone in FSW-1 (Section 9.3.9). This would have tended to concentrate deformations within the plastic hinge zone during the later stages of the test. Strain ageing could also have affected the distribution of rotation between the wall anchorage and plastic hinge zones. However, as Figure 9.25 shows, there was little change in the anchorage zone contribution between LR7 and LR10, whereas the relative effect of strain ageing on the post-elastic curvature distributions was probably greatest in LR9 and LR10 (Figures 9.14 and 9.15).

The additional gauges provided in FSW-2 permitted a more complete evaluation of the strains in the anchorage reinforcement than was possible for either FSW-1 or the beam-wall specimens. To examine these deformations in greater detail, three sets of strain distributions are considered; Figure 9.26 shows the distribution of strain under initial loading conditions (i.e., strains recorded when the specimen was first loaded to a particular load level), Figure 9.27 shows the distribution of strain during reloading (load less than previous maximum level), and Figure 9.28 shows the distributions recorded at the peaks of several post-elastic load reversals. Generally, only regions where the bars have not previously yielded are considered in these diagrams.

Several features of the behaviour of the anchorage bars are discussed below:

(a) Under initial loading in tension (Figure 9.26), strain gradients close to the maximum recorded, were reached at comparatively low load levels. Further loading resulted in significant strains spreading further along the anchored bar section (increasing anchorage length) but with only marginal increases in the strain gradients. This behaviour is clearly at variance with the constant anchorage length assumed for the theoretical model.

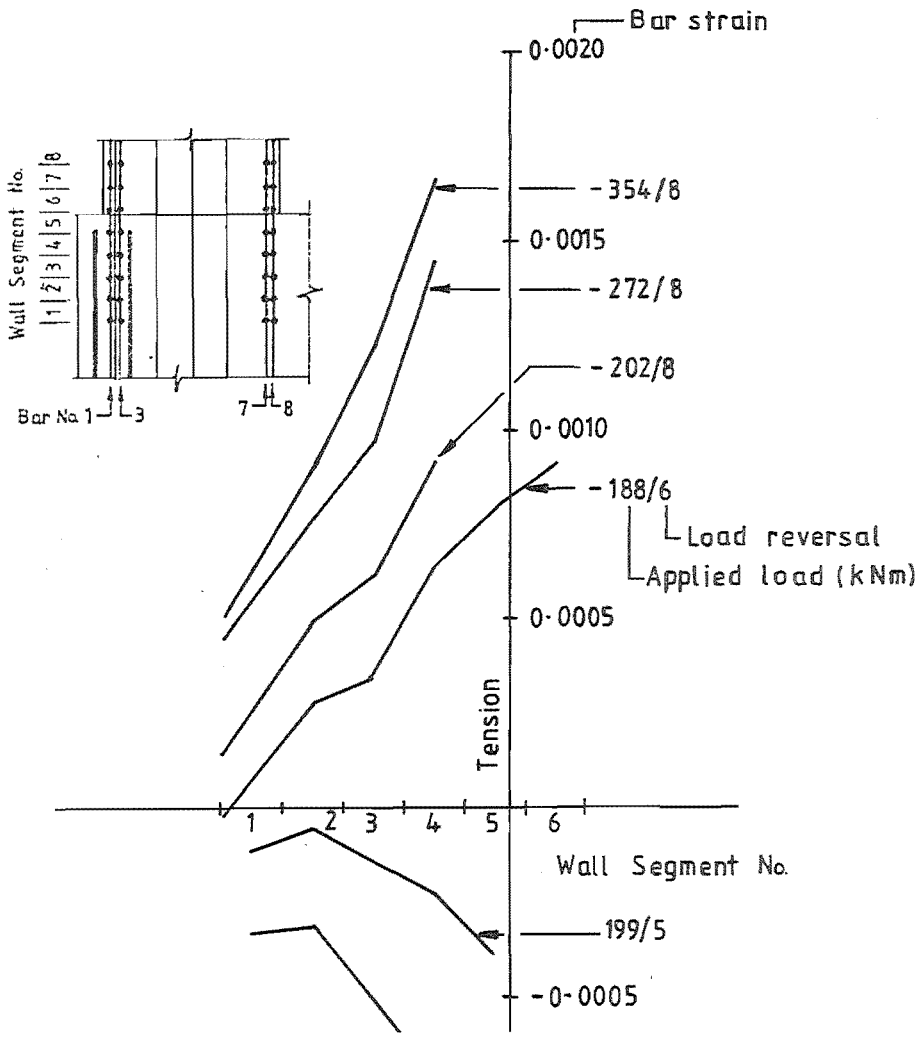

(a) Average tension strain in bars 1 and 3

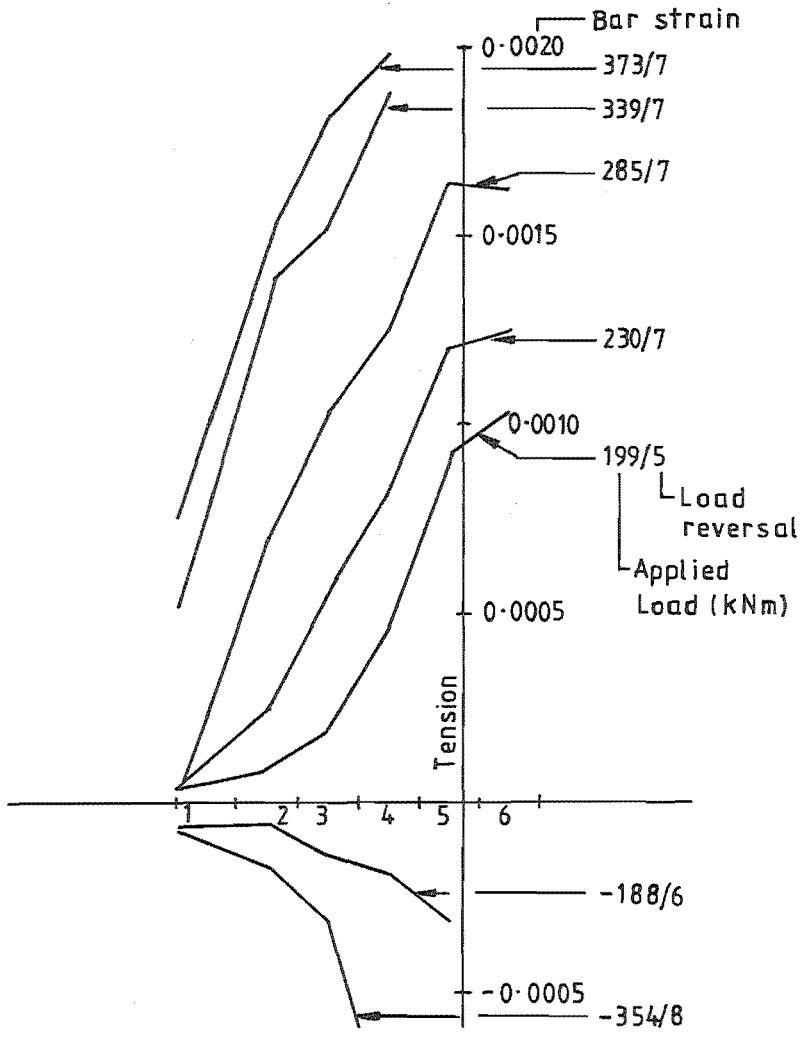

(b) Average tension strain in bars 7 and 8

FIGURE 9.26 : STEEL STRAIN DISTRIBUTION WITHIN ANCHORAGE REGION : INITIAL LOADING

(b) During reloading (bar strains below previous maximum value, Figure 9.27), the effective anchorage length appeared to remain reasonably constant while the strain gradient varied with load intensity. This is similar to the behaviour assumed in the theoretical model, except that the modelled anchorage length was fixed and not dependent on the maximum load previously imposed.

(c) The results for the two sets of bars considered in Figure 9.27 indicate a significant difference in behaviour at the start of the anchorage zone, i.e., near the base of the wall. This was largely due to the presence of the larger diameter base block flexural reinforcement close to the anchored ends of wall bars 1 and 3 (see Figure 7.14). This reinforcement considerably restricted cracking in this region of the anchorage zone. By contrast, there was only light stirrup reinforcement near the anchorages of bars 7 and 8, and large "V" cracks formed in the base block (Figure 9.7). As a result, most of the tension force was developed in the region beyond the cracks, where a compression strut could be formed between the tension bars and the wall compression zone. This behaviour is evident from the strain distributions shown in Figure 9.27b. For example, during LR9, the strain (and hence, the stresses) in segments 3 and 4 were approximately equal, indicating that almost no bond stress was developed in those segments.

(d) Beyond the end of the "V" cracks (i.e., in segments 1 and 2, Figure 9.27b), the strain gradient in bars 7 and 8 were even larger than those in bars 1 and 3. This was presumably a result of the smaller diameter of bars 7 and 8 (9.5 mm cf. 12.7 mm diameter for bars 1 and 3).

(e) As indicated in Figure 9.28 , yield eventually penetrated along bars 7 and 8 to the limit of the "V" cracks (i.e., as far as segment 3). This was only about one segment further than the yield penetration along bars 1 and 3. The results in Figure 9.28 also indicate that there was no significant deterioration

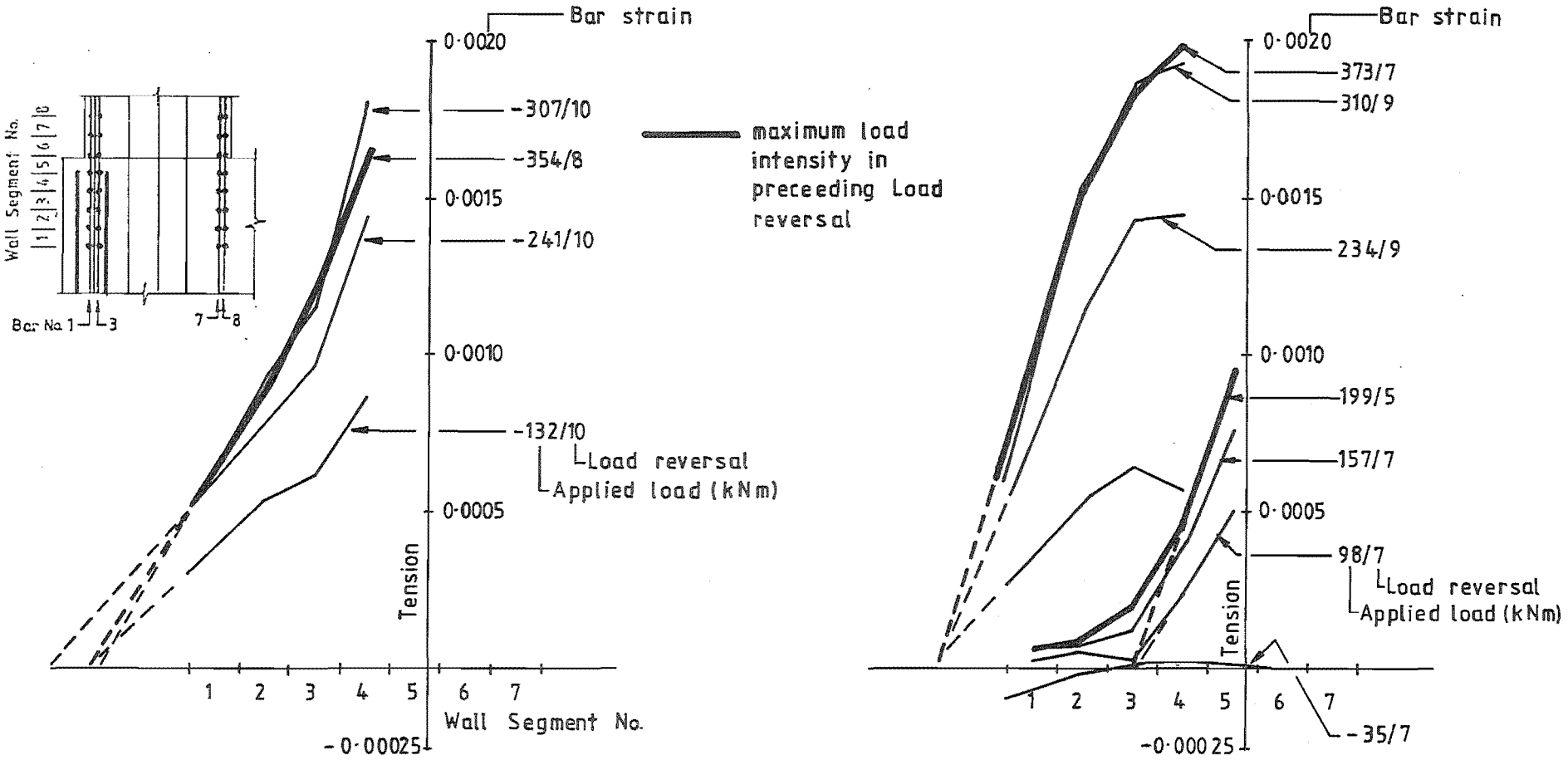

(a) Average strain in bars 1 and 3

(b) Average strain in bars 7 and 8

FIGURE 9.27 : STEEL STRAIN DISTRIBUTION WITHIN ANCHORAGE REGION : RELOADING BELOW PREVIOUS MAXIMUM LOAD INTENSITY

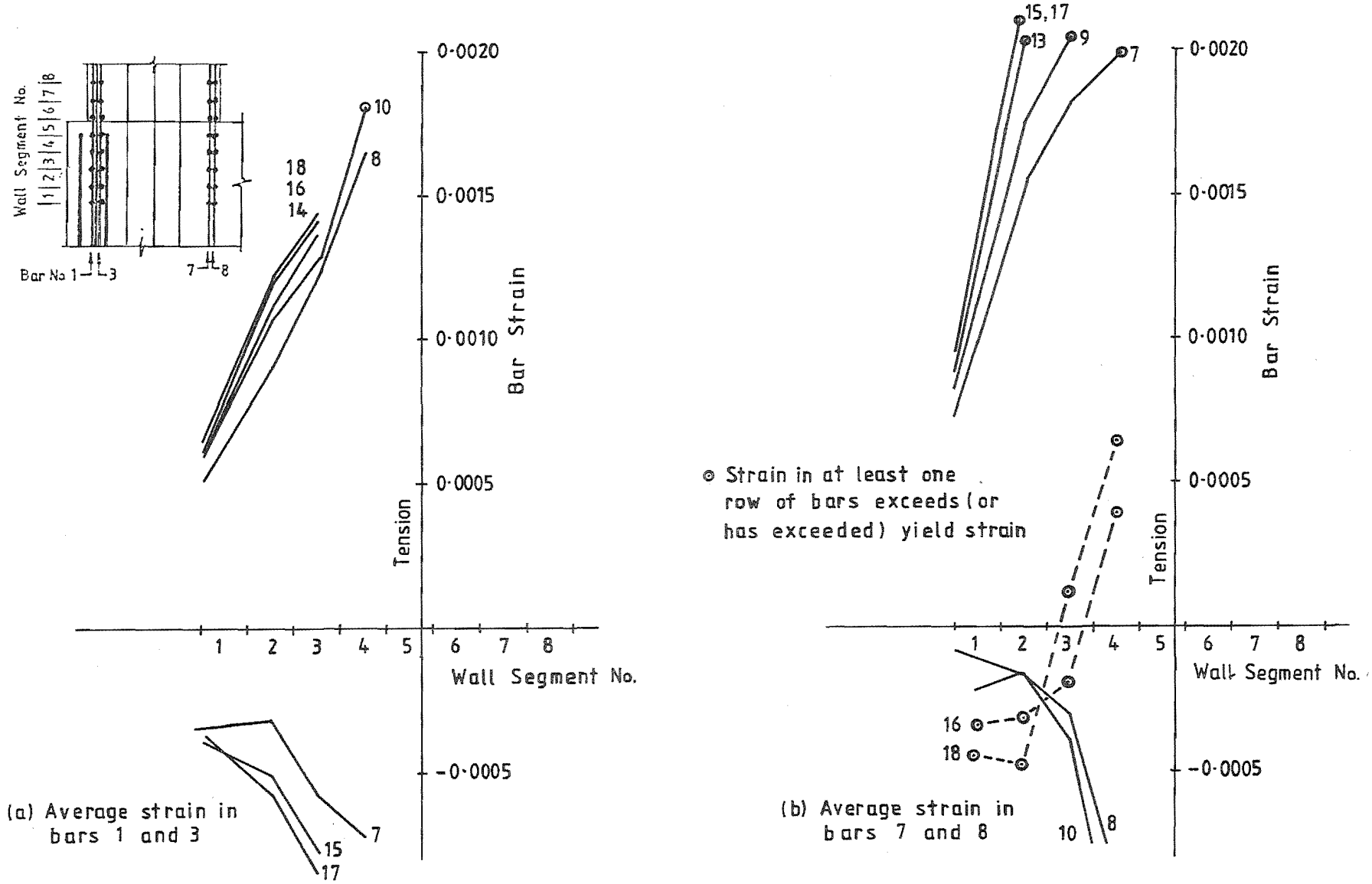

FIGURE 9.28 : STEEL STRAIN DISTRIBUTION WITHIN ANCHORAGE REGION : AT PEAKS OF EACH LOAD REVERSAL

in the bond performance outside of the yielded regions, even after 17 or 18 load reversals.

9.3.8 Stirrup Behaviour

Strains were measured along the length of eight stirrups in the bottom one and a half storeys of the wall in each specimen. Results obtained from these readings are shown in Figures 9.29 to 9.33*. Figures 9.29 and 9.30 compare the distribution of strains along the stirrups at the peaks of load reversals 7 to 10 with the locations of the corresponding main flexural and shear cracks in the tension region of the walls. Figures 9.31 and 9.32 show the strain histories recorded at selected gauge locations in each specimen, and Figure 9.33 compares the forces transferred across two cracks in each wall during LR7 and LR8. The locations of the gauges are indicated in Figure 9.29 ; the first digit of the gauge number specifies the stirrup number and the second, the position along the stirrup. Several features of the behaviour of these stirrups are discussed below:

(a) During the pre-yield load reversals, the maximum strains measured in the stirrups were generally less than 5% of the yield strain.

(b) Significant stirrup strains did not develop until the main inclined cracks began to form at a load of approximately $0.9 M_{by}$ in load reversal 7. These cracks did not fully develop until after the wall had yielded. The strains developed in the stirrups were generally localised in the vicinity of the cracks, at least until LR8. The large variation in strains along each stirrup shows that there was effective bond along the stirrups. This also means that significant transverse tensions must have been carried in the concrete between cracks, and even across cracks opened when the load was acting in the opposite direction, but which had subsequently closed. Clearly, any analysis based on a truss mechanism which assumes uniform tension in the stirrups, will tend to overestimate the shear deformation. This will apply especially in situations such as this where the maximum shear stresses were moderate

---

* The actual stirrup strains are likely to have been slightly smaller than the recorded values because of shrinkage induced compression strains in the stirrups at the time the zero readings were taken.

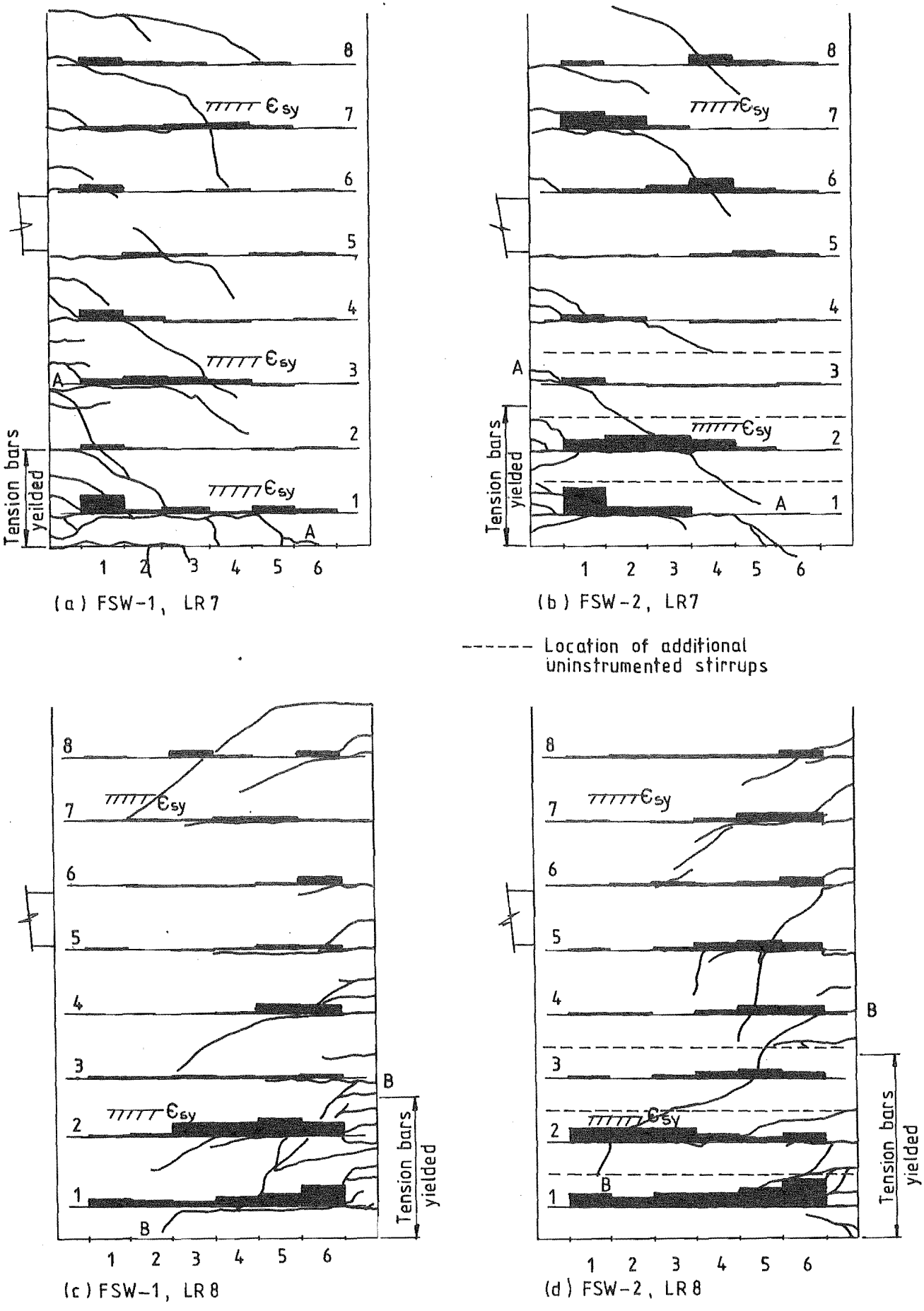

Note: A-A, B-B, locate position of cracks for which stirrup forces have been evaluated.

FIGURE 9.29 : STIRRUP STRAINS AT PEAKS OF LR7 AND LR8

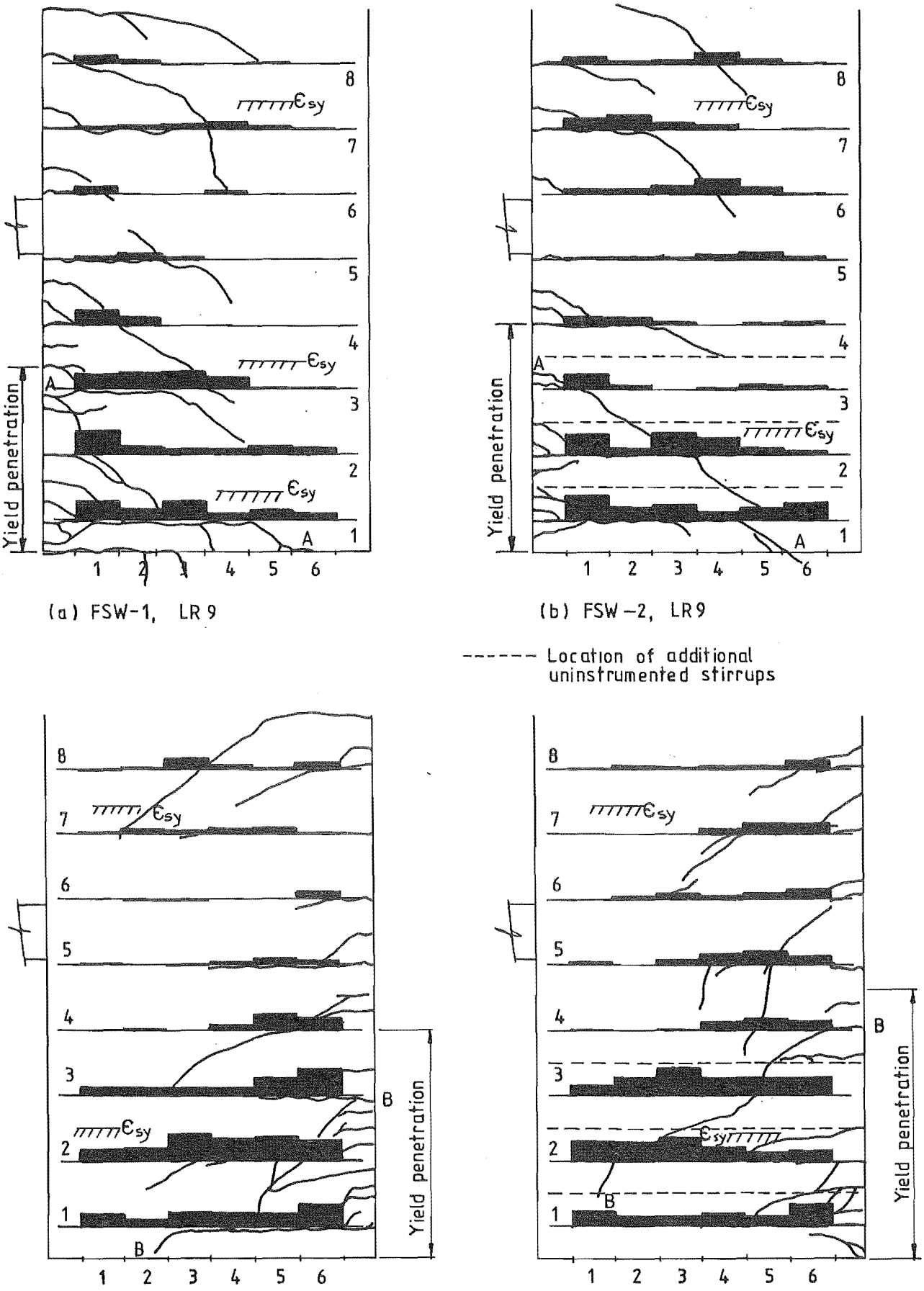

FIGURE 9.30 : STIRRUP STRAINS AT PEAKS OF LR9 AND LR10

($v_u \simeq 1.1$ MPa $= 0.18 \sqrt{f'_c}$) and the inclined cracks well spaced.

(c) The good bond apparent from the observed strains was achieved despite the fact that the bond conditions were in many cases worse than could be expected for a similar wall in a real building. This was because many of the flexural cracks in the wall plastic hinge regions tended to form along the gauged stirrups (Figures 9.29 and 9.30).

(d) Gauge WS1-6 was the only location where the initial large increase in strain occurred at low load intensity. This occurred in both FSW-1 and FSW-2 during LR8 (Figures 9.31 i and 9.32 i). When truss action is dominant, a large fraction of the wall shear force is transferred to the end support by a diagonal compression strut passing through the compression block at the base of the wall. However, at the start of LR8, the shear rigidities of the compression blocks in the wall plastic hinge zones were very low because of the flexural and interlock cracks which opened up during LR7 when the tension bars yielded. Consequently, during the initial stages of loading in LR8, most of the shear force in the plane of the bottom flexural crack was resisted by interlock in the vicinity of the tension bars and by dowel action. This resulted in high loading on the ends of the bottom stirrups at low applied shear levels, as they provided much of the support for the dowel action of the tension bars. Because this effect was very localised, the additional stirrups provided in FSW-2 made little difference to the loading on the bottom stirrup.

(e) Large localised strains were also induced at the other end (WS1-1) of the bottom stirrups ($0.65\ \varepsilon_{sy}$ in FSW-1 and $0.94\ \varepsilon_{sy}$ in FSW-2) at the peak of LR7. This was also largely due to the dowel loading from the main tension reinforcing, but in this case the initial straining occurred at high load levels after the tension bars had yielded.

(f) Three factors strongly indicate that coupling of flexural and shear actions occurred and that after yielding, the stirrup strains were significantly affected by the curvatures imposed

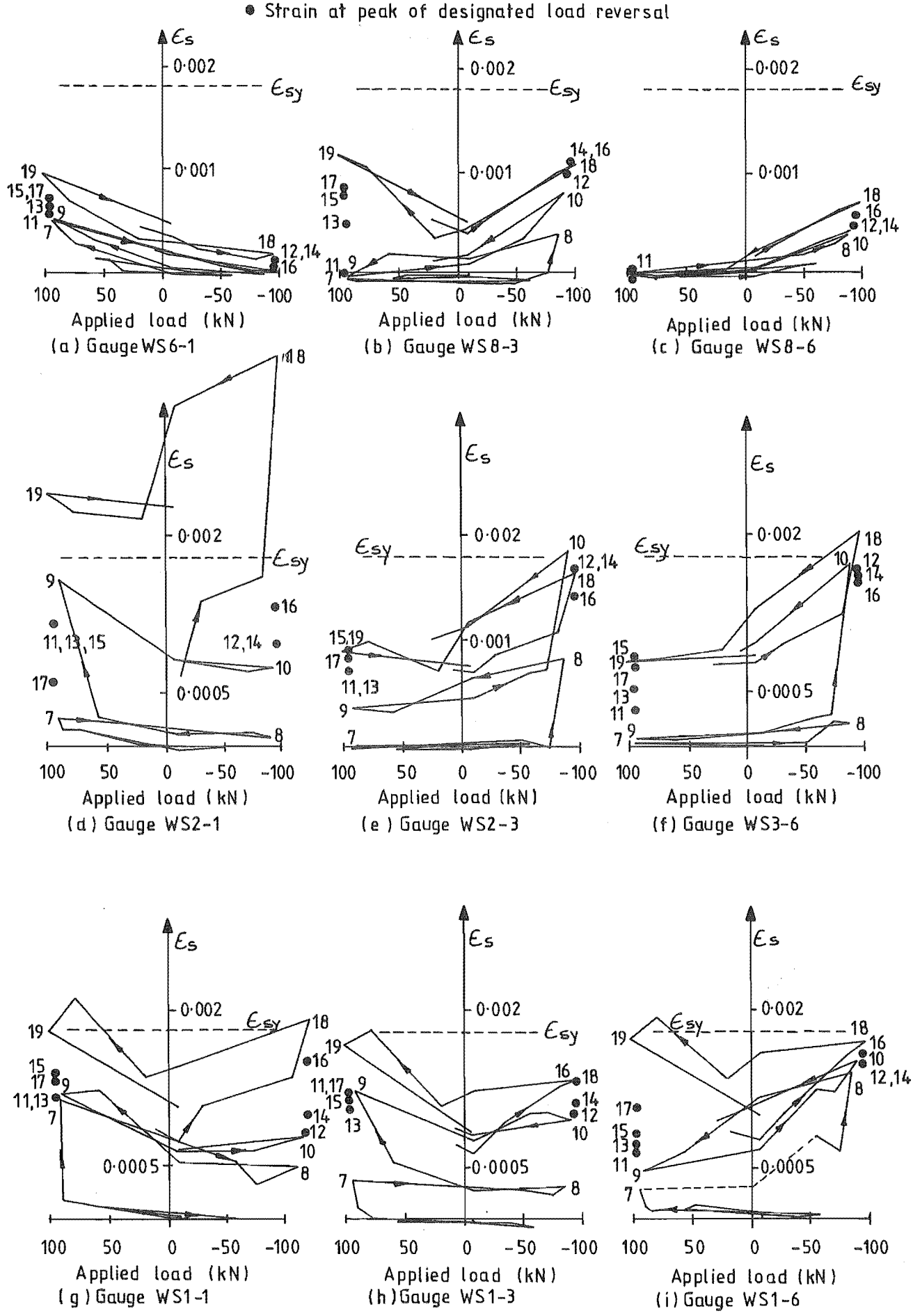

FIGURE 9.31 : STIRRUP STRAINS AT SPECIFIC GAUGE LOCATIONS, FSW-1

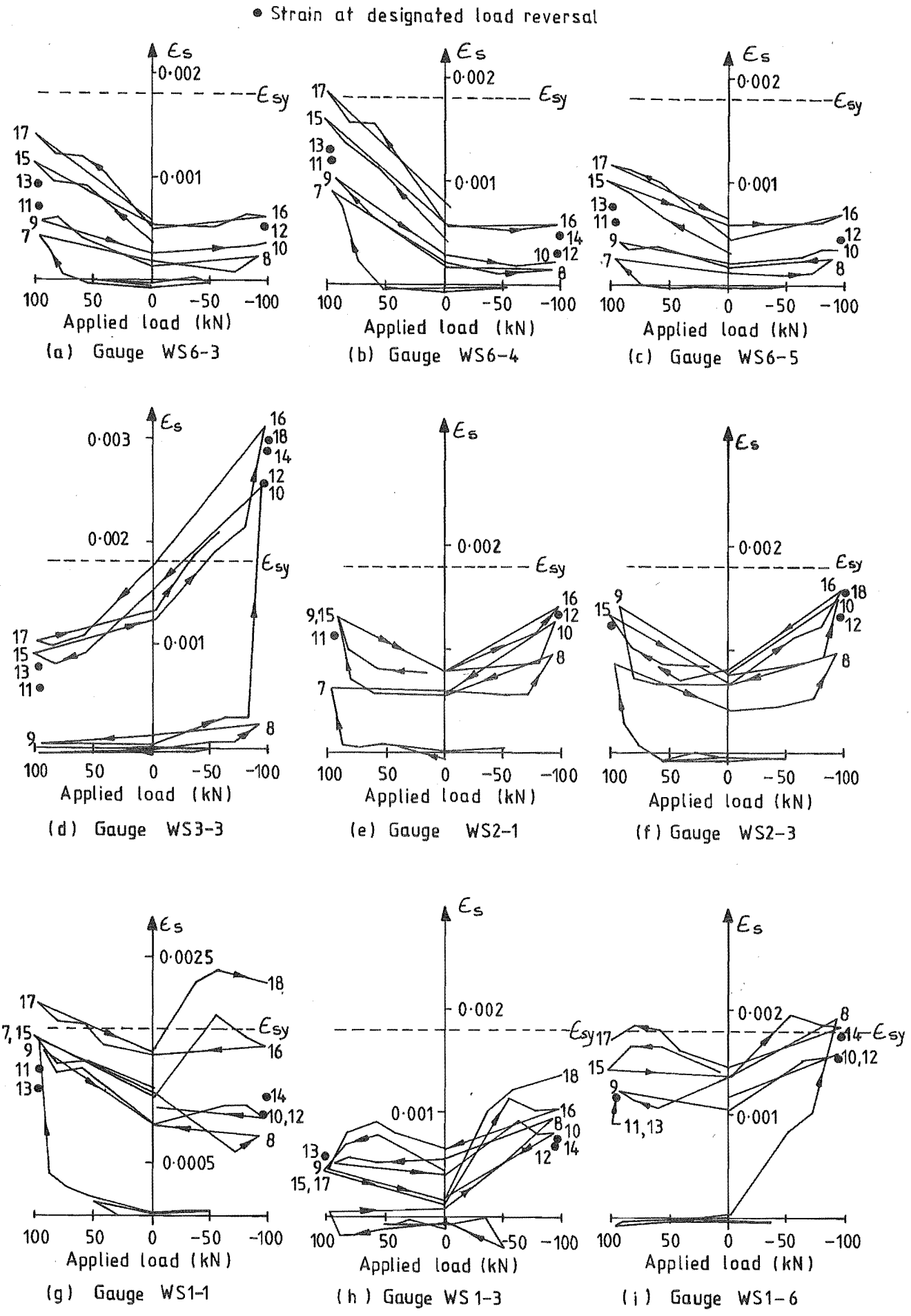

FIGURE 9.32 : STIRRUP STRAINS AT SPECIFIC GAUGE LOCATIONS, FSW-2

on the wall in the vicinity of stirrups:

(i) The patterns of cracking (e.g., crack slope, spacing and length) in the walls of both specimens were very similar. Despite the additional stirrups provided in FSW-2, the peak strains developed during LR7 and LR8 were generally slightly larger than at corresponding locations in FSW-1 (Figures 9.29 a to d). The larger strains in the FSW-2 stirrups are consistent with larger plastic deformations imposed on the wall (cf. Figures 9.14 and 9.15). Also, Figure 9.33 shows that even at equivalent displacements, the total force carried by the stirrups in the plastic hinge zone in FSW-2 was approximately double that in the corresponding stirrups in FSW-1. This indicates similar stirrup strains in FSW-2, since twice the number of stirrups crossed each crack.

(ii) Peak strains at locations on stirrups crossed by a crack generally occurred when maximum strains were induced in the main flexural bars crossing the same crack. As discussed in Section 9.3.2, the flexural reinforcement at the bottom of the wall was affected by strain ageing which occurred after initial plastic yielding. As a result, the maximum curvatures were developed during the first major yield excursion at each segment, with significantly smaller peak curvatures being developed in subsequent load reversals. This same general pattern of behaviour was also apparent in the strains recorded for the bottom three instrument stirrups. For example, large increases in strain were recorded when the cracks crossing the WS1-1 gauges in FSW-1 and FSW-2 opened due to initial flexural yielding during LR7. In subsequent load reversals in the same direction (LR9 to LR13), the peak strains developed at these gauge locations were approximately the same as or (in the case of FSW-2) even smaller than those in LR7, despite

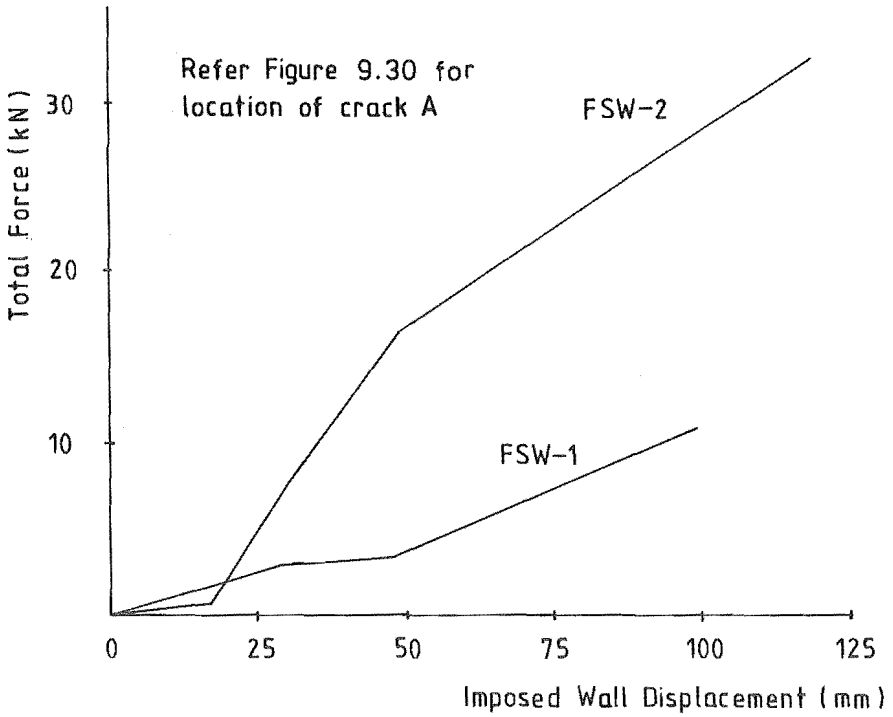

FIGURE 9.33 : TOTAL FORCE TRANSFERRED ACROSS CRACK 'A' BY STIRRUPS DURING LR7 LOAD REVERSALS

deterioration of the plastic hinge zone concrete. Similar behaviour was also observed at gauge locations on the bottom three stirrups, although in these cases the stirrup strains were not fully affected by yielding of the flexural bars until LR9 or LR10, e.g., gauges WS2-3 and WS3-6 in FSW-1, peak strain in LR10 was not exceeded until at least LR18. Because of the strain ageing, the recorded strains in the stirrups are not representative of wall stirrup behaviour under real earthquake loading. Nevertheless, the strain ageing has provided an unusual chance to assess the effect of wall plastic curvatures on stirrup strains.

(iii) As shown in Figures 9.31 and 9.32 , the "zero load" residual stirrup strains at gauge locations outside the plastic hinge zone were typically only 150 to 200 μs after the first post-elastic load reversal (e.g., WS6-4, FSW-2). By comparison, the "zero load" residual strains in stirrups within the plastic hinge zones were generally 700 μs to 1200 μs, or between 50% and 70% of the peak strains imposed. These large residual strains were a result of the cracks crossing the gauges being held open by the residual plastic strain in the wall tension reinforcement, and were clearly not due to the shear load (approximately zero) on the wall.

It should be stressed that the large increases in the strains in the lower stirrups during LR7 to LR10 were not solely due to flexural yielding. This is demonstrated by the large strains induced in stirrup 6 of FSW-2 during LR7 (Figure 9.32b). However, it is equally clear that the strains induced in the stirrups are not solely a function of the applied shear force, and that they can be significantly affected by the imposed curvatures, especially in the plastic hinge regions.

(g) As indicated by the cracking patterns (Figures 9.10 and 9.11)

TABLE 9.4 : STIRRUP FORCES TRANSFERRED ACROSS CRACKS IN THE WALL PLASTIC HINGE ZONES

LR	FSW-1			FSW-2			Crack++
	(a) Force+ Resisted by Stirrups (kN)	(b) Wall* Shear Force (kN)	(a)/(b) (%)	(a) Force+ Resisted by Stirrups (kN)	(b) Wall** Shear Force (kN)	(a)/(b) (%)	
7	10.8	85.6	12.6	33.0	88.2	37.6	A
8	19.5	71.6	27.2	42.9	73.4	58.4	B
9	28.0	82.8	33.8	68.1	83.6	81.4	A
10	54.8	76.4	71.7	64.1	76.9	83.6	B
11	24.7	85.5	28.9				A
12	56.3	78.5	71.7				B

\+ Total force carried by the stirrups crossing the crack. Estimated from measured stirrup strains and interpolation for the uninstrumented stirrups in FSW-2 wall.

++ Refer Figures 9.29 and 9.30.

* From analysis FSW-1/EV00, but scaled to adjust for the difference between the predicted and observed total loads resisted by the specimen.

** From analysis FSW-2/EV00, scaled as above.

and by the stirrup strains (Figures 9.29 to 9.32), the wall shear deformation responses for both directions of loading were similar. This indicates that the flexural reinforcement provided was effective in compensating for the effect of the varying frame-induced axial load* on the wall shear response as well as on the flexural response.

(h) Table 9.4 compares the stirrup forces transferred across cracks A and B in the wall plastic hinge zone of each specimen (see Figures 9.29 and 9.30). This shows that in both specimens there was a progressive increase in the forces carried by the stirrups during the first three or four post-

---

* Approximately 0 to 2.7 MPa compression on gross concrete section.

elastic load reversals, reaching a maximum of over 80% of the applied wall shear force in FSW-2. As discussed previously in point (f), the force transferred across cracks A and B in FSW-1 during LR7 and LR8 was only about half that transferred across the corresponding cracks in FSW-2. The force transferred across crack A in FSW-1 remained at a comparatively low level, probably because the crack ran into the base block some distance from the compression edge of the wall. By contrast, crack B (FSW-1) ran towards the edge of the wall and as a result the force transferred increased much more rapidly. By LR10 this had reached 71.7% of the shear force applied to the wall (cf. 81.4% for crack B in FSW-2 at the peak of LR10).

(i) Maximum strains in excess of yield were recorded in both FSW-1 and FSW-2 as early as LR10. However, this occurred at only one or two isolated points and as seen in Figure 9.32d for example, the response at these points remained stable. There was no evidence of onset of shear failure at any stage during the tests, i.e. yielding of all stirrups crossing a particular crack.

(j) During LR16 and LR18, there were further large increases in the stirrup strains, especially in the bottom stirrups in FSW-1, but also at WS1-1 in FSW-2. These increases in the stirrup strains were almost certainly caused by local buckling of the flexural compression bars on the inside edge of the walls between stirrups 2 and 3 in FSW-1 and between stirrup 1 and the base block in FSW-2 (see Section 9.3.9). By LR18, the core concrete in the vicinity of the buckled bars in FSW-1 had been severely damaged. This affected most of the stirrups below level 1.

(k) Outside of the plastic hinge zones, both the peak strains and the "zero load" residual strains generally increased progressively with each cycle, e.g., stirrup 6 in FSW-2 (Figure 9.32 a to c). At least three factors have probably contributed to this behaviour, i.e., deterioration of the bond between the stirrups and concrete; increasing flexural deformations in the vicinity of the stirrups (Figures 9.14 and 9.15), and mismatching of opposing crack surfaces.

9.3.9 Local Buckling of Flexural Reinforcing Bar Groups

Local buckling of wall compression bar groups occurred in both FSW-1 and, to a lesser extent, FSW-2. In both cases the buckling occurred in the bar group at the inside edge of the walls (Figures 9.34 to 9.37).

As discussed in Section 7.5.6, the transverse reinforcement provided in the wall plastic hinge zone of FSW-1 consisted of full depth R6.4 ties at 152 centres (approximately $d_w/4$ or 16 d_b) to resist the design shear force, plus additional small confining ties around the bar groups at each edge of the wall to reduce the unsupported length of bar to less than 6 d_b. The intention in using the local confining ties was to tie the outer bars back into the wall, or if this failed, to ensure that the bar groups acted as a composite strut. The minimum dimension of the cross-section enclosed at the inside edge of the wall was 35 mm or about 0.23 times the main tie spacing. For the bars at the outside edge, the minimum dimension was 64 mm or 0.42 times the main tie spacing.

In the test, the local ties around the bar group at the inside edge of the wall in FSW-1 did not function effectively. As shown in Figure 9.34 a, longitudinal splitting cracks developed along the junction between these bars and the core concrete as early as LR10, which was the first load reversal after tension yielding had penetrated past the second stirrup tie (Figures 9.29 and 9.30). By LR16, the cover concrete around these bars had spalled between the first and third stirrups and the bar group itself had buckled between the second and third stirrups* (Figure 9.34 b). The mode of buckling was in some respects similar to that observed in TB3, i.e., the deterioration of the confined concrete, loss of cover and large plastic tension strains developed during alternate load reversals permitted a "sliding shear" type buckling mechanism to develop, in which the two rows of bars in the group were only constrained to deform in parallel (Figure 9.34). Under these conditions, the stability of the bar group as a whole was little different from that of the individual bars.

---

* When fabricating the reinforcing cage, the second stirrup had to be moved towards the base block to avoid clashing with a strain gauge stud. As a result the gap between the stirrups 2 and 3 was 160 mm as compared with 133 mm between 1 and 2.

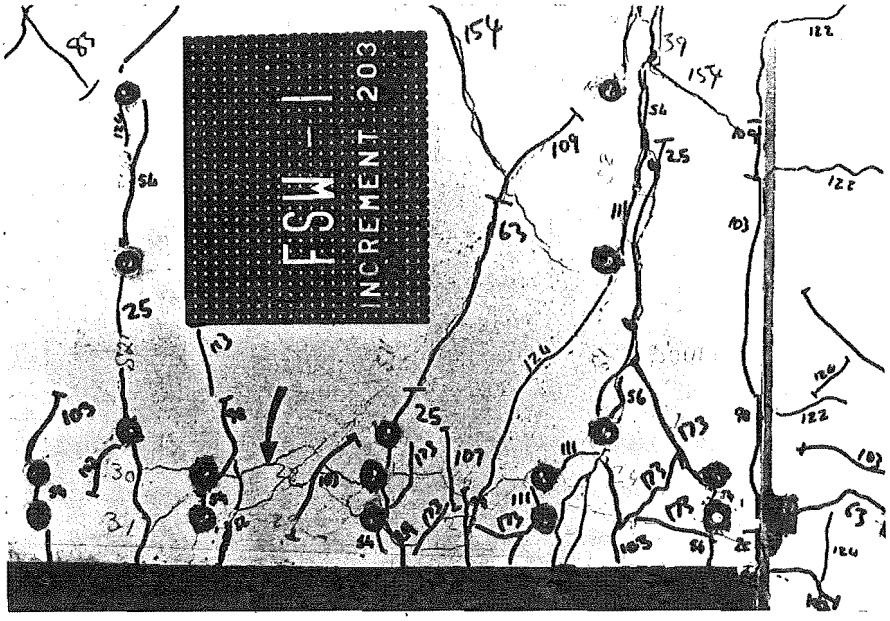

Note : Main longitudinal splitting cracks arrowed.

(a) Longitudinal splitting cracks, LR 10.

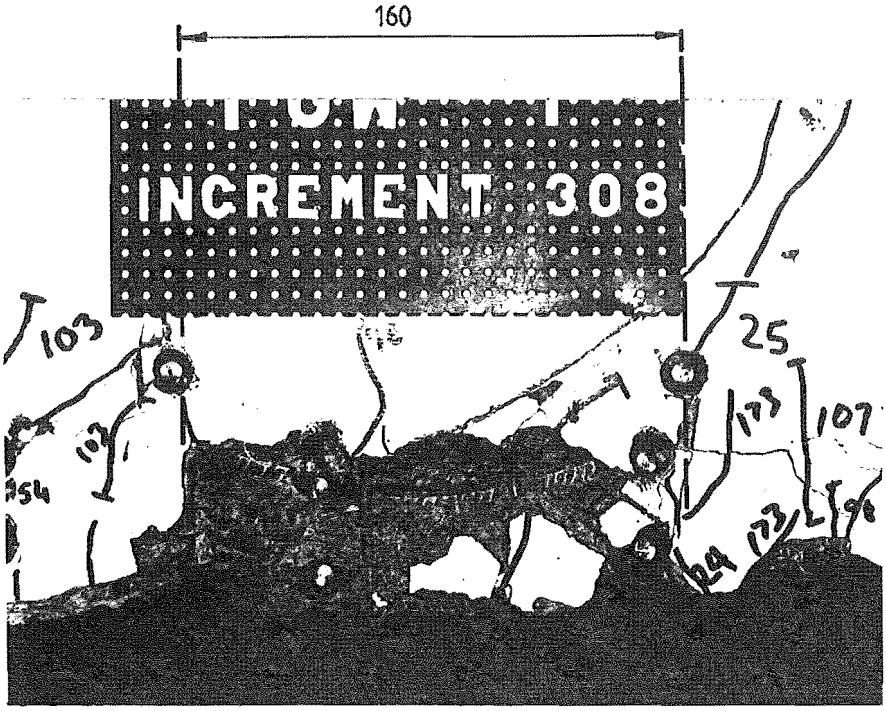

(b) Extent of buckling, LR 16

FIGURE 9.34 : LOCAL BUCKLING OF BAR GROUP, FSW-1

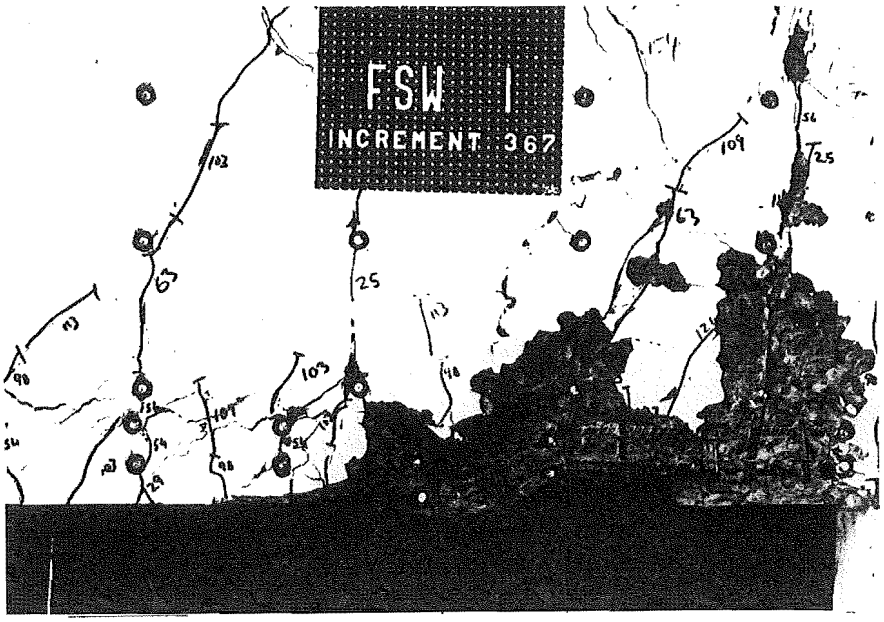

FIGURE 9.35 : LOCAL BUCKLING OF BAR GROUP AT PEAK OF FINAL NEGATIVE LOAD REVERSAL, LR20. CONCRETE CRUSHED (FSW-1)

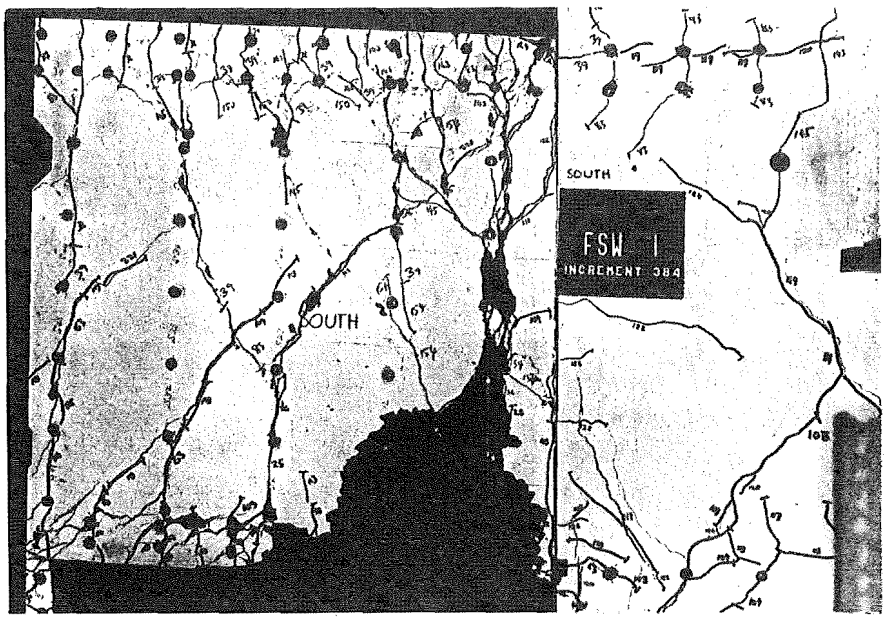

FIGURE 9.36 : FSW-1 WALL PLASTIC HINGE ZONE AT PEAK OF LR21 WITH LOOSE CRUSHED CONCRETE REMOVED

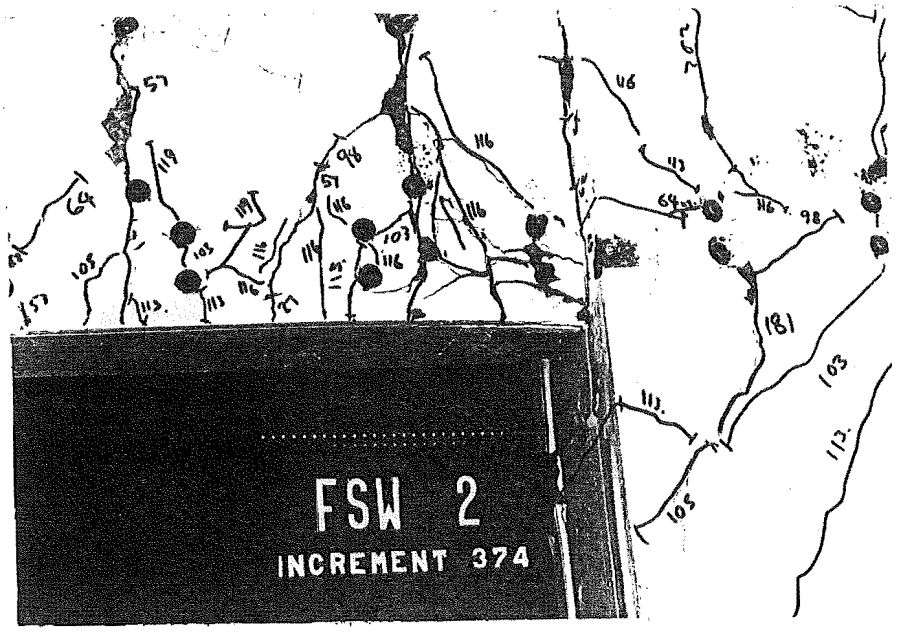

(a) Load reversal 18

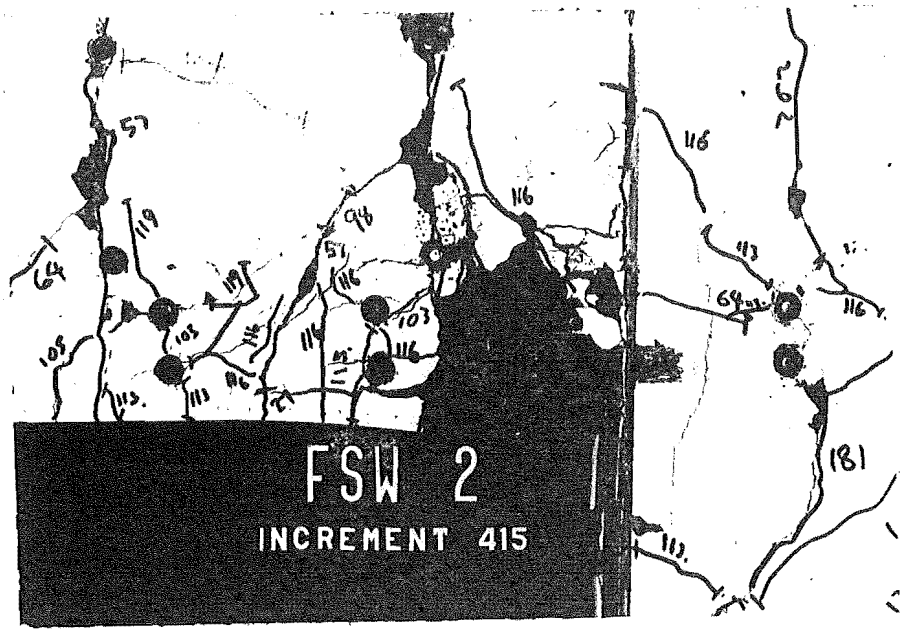

(b) Load reversal 20

FIGURE 9.37 : LOCAL BAR BUCKLING, WALL PLASTIC HINGE ZONE, FSW-2

With further cycling the effectiveness of these bars in compression decreased rapidly. During LR18 and LR20, the load-deflection response (Figure 9.5a) exhibited significant pinching at low loads due to the bars buckling and the region of the wall between the second and third stirrups was effectively only singly reinforced. Part of the core in this region eventually crushed at a ductility of DF ≃ 10 in LR20 (Figures 9.35 and 9.36). The crushing was accompanied by a significant reduction in the load carried by the specimen, and to avoid further damage, the direction of loading was reversed.

The bar group at the outside edge of the wall showed no sign of buckling. The better performance of this group of bars can be attributed to both the larger area confined by the local ties and the generally larger diameter of the bars in the group, i.e., 6D12.7 + 1D9.5 bars as opposed to 4D9.5 + 2D12.7 bars at the inside edge. Also, the peak tension strains induced in these bars between stirrups 2 and 3 were smaller than those induced in the bars that buckled, i.e., maximum average tensile strain ≃ 0.018 cf. 0.023* in the bars that buckled. This discrepancy became even greater during later stages of the test, partly because of the effect of the bars at the inside edge of the wall buckling.

As discussed in Section 7.5.6, additional full depth ties were provided in FSW-2 in an attempt to suppress this type of buckling failure. These ties reduced the unsupported lengths of the bar groups to about 75 mm, except between the base block and the first tie where the gap was almost 100 mm (approximately 10.5 times the minimum bar diameter). The bars at the inside edge of this wall did eventually buckle between the base block and the first stirrup, but only after about 10 large displacement load reversals had been imposed (Figure 9.37).

This type of buckling failure exhibited by these bars, although serious, should not be difficult to prevent. The results obtained from the tests generally indicate that the limit recommended by Bresler and Gilbert (112) of 6 d_b maximum unsupported length for

---

* At the peak of LR9 in the case of the bars at the inside edge and at the peak of LR10 for the bars at the outside edge.

compression bars in potential plastic hinge zones, is reasonable and should be effective in suppressing local buckling of the bars. However, the results also show that simply enclosing a small group of bars (even at 6 d_b spacing) may not be sufficient and that any supplementary ties used must adequately tie the bars back into the body of the wall to prevent the separation of a group of bars (19).

9.3.10 Out-of-Plane Buckling Failure, FSW-2 Wall

As noted in Section 9.2.2, the wall of the second specimen (FSW-2) failed by out-of-plane buckling at the outer edge of the wall plastic hinge zone. The failure occurred during LR21 after the wall had previously been subjected to 14 post-elastic load reversals, with the imposed displacement ductility being progressively increased from DF $\simeq \pm 4$ to DF $\simeq \pm 8$.

The load-deflection history for the final five load reversals is reproduced in Figure 9.38 . Out-of-plane buckling of the compression bars at the outside edge of the wall was first noticed at a ductility of DF = 3.7 in LR21 (increment 439 in Figure 9.38). By this stage the bars had already bent about 5 mm sideways and the weld joining the legs of the bottom local confining tie had fractured (Figure 9.39 a). With further loading the moment resisted by the specimen increased only marginally. At DF = 6 (increment 441 in Figure 9.38), the bars had buckled approximately 12 mm out-of-plane and a large inclined crack had developed across the end of the wall, just above where the bars were bent (Figure 9.39 b). The load resisted ultimately reached only 80% of the previous maximum value before suddenly reducing a further 20%. This sudden reduction in load occurred at a ductility of DF $\simeq$ 8, and was accompanied by explosive spalling of side cover concrete from the lower part of the wall and from the top edge of one side of the base block (Figure 9.40). The bars buckled to approximately 40 mm out-of-plane. Loading was continued up to a ductility of DF $\simeq$ 9.3, when there was a second, equally sudden reduction in strength. At this stage, the test was abandoned as the specimen had jammed against the test rig.

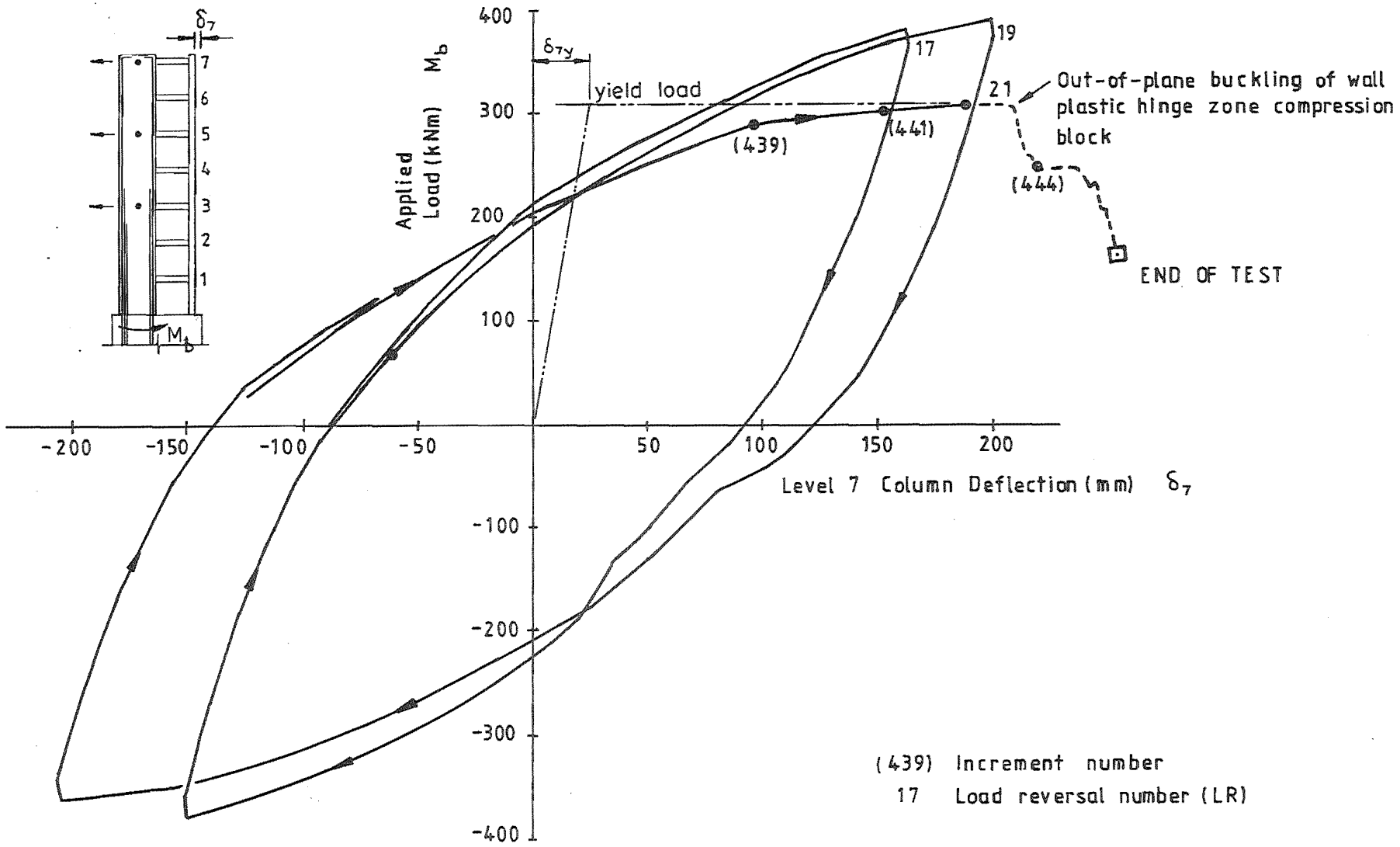

FIGURE 9.38 : LOAD COLUMN DEFLECTION RESPONSE FINAL FIVE LOAD REVERSALS, FSW-2

The mode of buckling was generally similar to that which occurred in TB3 (Section 8.10.3), i.e., the buckling at the base of wall was caused by a combination of instability of the compression bars as they approached yield and the low interlock and dowel rigidity of the compression block. The resulting large out-of-plane shear displacement of the bar group as can be seen in the photographs shown in Figure 9.39 and 9.40 . This shear deformation was confined to within a region of about 90 mm above the base of the wall, from which the cover concrete had already been spalled (Figure 9.39 a).

There are, however, two aspects in which the wall buckling differed from the behaviour of TB3. The first is the explosive manner in which the wall eventually buckled. The difference here was probably due to the wall being dependent on the concrete for part of its moment resistance. The sudden reduction in load caused by crushing and spalling of the concrete would therefore have released a large amount of energy. The concrete in TB3 had not previously been subjected to large compressions and consequently should have been in a better condition to resist the forces imposed after the compression bars had buckled (refer Section 8.10.3).

The second difference between the two buckling mechanisms was that, in the case of FSW-2, there were significant out-of-plane flexural and shear deformations in the section of wall above the region where the cover concrete had spalled (Figure 9.41). These deformations were largely a result of the restraint provided at level 1 (see Figure 9.41), which prevented the upper sections of wall from twisting freely. The out-of-plane flexural deformations* were therefore an important factor in the initiation of buckling. It is of interest to note that the storey height to wall thickness ratio for FSW-2 was only 7.5:1 and that the neutral axis was only 1 b_w ($\simeq 0.13\ \ell_w$) from the compression edge at the peak of LR7. By

---

* One noticeable feature of these deformations was that there was little or no out-of-plane mismatch between the faces of the cracks (Figure 9.39), despite there being sufficient lateral force to induce the large inclined crack. This demonstrates the effectiveness of intact cover concrete in restricting out-of-plane shear slip, e.g., by providing effective dowel restraint.

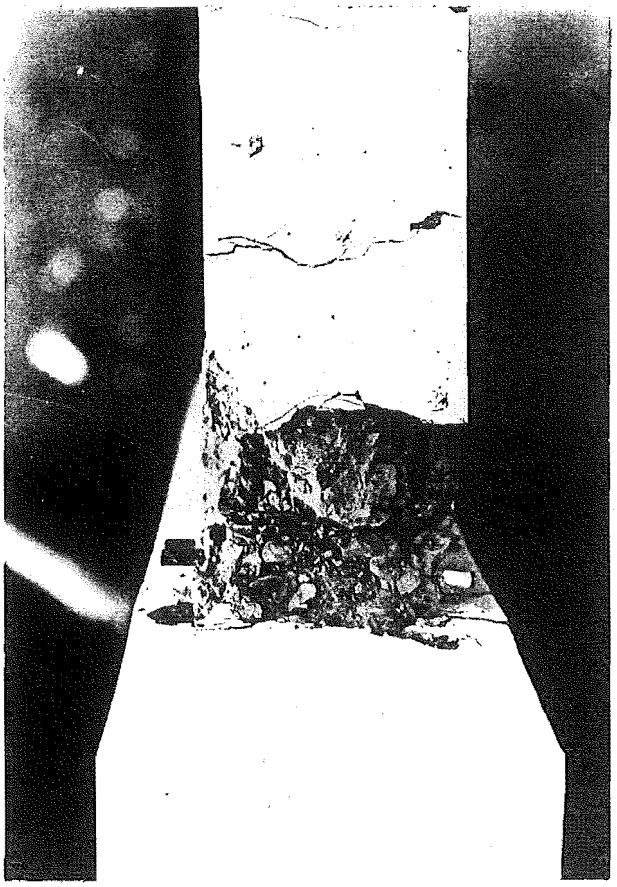

(a) Deformation when buckling first noticed at DF = 3·7 in LR 21. (Increment 439)

(b) Deformation at DF = 6 in LR 21. (Increment 441)

FIGURE 9.39 : BUCKLING FAILURE IN FSW-2, WALL COMPRESSION BLOCK

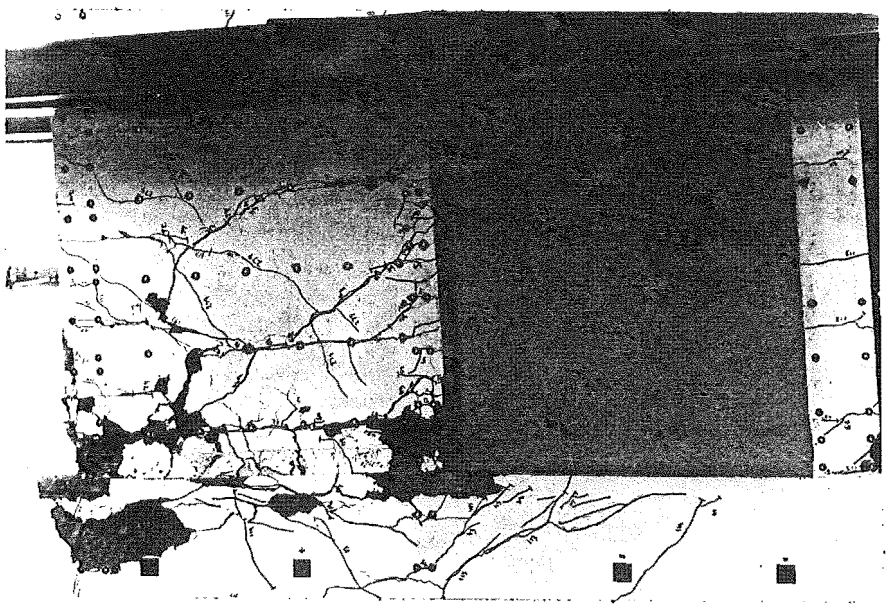

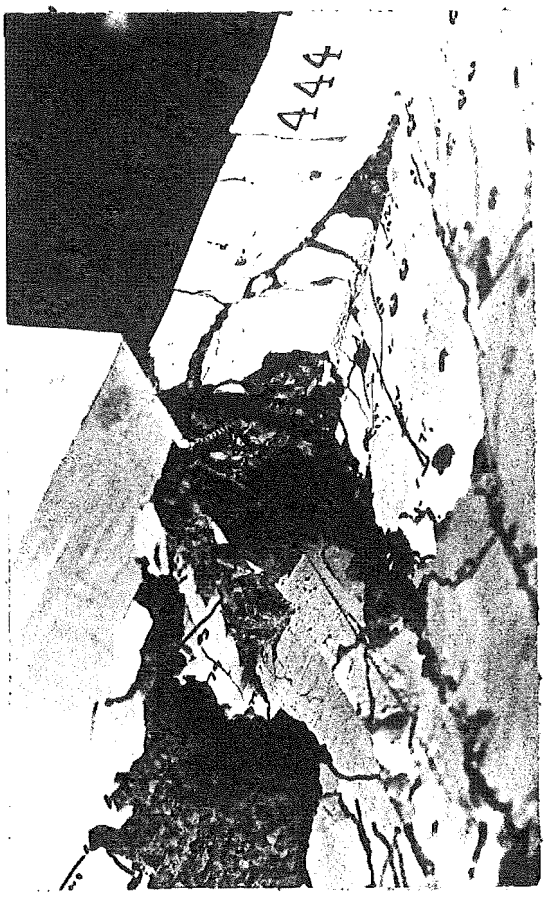

FIGURE 9.40 : BUCKLING FAILURE IN FSW-2 WALL COMPRESSION BLOCK.
DEFORMATION AFTER INITIAL SUDDEN REDUCTION IN STRENGTH
AT DF ≃ 8 IN LR21 (INCREMENT 444)

comparison, 'ductile' walls designed to the current New Zealand code only have to be one-tenth the storey height thick (or only 1/25 the storey height, if the neutral axis depth is not more than 3 b_w or 0.3 ℓ_w). However, the maximum member ductility (DF) expected under design earthquake loading would normally be smaller than imposed in these tests.

The large inclined crack across the end of the wall developed at some point between DF = 3.7 and DF = 6, and was a result of asymmetric compression (cracks closed on only one side, Figure 9.39) and transverse shear resulting from the restraint against twisting of the upper sections of the wall. This crack isolated a section of the wall compression block (Figure 9.39 b) and would have permitted the buckling failure to have proceeded, even if the upper sections of the wall had been rigidly restrained against twisting.

Previously it was stated that conventionally reinforced beams would not normally be susceptible to an out-of-plane shear-buckling failure (Section 8.10.3). However, as clearly demonstrated by the failure of FSW-2, conventionally reinforced walls are susceptible to this type of failure. There are two main reasons for this. The first is that the wall is more slender than a beam and therefore is more flexible in the out-of-plane direction. The second reason is that the presence of a net axial compression on the wall forces the closure of cracks at a lower lateral load (moment and shear). This results in smaller shear strains (Section 9.3.5), and consequently, a smaller mismatch between crack surfaces. Because of this, larger compressions are induced in the reinforcing bars, thereby increasing the risk of instability while the cracks are still open and hence out-of-plane sliding can occur.

One of the coupled shearwall specimens tested by Santhakumar (30) also failed by out-of-plane buckling. This failure was attributed to a vertical misalignment of approximately 0.004 radians between the planes of the walls and the base block, when the specimen was cast (30). However, although the misalignment may have accelerated the development of buckling, it seems likely that the wall would still have been susceptible to buckling at some stage. Because of the

problem experienced with Santhakumar's specimen, particular care was taken to minimise any misalignment in the present specimens (FSW-1 and FSW-2), and it is unlikely that this factor would have affected their behaviour.

Although the wall in FSW-2 sustained two load reversals to a ductility of DF ≃ 8*before buckling, walls with different geometries and reinforcing details, or subjected to different loading conditions could well buckle at much lower ductilities. There are several factors which could have inhibited buckling of the wall in FSW-2. These include:

(a) 12.7 mm diameter bars were used for the principal flexural reinforcement in the wall, whereas to satisfy similitude, only 7 mm - 8 mm diameter bars should have been used.

(b) Strain ageing of the bars considerably reduced the magnitude of the tension strains induced in the bars near the base of the wall (Section 9.3.2). In fact, during the period that the strains were monitored (i.e., up to LR18, DF = -5.7), the average tensile strain in the bottom 300 mm of the outer wall bars never exceeded the peak value reached (0.023) in LR8 (DF = -3.9).

(c) The wall was thicker relative to the storey height, or to the wall length, than is often the case (19).

(d) Local buckling of the bars at the inside edge of the wall will have caused some reduction in the peak tensile strains developed in the bars at the outside edge.

(e) The specimen was loaded only in the plane of the wall, and with significant restraint to twisting provided at levels 1, 3, 5 and 7. In a real building, earthquake loading will generally induce both in-plane and out-of-plane wall displacements. At the stage when buckling of the wall was first noticed (increment 439, Figure 9.39 a), the out-of-plane displacement of the compression edge of the wall was only about 0.7% of the storey height. Inter-storey displacements of this order can be expected during severe earthquakes, and

---

* Note that this value is the specimen ductility. In terms of actual deflection at wall yield, the maximum ductilities imposed were approximately only DF ±5.7 (see Fig. 9.2).

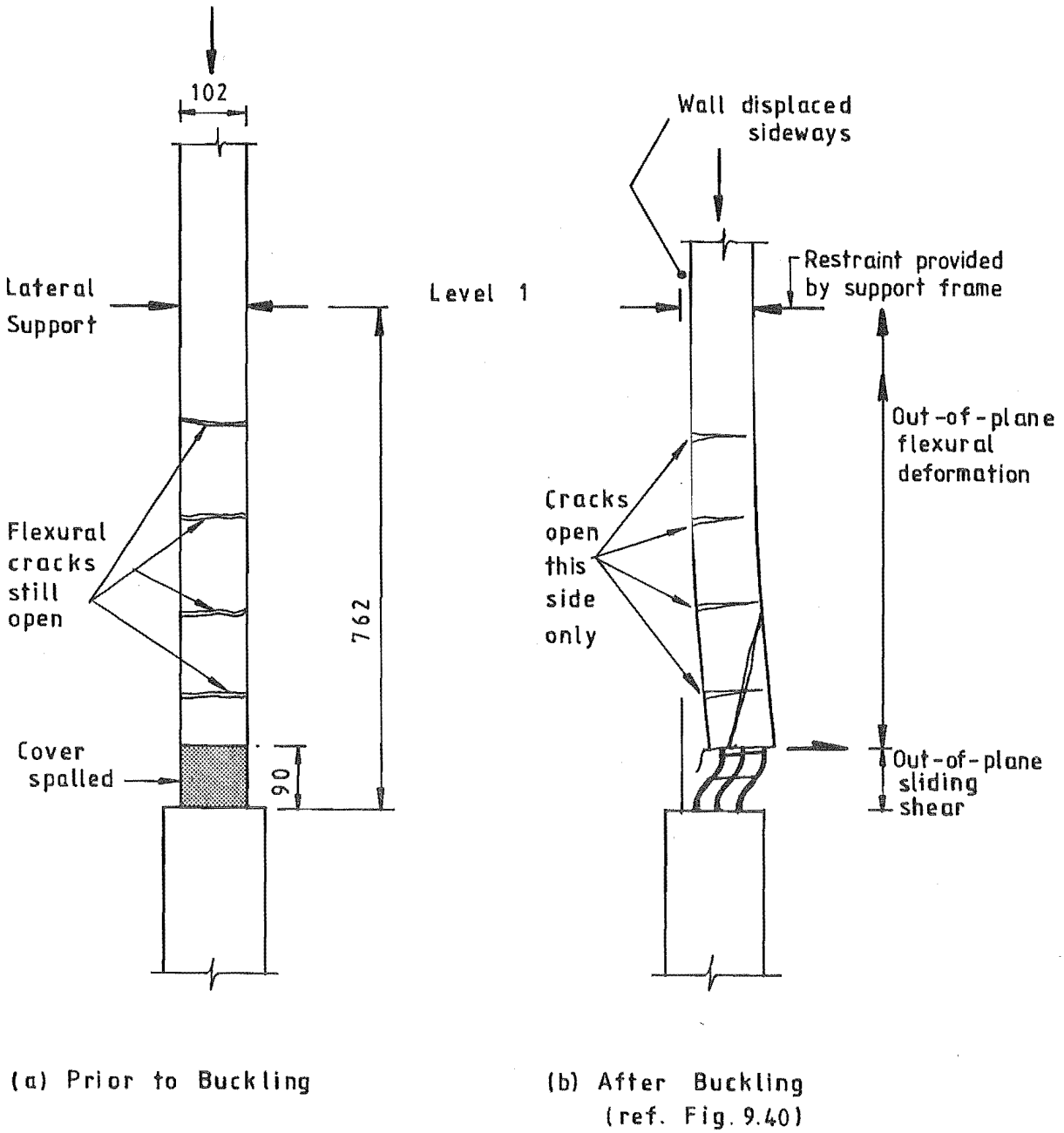

FIGURE 9.41 : MECHANISM OF BUCKLING FAILURE, FSW-2 WALL COMPRESSION BLOCK (SCHEMATIC ONLY)

therefore could possibly initiate buckling at significantly lower ductilities than the results from in-plane load tests suggest.

The fact that the wall in FSW-1 did not buckle in this manner, can largely be attributed to the more severe local buckling of the bars at the inside edge of the wall, and eventual failure of the compression block (see Section 9.3.9). Because of this, the maximum tensile strains in the outer wall bars were considerably smaller in FSW-1 than in FSW-2.

Because of the number of variables involved, generalisation from results of a single test is difficult. However, the results obtained from FSW-2 do indicate that some walls are susceptible to out-of-plane buckling. In view of the seriousness of this type of failure, it is important that more extensive testing be carried out to obtain a better understanding of wall buckling mechanisms.

9.4 BEHAVIOUR OF BEAMS

Aspects of the behaviour of the scale beams used in these specimens were investigated in detail in the beam-wall tests described in Chapter 8. In the frame-wall tests, only limited instrumentation of the beams was provided. This was principally directed at assessing interaction effects and evaluation of the theoretical model.

Factors investigated in this section include the magnitudes and distribution of imposed rotations, and the consequent flexural and shear deformations. In addition, the deterioration of the lapped splice regions of the beams in FSW-2 is investigated and an assessment made of the effect of this on the overall responses of the beams.

9.4.1 Pre-Yield Curvatures

Figure 9.42 compares the observed and predicted curvatures in the No. 2 segments of each beam at the peaks of load reversals 5 and 6.

The large scatter in the observed curvatures occurs because the loads acting on individual segments are not statistically determinate and are therefore dependent on the imposed beam displacements and the

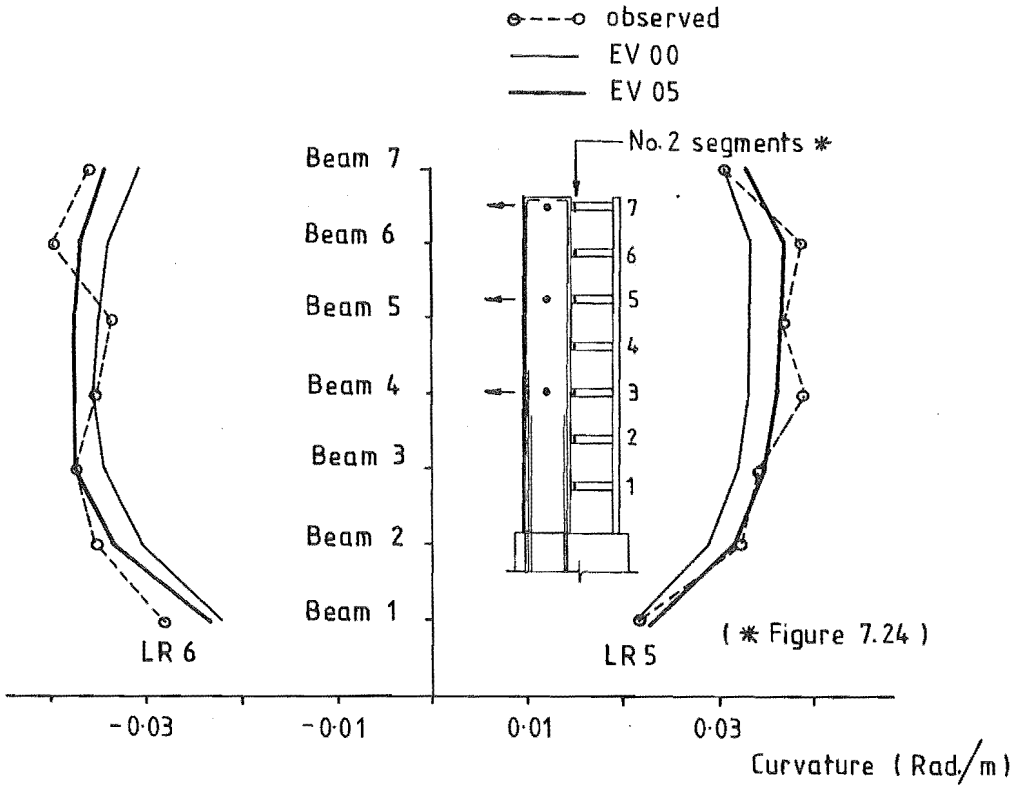

(a) FSW-1

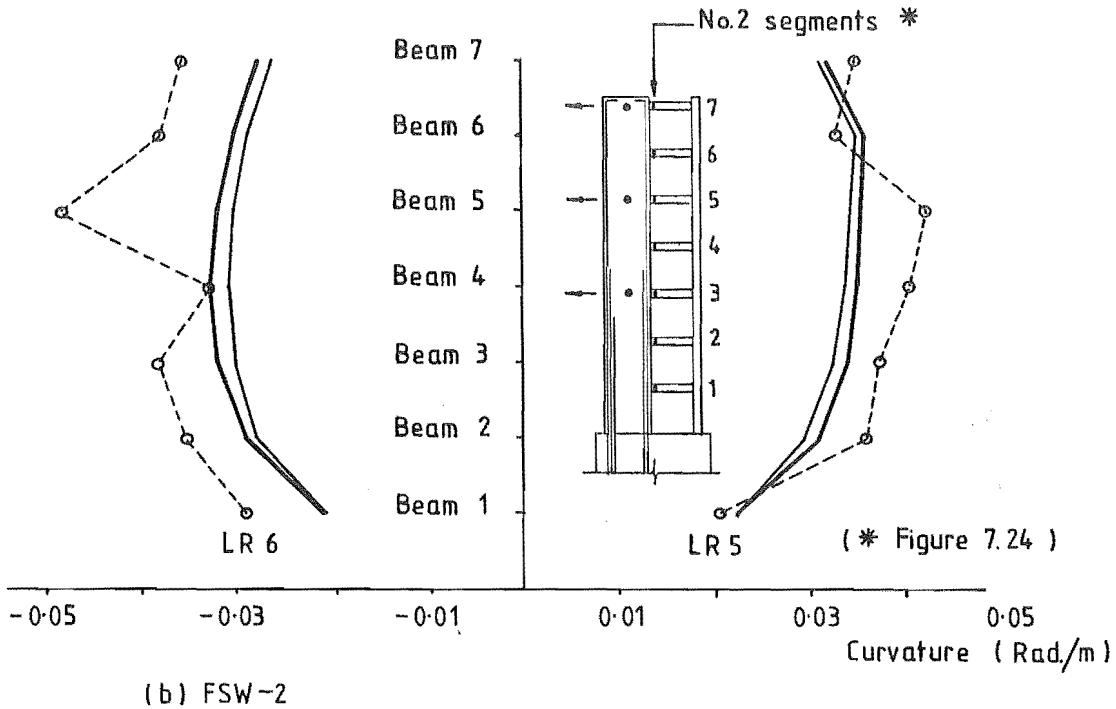

(b) FSW-2

FIGURE 9.42 : PRE-YIELD CURVATURES BEAM NO. 2 SEGMENT, LR5 AND LR6

overall flexibility of the beams. As a result, the segment curvatures developed are affected by variations in any of these factors, including for example, beam anchorage deformations, and even beam elongations*, as well as by variations in the segment flexibilities.

Despite the scatter in the experimental results, the general distribution of the curvatures for FSW-1 were predicted satisfactorily when allowance was made for the effect of inclined cracking (EV05 analysis). This result is dependent on the allowances made for shear and anchorage deformations in the beams and the anchorage deformations at the base of the walls. However, the parameters used for modelling the beam deformations were basically the same as used for analysing TB1 (see Section 7.6.3) and as indicated in Figure 8.3, the pre-yield load-deflection response for this specimen was predicted accurately.

Poorer agreement was obtained for FSW-2, with the curvatures generally being underestimated in the analyses. Similar results were obtained for TB3 and TB4 (Section 8.3.2).

Typical load-curvature responses of the beam No. 2 segments are shown in Figures 9.43 and 9.44 for load reversals 5 to 7. The predicted responses shown in these diagrams are from the EV00-S and EV05-S analyses. The load and displacement increments used in these analyses were reduced to 40% of the standard EV00 and EV05 values (Section 7.6.3), but all other model parameters were identical.

As indicated, the onset of yielding at the ends of the beams caused a sharp change in the slope of the load-curvature response curves for the No. 2 segments, with little or no subsequent increase in curvature until after the walls yielded. (Note that the curves are drawn as a function of the total load applied to the specimen, and not of the load acting on the beams, which could not be measured). This allowed the loads at beam yield to be determined even though the strains at the

---

* e.g. because of the constraining effect of the walls and columns, differences in the elongations of adjacent beams affect the axial loads induced in the beams.

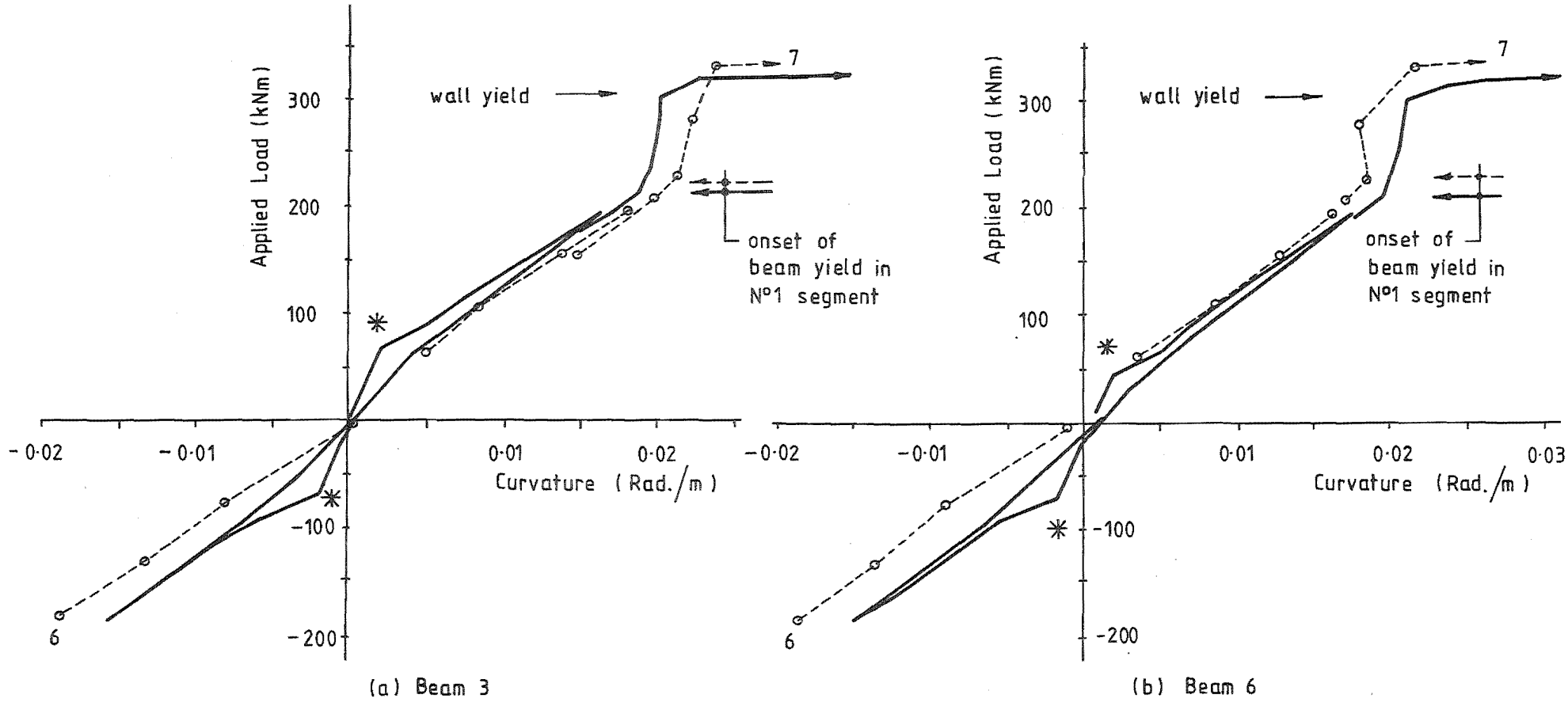

✳ Note : The initial four load reversals LR1 to LR4 were not imposed in the analyses and consequently the specimen was assumed uncracked at the start of LR 5 and LR 6

EV05-S (predicted)

observed

FIGURE 9.43 : PRE-YIELD LOAD-CURVATURE RESPONSES OF THE NO. 2 SEGMENT IN BEAMS 3 AND 6, FSW-2

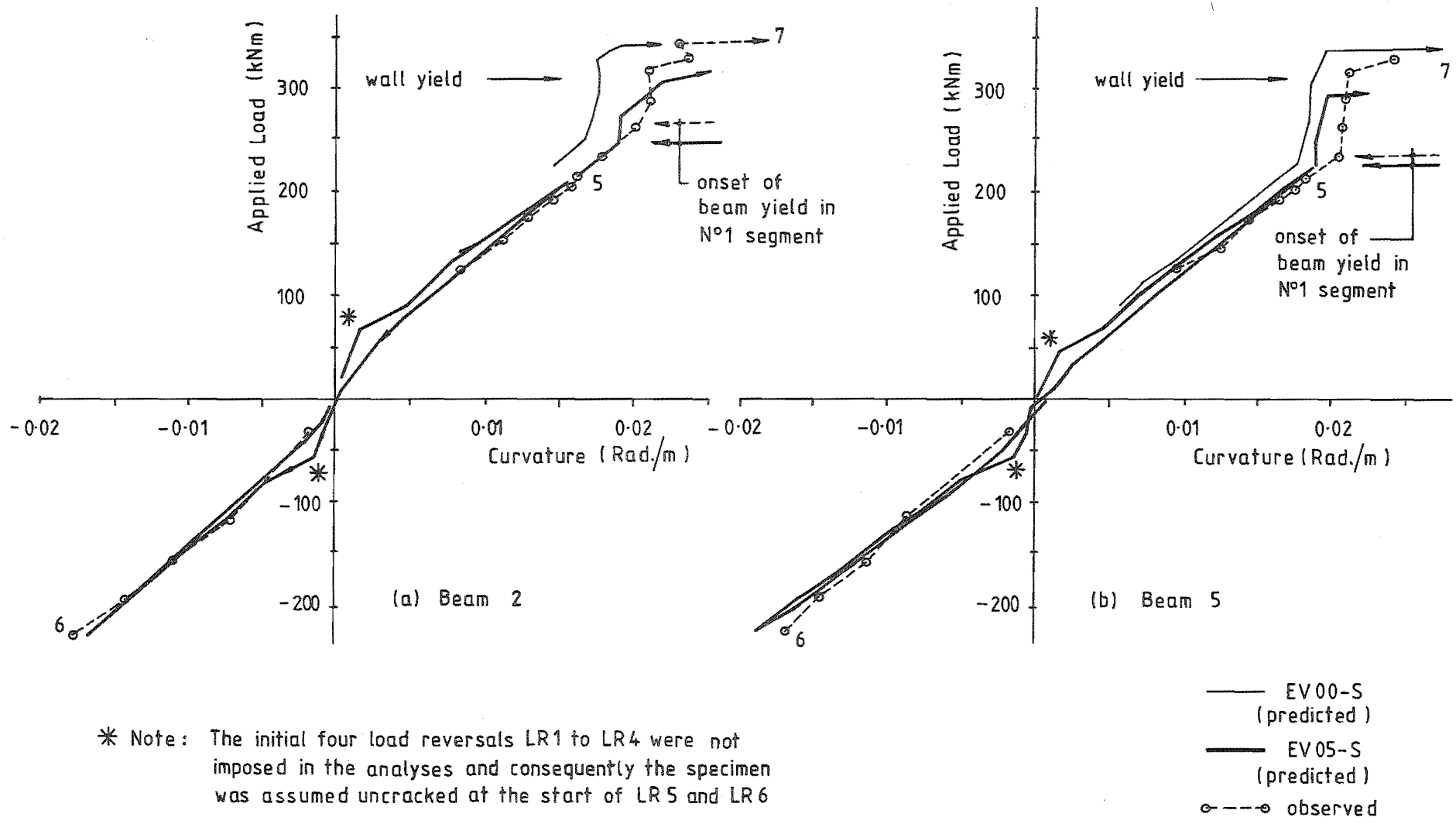

✳ Note: The initial four load reversals LR1 to LR4 were not imposed in the analyses and consequently the specimen was assumed uncracked at the start of LR5 and LR6

FIGURE 9.44 : PRE-YIELD LOAD-CURVATURE RESPONSES OF THE NO. 2 SEGMENT IN BEAMS 2 AND 5. FSW-1

ends where yielding occurred (No. 1 and 8 segments) were not measured.

The change in slope of the curves occurred because the wall was still elastic and continued to resist increased applied load, while the yielding at the ends of the beams meant that the moments applied to the beams remained almost constant. Because only limited rotations were imposed during this stage, beam yielding was confined to the end segments until after the walls yielded.

All analyses predicted the form of the responses accurately, although as indicated in Figure 9.42, the agreement for some individual beams was affected by the scatter in the observed values. The sequence of both observed and predicted yielding was similar to that indicated by the predicted curvature distribution at the peaks of the LR5 load reversals (Figure 9.42), i.e., the centre beams yielding first at a load of approximately 230 kNm, followed by beams 2 and 7, and finally beam 1. The analyses generally predicted onset of yielding at slightly lower loads than the corresponding observed results suggest. However, because of the size of load increments, it was often difficult to determine the observed yield loads accurately, especially for specimen FSW-2.

In most cases, the curvatures at onset of yielding were underestimated in the analyses. It is believed that this discrepancy was largely caused by slight softening of the steel just prior to reaching yield. This was observed in most of the (unmachined) bars tested in direct tension, but was not modelled. The effect of this softening is more obvious in these comparisons than is normally the case because the bars in the No. 2 segments were held at just below yield stress over a relatively large load interval. Failure to model softening of the steel just prior to yielding will also have contributed to the differences between the observed and predicted segment curvatures at onset of beam yielding.

The responses at the column ends of the beams were also evaluated. These were similar to those at the wall ends. Onset of yielding generally occurred at a slightly later stage.

9.4.2 Imposed Post-Elastic End Rotations

Figure 9.45 shows the rotations imposed at the wall ends of the beams just after the walls first yielded and at the peaks of load reversals 7 to 10. The observed values shown in these diagrams were reduced from the theodolite measurements of the wall and column displacements. Only the rotations at the wall ends of the beams could be determined, as corresponding data at the column ends were not obtained.

Only one set of predicted rotations (EV05) is shown for each specimen. The predicted yield rotations were used to compute the beam displacement ductilites (DF_b) indicated on the diagrams. These rotations are larger at wall ends of the beams because the beam-wall anchorage was modelled as being more flexible than the beam-column anchorage.

Several aspects related to the end rotation response shown in Figure 9.45 are discussed below:

(a) Although the observed rotations were affected by errors in the theodolite readings, most of the difference between the observed and predicted rotations was caused by overestimation of the predicted wall elongations (Section 9.3.6) and possibly*, column elongations. As Figure 9.45 shows, these errors caused a "zero shift" in the predicted beam rotations, with the result that the peak values were overestimated in positive load reversals. By load reversal 18, the predicted positive rotations were approximately 20% larger than the corresponding observed values.

(b) The peak negative end rotations were little more than half the positive values. This asymmetry is largely due to the changing location of the neutral axes in the wall plastic hinge regions, and net expansion of the wall. Due to the increasing residual wall elongations (Section 9.3.6), this effect became more pronounced with increasing numbers of load reversals.

---

* No output was obtained for the predicted column axial displacements.

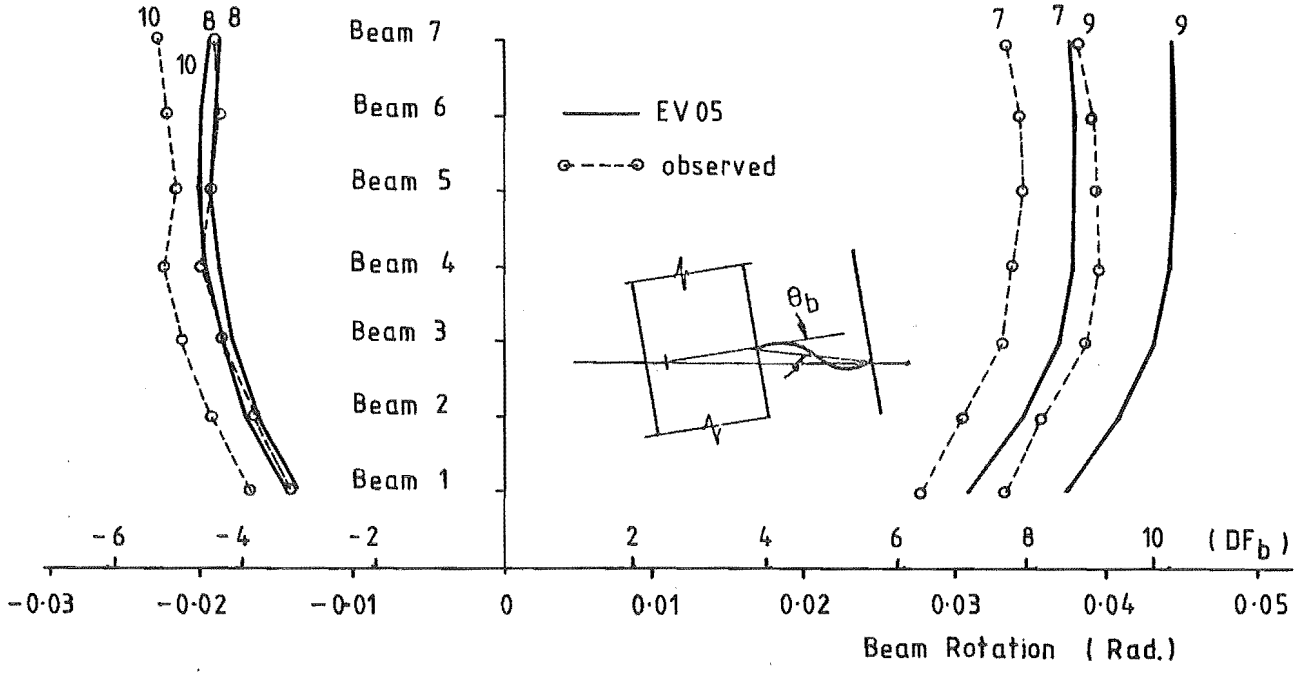

(a) FSW–1

$DF_b = \theta_b / \theta_{by}$ = Beam Displacement Ductility Factor

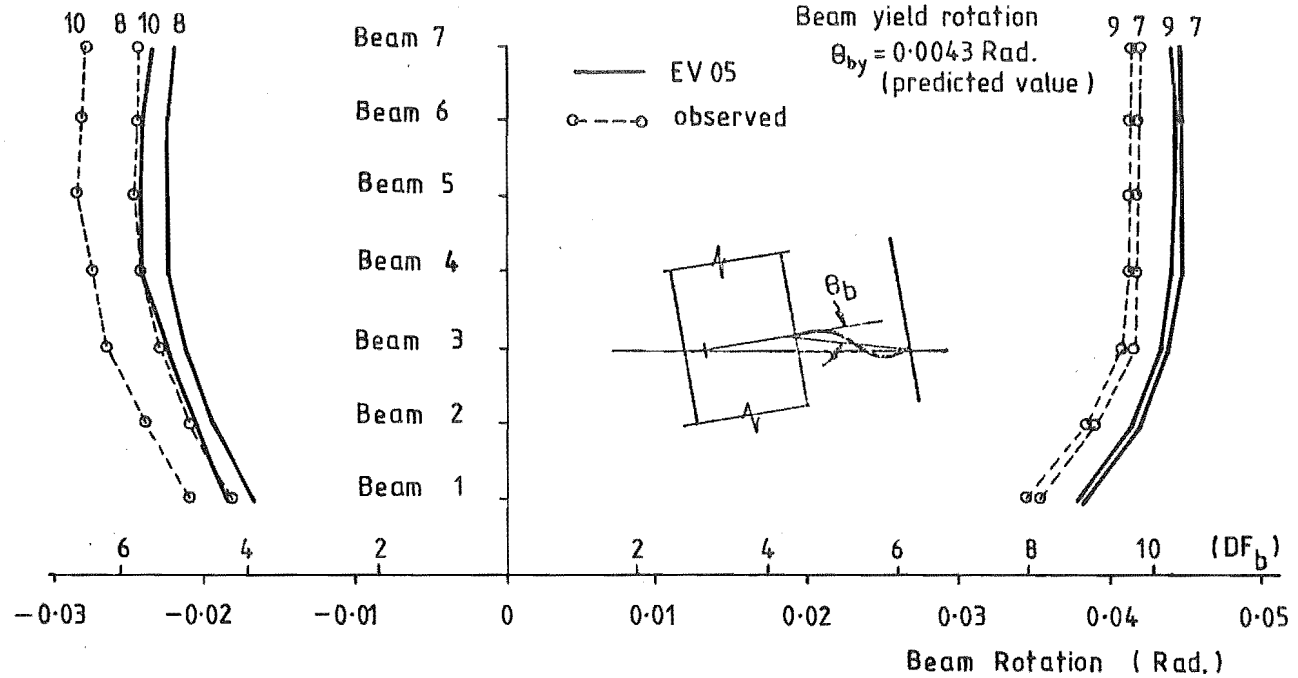

(b) FSW–2

FIGURE 9.45 : IMPOSED BEAM ROTATIONS, LR7 TO LR10

In FSW-1, this trend reversed when local buckling of the bars at the frame edge of the wall plastic hinge zone became significant. Because of the deterioration and eventual crushing of the compression concrete, the neutral axis moved closer to the centre of the wall during the last few negative load reversals.

(c) Although the maximum displacement ductilites imposed on the frame-wall specimen during LR7 to LR10 (the first four post-yield reversals) were less than 5, the resulting maximum end rotations imposed on the beams were over 0.04 radians. This is equivalent to a beam displacement ductility (DF_b) of 9.5. The maximum peak-to-peak end rotations during these load reversals were 0.061 radians in FSW-1 and 0.069 radians in FSW-2. These deformations are very large for the first few post-yield load reversals and show the extent to which the wall magnified the deformations imposed on the beams. The maximum peak-to-peak end rotations imposed during the tests were 0.17 radians ($\Delta DF_b \simeq 40$) for FSW-1 and 0.13 radians ($\Delta DF_b \simeq 30$) for FSW-2 (Figure 9.46). The beams in the first specimen appeared to sustain these loads satisfactorily, although they had been substantially softened by sliding shear deformations. In the second test, many of the splices between the diagonal and conventional beam reinforcing bars deteriorated seriously during the last three load reversals (Section 9.4.6) but there was no evidence of any significant deterioration in the plastic hinge zones.

9.4.3 Post-Elastic Flexural Deformations in Beams

Figure 9.47 shows the peak flexural deformations developed in the beam No. 2 segments during load reversals 7 to 10.

The large scatter in the observed results is caused in part by the low section rigidities after yielding. As a result, even very small differences in the relative strength of the segments or the cracking patterns can significantly affect the distribution of curvature within individual beams. The low post-yield section rigidities also caused problems during the later stages of the FSW-1 analyses, where up to

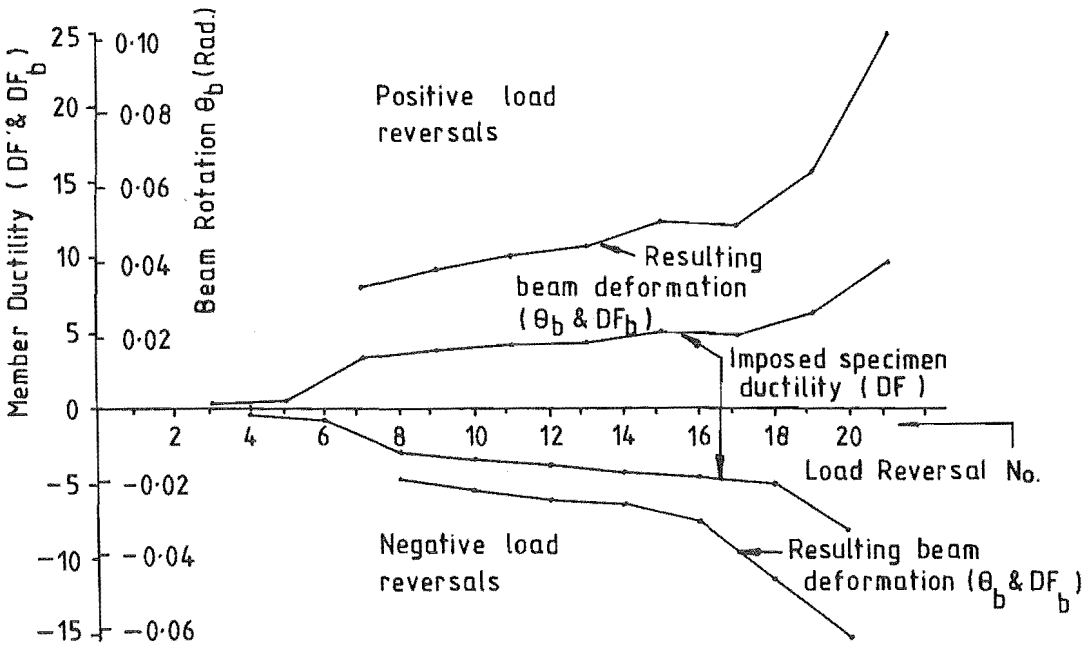

(a) FSW–1

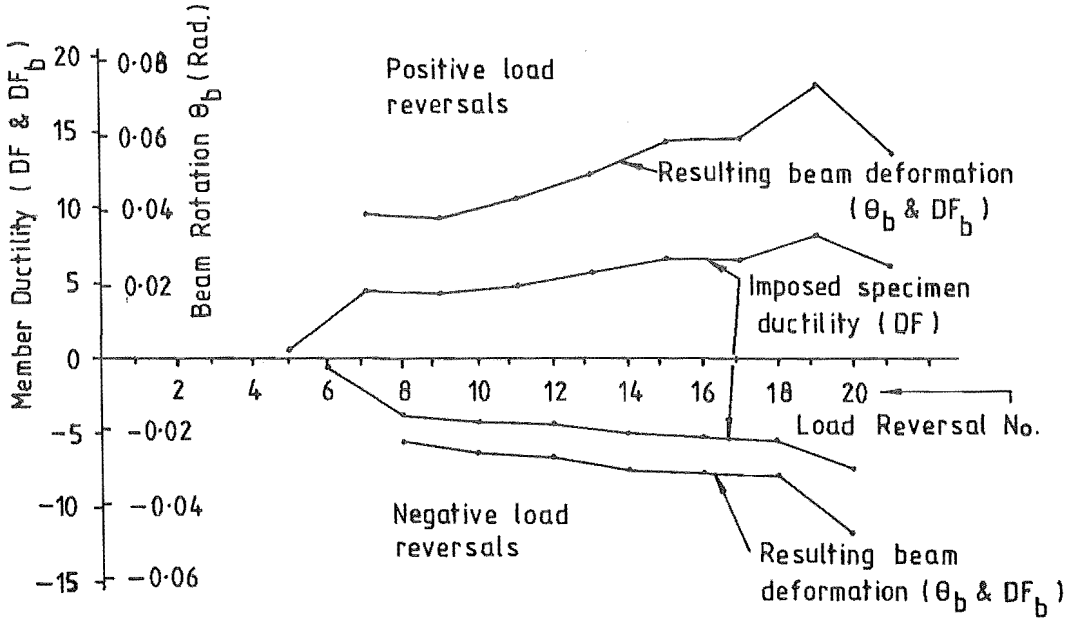

(b) FSW–2

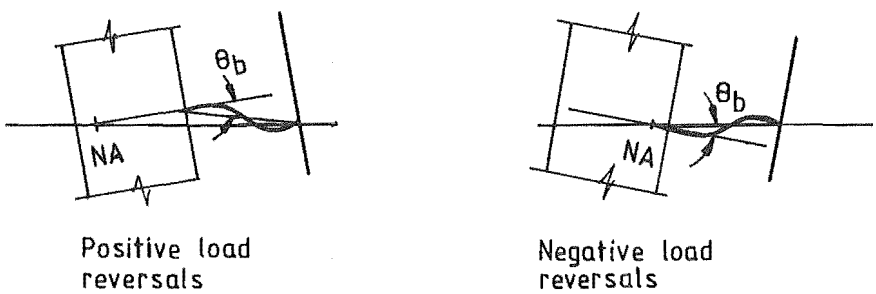

FIGURE 9.46 : IMPOSED BEAM ROTATIONS AND DUCTILITES (AVERAGE VALUES FOR TOP 5 BEAMS)

three segments at each end of the beams were yielding simultaneously. Two components of inelastic deformation occur in each segment, namely flexural and sliding shear. Therefore the solution procedure has to distribute correctly the total deformations between up to six components at each end. After LR12, there was considerable scatter in the predicted curvatures for the beam segments, indicating that some of the segment responses did not fully converge in the analyses. This was not detected in the solution convergence check because of the dominance of the wall response.

To obtain a more consistent assessment of the beam flexural responses, the peak values of curvature in the No. 2 and 3 segments were averaged over the top five beams. These are compared in Figure 9.48*, with the corresponding average observed rotations imposed by the walls at the ends of the beams at the peaks of the positive load reversals.

As indicated, the observed peak curvatures of the beams in FSW-1 and FSW-2 were initially similar, with a significant redistribution of curvature occurring in both specimens between LR7 and LR9. However, in subsequent load reversals, the total rotation of the beam No. 2 and 3 segments in FSW-1 actually decreased, despite increasing imposed beam rotations. The total rotations of the two segments during these load reversals were considerably smaller than predicted in the EV05 analysis. This behaviour is at variance with the results obtained for TB1, which showed good agreement between the observed curvature distributions and those predicted assuming e_v = 0.5 jd (Figure 8.9).

As in the case of the walls, the observed curvature distributions will have been significantly affected by strain ageing. For example, part of the redistribution of curvature between LR7 and LR9 will have been due to strain ageing. The fact that it was largely the No. 2, rather than No. 3 segment curvatures which were overestimated (EV05 analysis), suggests that strain ageing was also partly responsible for

---

* The segment curvature shown in Figure 9.48 are given in terms of rotation rather than as average curvatures, so that the contributions from the two segments can be summed and compared with the imposed rotations.

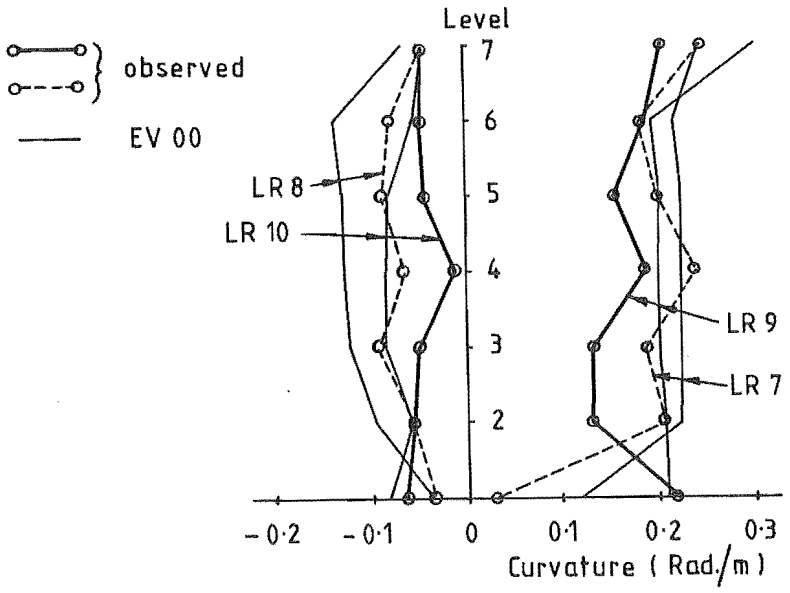

(a) FSW-1

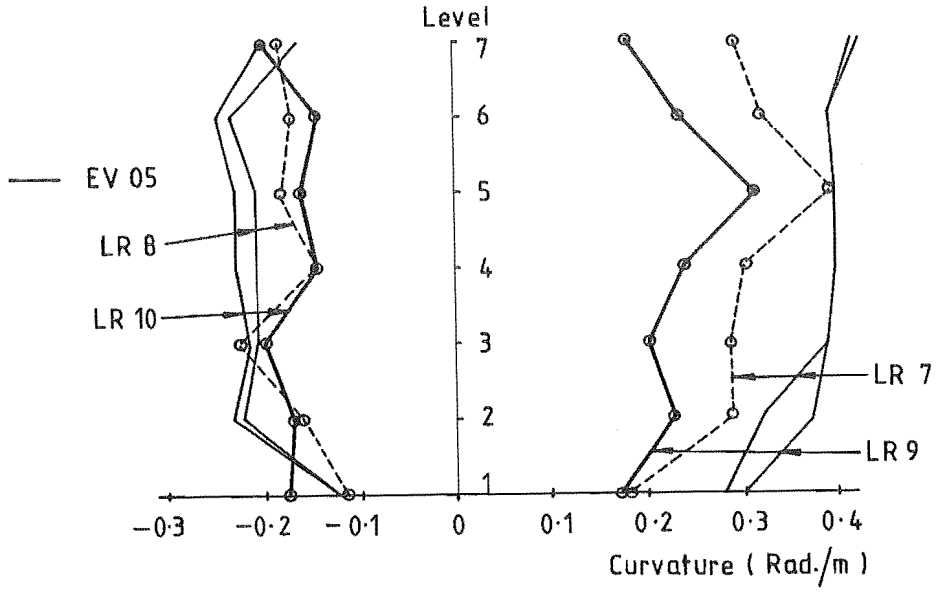

(b) FSW-2

FIGURE 9.47 : DISTRIBUTION OVER THE SPECIMEN HEIGHT OF THE CURVATURES OF THE BEAM NO. 2 SEGMENTS AT PEAKS OF LOAD REVERSALS LR7 TO LR10

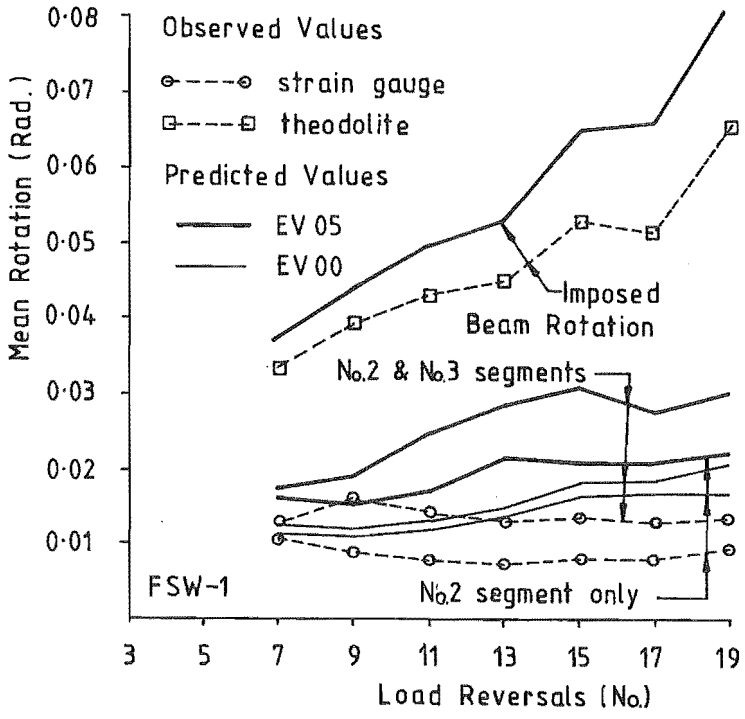

(a) Segment Rotations, No.2 and 3 Segments, FSW-1

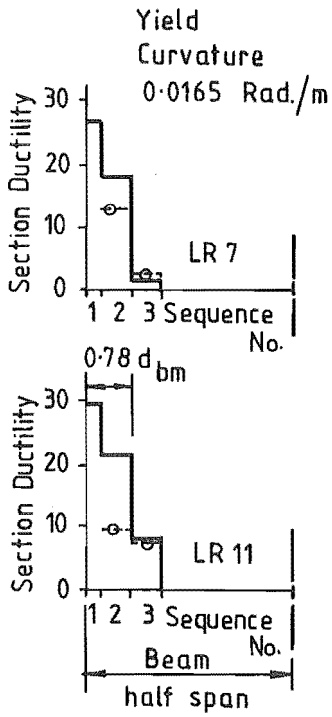

(c) Section Ductilities, No.1, 2 and 3 Segments, FSW-1

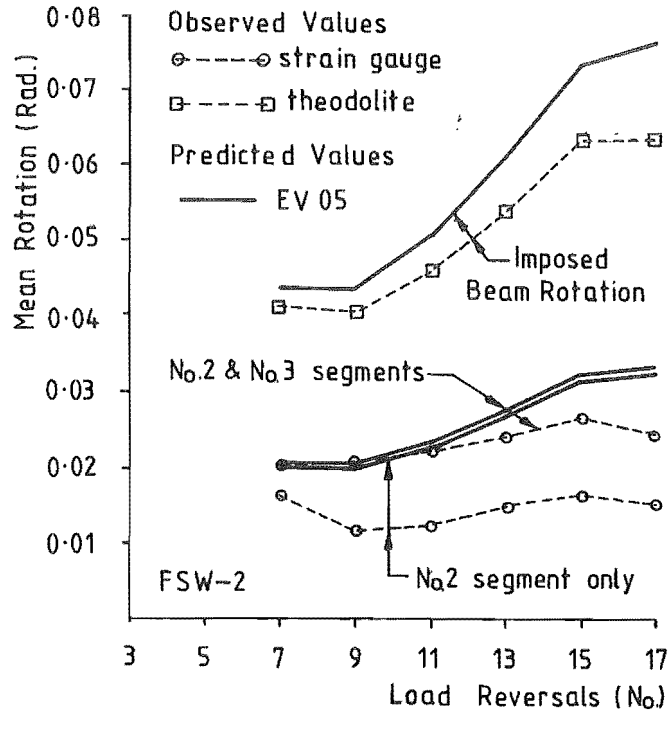

(b) Segment Rotations, No.2 and 3 Segments, FSW-2

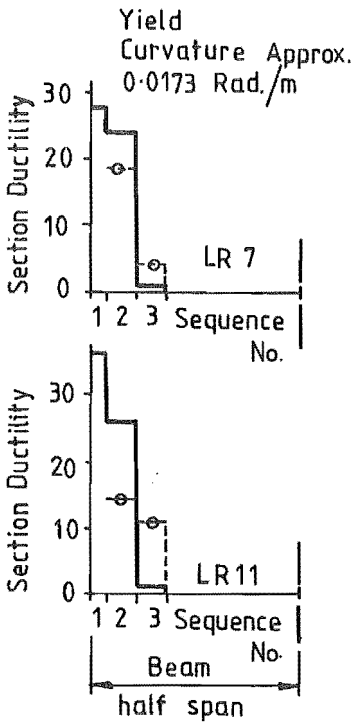

(d) Section Ductilities No.1, 2 and 3 Segments, FSW-2

FIGURE 9.48 : AVERAGE FLEXURAL DEFORMATIONS IN TOP FIVE BEAMS AT PEAKS OF POST-YIELD LOAD REVERSALS

the discrepancy between the observed and predicted curvatures during the later stages of loading, i.e., the observed curvature distributions imply that the No. 2 segments were 'stronger', relative to the No. 3 segments, than was allowed for in the EV05 analysis (Section 2.2.4). However, other factors such as incorrect modelling of the beam anchorage deformations may also have caused errors in the predicted responses.

In the case of FSW-2*, the total rotations of the two gauged segments generally increased in proportion to the magnitude of the imposed beam rotations and were considerably larger than the corresponding FSW-1 values. Although no yielding was predicted in the No. 3 segments**, the predicted total rotations of the two segments were similar to the observed values. Even better agreement would have been obtained if the imposed beam rotations had been predicted more accurately.

The large curvatures developed in the No. 2 and 3 beam segments in FSW-2 suggest that the spread of yielding due to strain ageing was probably more restricted than in FSW-1 because of the bends in the diagonal reinforcing and the presence of the additional parallel reinforcement.

Typical load-curvature responses for several of the beam No. 2 segments are shown in Figures 9.49 and 9.50. These indicate that apart from the magnitude of the peak curvatures (discussed above), the shapes of the response curves for FSW-2 were predicted accurately. The only apparent discrepancy was the sharp changes in slope of the predicted response curves at about -170 kNm and -225 kNm in LR8. This was presumably a result of onset of yield in the previously unyielded tension

---

* In the EV05 analysis of this specimen, only the walls were modified for the effect of inclined cracking (Section 7.6.4). Consequently the predicted beam curvature distributions were very similar to those predicted in the EV00 analysis.

** The No. 3 segments of the beams in FSW-2 were modelled as elastic segments in the analyses (Section 7.6.4). The maximum predicted curvatures of this segment were below yield level and consequently use of an inelastic section model would not have affected the results.

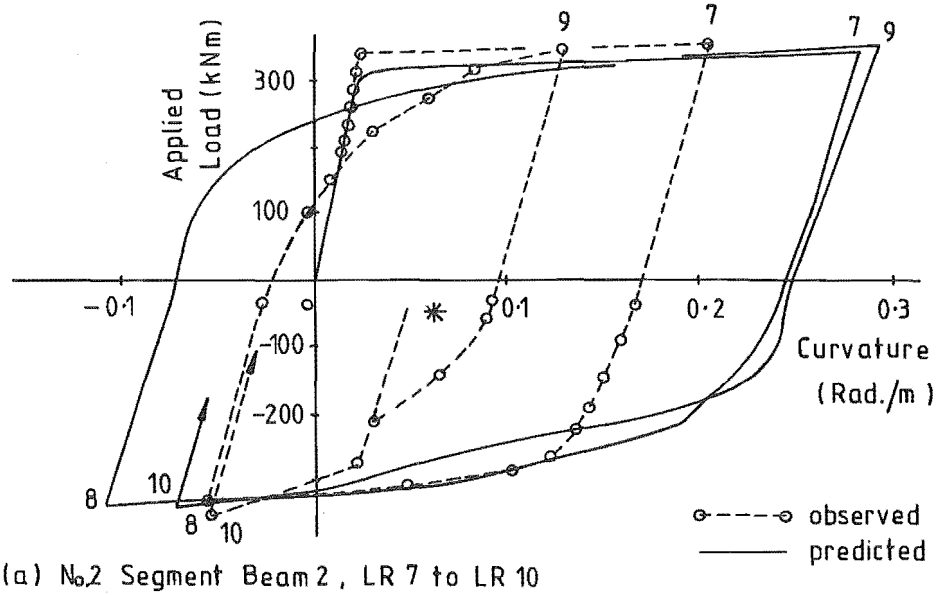

(a) No.2 Segment Beam 2, LR 7 to LR 10

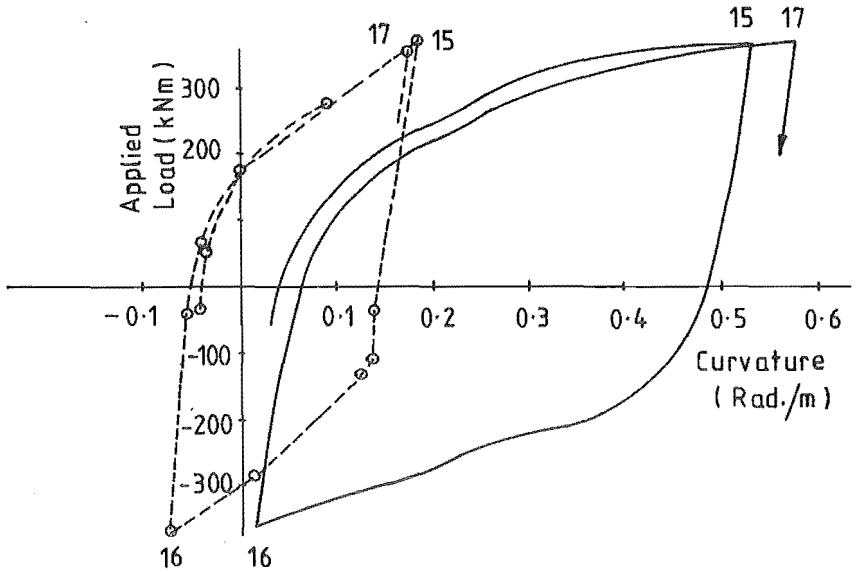

(b) No.2 Segment Beam 2, LR 15 to LR 17

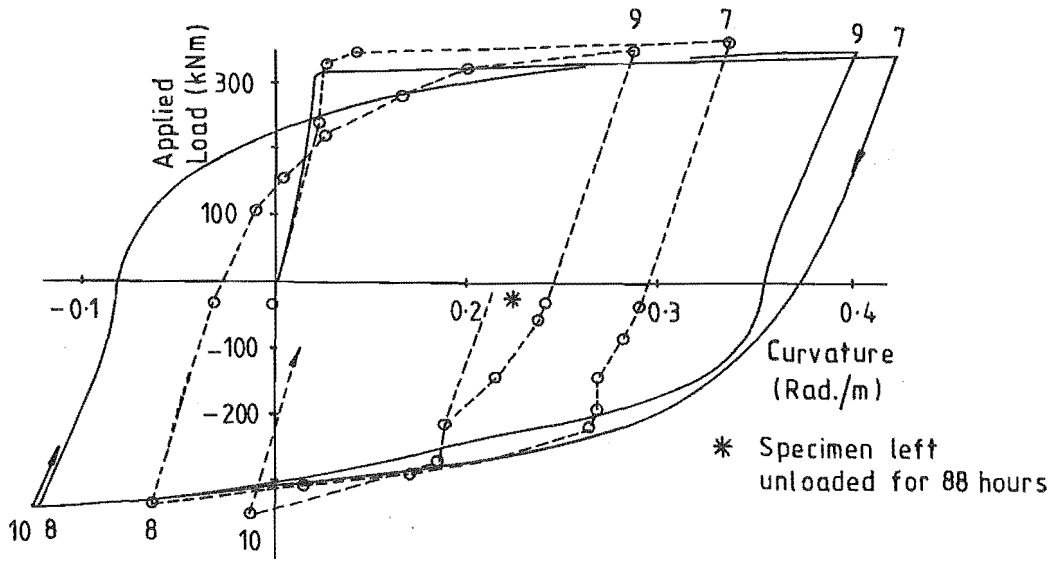

(c) No.2 Segment Beam 4, LR 7 to LR 10

FIGURE 9.49 : TYPICAL LOAD-CURVATURE RESPONSES, FSW-1 BEAMS

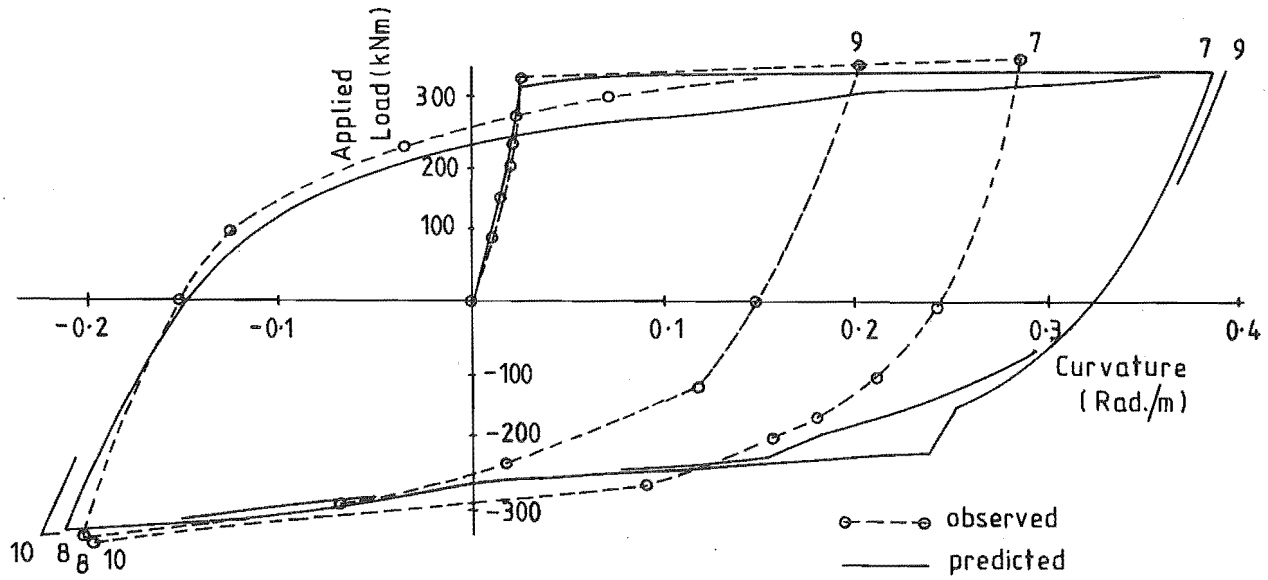

(a) No. 2 Segment Beam 3, LR 7 to LR 10

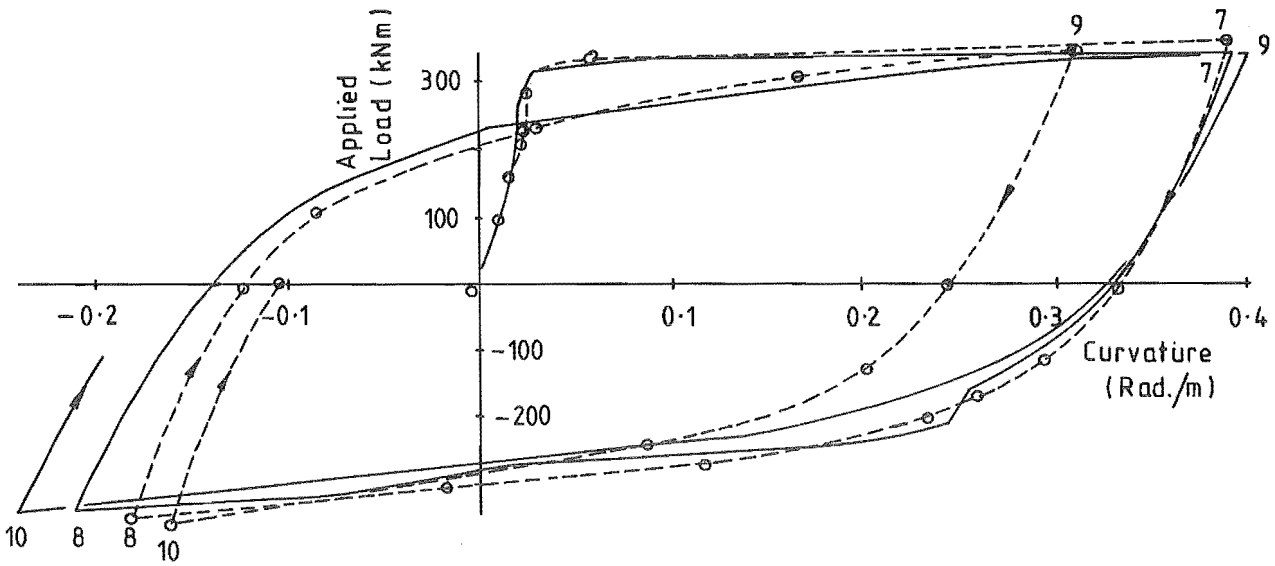

(b) No.2 Segment Beam 5, LR7 to LR 10

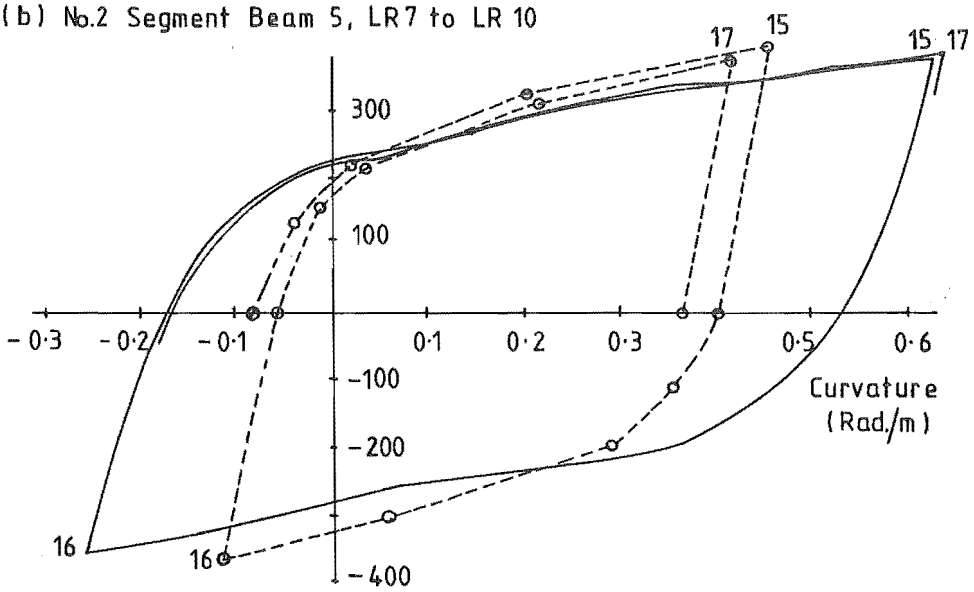

(c) No.2 Segment Beam 5, LR 15 to LR 17

FIGURE 9.50 : TYPICAL LOAD-CURVATURE RESPONSES, FSW-2 BEAMS

steel at the ends of the beams (cf. Section 9.4.1). The fact that no similar feature was indicated in the observed response curves could have been due to the large load increments between strain measurements. This behaviour would not have been evident in the predicted response if the load steps for the analysis had been displaced by 25 kNm from those actually used.

In the case of FSW-1, a similar effect due to tension yield in the beam No. 1 segments in LR8 was apparent in the observed response curves for Beam 4 (Figure 9.49c), but not in any of the predicted curves. The similar feature in the observed curves for LR9 was largely due to strain ageing (see Figure 9.49). This affected the responses of all the beams and caused a similar effect on the overall load-deflection response of FSW-1 (Figure 9.5). The other main feature in the beam load-curvature responses for FSW-1 is the increase in slope of the predicted curves which occurred near zero load, after LR8. This was due to the increase in the contribution of sliding shear at low beam shears, which reduced the flexural deformation demand, i.e., relative to the applied load. Unfortunately, too few readings of the beam strains were taken to be able to detect this behaviour from the observed curves.

9.4.4 Beam Shear Deformation

No beam shear deformations were measured during these tests, but the visual appearance of the plastic hinge zones confirmed that the shear responses were similar to those of the plastic hinge zones in the corresponding beam-wall specimens (Section 8.7).

As Figures 9.51 and 9.52 show, significant sliding shear displacements were developed in the plastic hinge zones of the conventionally reinforced beams in FSW-1. Lines were drawn on some of the beams to highlight the sliding displacement. (Note that these lines were drawn on at the peak of LR11, and therefore indicate the sliding movement relative to LR11, and not the absolute sliding movement). In the case of FSW-2, grids were drawn on the beams at the start of the test. These beams were diagonally reinforced (as for TB3 and TB4)

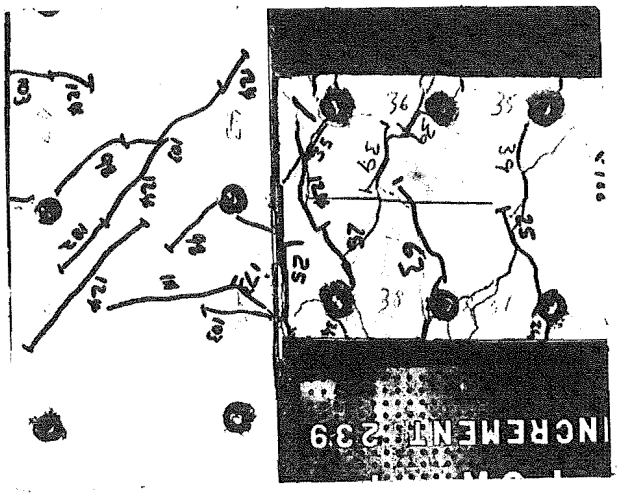

(a) Load Reversal 12

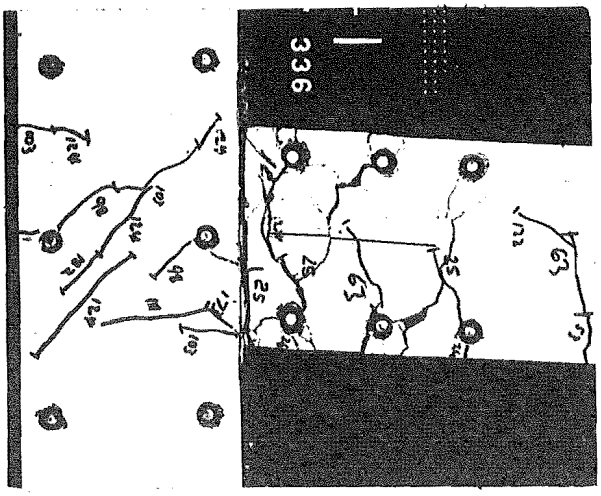

(b) Load Reversal 18

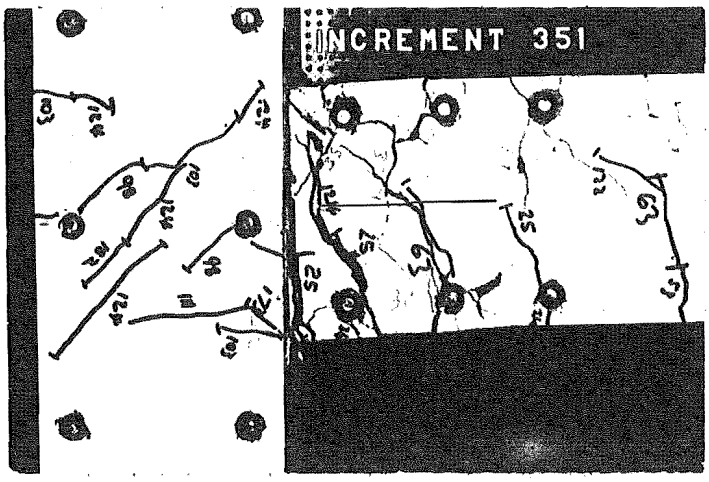

(c) Load Reversal 19

FIGURE 9.51 : BEAM 4 PLASTIC HINGE ZONE, FSW-1

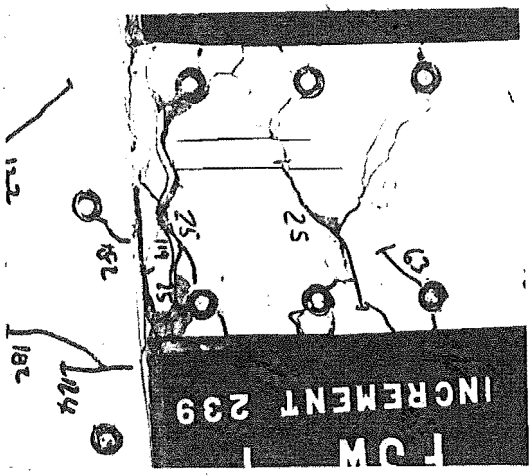

Column End

(a) Load Reversal 12

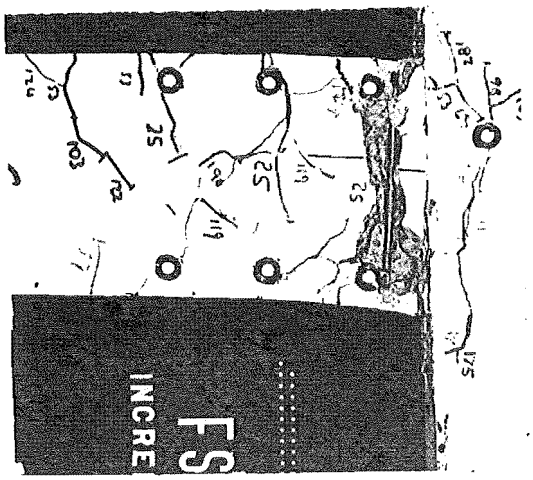

Wall End

(b) Load Reversal 18

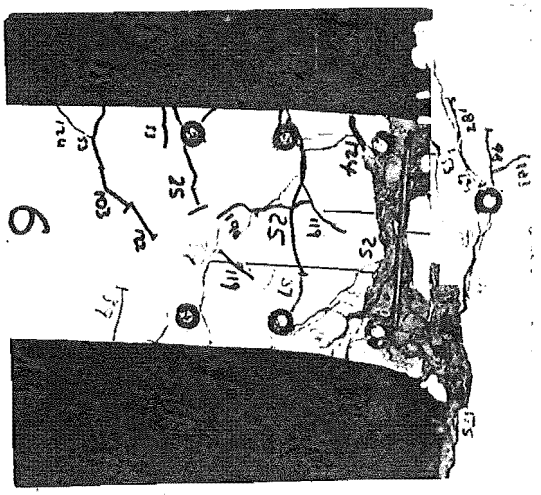

Wall End

(c) Load Reversal 20

FIGURE 9.52 : BEAM 6 PLASTIC HINGE ZONE, FSW-1

and as the grids show, no significant sliding shear deformations were observed in the plastic hinge zones (see Figure 9.56).

The predicted (EV00) shear force-shear displacement response of Beam 3 in FSW-1 is shown in Figure 9.53. This is typical of the predicted shear responses of the other beams in FSW-1 and of that for TB1 (Figure 8.20). Unlike the beam rotations, the predicted shear responses were not asymmetric with respect to loading direction. This is consistent with the observed deformed shapes of the plastic hinge zones (cf. Figures 9.51b and c). Comparison with the observed values for TB1 (Table 9.5) also indicates that the predicted peak shear deformations are reasonable.

9.4.5 Beam Elongations

Figure 9.54a compares the observed and predicted (EV00) elongations of the beams in FSW-1 at the peaks of load reversals 7 to 10. The observed values shown in this diagram were determined from the theodolite measurements of the wall and column deflections, and both sets of values (observed and predicted) include the components of elongation developed within the anchorage regions at either end of the beams.

As indicated, the elongations were predicted reasonably accurately at the peaks of the positive reversals (LR7 and LR9) but were under-estimated by 10% - 20% at the peaks of the negative load reversals (LR8 and LR10). The generally good agreement obtained at the peak of LR7 indicates that the observed values are reasonably accurate, despite the potential for error caused by having to interpolate or extrapolate the deflections at some levels*.

The nature of the discrepancy between the observed and predicted values can be seen more clearly from the load-elongation histories shown in

---

* Due to the theodolite targets being offset from the beam centre lines at some locations, especially at Levels 1, 3, 5 and 7 (obstructed by the loading frames). This potential for error was accentuated by the fact that the elongations were obtained from the difference between two sets of deflection measurements.

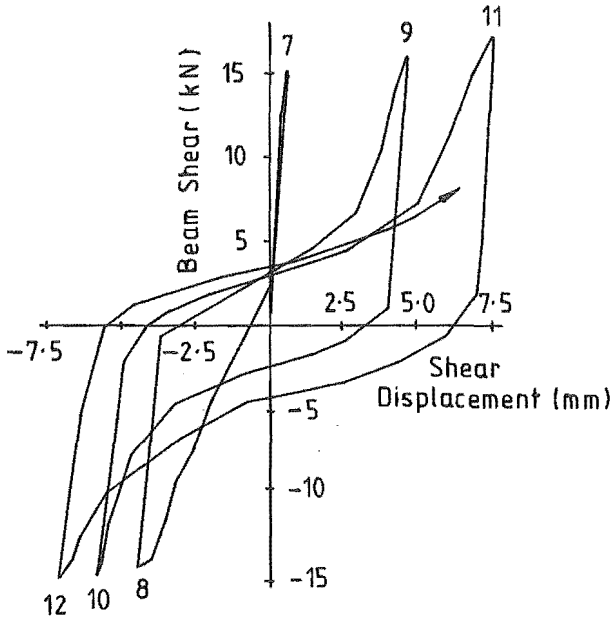

FIGURE 9.53 : PREDICTED SHEAR FORCE - SHEAR DISPLACEMENT RESPONSE FOR BEAM 3 (EVOO)

TABLE 9.5 : COMPARISON BETWEEN BEAM SHEAR DISPLACEMENTS IN FSW-1 (PREDICTED) AND TB1 (OBSERVED AND PREDICTED)

FSW-1 Beam 3 Predicted values ($e_v = 0.0$)				TB1 (Section 8.7)				
LR	DF_b	Rotation (Rad.)	δ_v (mm)	LR	DF_{TB1}	Rotation (Rad.)	$2\delta_v$ (mm)* observed	$2\delta_v$ (mm)* predicted
7	8.3	0.035	0.6	5	4.3	0.031	2.1	1.7
8	-4.3	-0.018	-4.5	6	-3.4	-0.024	-2.6	-2.8
9	9.8	0.041	4.7	9	4.1	0.030	4.8	3.7
10	-4.4	-0.019	-5.9	10	-4.5	-0.033	-4.3	-5.1

* TB1 shear displacements have been doubled to enable comparison with those for the beams in FSW-1 which had plastic hinge zones at each end.

DF_b = beam ductility factor, based on the beam end rotations.

DF_{TB1} = Ductility Factor for specimen TB1.

δ_v = shear displacement.

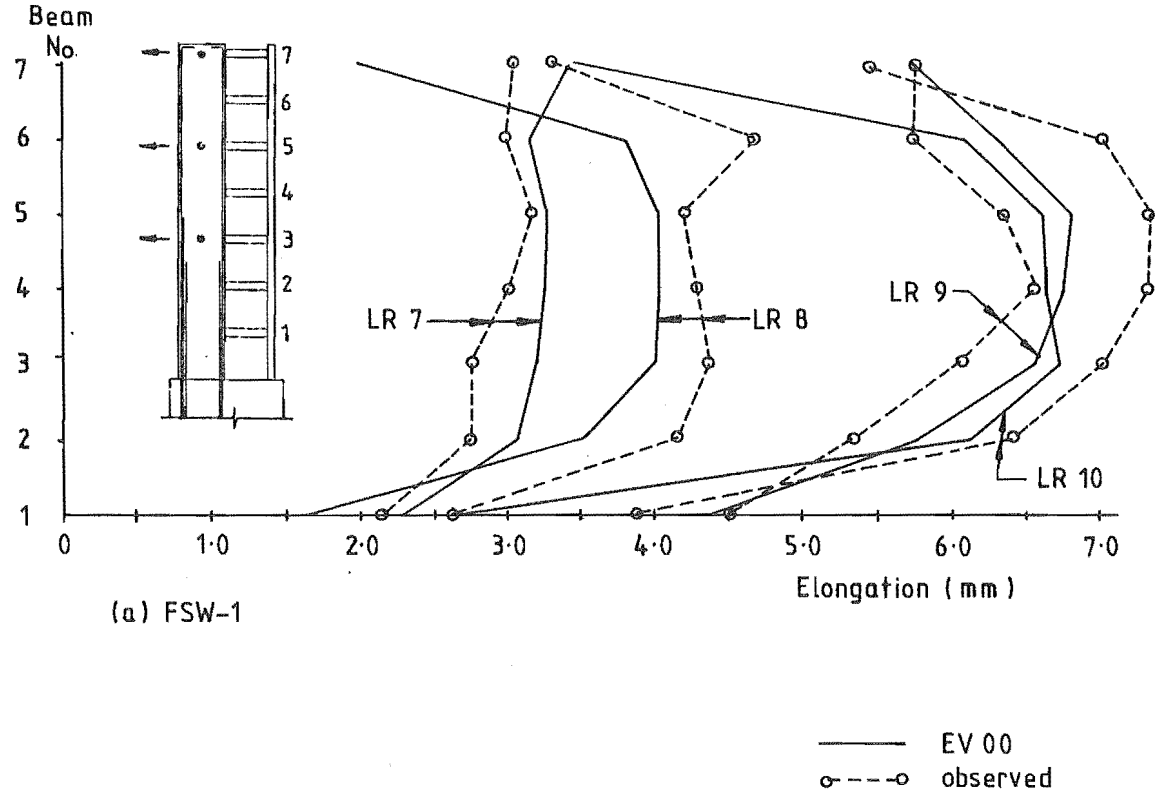

(a) FSW-1

EV 00
observed

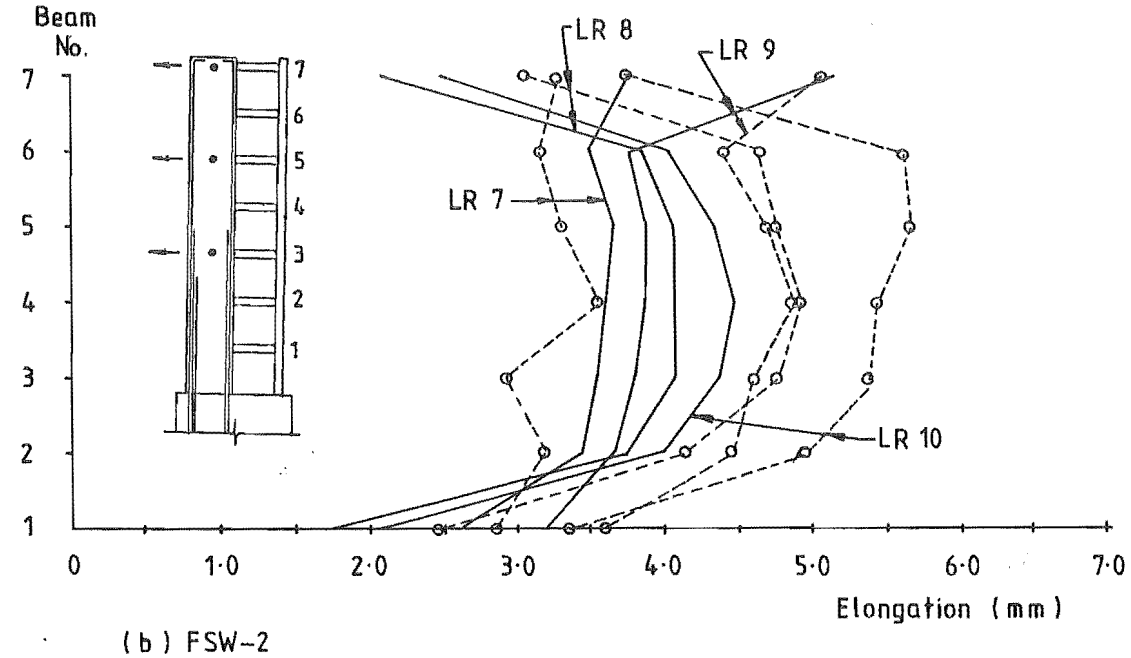

(b) FSW-2

FIGURE 9.54 : BEAM ELONGATIONS AT PEAKS OF LOAD REVERSALS 7 TO 10

Figure 9.55a. This shows that the increases in elongation were underestimated during the negative load reversals and, except in LR7, overestimated by a similar amount during the positive load reversals. These errors result partly from corresponding errors in the predicted beam rotations, which were under- and overestimated respectively in the positive and negative load reversals (Section 9.4.2) and partly from inadequate allowance for softening of the beam concrete due to mismatched crack surfaces (Section 5.4.5).

Corresponding comparisons between the observed and predicted elongations of the beams in FSW-2 are given in Figures 9.54b and 9.55b. As in the case of the diagonally reinforced beam-wall specimens, the model satisfactorily predicted the elongations in the initial post-yield load reversal, but not increases in elongation in subsequent load reversals (see Sections 8.5 and 8.6).

9.4.6 Lap Regions, FSW-2 Beams

The lap regions in the beams in FSW-2 did not perform as well as those in the two diagonally reinforced beam-wall specimens (Section 8.9).

Long inclined cracks formed across the terminated ends of the diagonal bars during the first two post-yield load reversals (LR7 and LR8). However, these did not widen significantly until after a further 3 to 4 load reversals (Figure 9.56), and there was no evidence indicating that either the flexural bars or the stirrups yielded during these initial post-yield load reversals. This is consistent with a theoretical assessment of the loads acting across the cracks which indicated that the continuing flexural reinforcement should have been just below yield when the overstrength (ϕ_o = 1.25) moments were developed at the ends of the beams.

The cracks began to widen slightly after 5 to 6 post-yield load reversals, but it was not until near the peak of LR17 that signs of serious deterioration of the lap regions were evident (Figure 9.56). By this stage, the inclined cracks had started to propagate along the plane of the diagonal bars in the lap region. In some beams (e.g.

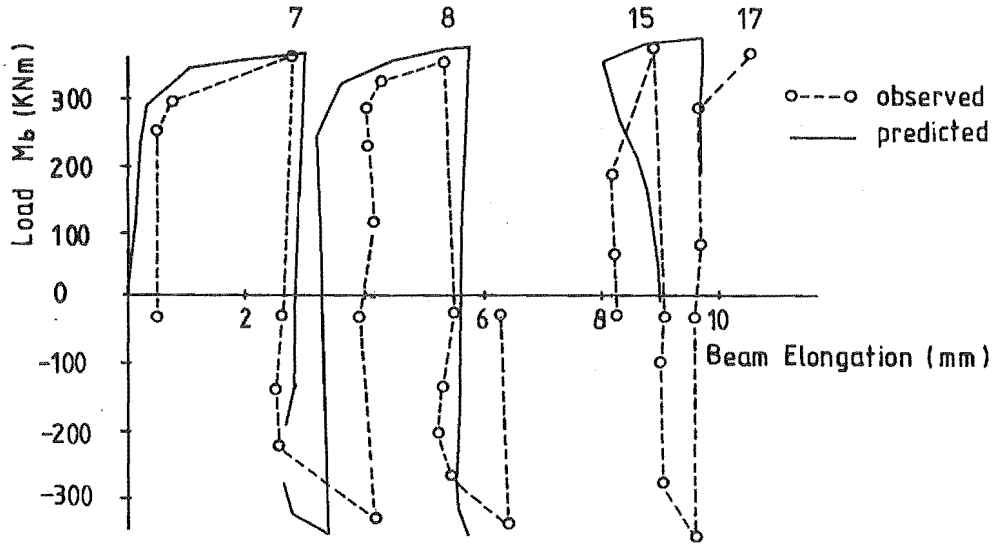

(a) Beam 2, FSW-1

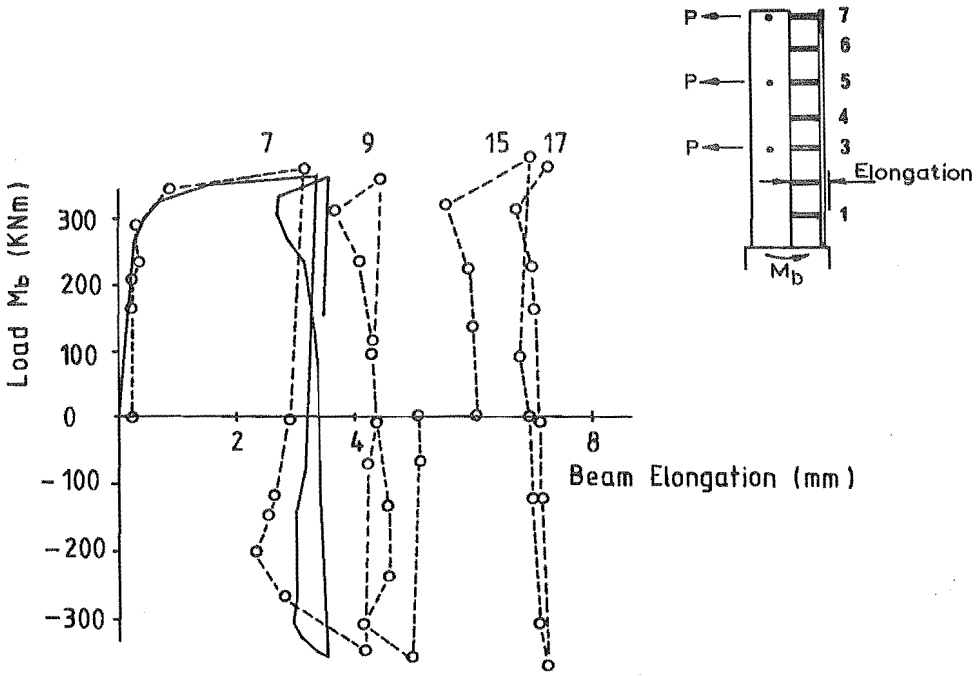

(b) Beam 2, FSW-2

FIGURE 9.55 : BEAM LOAD-ELONGATION RESPONSES

Figure 9.57) these cracks extended along most of the splice length. Generally the beams nearest the mid-height of the specimen were worst affected and in Beam 4, one crack was approximately 2 mm wide at the peak of LR17. However, in most other beams the cracks were still less than 0.8 mm wide.

After LR17, widening of the cracks resulted in rapid deterioration of the bond along the diagonal bars. In load reversals 20 and 21, these bars were sliding along the length of the lap region in some beams and part of the side cover concrete began spalling, particularly from Beams 3 and 4 (Figure 9.57). The bond slip that occurred in Beam 4 at the peak of LR20 is indicated in Figure 9.57 by the movement of two of the bottom strain gauge studs.

As discussed in Section 7.5.3, the design cut-off points for the diagonal bars did not take overstrength of the ends of the beams into account, and under rules of the current New Zealand concrete design code, the bars would have been required to extend considerably further into the beams. In the test, the effect of this design fault was undoubtedly accentuated by strain ageing which is likely to have significantly increased the strength of the bars in the plastic hinge regions and causes yielding to penetrate further into the beam.

Despite the apparent severity of damage to the lap regions, the affect on the overall response of the beams appears to have been comparatively small. This is evident from both the large curvatures still being induced in the beam segments during LR15 to LR17 (Section 9.4.3), and the curvatures induced in the columns by the beam end moments (Section 9.4.7). Also, even at as late a stage as LR19, the load-deflection response for FSW-2 still indicated considerably less softening of the specimen than occurred in FSW-1*, despite the generally larger displacements imposed (cf. Figures 9.5 and 9.6).

---

* Even after making allowanced for the effect of local buckling of the flexural reinforcement at the frame end of the wall.

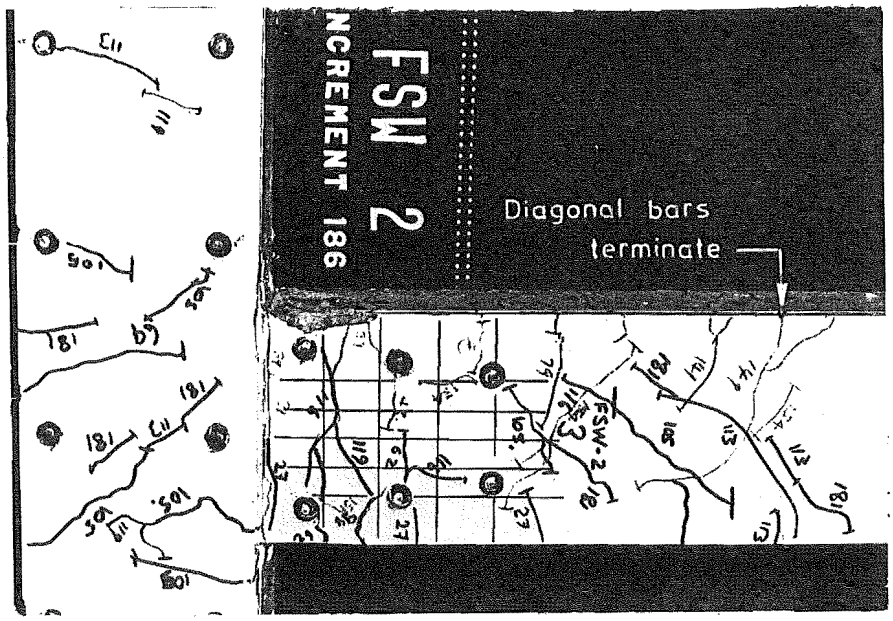

LR 9

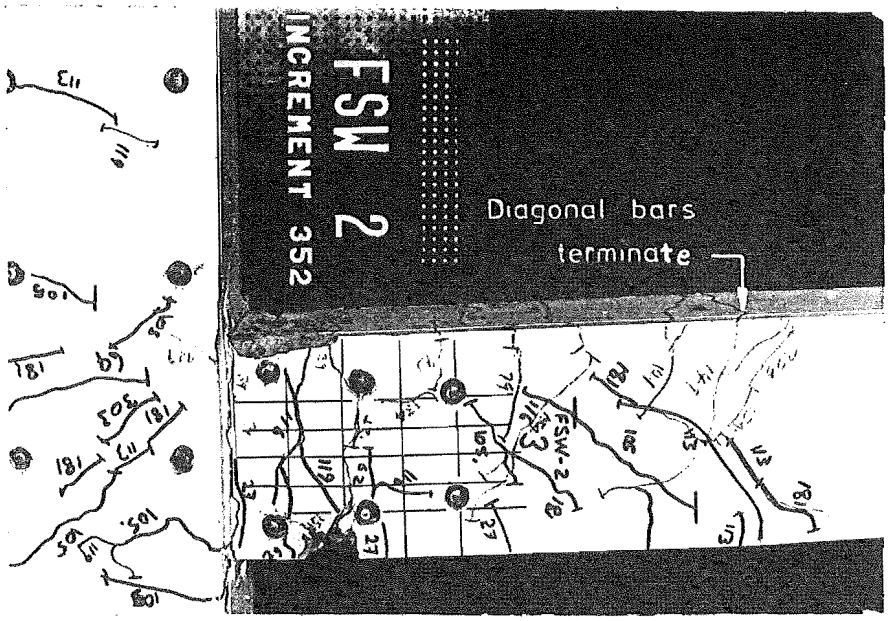

LR 17

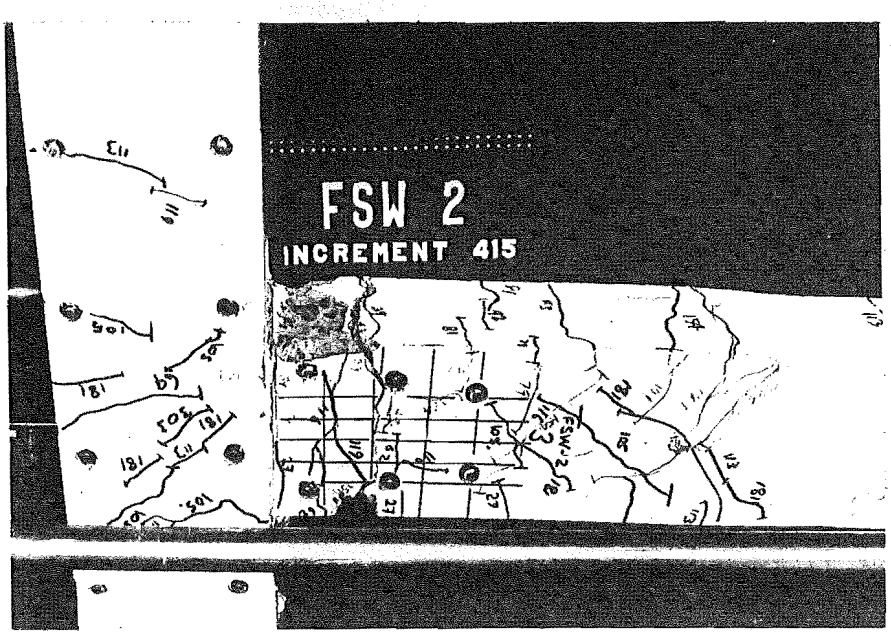

LR 20

FIGURE 9.56 : DETERIORATION OF LAP REGION IN BEAM 3, FSW-2

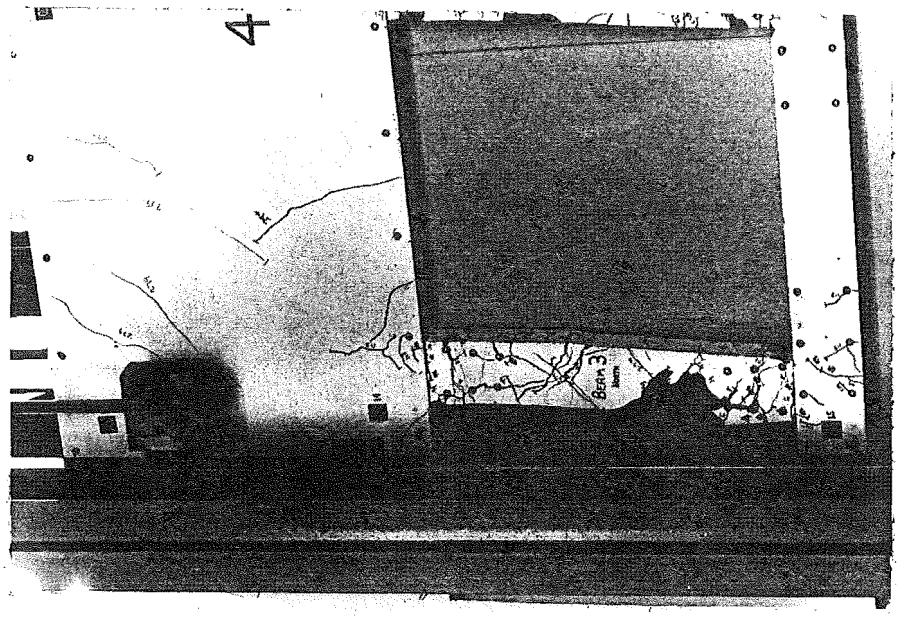

Beam 3 FSW-2
LR 21 (North face)

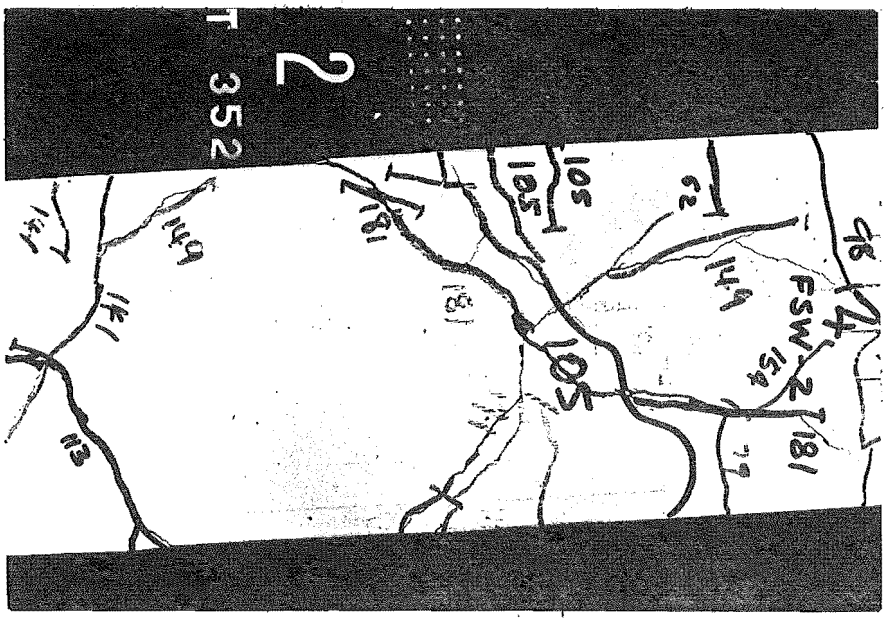

Beam 4 FSW-2
LR 17

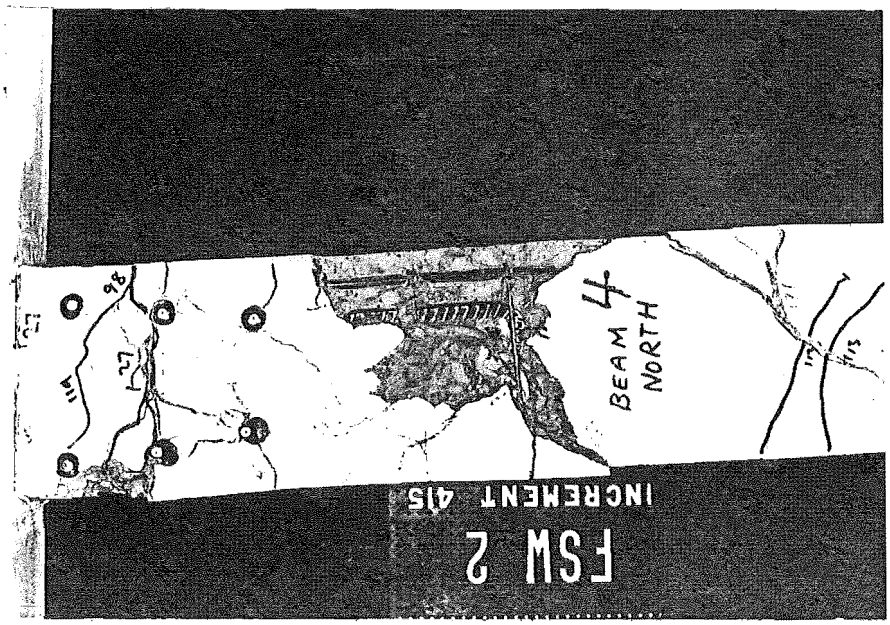

Beam 4 FSW-2
LR 20 (North face)

FIGURE 9.57 : DETERIORATION OF LAP REGION IN FSW-2 BEAMS

9.4.7 Beam Moments

Figures 9.58 and 9.59 compare the observed and predicted values for the differences between the column curvatures above and below each beam. These comparisons have been made primarily to assess the accuracy of the predicted beam moments and the effect of deterioration of the lap region on beam moments in FSW-2.

As indicated in the diagrams, there is a significant difference in behaviour between the positive and negative load reversals. In the negative load reversals the curvature difference values are approximately the same for most of the beams. This occurs because there is sufficient axial compression on the column to prevent cracks opening, except at the base plastic hinge zone (Level 0) and at Level 7 where the axial load was lowest and the section of column below the beam had to resist the full beam moment. Over the remainder of its height, the column was effectively uncracked and therefore had a reasonably uniform flexural rigidity ($= E_c I_g$).

The main discrepancies in the predicted values for the negative load reversals occur at the bottom beam (FSW-1) and above Beam 4 in LR10. These are believed to be largely due to differences between the observed and predicted beam elongations (Section 9.5.3). These have a greater relative effect during the negative load reversals because then the curvatures induced by the beam moments are small.

At the peaks of the positive load reversals, the axial load on the columns varied from a moderate compression (approximately $0.08\ f'_c$) at the top, to a net tension at the bottom (Figure 9.60). As a result, the columns were cracked over much of their length and there was a significant decrease in the values of curvature difference with height, even though the moments at the ends of all beams were similar. Concrete cracking also made the column curvatures more sensitive to the variations between the beam moments at different levels. In addition to the direct effect of the moment imposed on the columns, the associated beam shear forces affected the flexural rigidity of the columns because of their contribution to the column axial load. This increased sensitivity is

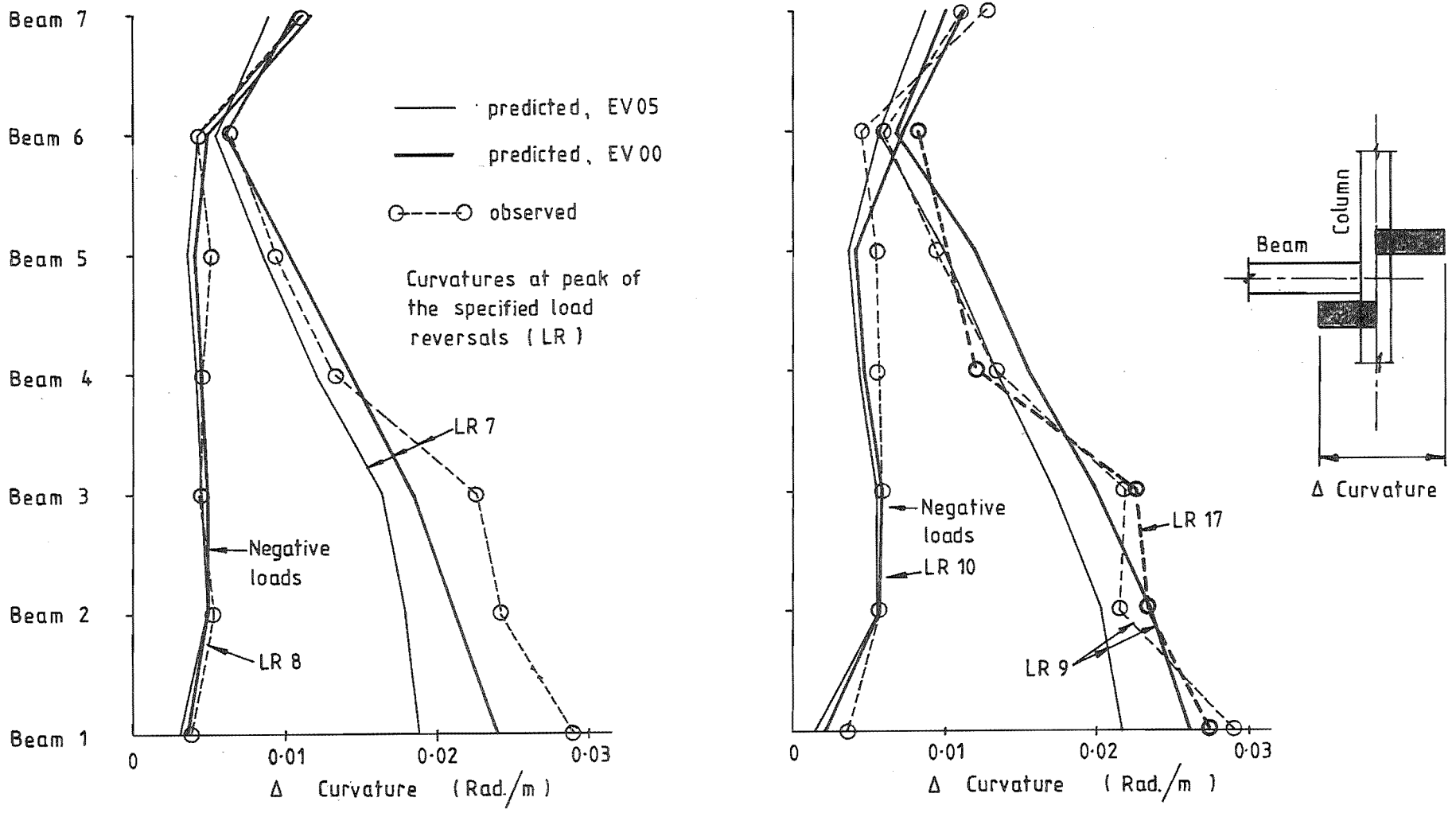

FIGURE 9.58 : DIFFERENCE BETWEEN COLUMN CURVATURE ABOVE AND BELOW EACH

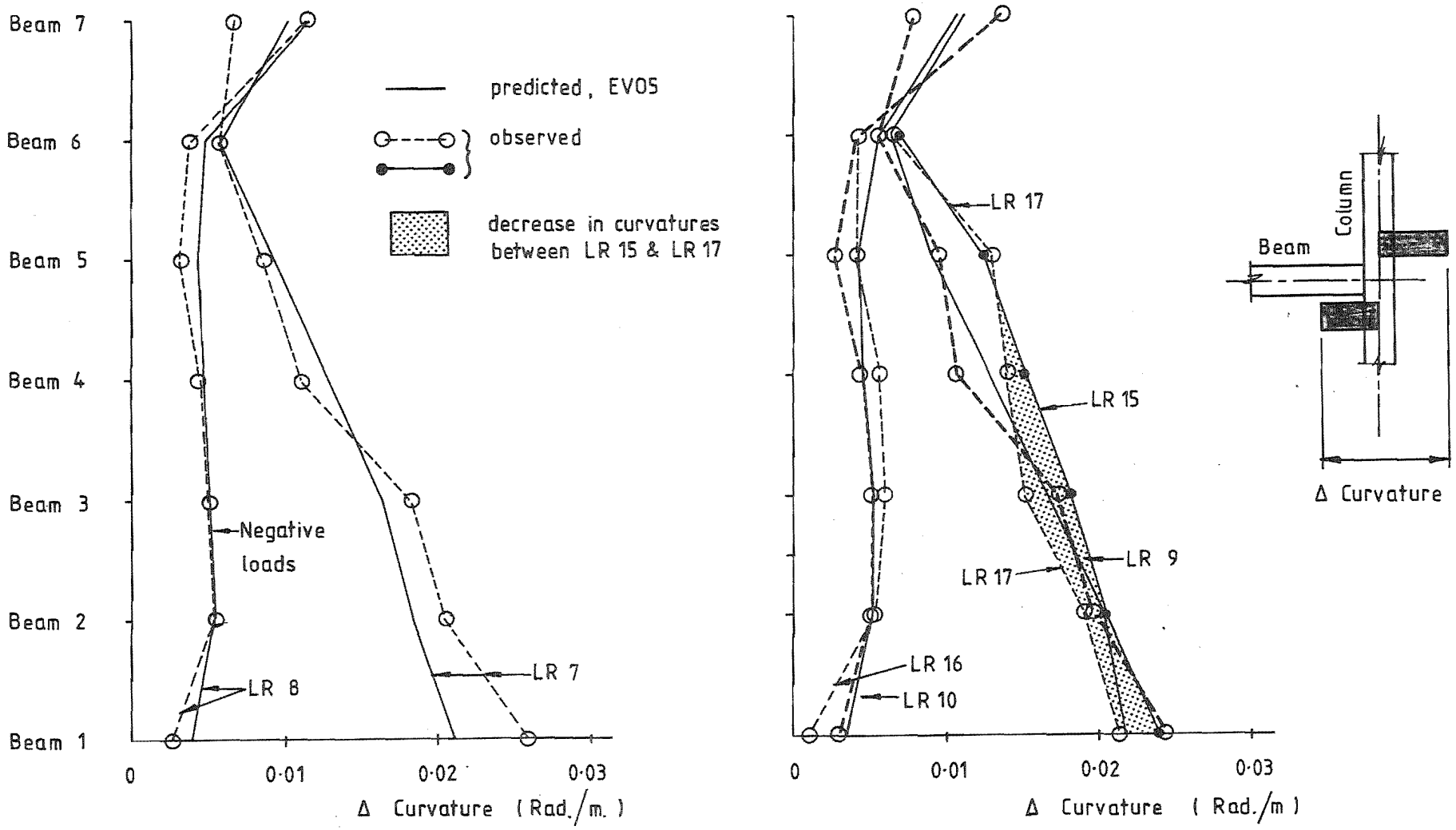

FIGURE 9.59 : DIFFERENCE BETWEEN COLUMN CURVATURE ABOVE AND BELOW EACH BEAM, FSW-2

indicated by the large (average 18%) difference between the values of curvature difference predicted by the EV05 and EV00 analyses of FSW-1. The difference between the predicted beam moments was only about 8%.

The theoretical model generally predicted the values of curvature difference for the positive load reversals satisfactorily, except at the bottom three beams in LR7. These discrepancies were confined to the sections of the columns which were in tension, and it is possible that they were due in part to the treatment of concrete cracking in the theoretical model*, or to errors in the predicted wall shear deformation (Section 9.3.4). Similar consistent discrepancies were not apparent at the peaks of the LR9 load reversals.

Although there were local discrepancies between the observed and predicted values, there is no evidence that the beam moments for either specimen were generally overestimated during the positive load reversals. In fact, they were underestimated in the EV05 analysis of FSW-1. It is therefore unlikely that the errors in the predicted curvatures in the unyielded regions of the walls at the peaks of the positive load reversals were caused by the wall moments being underestimated, since this would have required the frame component, and hence beam moments, to have been overestimated (see Section 9.3.1).

The observed values for FSW-2 during the later stages of loading indicate that the peak beam moments were of the same magnitudes in LR15 as they were in LR9, but may have decreased slightly between LR15 and LR17.

9.5 BEHAVIOUR OF COLUMNS

The columns in the two specimens behaved very similarly. Cracks opened over the full height of the columns during the positive post-yield load reversals when beam shears imposed upward forces on the columns (Figure 9.60), although above Levels 3 to 4 they were confined

---

* In the model, cracks were assumed to form only in regions where the tensile strength of the concrete was exceeded, and hence they were not assumed to propagate immediately to the neutral axis as soon as they had formed.

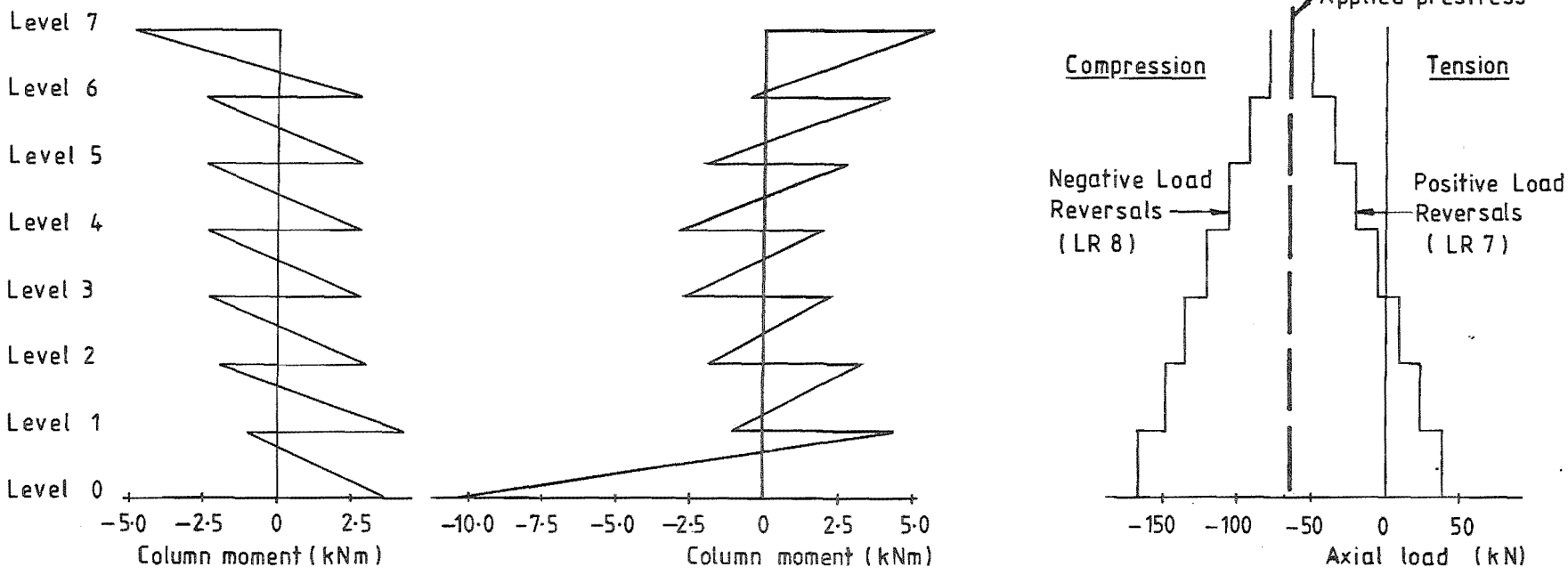

(a) Moment Diagram LR 7

(b) Moment Diagram, LR 8 (Maximum compression)

(c) Peak Axial Loads, LR 7 & LR 8

FIGURE 9.60 : PREDICTED MOMENT AND AXIAL LOADS ON FSW-2 COLUMN (EVO5 ANALYSIS) - FSW-1 VALUES SIMILAR

to the vicinity of the beam junctions. In the negative load reversals the beams imposed additional compression on the columns and open cracks were confined to the vicinity of the column bases (Level 0) and the top (Level 7) beams. Apart from the cracks and the expected plastic hinging at the bases, neither column was visibly damaged.

The main aspects of column behaviour investigated are the plastic hinge zone deformations and flexural deformations in other parts of the columns. Consideration is given to the factors affecting the pattern of column moments and to the effect of axial load on the plastic hinge zone shear deformations.

9.5.1 Base Plastic Hinge Zones

Figures 9.61 and 9.62 compare the observed and predicted curvatures in the lower part of the columns at the peaks of several load reversals and Figure 9.63 compares the observed and predicted load-curvature histories for segment CO-3 during load reversals 7 to 9. In both specimens, yielding initially developed at only two locations: at the bases of the columns (base plastic hinge zone) and in the vicinity of the top of the Level 1 beams.

As indicated in Figure 9.63, the standard EV05 analyses* significantly underestimated the curvatures of the bottom segments during the initial stages of LR7. This appears to have been due to pre-cracking of the segments during LR3, probably because shrinkage had reduced the effective tensile strength of the concrete, plus the effect of the holes for the strain gauge studs acting as crack initiators. Considerably better agreement was obtained when the concrete was assumed pre-cracked ($f'_t = 0$, Figure 9.63a).

Yielding of the base plastic hinge zone of the column in FSW-1 did not occur until ductility of DF ≈ 2.4 in LR7. At the peak of this load reversal, yielding was still confined to the bottom 25 mm of the column. Yield strains were therefore not directly detected in the tests.

---

* Similar results were obtained from the EV00 analyses (results not shown).

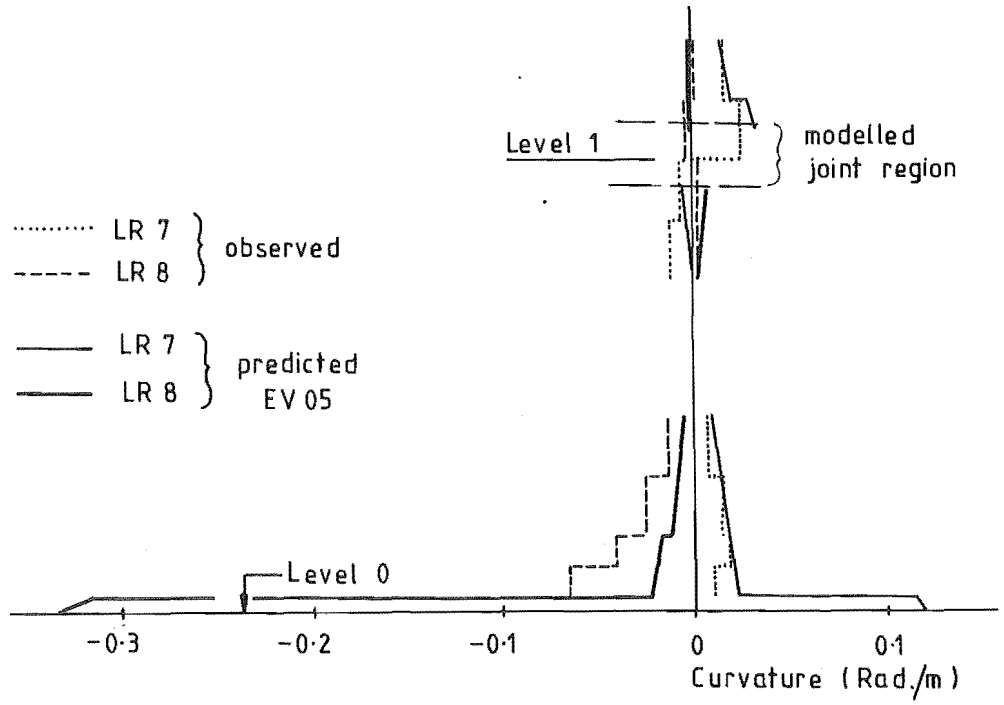

(a) Load Reversals 7 & 8

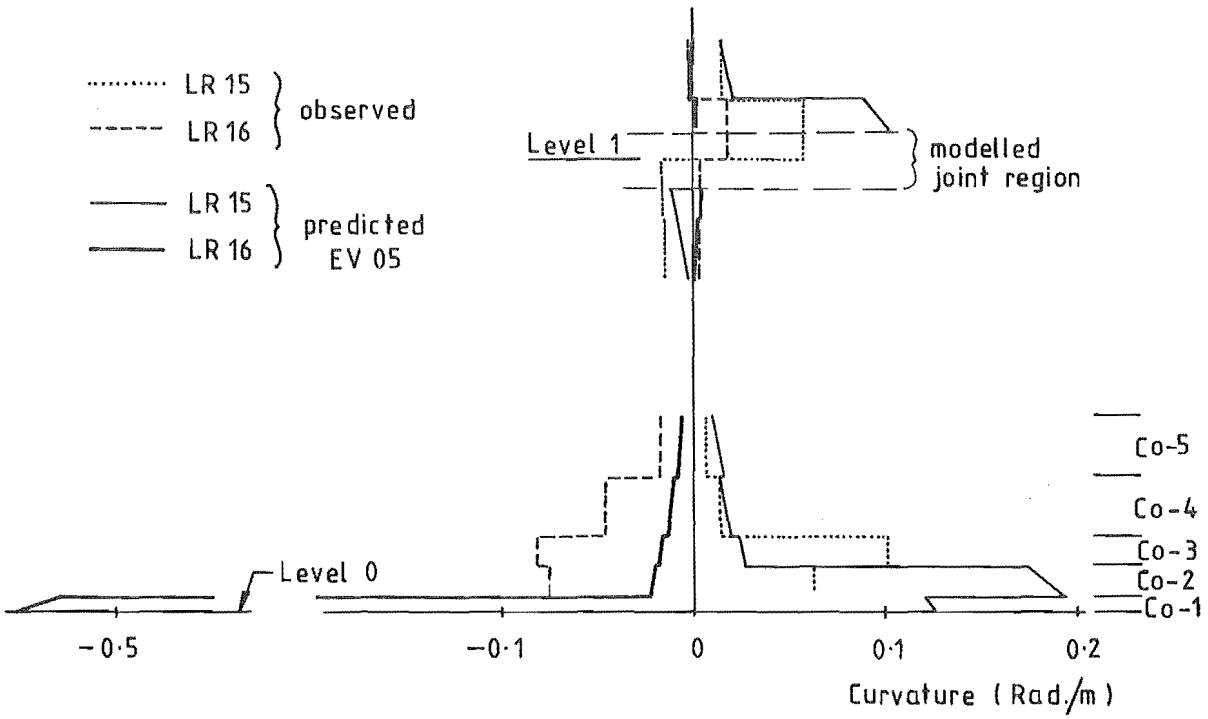

(b) Load Reversals 15 & 16

FIGURE 9.61 : DISTRIBUTION OF CURVATURE IN FIRST STOREY COLUMN IN FSW-1

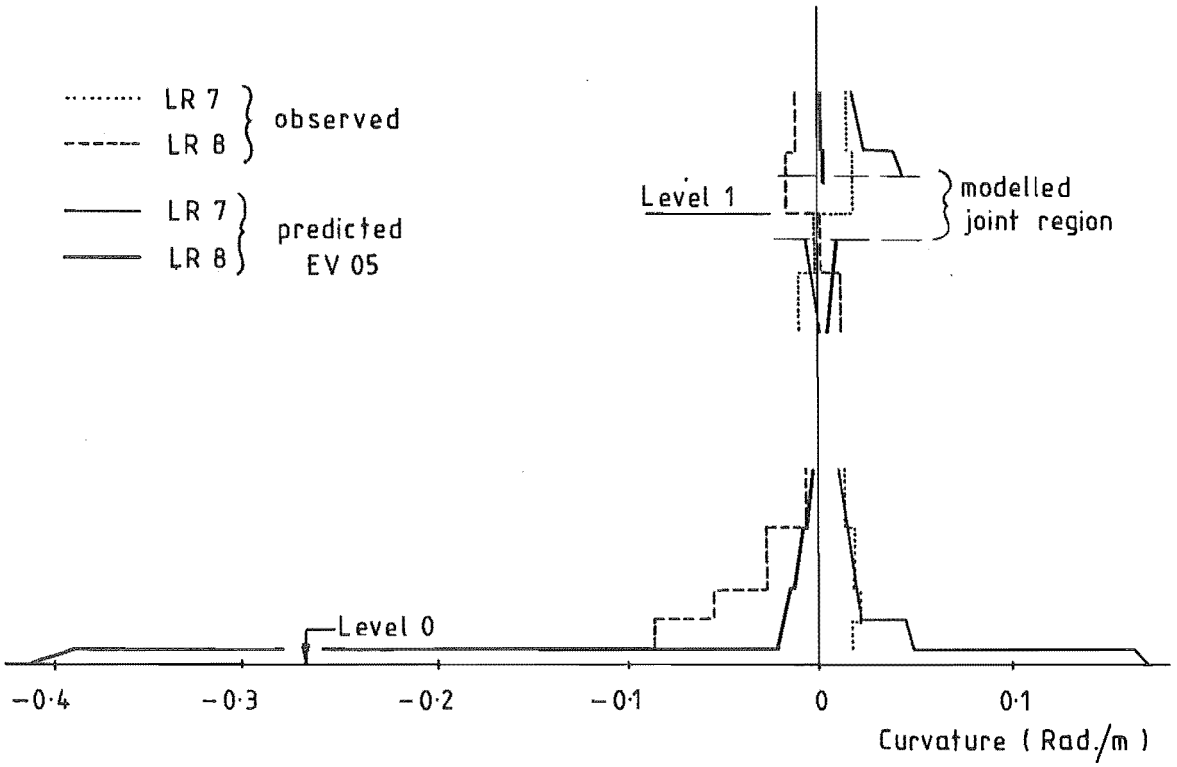

(a) Load Reversals 7 & 8

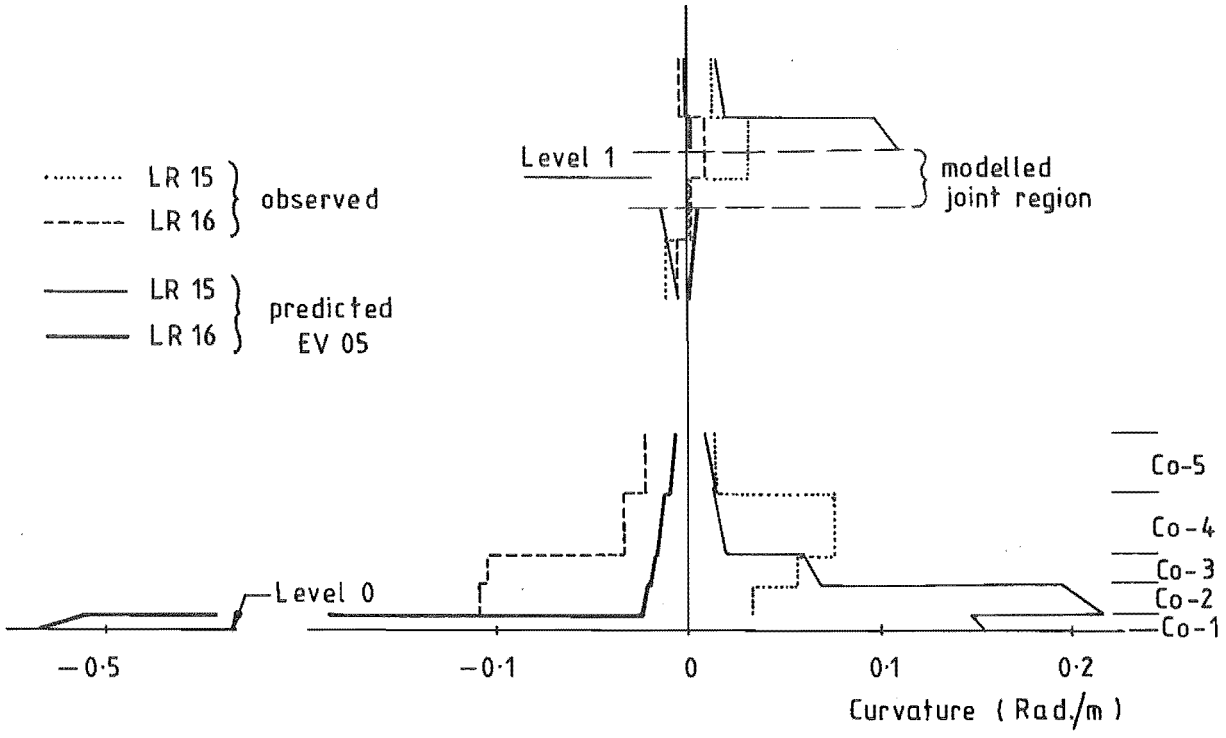

(b) Load Reversals 15 & 16

FIGURE 9.62 : DISTRIBUTION OF CURVATURE IN FIRST STOREY COLUMN IN FSW-2

However, as in the case of the beams, the onset of yielding limited the moment at the base of the columns. This caused a sharp change in slopes of the applied load-curvature response curves for the adjacent unyielded segments (see Figure 9.63a). Both the extent of yielding at the base of the columns (i.e. confined to the bottom 25 mm), and the effect of yielding on the curvatures of the adjacent segments were predicted accurately.

In the case of FSW-2, the onset of yield at the base of the column did not register on the observed load-curvature responses because of the large displacement increment between the final two sets of steel strain readings in LR7. The readings obtained did, however, indicate that the bottom of the column started to yield at a specimen ductility factor (DF) of between 1.9 and 4.7. The analyses predicted onset of column yielding at DF $\simeq$ 2.3, but as indicated in Figure 9.62, it also predicted that yielding would penetrate as far as the second segment above Level 0 (i.e. segment CO-2) at the peak of LR7. No yielding was observed in this segment in LR7. However, this result was possibly influenced by the fact that there were no cracks within segment 2.

In the following negative load reversals (LR8), the cover concrete at the compression face of the columns of both specimens spalled over an area extending into the third segment. This behaviour was not predicted correctly. As found previously (Section 6.2.2.2), the predicted loss of strength due to crushing of the end segment cover concrete significantly reduced the moments acting on other segments. In both specimens, the reduction in moment was sufficient to prevent further spread of yielding and, as a result, the curvatures in the gauged segments at the column bases (CO-2 to CO-5) were significantly underestimated in the analyses at the peaks of all negative load reversals (Figures 9.61 and 9.62).

After LR8, the observed post-elastic curvature-distributions for both positive and negative load reversals were affected by strain ageing. This causes the location of the maximum plastic curvature to migrate upwards (Figures 9.61b and 9.62b).

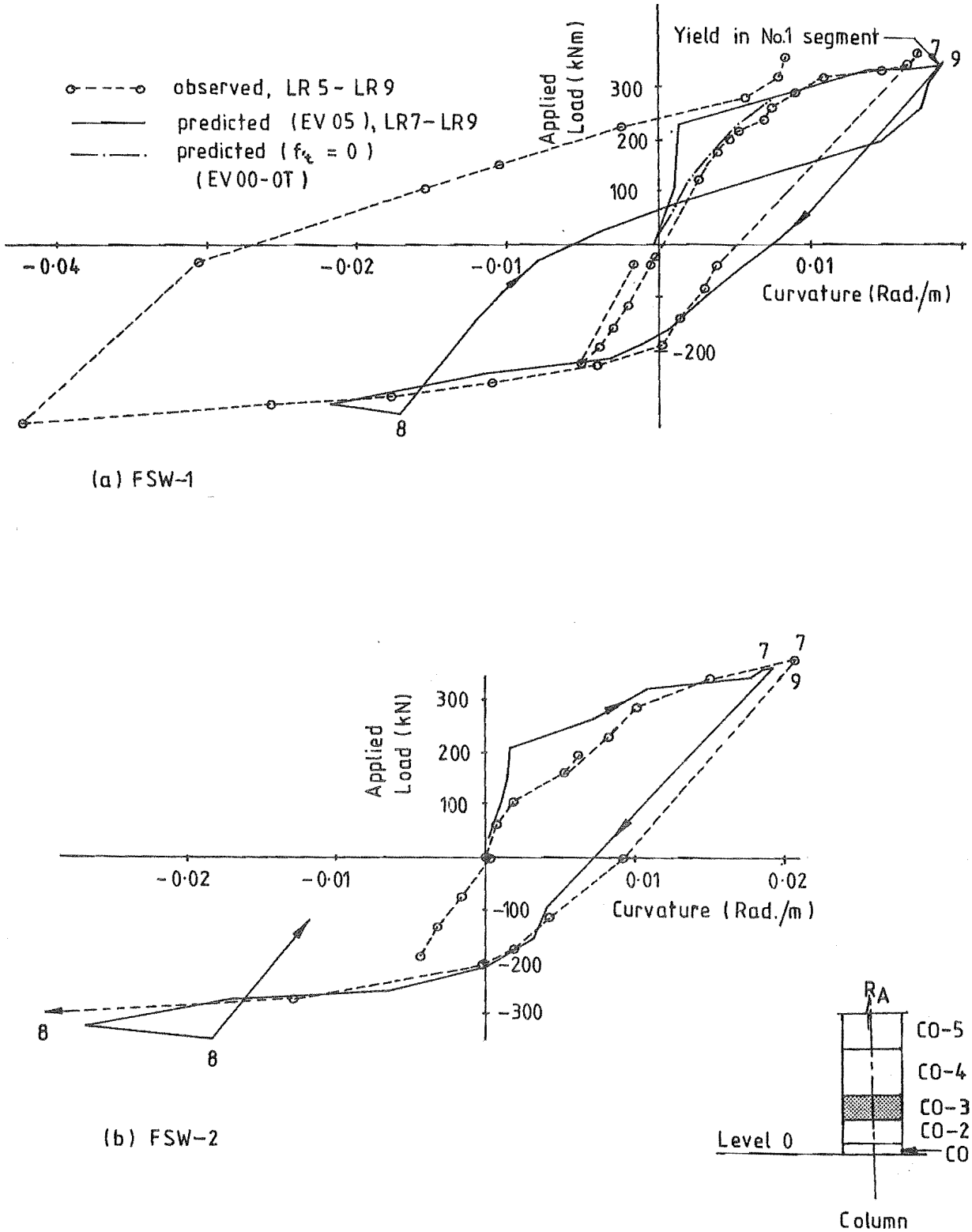

FIGURE 9.63 : LOAD-CURVATURE RESPONSES FOR THE CO-3 SEGMENTS OF THE FIRST STOREY COLUMNS

Despite the high net axial tensions on the columns at the peaks of the positive load reversals, no significant sliding shear deformations were apparent from the appearance of the plastic hinge zones (Figure 9.64). The analyses predicted an unsymmetric shear response with increasing drift of shear deformations in the negative load direction* (Figure 9.65). This predicted behaviour may not have been very realistic, but the peak values of shear displacement were only about one tenth of the beam shear deformations, and were therefore comparatively insignificant.

The shear behaviour of these plastic hinge zones again emphasises the effectiveness of an "average" net compression over a load cycle in reducing shear deformations in plastic hinge zones, even in situations where the member is in tension during part of the load cycle.

9.5.2 Yielding at Other Locations in the Columns

As indicated in Figures 9.61 and 9.62, the columns in both specimens yielded also at the top of the level 1 beam-column joint regions during the positive load reversals. The extent of yielding was, however, limited. The maximum measured bar strain in FSW-1 was 3360 μs in LR7 and 10100 μs in LR15, and there was no obvious sign of yielding in the column's appearance. Although the modelled segments do not directly correspond with the location of the strain gauge locations, it appears that the degree of yielding at these locations was predicted reasonably accurately.

Yielding also developed near the tops of the level 2 beams with a maximum strain of 4100 μs in FSW-1. However, this did not occur until LR11 and may have been partly a result of strain age strengthening of the beam plastic hinge zones. None of the analyses predicted yielding at this location.

---

* Negative loading induced maximum axial compression, but also maximum shear at the base of the columns (Figure 9.60).

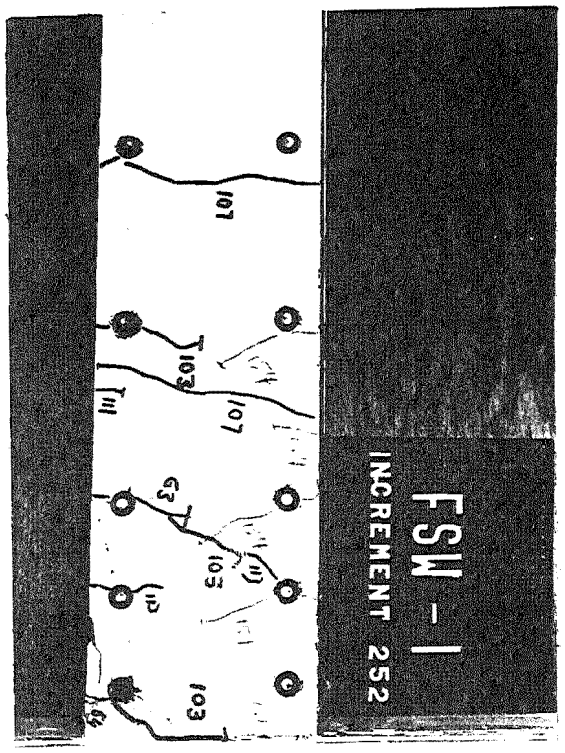

(a) FSW-1, LR 15 (South Side)

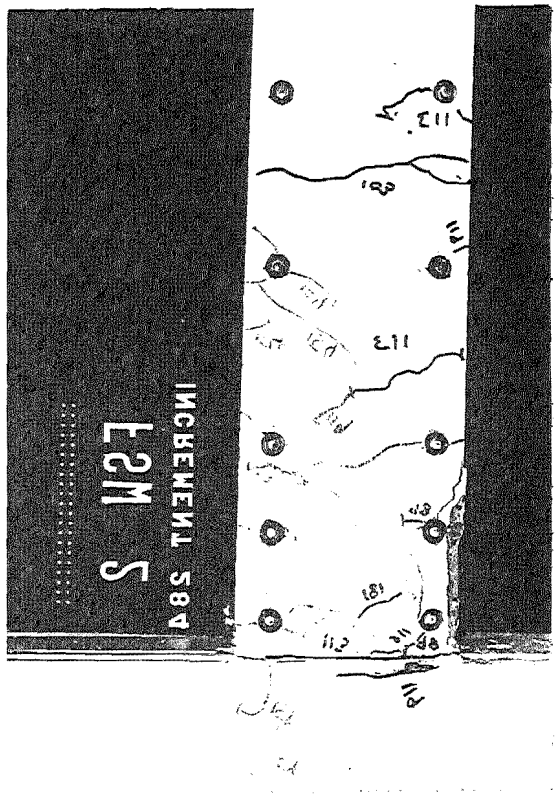

(b) FSW-2, LR 14 (North Side)

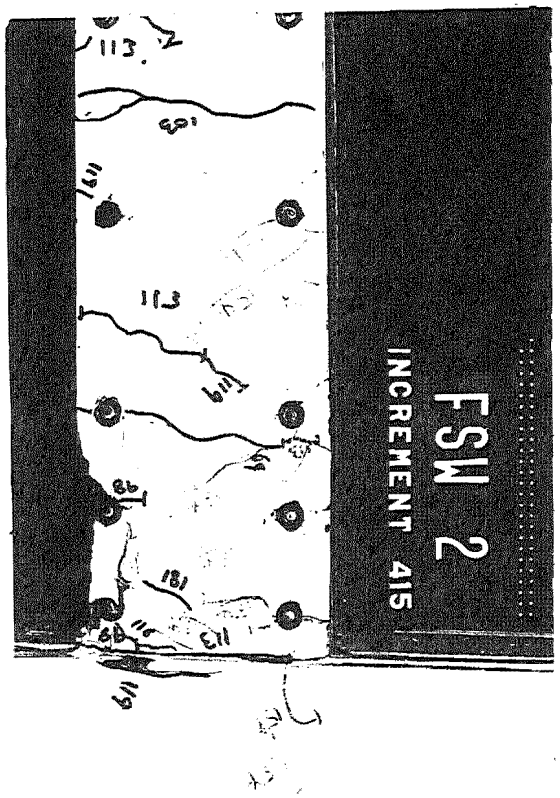

(c) FSW-2, LR 20 (South Side)

FIGURE 9.64 : COLUMN BASE PLASTIC HINGE ZONES

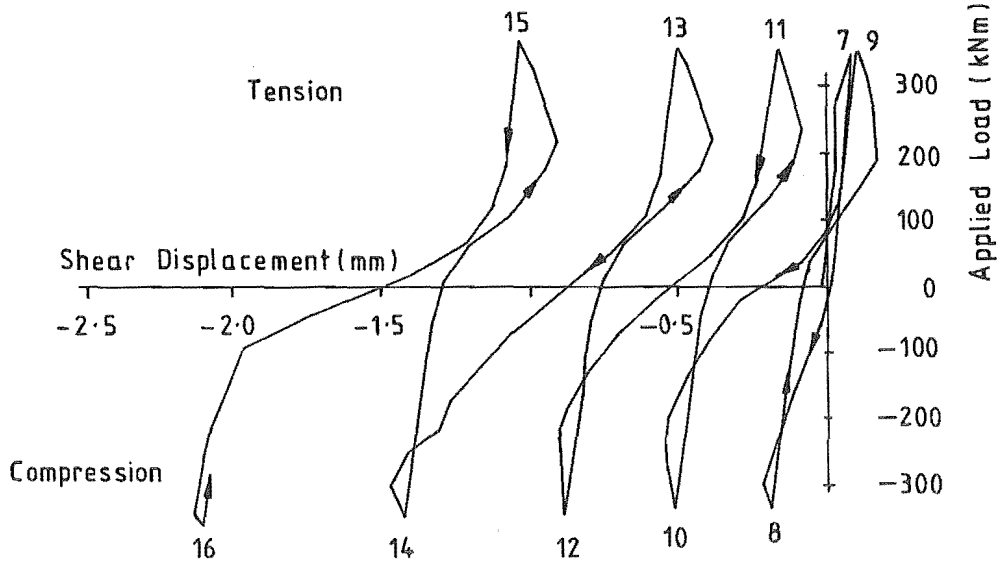

FIGURE 9.65 : PREDICTED SHEAR DISPLACEMENT RESPONSE LEVEL 0-1 SECTION OF COLUMN, FSW-1

9.5.3 Assessment of Moments Induced in the Columns

Figures 9.66 and 9.67 compare the observed and predicted curvatures above and below the four bottom beam-column joints, at the peaks of load reversals 7 to 10. These curvature distributions were derived in order to assess the column moment patterns (cf. Figure 9.60).

As seen, the overall agreement between the observed and predicted curvatures is generally reasonable. In most cases where there is a discrepancy, the curvatures both above and below the joint are similarly affected, with the difference between the values (Δ curvature in Figures 9.58 and 9.59) still predicted accurately, e.g. FSW-2: Level 1, LR7 and Level 2, LR10 (Figure 9.67).

The fact that the observed and predicted curvature differences across these joints are similar, indicates that the measured curvatures are likely to be reasonably accurate. The observed values of curvature difference were obtained from two independent measurements, i.e. one above and one below each joint. Compensating errors would have had to have been made in each measurement to obtain the same value. The similarity of the observed and predicted curvature differences also indicates that the errors are due to a "zero shift" in the moment pattern, rather than to errors in the predicted moments developed at the beam ends. In the case of these specimens, the moment zero shifts were most likely to have been caused by errors in the predicted relative elongations of adjacent beams, and possibly in the predicted shear displacement of the wall plastic hinge zone. For example, the errors in the Level 2 curvatures for FSW-1 at the peaks of LR8 and LR10 (Figure 9.66) were probably largely caused by the fact that the elongation of the Level 1 beam was significantly underestimated, whereas the elongations for the beams above Level 1 were overestimated (Figure 9.54a).

Because it was the relative, rather than absolute beam elongations which were important, the additional errors introduced by having to model sliding shear in the beam hinge zones meant that the predicted column curvatures for FSW-1 were generally more affected than those for

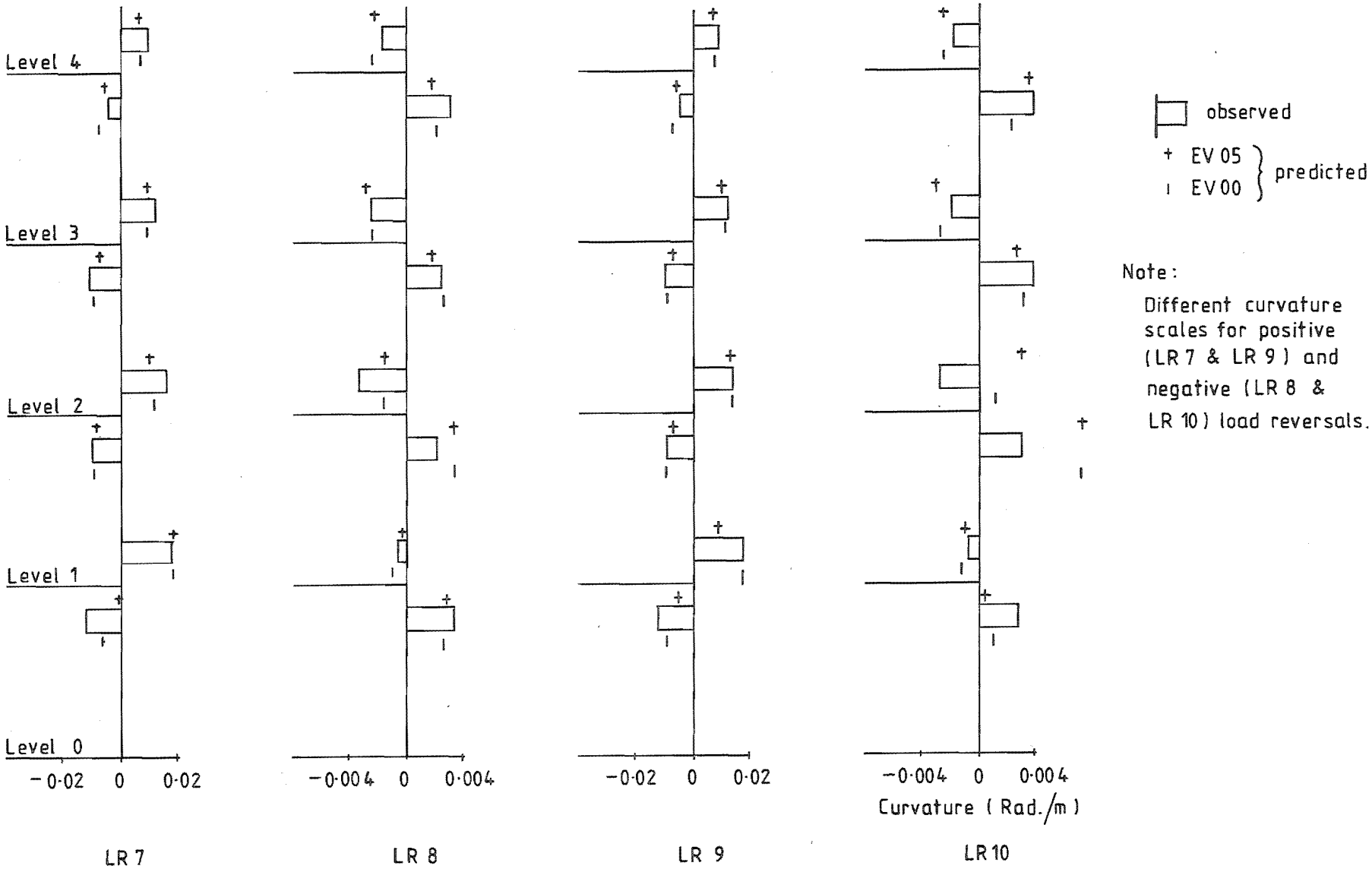

FIGURE 9.66 : DISTRIBUTION OF COLUMN CURVATURE IN VICINITY OF THE LEVEL 1 TO 4 BEAM COLUMN JOINTS, FSW-1

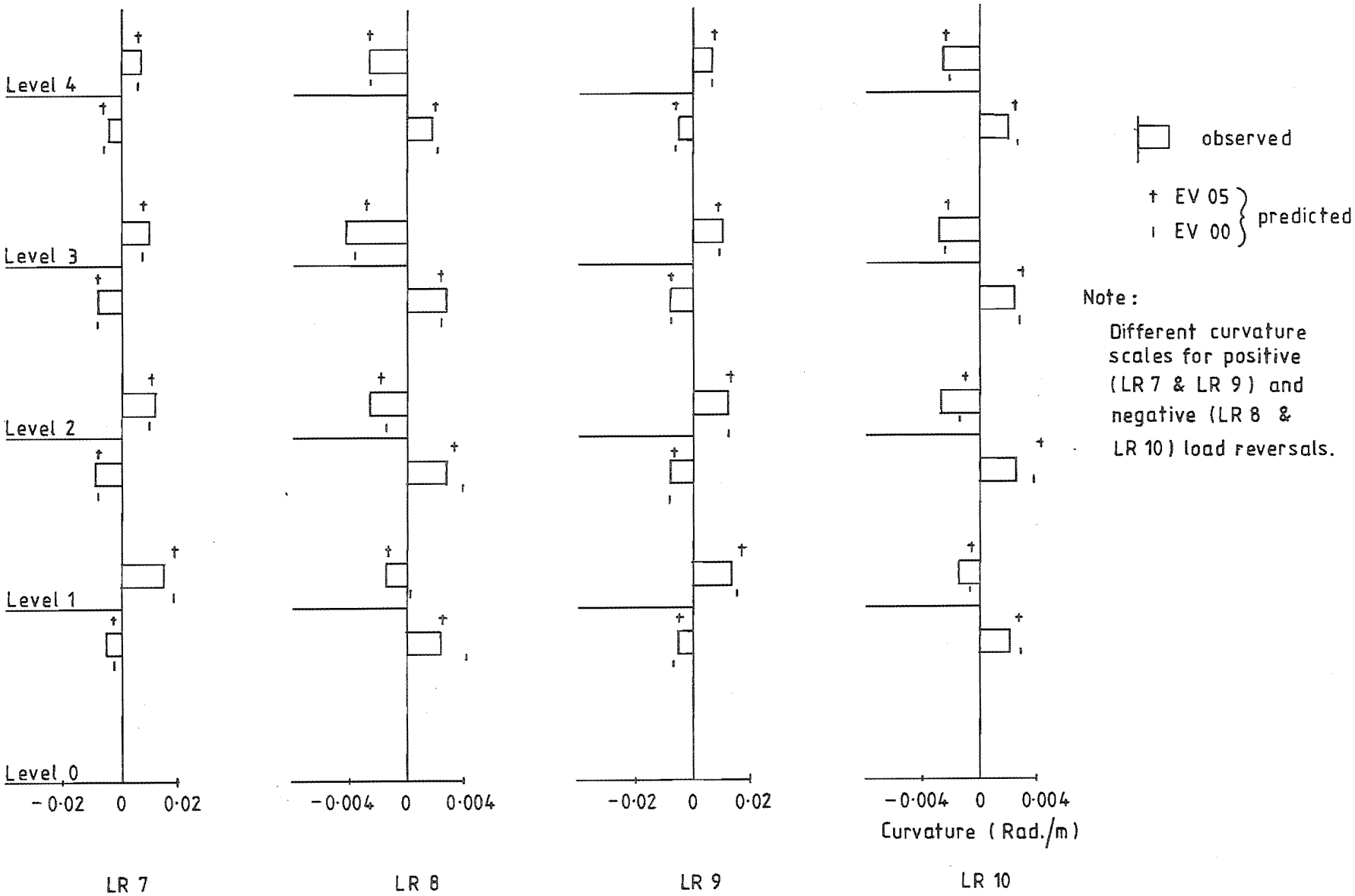
Level 4
Level 3
Level 2
Level 1
Level 0
-0·02
0
0·02
-0·004
0·004
Curvature (Rad./m)
observed
EV 05
EV 00
predicted
Note :
Different curvature scales for positive (LR 7 & LR 9) and negative (LR 8 & LR 10) load reversals.
LR 7
LR 8
LR 9
LR 10

FSW-2. These errors also had a greater relative effect in the negative load reversals. This was because the curvatures induced in the columns by the beam end moments were significantly smaller than during the positive load reversals (Section 9.4.7), whereas the effect of a given error in the beam elongations would be similar irrespective of the loading direction, i.e. a given displacement perturbation along the column would induce similar curvatures, irrespective of the stiffness of the column.

9.6 BEAM-COLUMN JOINTS

As indicated in Figures 9.68 and 9.69, the beam-column joint regions of both specimens performed well, with no sign of significant joint shear deformation. There was also no evidence of significant deterioration of the bond along the beam bars that were anchored in the columns. Increasing bar slip in the anchorage regions would have resulted in widening of the cracks at the beam-column interfaces and reduced the rotations developed in the adjacent plastic hinge zones in the beams. However, in both respects, the behaviour of the plastic hinge zones at the column and wall ends of the beams were very similar.

The good performance of the joints was achieved despite net axial tensions being developed in the columns below Level 3, at the peaks of the positive load reversals. Below Level 1, the tensile force reached approximately 40% of the column tensile yield strength, and was sufficient to induce yielding in the column flexural reinforcement in the vicinity of the Level 1 joint region (Section 9.5.2).

Three factors contributed to the good performance of the joint regions:

(a) The special reinforcing detail, with the anchored ends of the beam bars bent back diagonally through the centre of the joints (Section 7.5.4). This joint shear reinforcement was provided in addition to conventional joint ties and must have restricted the width of any diagonal cracks which developed.

---

* Predicted value, approximately the same for both specimens.

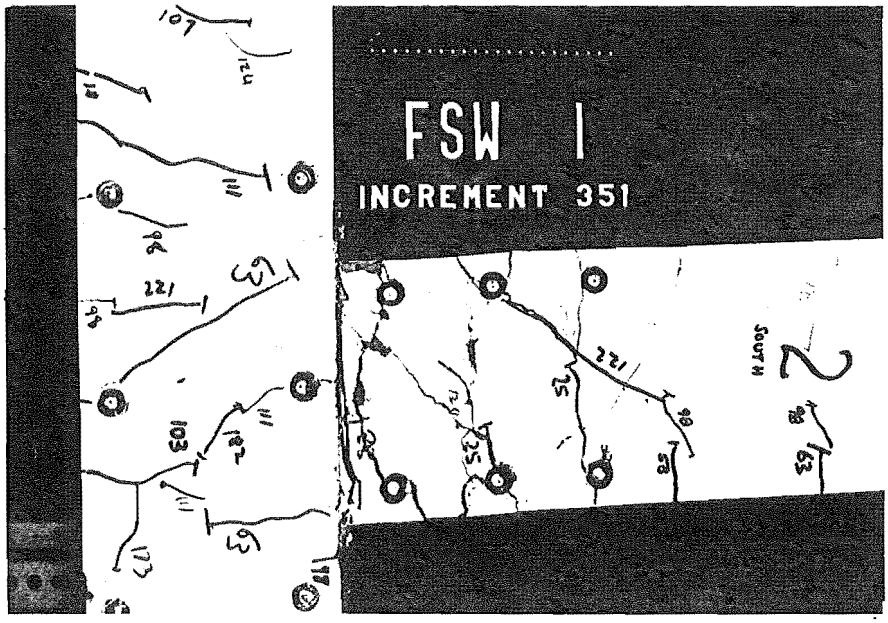

FIGURE 9.68 : FSW-1 LEVEL 2 BEAM COLUMN JOINT, PARTLY UNLOADED AFTER LR19

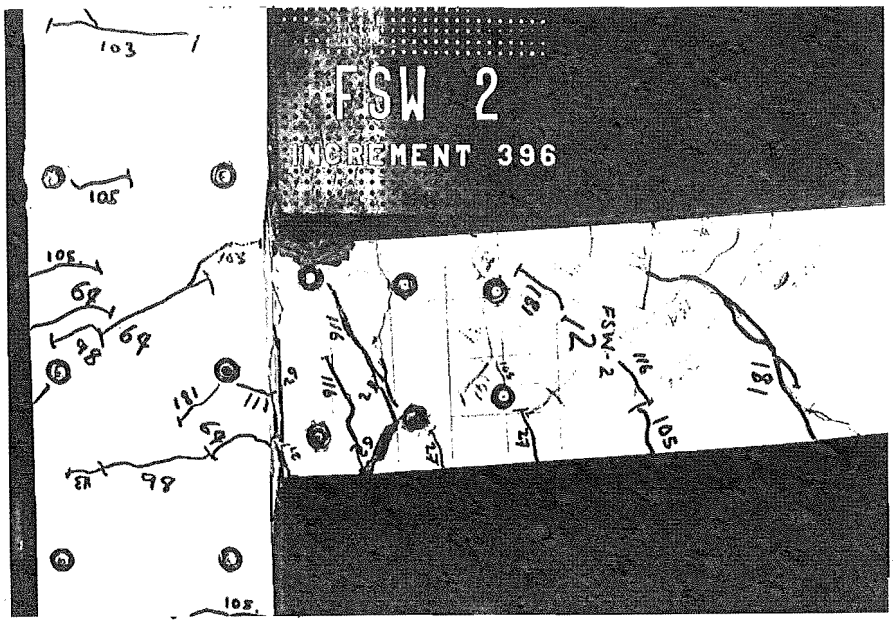

FIGURE 9.69 : FSW-2 LEVEL 2 BEAM COLUMN JOINT, AT PEAK OF LR19 (NET TENSION ON COLUMN)

(b) High net axial compressions (up to 0.28 f'_c) were induced in the columns during the negative load reversals, with the result that diagonal cracks formed only in one direction.

(c) The comparatively low maximum shear imposed on the joints, which was equivalent to about 0.44 $\sqrt{f'_c}$ (MPa) nominal shear stress on the gross concrete section.

It is not known whether the joints would have performed as well without the diagonal bars. However, the primary objective of the unconventional detailing of the joints was to minimise joint shear deformations and overall anchorage slip, both of which would have adversely affected the comparison of the specimen responses with those predicted by the theoretical model. As Figures 9.68 and 9.69 indicate, this objective was achieved.

10. DISCUSSION, CONCLUSIONS AND RECOMMENDATIONS

10.1 EXPERIMENTAL WORK

Four small scale beam-wall specimens and two small scale frame-wall assemblage specimens were tested under post-elastic reversed cyclic loading. Two of the beam-wall, and one of the frame-wall specimens had diagonally reinforced beam plastic hinge zones. All the specimens except for one of the beam-wall units exhibited good overall performance, with the diagonally reinforced specimens, in particular, exhibiting excellent stability and energy dissipation at very large ductilities.

Specific aspects related to this experimental work are discussed in the following subsections.

10.1.1 Beam-Wall Specimens

The first conventionally reinforced specimen (TB1) and the two diagonally reinforced specimens (TB3 and TB4) behaved well in terms of design expectation. The maximum values of deflection ductility sustained were well in excess of that required for ductile design. In the case of TB1 and TB3, ductilities in excess of DF = ±15 (± 0.09 Rad. beam rotation) were sustained before failure.

The behaviour of TB1 was very similar to that exhibited by similar larger scale conventionally reinforced beams. Sliding shear deformations contributed significantly to the overall load-deflection behaviour, but the hysteretic energy dissipation, while less than for the diagonally reinforced specimens, was still good by normal standards. Eventual failure of this beam resulted from the large sliding shear deformations during the final load reversals, but did not occur until after three load reversals to DF = ±15.

The performance of the second conventionally reinforced specimen (TB2) demonstrated that plain bars are not suitable for modelling the behaviour of deformed bars subjected to inelastic straining. However, it was of interest that the bond slip along the anchored bars caused

only limited loss of anchorage strength. There may therefore be situations where slightly bent plain bar anchorages would provide a better energy dissipation system than those presently used, as there would be minimal damage to the concrete.

Both specimens with diagonal reinforcing in the beam plastic hinge zones (TB3 and TB4) exhibited excellent energy dissipation and very stable, ductile responses. The diagonal reinforcement did prove to be susceptable to out-of-plane buckling at large deformations. However, the buckling behaviour exhibited was ductile and in the situation where a beam is fixed rigidly with a slab, the low torsional rigidity exhibited is probably an advantage. This is because the beam would be better protected against torsional damage resulting from building deformations perpendicular to the beam axis.

Measurements of the bar strains in the beam anchorage regions of TB1, TB3 and TB4 indicated that the anchorage rotations in these specimens contributed 25% to 35% of the total end deflection of the beams. This proportion remained reasonably constant, regardless of the intensity of load or the number of load cycles imposed.

10.1.2 Beams and Columns in the Frame-Wall Specimens

The beams in the frame-wall specimens behaved very similarly to the corresponding beams in the beam-wall specimens. The failure of the splice regions of the beams in FSW-2 due to inadequate splice length was an exception.

The ductilities imposed on the beams of the frame-wall specimens were significantly larger than indicated by the overall load-displacement responses of the specimens. This was due to early yielding of the beams relative to the walls and because of the vertical displacements at ends of the beams connected to the walls, i.e. due to elongation of the tension faces of the walls. Yielding of the beams occurred at a lower load than had been predicted using a simple elastic analysis model, because allowance had not been made for the shift of neutral axis position within the wall as a result of concrete cracking.

As expected, the peak member rotations imposed on the beams were reasonably uniform. Because the deformations imposed on the beams are largely determined by the deflected shape of the wall, the sequence of formation of plastic hinges is not significantly affected by varying the flexural reinforcement between beams. Consequently, there is little point in attempting to match accurately the beam reinforcement to any specific "elastic" moment distribution.

10.1.3 Wall Plastic Hinge Zone Shear Deformations (Frame-Wall Specimens)

Measurements and predictions of the sliding shear deformations in the wall plastic hinge zones indicate that even a relatively small mean axial compression can reduce significantly the magnitude of sliding shear deformation. The results also indicated that the magnitude of sliding shear deformation is largely dependent on the axial load at low lateral load intensities when the cracks are fully open, rather than on the peak axial loads.

Measurements of the wall stirrup strains indicated that significant bond developed along the stirrups and that after yielding of the flexural bars, the maximum forces developed in the stirrups at major diagonal cracks were related to the imposed plastic flexural deformations.

10.1.4 Local Buckling of Compression Bars

The flexural bars at the frame edge of the wall plastic hinge zones of both FSW-1 and FSW-2 buckled in compression. The buckling was most severe in the case of FSW-1, causing significant deterioration of the specimen response. Eventually, compression failure of the "confined" core concrete resulted.

The trend indicated by the local buckling of compression bars in both wall plastic hinge zones suggests that the recommended minimum of six bar diameter (19) spacing for confining ties in plastic hinge zones is reasonable. The results also demonstrated the need for confining ties to be adequately anchored into the main body of concrete to prevent simultaneous in-plane buckling of groups of bars tied by small ties or links (19).

10.1.5 Out-of-Plane Buckling

The behaviour of FSW-2 demonstrates that walls are susceptible to out-of-plane buckling. The axial load on a wall reduces the in-plane sliding shear deformation thereby increasing the stress required to be developed in the compression bars before the cracks close. This can result in buckling due to out-of-plane sliding shear displacements in the plastic hinge compression zone.

In this case, the behaviour exhibited was satisfactory with specimen ductilities significantly in excess of DF = ±4 being sustained for several cycles before the wall buckled. However, there were several factors related to these tests (e.g. bar size, strain ageing) which may have delayed the onset of buckling. Further investigation of the susceptibility of walls to this form of buckling is therefore necessary. In particular, the effect of deformations imposed by the earthquake component acting perpendicular to the plane of the wall, needs to be evaluated.

The behaviour exhibited by TB3 and FSW-2 suggests that use of diagonal reinforcement in a wall plastic hinge zone could accentuate the tendency of a wall to buckle out-of-plane by reducing the in-plane component of sliding shear deformations.

10.1.6 Strain Ageing

Results obtained for both the beam-wall and particularly the frame-wall specimens indicate that ordinary grades of steel can be significantly affected by strain ageing. Tests to evaluate the post-elastic behaviour of reinforced concrete components should therefore normally be carried out over as short a period of time as possible. However, there is also a need to evaluate the effect of strain ageing of steel on the behaviour of repaired structures and in this respect it would be desirable if repaired specimens were left to age for several months before retesting.

10.2 FRAME ANALYSIS COMPUTER PROGRAM

The computer program was developed with the intention of extending the degree of refinement available for moment curvature analyses to general analyses of frame assemblages. The main emphasis in this work was placed on adaption of the Newton-Raphson solution procedure, development of models for the steel and inelastic sliding shear responses, and on minimizing the computation time. Overall, the computer program performed well. The total load-deflection responses were predicted significantly more accurately than could be achieved if only the flexural deformations are considered. However, there were aspects of the shear response that were not modelled as accurately as would have been desirable and it was evident that, in some areas, the modelled behaviour could be improved. Several specific recommendations in this regard are made in Sections 10.2.3 to 10.2.8.

10.2.1 Newton-Raphson Solution Procedure for Materially Nonlinear Analyses

The solution procedure used for materially nonlinear analyses was based on generalised Newton-Raphson iteration. This proved to be very successful with generally good rates of convergence. Only in a very small number of cases did the solution fail to converge correctly.

Two significant adaptions were made to the generalised procedure in order to ensure satisfactory convergence when analysing reinforced concrete components subjected to post-elastic cyclic loading. In the first place, special measures were necessary to ensure that the constitutive models did not give rise to instability. Secondly, the complementary displacement control procedure was very important in the low-slope (generally post-yield) regions of the load displacement responses. This procedure made it possible to obtain uniform control of loading over the full range of the response, and because the imposed force was automatically adjusted in accordance with the forces resisted, there was no risk of structure overload in the analyses. The availability of displacement control also permitted convergence to specified cycle displacement limits, thereby enabling direct comparison with observed responses.

10.2.2 Steel Model

The steel model developed for the inelastic section analysis procedure proved to be both accurate for the range of data considered and very economical. The efficiency of this model was one of the main factors leading to reduction of computation times to a level which would make dynamic analyses of full frame assemblages practicable.

Some modifications are still required to make the model more general. A wider range of response data needs to be evaluated, particularly data from unmachined bar samples (e.g. unloading modulus, Section 3.5.1). However, the accuracy of the model is limited ultimately by variations in steel properties not only between bars, but also within lengths of individual bars. Hence spurious accuracy should not be sought at the expense of loss of computational efficiency of the model.

10.2.3 Concrete Model

The allowances made for sliding shear deformation, and particularly for the effect of mismatched crack surfaces, significantly increased the influence of the modelled response of the compression concrete. As a result, the treatment of the concrete response in both the uniaxial compression and the shear models, and interaction between the two, needs to be reviewed. Three of the more important aspects affected are discussed in Sections 10.2.7 to 10.2.9.

10.2.4 Member Idealization

The results obtained from the mesh refinement analyses indicated that relatively coarse member segmentations can be used without significantly affecting the accuracy of the response, particularly when allowance is made for shear induced stresses in the flexural reinforcing. In that case, a single inelastic segment would normally be adequate for representing a plastic hinge in ordinary frame members.

10.2.5 Shear Induced Stresses in the Flexural Reinforcement

Conflicting results were obtained from the attempts to model this behaviour, indicating that the approach used was possibly oversimplified. Both pre- and post-yield curvature distributions were predicted more

accurately when allowance was made for the effect of inclined cracking (e_v = 0.5 jd) but, in most cases, the peak loads during the initial post-elastic load reversals were underestimated. Also, measurements obtained from the frame-wall specimens showed that the wall stirrups were not strained significantly until after the flexural reinforcement yielded. This indicates that the stirrups could not have participated in shear resistance during the pre-yield load stages, as assumed in Section 2.2.4.

These results suggest that, except in cases where the shear stress is high, the effect of shear on the pre-yield curvatures is due primarily to the type of mechanism shown in Figure 10.1. However, this does not explain the low peak strengths predicted during the initial post-elastic load reversals, especially in view of the fact that the curvature distributions were predicted more accurately by the analyses with e_v = 0.5 jd. The only apparent explanation for this behaviour is that the concrete between cracks carried significant tension during the initial stages of post-elastic loading and hence that the average bar strains measured were significantly smaller than the peak strains developed at crack locations. The maximum forces resisted by the tension bars would therefore have been higher than indicated by the strain measurements.

The main exception to the general behaviour described above occurred in the case of the wall specimens tested by Wang et al (31). The peak shear stresses imposed on these walls were near to the maxima normally encountered and inclined cracking developed over the full depths of the webs before the flexural bars yielded (Figure 10.2). The behaviour of these walls was therefore probably close to that assumed in Section 2.2.4. Unlike the other specimens, the peak strengths in the first post-elastic load reversals were predicted reasonably accurately in the analyses with e_v = 0.5 jd.

10.2.6 Shear Deformation due to Inclined Cracking

Both shear deformation measurements and the magnitudes of stirrup strains recorded in the frame wall tests indicate that the shear deformation developed at high load intensity under monotonic loading, or initial

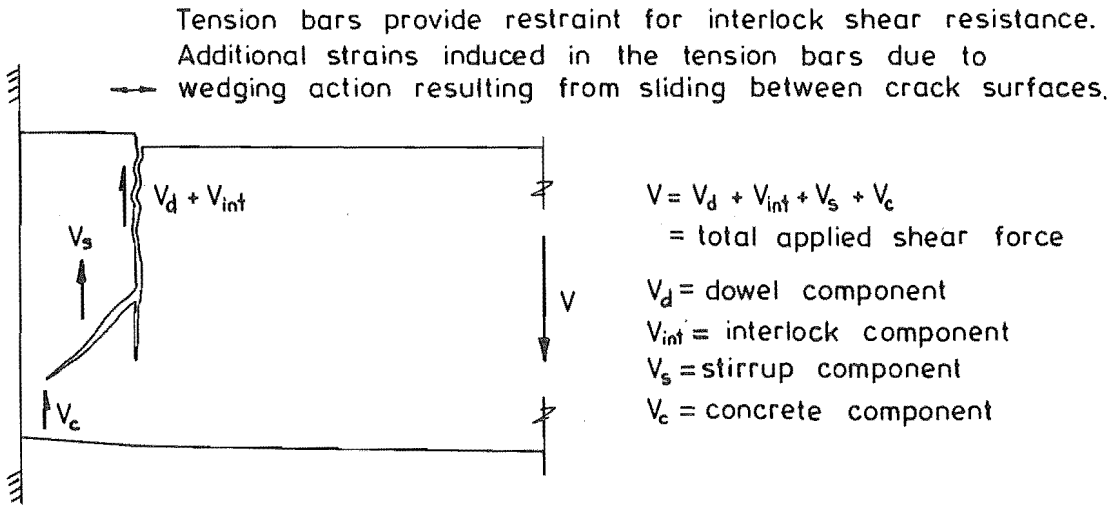

Before the tension bars yield, V_s is very small and the total shear (V) is largely resisted by $V_d + V_{int} + V_c$

FIGURE 10.1 : SHEAR RESISTANCE MECHANISM IN REINFORCED CONCRETE MEMBERS SUBJECTED TO LOW TO MODERATE SHEAR STRESS (SIMPLIFIED REPRESENTATION)

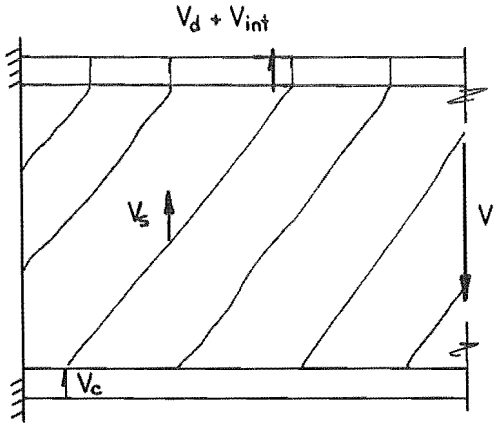

Full depth inclined cracks form before the tension bars yield. $V_{int.}$ and V_c components are small.

FIGURE 10.2 : CRACK PATTERN IN WEB SUBJECTED TO HIGH NORMAL SHEAR STRESSES

loading to increased displacement limits, are related to the magnitude of plastic hinge rotations*. These deformations appear to be due to inclined cracks opening as a result of the plastic strains developed in the tension bars. The peak shear deformations developed under these conditions were also generally of similar magnitude as the peak shear deformations in subsequent load cycles to the same displacement limits.

No provision was made for modelling the shear deformations occurring at high load intensities. This resulted in the shear deformations being significantly underestimated during initial post-elastic loading, with consequent overestimation of the plastic hinge flexural deformations. Inclusion of a model for shear deformations due to inclined cracking should not be difficult and would significantly improve overall correlation between the observed and predicted shear responses.

10.2.7 Interaction Between Concrete Shear and Normal Stress Actions

In the present model, the concrete shear and normal stress actions are uncoupled. Only normal stresses are assumed to strain the concrete. This limitation caused some difficulties as it meant that the onset of sliding shear displacements was entirely dependent on the normal stress response for opening cracks. Thus while any part of the concrete section is in compression, cracks can not be opened by imposing a shear force, regardless of how small the normal compression stress or how large the shear force might be. Not only is this unrealistic, but it also means that the predicted shear deformations are unnecessarily sensitive to the specific choice of increment size or of member segmentation (Section 6.2.6), as these choices can marginally affect the normal stress response.

Some form of coupling between the concrete normal and shear stress actions would therefore be desirable, although this would probably not need to extend to modelling the full biaxial stress field. This step was not taken in the present study as the resulting coupling of shear and normal stress actions would have had implications in other parts of

---

* Assuming that adequate stirrups have been provided to resist maximum imposed shear force.

the computer program (cf. Section 2.3.2) and also because of other aspects of the concrete model which need revision (e.g. Sections 10.2.8 and 10.2.9).

10.2.8 Concrete Softening due to Mismatched Crack Surfaces

No allowance was made for softening of the core concrete due to mismatched crack surfaces. As a result, the rigidity of the concrete, and hence the residual tensile strains in the compression reinforcement, were overestimated after the first post-elastic cycle. This in turn meant that the strains in the tension steel and therefore the predicted peak strength of the modelled plastic hinge zones were similarly overestimated.

The treatment of the concrete softening is probably the most serious deficiency in the shear model and was responsible for the largest discrepancies between the observed and predicted responses.

10.2.9 Unloading Shear Response

In the present model, a simple scaling factor, ϕ_{unl}, is used to artificially stiffen the shear unloading response. This was largely a stop-gap measure, designed to accentuate the difference between the stiffnesses of the shear loading and unloading responses. The model worked satisfactorily for the large displacement load cycles analysed in this study. However, scaling the unloading stiffness in this manner is a potential source of error under the more general loading conditions encountered in dynamic analysis. The use of this factor would probably not be necessary if adequate allowance were made for softening due to mismatched crack surfaces and for shear deformations resulting from inclined cracking.

10.2.10 Anchorage Model

The anchorage model developed for the program makes only an approximate allowance for the anchorage deformations at the ends of members which are subjected to inelastic deformations. This model worked satisfactorily for the cases analysed. However, with more experimental data now available, e.g. (67, 114), it should be possible to develop a more general model.

10.3 CONCLUSIONS

The following conclusions are made from the results obtained in this study:

10.3.1 Observed Behaviour of Test Units

(a) The beams designed in accordance with code requirements for ductile detailing, generally behaved well in terms of energy dissipation and stability of the load deflection responses.

(b) The flexural reinforcement in a plastic hinge zone in a conventionally reinforced beam exhibits a tendency to kink due to sliding shear deformation. This can cause the compression bars to buckle and lead to eventual failure of the core concrete. However, this effect only occurred at very large displacements and is likely to be significant only in the case of beams which are more critically loaded in shear than those tested in this study.

(c) Beams with diagonal reinforcing in the plastic hinge zones exhibit a tendency to twist. This may, however, be an advantage in the case of beams cast with a slab which are subjected to seismically induced torsion as well as flexure.

(d) A plastic hinge zone at the base of a reinforced concrete wall is susceptible to out-of-plane buckling. The mode of buckling exhibited by one of the walls involved out-of-plane sliding over a very small region at the base of the wall, where the cover concrete had spalled. The behaviour of the test specimen did not necessarily indicate any shortcoming in the code (19) provisions, but further investigation is required to establish acceptable ductility limits for various wall configurations.

(e) Even moderate net axial compression loads on a member significantly affect the magnitude of in-plane sliding shear.

(f) Limited yielding in a column subjected to tension during part of a load sequence is not serious if the magnitude of yielding is restricted by other stronger elements such as a wall.

(h) Anchorage deformations are significant even in well designed joints where there is little joint shear deformation or overall slip of the bars.

10.3.2 Theoretical Model

(a) Frame analyses based on refined section models are economically practical, but efficiency of modelling, solution procedure, and coding, are essential to achieving this.

(b) Accurate representation of the full inelastic response is possible providing shear and anchorage components are adequately accounted for.

(c) With suitable adaptions as outlined in this work, the Newton-Raphson solution procedure is an efficient and very effective means of analysing the inelastic response of reinforced concrete structures.

(d) The computer program satisfactorily predicts the response of components and structures providing the maximum nominal shear stresses are not high. However, to ensure greater generality, it would be desirable for the shear model to be revised as discussed in Section 10.2.

(e) The second-order formulations showed good agreement with results obtained from geometrically nonlinear formulations developed by other investigators. This facility proved useful in initial debugging of the numeric solution procedure. No problems were experienced in carrying out combined geometric and materially nonlinear analyses. The geometric nonlinear analysis capability also proved to be useful for simulating nonlinear effects resulting from the method of load application, e.g. as in the case of the wall specimens tested by Wang et al. (31).

(f) The member representation used exhibits good convergence with mesh refinement. For most applications one or two segments should be adequate to represent each beam or column plastic hinge zone.

10.4 SUGGESTIONS FOR FUTURE RESEARCH

10.4.1 Experimental Investigation

Some of the main areas related to the present study where more experimental data are required are discussed below. The data are required both for developing better theoretical models and for directly evaluating the seismic behaviour of reinforced concrete structures.

(a) More data are required for the inelastic responses of unmachined reinforcing bars to allow better calibration of existing theoretical steel models.

(b) Data for the inelastic flexural and shear response of reinforced concrete plastic hinge zones and of adjacent anchorage zones, are still inadequate. Results are required for specimens subjected to more complex load histories, and for different axial loads.

(c) The buckling behaviour of wall plastic hinge zones, including the effects of out-of-plane deformations induced by transverse components of building deformation, needs to be evaluated more fully. Attempts to suppress sliding shear deformations in wall plastic hinge zones, e.g. by use of diagonal bars, may make the walls more susceptible to buckling.

(d) The effect slabs have on the seismic response of frames needs to be studied for a range of realistic floor slab details. Few tests to date have modelled full width slabs.

(e) Large increases in effective yield stress in strain aged bars were observed in this study. The effect of this on the seismic performance of repaired structures needs investigating.

10.4.2 Computer Program

Generally the frame analysis program performed well in the analyses undertaken. This type of analysis has application not only in research but also for analysis and design of structures or components where redistribution of forces due to material nonlinearities may have significant effects. The results obtained in this study have demon-

strated that the inherent accuracy of a layered section model can be economically used in a general frame analysis procedure. However, only limited types of load sequence were considered. There is still a need for more general models of the concrete normal and shear stress responses and of the anchorage deformations. Upgrading the analytic models for concrete normal and shear stress along the lines suggested (Section 10.2), would improve the scope of the models and the accuracy of the predicted responses.

Other areas of development which would be desirable are the inclusion of optional two dimensional elements for modelling short members, more extensive modelling of failure models and one incorporation of a dynamic analysis capability. For accurate analyses of many structures, it will also be necessary to realistically model the effect of floor slabs.

REFERENCES

1. Park, R., Kent, D.C., and Sampson, R.A., "Reinforced Concrete Members with Cyclic Loading", Proceeding ASCE, Structural Division, Vol. 98, No. ST7, July 1972, pp. 1341-1360.

2. Smith, B.J., "Exterior Reinforced Concrete Joints with Low Axial Load Under Seismic Loading", M.E. Thesis Presented at University of Canterbury, Christchurch, New Zealand, 1972, 163 pp.

3. Patton, R.N., "Behaviour Under Seismic Loading of Reinforced Concrete Beam-Column Joints with Anchorage Blocks", Master of Engineering Report, University of Canterbury, February 1972, 103 pp.

4. Renton, G.W., "The Behaviour of Reinforced Concrete Beam-Column Joints Under Cyclic Loading", M.E. Thesis, Dept. of Civil Engineering, University of Canterbury, Christchurch, New Zealand, 1972.

5. Birss, G.R., "The Elastic Behaviour of Earthquake Resistant Reinforced Concrete Interior Beam-Column Joints", Research Report 78-13, Dept. of Civil Engineering, University of Canterbury, Christchurch, New Zealand, February 1978.

6. Beckingsale, C.W., "Post Elastic Behaviour of Reinforced Concrete Beam-Column Joints", Research Report 80-20, August 1980, Dept. of Civil Engineering, University of Canterbury, New Zealand, 359 pp.

7. Paulay, T. and Scarpas, A., "The Behaviour of Exterior Beam-Column Joints", Bulletin of the New Zealand National Society for Earthquake Engineering, Vol. 14, No. 3, September 1981, pp. 131-144.

8. Mahin, S.A., Bertero, V.V., Atalay, M.B., and Rea, D., "Rate of Loading Effects on Uncracked and Repaired Reinforced Concrete Members", Earthquake Engineering Research Center Report No. EERC 72-9, University of California, Berkeley, December 1972.

9. Bertero, V.V., Bresler, B., and Liao, H., "Stiffness Degradation of Reinforced Concrete Members Subjected to Cyclic Flexural Moments", Earthquake Engineering Research Center Report No. EERC 69-12, University of California, Berkeley, December 1969.

10. Bertero, V.V. and Popov, E.P., "Hysteretic Behaviour of Ductile Moment Resisting Reinforced Concrete Frame Components", Earthquake Engineering Research Centre, Report No. 75-16, University of California, Berkeley, April 1975.

11. Celebi, M. and Penzien, J., "Experimental Investigation into the Seismic Behaviour of Critical Regions of Reinforced Concrete Components as Influenced by Moment and Shear", Earthquake Engineering Research Center Report No. EERC 73-4, University of California, Berkeley, January 1973.

12. Ma, S.M., Bertero, V.V. and Popov, E.P., "Experimental and Analytical Studies on the Hysteretic Behaviour of Reinforced Concrete Rectangular and T-Beams", EERC Report 76-2, University of Californic, Berkeley, May 1976, 241 pp.

13. Viwathanatepa, S., Popov, E.P. and Bertero, V.V., "Seismic Behaviour of Reinforced Concrete Interior Beam-Column Subassemblages", Earthquake Engineering Research Center Report No. UCB/EERC 79/14, 1979.

14. Eto, H. and Takeda, T., "Dynamic Collapse Tests of Reinforced Concrete Frame Structures with a Column Subjected to High Compressive Stress", Proc. Seventh World Conference on Earthquake Engineering, Istanbul, September 1980.

15. Burns, N.H. and Seiss, C.P., "Repeated and Reversed Loading in Reinforced Concrete", Journal of the Structural Division, A.S.C.E., Vol. 92, No. ST5, October 1966.

16. Hanson, N.W. and Conner, H.W., "Seismic Resistance of Reinforced Concrete Beam-Column Joints", Proc. of the Structural Division, A.S.C.E., Vol. 93, No. ST5, October 1967, pp. 533-560.

17. Brown, R.H. and Jirsa, J.O., "Reinforced Concrete Beams Under Load Reversals", Jour. ACI, Proc. Vol. 68, No. 5, May 1971, pp. 380-390.

18. Fenwick, R.C. and Fong, A., "The Behaviour of Reinforced Concrete Beams Under Cyclic Loading", Bulletin of the N.Z. National Society for Earthquake Engineering, Vol. 12, No. 2, June 1979, pp. 158-167.

19. New Zealand Standard Code of Practice for the Design of Concrete Structures, NZS 3101 Parts 1 & 2, 1982, Standards Association of New Zealand, Wellington, 1982.

20. ACI Committee 318, "Building Code Requirements for Reinforced Concrete (ACI 318-77)", American Concrete Institute, Detroit, 1977, 102 p.

21. Seismology Committee, Recommended Lateral Force Requirements and Commentary, Structural Engineers' Association of California, San Francisco, 1973.

22. Paulay, T., "Coupling Beams of Reinforced Concrete Shear Walls", Jour. Struct. Div., ASCE, Vol. 97, No. ST3, March 1971, pp. 843-862.

23. Binney, J.R., "Diagonally Reinforced Coupling Beams", Master of Engineering Report, Dept. of Civil Engineering, University of Canterbury, February 1972.

24. Bertero, V.V., Popov, E.P. and Wang, T.Y., "Hysteretic Behaviour of Reinforced Concrete Flexural Members with Special Web Reinforcement", Report No. EERC 74-9, Earthquake Engineering Research Center, University of California, Berkeley, August 1974.

25. Bull, I.N., "The Shear Strength of Relocated Plastic Hinges", Department of Civil Engineering Report, No. 78-11, University of Canterbury, February 1978.

26. Thurston, S.J., "Cyclic Load Testing of Three Haunched Reinforced Concrete Beam-Column Assemblies", Bulletin of the New Zealand National Society for Earthquake Engineering, Vol. 15, No. 3, September 1982, pp. 141-153.

27. Galunic, B., Bertero, V.V. and Popov, E.P., "An Approach for Improving Seismic-Resistant Behaviour of Reinforced Concrete Interior Joints", Report No. EERC 77/30, Earthquake Engineering Research Centre, University of California, Berkeley, U.S.A., 1977.

28. Cardenas, A.E., Hanson, J.M., Corley, W.G. and Hognestad, E., "Design Provisions for Shear Walls", Journal of the American Concrete Institute, Vol. 70, pp. 221-230, March 1973.

29. Fiorato, A.E., Oesterle, R.G. and Corley, W.G., "Ductility of Structural Walls for Design of Earthquake Resistant Buildings", Proc. Sixth World Conference on Earthquake Engineering, New Delhi, 1977 (in print).

30. Santhakumar, A.R., "Ductility of Coupled Shear Walls", Research Report 74-10, University of Canterbury, Department of Civil Engineering, New Zealand, October 1974, 385 pp.

31. Wang, T.Y., Bertero, V.V. and Popox, E.P., "Hysteretic Behaviour of RC Framed Walls", Report No. EERC 75-23, Earthquake Engineering Research Centre, University of California, Berkeley, U.S.A., December 1975, 367 pp.

32. Nikhed, R.P., MacGregor, J.G. and Adams, P.F., "Studies of Reinforced Concrete Shear Wall-Frame Structures", Structural Engineering Report No. 25, Dept. of Civil Engineering, University of Alberta, Edmonton, Canada, June 1970.

33. Hidalgo, P. and Clough, R.W., "Earthquake Simulator Study of a Reinforced Concrete Frame", Report No. EERC 74-13, Earthquake Engineering Research Centre, University of California, Berkeley, U.S.A., 1974.

34. Oliva, M.G., "Shaking Table Testing of a Reinforced Concrete Frame with Biaxial Response", Earthquake Engineering Research Center Report No. UCB/EERC 80/28, 1980.

35. Lybas, J.M., "Concrete Coupled Walls : Earthquake Tests", Journal of the Structural Division, ASCE, Vol. 107, No. ST5, May 1981, pp. 835-855.

36. Sozen, M.A., "Earthquake Simulator in the Laboratory", Workshop on ERCBC, University of California, Berkeley, July 1977.

37. Okada, T., "The Experimental Investigation on ERRCBC with Emphasis on the Use of Earthquake Response Simulators in Japan", Workshop on ERCBC, University of California, Berkeley, July 1977.

38. Koike, K., Omote, Y., Eto, H. and Takeda, T., "Reinforced Concrete Wall-Frame Structures Subjected to Dynamic and Static Loadings : Model Tests and the Simulations", Proc. Seventh World Conference on Earthquake Engineering, Istanbul, September 1980.

39. Kanaan, A., Powell, G., "DRAIN2D A General Purpose Computer Program for Dynamic Analysis of Inelastic Plane Structures", Earthq. Engng. Res. Ctr., EERC 73-22, University of California, Berkeley, 1973.

40. Giberson, M.F., "Two Nonlinear Beams with Definitions of Ductility", Journal of the Structural Division, ASCE, Vol. 95, No. ST2, February 1969, pp. 137-157.

41. Clough, R.W., "Effect of Stiffness Degradation on Earthquake Ductility Requirements", Report No. 66-16, Structural Engineering Laboratory, University of California, Berkeley, October 1966, 67 pp.

42. Saiidi, M. and Sozen, M.A., "Simple Nonlinear Seismic Analysis of R/C Structures", Journal of the Structural Division, ASCE, Vol. 107, No. ST5, May 1981.

43. Shiga, T., Shibata, A., Shibuya, J. and Takahashi, J., "Performance of the Building of Faculty of Engineering, Tohoku University, During the 1978 Miyagi-Ken-Oki Earthquake", Proc. Seventh World Conference on Earthquake Engineering, Istanbul, September 1980.

44. Thompson, K.J., "Ductility of Concrete Frames Under Cyclic Loading", Ph.D. Thesis, University of Canterbury, Christchurch, New Zealand, 1975, 341 pp.

45. Saatcioglu, M., Takayanagi, T. and Derecho, A.T., "Dynamic Response of Reinforced Concrete Wall Systems", Proc. Seventh World Conference on Earthquake Engineering, Istanbul, Vol. 5, 1980.

46. Smith, J.K., Gergely, P. and White, R.N., "The Effects of Cracks on the Seismic Analysis of Reinforced Concrete Nuclear Containment Vessels", Report No. 368, Department of Structural Engineering, Cornell University, Ithaca, New York, April 1977.

47. Aoyama, H., "Moment-Curvature Characteristics of Reinforced Concrete Members Subjected to Axial Load and Reversal of Bending", Proceedings of the International Symposium on the Flexural Mechanics of Reinforced Concrete, ASCE-ACI, Miami, November 10-12, 1964, pp. 183-212.

48. Kent, D.C., "Inelastic Behaviour of Reinforced Concrete Members with Cyclic Loading", Ph.D. Dissertation, University of Canterbury, Christchurch, New Zealand, 1969.

49. Singh, A., Gerstle, K.H., and Tulin, L.G., "The Behaviour of Reinforcing Steel Under Reversed Loading", Journal A.S.T.M., Materials Research and Standards, Vol. 5, No. 1, January 1965.

50. Menegotto, M. and Pinto, P.E., "Method of Analysis for Cyclically Loaded R.C. Plane Frames Including Changes in Geometry and Non-Elastic Behaviour of Elements Under Combined Normal Force and Bending", Symposium on the Resistance and Ultimate Deformability of Structures Acted on by Well Defined Repeated Loads, International Assn. for Bridge and Structural Engineering, Preliminary Report, Vol. 13, Lisbon, 1973, pp. 15-22.

51. Blaauwendraad, J., "Realistic Analysis of Reinforced Concrete Framed Structures", Heron, Vol. 18, No. 4, Delft, 1972, 31 pp.

52. Taylor, R.G., "The Non-Linear Seismic Response of Tall Shear Wall Structures", Research Report 77-12, Dept. of Civil Engineering, University of Canterbury, November 1977.

53. Sharpe, R.D., "The Seismic Response of Inelastic Structures", Ph.D. Thesis, University of Canterbury, Christchurch, New Zealand, 1974.

54. Blakeley, R.W.G., Megget, L.M. and Priestley, M.J.N., "Seismic Performance of Two Full-Size Reinforced Concrete Beam-Column Joint Units", Bull. N.Z. National Society for Earthquake Engineering, Vol. 6, No. 1, March 1975, pp. 38-69.

55. Bhatt, P., "Effect of Beam-Shearwall Junction Deformations on the Flexibility of the Connecting Beams", Building Science, Vol. 8, 1973, pp. 149-151, Pergamon Press, Great Britain.

56. Jennings, A., "Frame Analysis Including Change of Geometry", Journal of the Structural Division, ASCE, Vol. 94, No. ST3, Proc. Paper 5839, March 1968, pp. 627-664.

57. Rajasekaren, S. and Murray, D.W., "Incremental Finite Element Matrices", Journal of the Structural Division, ASCE, Vol. 99, No. ST12, December 1973.

58. Franklin, H.A., "Nonlinear Analysis of Reinforced Concrete Frames and Panels", Report No. SESM-70-5, March 1970, College of Engineering, University of California, Berkeley, California.

59. Tillerson, J.R., Stricklin, J.A. and Haisler, W.E., "Numerical Methods for the Solution of Nonlinear Problems in Structural Analysis", Numerical Solution of Non-Linear Structural Problems, AMD - Vol. 6, ASME, 1973 (Applied Mech. Div.) Winter Meeting, November 1973.

60. Phillips, D.V. and Zienkiewicz, O.C., "Finite Element Non-Linear Analysis of Concrete Structures", Proc. Institution of Civil Engineers, Vol. 61, Part 2, March 1976, pp. 59-88.

61. Horringmoe, G., "Finite Element Instability Analysis of 'Freeform' Shells", Report No. 77-2, May 1977, Division of Structural Mechanics, Norwegian Institute of Technology, University of Trondheim, Norway.

62. Bergan, P.G. and Clough, R.W., "Convergence Criteria for Iterative Processes", AIAA Journal, Vol. 10, No. 8, 1972, pp. 1107-1108.

63. Aktan, A.E., Karlson, B.J. and Sozen, M.A.,"Stress-Strain Relationships of Reinforcing Bars Subjected to Large Strain Reversals", Civil Engineering Study No. 397, University of Illinois, June 1973.

64. Ramberg-Osgood, W.R., "Description of Stress Strain Curves by Three Parameters", NACA, Technical Note 902, July 1943.

65. Burns, N.H., and Seiss, C.P., "Load-Deformation Characteristics of Beam-Column Connections in Reinforced Concrete", Civil Engineering Studies, Structural Research Series No. 234, University of Illinois, January 1962.

66. Leslie, P.D., "Ductility of Reinforced Concrete Bridge Piers", M.E. Report, Department of Civil Engineering, University of Canterbury, Christchurch, New Zealand, 1974, 147 pp.

67. Stanton, J.F. and McNiven, H.D., "The Development of a Mathematical Model to Predict the Flexural Response of Reinforced Concrete Beams to Cyclic Loads, Using System Identification", Earthquake Engineering Research Centre, Report No. UCB/EERC - 79/02, January 1979.

68. Blakeley, R.W.G., "Ductility of Prestressed Concrete Frames Under Seismic Loading", Ph.D. Thesis, University of Canterbury, Christchurch, New Zealand, 1971, 230 pp.

69. Sinha, B.P., Gerstle, K.H., and Tulin, L.G., "Stress-strain Relationships for Concrete Under Cyclic Loading", Journal of the American Concrete Institute, Vol. 61, No. 2, February 1964, pp. 195-212.

70. Karsan, I.D. and Jirsa, J.O., "Behaviour of Concrete Under Compressive Loadings", Journal of the Structural Division, ASCE, Vol. 95, No. ST12, December 1969, pp. 2543-2363.

71. Lampert, P., Luchinger, P. and Thurlimann, B., "Torsionsversuche un Stahl-und Spannbetonbalken", Institut fur Baustatik ETH Zurich, Bericht Nr. 6506-4, Febraur 1971 (in German).

72. Scott, B.D., "Stress-Strain Relationships for Confined Concrete: Rectangular Sections", Research Report 80-6, Dept of Civil Eng., University of Canterbury, Christchurch, February 1980.

73. Fenwick, R.C., "The Shear Strength of Reinforced Concrete Beams", Ph.D. Thesis, University of Canterbury, Christchurch, New Zealand, 1966.

74. "Shear in Reinforced Concrete", Vol. 1 and 2, Special Publication No. 42, American Concrete Institute, 1974.

75. Kupfer, H., Hilsdorf, H. and Rusch, H., "Behaviour of Concrete Under Biaxial Stress", Proc. ACI, Vol. 66, August 1969, pp. 656-666.

76. Houde, J. and Mirza, M.S., "A Finite Element Analysis of Shear Strength of Reinforced Concrete Beams", Shear in Reinforced Concrete, Publ. SP-42, ACI, Detroit, 1974.

77. Paulay, T. and Loeber, P.J., "Shear Transfer by Aggregate Interlock, Shear in Reinforced Concrete," Publ. SP-42, ACI, Detroit, 1974.

78. Colley, B.E. and Humphrey, H.A., "Aggregate Interlock at Joints in Concrete Pavements", Highway Research Record No. 189, 1967, pp. 1-8, Bulletin D124, PCA Research and Development Lab.

79. Newton, W.J., "Influence of Aggregate Properties on Effectiveness of Joints in Concrete Pavements", Journal of the PCA Research and Development Lab., Bulletin D139, Vol. 10, No.2, May 1968, pp. 2-8.

80. Taylor, H.P.J., "The Fundamental Behaviour of Reinforced Concrete Beams in Bending and Shear", ACI Publication SP-42, Shear in Reinforced Concrete, Vol. 1, 1974.

81. Mattock, A.H., Hofbeck, J.F. and Ibrahim, I.O., "Shear Transfer in Reinforced Concrete", ACI Journal, Proceedings, Vol. 66, No. 2, February 1969, pp. 119-128.

82. Phillips, M.H., "Horizontal Construction Joints in Cast-in-Situ Concrete", M.E. Report, University of Canterbury, Christchurch, New Zealand, 1972.

83. Taylor, H.P.J., "Fundamental Behaviour in Bending and Shear of Reinforced Concrete", Ph.D. Thesis, Civil Engineering, The City University, London, 1971.

84. Baumann, T., "Versuche zum Studium der Verdubelungswirkung der Biegezugbewebrugg eines Stahlbetonbalken", Bericht No. 77, Materialprufungsamt fur das Bauwesen der Technischen Hochschule Munchen, 1968.

85. Regan, P.E., "Shear Tests of Reinforced Concrete Beams", Interim Report, CRIRIA Project No. 91, August 1969.

86. O'Leary, A.J., "Shear, Flexure and Axial Tension in Reinforced Concrete Members", Ph.D. Thesis, University of Canterbury, Christchurch, New Zealand, 1970.

87. Joint ASCE-ACI Task Committee 426, "The Shear Strength of Reinforced Concrete Members", Journal of the Structural Division, ASCE, Vol. 99, ST6, June 1973, pp. 1091-1187.

88. Regan, P.E. and Khan, M.H., "Bent-Up Bars as Shear Reinforcement", Shear in Reinforced Concrete, ACI Publication SP-42-11, Vol. 1, 1974, pp. 249-266.

89. Ma, S.M., "Experimental and Analytical Studies of Hysteretic Behaviour of Reinforced Concrete Rectangular and T-Beams", Ph.D. Dissertation, Department of Civil Engineering, University of California, Berkeley, 1975.

90. Ebner, A.M. and Ucciferro, J.J., "A Theoretical and Numerical Comparison of Elastic Nonlinear Finite Element Methods", Computers and Structures, Vol. 2, pp. 1043-1061, Pergamon Press, Great Britain.

91. Sabir, A.B. and Lock, A.C., "Large Deflexion, Geometrically Non-Linear Finite Element Analysis of Circular Arches", International Journal of Mechanical Science, Vol. 15, pp. 37-47, Pergamon Press, Great Britain.

92. Powell, G.H., "Theory of Nonlinear Elastic Structures", Journal of the Structural Division, A.S.C.E., Vol. 95, No. ST12, December 1969, pp. 2687-2701.

93. Manuel, F.S. and Lee, S., "Flexible Bars Subjected to Arbitrary Discrete Loads and Boundary Conditions", Journal of the Franklin Institution, Vol. 285, 1968, pp. 452-474. (From Ref. 90).

94. Mallett, R.H. and Marcal, R.V., "Finite Element Analysis of Nonlinear Structures", Journal of the Structural Division, A.S.C.E., Vol. 94, No. ST9, September 1968, pp. 2081-2105.

95. Park, R. and Paulay, T., "Reinforced Concrete Structures", John Wiley and Sons, New York, 1975.

96. Uniform Building Code, International Conference of Building Officials, Pasadena, 1973 edition.

97. Taylor, R.G., Personal communication.

98. Little, W.A. and Paparoni, M., "Size Effect in Small-Scale Models of Reinforced Concrete Beams", Journal of the American Concrete Institute, Vol. 63, No. 9, November 1966, pp. 1191-1204.

99. White, R.N. and Chowdhury, A.H., "Behaviour of Multi-Storey Reinforced Concrete Frames Subjected to Severe Reversing Loads", Preliminary Report, Symposium, Resistance and Ultimate Deformability of Structures Acted on by Well Defined Repeated Loads, International Association for Bridge and Structural Engineering, Lisbon, Portugal, 1973.

100. Wilby, G.K., "Response of Concrete Structures to Seismic Motions", Ph.D. Thesis, Research Report 75-11, Dept. of Civil Engineering, University of Canterbury, New Zealand, July 1975, 225 pp.

101. Alami, Z.Y. and Fergusson, P.M., "Accuracy of Models used in Research on Reinforced Concrete", Journal of the American Concrete Institute, Proceedings Vol. 60, No. 11, November 1963, pp. 1643-1662.

102. Loeber, P.J., "Shear Transfer by Aggregate Interlock", M.E. Thesis, University of Canterbury, Christchurch, New Zealand, 1970.

103. "Building Code Requirements for Reinforced Concrete", ACI Standard 318-71, Detroit, Michigan.

104. NZS 1900, Chapter 8, "Basic Design Loads", New Zealand Standard Model Building Bylaw, Standards Association of New Zealand, Wellington, 1965.

105. Blakeley, R.W.G., Cooney, R.C. and Megget, L.M., "Seismic Shear Loading at Flexural Capacity in Cantilever Wall Structures", Bulletin of the N.Z. National Society for Earthquake Engineering, Vol. 8, No. 1, March, 1975.

106. Bertero, V.V., "Experimental Studies Concerning Reinforced, Prestressed and Partially Prestressed Concrete Structures and Their Elements", Symposium on Resistance and Ultimate Deformability of Structures Acted on by Well Defined Repeated Loads, IABSE, Lisbon, 1973, pp. 67-99.

107. Mahin, S.A. and Bertero, V.V., "Rate of Loading Effects on Uncracked and Repaired Reinforced Concrete Members", Earthquake Engineering Research Center, Report No. EERC 72-9, University of California, Berkeley, December 1972.

108. Paulay, T., "Simulated Seismic Loading of Spandrel Beams", Jour. Struct. Div., ASCE, Vol. 97, No. ST9, September 1971, pp. 2407-2419.

109. Morice, P.B., "The Design and Use of a Demountable Mechanical Gauge for Concrete Structures", Magazine of Concrete Research, Vol. 5, No. 13, August 1953, pp. 37-42.

110. Fritz Staeger, Manual for Contact-Type Strain Gauge, designed by Pfender CTA-MPA, Berlin-Dahlem, 1 Berlin 61 Zossener Strabe, 56-58.

111. NZS 4203 : 1976, "Code of Practice for General Structural Design and Design Loadings for Buildings", Standards Association of New Zealand, Wellington, 1976, 80 pp.

112. Bresler, B., and Gilbert, P.H., "Tie Requirements for Reinforced Concrete Columns", Proceedings ACI Journal, Vol. 58, No. 5, November 1961, pp. 555-570.

113. Paulay, T. and Spurr, D.D., "Frame-Shear Wall Assemblies Subjected to Simulated Seismic Loading", Proc., Sixth World Conference on Earthquake Engineering, New Delhi, 1977.

114. Ciampi, V., Eligehausen, R., Bertero, V.V. and Popov, E.P., "Analytical Model for Concrete Anchorages of Reinforcing Bars Under Generalized Excitations", Earthquake Engineering Research Center Report No. UCB/EERC 82/23, November 1982, University of California, Berkeley.

APPENDIX A

EFFECTS OF STRAIN AGEING

A.1 STRAIN AGEING PHENOMENA

Ambient temperature strain ageing in structural grade reinforcing bars is normally considered as being predominantly due to the interstitial nitrogen in the steel. Its effect on the mechanical properties of the steel is primarily dependant on the nitrogen content, the extent and nature of prestraining, and on the temperature and elapsed time of ageing. The processes occurring during strain ageing in these steels are generally divided into three or four stages, although only the first two are relevant here:

Stage 1 : (Figure A.1a)

Return of a distinct yield point and increases in the elastic modulus, the reloading yield stress and in the "length" of the yield plateau. These are assumed to occur as a result of migration of free nitrogen to the strain dislocations and the formation of a Cottrell atmosphere which locks the dislocation. This stage continues until the atmosphere is saturated, typically 5-10 days at a temperature of approximately $14^{o}C$ - $18^{o}C$. Reloading past the yield stress during this stage disperses the atmosphere, but generally it reforms faster than when originally formed. The dislocation sources operative for reverse loading are different from those for forward loading and the locking is generally slower. Immediate reverse loading results in the well known Bauschinger softening of the steel response, but with time, i.e. into stage 2, the steel will recover its initial elastic modulus over most of the original elastic loading range (Figure A.3, bar type I).

Stage 2 : (Figure A.1b) If sufficient nitrogen.

After saturation, iron nitride begins to precipitate into the dislocation. This results in partial permanent locking of the dislocation with a consequent increase in the ultimate tensile strength and reduction in the ultimate elongation. The yield

stress continues to increase, but not the "length" of the yield plateau.

A.2 STRAIN AGEING EFFECTS IN TEST SPECIMENS

The tests on TB1 and TB3 took approximately one week to complete after the specimens first yielded. In the case of specimen TB1, the only significant delay between load reversals (5 days between LR11 and LR12) was after the steel strain readings had been completed. Hence the results derived from the strain readings for this specimen are unlikely to have been significantly affected by strain ageing. In the case of specimen TB3, there was 5 days delay between the first and second post-elastic load reversals. As noted in Section 8.2.3e this caused a noticeable increase in stiffness of the specimen when it was first reloaded after the delay. However, as the delay was only 5 days, only the first stage of strain ageing will have developed. Consequently the curvature distributions at the peaks of subsequent load reversals are unlikely to have been significantly affected.

Both frame-wall tests took approximately 3 months to complete and it is evident from the observed curvature distributions for the walls (Section 9.3.2), that the effects of strain ageing in these specimens were more pronounced.

In order to obtain a more quantitative assessment of the effects of strain ageing on the reinforcing steels used in the specimens, two sets of tests were performed.

In the first of these, sample lengths of reinforcement were prestrained to a strain of approximately 0.02, then unloaded. The specimens were then reloaded to "yield" at various times after a delay of up to 4½ days. The results obtained from these tests were consistent with the behaviour expected during the first stage of strain ageing, with a maximum increase in yield stress ($\Delta\sigma_{sy}$) of 9.1% σ_{sy} (Figure A.2), but with no discernable effect on the ultimate strength of the bars.

For the second set of tests, several lengths of bars were salvaged from the wall plastic hinge zones of the frame-wall specimens. These were reloaded approximately 5 months (bars from FSW-1) and 44 months (bars

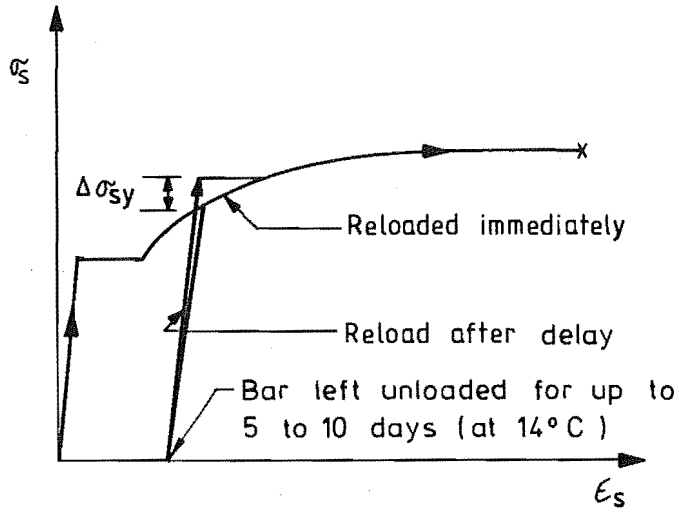

(a) Stage 1

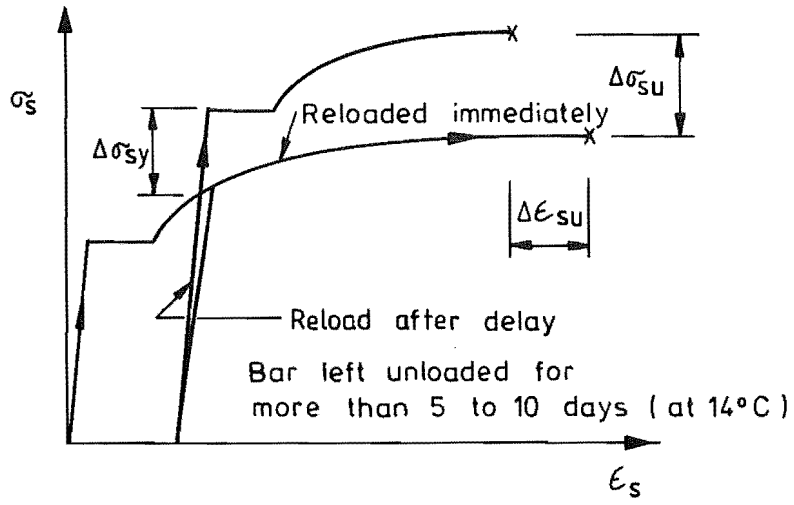

(b) Stage 2

FIGURE A.1 : FIRST TWO STAGES OF STRAIN AGEING; EFFECT ON STEEL STRESS-STRAIN RESPONSE

from FSW-2) after they had been first yielded. A comparison of the stress-strain responses of three of these bars and the original stress-strain relationship for the steel used is shown in Figure A.3, together with a description of the approximate strain history imposed on the bars when the frame wall specimens were tested*.

The stress-strain responses of both the 5 month and the 44 month aged specimens were similar. The ultimate strengths of both sets of bars were approximately 10% greater than that of the non-strain aged steel and the ultimate strain measured over a 254 mm gauge length was reduced to approximately 0.12 to 0.13. More importantly, the yield strength of the bar reloaded in the same direction as it had last been loaded in the test, i.e. type II bar in Figure A.3, was approximately 43% greater than the yield strength of the non-aged steel and 69% greater than the nominal yield strength.

A.3 EFFECT OF STRAIN AGEING ON REPAIRED STRUCTURES

The increases in yield strength of the bars extracted from the frame-wall specimens are large by comparison with the 25% increase over nominal yield strength normally used for computing overstrength (19). Part of this increase in yield stress was due to strain hardening. However, this is not important from the point of view of repair, as the action of epoxy injection or of casting new concrete in a damaged area effectively resets the strain origin to zero.

Because of the limited length over which strain ageing affects bar properties, i.e. over the length of the original plastic hinge zone, the corresponding increase in member strength will depend on the member geometry and other factors, and could be accurately assessed only by testing repaired and aged specimens. However, large increases in bar yield strength will cause new yielding to spread to weaker previously unyielded regions if the structure were later subjected to a second large earthquake. Yielding could penetrate regions that were not intended to provide ductility and cut off lengths may also be insufficient for the increased yield penetration. In the case of beams which

---

* The complete strain histories are not known as no steel strains were measured in the final load cycles of the frame-wall tests.

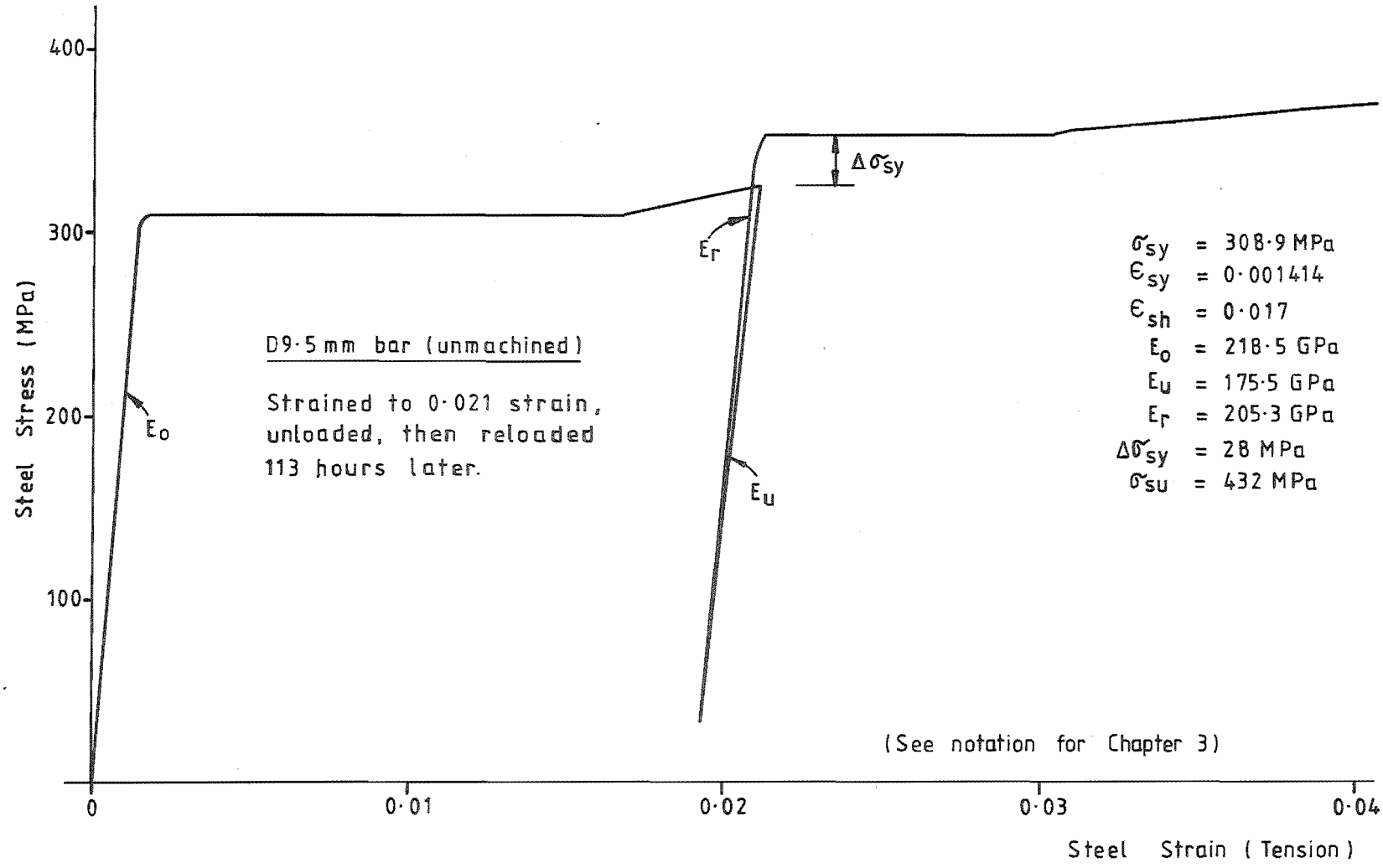

FIGURE A.2 : EFFECT OF STRAIN AGEING ON THE RESPONSE OF A PREVIOUSLY UNSTRAINED BAR

have been designed so that the plastic hinge forms away from the column face, the increased strength of the bars in the original plastic hinge zone could force yielding into the now relatively weaker column face region.

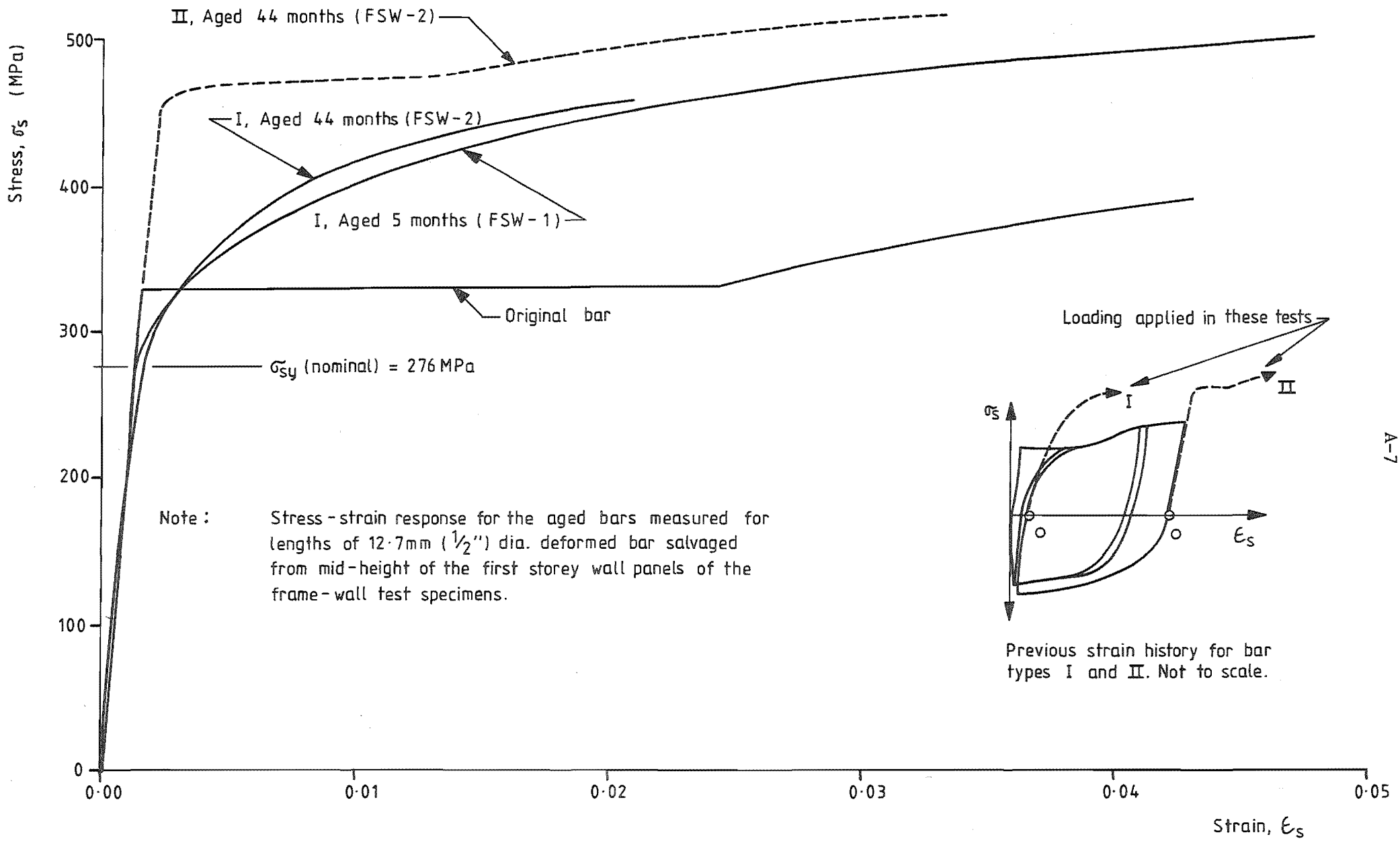

FIGURE A.3 : STRESS-STRAIN RESPONSES OF BARS SALVAGED FROM THE FRAME-WALL SPECIMENS

Classn:

POST-ELASTIC BEHAVIOUR OF REINFORCED CONCRETE FRAME-WALL COMPONENTS AND ASSEMBLAGES SUBJECTED TO SIMULATED SEISMIC LOADING

David D. Spurr

ABSTRACT: Four beam-wall and two 7 storey × 1 bay frame-wall specimens, all approximately one quarter scale, were tested. An inelastic frame analysis computer program was subsequently developed. This models the inelastic shear flexural and anchorage deformations of plastic hinges in reinforced concrete flexural members. Solution efficiency and stability were emphasized.

Department of Civil Engineering, University of Canterbury Research Report No. 84- , 1984.